THÈSE POUR OBTENIR LE GRADE DE DOCTEUR DE L'UNIVERSITÉ DE MONTPELLIER

En Sciences de la Terre

École doctorale GAIA

Unité de recherche Géosciences Montpellier

En partenariat international avec l'Université de Johannesburg – Afrique du Sud

Distribution and Structural Control of the Hydrothermal Events within the Barberton Greenstone Belt (South Africa, Eswatini) – implications for Gold Mineralisation Formation

Présentée par Laurine TRAVERS
Le 17 Novembre 2023

Sous la direction de Alain CHAUVET
et Jérémie LEHMANN

Devant le jury composé de

Alexander KISTERS, Professor, Department of Earth Sciences, Stellenbosch University	Rapporteur
Dominique CHARDON, Directeur de Recherche, IRD	Rapporteur
Aude GEBELIN, Professeure, GéoRessources, Université de Lorraine	Examinatrice
Lenka BARATOUX, Chargée de Recherche, IRD	Examinatrice
Jean-François MOYEN, Professeur, Laboratoire Magma Volcan, Université Clermont – Auvergne	Examinateur
Alain CHAUVET, Directeur de Recherche, Géosciences Montpellier, Université de Montpellier	Directeur de thèse
Jérémie LEHMANN, Associate Professor, Department of Geology, University of Johannesburg	Co-directeur de thèse

UNIVERSITÉ DE MONTPELLIER

Declaration

I declare that the work presented in this thesis is the result of my own original research unless explicitly stated otherwise. Any external sources, including published work, ideas, or data, are appropriately cited and referenced. I acknowledge and confirm that no unethical research practices, including plagiarism or any form of dishonesty, were employed during the research and preparation of this thesis. This research was conducted under the joint supervision of Alain Chauvet and Jérémie Lehmann and was undertaken as part of a collaborative program between the University of Johannesburg and the University of Montpellier. This thesis has not been previously submitted, either in part or in whole, to any other university or educational institution besides the University of Montpellier and the University of Johannesburg. Furthermore, I declare that this thesis is consistent with the Plagiarism Policy of both the University of Johannesburg and the University of Montpellier, with which I am familiar.

Publication

Travers, L., Chauvet, A., Lehmann, J., 2023. Structure and Distribution of the Gold-Related Quartz Vein Systems in the Southwestern Part of the Barberton Greenstone Belt (South Africa, Eswatini). Minerals 13, 1034.

Conference abstracts

Travers, L, Chauvet, A., Lehmann, J., Moyen, J-F., 2021. Evolution tectonique de la partie Sud Est de la Ceinture de Roche Vertes de Barberton (Afrique du Sud, Eswatini). Place de l'évènement minéralisateur magmato-hydrothermal et implications sur le style tectonique archéen. In 27e édition de la Réunion des Sciences de la Terre, Lille, France, 284.

Travers, L., Lehmann, J., Chauvet, A., 2023. Structural control on gold mineralisation in the southwestern part of the Barberton Greenstone Belt (South Africa, Eswatini). GeoCongress, Stellenbosch, South Africa, 238.

Travers, L., Lehmann, J., Chauvet, A., 2023. Spatial distribution and structural control on gold mineralisation in the Barberton Greenstone Belt (South Africa, Eswatini). 17th SGA Biennial Meeting.

Signed by Laurine Travers, September 2023

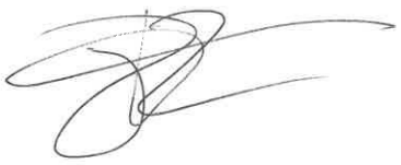

Abstract

The Barberton Greenstone Belt (BGB) is a significant gold-rich geological domain, hosting over 350 gold occurrences with an estimated 342 tons of gold production. Prior studies have focused on large active mining sites like Fairview, New Consort, and Sheba. Our investigations encompass a broader exploration into the distribution and structural control of hydrothermal veins across historical mining regions and lower-grade gold occurrences. Our multifaceted research approach combines spatial analysis with field structural geology complemented by petrological and microstructural analyses. The objective is to understand the structural control of the gold-bearing large-scale event within the BGB. Our findings reveal four main clusters of gold occurrences and deposits within the Barberton Greenstone Belt distributed into high gold grade northern and lower gold grade southern parts.

Two distinct tectonic events have been identified, forming hydrothermal veins. The first one, trending NW-SE and EW within the north and south belt, respectively, is related to the main deformation that structures the BGB, forming large-scale folding, thrusts and schistosity. The variation of trends is due to the arcuate geometry of the BGB. Both north and south, this event is related to the emplacement of the mineralised gold quartz veins responsible for gold economic grade. Different morphologies occur with, more frequently, vertical veins associated with horizontal ones and sometimes back-thrusting. The texture of the horizontal ones yields vertically elongated minerals (quartz, feldspars, tourmaline or carbonate). The second deformational event, attributed to NE-SW shortening, forms late barren quartz veins. This shortening event is also responsible for the development of a sub-vertical NW-SE schistosity prominently observed in the Malolotja Synform to the south of the belt.

In summary, our research presents a comprehensive model of regional deformation and structural control of the gold mineralisation within the Barberton Greenstone Belt. An enigmatic NE-SW shortening event has been discovered, linked to a late hydrothermal event. These findings enhance our understanding of the geological evolution of the Barberton Greenstone Belt and its gold-bearing event.

Keywords: Gold Mineralisation; Structural Geology; Greenstone Belt; Archean, Barberton.

Résumé

La Ceinture de Roches Vertes de Barberton (CRVB), renommée comme domaine archéen aurifère, abrite plus de 350 indices et gisements d'or avec une production d'or totale estimée à 342 tonnes. De nombreuses études antérieures se sont focalisées sur les grandes mines actives, tels que Fairview, New Consort et Sheba. Les recherches présentées ici sont complémentaires et englobent une étude plus large de la distribution des indices et anciens gisements aurifères ainsi que de leur contrôle structural. Notre travail a combiné l'analyse spatiale à la géologie structurale de terrain, complétée par des observations pétrologiques et microstructurales. L'objectif est de comprendre l'hydrothermalisme et notamment l'événement aurifère à grande échelle au sein de la CRVB. L'analyse spatiale a mis en évidence quatre clusters d'indices aurifères, répartis entre une partie nord qui contient les gisements les plus importants et une partie sud porteuse de petits indices aurifères et d'anciennes mines abandonnées. Deux événements tectoniques distincts ont été identifiés pour la formation de veines hydrothermales. Dans la partie sud de la CRVB, un régime de raccourcissement E-O a formé des plis majeurs, une schistosité et des veines aurifères orientées N-S. Dans la partie nord de la CRVB, c'est un raccourcissement NNO-SSE à NO-SE qui produit les plis et failles majeurs ainsi qu'une schistosité et des veines de quartz liées à l'or principalement orientées ENE-OSO à NE-SO. Ces deux évènements sont corrélés à l'échelle de la ceinture et la variation de direction est due à sa géométrie en arc. Les veines de quartz liées à la minéralisation présentent diverses morphologies. La majorité d'entre elles sont des veines à fort pendage associées à des veines sub-horizontales qui portent des minéraux allongés verticalement (quartz, feldspaths, tourmaline et/ou carbonate), des veines parallèles à la stratification, des zones très riches en veines appelées stockwerks. De plus, un événement de déformation ultérieur, attribué à un raccourcissement NE-SO dans la CRVB, vient former des veines de quartz stériles tardives. Cet événement de raccourcissement est également responsable de la création d'une schistosité sub-verticale NO-SE observée dans la synforme de Malolotja au sud de la ceinture. En résumé, nos recherches contribuent à un modèle de déformation régionale dans lequel le contrôle structural est fondamental pour la mise en place de la minéralisation aurifère de la Ceinture de Roches Vertes de Barberton.

Mots clés : Minéralisation aurifère, Tectonique, Ceinture de Roches Vertes, Archéen, Barberton.

Résumé Étendu

Préambule

Ce doctorat a été réalisé dans le cadre d'une cotutelle entre l'Université de Montpellier en France et l'Université de Johannesburg en Afrique du Sud, en co-supervison entre Alain Chauvet (UM) et Jérémie Lehmann (UJ). La thèse s'inscrit dans le cadre de l'IRP (Projet de Recherche International) BuCOMO (Building Continents - From Mantle to Ore) piloté par Jean-François Moyen et Gary Stevens et visant à étudier l'origine et l'évolution de la croûte continentale. Ce programme de recherche collaboratif implique des chercheurs de diverses universités françaises et sud-africaines (plus d'informations sur le site web de l'IRP BuCOMO : https://bucomo.fr/).

Introduction

L'archéen constitue une période de l'histoire de la Terre qui s'étend de 4 à 2.5 Ga, marquée par des caractéristiques uniques, qui ne s'observe plus dans les paysages géologiques modernes. L'un des traits marquants de cette époque, est son intense activité magmatique, facilitée par un manteau plus chaud, entrainant la formation de grands domaines de croûte continentale (Belousova et al., 2010; Herzberg et al., 2010). Ces zones continentales sont en grande partie composées de roches granitiques et gneissiques, connues sous le nom de suite Tonalite-Trondhjémite-Granodiorite (TTG). Une autre particularité des dominants archéen est la prédominance des ceintures de roches vertes déposées sur les TTG. Ces ceintures, composées principalement de roches volcano-sédimentaires, ont subi un métamorphisme au faciès schiste verte à amphibolitique (Cutts et al., 2014; Brown, 2015). Structuralement ils sont allongés en forme de synclinorium étroits, ce qui justifie leur nom de ceinture. De nombreuses études s'attachant à comprendre la géodynamique archéenne ont montré des spécificités uniques (Kohler and Anhaeusser, 2002; Condie and Benn, 2006; Korenaga, 2006; Liu et al., 2022). En effet, l'observation de nombreux domaines en dômes et bassins, a été décrit comme de la tectonique dite verticale crée par de l'effondrement gravitaire des ceintures de roches vertes très denses bordées par les granites peu denses (Gorman et al., 1978; Bouhallier et al., 1995; Collins et al., 1998). De nombreux débats animent le monde scientifique sur l'existence d'une tectonique des plaques similaire à celle observée actuellement, avec par exemple la présence de subduction (Hamilton, 1998; Cawood et al., 2006; Condie and Benn, 2006; van Hunen and

Moyen, 2012; Brown et al., 2020). De plus, l'ère archéenne se caractérise par un enrichissement exceptionnel en métaux, et en particularité, porte des gisements d'or de classe mondiale (Barley and Groves, 1992; Goldfarb et al., 2001; Groves et al., 2005; Frimmel, 2008).

La Ceinture de Roches Vertes de Barberton, situé à cheval entre l'Afrique du Sud et l'Eswatini, ne fait pas exception et illustre ces caractéristiques uniques. Cette ceinture est en particulier connue pour ces nombreux indices et gisements d'or qu'elle abrite. La distribution de ces gisements n'est pas uniforme sur toute la ceinture, elle semble être préférentiellement le long des principales structures tectoniques, en particulier des failles et les plis. Les mines en activité sont réparties dans la partie nord de la ceinture, dont trois sont dans un rayon à moins de quatre kilomètres de distances. Plusieurs études scientifiques ont ciblé cette zone pour comprendre la mineralisation aurifère de la ceinture (e.g., Anhaeusser, 1976, 1976, 2019; Schouwstra, 1995; Dziggel et al., 2007; Otto et al., 2007; Dirks et al., 2009; Munyai et al., 2011; Agangi et al., 2014, 2016; Altigani et al., 2016; Argapadmi et al., 2018; Gloyn-Jones and Kisters, 2018, 2019; Dziggel and Kisters, 2019; Pintos Cerda et al., 2020, 2022; Altigani, 2021; Jones and Kisters, 2022). L'une des principales énigmes entourant cette minéralisation est son contrôle structural. En effet, il n'y a pas de consensus sur celui-ci, deux théories semblent émergées : i) des études proposent que la minéralisation se forme au cours d'une phase tardive du raccourcissement régional majeur NO-SE, en réactivant des anciennes structures (de Ronde et al., 1992; Gloyn-Jones and Kisters, 2019; Jones and Kisters, 2022; Pintos Cerda et al., 2022) ; ii) d'autres auteurs suggèrent que la minéralisation s'est produite pendant une phase d'extension régionale NO-SE, qui a suivi la stabilisation tectonique et thermique du craton du Kaapvaal (Otto et al., 2007; Munyai et al., 2011; Dirks et al., 2013). Cependant des centaines d'autres indices et gisements sont présents dans la CRVB, et sont assez peu étudiés, représentant une immense source d'information inexploitée. Cette thèse porte sur l'étude de leur distribution et de leur contrôle structural à l'échelle de la Ceinture de Roches Vertes de Barberton. À l'aide d'analyses spatiales, de travaux de terrain approfondis, d'études minéralogique et microstructurales, ce travail vise à caractériser la distribution spatiale à grande échelle des occurrences et des gisements d'or, à identifier les différents événements tectoniques liés à leur formation et enfin à discuter des implications de ces découvertes dans la cadre de cette ceinture et plus globalement des domaines archéens.

Contexte Géologique

La Ceinture de Roches Vertes de Barberton est située dans la partie orientale du craton de Kaapvaal en Afrique du Sud et en Eswatini. Elle est composée d'unités volcano-sédimentaires, entourées de TTG et intrudées par des batholithes potassiques tardifs (Fig. 1).

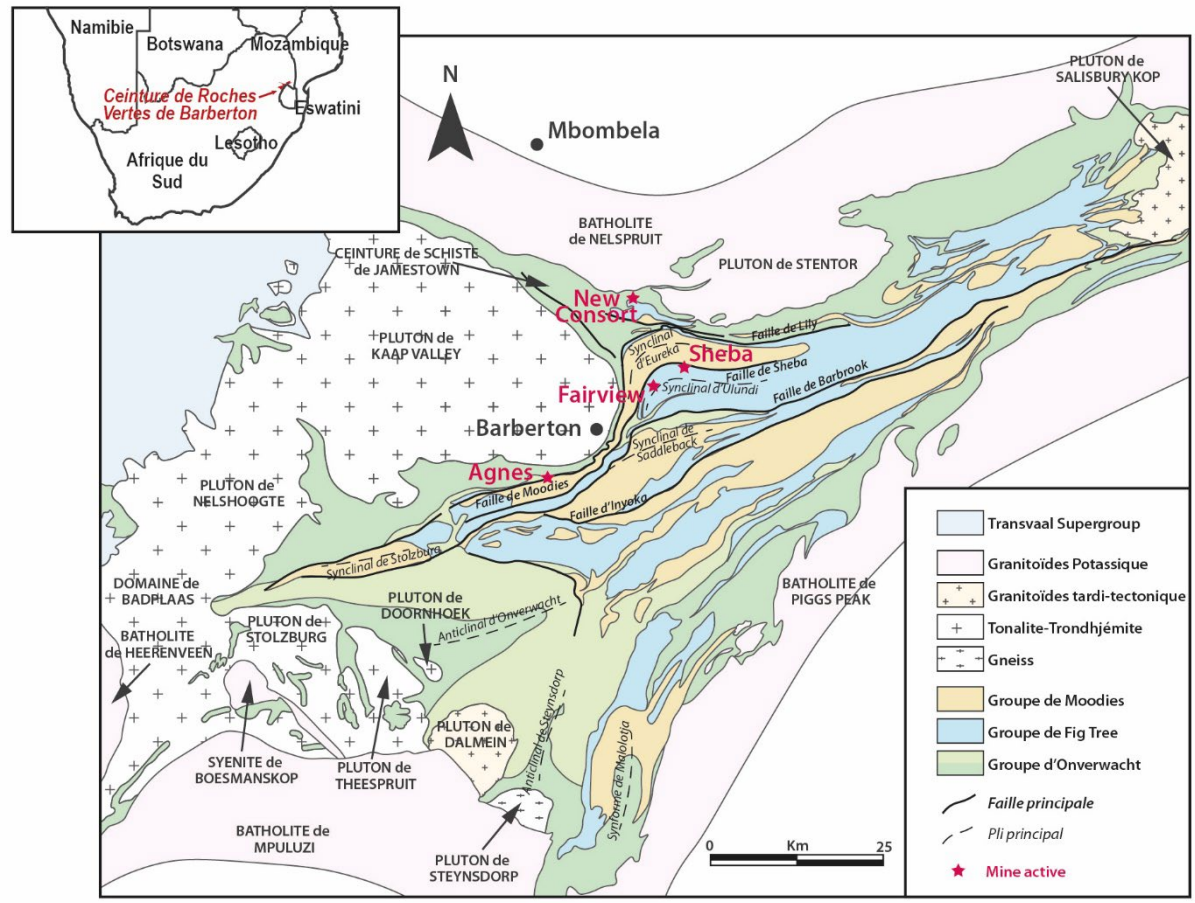

Fig. 1. Carte géologique de la région de Barberton, montrant les trois unités stratigraphiques composant la Ceinture de Roches Vertes de Barberton (Moodies, Fig Tree et Onverwacht), les granitoïdes l'entourant ainsi que les quatre mines d'or en activité de la zone (modifiée d'après Anhaeusser, 2019)

La succession stratigraphique de la CRVB est formée par trois groupes principaux : Onverwacht, Fig Tree et Moodies (Fig. 1). Le groupe d'Onverwacht (ca. 3,55 à 3,29 Ga) est principalement une série méta-volcano-sédimentaire mafique à ultramafique (Viljoen and Viljoen, 1969; Byerly, 1999; Furnes et al., 2013). Le groupe de Fig Tree (ca. 3,26 à 3,22 Ga) est formé de laves calco-alcalines et de roches détritiques (Condie et al., 1970; Hofmann, 2005). Enfin, le groupe Moodies (ca. 3,22 à 3,21 Ga) représente la série détritique supérieure de la ceinture (Heubeck and Lowe, 1994a, 1994b). L'architecture de la BGB semble résulter de

plusieurs événements de raccourcissement principalement orientés NO-SE (de Ronde and de Wit, 1994).

La Ceinture de Roches Vertes de Barberton porte environ 350 indices et gisements aurifères (Dirks et al., 2009). Les plus étudiées sont les mines en activité de Fairview, Sheba et New Consort, qui sont toutes situées au nord de la CRVB à la jonction avec la Ceinture de Schiste de Jamestown (Fig. 1). Comme énoncé dans l'introduction, deux théories s'opposent sur l'interprétation de leur contrôle structural, les minéralisations aurifères peuvent donc s'être formées au cours : i) d'une phase tardive d'extension régionale (Otto et al., 2007; Munyai et al., 2011), postérieure à la stabilisation tectonique et thermique de la ceinture (Dirks et al., 2013), et/ou ii) d'un épisode tardif du raccourcissement NO-SE (Gloyn-Jones and Kisters, 2019; Jones and Kisters, 2022; Pintos Cerda et al., 2022).

Plusieurs âges de minéralisation aurifère ont été publiés dans la partie nord de la CRVB. Dans la mine Fairview, (de Ronde et al., 1991) ont daté un dyke porphyrique qui recoupe la minéralisation et un rutile hydrothermal pour avoir une fourchette de mise en place de la minéralisation entre ca. 3126 et ca. 3084 Ma. D'autres âges plus jeunes ont été publiés à la mine New Consort, en datant une titanite hydrothermale, liée à l'altération de la minéralisation, à ca. 3027 Ma (U-pb ; Dziggel et al., 2010). Et enfin, la datation (zircon U-Pb) d'un dyke felsique interprété comme syn-minéralisation a révélé un âge de ca. 3015 Ma à Golden Quarry (située à proximité de la mine de Sheba, (Dirks et al., 2013). Dans l'ensemble, deux périodes de minéralisation semblent émerger de la littérature, la première entre 3126-3084 Ma et une plus jeune à 3027-3015 Ma. Ainsi, la formation de l'événement aurifère de la CRVB semble s'étaler sur une longue période, avec peut-être deux épisodes de minéralisation.

Distribution des Indices et Gisements Aurifères

L'analyse spatiale prédictive a été réalisée sur la carte métallogénique de la Ceinture de Roches Vertes de Barberton à l'échelle 1:100 000 compilée par Ward (2000). La carte a préalablement été numérisée avec ses indices et gisements et leurs caractéristiques (c'est-à-dire leurs orientations, leurs tailles, leurs morphologies, leurs statuts miniers, et leurs noms), le tout réalisé sur la plate-forme de SIG ArcGIS Pro.

Plusieurs méthodes d'analyse ont été utilisées pour étudier la distribution des occurrences et gisements d'or de la Ceinture de Roches Vertes de Barberton. Les indices ont été analysés selon

le groupe stratigraphique de leur roche encaissante, les structures régionales à proximité d'eux, leur densité et de leur teneur en or.

Le contrôle lithologique sur la minéralisation a été explorée par la méthode du 'Poids de la Preuve' (Weight of Evidence). On a donc pondéré le nombre d'indices par groupe lithologique par leur taille. Cette analyse a montré que le groupe Onverwacht a peut-être un faible poids sur le contrôle stratigraphique, deux autres groupes lithologiques ont aussi montré une favorabilité à porter des minéralisations d'or, cependant des sous-unités font eux-mêmes partie d'autres unités lithologiques, ce qui biaise le calcul.

En récupérant l'orientation des indices de la carte métallogenique (Ward, 2000), et les plotant sur un diagramme de rose, deux directions principales sont mis en évidences : la grandes majorité sont orientées NE-SO à E-O avec un pic orienté NE-SO (Fig. 2).

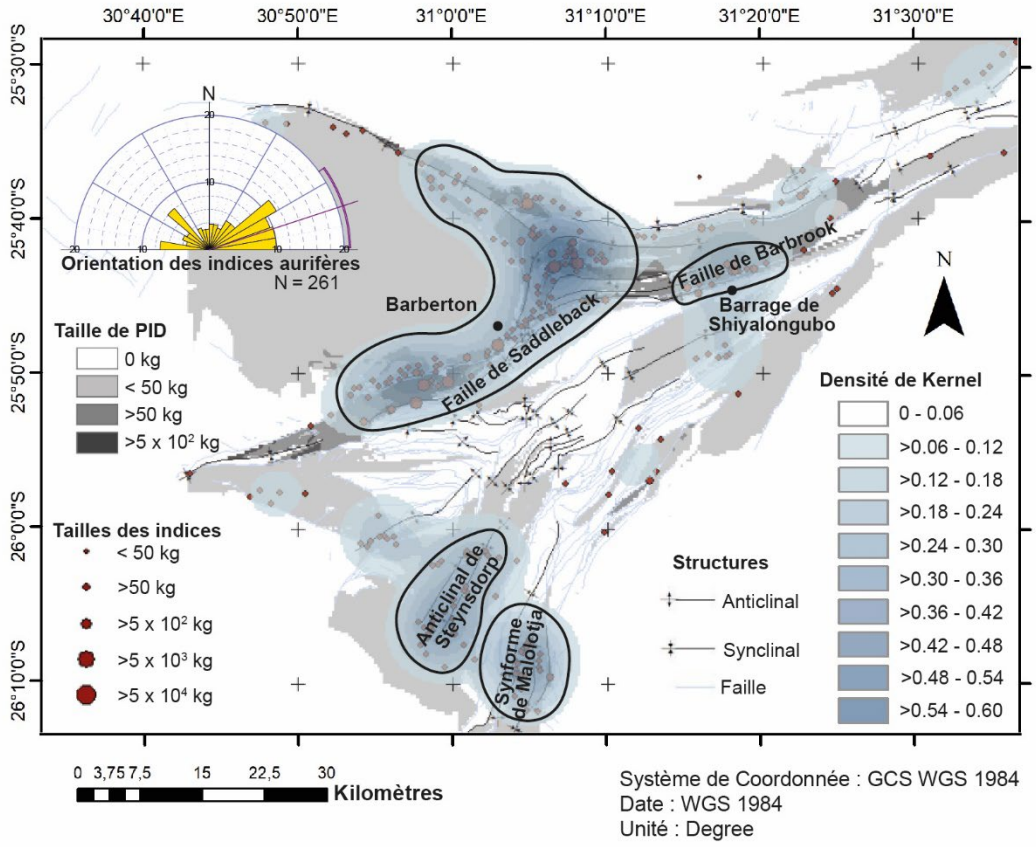

Fig. 2. Carte synthétique de la répartition des indices et gisements aurifères (points rouges) ainsi que leurs différents clusters obtenus avec la densité de Kernel (gradient bleu) et des plus fortes productions d'or dans la partie nord imagées avec l'interpolation PID (gradient gris) de la Ceinture de Roches Vertes de Barberton. Le diagramme de rose compile leurs différentes orientations.

L'orientation de ces indices a été comparée avec l'orientation des failles et des plis les plus proches dans un rayon donné. Dans l'ensemble, la différence angulaire entre l'orientation des indices et la direction de la faille la plus proche est plutôt faible (55% des indices d'or ont une différence angulaire inférieure à 22.5°) ; de même avec les plis (avec 58% d'orientation indices inférieure à 22.5° avec l'orientation des plans axiaux des plis). Ces données suggèrent que les indices d'or sont structuralement contrôlés et peuvent avoir un lien direct avec les plis et failles majeurs de la CRVB.

Une Pondération Inverse à la Distance (PID) a permis d'obtenir une carte d'interpolation des productions des gisements aurifères, cette carte montre que la partie nord de la CRVB est plus propice a porté des tonnages plus élevés (Fig. 2), ce qui semble se vérifier par la présence des plus gros gisements.

Une carte de densité de Kernel des indices a aussi été réalisée, et montre qu'ils sont préférablement répartis dans quatre clusters principaux : Barberton, Steynsdorp, Malolotja et Shiyalongubo (Fig. 2). Ces résultats, qui nous semblent les plus démonstratifs, ont permis de mieux cibler les différentes missions de terrains.

Provinces Aurifères de la Partie Sud

Dans la partie Sud de la Ceinture de Roches Vertes de Barberton, des observations détaillées dans l'anticlinal de Steynsdorp et la synforme de Malolotja nous ont conduits à proposer un modèle en trois étapes décrivant l'évolution tectonique et hydrothermales de cette zone :

Un stade initial (Fig. 3a) a été caractérisé par une schistosité dénommée Se, qui est sub-verticale. Cette schistosité se superpose localement aux couches lithologiques du groupe d'Onverwacht, elle résulterait du chevauchement des roches du groupe d'Onverwacht sur le groupe de Moodies, comme l'ont suggéré d'autres études (Lamb, 1986 ; Lamb et Paris, 1988 ; Heubeck et al., 2023). Cette phase voit la formation des premières veines de quartz, qui sont généralement centimétriques en formes de lentilles sont associées à la schistosité Se et ne contiennent pas d'or.

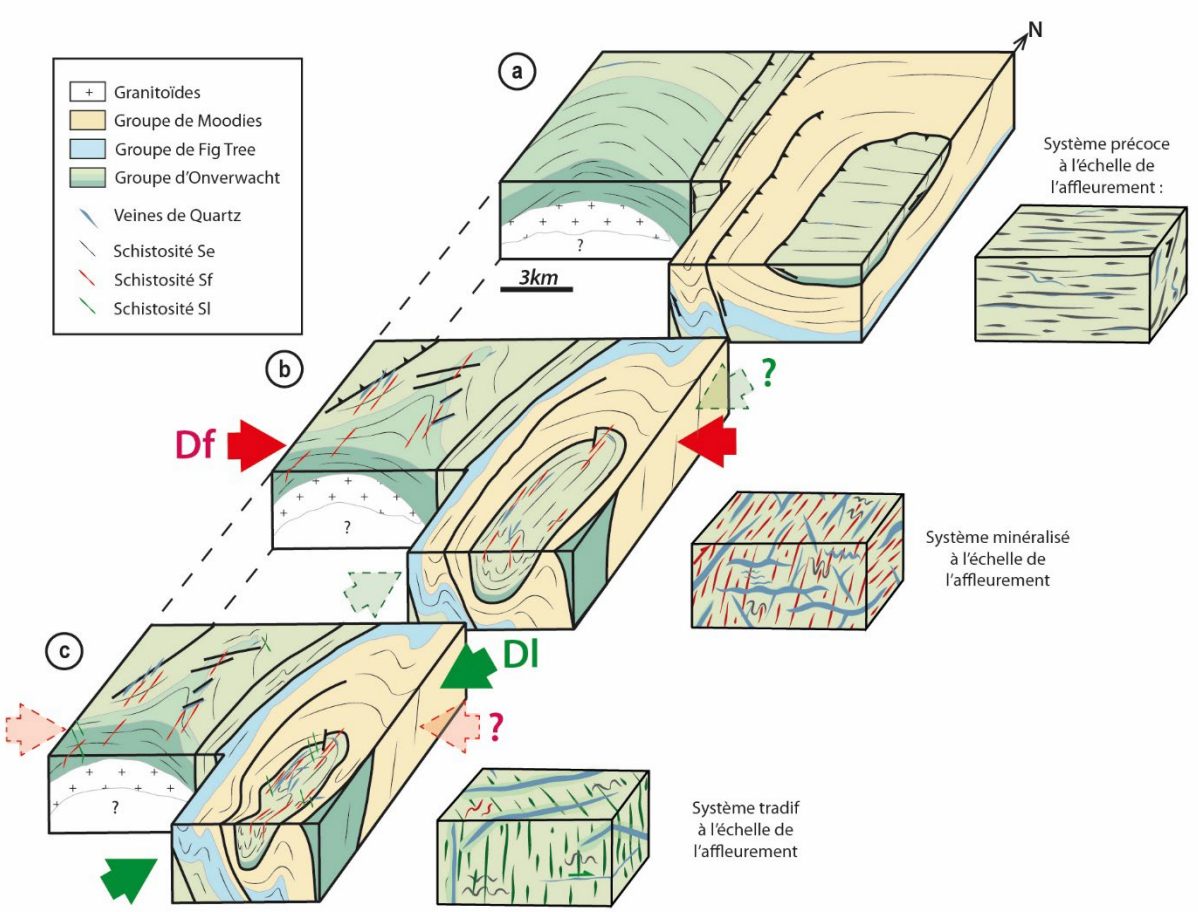

Fig. 3. Bloc 3D synthétique de l'évolution tectonique et hydrothermale de la partie sud de la Ceinture de Roches Vertes de Barberton. **(a)** Stade précoce De. **(b)** Stade de formation des plis et de mise en place de la minéralisation aurifère Df. **(c)** Stade tardif Dl (modifié d'après Travers et al., 2023).

Le deuxième événement (Fig. 3b), appelé Df, est en grande partie responsable de l'architecture du sud de la CRVB, et se caractérise par un raccourcissement E-O. En effet, cet épisode tectonique donne lieu au développement de plis à grande échelle, illustrés par l'anticlinal de Steynsdorp et la synforme de Malolotja qui ont un plan axial de pli globalement N-S. Une schistosité verticale N-S, nommé Sf, est également associée à cette déformation. On observe d'ailleurs la schistosité Se ainsi que les veines précoces plissées avec des plans axiaux de plis parallèles à Sf. Parallèlement, la majorité des veines de quartz aurifères et/ou liées à l'or se mettent en place lors de cet évènement. Nombreuses de ces veines sont centimétriques à métriques, à fort pendage et montrent des critères de chevauchement. D'autres sont sub-horizontales et très souvent ondulées. Ces veines sont composées majoritairement de quartz, avec localement la présence de carbonate, de feldspaths et de tourmaline. La texture interne des veines sub-horizontales présente des peignes de quartz et des tourmalines allongées

verticalement, ce qui a été interprété comme de l'ouverture de mode I, formée par un raccourcissement horizontal.

Le troisième événement (Fig. 3c) est attribué à un raccourcissement NE-SO. Cet événement produit localement des plis, et forme une schistosité, nommée Sl, qui est verticale et orientée NO-SE. Lors de cette déformation, des veines tardives se mettent aussi en place, caractérisées par des veines centimétriques à métriques, sub-verticales et orientées NE-SO, et aussi par des veines à faibles pendage en cisaillement qui décalent le système minéralisé.

Provinces Aurifères de la Partie Nord

Dans la partie nord de la ceinture de roches vertes de Barberton, six gisements ont été pris en exemple dans cette thèse pour illustrer les différents types de veines minéralisées observées : Tiger Trap/Pioneer, Agnes, Victoria, Clutha, Golden Quarry et la région de Shiyalongubo. D'autres affleurements clés ont aussi relevés la présence d'un autre système hydrothermal qui est tardif et stérile. Le système de veines associées à la minéralisation ainsi que les veines tardives sont chacun associés à des évènements de déformation distincts.

D'un point de vue déformation des roches encaissantes, un important raccourcissement, nommé Df, et orienté NO-SE à NNO-SSE est prépondérant et a permis la formation de plis fermés et d'une schistosité d'ampleur régionale orientée ENE-OSO. La région nord de la ceinture est aussi marquée par de nombreuses failles chevauchantes très pentées orientées NE-SO à ENE-OSO. Localement, ces structures sont plissées avec un plan axial de pli NO-SE dans la région de Sheba-Fairview. Cette déformation est attribuée à un épisode tardif de raccourcissement NO-SE qui pousse la ceinture contre la tonalite du Kaap Valley jouant alors le rôle d'un corps rigide (Jones and Kisters, 2022).

Cinq types de veines principaux sont identifiés dans les différents gisements (Fig. 4) : i) les veines très fortement pentées vers le nord qui montrent des critères de chevauchement vers le sud. ii) des veines sub-horizontales avec des peignes de quartz, de carbonates et de feldspaths ainsi que des tourmalines allongées verticalement. iii) des veines parallèles à la stratification de l'encaissant qui sont localement boudinées. iv) des réseaux veines en stockwerks. Et v) des zones à structures plus complexes. Toutes ces veines ont été interprétées comme se formant au cours d'un épisode de la déformation Df, c'est-à-dire lors d'un raccourcissement horizontal NNO-SSE à NO-SE.

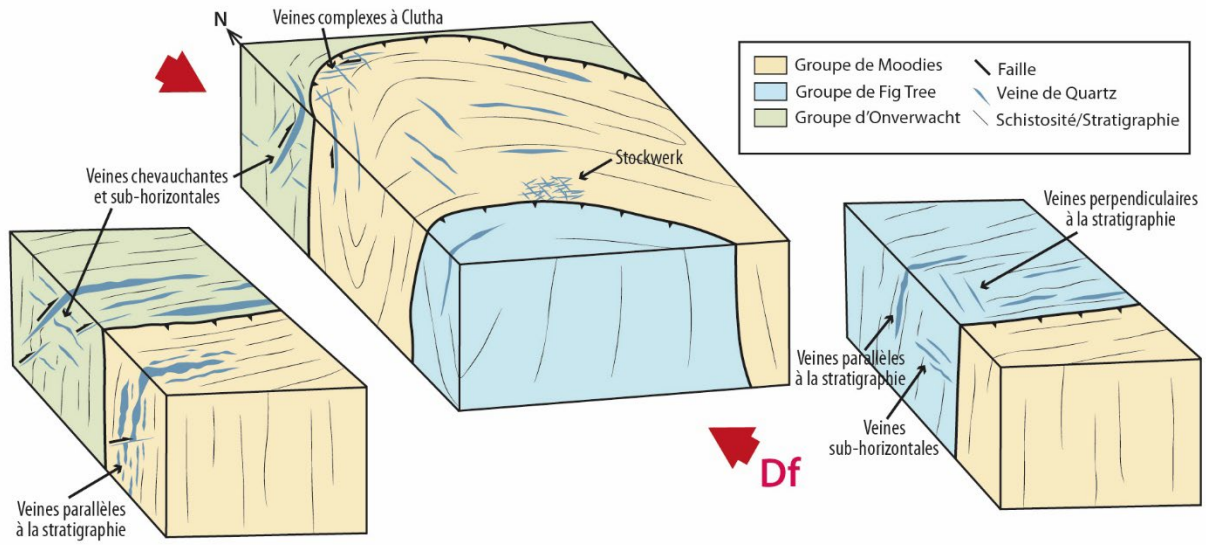

Fig. 4. Blocs schématiques illustrant les différents types de veines de quartz liés à la minéralisation aurifère et leur emplacement dans la partie nord de la Ceinture de Roches Vertes de Barberton. Les diagrammes ne sont pas à l'échelle, il représente schématiquement les géométries des principales structures.

Un système de veines tardif et stérile a également été observé. Ce système présente divers types de veines, notamment : i) des veines en échelon sub-horizontales avec des fibres sub-verticales ; ii) des veines à faible pendage montrant des critères de cisaillement vers l'Ouest et le Sud-Ouest ; et iii) des réseaux de veines complexes mis en place à proximité de failles décrochantes senestres. Toutes ces veines ont été interprétés comme contrôlées par un raccourcissement NE-SO.

Conclusions

La Ceinture de Roches Vertes de Barberton contient de nombreux indices et gisements d'or, dont une grande partie sont peut étudiés. Actuellement deux grandes théories s'opposent sur la caractérisation de l'évènement aurifère de la CRVB. En effet, la minéralisation aurifère a été interprétée comme s'étant formée au cours d'une phase tardive d'extension régionale ou par un épisode tardif de raccourcissement NO-SE. L'objectif principal de cette étude a été d'obtenir des informations complètes sur la distribution et les contrôles structuraux de la minéralisation aurifère dans la Ceinture de Roches Vertes de Barberton en Afrique du Sud et en Eswatini, en utilisant des occurrences et des gisements d'or peu étudiés. Via différents outils d'analyses spatiales, il a été montré que les indices aurifères sont répartis de manière hétérogène sur l'ensemble de la région. En effet certaines zones présentent une plus forte concentration d'indices aurifères, ces zones sont préférentiellement développées autour des structures

majeures telles que les plis et les zones de chevauchement, et semblent plus importantes dans la partie nord de la CRVB. Une étude de terrain détaillée a mis en évidence deux systèmes hydrothermaux, qui sont structuralement contrôlés par deux directions de raccourcissement. Le premier système résulte d'un événement de déformation associé la formation de failles et de plis majeurs ainsi qu'à une schistosité orientée globalement NE-SO. Cette déformation est caractérisée par un raccourcissement horizontale NO-SE à l'échelle de CRVB. Localement, on observe une rotation de ses structures avec une direction plutôt EO dans le sud de la ceinture. L'hydrothermalisme associé à cette déformation produit des veines minéralisées qui présentent des morphologies diverses mais toutes répondant au même système de raccourcissement NO-SE. Deuxièmement, un événement de déformation tardive est aussi observé dans cette région. Cette deuxième déformation est créée par un raccourcissement NE-SO énigmatique, qui est également lié à la formation de veines de quartz. Cet événement de déformation tardive ajoute une complexité supplémentaire dans l'histoire géologique de la Ceinture de Roches Vertes de Barberton et pose notamment la question du rôle des granites à la fois dans la formation des structures arquées et plissée de la région (arc grand format à l'échelle de la ceinture et are de Sheba-Fairview à plus petite échelle) mais aussi dans la formation de l'hydrothermalisme tardif stérile. Ce caractère, si démontré un jour, pourrait représenter une persistance de la tectonique molle archéenne dominé par la mise en place continue et significative de magmas (Gapais, 2018).

Références

Agangi, A., Hofmann, A., Eickmann, B., Marin-Carbonne, J., Reddy, S.M., 2016. An atmospheric source of S in Mesoarchaean structurally-controlled gold mineralisation of the Barberton Greenstone Belt. Precambrian Research 285, 10–20. https://doi.org/10.1016/j.precamres.2016.09.004

Agangi, A., Hofmann, A., Przybyłowicz, W., 2014. Trace element zoning of sulfides and quartz at Sheba and Fairview gold mines: Clues to Mesoarchean mineralisation in the Barberton Greenstone Belt, South Africa. Ore Geology Reviews 56, 94–114. https://doi.org/10.1016/j.oregeorev.2013.08.016

Altigani, M.A.H., 2021. Insights on Mineralogy and Chemistry of Fairview Gold Mine, Barberton Greenstone Belt, South Africa. Indonesian Journal on Geoscience 8, 73–99. https://doi.org/10.17014/ijog.8.1.73-99

Altigani, M.A.H., Merkle, R.K.W., Dixon, R.D., 2016. Geochemical identification of episodes of gold mineralisation in the Barberton Greenstone Belt, South Africa. Ore Geology Reviews 75, 186–205. https://doi.org/10.1016/j.oregeorev.2015.12.016

Anhaeusser, C.R., 2019. The geology and tectonic evolution of the northwest part of the Barberton Greenstone Belt, South Africa: A review. South African Journal of Geology 122, 421–454. https://doi.org/10.25131/sajg.122.0033

Anhaeusser, C.R., 1976. Archean metallogeny in southern Africa. Economic Geology 71, 16–43. https://doi.org/10.2113/gsecongeo.71.1.16

Argapadmi, W., Toth, E.R., Fehr, M.A., Schönbächler, M., Heinrich, C.A., 2018. Silver Isotopes as a Source and Transport Tracer for Gold: A Reconnaissance Study at the Sheba and New Consort Gold Mines in the Barberton Greenstone Belt, Kaapvaal Craton, South Africa☼. Economic Geology 113, 1553–1570. https://doi.org/10.5382/econgeo.2018.4602

Barley, M.E., Groves, D.I., 1992. Supercontinent cycles and the distribution of metal deposits through time. Geology 20, 291. https://doi.org/10.1130/0091-7613(1992)020<0291:SCATDO>2.3.CO;2

Belousova, E.A., Kostitsyn, Y.A., Griffin, W.L., Begg, G.C., O'Reilly, S.Y., Pearson, N.J., 2010. The growth of the continental crust: Constraints from zircon Hf-isotope data. Lithos 119, 457–466. https://doi.org/10.1016/j.lithos.2010.07.024

Bouhallier, H., Chardon, D., Choukroune, P., 1995. Strain patterns in Archaean dome-and-basin structures: The Dharwar craton (Karnataka, South India). Earth and Planetary Science Letters 135, 57–75. https://doi.org/10.1016/0012-821X(95)00144-2

Brown, M., 2015. Paleo- to Mesoarchean polymetamorphism in the Barberton Granite-Greenstone Belt, South Africa: Constraints from U-Pb monazite and Lu-Hf garnet geochronology on the tectonic processes that shaped the belt: Discussion. Geological Society of America Bulletin 127, 1550–1557. https://doi.org/10.1130/B31198.1

Brown, M., Johnson, T., Gardiner, N.J., 2020. Plate Tectonics and the Archean Earth. Annual Review of Earth and Planetary Sciences 48, 291–320. https://doi.org/10.1146/annurev-earth-081619-052705

Byerly, G.R., 1999. Komatiites of the Mendon Formation: Late-stage ultramafic volcanism in the Barberton Greenstone Belt. Geologic Evolution of the Barberton Greenstone Belt, South Africa. Geological Society of America. https://doi.org/10.1130/0-8137-2329-9.189

Cawood, P.A., Kröner, A., Pisarevsky, S., 2006. Precambrian plate tectonics: Criteria and evidence. GSA Today 16, 4. https://doi.org/10.1130/GSAT01607.1

Collins, W.J., Van Kranendonk, M.J., Teyssier, C., 1998. Partial convective overturn of Archaean crust in the east Pilbara Craton, Western Australia: driving mechanisms and tectonic implications. Journal of Structural Geology 20, 1405–1424. https://doi.org/10.1016/S0191-8141(98)00073-X

Condie, K.C., Benn, K., 2006. Archean geodynamics: Similar to or different from modern geodynamics? In: Benn, K., Mareschal, J.-C., Condie, K.C. (Eds.), Geophysical Monograph Series. American Geophysical Union, Washington, D. C., 47–59. https://doi.org/10.1029/164GM05

Condie, K.C., Macke, J.E., Reimer, T.O., 1970. Petrology and Geochemistry of Early Precambrian Graywackes from the Fig Tree Group, South Africa. Geological Society of America Bulletin 81, 2759. https://doi.org/10.1130/0016-7606(1970)81[2759:PAGOEP]2.0.CO;2

Cutts, K.A., Stevens, G., Hoffmann, J.E., Buick, I.S., Frei, D., Munker, C., 2014. Paleo- to Mesoarchean polymetamorphism in the Barberton Granite-Greenstone Belt, South Africa: Constraints from U-Pb monazite and Lu-Hf garnet geochronology on the tectonic processes that shaped the belt. Geological Society of America Bulletin 126, 251–270. https://doi.org/10.1130/B30807.1

de Ronde, C.E.J., de Wit, M.J., 1994. Tectonic history of the Barberton greenstone belt, South Africa: 490 million years of Archean crustal evolution. Tectonics 13, 983–1005. https://doi.org/10.1029/94TC00353

de Ronde, C.E.J., Kamo, S., Davis, D.W., De Wit, M.J., Spooner, E.T.C., 1991. Field, geochemical and U-Pb isotopic constraints from hypabyssal felsic intrusions within the Barberton greenstone belt, South Africa: Implications for tectonics and the timing of gold mineralization. Precambrian Research 49, 261–280. https://doi.org/10.1016/0301-9268(91)90037-B

de Ronde, C.E.J., Spooner, E.T.C., de Wit, M.J., Bray, C.J., 1992. Shear zone-related, Au quartz vein deposits in the Barberton greenstone belt, South Africa; field and petrographic characteristics, fluid properties, and light stable isotope geochemistry. Economic Geology 87, 366–402. https://doi.org/10.2113/gsecongeo.87.2.366

Dirks, P.H.G.M., Charlesworth, E.G., Munyai, M.R., 2009. Cratonic Extension and Archaen Gold Mineralisation in the Sheba-Fairview Mine, Barberton Greenstone Belt, South Africa. South African Journal of Geology 112, 291–316. https://doi.org/10.2113/gssajg.112.3-4.291

Dirks, P.H.G.M., Charlesworth, E.G., Munyai, M.R., Wormald, R., 2013. Stress analysis, post-orogenic extension and 3.01Ga gold mineralisation in the Barberton Greenstone Belt, South Africa. Precambrian Research 226, 157–184. https://doi.org/10.1016/j.precamres.2012.12.007

Dziggel, A., Kisters, A.F.M., 2019. Tectonometamorphic Controls on Archaean Gold Mineralization in the Barberton Greenstone Belt, South Africa. Earth's Oldest Rocks. Elsevier, 655–674. https://doi.org/10.1016/B978-0-444-63901-1.00026-5

Dziggel, A., Otto, A., Kisters, A.F.M., Meyer, F.M., 2007. Chapter 5.8 Tectono-Metamorphic Controls on Archean Gold Mineralization in the Barberton Greenstone Belt, South Africa: An Example from the New Consort Gold Mine. Developments in Precambrian Geology. Elsevier, 699–727. https://doi.org/10.1016/S0166-2635(07)15058-1

Dziggel, A., Poujol, M., Otto, A., Kisters, A.F.M., Trieloff, M., Schwarz, W.H., Meyer, F.M., 2010. New U–Pb and 40Ar/39Ar ages from the northern margin of the Barberton greenstone belt, South Africa: Implications for the formation of Mesoarchaean gold deposits. Precambrian Research 179, 206–220. https://doi.org/10.1016/j.precamres.2010.03.006

Frimmel, H.E., 2008. Earth's continental crustal gold endowment. Earth and Planetary Science Letters 267, 45–55. https://doi.org/10.1016/j.epsl.2007.11.022

Furnes, H., de Wit, M., Robins, B., 2013. A review of new interpretations of the tectonostratigraphy, geochemistry and evolution of the Onverwacht Suite, Barberton Greenstone Belt, South Africa. Gondwana Research 23, 403–428. https://doi.org/10.1016/j.gr.2012.05.007

Gapais, D., 2018. Tectonics-mineralisation relationships within weak continental lithospheres: a new structural framework for Precambrian cratons. BSGF - Earth Sciences Bulletin 189, 14. https://doi.org/10.1051/bsgf/2018014

Gloyn-Jones, J., Kisters, A., 2019. Ore-shoot formation in the Main Reef Complex of the Fairview Mine—multiphase gold mineralization during regional folding, Barberton Greenstone Belt, South Africa. Mineralium Deposita 54, 1157–1178. https://doi.org/10.1007/s00126-019-00865-9

Gloyn-Jones, J., Kisters, A., 2018. Regional folding, low-angle thrusting and permeability networks: Structural controls of gold mineralization in the Hope reef at Fairview Mine, Barberton Greenstone Belt, South Africa. Ore Geology Reviews 102, 585–603. https://doi.org/10.1016/j.oregeorev.2018.09.024

Goldfarb, R.J., Groves, D.I., Gardoll, S., 2001. Orogenic gold and geologic time: a global synthesis. Ore Geology Reviews 18, 1–75. https://doi.org/10.1016/S0169-1368(01)00016-6

Gorman, B.E., Pearce, T.H., Birkett, T.C., 1978. On the structure of Archean greenstone belts. Precambrian Research 6, 23–41. https://doi.org/10.1016/0301-9268(78)90053-0

Groves, D.I., Vielreicher, R.M., Goldfarb, R.J., Condie, K.C., 2005. Controls on the heterogeneous distribution of mineral deposits through time. Geological Society, London, Special Publications 248, 71–101. https://doi.org/10.1144/GSL.SP.2005.248.01.04

Hamilton, W.B., 1998. Archean magmatism and deformation were not products of plate tectonics. Precambrian Research 91, 143–179. https://doi.org/10.1016/S0301-9268(98)00042-4

Herzberg, C., Condie, K., Korenaga, J., 2010. Thermal history of the Earth and its petrological expression. Earth and Planetary Science Letters 292, 79–88. https://doi.org/10.1016/j.epsl.2010.01.022

Heubeck, C., Lowe, D.R., 1994a. Late syndepositional deformation and detachment tectonics in the Barberton Greenstone Belt, South Africa. Tectonics 13, 1514–1536. https://doi.org/10.1029/94TC01809

Heubeck, C., Lowe, D.R., 1994b. Depositional and tectonic setting of the Archean Moodies Group, Barberton Greenstone Belt, South Africa. Precambrian Research 68, 257–290. https://doi.org/10.1016/0301-9268(94)90033-7

Hofmann, A., 2005. The geochemistry of sedimentary rocks from the Fig Tree Group, Barberton greenstone belt: Implications for tectonic, hydrothermal and surface processes during mid-Archaean times. Precambrian Research 143, 23–49. https://doi.org/10.1016/j.precamres.2005.09.005

Jones, C., Kisters, A., 2022. Regional and local controls of hydrothermal fluid flow and gold mineralization in the Sheba and Fairview mines, Barberton Greenstone Belt, South Africa. Ore Geology Reviews 144, 104805. https://doi.org/10.1016/j.oregeorev.2022.104805

Kohler, E.A., Anhaeusser, C.R., 2002. Geology and geodynamic setting of Archaean silicic metavolcaniclastic rocks of the Bien Venue Formation, Fig Tree Group, northeast Barberton greenstone belt, South Africa. Precambrian Research 116, 199–235. https://doi.org/10.1016/S0301-9268(02)00021-9

Korenaga, J., 2006. Archean geodynamics and the thermal evolution of Earth. In: Benn, K., Mareschal, J.-C., Condie, K.C. (Eds.), Geophysical Monograph Series. American Geophysical Union, Washington, D. C., 7–32. https://doi.org/10.1029/164GM03

Liu, S., Bao, H., Sun, G., Wang, W., Fu, J., Gao, L., Guo, R., Hu, Y., 2022. Archean crust-mantle geodynamic regimes: A review. Geosystems and Geoenvironment 1, 100063. https://doi.org/10.1016/j.geogeo.2022.100063

Munyai, M.R., Dirks, P.H.G.M., Charlesworth, E.G., 2011. Archaean Gold Mineralisation during Post-orogenic Extension in the New Consort Gold Mine, Barberton Greenstone Belt, South Africa. South African Journal of Geology 114, 121–144. https://doi.org/10.2113/gssajg.114.2.121

Otto, A., Dziggel, A., Kisters, A.F.M., Meyer, F.M., 2007. The New Consort Gold Mine, Barberton greenstone belt, South Africa: orogenic gold mineralization in a condensed metamorphic profile. Mineralium Deposita 42, 715–735. https://doi.org/10.1007/s00126-007-0135-5

Pintos Cerda, L.R., Jones, C., Kisters, A.F.M., 2022. The effects of fault-zone architecture, wall-rock competence and fluid pressure variations on hydrothermal veining and gold mineralization along the Sheba Fault, Barberton Greenstone Belt, South Africa. Journal of African Earth Sciences 192, 104554. https://doi.org/10.1016/j.jafrearsci.2022.104554

Pintos Cerda, L.R., Jones, C., Kisters, A.F.M., 2020. Multi-stage alteration, rheological switches and high-grade gold mineralization at Sheba Mine, Barberton Greenstone Belt, South Africa. Ore Geology Reviews 127, 103852. https://doi.org/10.1016/j.oregeorev.2020.103852

Schouwstra, R.P., 1995. Wall-rock alteration as a guide to gold-bearing fracture zones in the Zwartkoppie Section, Sheba Gold Mine, South Africa. 16.

Travers, L., Chauvet, A., Lehmann, J., 2023. Structure and Distribution of the Gold-Related Quartz Vein Systems in the Southwestern Part of the Barberton Greenstone Belt (South Africa, Eswatini). Minerals 13, 1034. https://doi.org/10.3390/min13081034

van Hunen, J., Moyen, J.-F., 2012. Archean Subduction: Fact or Fiction? Annual Review of Earth and Planetary Sciences 40, 195–219. https://doi.org/10.1146/annurev-earth-042711-105255

Viljoen, M.J., Viljoen, R.P., 1969. An introduction to the geology of the Barberton granite-greenstone terrain. Spec. Publ. Geol. Soc. S. Afr. 2, 9–27.

Ward, J.H.W., 2000. Metallogenic map of the Barberton Greenstone Belt, South Africa and Swaziland., scale 1:100000, Council for Geoscience. ed.

Table of Contents

Declaration ..... **v**

Abstract ..... **vi**

Résumé ..... **vii**

Résumé Étendu ..... **viii**

Préambule viii

Introduction viii

Contexte Géologique x

Distribution des Indices et Gisements Aurifères xi

Provinces Aurifères de la Partie Sud xiii

Provinces Aurifères de la Partie Nord xv

Conclusions xvi

Références xvii

Table of Contents ..... **xxii**

Chapter I: Introduction **1**

I.A. The Archean specificities 3

I.B. Gold deposit 8

I.C. Gold Mineralisation in the Barberton Greenstone Belt: debates on the Structural Controls 10

I.D. Objectives of the thesis 12

I.E. Study framework 14

Chapter II: Geological Setting **17**

II.A. The Kaapvaal Craton 17

II.B. The Barberton Greenstone Belt and Surrounding Granitoids 19

II.B.1. The Barberton Greenstone Belt 20

II.B.1.1. Lithological assemblages *20*
II.B.1.2. Stratigraphic formations *20*
II.B.1.3. Metamorphic conditions *22*
II.B.2. The surrounding Granitoid rocks 23
II.B.2.1. TTG suites *23*
II.B.2.2. GMS suite *24*
II.B.3. The tectonic models 25
II.C. The gold mineralisation of the Barberton Greenstone Belt 28
II.C.1. The Southern part of the Belt 29
II.C.1.1. The structural setting of the southern part of the BGB *30*
II.C.1.2. Southern gold mineralisation *32*
II.C.2. The Northern part of the BGB 33
II.C.2.1. The structural setting of the northern flank *33*
II.C.2.2. Northern gold mineralisation *35*
Chapter III: Spatial distribution of gold mineralisation 41
III.A. Methods 41
III.A.1. Inverse Distance Weighted technique 42
III.A.2. Weight of Evidence method 42
III.A.3. Kernel Density Estimation 42
III.B. Results of Cartographic Analysis 43
III.B.1. Cartography of Dykes 44
III.B.2. Cartography of Lithostratigraphic units 45
III.B.3. Cartography of Bedding 46
III.B.4. Cartography of Mineralised occurrences 48
III.C. Gold distribution 49
III.C.1. Lithostratigraphy control? 50
III.C.2. Structural control? 52
III.C.2.1. Axial planes control? *52*
III.C.2.1. Fault control? *55*
III.C.3. Spatial control? 57

III.D. Synthesis 60

Chapter IV: Southern Gold Provinces 63

IV.A. The Malolotja area 64

IV.A.1. Main Gold occurrences 64

IV.A.1.1. The She Mine occurrence (942) 64
IV.A.1.2. Waverley Reefs occurrences (947&948) 66
IV.A.1.3. Ivanhoe occurrence (950) 72
IV.A.1.4. The Avalanche occurrence (951) 74
IV.A.1.5. The Rosehill Occurrence (952) 76
IV.A.1.6. The Primrose Occurrence (953) 79
IV.A.1.7. The Welcome Occurrence (956) 82
IV.A.1.8. The Waterfall Occurrence (957) 84
IV.A.1.9. Forbes Reef Mine (960) 86

IV.A.2. Minor gold occurrences 87

IV.A.3. Other geological observations 89

IV.A.3.1. Outcrop Lo14 89
IV.A.3.2. Outcrop Lo43 90
IV.A.3.3. Outcrop Lo37 93
IV.A.3.4. Outcrop Lo181 94
IV.A.3.5. Outcrop Lo186 95
IV.A.3.6. Outcrops in the Piggs Peak Batholith 96

IV.B. The Steynsdorp area 97

IV.B.1. Main Gold occurrences 97

IV.B.1.1. Occurrence n°817 97
IV.B.1.2. Occurrence n°818 100
IV.B.1.3. Occurrence n°819 102
IV.B.1.4. The Gypsy Queen occurrence (827) 104
IV.B.1.5. The Post Office occurrence (830) 105
IV.B.1.6. The Homestead occurrence (925) 107
IV.B.1.7. The Idaho occurrence (930) 110
IV.B.1.8. The Beaconsfield occurrence (931) 112
IV.B.1.9. The Unity occurrences (932&933) 114

IV.B.2. Minor Gold occurrences 116

IV.B.3. Other geological observations 118

IV.B.3.1. Outcrop Lo129 - Vlakplaas granodiorite 118

IV.B.3.2. Contact zone: Steynsdorp gneiss - lower Onverwacht Group rocks 118

IV.C. Synthesis 120

1. Introduction 1

2. Geological Setting 3

2.1. The Barberton Greenstone Belt and Surrounding Granitoids 3

2.2. Gold Mineralisation throughout the Barberton Greenstone Belt 4

2.3. The Malolotja Synform and the Steynsdorp Anticline Areas and Their Gold Occurrences . 6

3. Lithostratigraphy 7

4. Regional Deformation 9

4.1. Early Event (De) 9

4.2. Main Fold-Related Event (Df) 11

4.3. Late Event (Dl) 11

5. Hydrothermal Vein System 12

5.1. Vein Macroscopic Study 12

5.1.1. Early Veins System 12

5.1.2. Mineralised Veins System 12

5.1.3. Late Vein System 15

5.2. Vein Microscopic Study 16

5.2.1. Petrography 16

5.2.2. Microstructures 18

5.3. Alteration 18

6. Interpretation 21

6.1. Main Results 21

6.2. Tectono-Hydrothermal Evolution of the Southern Barberton Greenstone Belt 22

7. Discussion 23

7.1. Vein Formation Model 23

7.2. Significance of the Deformation Events 24

7.3. Timing of the Mineralisation Event 25

8. Conclusions 26

References 26

Chapter V: Northern Gold Provinces 150

V.A. Regional Deformation 151

V.A.1. Bedding 151

V.A.2. Main Folds 153

V.A.3. Schistosities 155

V.A.4. Other Local Folds 157

V.A.5. Faults 158

V.B. Mineralised quartz vein system 159

V.B.1. Field macroscopy study 160

V.B.1.1. Tiger Trap and Pioneer mines 160

V.B.1.2. The Agnes Mine 163

V.B.1.3. Victoria Mine 166

V.B.1.3. Clutha Mine 168

V.B.1.3. Golden Quarry 173

V.B.1.4. Shiyalongubo 175

V.B.1.5. Synthesis 178

V.B.2. Microscopy study 178

V.B.2.1. Petrography 178

V.B.2.2. Microstructures 179

V.B.2.3. Metallogeny 182

V.C. Late quartz vein system 186

V.C.1. Field macroscopy study 186

V.C.1.1. En-echelon veins 186

V.C.1.2. Shallow-dipping shear veins 189

V.C.1.3. Complex quartz vein network 190

V.C.2. Microscopy study 194

V.C.2.1. Petrography 194

V.C.2.2. Microstructures 194

V.D. Interpretation 196

V.D.1. Main Results 196

V.D.2. Vein formation model for the northern domain 199

V.E. Discussion 203
V.E.1. Structural control of the gold mineralisation 203
V.E.2. Significance and timing of deformation event 205
V.F. Conclusions 206
Chapter VI: General Interpretation and Discussion 207
V.I.A. Main Findings 207
VI.A.1. Gold Distribution 207
VI.A.2. Southern Domain 208
VI.A.3. Northern Domain 209
VI.B. Discussion 210
VI.B.1. The Deformation Events and their Significance 210
VI.B.2. The Structural Control of the Gold Mineralisation 213
VI.B.3. Typology of the mineralisation 215
Conclusions 217
References 219
Annexes 235

Chapter I: Introduction

The geological record of the Archean Eon exhibits unique features that set it apart from the modern geological domains. Several key distinctions define this ancient eon. Firstly, Archean is marked by remarkably high levels of magmatic activity (Belousova et al., 2010). During this period, a hotter mantle (Nisbet et al., 1993; Herzberg et al., 2010) contributed to the formation of extensive continental crust characterised by Na-rich granite-gneissic rocks known as TTG (Tonalite, Trondhjemite, Granodiorite; Martin, 1994).

Another hallmark of the Archean Eon is the presence of greenstone belts surrounding TTG domains. These greenstone belts exhibit distinctive characteristics, manifested as elongated structures in tight synclinorium and fault-bounded domains. Comprising primarily of volcano-sedimentary rocks, they have undergone metamorphism at greenschist to amphibolite facies conditions (Condie, 1981).

Moreover, Archean geodynamics seems diverged significantly from modern tectonic patterns. Unlike the horizontal plate tectonics motion observed today, Archean geology has been frequently associated with vertical deformation illustrated by domes-and-keel geometry (Gorman et al., 1978; van Hunen and Moyen, 2012) or sagduction processes (Bouhallier et al., 1995; Chardon et al., 2002). This unique configuration adds complexity to the structural geology of greenstone belts where Archean deformation tends to exhibit weaker intensity compared to modern orogenic belts, resulting in fewer distinct kinematic indicators (Gapais, 2018).

In addition, Archean domains stand out for their exceptional metal enrichment, with a particular emphasis on world-class gold deposits (Barley and Groves, 1992; Goldfarb et al., 2001; Groves et al., 2005), although the gold level in some Paleoarchean rocks are considered low (Hofmann et al., 2017). With few exceptions in more recent geological history and as example for Au-rich porphyric deposits, most of the world's class gold deposits are concentrated within the Archean to Paleoproterozoic periods (e.g., Witwatersrand gold deposit, South Africa; Kalgoorlie-Super Pit deposit, Western Australia; Homestake deposit, USA; Red Lake Gold Mine, Canada). These examples highlight the significance of early Earth geological domains in hosting some of the world's most prolific gold deposits. The unique geological conditions and

long geological history of Archean terrains have contributed to the formation of these exceptional gold resources.

Transitioning to our specific focus, the Barberton Greenstone Belt (BGB) in South Africa and Eswatini emerges as a good illustration of these unique Archean characteristics. Indeed, the BGB is surrounded by numerous TTGs and batholiths (e.g., Kisters and Anhaeusser, 1995; Kisters et al., 2010; Moyen and Martin, 2012; Laurent et al., 2020), that testify to intense magmatic activity in the Archean period. The synclinorium-shaped BGB reveals meta-sedimentary rocks showing mainly greenschist metamorphism with local amphibolite facies (Heubeck and Lowe, 1994; Cutts et al., 2014; Brown, 2015). Many questions and debates about the tectonic events that shaped the BGB contribute to discussions on Archean geodynamics (Anhaeusser, 1984; Jackson et al., 1987; Heubeck and Lowe, 1994; Lowe et al., 1999; Kisters et al., 2003; Moyen et al., 2006, 2019; Schoene and Bowring, 2010; Van Kranendonk, 2011; de Wit et al., 2018). It also stands as a testament to the geological richness of this eon, boasting an estimated production of 342 tons of gold (Anhaeusser, 2019), along with over 350 gold deposits and occurrences and four major operating mines (Fairview, Sheba, New Consort, and Agnes mines).

The spatial distribution of these gold deposits and occurrences within the BGB is not uniform. They predominantly cluster are along major tectonic structures such as faults and folds, primarily within volcano-sedimentary units at the margins of the belt (Ward, 2000). Notably, major mines like New Consort, Sheba, and Fairview are concentrated in the Eureka and Ulundi Synclines in the northern part of the belt, at the intersection with the Jamestown schist belt. These three mines account for approximately 76% of the gold produced in BGB (Pearton and Viljoen, 2017). Conversely, there are also regions of low-grade gold occurrences, exemplified by Steynsdorp and Malolotja, which have yielded limited quantities of gold through historical small-scale artisanal mining (gold production estimated at about 1770 kg; Anhaeusser, 1976).

The non-uniform spatial distribution of gold deposits and varying grades within the BGB suggests a strong structural and/or lithological influence. It is plausible that the regional deformation of the belt influenced gold mineralisation processes. While the most studied gold deposits are found in active mines like Fairview, Sheba, and New Consort, the numerous low-grade occurrences remain relatively under-examined. To address this gap, this study focuses on

the structural framework of these gold-related occurrences throughout the Barberton Greenstone Belt.

This study aims to establish a comprehensive tectonic-hydrothermal model for gold mineralisation within the Barberton Greenstone Belt. We intend to achieve this goal by conducting in-depth investigations of vein systems, their associated alterations, and the structural characteristics of host rocks. Our approach combines Geographic Information System-based spatial analyses with extensive fieldwork, structural, microstructural, and mineralogical analyses of the study area, ultimately shedding light on the structural controls influencing gold-related quartz veins within the Barberton Greenstone Belt.

To provide a solid foundation for understanding the complexities of gold mineralisation within the Barberton Greenstone Belt, it is essential to begin with an introduction on Archean geological record and its unique characteristics, and on gold deposits classification and formation processes. Then, the different objectives of this study will be exposed, and the study framework explicated.

I.A. The Archean specificities

Since its formation, Earth endures various modifications which transformed the primitive shape to its present-day architecture. This includes differentiation processes related to geodynamic, chemical and physical changes. One notable outcome of this differentiation is the formation of continental crust (Dewey and Windley, 1997; Capitanio et al., 2019). Due to a good preservation (oppositely to oceanic domains, Karato, 2010; Condie, 2014; Spencer et al., 2017), these continental areas record the earth geological history, including the early time with preserved Archean craton and shield. The Archean domains represent therefore ideal areas to study the primitive Earth's geological history.

The earth evolution is globally marked by a long and continuous general cooling. Indeed, the Archean eon is marked by a significantly warmer mantle than the present day one (Nisbet et al., 1993; Herzberg et al., 2010). This higher mantle temperature had deep implications for lithospheric dynamics, as for example, elevated mantle melting rates (Drummond and Defant, 1990), or lowering the viscosity of the mantle (van Hunen and van den Berg, 2008). This process gave rise to large granitoid-dominated crustal regions (Condie and Benn, 2006) and created a depletion of incompatible elements in the residual lithospheric mantle (Sleep and Windley, 1982; Korenaga, 2006). Paradoxically, this depletion made the lithospheric mantle

less dense than the one of the modern domain while simultaneously causing the crust to thicken (Sleep and Windley, 1982; Korenaga, 2006).

To appreciate the singularities of the Archean geodynamics, it is essential to compare this with the well-established modern plate tectonics one. While modern plate tectonics involves displacement of rigid lithospheric plates, with important deformation mainly located at the plate boundaries (Dewey et al., 1973; Sleep, 1992). Archean geodynamic regime differed because of the divergent thermal regime, Archean geodynamics operated in a context where the lithospheric behaviour was influenced by, as previously stated, a warmer mantle, and higher rates of melting. These unique Archean conditions gave rise to specific consequences: i) Archean lithospheric plates may have been smaller and less well-defined than the modern ones (Fig. I.1; de Wit and Hart, 1993; Martin, 2005). ii) The deformation is more distributed across wider regions, leading to less localised stress and strain patterns (Sleep, 1992).

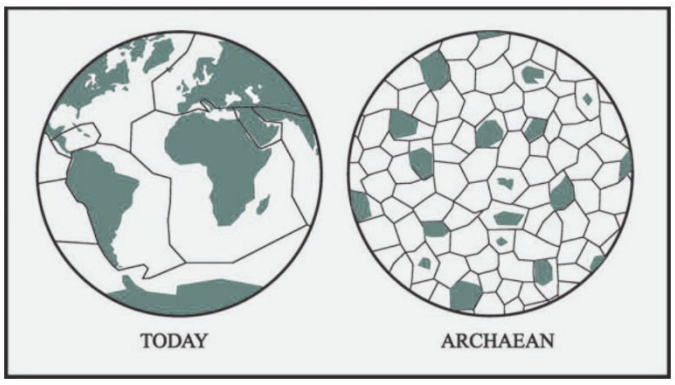

Fig. I.1. Schema illustrating the size of the modern (left) plates to its possible Archean (right) equivalents (modified from Martin, 2005).

As for the tectonic model operating in the Archean eon, numerous debates on the existence of subduction are still active in the scientific community (Hamilton, 1998; Cawood et al., 2006; Condie and Benn, 2006; van Hunen and Moyen, 2012; Brown et al., 2020). Indeed, the hot temperature and low viscosity of the mantle challenge the subduction of lithospheric plates. However, numerous studies testify of subduction in Archean domains (Chen et al., 2009; Jenner et al., 2009). However, this subduction "system" seems different from the modern one, especially in the upper part of the crust where structural features are mostly sub-vertical, and the deformation seems more diffused in smaller suture areas (Chardon et al., 2009; Gapais et al., 2009). In comparison, modern orogen exhibits large mountain ranges with significant crustal thickening accommodated by large, shallow dipping thrust faults and a high variability of metamorphic grades and localised deformation (Yin and Harrison, 2000; Brown, 2007).

Nevertheless, it seems that, subduction could become more recurrent in its classical scheme within domains more moderns in relation with cooling of the entire system (Fig. I.2; Cagnard et al., 2006; Chardon et al., 2009).

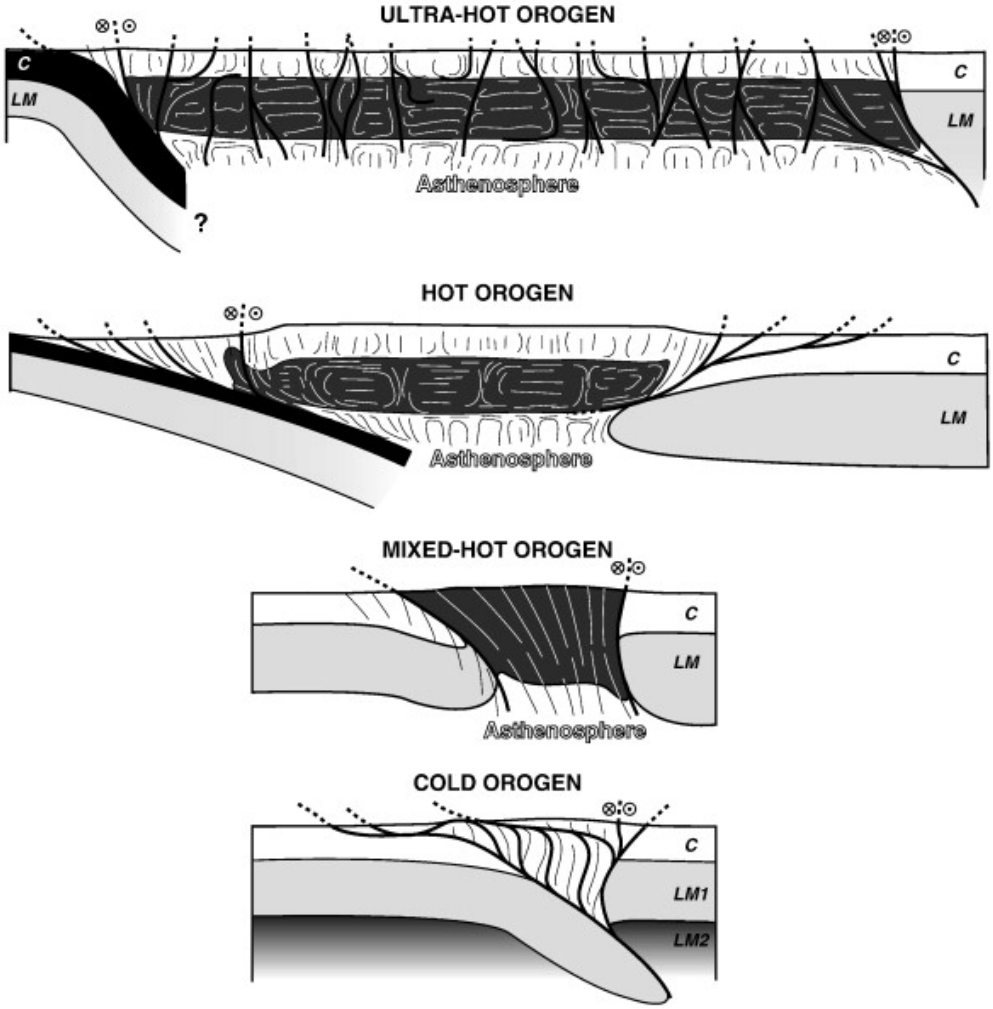

Fig. I.2. Diagrams representing different orogen building modes in time and space, from ultra-hot to cold. C: crust; LM: lithospheric mantle; LM1: stiff upper mantle lithosphere; LM2: ductile, lower viscosity, lower lithospheric mantle (after Chardon et al., 2009).

Typical structures of Archean domains, like the dome-and-keel geometry, have also been interpreted by other tectonic processes. Dome-and-keel domains are formed by granitoid domes, which can exhibit dome-shape foliation, surrounded by narrow and elongated supracrustal formations named the greenstones belts (e.g., the Pilbara Craton in Australia or Dharwar Craton in India). These greenstone terrains have tight pluri-km long synform shapes. The dome-and-keel structures are typically interpreted as the result of a “vertical” tectonics related to the gravity instability of density variation between denser greenstone belt lithologies on less dense granite-gneissic plutons. This gravitational instability will lead to the burial of

supracrustal crust portions and the granitoid plutons' diapiric-like rising (Fig. I.3; Gorman et al., 1978; Bouhallier et al., 1995; Collins et al., 1998). This concept is sometimes referred as sagduction (Bouhallier, 1994).

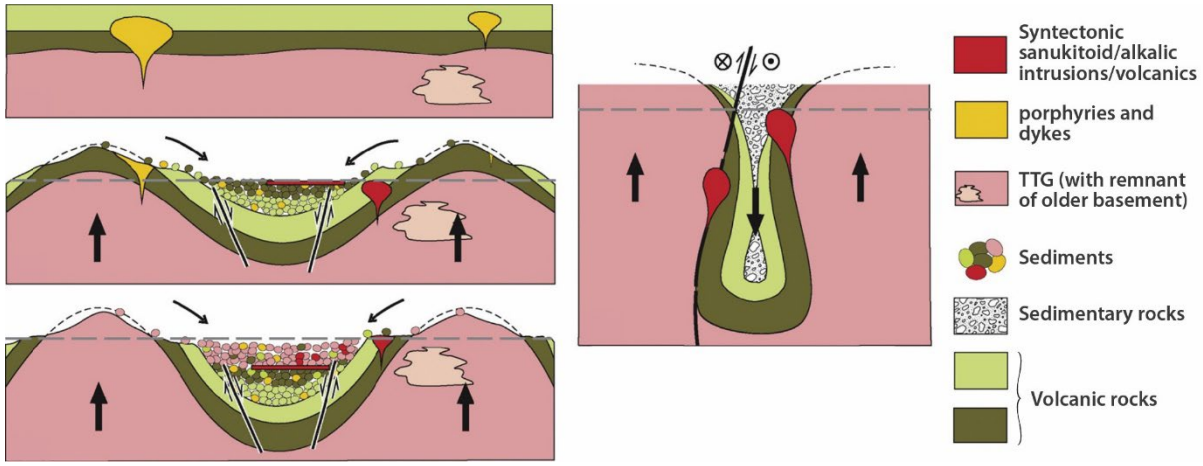

Fig. I.3. Schematic diagram illustrating the sagduction mechanism (after Lin et al., 2013; legend modified).

The lithology of Archean rocks exhibits distinctive specificities that set them apart from their modern counterparts (Fig. I.4). In terms of magmatic rocks, the Archean eon is notably characterised by the prevalence of the Tonalite-Trondhjemite-Granodiorite suite (TTG), which are granitoids containing minimal K-feldspar (Moyen and Martin, 2012). These TTG intrusions constitute the predominant rock type within Archean cratons (Goodwin, 1996). In contrast to present-day volcanic rocks, Archean volcanic units display also a specific composition. Indeed, the volcanic series exhibit a bimodal composition, featuring both mafic and felsic units (Lowe, 1980; Condie, 1981). Moreover, Archean greenstone belts frequently host komatiites (Fig. I.4), which are ultramafic magmas (Byerly, 1999; Robin, 2011). Sedimentary rocks from the Archean eon also carry unique characteristics (Fig. I.4) within dominant poorly evolved detrital sediments including conglomerates and greywackes, which often have a substantial volcanic component (Lowe, 1980). Additionally, Archean sediments also include ortho-chemical formations like cherts (Ledevin, 2019) and abundant Banded Iron Formations (BIFs), both well-known in Archean supracrustal domains. These rock sequences alternate between iron-bearing quartzite layers, rich in magnetite and hematite—minerals of substantial economic importance—and pelitic levels. The origin of these BIFs is thought to be linked to an increase in oxygen in the oceans, leading to the oxidation of ferrous iron Fe^{2+} (Dodd et al., 2022).

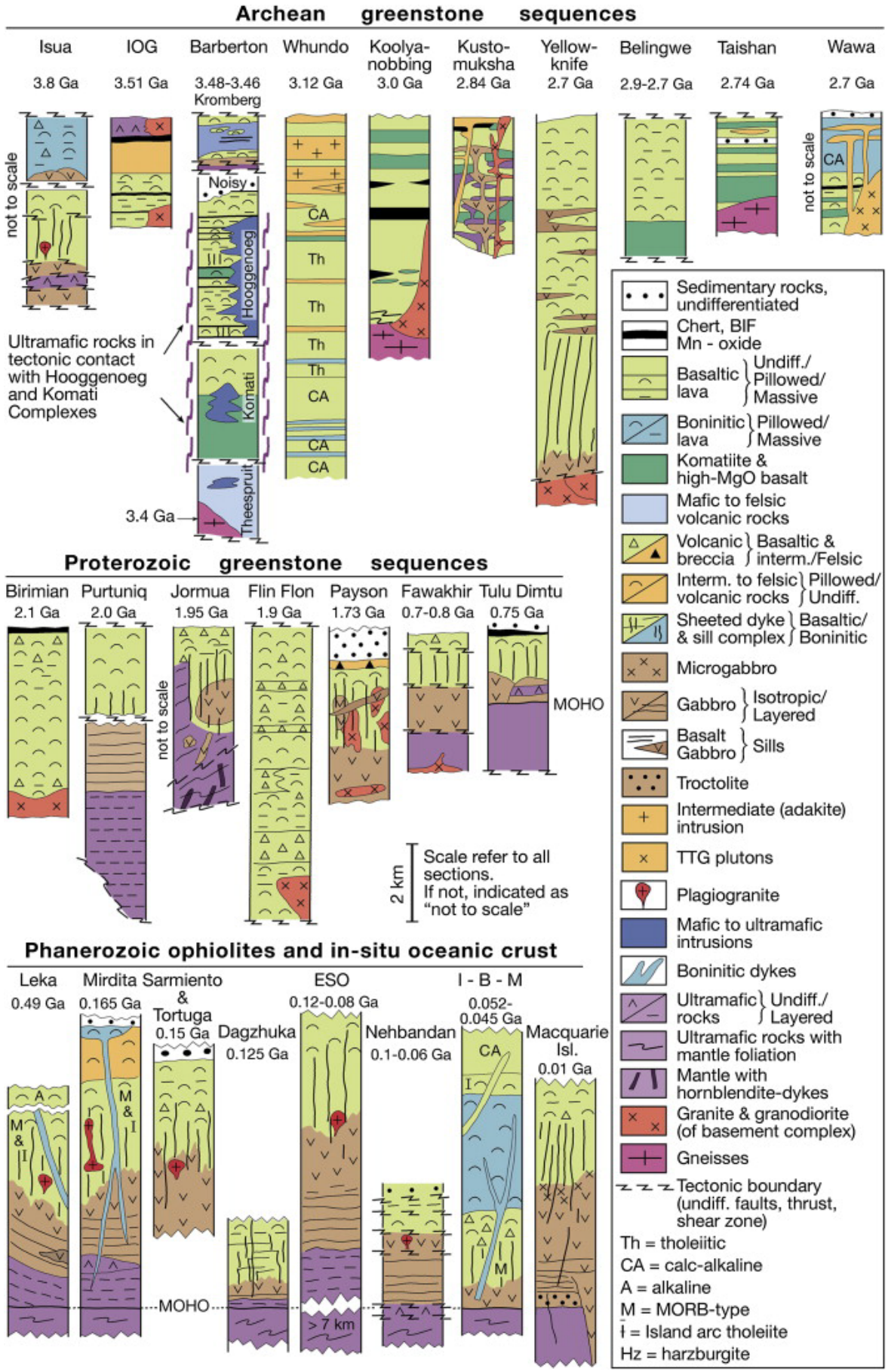

Fig. I.4. Typical stratigraphic sections of Archean greenstones, Proterozoic greenstones and Phanerozoic crust (after Furnes et al., 2014 and references therein). See the lithological differences with times.

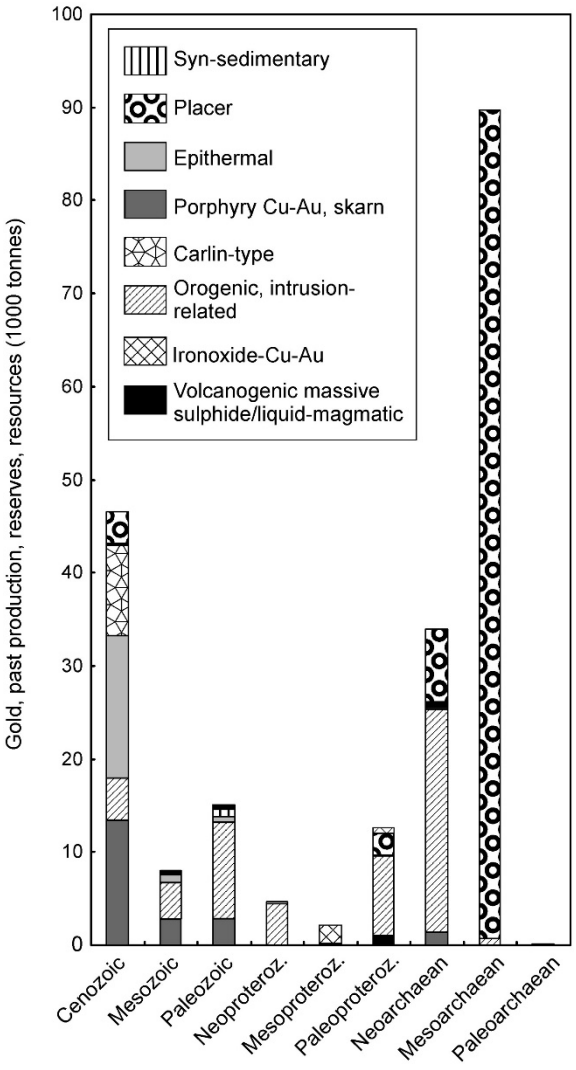

Archean domains, serve as reservoirs of diverse and abundant metallic resources: i) BIFs offer extensive deposits of iron that has already mentioned (Li et al., 2014; Hagemann et al., 2016); ii) Archean greenstone belts bears substantial nickel deposits, often associated with the komatiite formations (Hoatson et al., 2006; Bekker et al., 2009); iii) Archean domains also yielded some of the world's most substantial gold deposits (Fig. I.5), exemplified by the renowned Witwatersrand gold deposits (Tucker et al., 2016). The concentration of diverse metallic resources, encompassing iron, nickel, and gold, make Archean domains interesting to mineral exploration and resource industry.

Fig. I.5. Distribution of gold deposits and its types over geologic time (after Frimmel, 2008).

I.B. Gold deposit

Mankind has been mining gold for 7,000 years (Frimmel, 2008). Because of its rarity and economic value, it was at the origin of the great gold rushes of the 19th century with for example, the famous gold rushes of California in USA, of Klondike in Canada, of Victoria in Australia, or even of Transvaal in South Africa. The rarity of the gold is explained by its low content in Earth, with an average gold content estimated at 0.88 ppb in the upper mantle (Palme and O'Neill, 2007), and less than 1 ppb in the crust (Gao et al., 1998). Locally, the gold content of the crust can become enriched, referred to as gold occurrences. If the concentration reaches an economically level, it is classified as a gold deposit.

The formation of gold deposits has not occurred uniformly throughout geological time. A peak in gold mineralisation is identified in the Mesoarchean era (Fig. I.5; Goldfarb et al., 2001; Frimmel, 2008), spanning from ca. 3.2 Ga to 2.8 Ga. This peak is largely attributed to the exploitation of the Witwatersrand paleoplacer within the Kaapvaal Craton, South Africa, which

produced ca. 52,000 tonnes of gold (Pearton and Viljoen, 2017). Nonetheless, the Witwatersrand deposit type remains a subject of debate, possibly encompassing not only paleoplacers but also orogenic gold or intrusion-related gold (e.g., Muntean et al., 2005) certainly because not only the pebbles were mineralised such as in any type of paleoplacer but also the matrix between the pebble.

Deposits can be classified based on various criteria, including production type, host rock type (telethermal, epithermal, mesothermal, hypothermal), geodynamic context (oceanic rifts, convergence, intra-cratonic rifts), and mineralisation process. Globally, three main types of mineralisation have been identified: magmatic deposits, hydrothermal deposits, and deposits formed via sedimentary and/or surface processes.

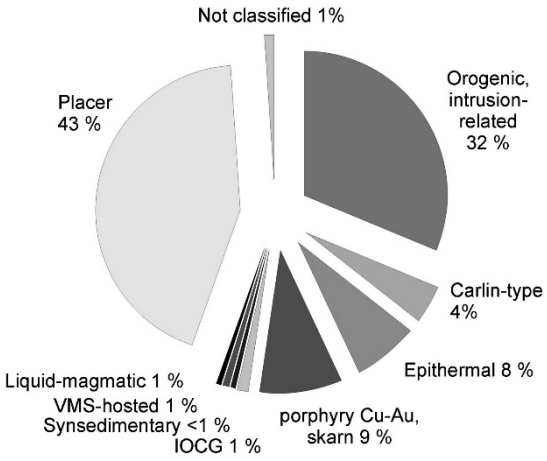

Fig. I.6. Relative distribution of different types of gold deposit in total production (after Frimmel, 2008).

The richest types of deposits, in terms of gold production, include placer deposits, orogenic and intrusion-related gold deposits, both part of the so-called hydrothermal ones (Fig. I.6; Frimmel, 2008). They exhibit the following characteristics:

1) **Gold Placers Deposits.** They are formed by sedimentary processes and are referred as secondary. Indeed, they resulted in the reconcentration of a pre-existing gold-enriched rocks. Due to weathered processes, the gold is remobilised from its source and re-concentrate in a placer (Yeend and Shawe, 1989). Most of these deposits are alluvial (Yeend and Shawe, 1989). Due to the fact that gold is a heavy particle it tends to sediments at the base of channels and get stuck in morphological traps, within river.
2) **Orogenic Gold Deposits**. Also known as "mesothermal" gold deposits, these are part of hydrothermal type of mineralisation. In fact, they are related to metamorphosed terrains, mostly in accretion and collision areas (Groves et al., 1998, 2018). Orogenic gold deposits are commonly associated with quartz and sulphides veins, notably arsenopyrite in metasedimentary rocks (Groves et al., 2018). The mineralogy are mainly quartz-carbonate veins associated with gangue alteration of albite, white mica or fuchsite, chlorite, scheelite and tourmaline in greenschist-facies host-rock (Groves et

al., 1998). The fluid carrying the gold is mostly low-salinity and rich-CO_2 fluids (Groves et al., 1998), and has a metamorphic origin.

3) **Intrusion-Related Gold Deposit (IRGD).** These deposits have a magmatic-hydrothermal origin. The IRGD are genetically related to felsic intrusive rocks (Thompson et al., 1999; Lang and Baker, 2001). They are frequently hosted in veins or brecciated areas filled with quartz, carbonate, and sulphides (Thompson et al., 1999). Mineralogically, they feature carbonates, K-feldspar, albite and/or sericitic alteration assemblages (Thompson et al., 1999). The ore is generally present with sulphides, mainly pyrite and arsenopyrite in smaller quantities (Thompson et al., 1999). The fluids are generally low to high-salinity and carbonic (Thompson et al., 1999). The main difference with orogenic deposits is the fact that the hydrothermal fluid that leached and carried gold within the neighbouring metasediments has a magmatic-hydrothermal origin and come from the granite, during the ongoing magmatic-hydrothermal transition.

The description of these three rich gold deposit types in the preceding paragraphs indicates that gold deposits can form in a wide variety of geological contexts. Therefore, gold deposits serve as indicators of the geological events that led their formation.

I.C. Gold Mineralisation in the Barberton Greenstone Belt: debates on the Structural Controls

The story of gold mining in the Barberton Greenstone Belt began in 1883 and continues to this day (Pearton and Viljoen, 2017). The region hosts a remarkable gold production, estimated at ca. 342 tons of gold (Anhaeusser, 2019). Notably, approximately 76% of this production provided from the three major mines: Sheba, Fairview, and New Consort (Pearton and Viljoen, 2017). These mines not only stand as pillars of the gold production but also serve as the focal points of extensive geological studies, making them renowned and well-documented deposits in the area (e.g., Anhaeusser, 1976, 1976, 2019; Schouwstra, 1995; Dziggel et al., 2007; Otto et al., 2007; Dirks et al., 2009; Munyai et al., 2011; Agangi et al., 2014, 2016; Altigani et al., 2016; Argapadmi et al., 2018; Gloyn-Jones and Kisters, 2018, 2019; Dziggel and Kisters, 2019; Pintos Cerda et al., 2020, 2022; Altigani, 2021; Jones and Kisters, 2022). Beyond these prolific gold mines, the Barberton Greenstone Belt holds over 350 additional gold occurrences and deposits (Dirks et al., 2009; Fig.I.7). The belt northern domains, particularly near the town of Barberton,

are especially well-endowed with gold (Fig. I.7). It is from this area that the majority of the gold has been extracted over the years. Furthermore, in the late 19th century, small-scale artisanal mines delved into minor gold deposits in the southern part of the belt, specifically within the Steynsdorp goldfield and extending into Eswatini (Anhaeusser, 1986).

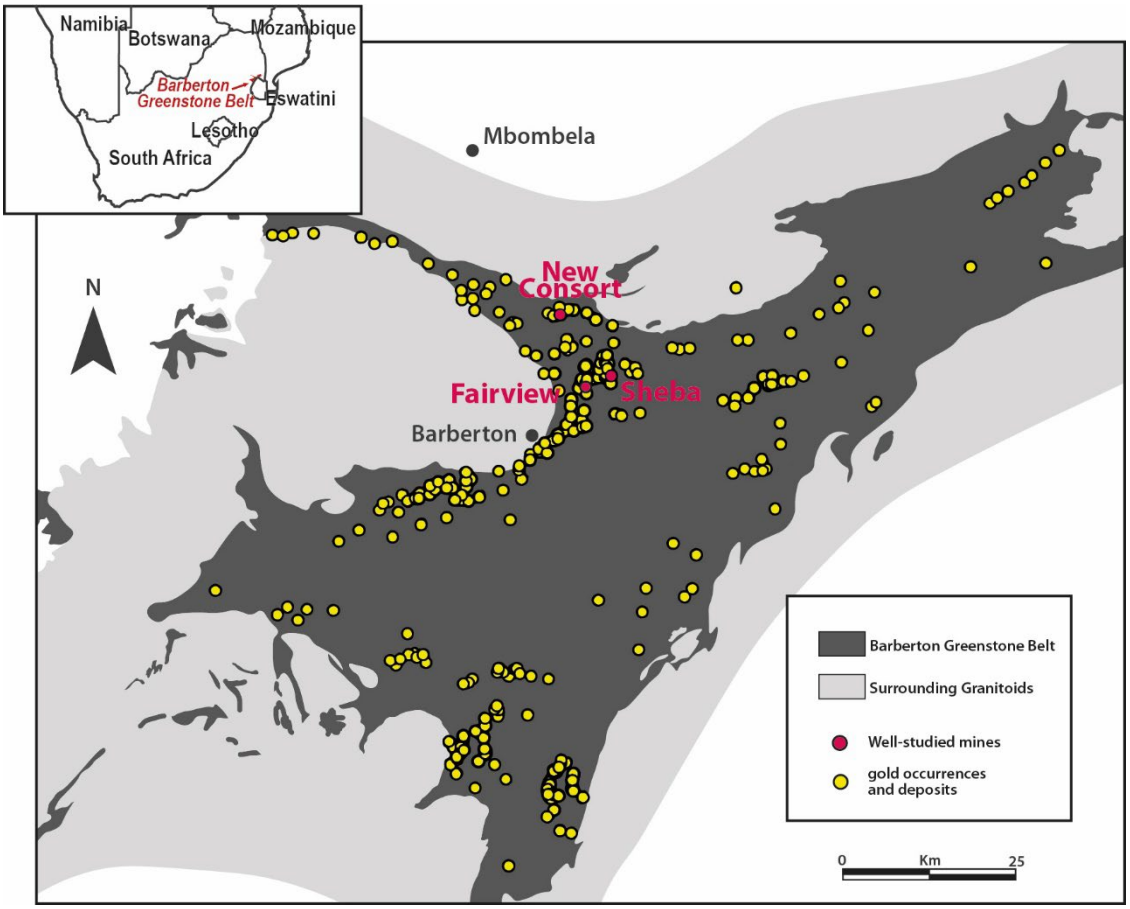

Fig. I.7. Map of the Barberton granite-greenstone terrane showing the distribution of the gold occurrences and deposits and the localisation of well-studied deposits.

One of the main enigmas surrounding the Barberton Greenstone Belt mineralisation is the structural control of its gold deposits. Indeed, there are no consensus on the gold formation, actually two main theories have emerged. The first theory posits that gold mineralisation may have occurred during a late phase of NW–SE regional shortening (de Ronde et al., 1992; Gloyn-Jones and Kisters, 2019; Jones and Kisters, 2022; Pintos Cerda et al., 2022). This phase involved the reactivation of older geological structures, providing a fluid path for the deposition of gold (Jones and Kisters, 2022; Pintos Cerda et al., 2022). In contrast, an alternative theory suggests that gold mineralisation occurred during a regional NW–SE extension phase (Dirks et al., 2013). This extensional phase followed the tectonic and thermal stabilisation of the belt

(Otto et al., 2007; Munyai et al., 2011), presenting a distinct set of geological conditions for the formation of gold deposits.

Old gold mines and less economically significant gold occurrences areas but can records valuable information on gold mineralisation processes. A detailed structural investigation on these areas promises to yield a fresh look and findings on the tectono-hydrothermal gold formation. By conducting this study on a belt-wide scale will also provide a new insight and a constructive overview of the potential structural control of the Barberton Greenstone Belt gold mineralisation, giving new impetus to the discussions surrounding gold formation. In doing so, we aim to not only unveil the geological history of the Barberton Greenstone Belt.

I.D. Objectives of the thesis

The primary objective of this study is to gain comprehensive insights into the distribution and structural controls on gold mineralisation within the Barberton Greenstone Belt in South Africa and Eswatini, focusing on poorly/never studied gold occurrences and deposits. Indeed, we firstly aim to characterise the large-scale spatial distribution of the gold occurrences and deposits in the belt, secondly to identify the different tectonic events related to hydrothermal gold-related system in the belt, and its mineralogy, and lastly to discuss the implications of the findings for the Archean deformation and hydrothermal mineralisation. Specifically, this study aims to achieve the following key objectives:

Objective 1: Determining the large-scale distribution of gold-related features

The first objective of this study is to elucidate the large-scale spatial distribution of gold-related occurrences and deposits at the scale of an entire Greenstone Belt. This will be accomplished using several spatial analysis methods on a digitised map from an existing metallogenic data (Ward, 2000) and with a Geographic Information System (GIS) software (ArcGIS). The relationship between gold occurrences and various geological features, such as faults, fold axes, schistosity, stratigraphy, and lithological units, will be closely examined to identify any potential correlations. Additionally, individual deposits will be examined, with a focus on parameters like their orientation, size, and morphology, to group them based on similarities and differences. Ultimately, the objective is to create a spatial representation of the distribution of the gold occurrences and deposits in the belt, facilitating the recognition of fieldwork targets.

Objective 2: Understanding the role of structural geology in gold mineralisation formation

The second and central objective of this study is to identify the structural controls governing gold-related veins within the Barberton Greenstone Belt. This objective necessitates extensive fieldwork and structural investigations at multiple sites (approximately 220 locations were examined) and scales. On-site, detailed structural measurements and descriptions of structures associated with gold deposits, including their alteration patterns and host rocks, will be conducted.

Extensive sampling, involving a significant number of oriented samples, will be undertaken (approximately 240 samples were collected). These samples will enable a comprehensive microstructural analysis via oriented thin-sections (approximately 230 thins sections were realised), shedding light on the relationship between mineral crystallisation and deformation, specifically, whether minerals formed before, during (syn-deformation), or after deformation (post-deformation). Subsequently, the structural data will be synthesised to produce a structural model explaining the formation of gold mineralisation within the global structural evolution of the Barberton Greenstone Belt.

Objective 3: Mineralogical and Fluid inclusion characterisation within hydrothermal veins

Another objective of this study is to characterise the mineralogy associated with gold mineralisation and identify the composition of the mineralising fluid. To achieve this, the mineralogy of mineralisation-related veins and their associated alteration halos will be determined. A preliminary fluid inclusion study will be conducted to ascertain the conditions under which fluids were trapped and their composition. This synthesis of mineralogical and microthermometry data will contribute to a preliminary but comprehensive physico-chemical characterisation of veins and their associated fluids.

Objective 4: Building a tectono-hydrothermal model for the gold mineralisation

The final objective is to integrate the findings from the previous objectives to reconcile the history of vein formation with deformation events. Additionally, it aims to propose a model explaining the formation of gold mineralisation in the Barberton Greenstone Belt in relation to the structural evolution. A discussion of the new findings will be conducted, and a comparison

of the proposed model with existing models of well-studied mining deposits such as Fairview, Sheba, and New Consort mines will be made. Furthermore, the comparison with the depicted tectonic events documented in the literature on the Barberton Greenstone Belt will also be discussed.

In conclusion, this study is set to comprehensively explore the distribution, structural controls and mineralogy of the hydrothermal events related to gold mineralisation in the Barberton Greenstone Belt. Through the attainment of these objectives, it aims to contribute valuable insights into the geological history and mineralisation formation of this region, advancing our understanding of Archean deformation and hydrothermal mineralisation.

I.E. Study framework

This Ph.D. research was conducted as part of a collaborative program between the University of Montpellier in France and the University of Johannesburg in South Africa. It was co-supervised by Alain Chauvet and Jérémie Lehmann, involving structural analysis, microscopy observations, and SEM analysis at both institutions. Over the three years, multiple field trips were conducted in the Barberton Greenstone Belt in South Africa and Eswatini, facilitated by the International Research Project (IRP) BuCOMO (Building Continents – From Mantle to Ore). The BuCOMO project, headed by Jean-François Moyen and Gary Stevens, aims to investigate the origin and evolution of continental crust. This collaborative research program involves researchers from various French and South African universities (more information on the IRP's website https://bucomo.fr/). Additionally, a preliminary fluid inclusions mapping and microthermometry analysis were conducted at Stellenbosch University in South Africa under the supervision of Bjorn van der Heyden. Spatial analysis using ArcGIS software was initiated in collaboration with students from the BRGM school and the University of Orléans in France, under the advises of Johann Tuduri. Microprobe analysis was conducted at Géosciences Montpellier with assistance from Olivia Mauguin. Thin-section scanning, cathodoluminescence imagery, and an ore microscopy course were overseen by Kalin Kouzmanov at the University of Geneva in Switzerland. An attempt was made to model an Archean crust using COMSOL software at the University of Montpellier under the collaboration and supervision of Diane Arcay, though this remains unfinished and therefore not presented in the thesis. Similarly, an attempt of identifying alteration halos related to gold mineralisation using ASTER imagery was undertaken at the University of Montpellier, supervised by Matthieu Ferry, but did not yield successful results because of the small size of the alteration haloes with respect to the pixel size

of the available imagery, and because of the extensive vegetation cover, pre-empting acquisition of ground surface reflectance.

This thesis is structured into six several chapters, each contributing to the resolution of the scientific aims:

Chapter I: Provides an introduction to the thesis, outlining the characteristics of Archean domains and their enrichment, the knowledge on gold deposits, and the specific issue of gold in the Barberton Greenstone Belt. It also delineates the objectives and study framework.

Chapter II: Offers the geological context of the study area, focusing on the Kaapvaal Craton, the greenstone belts, the surrounding granitoids, and the state of the art regarding gold mineralisation in the belt. This chapter provides essential background for understanding the research problem and approach.

Chapter III: Presents the distribution of gold occurrences and deposits in the belt through spatial analysis conducted using ArcGIS software and the metallogenic map. The aim is to visualise the distribution of gold at the belt scale and identify potential controlling factors and targeting the fieldwork.

Chapter IV: Focuses on a petro-structural study of mineralisation in the southern part of the Barberton Greenstone Belt, an area with limited scientific documentation on the gold ores. The chapter examines structural, microstructural, and mineralogical aspects of quartz veins associated with gold mineralisation and their alteration. Detailed observations centre around the Steynsdorp Anticline and the Malolotja Synform is exposed and these observations will be synthesised and interpreted in a scientific publication (Travers et al., 2023), with the intent to provide a tectono-hydrothermal evolutionary model of the southern part of the belt and discussing these new findings.

Chapter V: Explores the petro-structural study of mineralisation in the northern part of the Barberton greenstone Belt. The chapter investigates structural, microstructural, and mineralogical aspects of quartz veins related to gold mineralisation and their alteration. Observations will be focused on seven deposit examples (Tiger Trap/Pioneer, Agnes, Golden Quarry, Victoria, Clutha and the Shiyalongubo area), aiming to propose and discuss a tectono-hydrothermal evolutionary model for the northern part of the belt.

Chapter VI: Provides a synthesis and overall interpretation of the results of this study. This chapter aims to propose models for the formation of observed vein types and an evolutionary model for mineralisation in association with the belt's architecture and distribution on a belt-larger-scale. And engages in a final discussion regarding the formation models of mineralised systems presented in Chapter VII and their impact on the current understanding of the belt and Archean domains as a whole.

Conclusions: Summarises the key conclusions drawn from this study.

This structure provides a comprehensive framework for addressing the research aims and presenting the findings.

Chapter II: Geological Setting

II.A. The Kaapvaal Craton

The Kaapvaal Craton is one of Earth's most ancient, vast, and well-preserved Archean shields, and is a part of the large-scale Kalahari Craton. It extends for about $1.2x10^6$ km^2 across multiple countries including South Africa, Eswatini, Botswana, Zimbabwe and Mozambique (de Wit et al., 1992; Fig. II.1). The Kaapvaal Craton formed ca. 3.5 - 3.2 Ga and appears to have stabilised around 3.1 - 2.7 Ga ago (de Wit et al., 1992), making this ca. 200-250 km thick lithosphere (Evans et al., 2011) serves as a valuable window into the early history of our planet. The craton is composed predominantly of variably gneissified granitoid rocks and a few greenstone belts. It is largely covered by Mesoarchean to Paleoproterozoic sedimentary rocks (Catuneanu and Eriksson, 1999; Kröner et al., 2019).

The Kaapvaal Craton can be categorised into four different terranes (Poujol et al., 2003; Kgaswane et al., 2018; Fig. II.1): a) the Eastern domain, or the Swaziland terrain dated 3.6 - 3.1 Ga (Poujol et al., 2003). Notably, it includes the Barberton Greenstone Belt, surrounded by granitoids and the Ancient Gneiss Complex (Hunter, 1970), and overlain to the south by the Pongola basin. b) The Central domain, situated in the Witwatersrand terrane, is dated 3.2 - 2.7 Ga (Poujol et al., 2003). This domain is well-known for its rich goldfield province. c) The Northern domain, around the Pietersburg terrane, is formed ca. 3.2 - 3.0 Ga (Poujol et al., 2003). This area encompasses several greenstone belts, including the Murchison, Giyani, and Pietersburg greenstone belts. d) The Western domain with the Kimberly terrane, dated 3.0 - 2.7 Ga (Poujol et al., 2003), is formed by a few belts (Kraaipan, Amalia and Madibe greenstone belts) and extensively covered by Neoarchean to Phanerozoic sediments, including the rocks of the Ventersdorp, the Transvaal and the Karoo supergroups.

The Kaapvaal Craton formation from ca. 3.6 to 3.2 Ga results from magmatic accretion and tectonic amalgamation (de Wit et al., 1992; Poujol et al., 2003). Subsequently, at approximately 3.1 Ga, a period of heightened magmatic activity produced numerous potassic granitoid batholiths (Hunter, 1991; Poujol et al., 2003). These marks the begging of the stabilisation of the craton. Between 3.0 and 2.8 billion years ago, multiple episodes of accretion and collision events occurred (Schmitz et al., 2004) leading to the formation of basins, including the Witwatersrand basin (Poujol et al., 2003; Tucker et al., 2016). A late extension ca. 2.8 Ga formed

intrusion of post-tectonic plutons and the deposition of the Ventersdorp Supergroup (Van der Westhuizen et al., 1991; Gumsley et al., 2020). Between 2.7 – 2.1 Ga the Transvaal Supergroup is deposited (Eriksson and Altermann, 1998; Catuneanu and Eriksson, 1999). Evidence of a large collision between the Kaapvaal Craton and the Zimbabwe Craton is identified in the Limpopo belt with large shear zone (Van Reenen et al., 1987). Lastly, at ca. 2.05 Ga the world's largest layered mafic intrusion of the Bushveld complex emplaced (Scoates and Friedman, 2008).

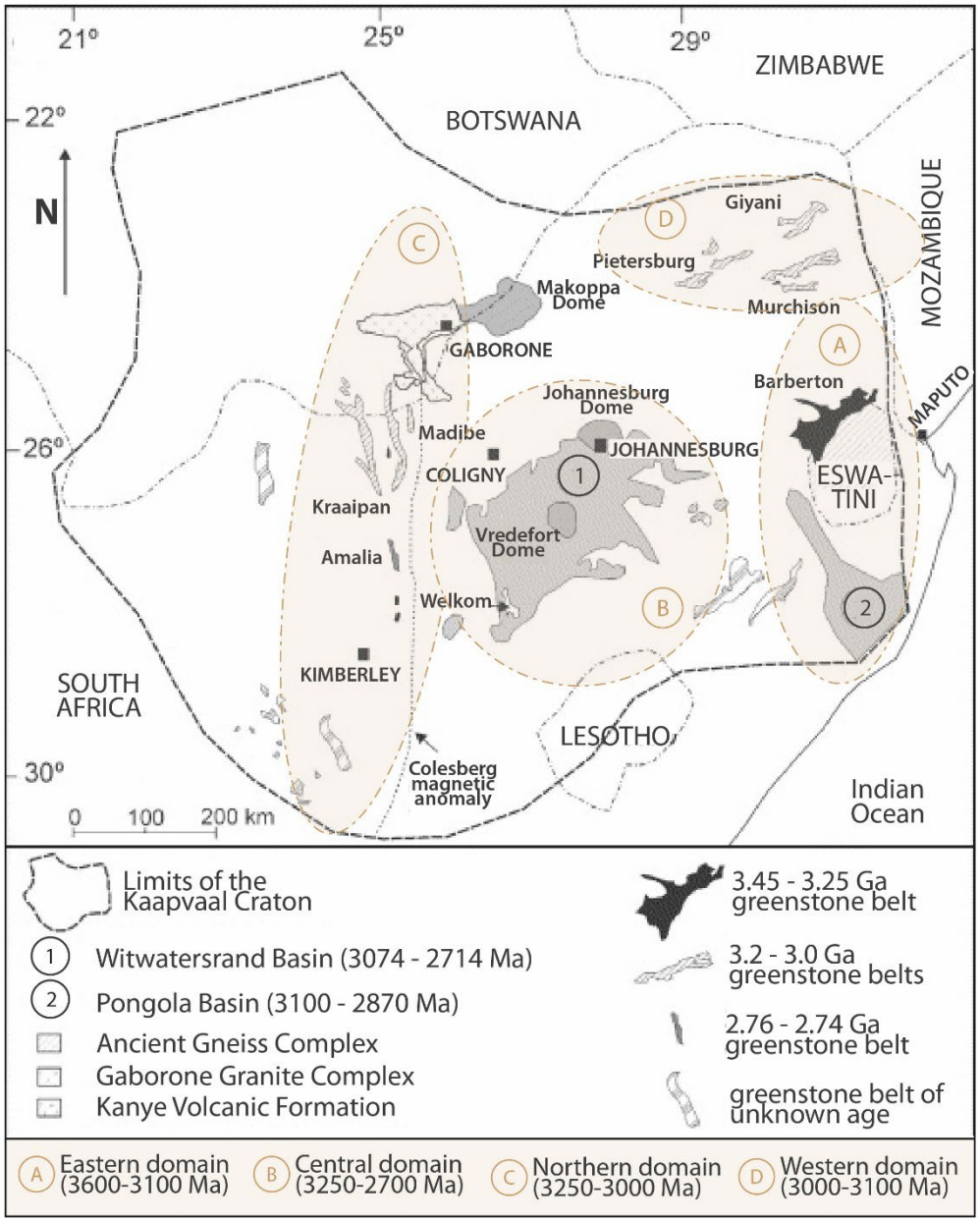

Fig. II.1. Simplified Kaapvaal craton map with its diagram showing main geological components (modified from Poujol et al., 2003).

II.B. The Barberton Greenstone Belt and Surrounding Granitoids

The Barberton Greenstone Belt (BGB) is situated along the northeastern margin of the Kaapvaal Craton (Fig. II.1), expanding the northeastern region of South Africa and the northwestern area of Eswatini. Covering an area of approximately 120 kilometres in length and 50 kilometres in width, the BGB is characterised by volcano-sedimentary units intruded by TTG (tonalite-trondhjemite-granodiorite) and numerous late potassic batholiths (Fig. II.2).

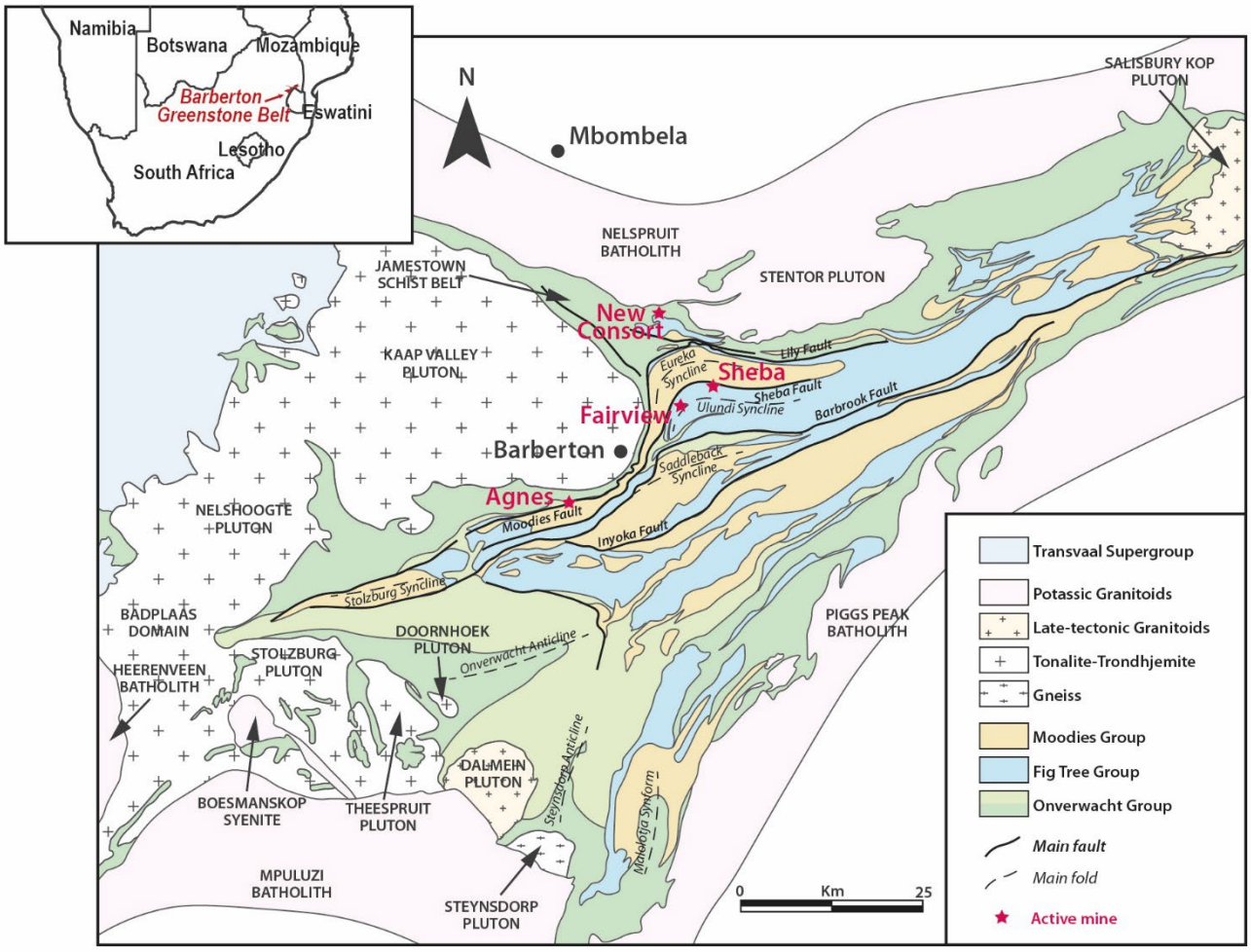

Fig. II.2. Simplified geological map of the Barberton granite-greenstone terrane showing the three volcanic-sedimentary units (Moodies, Fig Tree and Onverwacht), the main granites, and the four main gold deposits (modified from Anhaeusser, 2019). The location of the BGB is shown in inset.

II.B.1. The Barberton Greenstone Belt

II.B.1.1. Lithological assemblages

The lithostratigraphic succession of the BGB is formed by three principal lithostratigraphic units, from older to younger: the Onverwacht, Fig Tree, and Moodies groups (Jackson et al., 1987; Fig. II.3).

The Onverwacht Group, with an age range from roughly 3.55 to 3.29 Ga, is predominantly composed of mafic to ultramafic meta-volcano-sedimentary rocks (Anhaeusser, 1976a; Jackson et al., 1987; Byerly et al., 1996; Kröner et al., 1996; Poujol et al., 2003; Lowe and Byerly, 2007a). This group is characterised by the intercalation of mafic to ultramafic volcanic units with felsic volcanic lithologies and minor cherts (Viljoen et al., 1969; Byerly et al., 1996).

The Fig Tree Group, constrained temporally between 3.28 to 3.22 Ga (de Ronde and de Wit, 1994; Byerly et al., 1996; Kröner et al., 1996; Poujol et al., 2003), is formed by felsic volcanic successions interbedded with sedimentary facies (Byerly et al., 1996; Hofmann, 2005). This group exhibits a lithological composition including sandstone, shale, chert, banded iron formations (BIF), and minor felsic volcanic rocks (Hofmann, 2005; Drabon et al., 2019).

The Moodies Group, corresponding to an age range from 3.22 to 3.21 Ga, constitutes the upper detrital sequence (Heubeck and Lowe, 1994a, 1994b; Kamo and Davis, 1994). This package is predominantly composed of mudstones, quartz-rich and felsic sandstones, and conglomerates (Heubeck and Lowe, 1994a).

Disparities in lithofacies and ages across the southeastern and northwestern part of the BGB have been attributed to the existence of distinct island arc terranes, named the southern and northern terranes separated by the Saddleback-Inyoka fault networks (de Wit et al., 1992; de Ronde and de Wit, 1994; Lowe and Byerly, 2007b).

II.B.1.2. Stratigraphic formations

The three main groups of the BGB (Onverwacht, Fig Tree and Moodies) are subdivided in different stratigraphic formations (Fig. II.3), which can differ from the southern and the northern terranes.

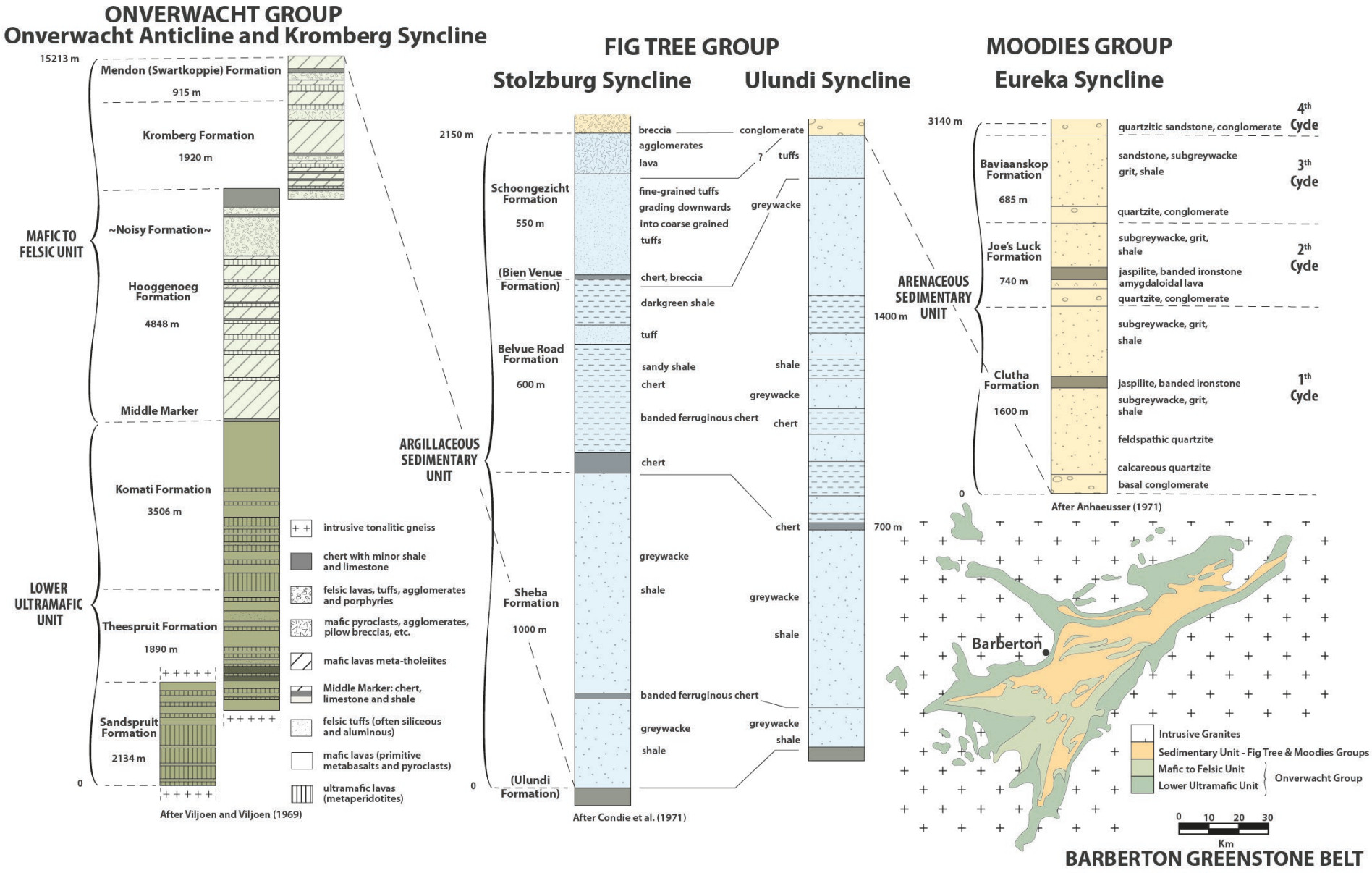

Fig. II.3. Stratigraphic sections illustrating the different stratigraphic formations of the Barberton Greenstone Belt (modified from (modified from Anhaeusser, 1973 and references therein).

Stratigraphically, the Onverwacht Group in the southern sector consists of seven formations (Furnes et al., 2013): Sandspruit, Theespruit, Komati, Hooggenoeg, Noisy (which is also described as part of the Hooggenoeg Formation; Viljoen and Viljoen, 1969; Lowe and Byerly, 2007b), Kromberg and Mendon complexes (also recognised as the Swartkoppie Formation; de Wit et al., 2011). An additional eighth formation, designated the Weltevreden Formation, is exclusively identified within the northern sector of the belt and is correlated with the Mendon Formation found in the southern part (Byerly, 1999; Thompson Stiegler et al., 2012).

The Fig Tree Group is stratigraphically divided into five principal formations in the northern part: Ulundi, Sheba, Belvue Road, Bien Venue, and Schoongezicht formations (Condie et al., 1970; Hofmann, 2005). In the southern part of the belt, the Fig Tree Group is subdivided into the Loenen, Ngwenya, Mapepe, and Auber Villiers formations (Hofmann, 2005; Hofmann et al., 2006; Lowe and Byerly, 2007b).

The Moodies Group is represented by three main formations: Clutha, Joe's Luck and Baviaanskop formations (Anhaeusser, 1971, 1976b; Heubeck and Lowe, 1994a).

II.B.1.3. Metamorphic conditions

The Barberton Greenstone Belt is dominated by lower greenschist facies of metamorphism (Tice et al., 2004; Grosch et al., 2012). Higher metamorphic conditions have been recorded in the proximity to the Stolzburg block in the southwestern part of the belt (Diener et al., 2005; Moyen et al., 2006; Stevens and Moyen, 2007; Cutts et al., 2014), and around the Stentor Pluton in the northern part of the belt (Dziggel et al., 2006). The southern block exhibits metamorphic conditions of approximately 650-700°C and pressures ranging from 0.8-1.1 GPa (Dziggel et al., 2002; Cutts et al., 2014), indicative of a metamorphic gradient of approximately 20°C/km (Diener et al., 2005; Stevens and Moyen, 2007). The peak pressure of metamorphism was found along the Inyoni shear zone with a pressure of 1.2-1.5 GPa representing a gradient of 12°C/km (Moyen et al., 2006). The northern domain exhibits high-grade metamorphism with peak PT conditions reaching a temperature of 600-700°C at a pressure of about 0.5 GPa, corresponding of a 30-40°C/km metamorphic gradient (Dziggel et al., 2006; Stevens and Moyen, 2007).

II.B.2. The surrounding Granitoid rocks

The Barberton greenstone belt is surrounded by numerous granitoid rocks, including TTG (Tonalite-Trondhjemite-Granodiorite) and late GMS (Granodiorite-Monzogranite-Syenite) batholiths.

II.B.2.1. TTG suites

Three distinct generations of TTG were identified in the surroundings of the Barberton Greenstone Belt (Moyen et al., 2007; Fig. II.4):

- To the south of the belt, the oldest Steynsdorp Pluton belongs to the first generation of TTG. It is dated at ca. 3.5 Ga (Kamo and Davis, 1994; Kröner et al., 1996), and is composed of variably deformed tonalite and trondhjemite (Kisters and Anhaeusser, 1995a; Moyen et al., 2007).

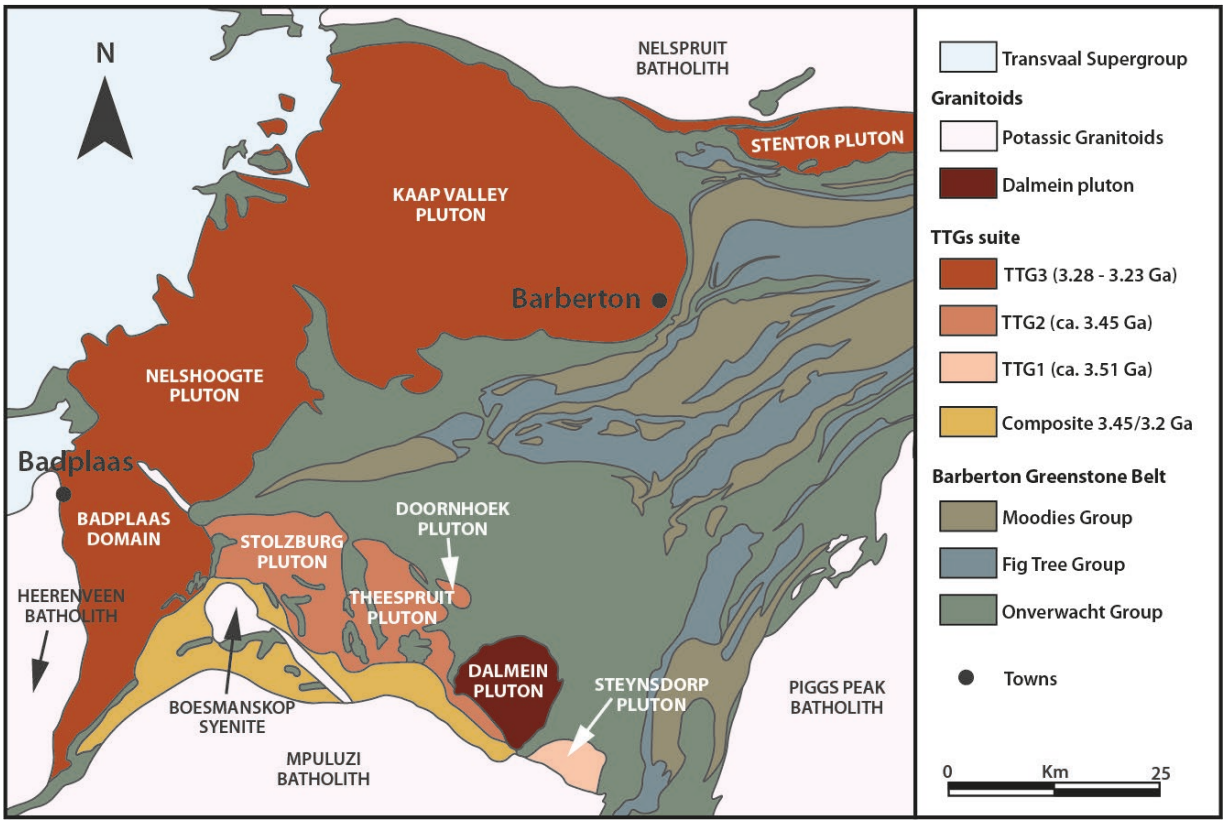

Fig. II.4. Simplified geological map of the southwestern part of the Barberton Granitoid-Greenstone Terrain, focusing on the TTG suite (modified from Anhaeusser, 2019; and Moyen et al., 2019).

- The second generation, dated between 3460 and 3440 Ma, is formed by the Stolzburg block (Kamo and Davis, 1994; Moyen et al., 2019). Located in the southwestern part of the belt, the Stolzburg block encompasses three plutons, from east to west: the

Doornhoek Trondhjemite, Theespruit Gneiss and Stolzburg Gneiss. These plutons show either discordant or concordant contact relationships with the surrounding belt (Kisters and Anhaeusser, 1995b; Kisters et al., 2003).

- The third generation of TTGs was formed at ca. 3.2 Ga, primarily clustering in two different geographical areas. In the west of the belt, Badplaas domain comprises several plutons: the Rooihoogte pluton, Batavia pluton, Badplaas gneiss, and Elandsfontein gneiss (Poujol et al., 2003; Kisters et al., 2010). In the northwest of the belt, the Kaap Valley domain is formed by the Nelshoogte trondhjemite dated at 3236-3212 Ma (de Ronde and Kamo, 2000; Robb et al., 2006) and the Kaap Valley tonalite dated at 3227 ± 1 Ma (Kamo and Davis, 1994).

Outside this classification, the youngest TTG dated at 3215 ± 2 Ma (Kamo and Davis, 1994), named the Dalmein Pluton is located in the southern part of the belt. This granodiorite seems to crosscut the main NE-SW trending structural grain of the BGB (de Ronde and de Wit, 1994; Kisters et al., 2003).

II.B.2.2. GMS suite

Late-stage potassic granitoid plutons intruded the Barberton granitoid-greenstone terrane belt and its surroundings (Fig. II.5). These plutons are referred to as Granite-Monzogranite-Syenite (GMS) suite, and are formed around 3.1 Ga. These batholiths mark the shift from sodic to potassic magmatism in the region (Murphy, 2022).

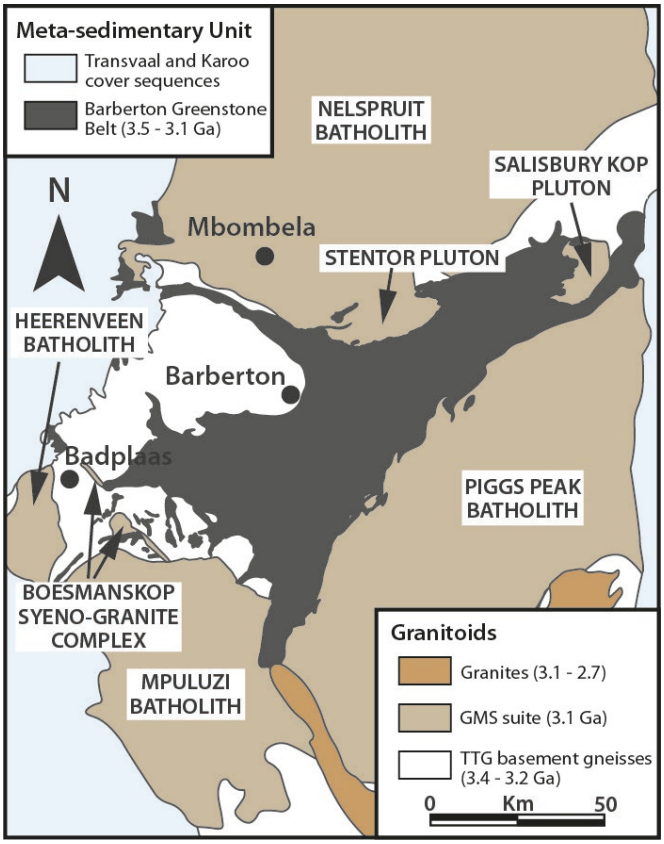

Fig. II.5. Simplified geological map of the Mesoarchean Barberton Granitoid-Greenstone Terrain, focusing on the GMS suite (modified from Belcher and Kisters, 2006).

Four large batholiths are identified: i) The Nelspruit Batholith, located to the north, dated at 3106 ± 3 Ma (Kamo and Davis, 1994). ii) In the eastern region, the Pigg's Peak Granite is dated at either 3140 ± 4 Ma or 3074 ± 4 Ma (Robb et al., 2006; Schoene and Bowring, 2007). iii and iv) The southwestern Mpuluzi and the smaller Heerenveen batholiths, situated in the southwest, are dated respectively 3107+4/-2 Ma and ca. 3110 Ma (Kamo and Davis, 1994; Moyen et al., 2021). These batholiths are described as thin, tabular geometries and composed of K-feldspar rich granite sheets (Westraat et al., 2005; Belcher and Kisters, 2006; Clemens et al., 2010).

These large batholiths are synchronous with the Kees Zyn Doorns and Boesmanskop syenites, intruding the Badplaas and the Stolzburg domains (Anhaeusser et al., 1983). Another pluton is reported, the Salisbury Kop granodiorite dated at ca. 3079 Ma intruded the eastern part of the belt (Heubeck et al., 1993).

II.B.3. The tectonic models

The Barberton Greenstone Belt is arousing controversy and debate over its tectonic models of formation, with several theories proposed in the availed scientific literature (e.g., Anhaeusser, 1984; Jackson et al., 1987; Heubeck and Lowe, 1994b; Lowe et al., 1999; Kisters et al., 2003; Moyen et al., 2006, 2019; Schoene and Bowring, 2010; Van Kranendonk, 2011; de Wit et al., 2018; Fig. II.6).

This complex geological history of the belt can be summarised in two main different interpretations of its tectonic model of formation. On one hand some authors propose for the "gravitational collapse" model, suggesting that the synform-shaped structure of the belt is a result of vertical movements (Anhaeusser, 1981). Especially, in the western part of the belt, where dome-and-keel structures are identified. In these areas, the high-grade metamorphosed plutons are juxtaposed with lower-greenschist facies of the supracrustal rocks of Barberton Greenstone Belt (Anhaeusser, 2001; Van Kranendonk et al., 2009; Lana et al., 2010). These models imply vertical displacement of granitoid plutons causing extension and the synform folding of the supracrustal belt (Van Kranendonk, 2011, 2021; Van Kranendonk et al., 2014).

Other researchers suggest that the Barberton Greenstone Belt is formed through the juxtaposition of terranes separated by major thrusts (de Wit et al., 1987). These domains were formed by the accretion and the subduction of island arcs during a period of horizontal shortening, similar to modern tectonic deformation (de Wit et al., 1992; Moyen et al., 2006; Schoene et al., 2008; Schoene and Bowring, 2010). In such a scenario, detrital rocks of the Fig

Tree Group are interpreted to form in fore- and back-arc basins, while the Moodies Group sedimentary rocks are likened to syntectonic basin formed during the orogenic collapse (Jackson et al., 1987; Heubeck and Lowe, 1994a; Drabon and Lowe, 2021).

Finally, other studies describe a mixed model positing a complex, polyphase history of belt formation (Kisters et al., 2003; Moyen et al., 2019). They suggest that there was a transition in the mode of deformation from early Earth history to the modern deformation of plate tectonics, reflecting a progressive shift of the dynamic Earth's geological processes over time.

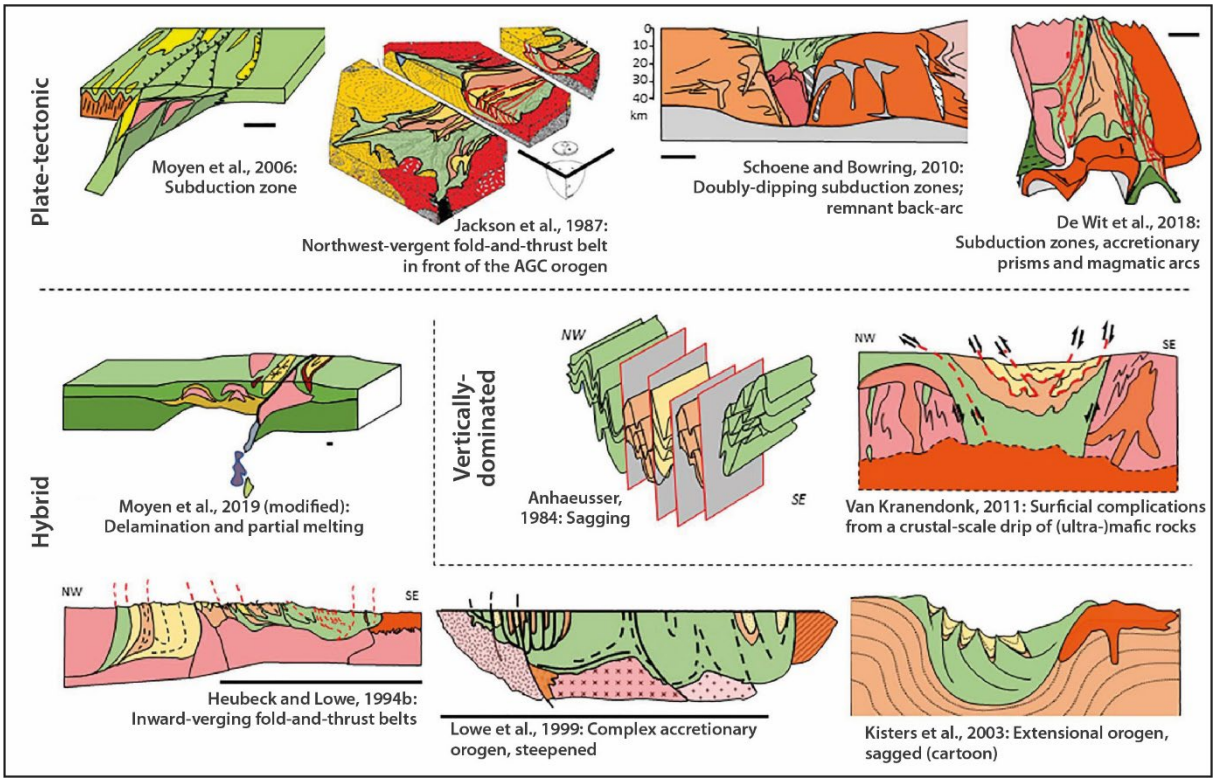

Fig. II.6. Diagrams depicting the various tectonic models realised to illustrate the architecture of the Barberton Greenstone Belt (after Schmitz and Heubeck, 2021; legend modified).

The complex geological history of the Barberton Greenstone Belt has been explored by numerous researchers (e.g., Ramsay, 1963; Jackson et al., 1987; de Ronde and de Wit, 1994; Lowe et al., 1999; Van Kranendonk, 2021), each proposing various interpretations of the deformation record and nomenclatures. According to their findings, the framework of the belt formation can be explained through several key tectono-metamorphic and magmatic phases. These phases can be globally summed up through the five principal deformation events, using the classification model established by de Ronde and de Wit (1994).

- Around. 3.55 Ga, the lower Onverwacht Group, composed by mafic to ultramafic lavas, is formed over the Ancient Gneiss Complex (Anhaeusser, 1973; Lowe, 1994; Hoffmann et al., 2016). It is possible that a period of intra-oceanic activity was genetically linked to these lavas (Lowe, 1994). Subsequently, the melting of a continental shield gave rise to the Steynsdorp Pluton (Kröner et al., 1996; Moyen et al., 2007). A early event (D0) took place around 3458 Ma, marked by hydrothermal alteration (de Ronde and de Wit, 1994).
- Between ca. 3445 and 3416 Ma, the Onverwacht Group experienced an early phase of deformation known as D1 (de Ronde and de Wit, 1994). This deformation is closely associated in time with the second generation of TTGs (de Ronde and de Wit, 1994; Kamo and Davis, 1994; Moyen et al., 2007).
- At 3229-3227 Ma, a second deformation phase, D2, affected the entire belt during NW-SE shortening. This period coincided with the intrusion of several TTG plutons (Kaap Valley, Badplaas, Nelshoogte; (de Ronde and de Wit, 1994). The cause of this tectono-magmatic event is attributed to either the subduction of the southern flank beneath an northern arc (Armstrong et al., 1990; de Ronde and de Wit, 1994; Kohler and Anhaeusser, 2002; Kisters et al., 2003; Moyen et al., 2006) or vertical mass redistribution driven by the density inversion between the rising lighter TTG magmas and the denser upper crustal material above (Van Kranendonk et al., 2009). The D2 deformation is interpreted to be coeval with the formation of the Fig Tree Group in a foreland setting (Drabon and Lowe, 2021).
- Between ca. 3226 and 3080 Ma, a renewed or continued NW-SE shortening led to the D3 deformation, which involved the creation of strike-slip shear zones and the folded the earlier structures (de Ronde and de Wit, 1994). This marks the beginning of the collision and the suture formation between northern and the southern domains (Stevens and Moyen, 2007). The Inyoka fault system within the belt corresponds to a large-scale thrust that brought the two domains in contact (Lowe, 1994). Within the surrounding granitoid terranes, this fault extended to a ductile deformation zone, bringing in contact the northern Badplaas domain with the southern Stolzburg block (Moyen et al., 2006, 2007). In this scenario, the Moodies Group sediments are interpreted as having been deposited in a syntectonic basin formed during the orogenic collapse that followed this event at 3.2 Ga (Heubeck and Lowe, 1994a).

- Around ca. 3080 Ma, the fourth and final deformation event, D4, is characterised by extensional or transtension tectonics (de Ronde and de Wit, 1994; Lana et al., 2011). De Ronde and de Wit (1994) linked this D4 deformation to the emplacement of the late Granite-Monzogranite-Syenite (GMS) batholiths.

II.C. The gold mineralisation of the Barberton Greenstone Belt

The history of gold mining in Barberton dates back to 1883 (Pearton and Viljoen, 2017), and this mining activity continues to this day through four active mines situated in the northern part of the belt (Fig. II.7; Agnes, Sheba, Fairview and New Consort).

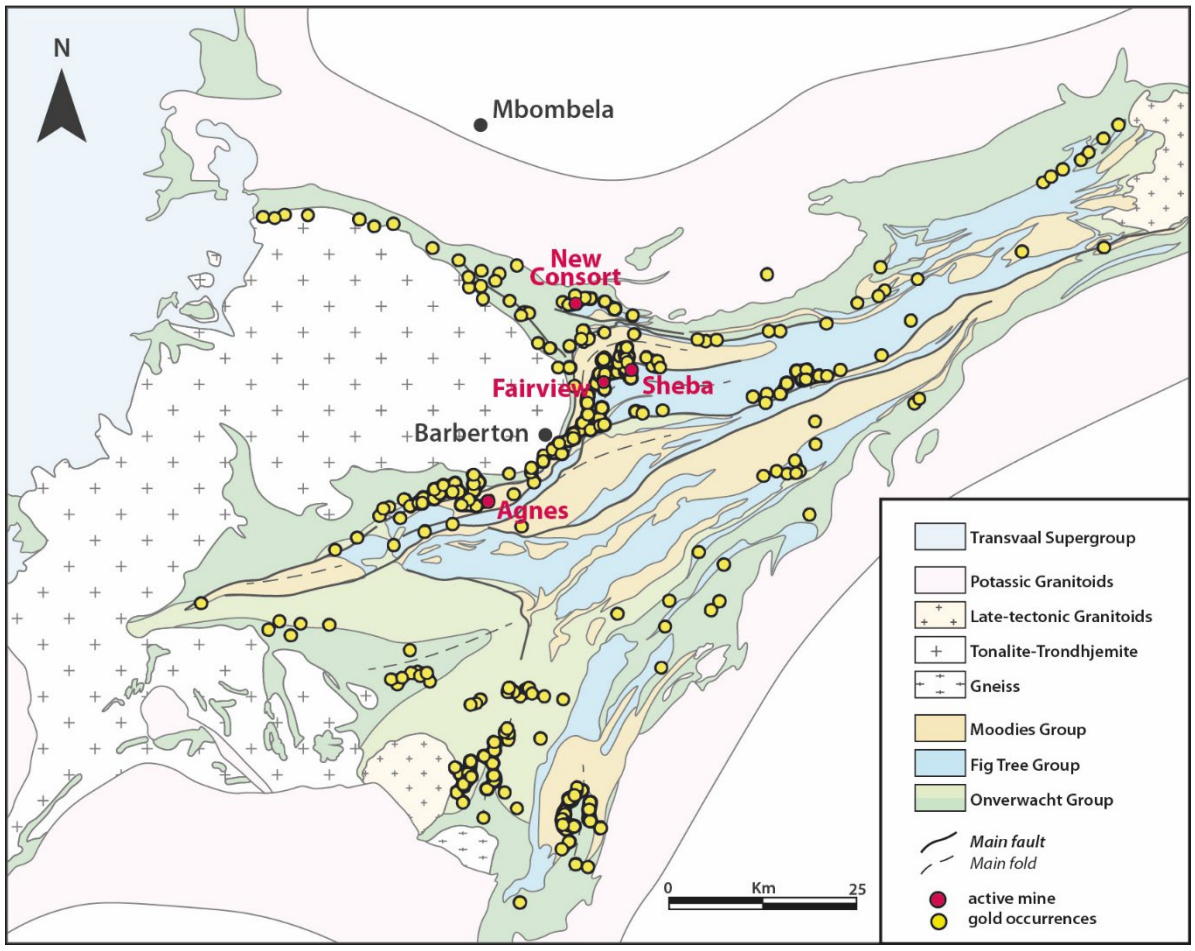

Fig. II.7. Simplified geological map of the Barberton granite-greenstone terrane showing the distribution of the gold occurrences and deposits.

The cumulative gold production in Barberton has been substantial, amounting to an estimated 342 tons of gold (Anhaeusser, 2019). Notably, a significant portion of this production, approximately 76%, is concentrated in three major mines: Sheba, Fairview, and New Consort (Pearton and Viljoen, 2017). These mines, aside from being major gold producers, also happen

to be the most extensively studied and widely recognised deposits in the area (e.g., Dziggel et al., 2007; Otto et al., 2007; Dirks et al., 2009; Munyai et al., 2011; Agangi et al., 2014; Gloyn-Jones and Kisters, 2019; Altigani, 2021).

In addition to these large gold deposits, the Barberton Greenstone Belt hosts over 350 gold occurrences and deposits (Fig. II.7 Dirks et al., 2009). The belt is significantly well-endowed in its northern part, near the town of Barberton (Fig. II.7). It is from this specific area that most of gold has been extracted over the years. Furthermore, in the late 19th century, small-scale artisanal mines have also been exploited minor gold deposits in the southern part of the belt, specifically in the Steynsdorp goldfield and in Eswatini (Anhaeusser, 1986).

II.C.1. The Southern part of the Belt

In the southern sector of the Barberton Greenstone Belt, there are approximately a hundred gold occurrences and deposits, although none of them are currently active. Notably, nearly half of these occurrences are concentrated along the Steynsdorp and Malolotja folds, making these two geological structures the focal points of this research (Fig. II.8).

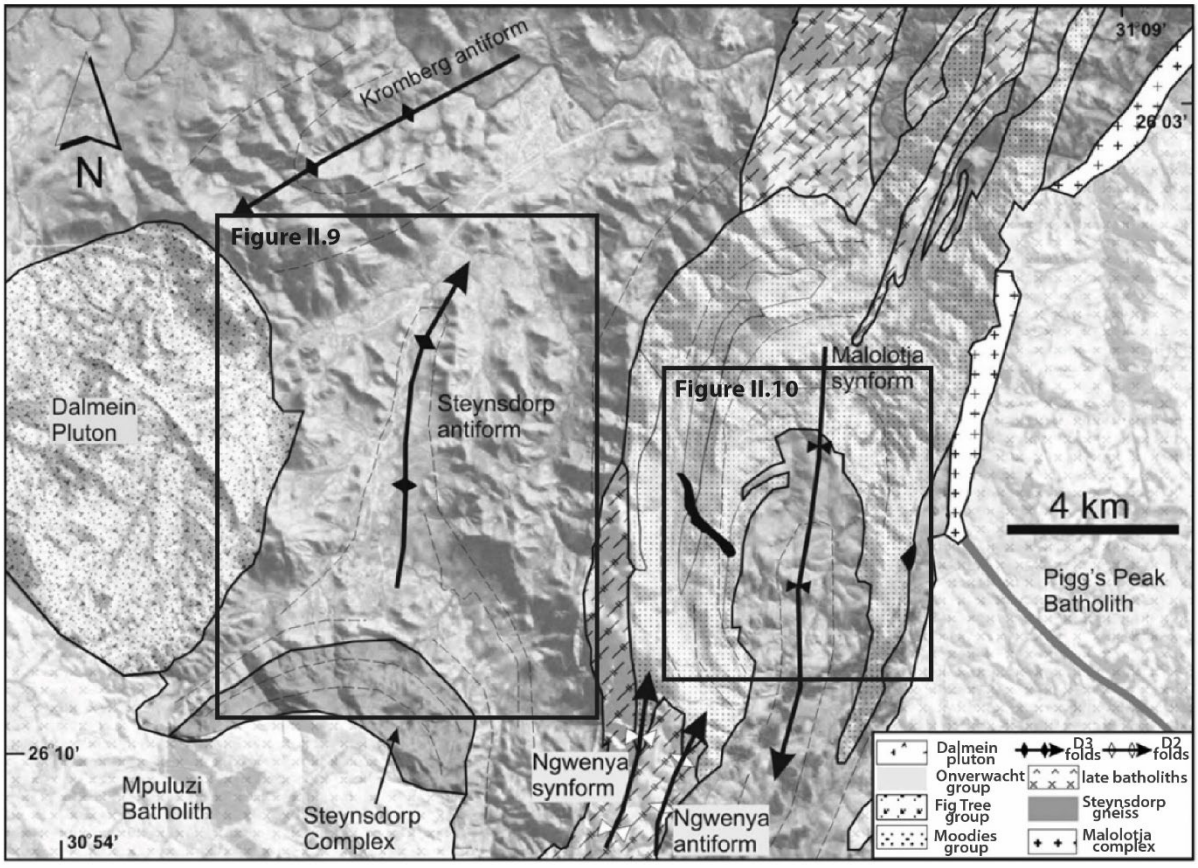

Fig. II.8. Geological map of the southern part of the Barberton Greenstone Belt and surrounding granitoids (after Lana et al., 2011; legend modified and localisation of Figures II.9 and II.10 added).

II.C.1.1. The structural setting of the southern part of the BGB

In the southern part of the Barberton Greenstone Belt, the Steynsdorp and Malolotja folds straddle the border between South Africa and Eswatini. This region encompasses a series of broadly NNE-SSW-striking regional-scale folds, including the Kromberg Antiform, Steynsdorp Antiform, Ngwenya Synform, Ngwenya Antiform, and Malolotja Synform (Fig. II.8; Lana et al., 2011).

The Steynsdorp Anticline, with a width of approximately 5 kilometres and a length of 11 kilometres, is exclusively composed of the Onverwacht Group (Fig. II.9). It is situated to the north of the Barberton Greenstone Belt's oldest pluton, the ca. 3510 Ma Steynsdorp gneiss (Kröner et al., 1996). This fold exhibits a north-plunging anticlinal structure, with a conical geometry in the vicinity of the pluton and a more concentric structure to the north (Fig. II.8; Kisters and Anhaeusser, 1995a).

From a stratigraphic standpoint, the Steynsdorp Anticline is composed of three out of the seven formations of the Onverwacht Group. The lowest Theespruit Formation, enveloping the Steynsdorp gneiss, while the upper Komati Formation, along with its Middle-Marker upper horizon, and the Hooggenoeg Formation, formed the concentric part of the fold (Viljoen et al., 1969; Kisters and Anhaeusser, 1995a).

The Steynsdorp sector is interpreted as a result of a doming effect associated with the emplacement of the Steynsdorp pluton during the regional WNW-ESE shortening (Kisters and Anhaeusser, 1995a). Alternatively, another model suggests the exhumation of the Steynsdorp gneiss followed by extensional detachment at the boundary between the Komati formation and the Theespruit formation during NE-SW striking extension, resulting in a dome-and-keel structure (Lana et al., 2010).

The Malolotja Synform, spanning approximately 4 kilometers in width and 12 kilometers in length, is adjacent to the ca. 3140 Ma Pigg's Peak batholith (Schoene and Bowring, 2007). This synform is composed by talc schists and cherts of the Onverwacht Group (Fig. II.9), which have recently been correlated with the Kromberg and Mendon formations based on new U-Pb ages (Heubeck et al., 2023). Surrounding the Onverwacht Group, the Moodies Group formed the high relief of the area. The Moodies Group in the core of the synform is composed of sandstones and minor conglomerates (Fig. II.10).

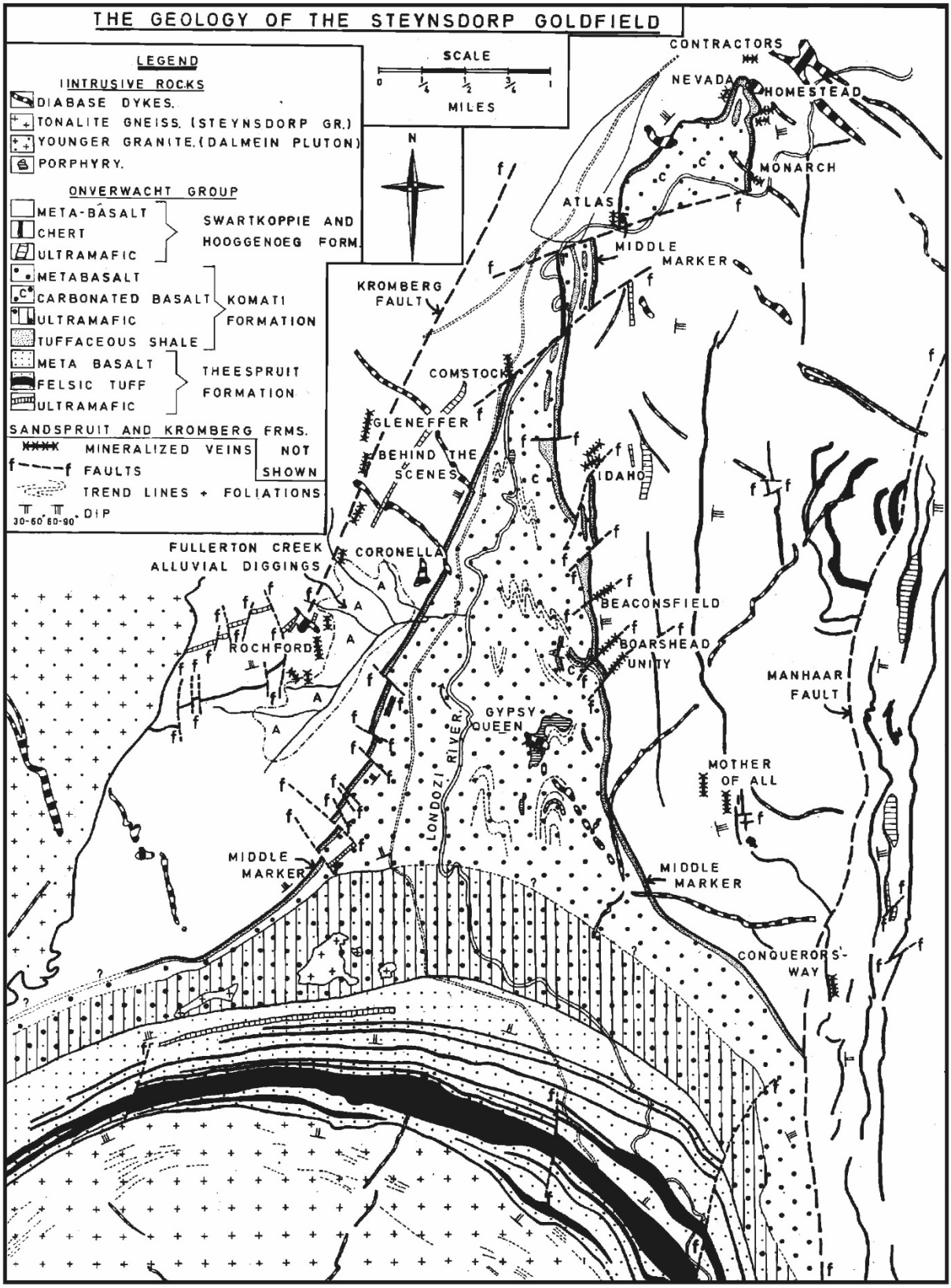

Fig. II.9. Geological map of the Steynsdorp goldfield (after Viljoen et al., 1969).

The Malolotja Synform is a tight and south-plunging synform (Lamb, 1987). This area has been interpreted as early NW-directed nappe of the upper Onverwacht Group over syn-tectonic sediments of the Moodies Group, which have been folded later (Lamb, 1984, 1987; Heubeck et al., 2023).

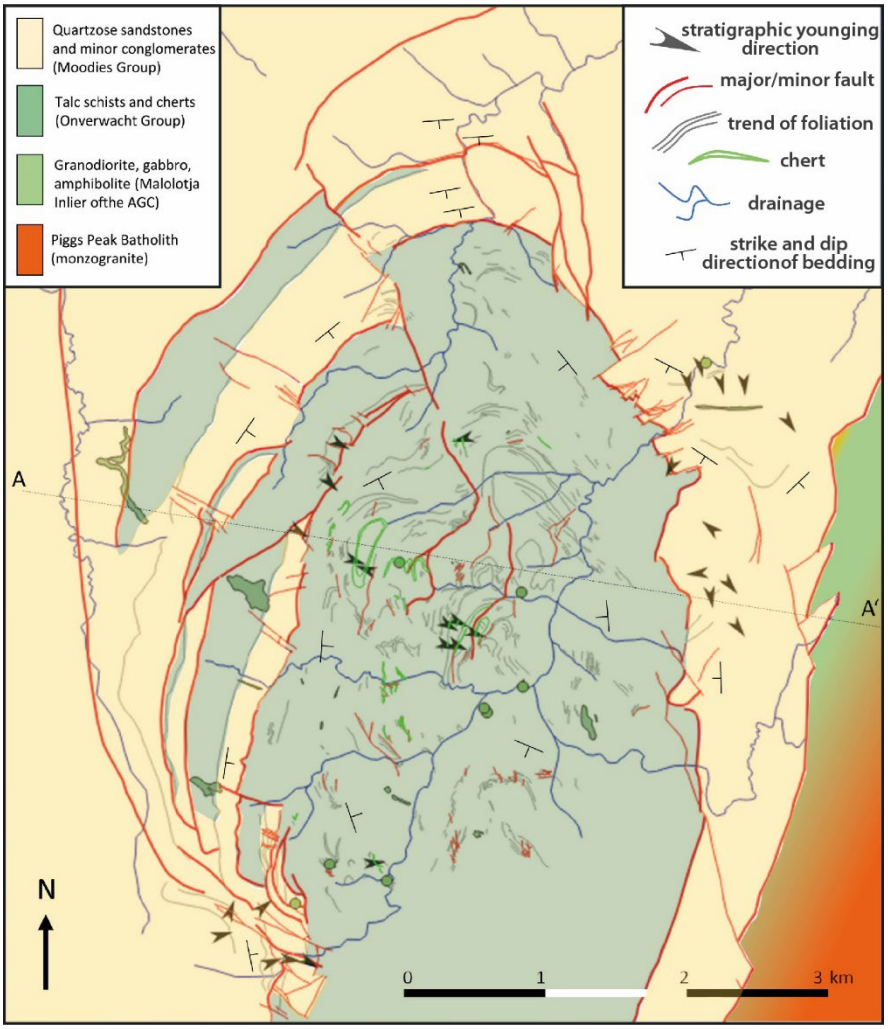

Fig. II.10. Geological map of the Malolotja Synform (after Heubeck et al., 2023; legend modified).

II.C.1.2. Southern gold mineralisation

Small-scale gold mining operations were initiated in the southern region of the Barberton Greenstone Belt in the end of the 19th century, specifically in the Steynsdorp gold field and in Eswatini, which encompasses the Malolotja Synform (Anhaeusser, 1986). Over 45 gold occurrences have been identified in this area, globally characterised as shear zone mineralisation, as documented in the metallogenic map of the Barberton Greenstone Belt (Ward, 2000). These gold occurrences correspond to historical mining sites.

Within the Steynsdorp Anticline, there are over 25 documented gold occurrences, with an estimated 68 kg of gold having been extracted from this area (Anhaeusser, 1986). Viljoen et al. (1969) categorised four primary types of gold occurrences:

1. **Gold Quartz Veins:** These are the most prevalent occurrences and involve mineralised veins composed of quartz and carbonate (ankerite and siderite).
2. **Pyritic Ores in Fractured Chert Horizons:** This type is characterised by stratiform occurrences within chert, particularly in the Middle Marker chert horizon.
3. **Complex Sulphide-related Ores Associated with Intrusive Porphyries:** This category is primarily exemplified by the Gypsy Queen Mine (see location in Figure II.8), where mineralisation is hosted in the fracture network of a porphyry.
4. **Alluvial Diggings:** These occurrences are linked to alluvial gold found in channels, mainly originating from quartz vein systems.

The gold of the Steynsdorp area is mostly hosted as inclusion in pyrite and to a lesser extent in arsenopyrite (Viljoen et al., 1969). The source of this gold is interpreted to be the mafic to ultramafic volcanic rocks of the Onverwacht Group, based on trace element analyses of gold within rocks from the Steynsdorp area (Viljoen et al., 1969).

Similarly, the Malolotja Synform hosts over 20 gold occurrences, primarily listed as "gold-quartz veins" in an appendix of Anhaeusser (1986). However, these occurrences are not extensively documented in the available scientific literature.

II.C.2. The Northern part of the BGB

In the northern domain of the Barberton Greenstone Belt, more than 200 gold occurrences and deposits have been identified, and the area hosts four operational mines (New Consort, Fairview, Sheba, and Agnes mines). Notably, a significant proportion of these occurrences are clustered along main structural features such as the Moodies, Lily, Sheba, Barbrook faults, as well as within the Ulundi and Eureka synclines (Figs. II.2 and II.7).

II.C.2.1. The structural setting of the northern flank

The northern region of the Barberton Greenstone Belt is characterised by a complex geological structural framework showing numerous synclines, including the Eureka, Ulundi, Dycedale, and Saddleback synclines (Heubeck and Lowe, 1994b, 1994b). These synclines are separated by major faults, such as the Inyoka, Saddleback, Moodies, Sheba, Lily, and Barbrook faults (de Ronde et al., 1992).

This expansive part of the Barberton Greenstone Belt encompasses various distinct areas. Notably: i) the **Jamestown Schist Belt** is a NW-SE striking ultramafic to mafic assemblage of the belt enclosed between the Kaap Valley Tonalite and the Nelspruit batholith (Fig. II.11); ii) the **Sheba Hills**, forming the area at the triple junction between the Jamestown Schist Belt, the Kaap Valley Tonalite, and the Stentor Pluton (Fig. II.11; Anhaeusser, 1972). This region includes the Sheba and Ulundi synclines; iii) The **Moodies Hills**, these hills create a NE-SW striking topography extending from the southwestern part of the BGB to the town of Barberton (Fig. II.11). iv) the entire **northeastern part of the belt,** which is mainly composed of the Fig Tree Group and is characterised by a NE-SW striking bedding orientation.

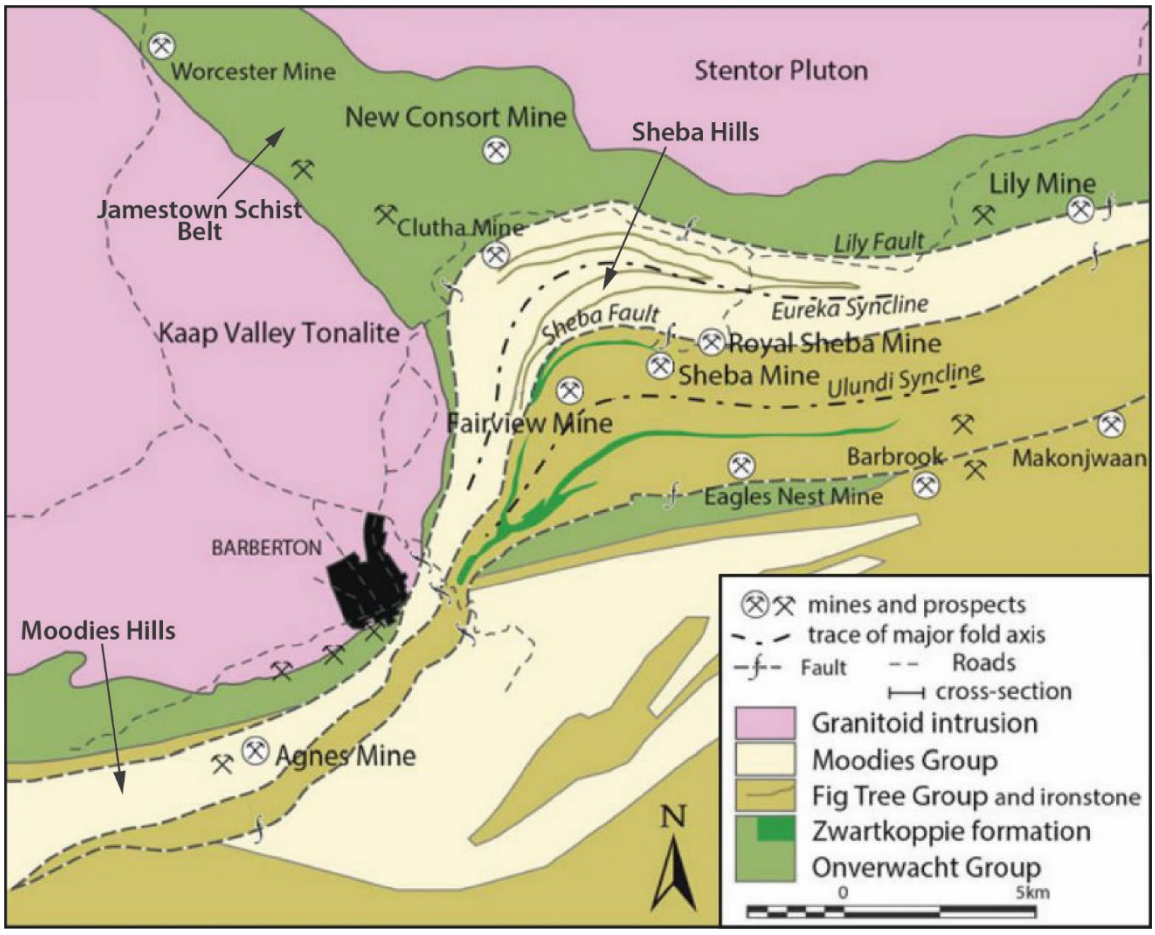

Fig. II.11. Geological map of the northern part of the Barberton Greenstone, depicting the some of the gold deposits in the Sheba Hills, Moodies Hills and in the Jamestown Schist Belt (after Agangi et al., 2019; localisation of Moodies Hills, Sheba Hills and Jamestown Schist Belt added).

The structural configuration of this northern sector of the Barberton Greenstone Belt has evolved through a series of folding and faulting events associated with northwest-to-southeast shortening deformations (de Ronde and de Wit, 1994; Heubeck and Lowe, 1994b).

The Sheba Hills region is particularly structurally intricate, presenting an arc-shaped in the Ulundi and Eureka synclines and the Lily and Sheba faults (Fig. II.11). In this area, close to the Fairview-Sheba gold mines, the Sheba Fault juxtaposes the Moodies Group rocks of the Eureka Syncline with the Fig Tree Group rocks of the Ulundi syncline.

The Eureka syncline predominantly consists of Moodies Group rocks, formed by the Clutha, Joe's Luck, and Baviaanskop formations, composed of conglomerate, quartzite, sandstone and shale (Anhaeusser, 1976b). On the other hand, the Ulundi Syncline is mainly composed of the Fig Tree Group. In this syncline, the Fig Tree Group rocks are formed by greywacke, mudstone and sandstone of the Ulundi, Sheba, and Belvue Road formations (Anhaeusser, 2019). Additionally, some fine layers of the Onverwacht Group are also present in the Ulundi Syncline (Visser, 1956).Across this area, the Onverwacht Group exhibits a diverse composition, comprising carbonate-chlorite-talc schist, quartz-sericite schist, and chert (Anhaeusser, 2019). And, to the north of the Lily fault, in the Jamestown Schist Belt, the Onverwacht Group is composed of ultramafic-mafic rocks, occasionally interlayered with felsic shists and cherts (Anhaeusser, 1972, 2019). Throughout this entire area, the Weltevreden Formation is the predominant unit of the Onverwacht Group.

The structural arrangement of this domain is the result of at least three successive folding phases (Dziggel and Kisters, 2019). Initially, an early stage of folding created high-amplitude folds, partially transposing bedding (Dziggel and Kisters, 2019). Subsequently, a significant fold-and-thrust deformation event occurred, refolding the early folds and giving rise to major thrust folds during a regional D3 event (Heubeck and Lowe, 1994b; Anhaeusser, 2019). Finally, a third episode of folding shaped the NW-SE striking arcuate form of the Ulundi and Eureka synclines. This late folding phase is associated with the diapiric emplacement of the Kaap Valley Pluton (Anhaeusser, 1976b) or is attributed to progressive NW-SE shortening of the belt, interacting with rigid TTG plutons, inducing folding (Jones and Kisters, 2022). During this late refolding phase, the Sheba Fault underwent reactivation, recording both folding and strike-slip horizontal motion (Visser, 1956; Dziggel and Kisters, 2019).

II.C.2.2. Northern gold mineralisation

In the northern part of the Barberton Greenstone Belt, several sizable gold mines operate, while a few historical mining operations still exist. In this area, more than two hundred gold occurrences and deposits have been documented, with the majority concentrated in the Moodies Hills and its surrounding. These occurrences and deposits are classified as shear zone

mineralisation, veins, and stockworks according to the metallogenic map of the Barberton Greenstone Belt (Ward, 2000). Extensive research has been conducted on the Sheba-Fairview mining complex and the New Consort mine, while the remaining occurrences and deposits have received comparatively less attention.

Within the Sheba-Fairview complex, gold mineralisation is predominantly described as shear quartz-carbonate-sulphide lodes, sulphide dissemination within fractures, or bedding-parallel to shear zones (Gloyn-Jones and Kisters, 2019; Pintos Cerda et al., 2022). This mineralisation occurs under greenschist facies conditions (Agangi et al., 2019). Alteration halos characterised by fuchsite-carbonate-sericite-graphite associations are closely associated with gold mineralisation (Gloyn-Jones and Kisters, 2018; Pintos Cerda et al., 2020). Gold mineralisation is present as either refractory or micro-inclusions within sulphides, mostly in arsenopyrite and pyrite, or as free gold grains in veins and alteration halos (de Ronde et al., 1992; Agangi et al., 2019). De Ronde et al. (1992) and de Ronde and de Wit (1994) suggest that the gold event resulted from the reactivation of older D2/D3 structures during the late stage of D3 NW-SE shortening. More recent work corroborates that mineralisation formed during a late stage of the D3 NW-SE shortening (Gloyn-Jones and Kisters, 2018; Jones and Kisters, 2022; Fig. II.12). Nevertheless, other researchers have linked the gold-bearing event to the regional D4 extension tectonic event (Dirks et al., 2009, 2013).

The New Consort gold mine is situated north of the Sheba and Fairview mines, within the southern part of the Jamestown Schist Belt. The New Consort mine is associated with highly deformed country rocks that have undergone metamorphism at amphibolite facies conditions (Viljoen, 1963; Anhaeusser, 1972; Otto et al., 2007; Fig. II.13). Otto et al. (2007) have identified two distinct mineralisation phases: i) the earlier mineralisation is characterised by disseminated sulphides with calc-silicate alteration (Otto et al., 2007); ii) the second phase mineralisation is defined as high-grade brittle-ductile shear zones marked by quartz veining, silicate alteration, and abundant arsenopyrite (Munyai et al., 2011). Gold mineralisation is closely associated with sulphides, mainly appearing as native gold within arsenopyrite in veins and alteration halos (Otto et al., 2007). The interpretation of New Consort mineralisation linked it to the D3 event, which is associated with the diapiric emplacement of the neighbouring Nelspruit Batholith or D4 extensional shear zone networks (Viljoen, 1963; Munyai et al., 2011).

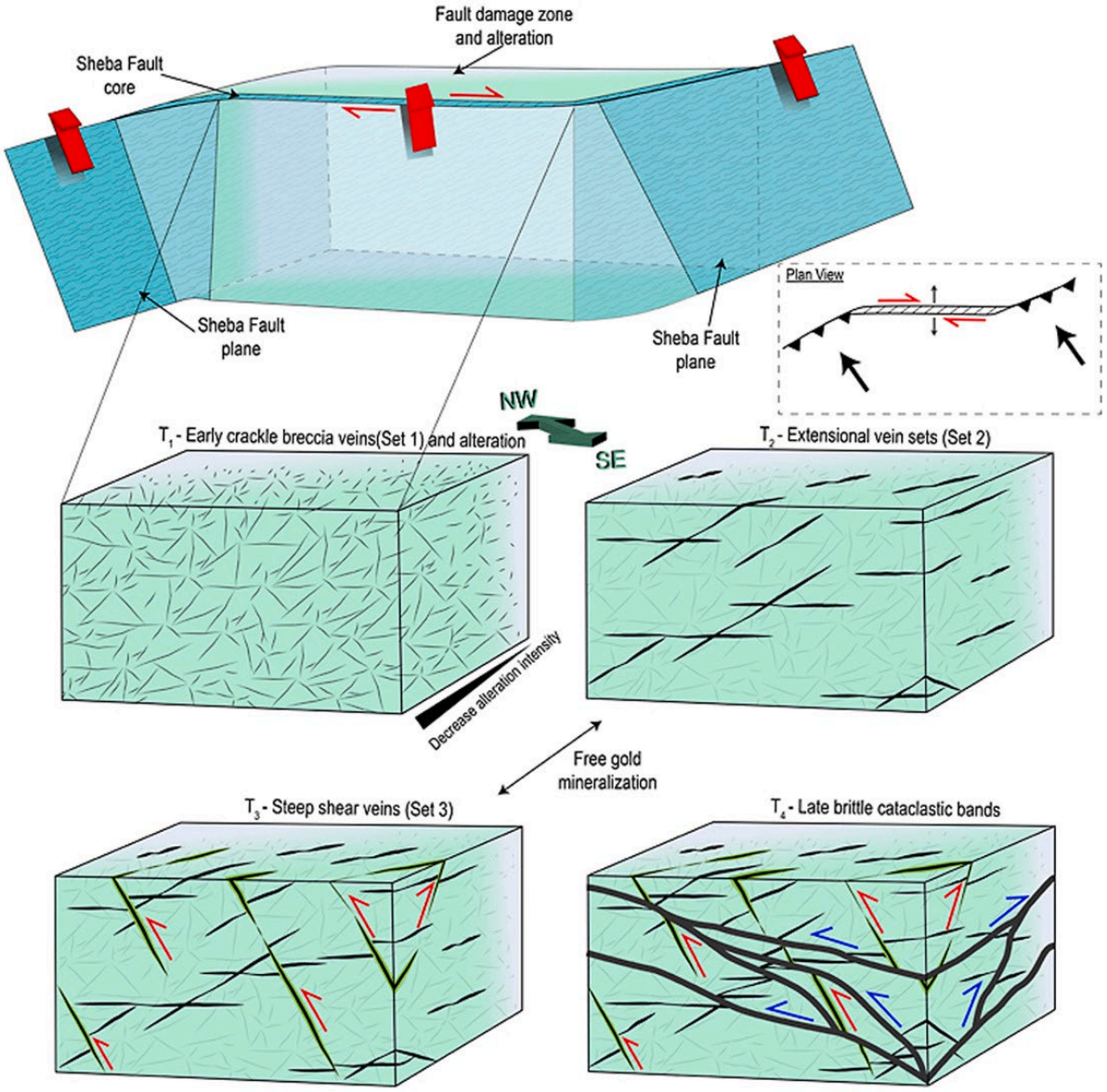

Fig. II.12. Tectono-hydrothermal model of Pintos Cerda et al. (2022) depicting the development of vein sets and brittle deformation associated with the Sheba mineralisation, structurally controlled during a NW-SE shortening event.

Few documentations have been found regarding information on the Agnes mine, former Lily Mine and in the mines around the Barbrook fault. The Agnes mine is located to the southwest of Barberton town in the Moodies Hills (Fig. II.14a). The gold ores are structurally hosted in vertical and east-west striking planes (Fig. II.14b). The host rocks is composed of siltstone and jaspilitic ferruginous shale sediments of the Clutha formation (Pearton and Viljoen, 2017).

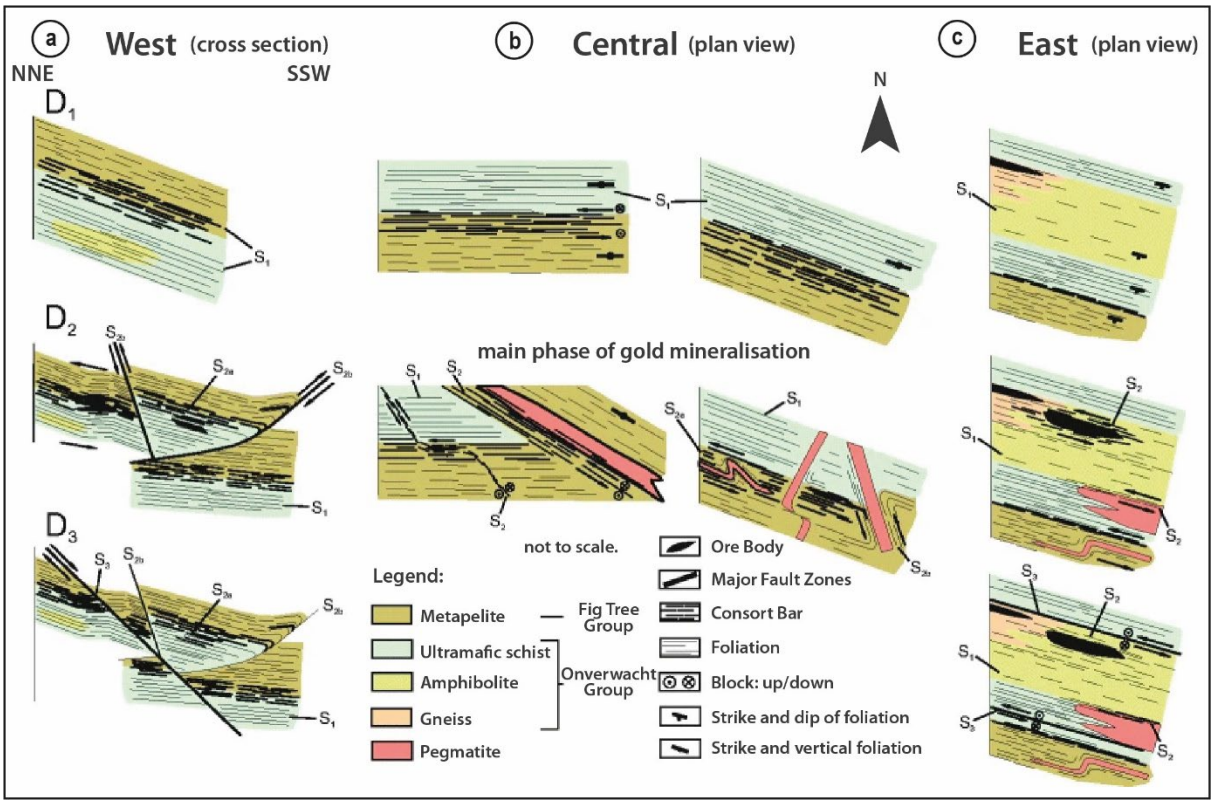

Fig. II.13. Sketches depicting the structure of the gold mineralisation and its relative timing in the New Consort mine. **(a)** Western zone, **(b)** central zone and **(c)** eastern zone (after Otto et al., 2007; legend modified).

The former Lily Mine is situated along the Lily fault, east of the Sheba-Fairview complex, with the Lily fault acting as a geological boundary between the Onverwacht Group and the Fig Tree Group. The gold ores seem to occur in abundant non-refractory pyrrhotite and minor arsenopyrite, as well as native gold associated with quartz-carbonate veins (Pearton and Viljoen, 2017). Mining operations primarily focused on quartz veins and brecciated shoots filled with quartz (Anhaeusser, 1986). The country rock in the mine is composed of shale, BIF, chert, greywacke of the Fig Tree Group, and minor ultramafic schists of the Onverwacht Group (Pearton and Viljoen, 2017).

Around the Barbrook fault in the northeastern part of the belt, several occurrences and deposits are present. Mineralisation appears to be controlled by the reactivation of regional fault planes associated with second-order sub-horizontal displacement (Anhaeusser, 1986). The gold mineralisation is described as weathered or oxidised gold ores (Anhaeusser, 1986). The lithology of the host rock consists of greywacke, shale, BIF, and chert of the Fig Tree Group (Anhaeusser, 1986).

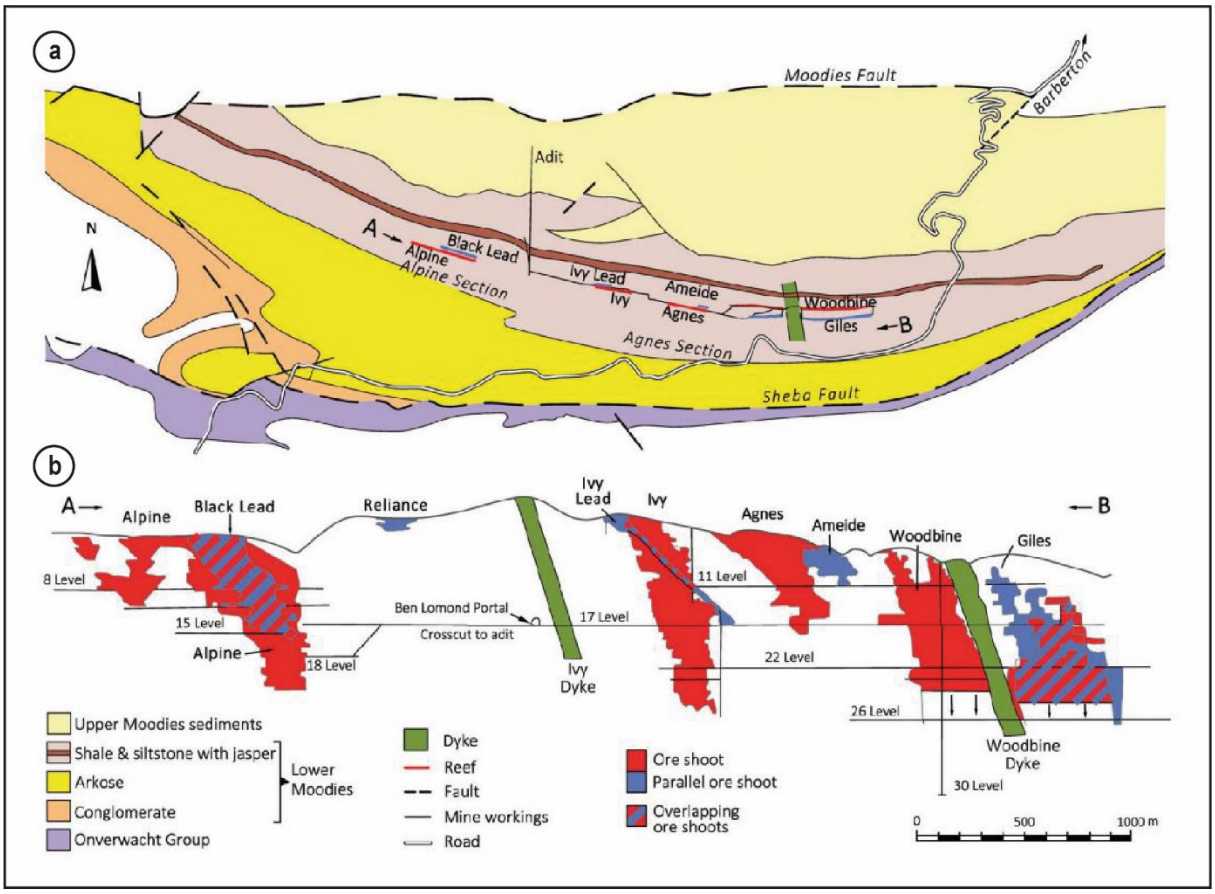

Fig. II.14. Gold occurrences and deposits of the Moodies Hills domains (from Pearton and Viljoen, 2017). **(a)** Geological map of the Moodies Hills and location of the gold mineralisation. **(b)** Longitudinal cross-section of the Agnes mines showing sub-vertical mineralisation.

Several gold mineralisation ages have been documented. These ages provide valuable insights into the temporal evolution of gold deposition:

- The oldest age for mineralisation was determined at Fairview mine by de Ronde et al. (1991), who dated a porphyry body cross-cut by the mineralisation. The obtained age is at ca. 3126 Ma using U-Pb zircon dating. They also dated a hydrothermal rutile at ca. 3084 Ma (U-Pb), which provides a lower age constraint.
- Younger ages have been reported at the New Consort mine, where a hydrothermal titanite associated with alteration was dated at around 3027 ± 7 Ma (U-Pb, Dziggel et al., 2010).
- The dating of a felsic dyke interpreted as coeval with the gold mineralisation at Golden Quarry, located near the Sheba mine, produced an age of ca. 3015 Ma (U-Pb zircon, Dirks et al., 2013).

These age determinations suggest the presence of two distinct periods of mineralisation: an older one ranging from 3126 to 3084 Ma and a younger one occurring between 3027 and 3015 Ma. This distribution of ages implies the possibility of at least two distinct mineralisation episodes, or that the dating of mineralisation events may not be tightly constrained.

Regarding the interpretation of Barberton's gold mineralisation, two main theories have been proposed based on various geological models: i) gold mineralisation may have occurred during a late stage of NW-SE regional shortening, involving the reactivation of older geological structures, leading to the deposition of gold (de Ronde et al., 1992; Gloyn-Jones and Kisters, 2019; Jones and Kisters, 2022; Pintos Cerda et al., 2022); (ii) An alternative theory suggests that gold mineralisation took place during a regional NW-SE extensional phase, which occurred after the tectonic and thermal stabilisation of the belt (Otto et al., 2007; Dirks et al., 2013).

Chapter III: Spatial Distribution of Gold ineralisation

A preliminary mapping study was conducted to enhance the characterisation of the study area in term of gold occurrences distribution and effectively identify favourable areas for potential exploration. One aim of this study is to analyse the spatial distribution of gold occurrences using Geographical Information Systems (GIS) and determine if any preferential patterns exist.

III.A. Methods

This predictive spatial analysis was performed using ArcGIS, a geospatial software developed by ESRI, that enables the collection, management, processing, analysis and editing of geospatial data. In addition, ArcGIS allows for quantitative comparison and correlation between various datasets and sources of information.

The Metallogenic map of Barberton Greenstone Belt (1 : 100 000) compiled by Ward (2000) was used as a base map for this analysis. This map was selected because it provides at once information on gold occurrences, lithology and structural geology data across the entire study area, which is the Barberton Greenstone Belt.

To extract the data from this map, it was first georeferenced using the CGS WGS 1984 coordinate system (that uses the WGS84 datum) and then digitised. Multiple layers of polygons, lines and points were created to digitise the map. Specifically, one polygon layer was created for lithology data, three polyline layers for faults, fold axial planes and dykes; and three point layers for mineralised occurrences, bedding measurements and formation labels. The greatest number of attributes were identified for each type of features, to recover as much information as possible from the base map. For example, for mineralised occurrences: their ID number, name, commodity type, deposit morphology, size, mining status, orientation (as strike direction and dip angle) and coordinates were extracted and reported under different attribute groups. This is a laborious and time-consuming step, but valuable for predictive spatial analysis, and should not be overlooked.

Once the map has been digitised, the spatial analysis can be carried out. Several ArcGIS tools were used to highlight, compare, extract and calculate data. These tools will be explained in the

subsequent section where they are employed. Additionally, three major spatial analysis methods were applied: the Inverse Distance Weighted (IDW) technique, the Weight of Evidence (WoE) method and the Kernel Density estimation. A brief description and the principle of these methods are summarised below.

III.A.1. Inverse Distance Weighted technique

The Inverse Distance Weighted (IDW) method is an interpolation technique that converts a database of points into a continuous surface represented by a raster layer (a raster layer is a grid image formed from a matrix of pixels with eigenvalues). This interpolation method calculates the value of unknown pixels located in between the points with known values, by taking a linear weighted combination of the database of points, and the weighting is an inverse function of distances. Therefore, this method assumes that the unknown values are decreasingly influenced by the increasing known value distance from a point with a known value (Bartier and Keller, 1996; Deveaud et al., 2013; Setianto and Triandini, 2015; ArcGIS - Documentation). In other words, the further away an unknown pixel is from an input database point, the less its value will be impacted by the value of the point database. Several parameters can influence this interpolation, such as barriers. Barriers are implemented as polylines that act as boundaries constraining the interpolation process.

III.A.2. Weight of Evidence method

The Weight of Evidence (WoE) method is a statistical approach widely employed in various scientific fields, particularly in medicine, and also more recently in mineral prospectivity mapping (Weed, 2005; Porwal et al., 2010). This method applies Bayes' theory of conditional probability and assumes that all the database points (e.g., the mineralised occurrences) are spatially located in predictive zones. It calculates the probability of a specific area hosting a mineralised occurrence relative to the probability of it being situated outside that area by applying linear weights based on the surface area ratio of the predictive zones (Agterberg et al., 1990; Bonham-Carter and Agterberg, 1990; Porwal et al., 2010). In simple terms, the WoE method is used to estimate the favourability of an area to host occurrences, taking into account its size ratio and the proportion of occurrences it contains.

III.A.3. Kernel Density Estimation

The Kernel Density estimation is a point-to-raster or polyline-to-raster estimation method. It is a statistical and non-parametric technique to estimate the density of the input data foreach pixel.

To calculate the density, the method employs symmetric and gradient "kernels" to image each data point, and then combines all these kernels. The result will form a smoothed estimation map reflecting the density of the input data (Silverman, 1986; Salvo et al., 2005; ArcGIS - Documentation). This method provides the visualisation of the input data distribution without assuming a data parametric distribution. In summary, Kernel Density estimation provides the output data frequency by a colour gradient, based exclusively on input data.

III.B. Results of Cartographic Analysis

The predictive spatial analysis was carried out using the digitised Metallogenic map of the Barberton Greenstone Belt (Ward, 2000; Fig. III.1).

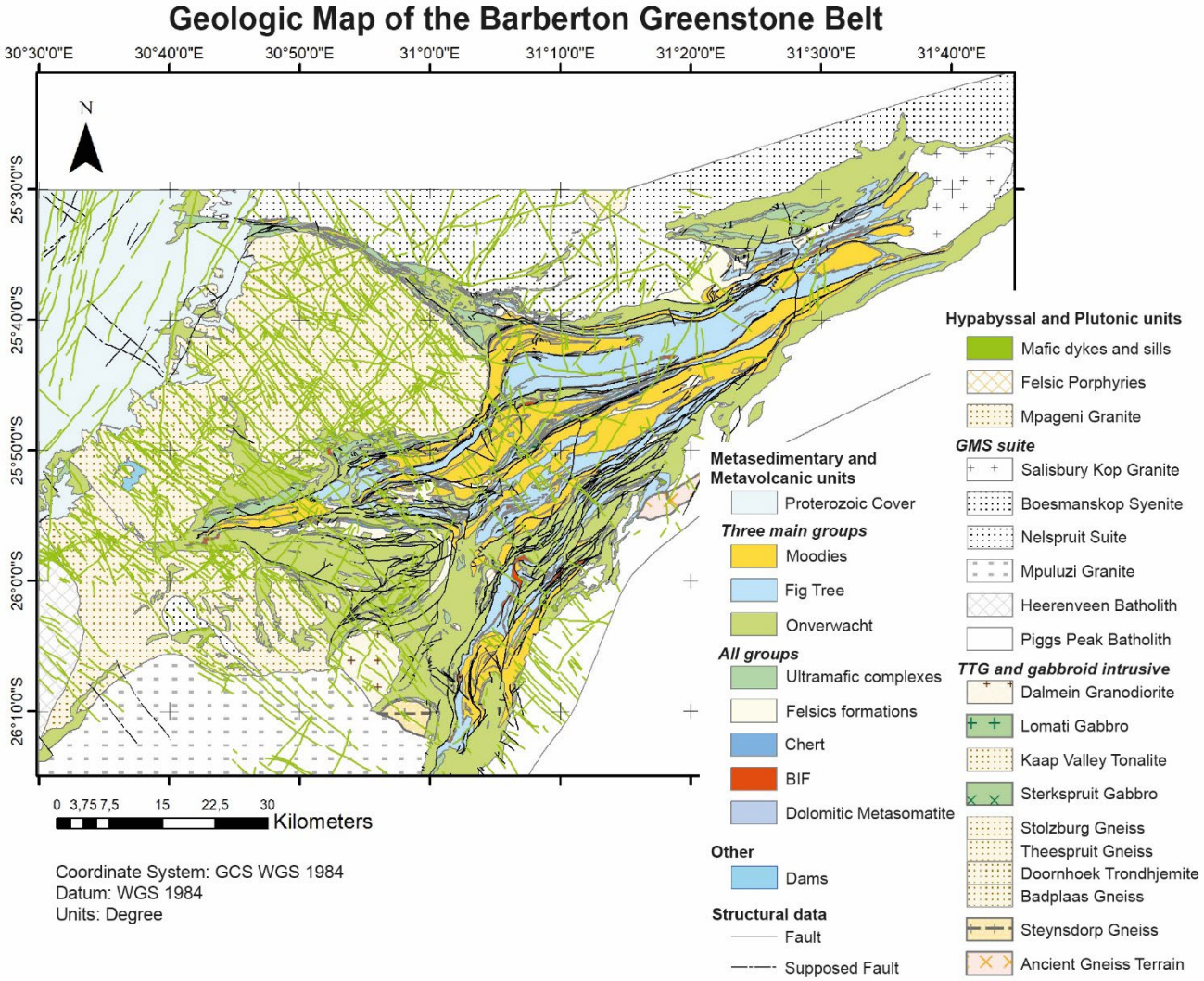

Fig. III.1. ArcGIS-georeferenced and digitised 100 000 scale metallogenic map of the Barberton Greenstone Belt (Ward, 2000).

III.B.1. Cartography of Dykes

The Belt and its surrounding plutonic rock are intersected by numerous rectilinear mafic dykes (green lines in Figure III.1). To see if a spatial pattern is emerging, the striking orientations of these dykes were extracted using the "Calculate Geometry Attributes" function. This provided the coordinates of the two extremities of each dyke, enabling the calculation of their striking directions. The data were plotted on a rose diagram (Fig. III.2), which revealed two main striking directions. The first one is NW-SE striking (green histogram in Figure III.2) and the second one strikes NE-SW (purple histogram in Figure III.2).

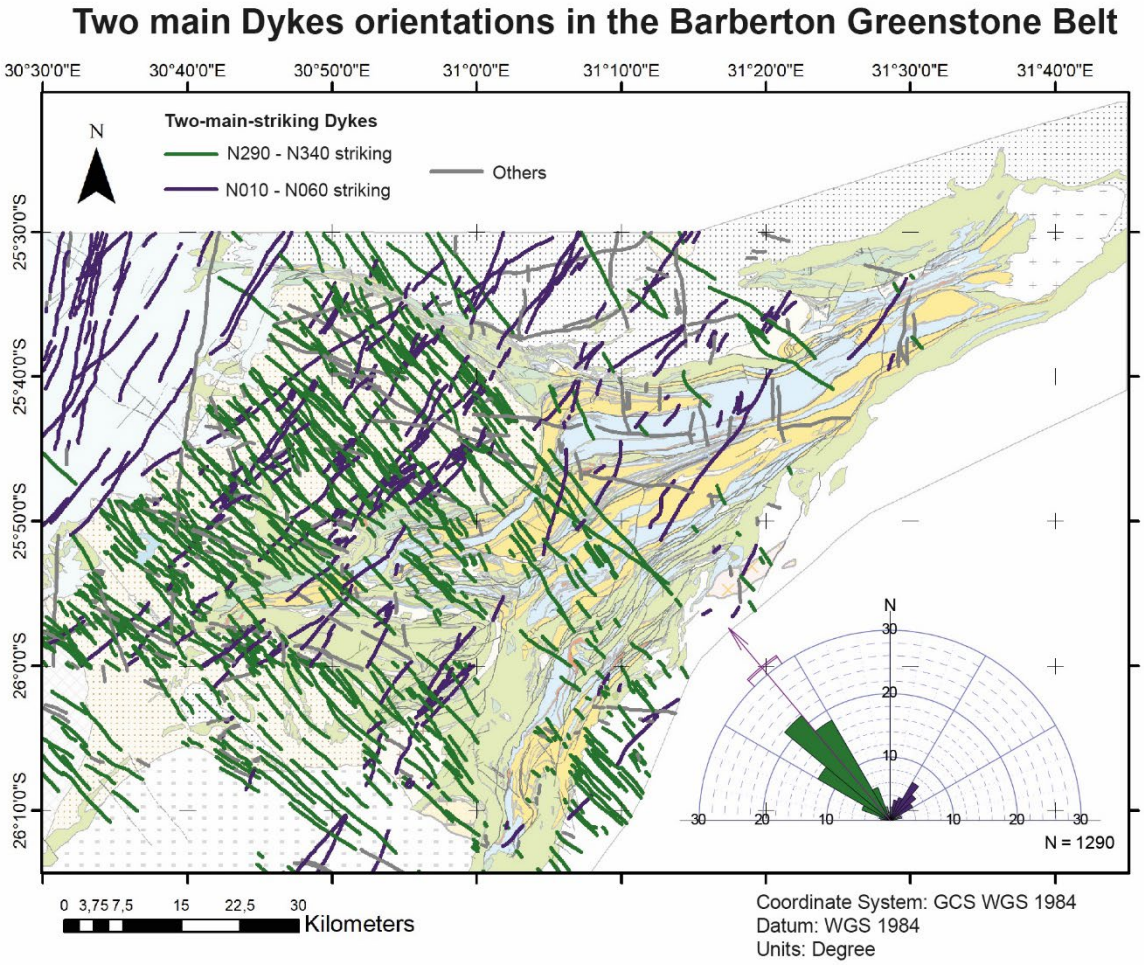

Fig. III.2. Bimodal orientations of the mafic dykes of the Barberton Greenstone Belt with the rose diagram of the two main striking directions (NW-SE striking in green and NE-SW striking in purple). Note the purple dykes transecting the Proterozoic cover in the NW part of the map.

The map in Figure III.2 shows by different colours these two main directions:

- Many NE-SW striking dykes cut the Proterozoic cover. Assuming that all these dykes belong to the same generation, even those which are not cutting the Proterozoic cover, they are interpreted to be late in the history of the BGB.
- The NW-SE striking dykes do not intersect the Proterozoic cover but intersect the late surrounding batholith of the BGB, such as the Piggs Peak Batholith, Mpuluzi Granite and the Nelspruit Batholith. This may indicate that they are earlier than the NE-SW striking dykes, although still relatively late in the BGB history.

To sum up, the mafic dykes cutting across the BGB, and the surrounding plutons appear to be structurally controlled. Two major directions emerge, suggesting by relative intersection relationship, a different timing of emplacement. As these dykes appear to be late-stage or even to post-date the formation of the BGB, their study is out of the scope of the thesis.

III.B.2. Cartography of Lithostratigraphic units

To enhance the information provided by the map of the Figure III.1, an interpolation of the formation labels (represented by red dots in Figure III.3) was attempted.

Indeed, the map includes the formation names as labels but does not detail their boundaries, the aim is therefore to define the formation boundaries. The interpolation was constrained by the unit borders as barriers (see section *I.A.1. Inverse Distance Weighted technique*) of the Moodies, Fig Tree and Onverwacht groups.

However, the outcome of the formation labels IDW interpolation (Fig. III.3) was inconclusive. The number of input data (the formations labels) was insufficient to achieve a precise and representative interpolation.

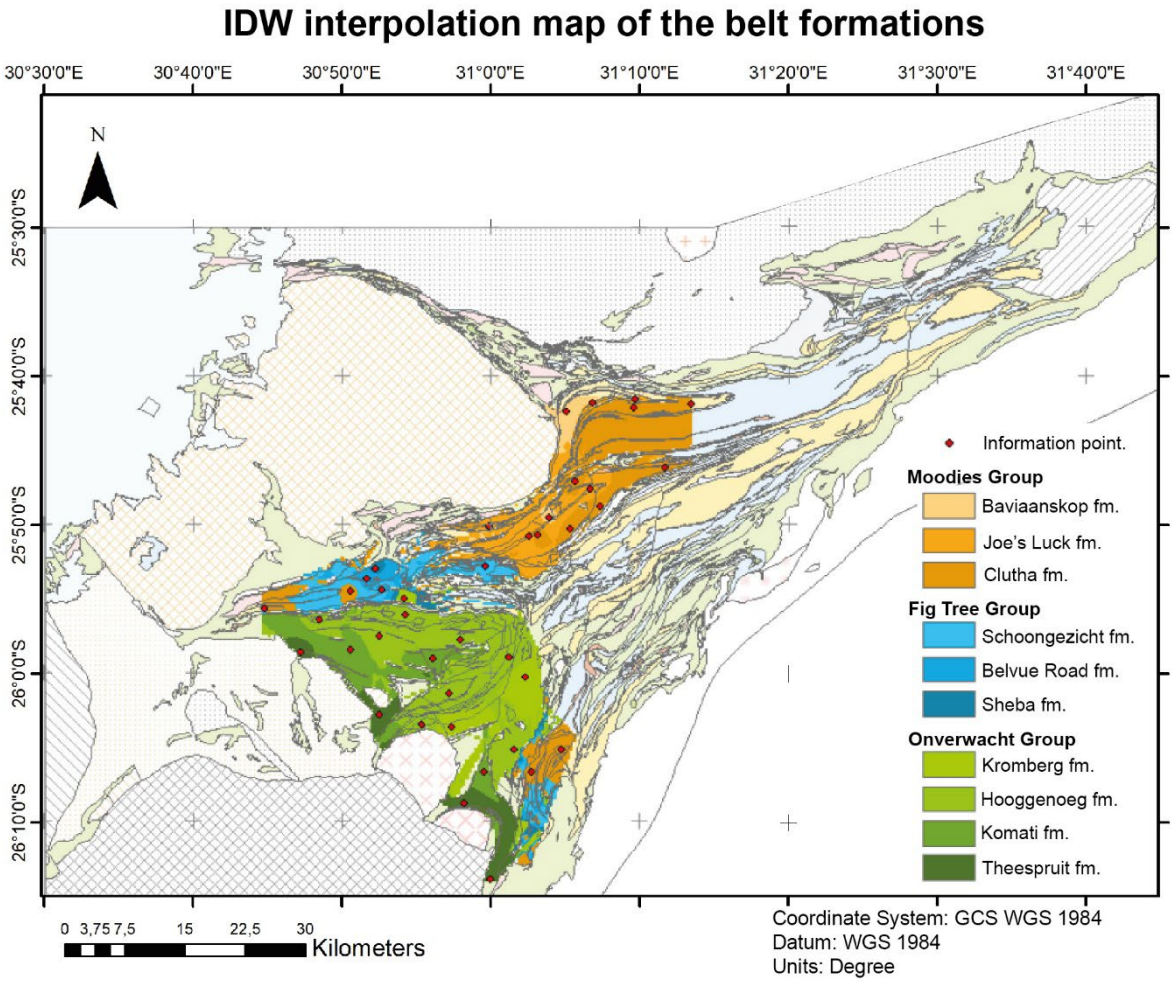

Fig. III.3. IDW interpolation map of the formation label with the Barberton Greenstone Belt geological map in the background.

III.B.3. Cartography of Bedding

The map also contains numerous bedding strike and dip data. Two IDW interpolations were conducted on these data using the fold axial planes and the faults as barriers.

- The first interpolation, displayed in Figure III.4a, represents the dip azimuth (indicated by the black arrow in Figure III.4a) and dip (colour bar in Figure III.4a) over the entire study area. The map reveals that the majority of beds in the belts are sub-vertical, as indicated by the prevalence of yellow-green colours in Figure III.4a, representing beds with a dipping greater than 70°.

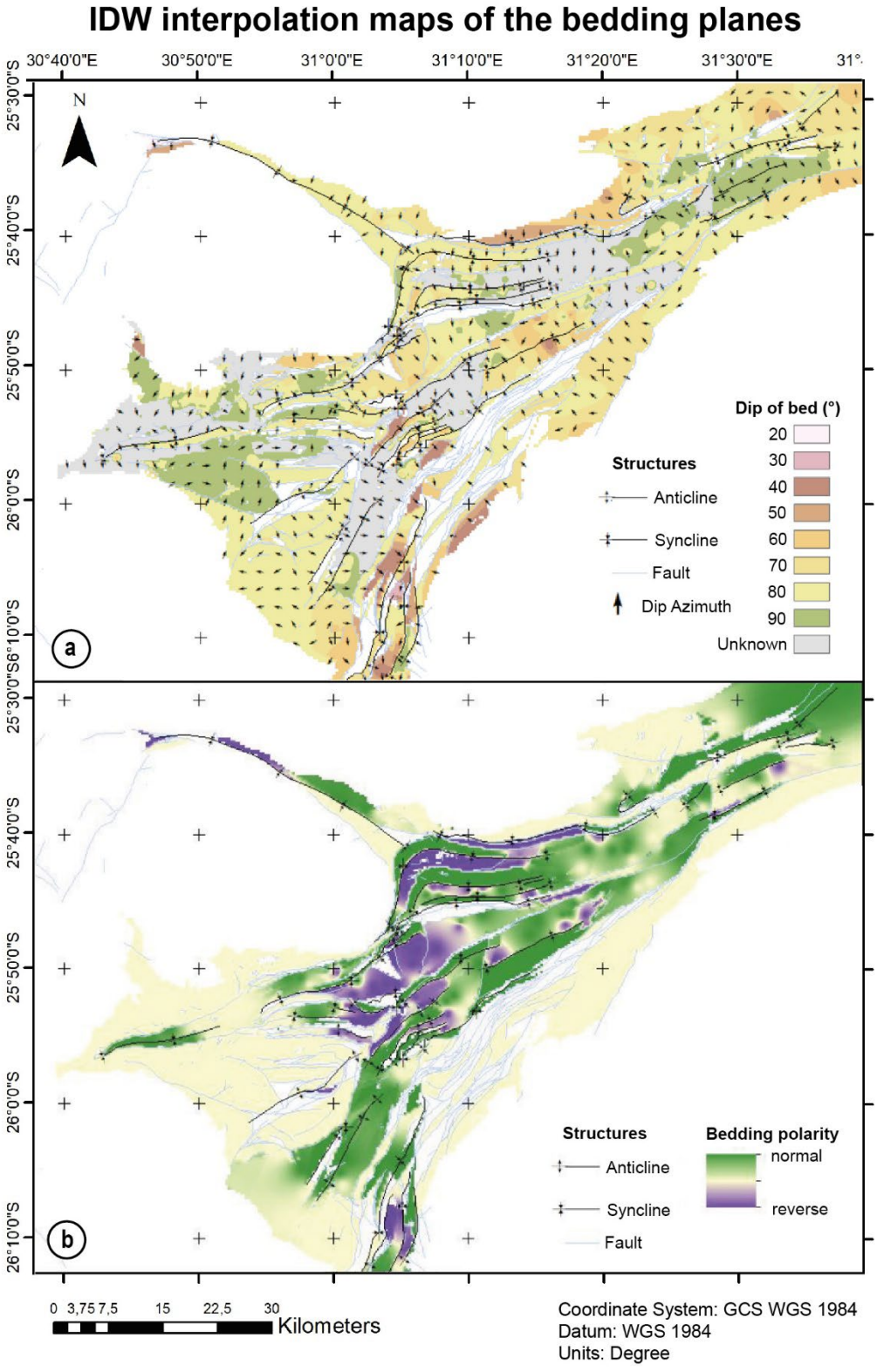

Fig. III.4. IDW interpolation maps of bedding data. **(a)** IDW interpolation map of the strike and dips of the bedding data of the Barberton Greenstone Belt, the arrow shows the Dip Azimuth of the bed and the dip of the colours map. **(b)** IDW interpolation map of the polarity of the bedding data of the Barberton Greenstone Belt, (in green the normal polarity beds and in purple the reverse polarity beds). Grey- and light-yellow-shaded zones are areas with no available information.

- The second IDW interpolation, shown in Figure III.4b, focuses on the strike and dip data to give access to the bedding polarity. This figure represents the interpolation of the bedding polarity (reverse polarity depicted by shades of purple colours). It should be noted that due to numerous faults cutting across the belt, particularly in its western part, several areas leak information or have poorly defined data in Figure III.4b.

III.B.4. Cartography of Mineralised occurrences

The Barberton Greenstone Belt host numerous mineralised occurrences, mainly gold occurrence but also asbestos, iron, baryte, verdite, etc. (Fig. III.5). These occurrences are contained in several morphology deposits, most of them are identified on the map as 'mineralised shear zone', ‘vein’, ‘stratiform’, ‘stockworks’ and ‘placer’. Scattered other morphologies are present like ‘irregular/disseminated or ‘pegmatite’ morphology deposits. This study will focus on gold occurrences.

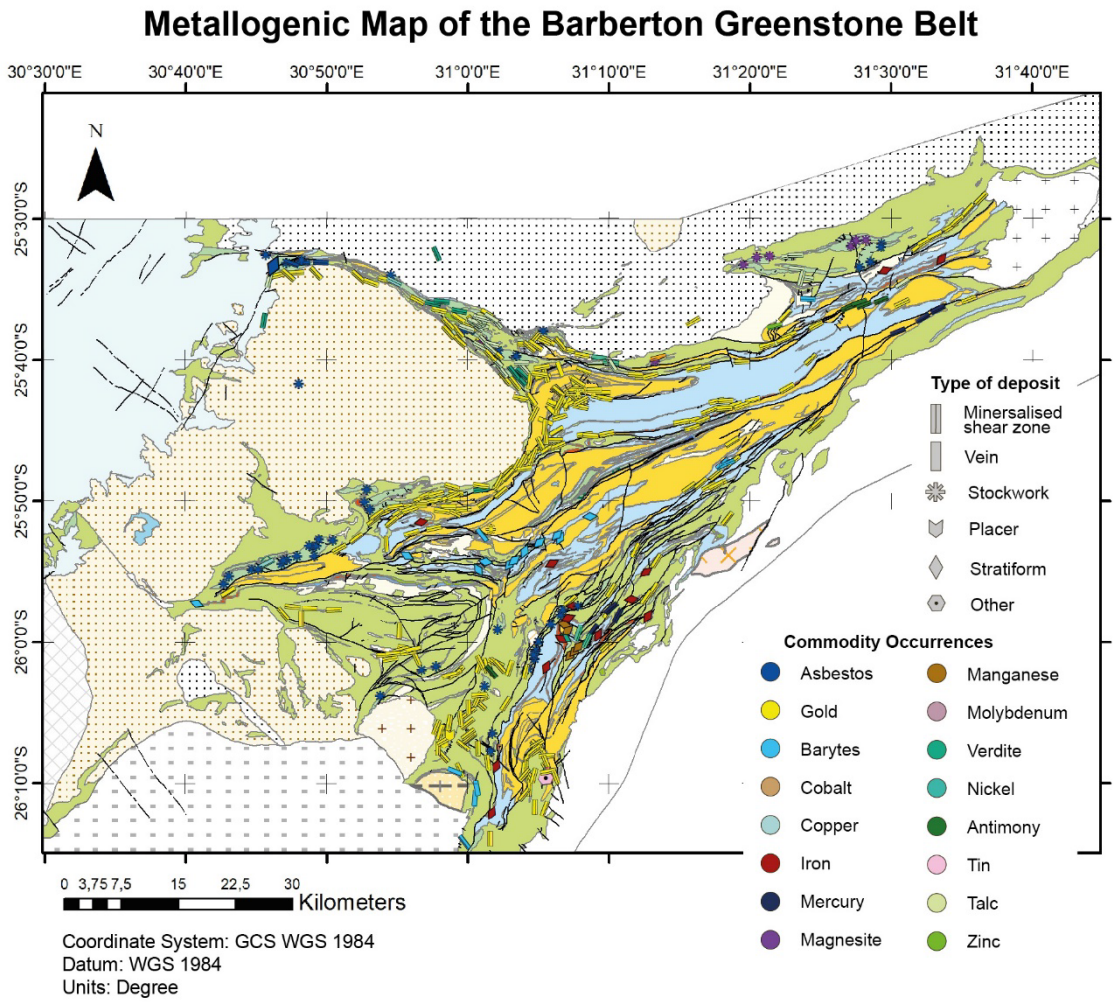

Fig. III.5. Metallogenic Map of the Barberton Greenstone Belt digitised on ArcGIS based on the metallogenic map of the Barberton Greenstone Belt (Ward, 2000).

III.C. Gold distribution

The Barberton Greenstone Belt contains 265 gold occurrences according to the Metallogenic map (Ward, 2000). These occurrences are classified into five deposit sizes (in kg, Fig. III.6), and categorised based on morphology. The most common morphology is the 'mineralised shear zone' with 255 gold occurrences. The second most represented morphology is the ‘vein’ morphology with six deposits. ‘Stockwork’ and ‘placer’ each have two occurrences, making them the least common morphologies.

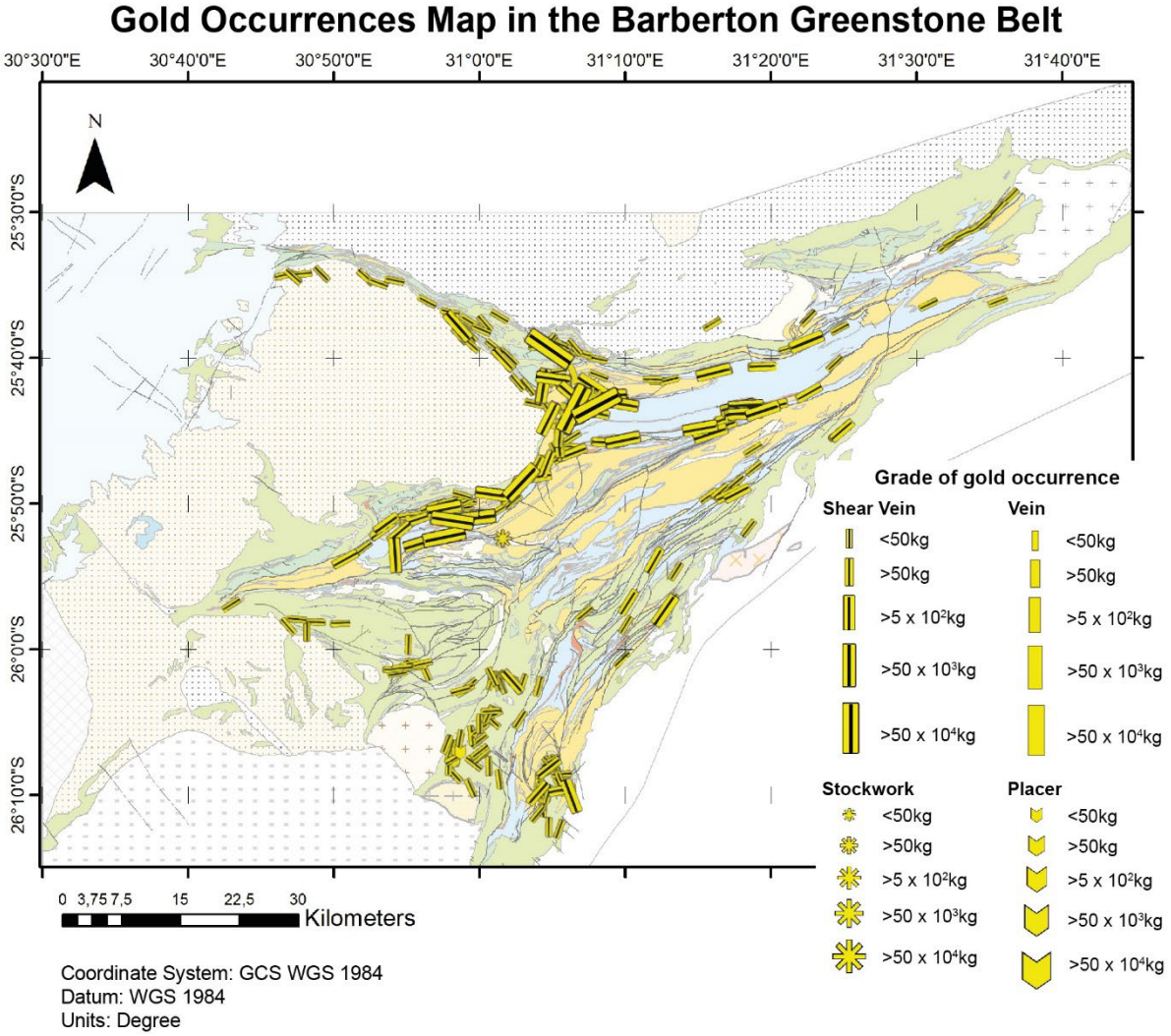

Fig. III.6. Gold occurrence map of the Barberton Greenstone Belt, the symbology shows the different types of the morphology of the occurrences and the size of the gold grade.

These occurrences are not homogeneously distributed on the map (Fig. III.6). To understand the heterogenous distribution of these deposits, several factors will be investigated using spatial analysis tools.

III.C.1. Lithostratigraphy control?

In Figure III.6, the gold occurrences seem preferentially localised in the belt, indeed a very low number of occurrences are hosted in the surrounding plutons. The lithostratigraphy control of the gold occurrences was therefore investigated.

To test the impact of the lithostratigraphy on the gold occurrence distribution, a join was created between the gold occurrence point layer and the lithostratigraphy category polygon layer. This join layer provides the lithological group attributes for each occurrence, indicating the lithostratigraphy category of the host rock. By performing a simple frequency calculation on the newly created join layer, the number of gold occurrences for each lithostratigraphic group was determined. The results show that the Onverwacht Group contains 129 occurrences, the Fig Tree Group hosts 49 occurrences, the Moodies Group has 41 occurrences; and small sub-units of BIF contain 13 gold occurrences, the ultramafic complex in the northwestern part of the belt hosts 11 gold occurrences, the dolomitic metasomatite eight occurrences and the chert five occurrences; among the hypabyssal and plutonic units, the Kaap Valley Pluton has the highest number of occurrences with seven, followed by the felsic porphyries group and the Nelspruit Suite with one occurrence each. The map representing the number of gold occurrences by lithostratigraphic category with red gradient is shown in Figure III.7a. The BGB is depicted in deeper red colours and the surrounding granite is shown in a lighter shade of red. It is here demonstrated that the belt bears the majority of the gold occurrences. The Kaap Valley tonalite, northwest of the belt (Fig. II.2), singularly contains more gold occurrences than the other surrounding plutonic rocks.

However, this processing method does not accurately represent the lithostratigraphic control of the gold occurrences, as it is too dependent on the unit size. For example, a larger unit is statistically more likely to contain more occurrences. To address this bias, the Weight of Evidence method was applied. The number of gold occurrence for each unit was weighted by the unit size. Figure III.7b shows the results of the WoE analysis, a unit is considered favourable if its ratio is higher than one. According to this method, the units most likely to contain gold occurrences, in order of favourability, are the dolomitic metasomatite sub-unit, the BIF sub-unit and the Onverwacht Group. All other lithostratigraphic categories exhibit a negative favourability index and are therefore unfavourable for hosting gold occurrences.

These results will be discussed in the *III.D. Synthesis* section.

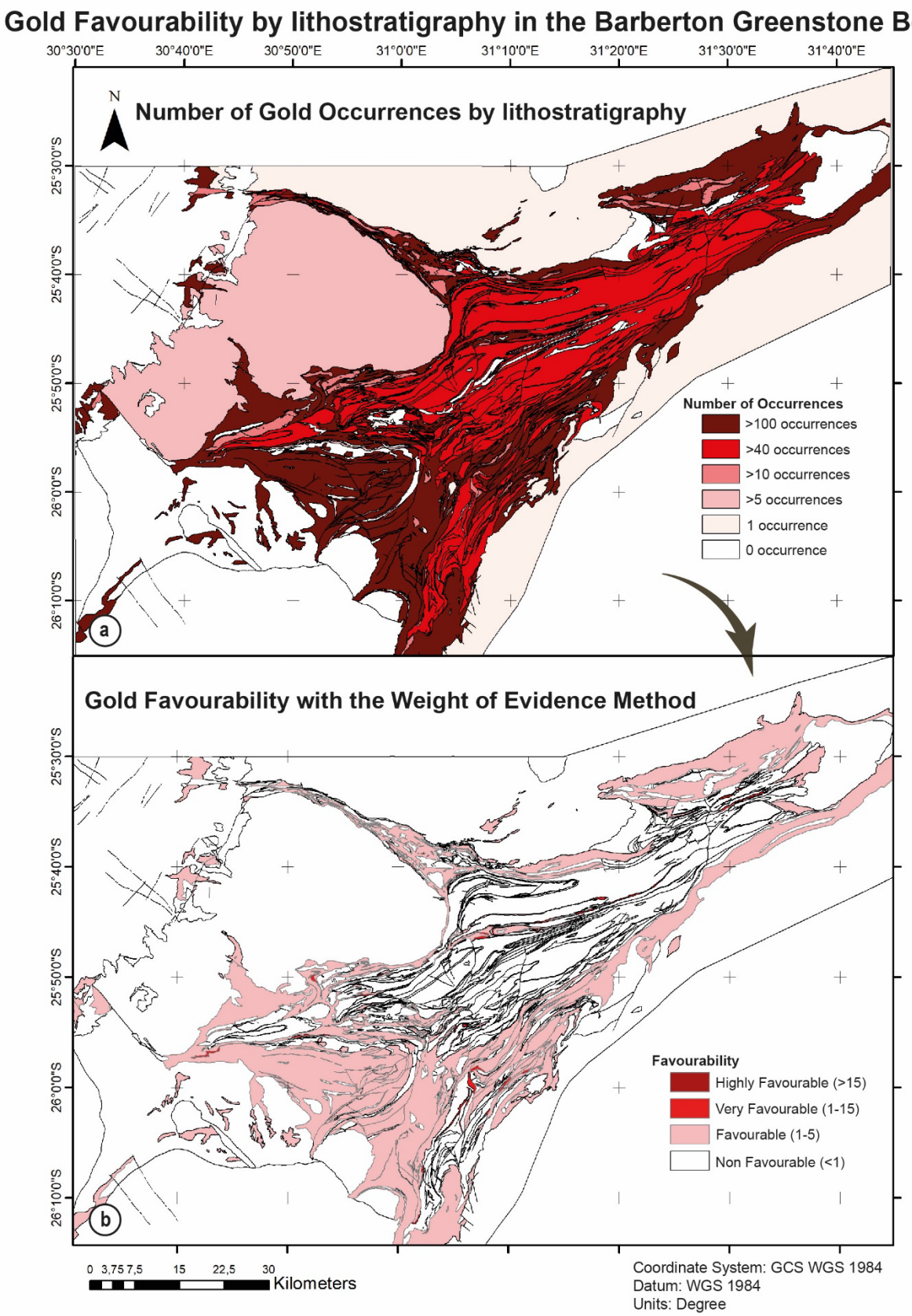

Fig. III.7. Gold Favourability of the lithostratigraphic units in the Barberton Greenstone Belt. **(a)** Number of gold occurrences per lithostratigraphy classified by colour (few occurrences in light pink and numerous occurrences in dark red). **(b)** Gold occurrence favourability with the weight of Evidence Method (non-favourable in white and highly favourable in dark red).

III.C.2. Structural control?

The 'mineralised shear zone' and 'vein' gold occurrence– i.e., the gold occurrences majority – are reported in the map with an information about their strike. The strike data for these occurrences have been extracted and presented in a rose diagram (Fig. III.8). It reveals that most gold occurrences have an orientation ranging from NE-SW to E-W, although a peak of NW-SE striking data is also observed. Gold occurrences, therefore, appear to be structurally controlled.

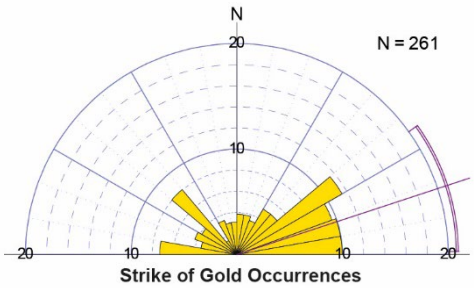

Fig. III.8. Rose diagram of the gold occurrence strikes. Note the main clusters: NE-SW to E-W and NW-SE trends.

The structural control of the gold occurrences is investigated below, according to the major belt structures, i.e., folds and faults.

III.C.2.1. Axial planes control?

When the gold occurrences are plotted on a map alongside the axial planes of the main folds (Fig. III.9a), they seem to be predominantly located in close proximity to these folds. To study the influence of these folds on the occurrences, buffer zones were created to highlight the occurrences near these folds. The largest folds have an average wavelength of 5-6 kilometres, so the buffer zone radius has been set at 3 km, to encompass as many occurrences as possible within the folds (Fig. III.9b). These buffers were generated using the buffer tool in ArcGIS. Out of the 265 gold occurrences, 194 were identified within a buffer zone of a 3 km radius around the axial planes, i.e., ca. 73%.

Strike data from the main axial planes were extracted (processed the same way as dykes, section *III.B.1. Cartography of Dykes*) and compiled in the Figure III.9b rose diagram. These fold axial planes exhibit a predominant striking direction ranging from NE-SW to ENE-WSW. As most of the gold occurrences have a preferential strike (Fig. III.8), a comparison was made between the gold occurrences strikes and closest axial plane strikes.

To facilitate the comparison of these two orientations, the angular differences have been calculated. A join between the occurrences layers and the buffers was made, giving access to the nearest axial plane attribute table data for each occurrence. By performing a subtractive calculation of the occurrence and fold axial plane strikes, the angular difference between the occurrence and fold axial plane directions was obtained.

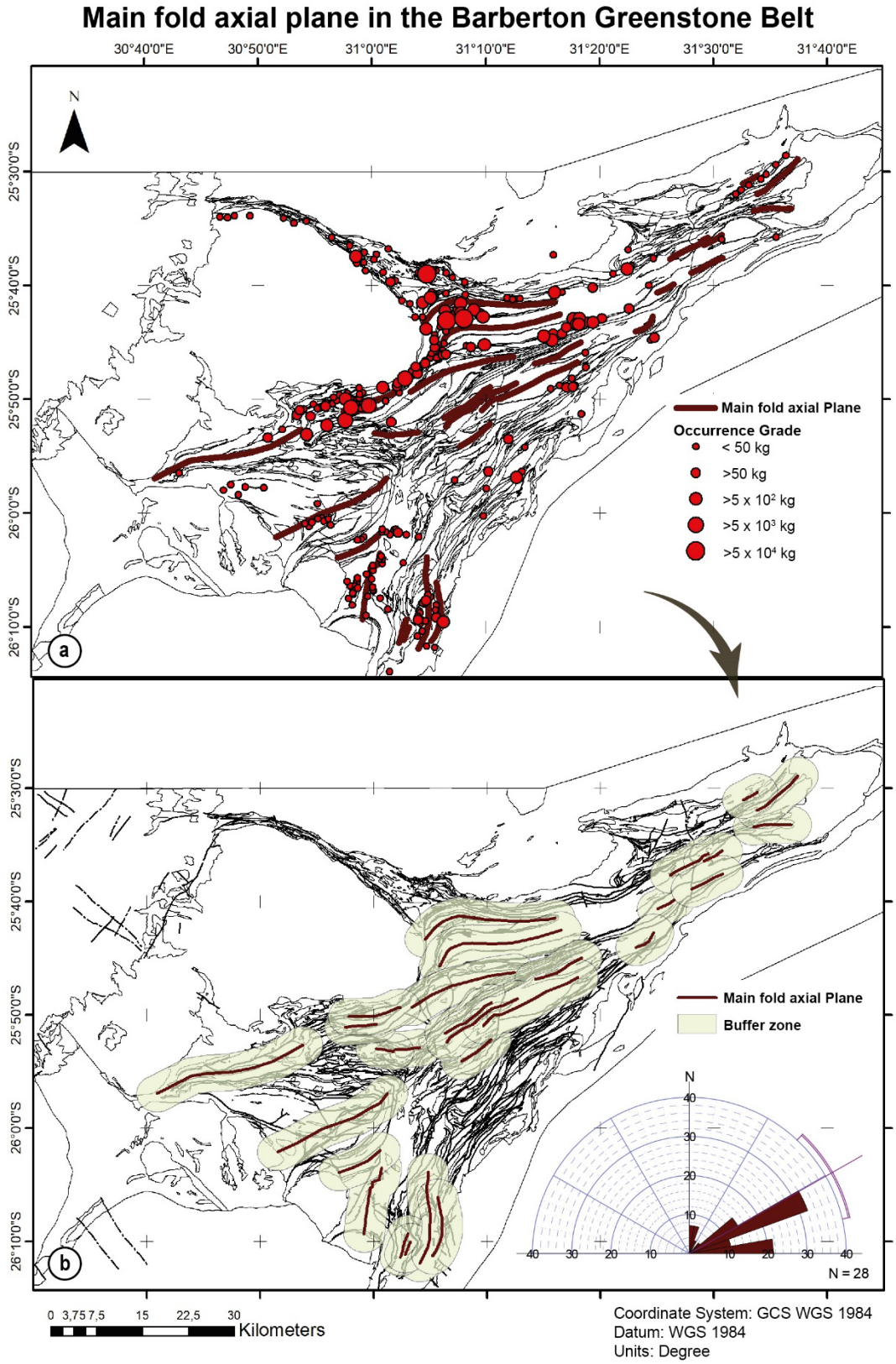

Fig. III.9. Main-fold axial plane map of the Barberton Greenstone Belt. **(a)** Main-fold axial plane (thick dark red line) and gold occurrences (red dots) map of the Barberton Greenstone Belt. Note the numerous gold occurrences close to the folds. **(b)** Main-fold axial plane and buffer zone (beige polygon) map and Rose diagram of the fold axial plane striking direction. Note the NE-SW to ENE-WSW main direction in the rose diagram.

The result of this calculation is illustrated in Figure III.10, which includes a map displaying occurrences of different colours according to their angular difference, as well as a colour pie chart representing the proportions of the occurrences according to their angular difference.

Overall, the angular difference between the orientation of the deposits and the orientation of the nearest axial plane is fairly small (58% of the gold occurrence have an angular difference less than 22,5°).

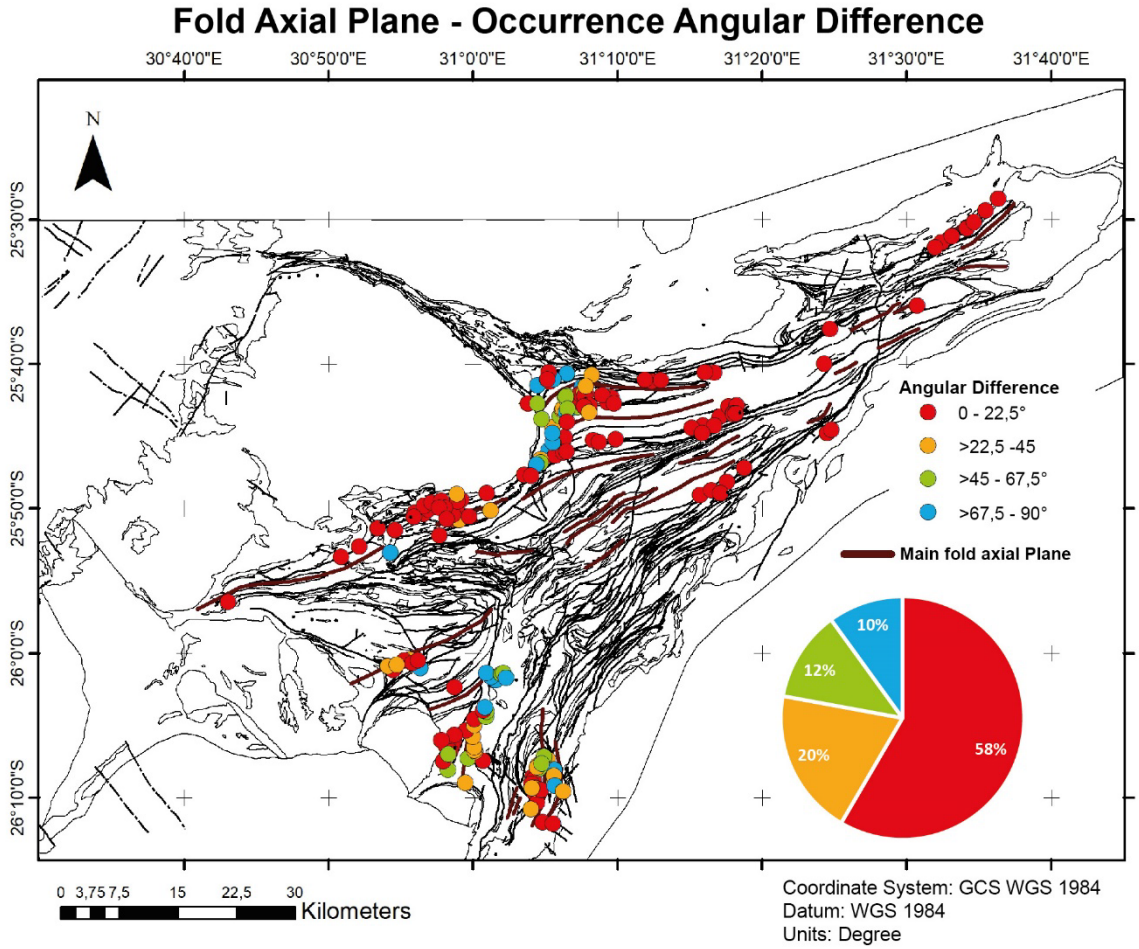

Fig. III.10. Map showing the angular difference between the strikes of the first-order axial planes and their closest gold occurrence; and the colour pie chart representing the gold occurrence proportions according to their angular difference from the nearest axial plane. Red colour represents occurrences sub-parallel to the nearest axial plane, and the blue colour the highly oblique to sub-perpendicular occurrences. Note that the gold occurrences represented here are in the buffer zone of Figure III.9b and have a reported strike direction on the map (shear vein and veins only, Fig. III.6).

III.C.2.1. Fault control?

Similar to the study on folds, an analysis was conducted to examine the influence of faults on the gold occurrence distribution. Figure III.11a illustrates a map displaying the gold occurrences alongside the faults, the gold occurrences appear to be in close proximity to the faults.

To assess the control of these faults on the gold occurrences, similar to the approach used for folds, buffer zones were created to investigate the occurrences in the vicinity of faults. According to existing literature, the damage zone of a fault generally extends a few hundred metres wide, with a maximum thickness of around 1000 m (Savage and Brodsky, 2011; Torabi and Berg, 2011; Solum and Huisman, 2017). Therefore, a buffer with a radius of 500 m was established to encompass as many occurrences as possible near a fault (Fig. III.11b). A total of 179 gold occurrences were identified within a fault buffer zone with a 500 m radius, representing approximately 67% of all the gold occurrences.

The fault shape is not rectilinear, but in some places very curved. To obtain the fault orientations that are as representative as possible of reality, the faults were manually truncated. From the fault segments, the fault striking directions were calculated in the same way as for the dykes. The striking directions of the faults were then extracted and presented in the Figure III.11b rose diagram. The majority of the faults are NE-SW striking.

To compare the variation in strike angles between the gold occurrences and the faults, a similar approach to the one used for folds was employed. A join was established between the occurrence layers and the buffer layers. This join facilitated the retrieval of the nearest fault attribute table data corresponding to each occurrence, enabling the calculation of the angular difference. The output of the angular difference is illustrated in Figure III.12, with a map displaying occurrences with different colours according to their angular difference. Additionally, a colour pie chart illustrates the proportions of the occurrences according to their angular difference.

The findings indicate that a significant number of gold occurrences exhibit similar strike directions to their nearest fault (approximately 60% of occurrences have an angular difference inferior to 22.5°).

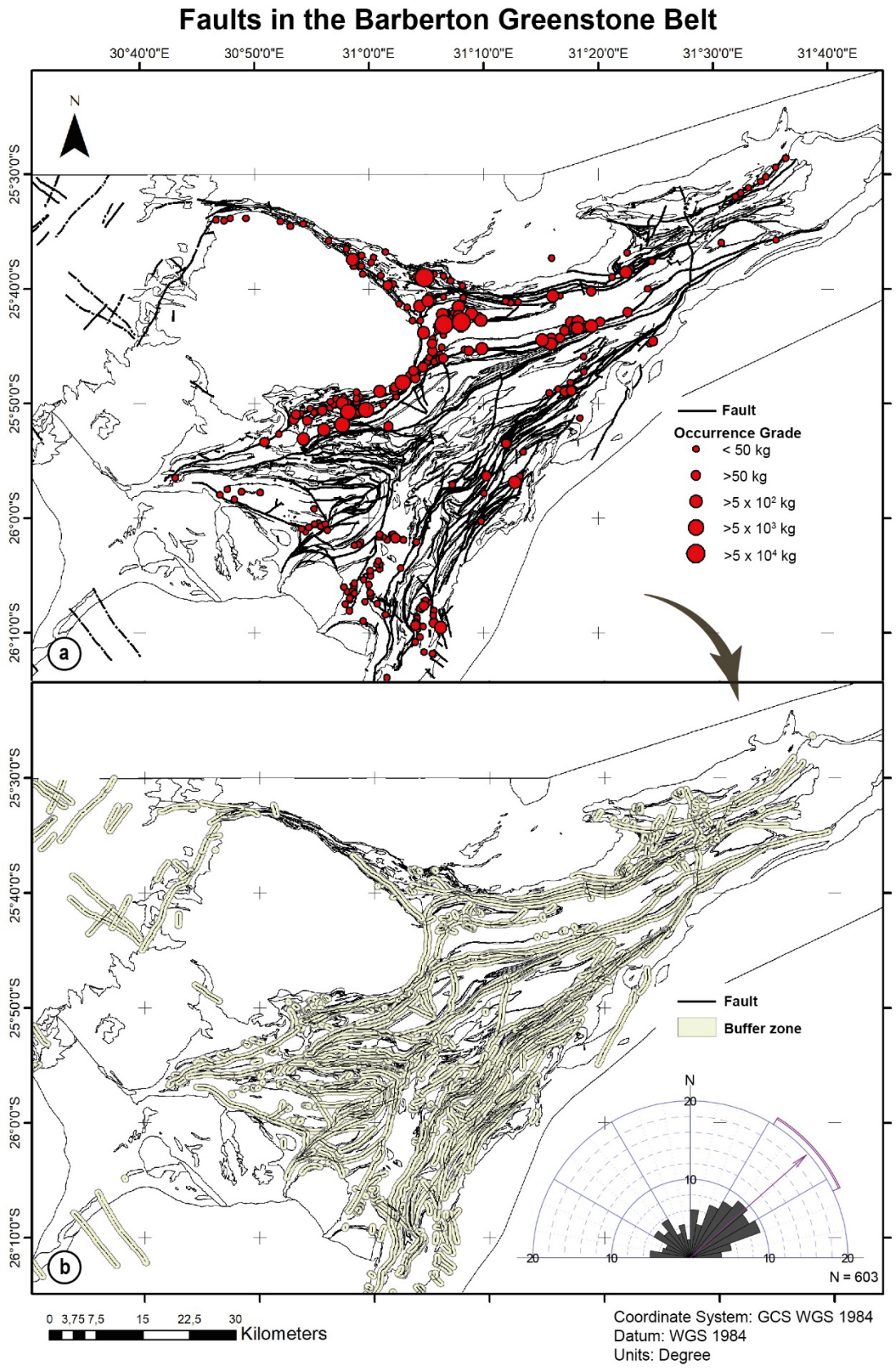

Fig. III.11. Faults map of the Barberton Greenstone Belt. **(a)** Faults (thick black line) and gold occurrences (red dots) map of the Barberton Greenstone Belt. Note the numerous gold occurrences close to faults. **(b)** Faults and their associated buffer zones (beige polygon) map and rose diagram of the faults striking direction. Note the NE-SW main direction in the rose diagram.

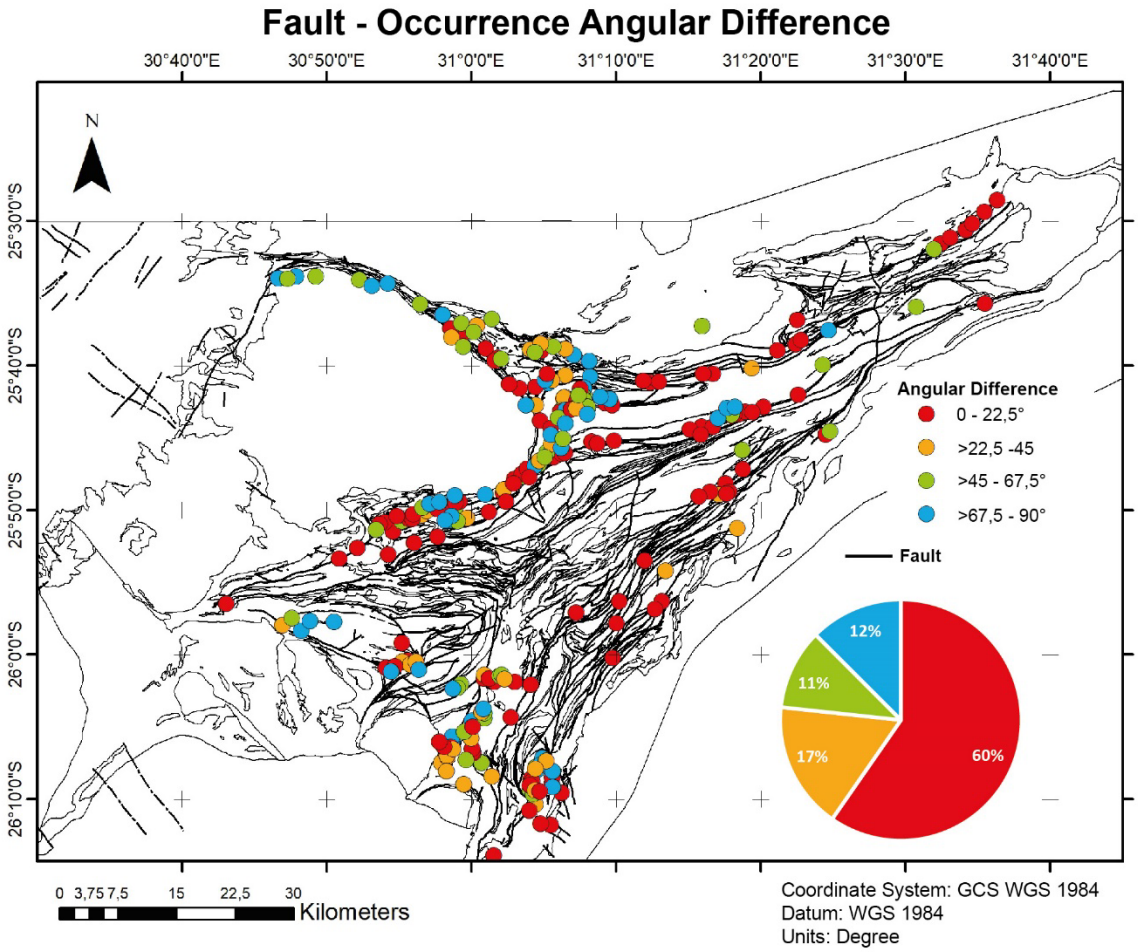

Fig. III.12. Faults and their closest gold occurrence striking direction angular difference map; and the colour pie chart representing the gold occurrence proportions according to their angular difference from the nearest fault (red colour represents occurrences sub-parallel to acute angle to the nearest fault, and the blue colour the sub-perpendicular to highly oblique occurrences). Note that the gold occurrences represented here are in the buffer zone of Figure III.11b and have a strike direction (shear vein and veins only, Fig. III.6).

III.C.3. Spatial control?

In the previous sections, the connections between the gold occurrences and lithostratigraphy, and the major structures were examined. However, in the central part of the belt as well as its north-eastern and western extremities, there are relatively few gold occurrences despite a 'favourable' lithology or the existence of numerous folds and faults (Figs. III.7, III.9 and III.11). Therefore, the spatial distribution of occurrences will be studied.

Each occurrence is associated with an attribute representing the deposit size. These sizes were interpolated using the IDW method to visualise the spatial location of high-grade areas, i.e., regions with a high concentration of gold. In this interpolation, it was considered that the main

faults and axial planes acted as geospatial barriers for the interpolation (see section *III.A.1 Inverse Distance Weighted technique*).

The result of this interpretation is presented in Figure III.13, displayed as a grey gradient. Overall, the northern part of the belt appears more likely to contain high gold grades, particularly in the junction with the Jamestown Schist Belt. The limit between north and south seems to be bounded by the Barbrook and Saddleback faults (Figs. III.13 and III.15). The southern part of the belt exhibits a very low-grade concentration of gold, even though there are localised areas of higher grade.

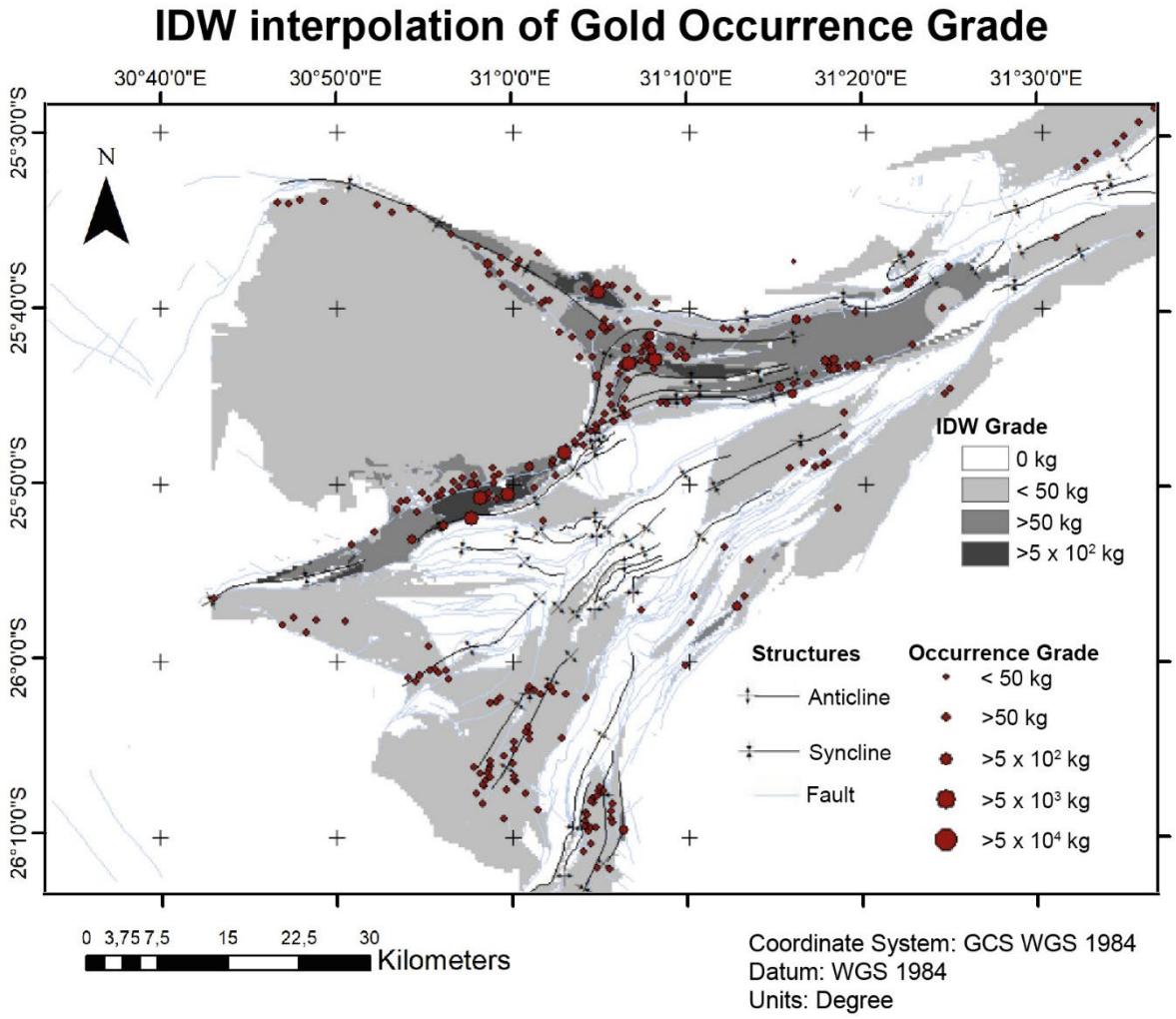

Fig. III.13. IDW interpolation (grey shades) of the gold grade (size of the red dot) in the Barberton Greenstone Belt.

Another method used to visualise the spatial distribution of gold occurrences is the Kernel density estimation, implemented through the kernel density tool in ArcGIS. The result of this analysis is depicted in Figure III.14, where the density is represented by blue colour gradient.

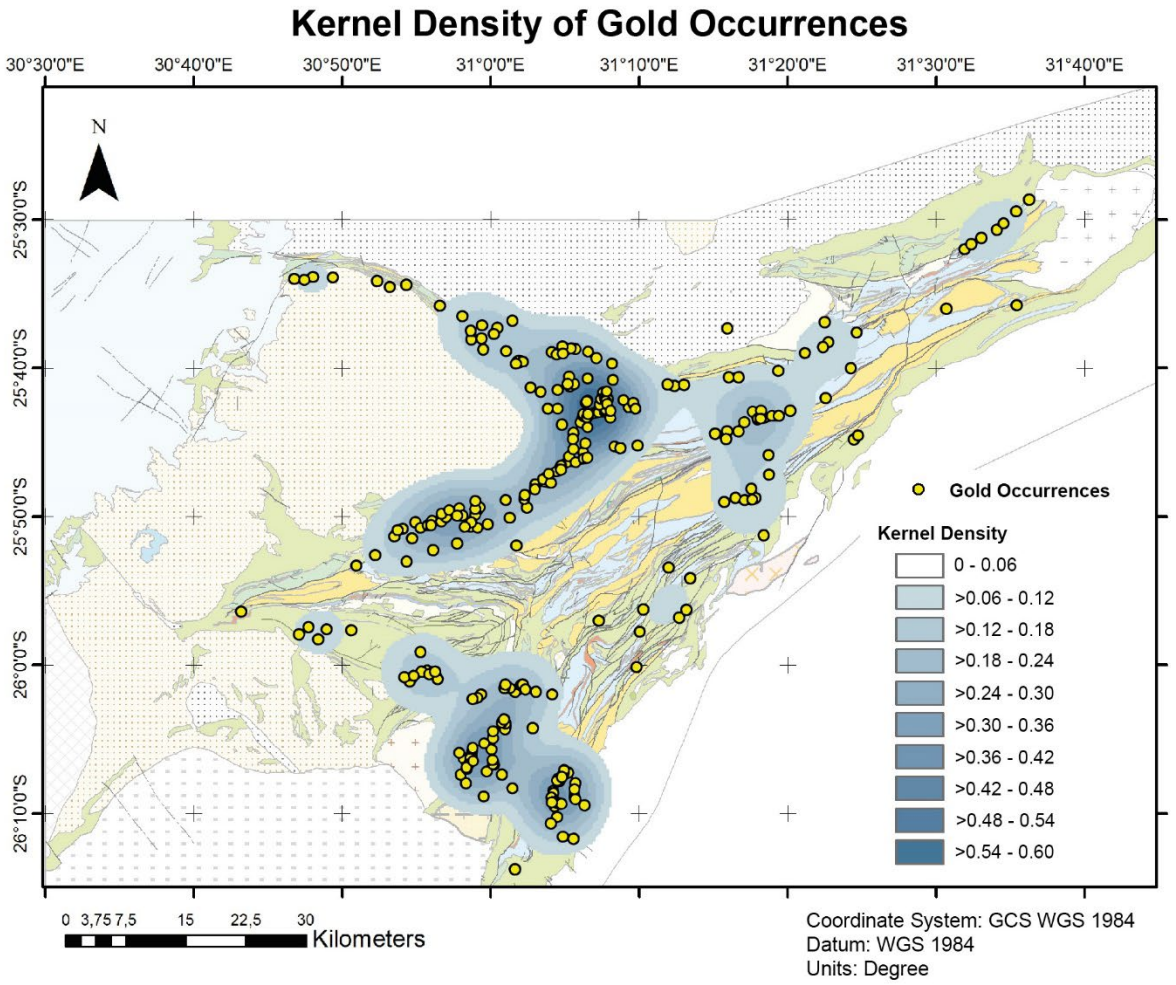

Fig. III.14. Kernel Density (blue shades) of the gold occurrences (yellow dot) with the Barberton Greenstone Belt geological map in the background.

The density map reveals several clusters of gold mineralisation, with four main clusters identified.

- i) The largest cluster forms a crescent shape around Barberton town, encompassing the Sheba-Fairview area (Figs. III.14 and III.15).
- ii) and iii) There are two round clusters around the Steynsdorp and Malolotja regional folds, which are very close together.

- iv) A smaller cluster is observed along the Barbrook fault near the Shiyalongubo dam (Figs. III.14 and III.15).

Occurrences outside these clusters seem more scattered.

III.D. Synthesis

The predictive spatial analysis enables the examination of the relationships between various parameters and gold occurrences to identify any emerging patterns.

It appears that the gold-bearing/related occurrences are predominantly distributed within the volcano-sedimentary part of the Barberton Greenstone Belt, although some occurrences are also found within the outer margins of the surrounding plutons, particularly in the Kaap Valley tonalite (Fig. III.7a). According to the Weight of Evidence method, the most favourable lithostratigraphic units for hosting gold occurrences are the dolomitic metasomatite, the BIF and the Onverwacht Group (Fig. III.7b). However, it should be noted that the dolomitic metasomatite and BIF layers are mapped as sub-units that could belong to any of the three groups of the belt (Moodies, Fig Tree and Onverwacht groups). Therefore, the results presented in Figure III.7b need to be interpreted with caution as the presence of these sub-units may distort the favourability assessment. Additionally, the WoE favourability map (Fig. III.7b) does not align with the occurrence distribution (Figs. III.6, III.13 and III.14). This raises questions regarding the lithostratigraphic influence on the gold occurrence distribution. While it is clear that the gold occurrences are more localised in the supracrustal rocks of the belt, particularly in the Onverwacht group, there does not appear to be an obvious lithological control on the gold occurrences.

Gold occurrences appear to be structurally controlled, as evidenced by the observation of a preferential direction (Fig. III.8). Although many gold occurrences are found in the vicinity of folds and faults, it is questionable how much weight these have on the structural control of occurrence. The angular difference between the occurrence orientation and the folds or faults orientations may provide some indications (Figs. III.10 and III.12). However, this method has limitations due to the fact that fault and fold zones can exhibit different styles and orientation of fractures and faults (e.g., a fold can have oblique fractures, axial plane perpendicular fractures or axial plane parallel fractures). Consequently, quantifying the influence between these occurrences and nearby folds and faults is challenging using a spatial analysis approach, and clearly ground truthing is required to address these issues. Another problem, in studying

the link between occurrences and major structures, lies in the fact that numerous major belt structures were formed by repeated episodes of NW-SE shortening (e.g., de Ronde and de Wit, 1994; Lowe, 1994; Dziggel and Kisters, 2019; see *Chapter II Geological Setting*). Therefore, even if a structural link between a structure and a gold occurrence is established, it is not possible to make temporal links because older structures may have been reactivated.

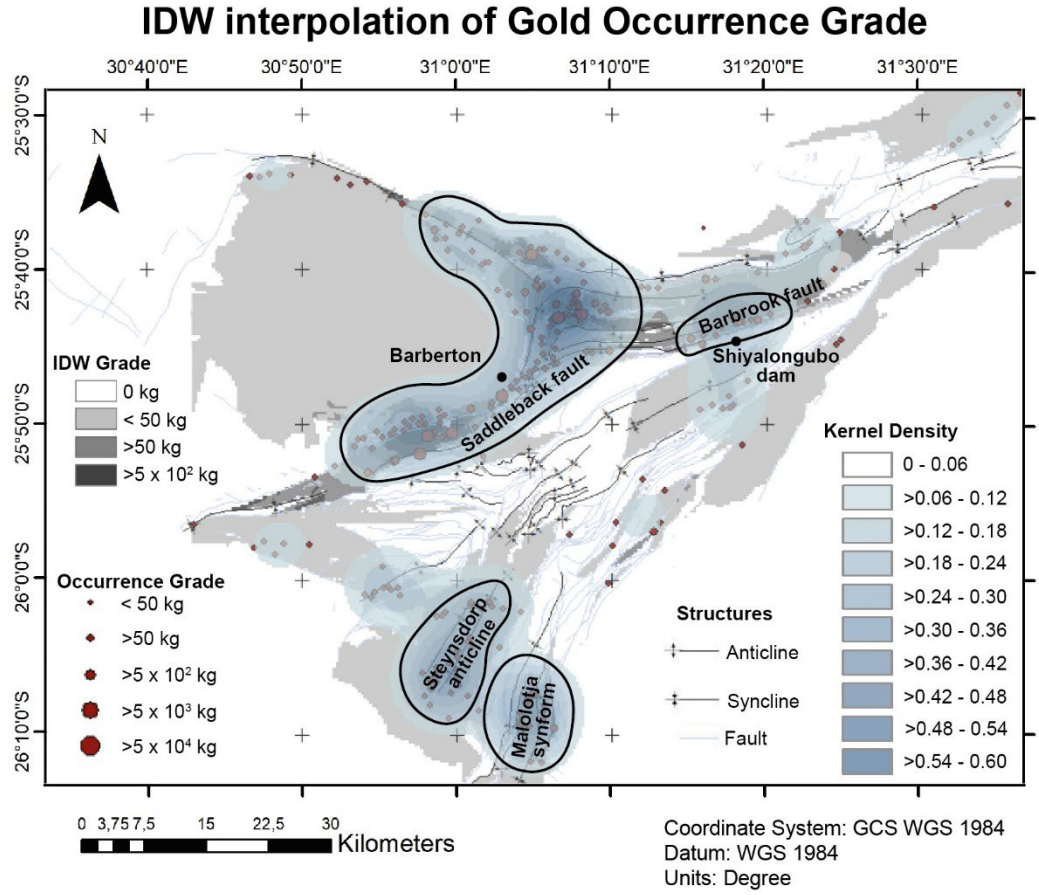

Fig. III.15. Synthetic map of the cluster's zone according to the Kernel Density (blue gradient) and the IDW interpolation of occurrence size (grey gradient) in the Barberton Greenstone Belt.

The spatial distribution analysis of gold occurrences reveals three main findings.

- Firstly, the gold occurrence orientations have a low angle (<22.5°) with fold axial plane and fault orientations (Figs. III.10 and III.12).
- Secondly, there is a noticeable heterogeneity between the northern and the southern parts of the belt, with higher grade areas found in the northern part (Fig. III.13).

- Lastly, four main clusters have been identified, indicating high occurrence-density areas. The southern zone hosts two clusters surrounding the Malolotja and the Steynsdorp regional folds. The northern zone bears two additional clusters, one near the town of Barberton and encompassing the Sheba-Fairview area, and another one near the Shiyalongubo dam, along the Barbrook fault (Figs. III.14 and III.15). These findings provide a base map for targeting fieldwork activities.

It is important to note that all the data obtained from these analyses must be interpreted with caution because they are entirely dependent on the input data, i.e., the Metallogenic map of the Barberton Greenstone belt (Ward, 2000).

Chapter IV: Southern Gold Provinces

A gold occurrence cluster density has been identified in the south of the belt, correlating with two major structures: the Malolotja synform and the Steynsdorp Anticline. The Malolotja and the Steynsdorp areas host more than 20 and 25 gold occurrences, respectively. Figure IV.1 shows the distribution of these occurrences in the southern part of the Barberton Greenstone Belt (numbers or names from the metallogenic map of the Barberton Greenstone Belt, compiled by Ward (2000), and outcrops out of the zones with mineralisation.

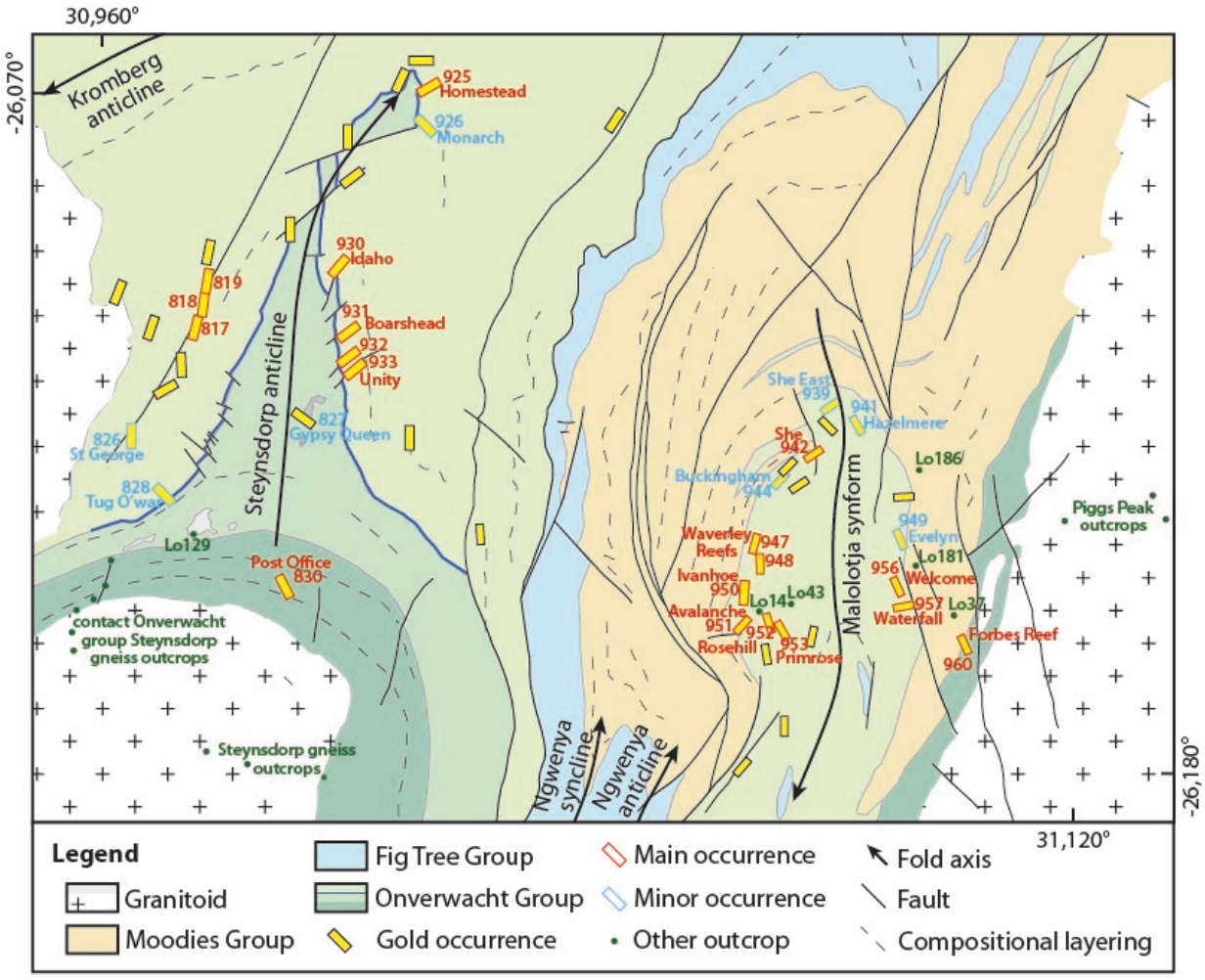

Fig. IV.1. Geological map of the southern part of the Barberton Greenstone Belt (after the metallogenic map of the Barberton Greenstone Belt compiled by Ward (2000) and Viljoen et al. (1969)) and localisation and names of the main gold occurrences and studied outcrops.

The data from these two folds, described in the first two sub-sections of this chapter, have been published in a scientific publication in *Minerals*, which will be presented in the *IV.C. Synthesis* section.

IV.A. The Malolotja area

All the outcrops studied during fieldwork have been classified into three categories: i) main occurrences corresponding to old mines. ii) minor occurrences corresponding to exploration trenches and small scrapings. iii) other outcrops which are outside of gold occurrences.

IV.A.1. Main Gold occurrences

IV.A.1.1. The She Mine occurrence (942)

The gold occurrence 942 designates the former She gold Mine located north of the regional Malolotja synform. Today, many collapsed galleries and pits remain.

In this zone, the main schistosity is ENE-WSW striking and dipping 40° to the SSE (Fig. IV.2a). This schistosity is parallel to a compositional layering of alternating red, brown, ochre and green planes (Fig. IV.2b); and carries a well-expressed down-dip mineral stretching lineation. On the XZ observation plane (normal to the schistosity and parallel to the lineation), sigmoids wrapped by the schistosity show a reverse sense of shear, top to the NNW (Fig. IV.2a,b,d,c). West of the mine, the schistosity and parallel compositional layering are striking NE-SW and dipping 70° to the SW (Fig. IV.2d,f). This schistosity is folded by tight cm-scale fold, with steeply SW-dipping axial plane (Fig. IV.2d,e). Instead, east of the mine, a N-S striking schistosity is folded in open folds, associated with a SE-dipping, poorly defined axial plane (Fig. IV.2g,h).

Two types of quartz veins were observed, both were mined (Fig. IV.2a): 1) mm- to cm-thick reverse sigmoids filled by quartz and wrapped by the schistosity (Fig. IV.2b). 2) dm-wide schistosity-parallel veins (Fig. IV.2c). Microscopically, these two types of veins are different. The quartz sigmoids are formed by comb quartz and K-feldspar (Fig. IV.3a,c), while the schistosity-parallel veins are composed of highly recrystallised quartz, chlorite, tourmaline and numerous oxides (Fig. IV.3b,d).

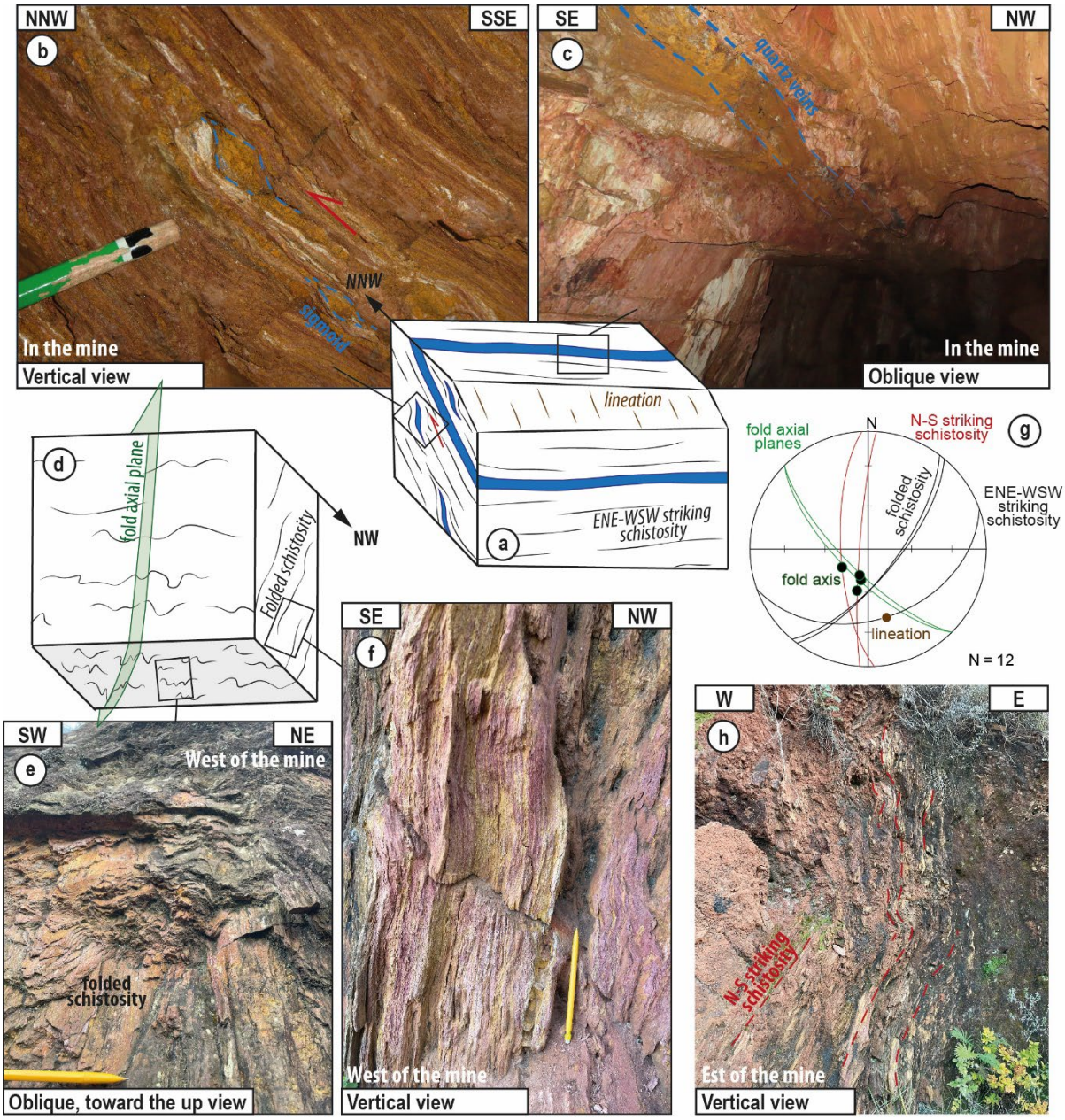

Fig. IV.2. Field observations documenting the geology of the She Mine occurrence. **(a)** Schematic diagram of the main structures in the mine, with the schistosity associated with top to NNW-thrusting, the two types of quartz veins (in blue) and down-dip lineation (brown line). **(b)** XY observation plane of sigmoids in the schistosity attesting of a reverse sense of shear. **(c)** Schistosity-parallel, 50 cm-thick quartz vein highlighted by the blue dashed line. **(d)** Schematic diagram of the outcrop west of She Mine, with a NE-SW striking folded schistosity and associated NW-SE striking axial plane (green plane). **(e)** View toward the top of the folded schistosity depicted in (e). **(f)** Alternating red, brown, and ochre layers of schistosity. **(g)** Stereonet diagram representing all schistosities measured in She Mine and surroundings (Schmidt diagram, lower hemisphere). **(h).** Outcrop east of She Mine showing a folded N-S striking schistosity (red dash line).

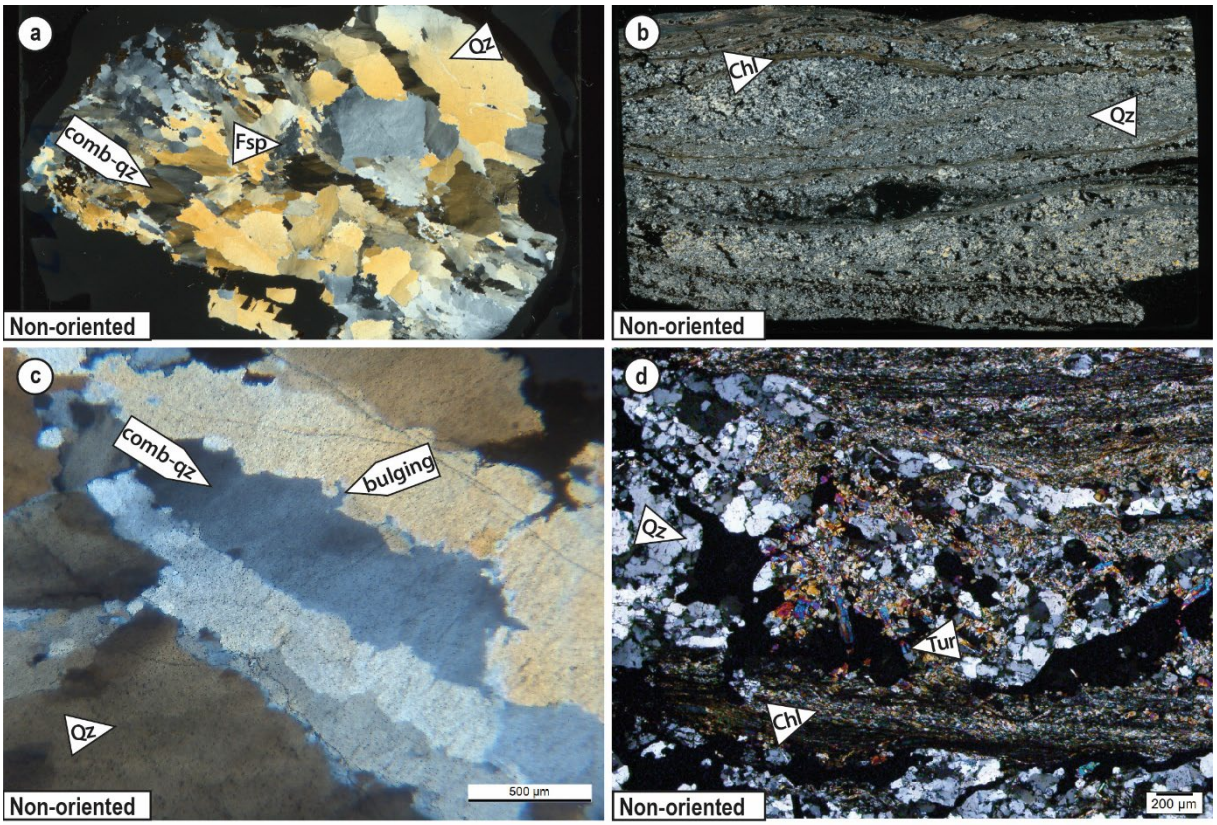

Fig. IV.3. Microscopic observations of the two types of veins in She Mine. **(a)** Thin section scan of a sigmoid vein (crossed polars). **(b)** Thin section scan of a schistosity-parallel vein (crossed polars). **(c)** Comb quartz within a sigmoidal quartz vein (crossed polars). **(d)** Elongated chlorite and tourmaline grains in a core of a matrix composed by quartz (crossed polars).

IV.A.1.2. Waverley Reefs occurrences (947&948)

The n°947 and 948 gold occurrences are large open pits with some galleries, numerous trenches, and wells (Fig. IV.4a,b,c,d). Occurrence n°948 is a vast open pit about 30 m wide and 25 m deep; only a tiny part of the south pit is easily reachable (Fig. IV.4b). Occurrence n°947 corresponds to two small pits about 20 m-wide and 10 m-deep, with multiple galleries (few are collapsed), trenches and wells (Fig. IV.4c,d). These two occurrences are named « Waverley Reefs ».

The schistosity in this area is hardly visible because the country rocks are significantly altered. However, two different directions have been observed (Fig. IV.4e). A preponderant NNW-SSE striking sub-vertical schistosity, locally superimposed on a compositional layering and is parallel to a pinkish chert horizon (Fig. IV.5a,c,g). Another schistosity, N-S striking and steeply dipping to the east, is visible by the alignment of mm-scale mica grains.

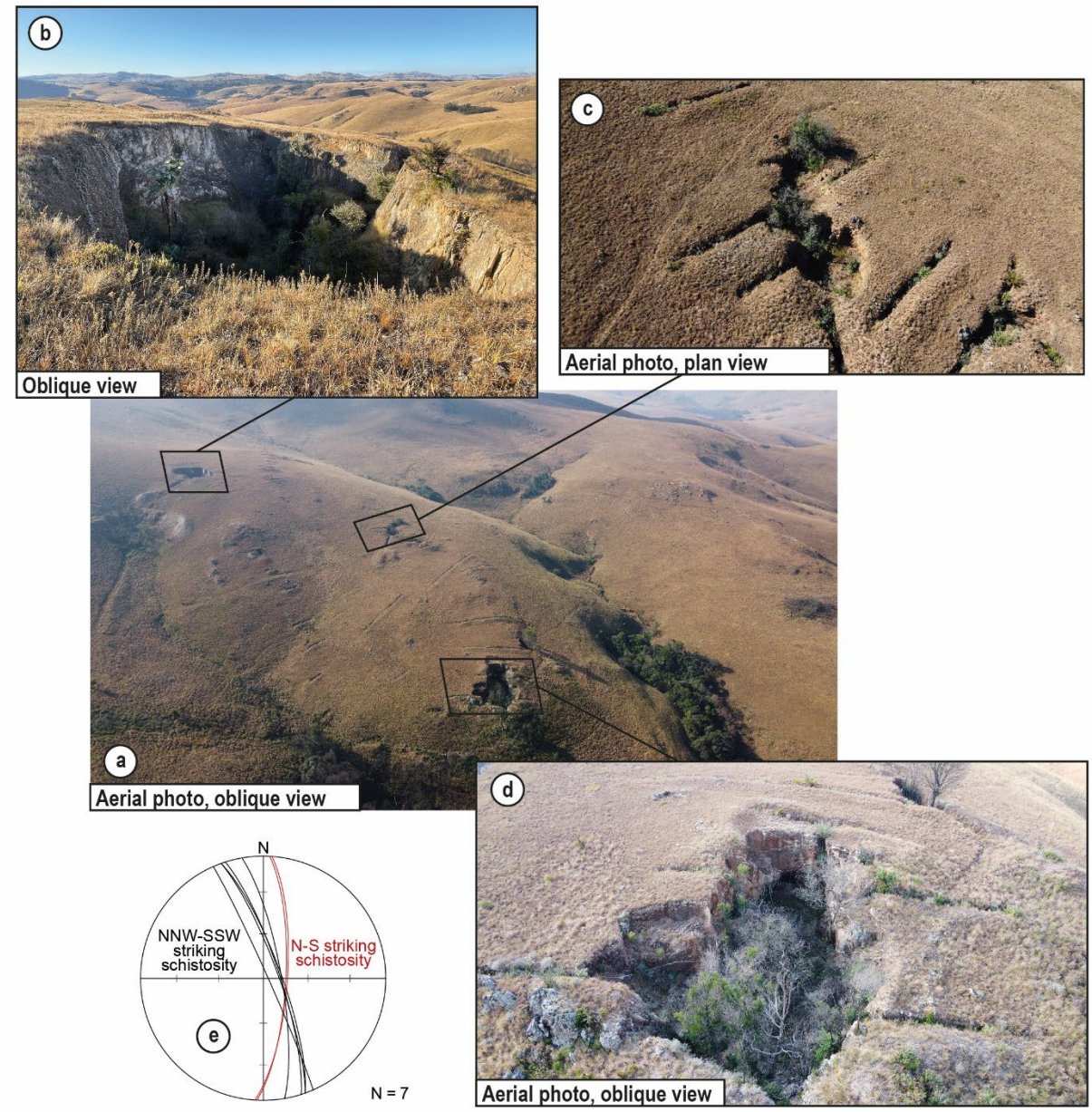

Fig. IV.4. Aerial (drone) photo of the Waverley Reefs occurrences and schistosity stereonet. **(a)** Overview of the Waverley Reefs area. **(b)** the topographically upper pit corresponds to the n°948 occurrence and **(c)** and **(d)** the two smaller pits belong to the n°947 one. **(e)** Stereonet diagram representing all schistosities measured in Waverley Reefs area (Schmidt diagram, lower hemisphere).

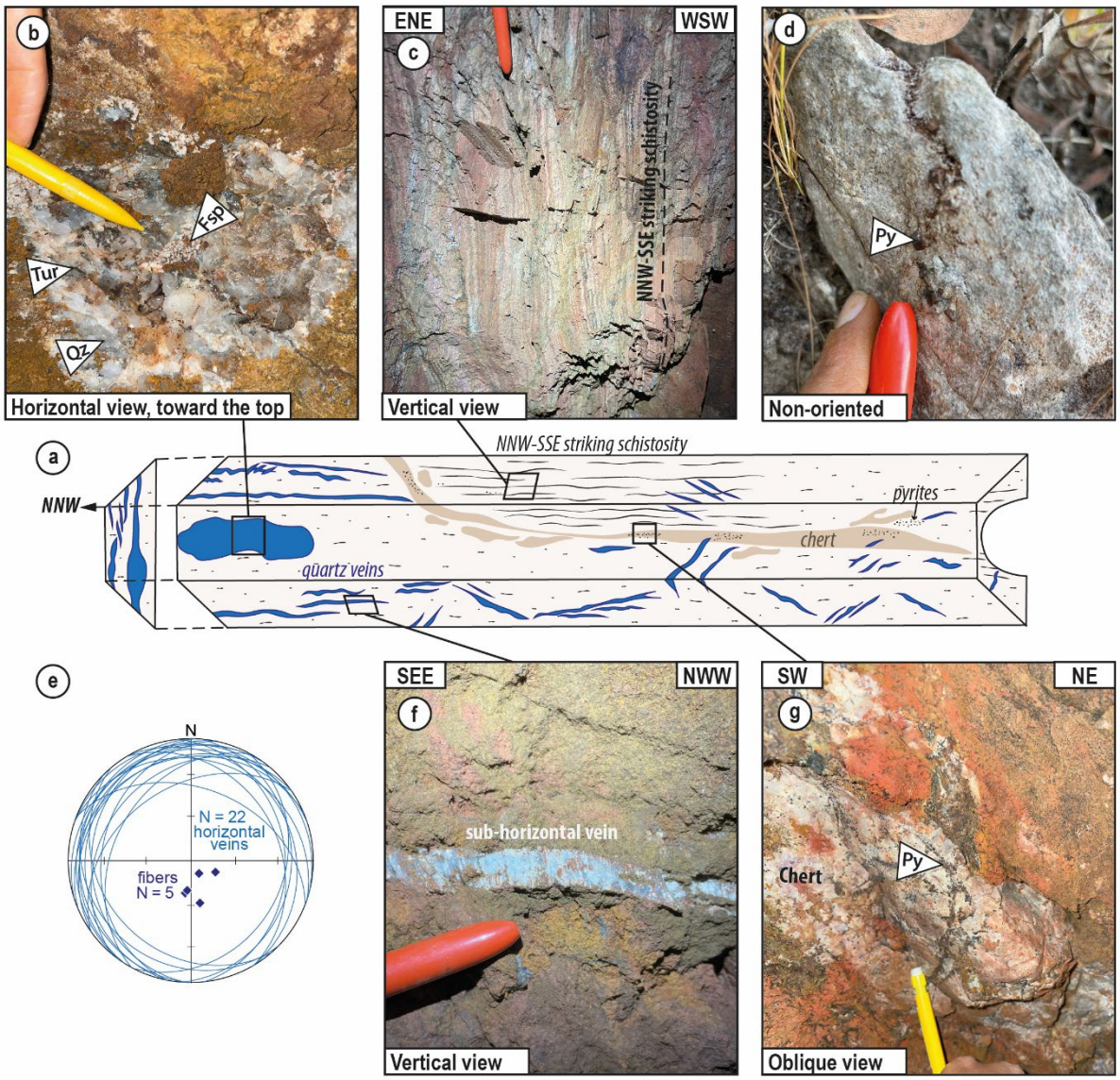

Fig. IV.5. Field observation of a gallery in Waverley Reefs occurrences. **(a)** Schematic diagram of the main gallery, view from the top with quartz vein shown in blue, the schistosity in black and the chert in beige. **(b)** View toward the top of a horizontal vein composed of quartz, feldspar, and tourmaline. **(c)** Compositional layering parallel to an NNW-SSE striking schistosity. **(d)** Pyrites in schist. **(e)** Stereonet diagram of all horizontal veins and associated sub-vertical quartz and feldspar fibres (Schmidt diagram, lower hemisphere). **(f)** Horizontal quartz-feldspar vein with infilling marked by feldspar vertical fibres. **(g)** Pinkish chert with pyrites.

Vein's geometry shows strong lateral variations in all Waverley Reefs area. Southward, topographically lower down (Fig. IV.4c,d), numerous sub-horizontal undulous quartz veins have been observed (Fig. IV.6). These veins are composed of quartz, feldspars (mostly appearing strongly altered and transformed in kaolinite powder), few tourmalines, sulphides (mostly pyrites) either in the veins or disseminated in the host-rock). Some malachite grains occur in the country rock a cm-away from the main quartz veins (Figs. IV.5b,d, IV.6a, and

IV.7a,b,c,d). Some vertical fibres of feldspars and comb quartz filled the horizontals veins (Figs. IV.5e,f and IV.7b). Under the microscope, quartz grains show evidence for bulging sub-grains formation, even if quartz seems weakly recrystallised (Fig. IV.7a). Steeper veins, measured NW-SE striking and dipping to the NE, have also been observed in this zone (Figs. IV.6b and IV.8a,c).

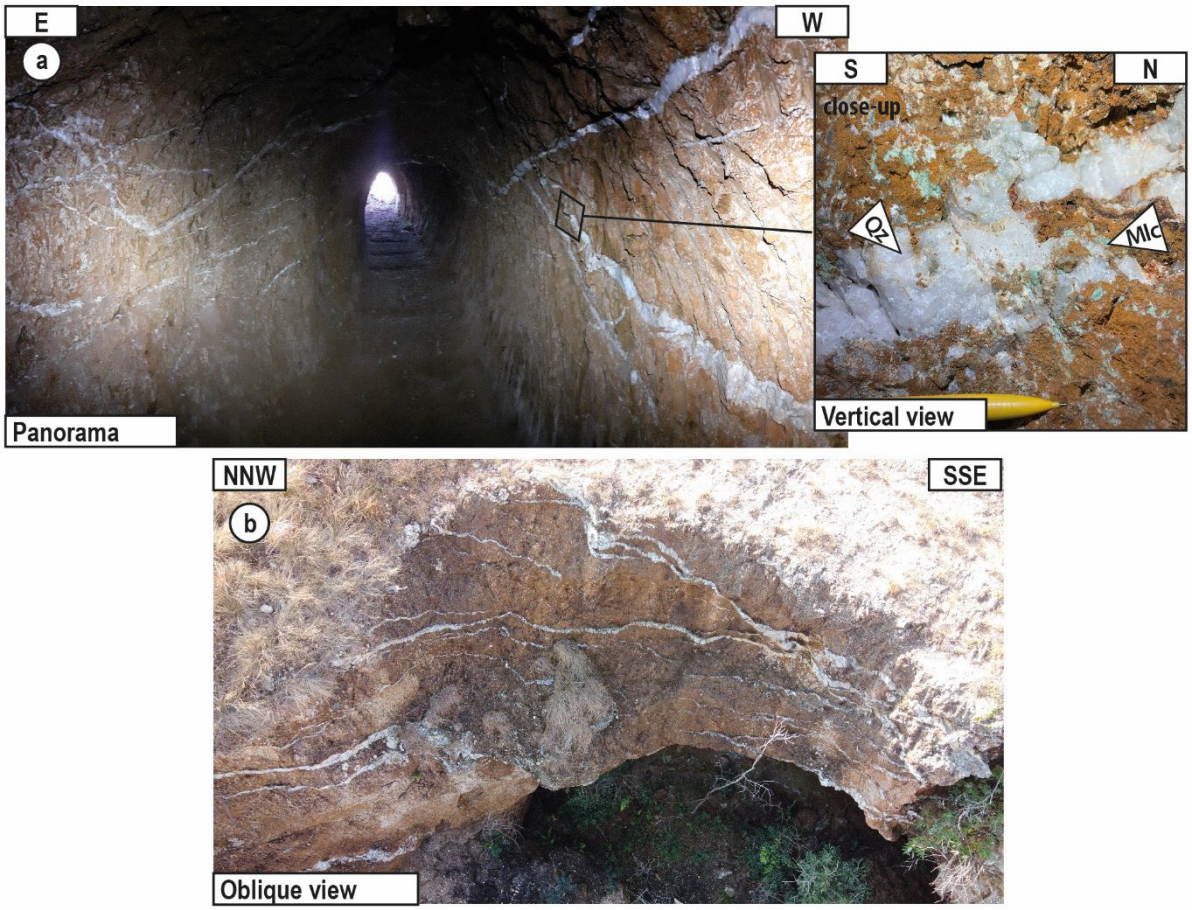

Fig. IV.6. Field observation of the n°947 Waverley Reefs occurrence. **(a)** Panoramic view of a gallery and close-up view of a quartz vein. Note the undulating quartz vein, and the malachite grain surrounding the vein. **(b)** Wall of the pit located at the bottom of the mined sector, with sub-horizontal undulating veins and a steeper one.

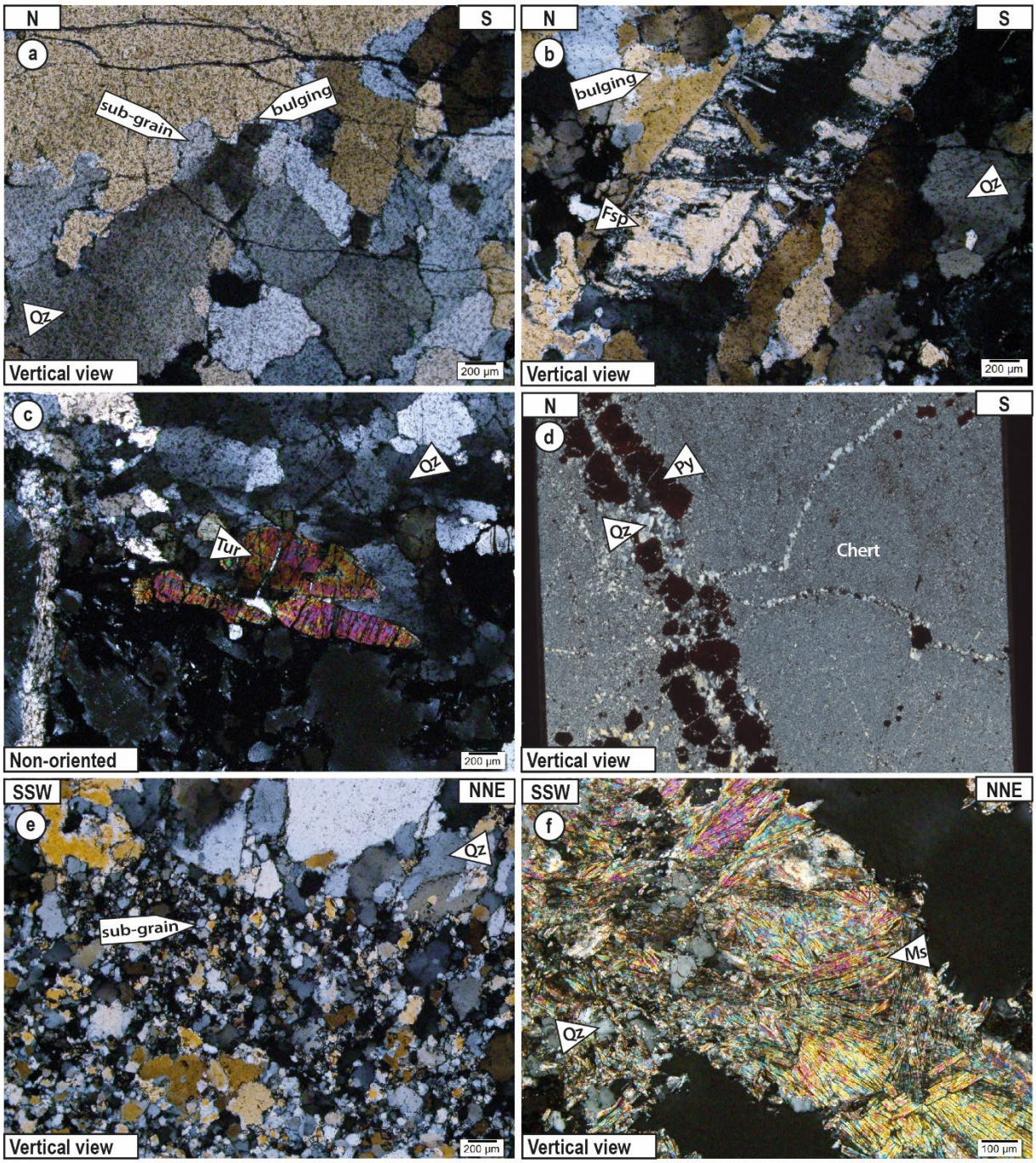

Fig. IV.7. Microscopic observations of the hydrothermal features in Waverley Reefs. **(a)** Horizontal vein infilled by quartz exhibiting bulging and sub-grain recrystallisation (crossed polars). **(b)** Feldspar grain in a horizontal vein, note bulging recrystallisation along quartz grain rims (crossed polars). **(c)** Tourmaline grains in a horizontal vein (crossed polars). **(d)** Thin section scan of aligned pyrites in a chert; note the systematic location of quartz grains surrounding the pyrites (crossed polars). **(e)** Highly recrystallised quartz grains from a horizontal shearing vein (crossed polars). **(f)** Large muscovite grains in a horizontal shearing vein (crossed polars).

One of these veins steeper dipping to the NE veins is offset by a sub-horizontal vein (Fig. IV.8a), microscopically composed of mm-wide muscovite and highly recrystallised quartz with µm-wide quartz sub-grain (Fig. IV.7e,f).

Upper topographically and to the north (Fig. IV.4b), numerous vertical veins appear with a lense or rectilinear geometry (Fig. IV.8b). They are N-S striking and steeply dip to the west in contrast to the N-S striking schistosity that dips to the east (Fig. IV.8c).

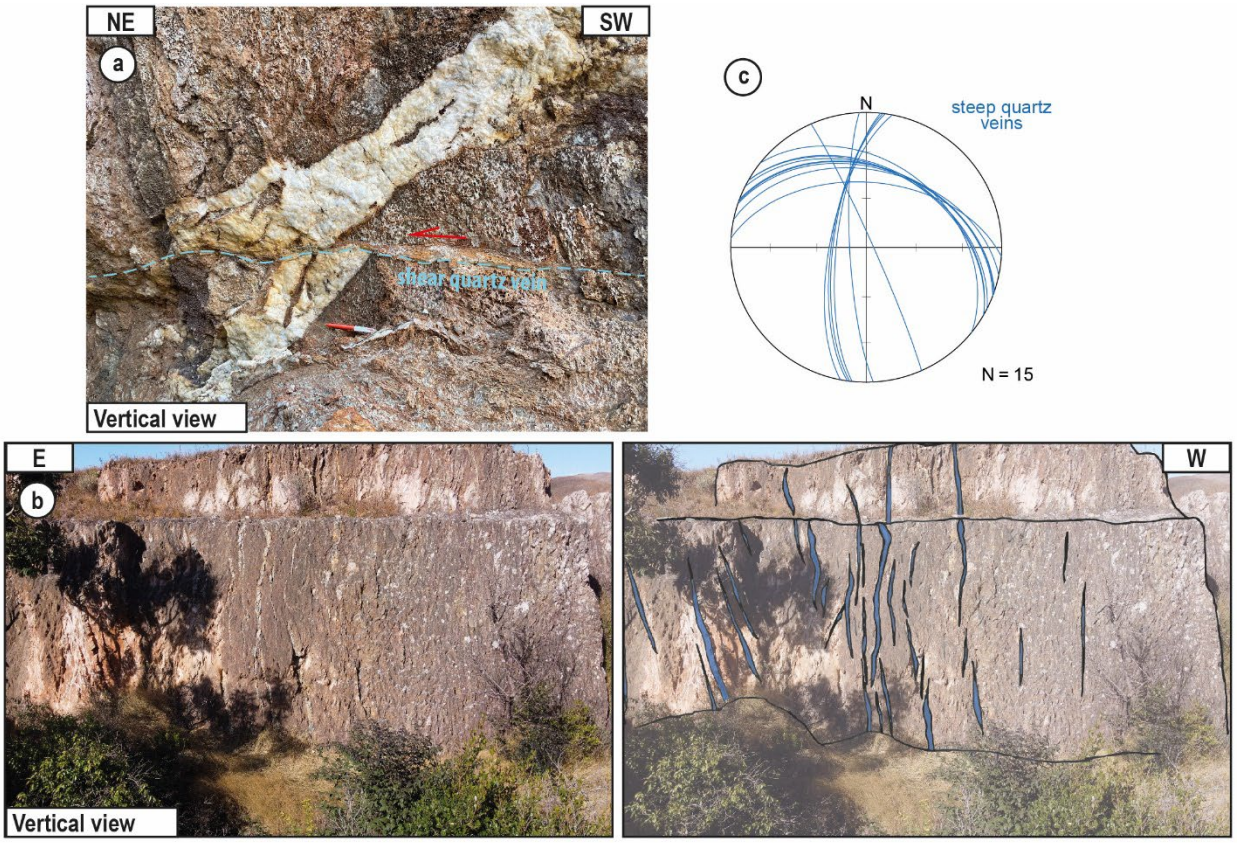

Fig. IV.8. Field observation of the steeper veins in the Waverley Reefs occurrences. **(a)** NW-SE striking dipping to the NE vein onset by a centimetric horizontal vein (light blue dash line). **(b)** Photo and sketch of sub-vertical veins of the n°948 occurrence. **(c)** Stereonet diagram of all sub-vertical veins measured in Waverley Reefs (Schmidt diagram, lower hemisphere).

IV.A.1.3. Ivanhoe occurrence (950)

Occurrence n°950, called Ivanhoe is a former mine with a large open pit and some unsafe galleries and shafts (Fig. IV.9).

Fig. IV.9. Drone photo of the Ivanhoe gold occurrence (the western pit is ca. 40 m long).

In the main pit, the schistosity is difficult to observe due to strong weathering of the country rocks. Nevertheless, it has been measured in few places and is N-S striking, vertical. Within a silicified area located 100 m outside the mined zone, a sub-vertical E-W striking cm to dm-wide tight folded schistosity has been observed, and the fold axial plane is also N-S striking and vertical, parallel to the main schistosity observed everywhere at this occurrence (Fig. IV.10a,b,c).

Exploited quartz veins show a complex association between sub-horizontal folded veins and steep veins dipping mainly dipping to the east, although a few veins are dipping west. They all strike N-S. Sub-horizontal veins are tightly folded with axial fold plane parallel to the N-S schistosity (Fig. IV.10c,d,e). All these veins are in petrographic continuity (i.e., show a similar infilling; Fig. IV.10d). These veins are composed of quartz with feldspars at the edge and few tourmaline and muscovite grains. Microscopically, the quartz is weakly recrystallised (Fig. IV.11).

Silicified rocks outside the mined area show an accumulation of quartz veins, all oriented approximately NE-SW striking.

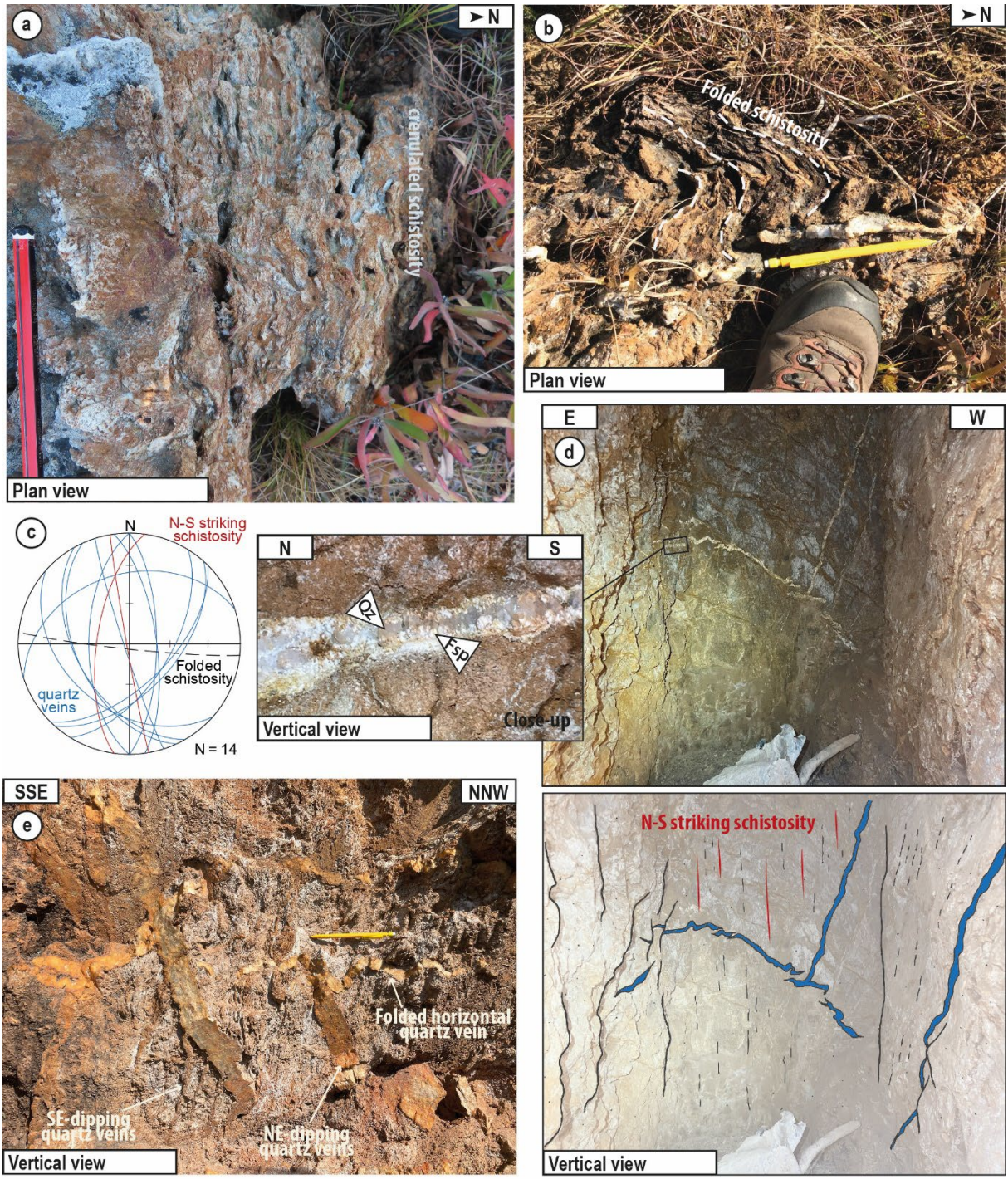

Fig. IV.10. Field observations of the Ivanhoe occurrence and surroundings. **(a)** E-W striking, steep, folded schistosity in surrounding rocks. **(b)** Tight folds affecting the E-W striking schistosity (white dash line) in the vicinity of the main occurrence; note the N-S-striking, steep quartz vein parallel to the axial plane. **(c)** Stereonet diagram showing folded schistosity (black dash great circle), N-S striking veins in the mine (red great circle) and other veins (blue great circle) (Schmidt diagram, lower hemisphere). **(d)** Photo and sketch of a shallow dipping folded vein coeval with steeply east-dipping quartz veins. Inset: the close-up view of the veins shows elongated feldspars grains perpendicular to vein edge. **(e)** Photo of folded horizontal veins and steep SE and NE dipping veins, the fold axial plane is N-S striking and sub-vertical.

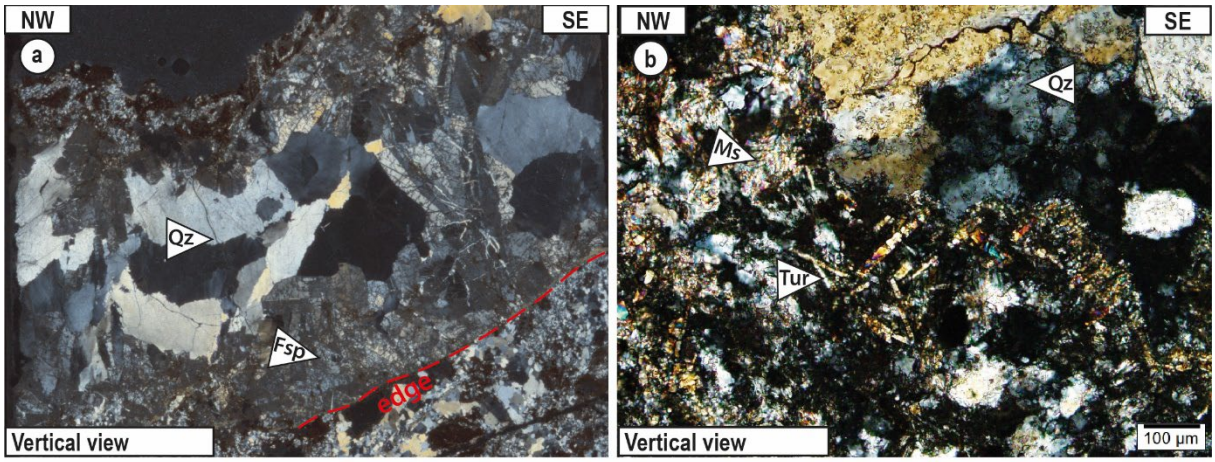

Fig. IV.11. Microscopic observations of the veins in the Ivanhoe occurrence. **(a)** Feldspars at the edge of the sub-horizontal veins exhibiting unrecrystallised quartz grain (crossed polars). **(b).** Tourmaline, muscovite and quartz in a vein (crossed polars).

IV.A.1.4. The Avalanche occurrence (951)

The former Avalanche Mine is a large open pit of about 100x80m in surface, with small drifts and galleries (Fig. IV.12a).

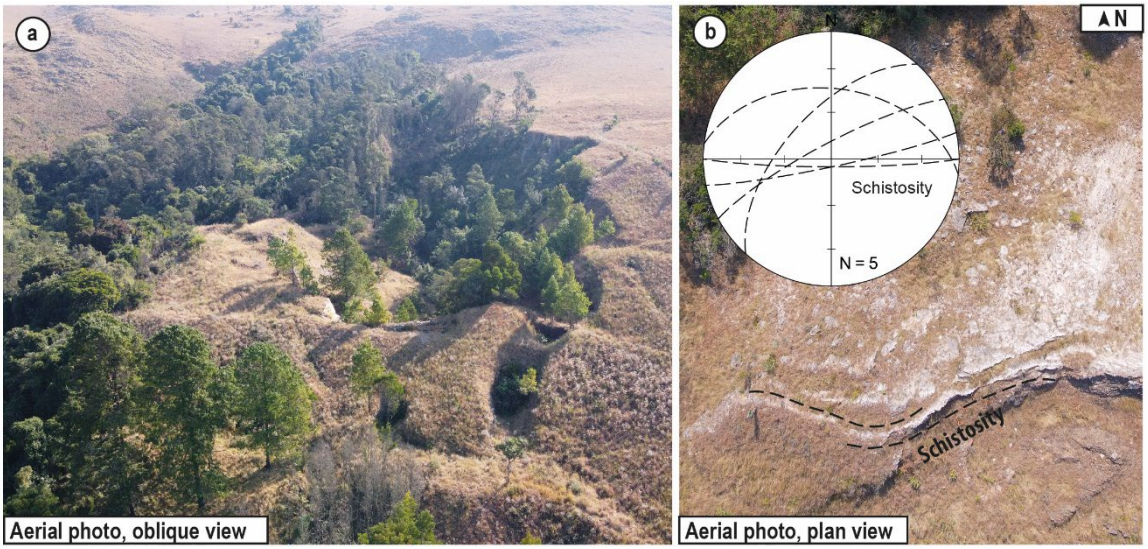

Fig. IV.12. Aerial (drone) photo of the Avalanche gold occurrence. **(a)** Overview of the Avalanche pit, view to the West. **(b)** ENE-WSW striking large-scale folded schistosity aerial photo and associated stereonet diagram (Schmidt diagram, lower hemisphere).

Two directions of schistosity have been measured in this area, the first is ENE-WSW striking and visible as a large 20 m-scale open folded band on the southern edge of the pit (Fig. IV.12b), Similarly oriented schistosity is observed in the northern side of the pit, but with a shorter fold wavelength (4 metres).

The predominant schistosity in the remaining of the pit is NW-SE striking and steeply dipping to the NE (Fig. IV.13a) and host a down-dip stretching lineation.

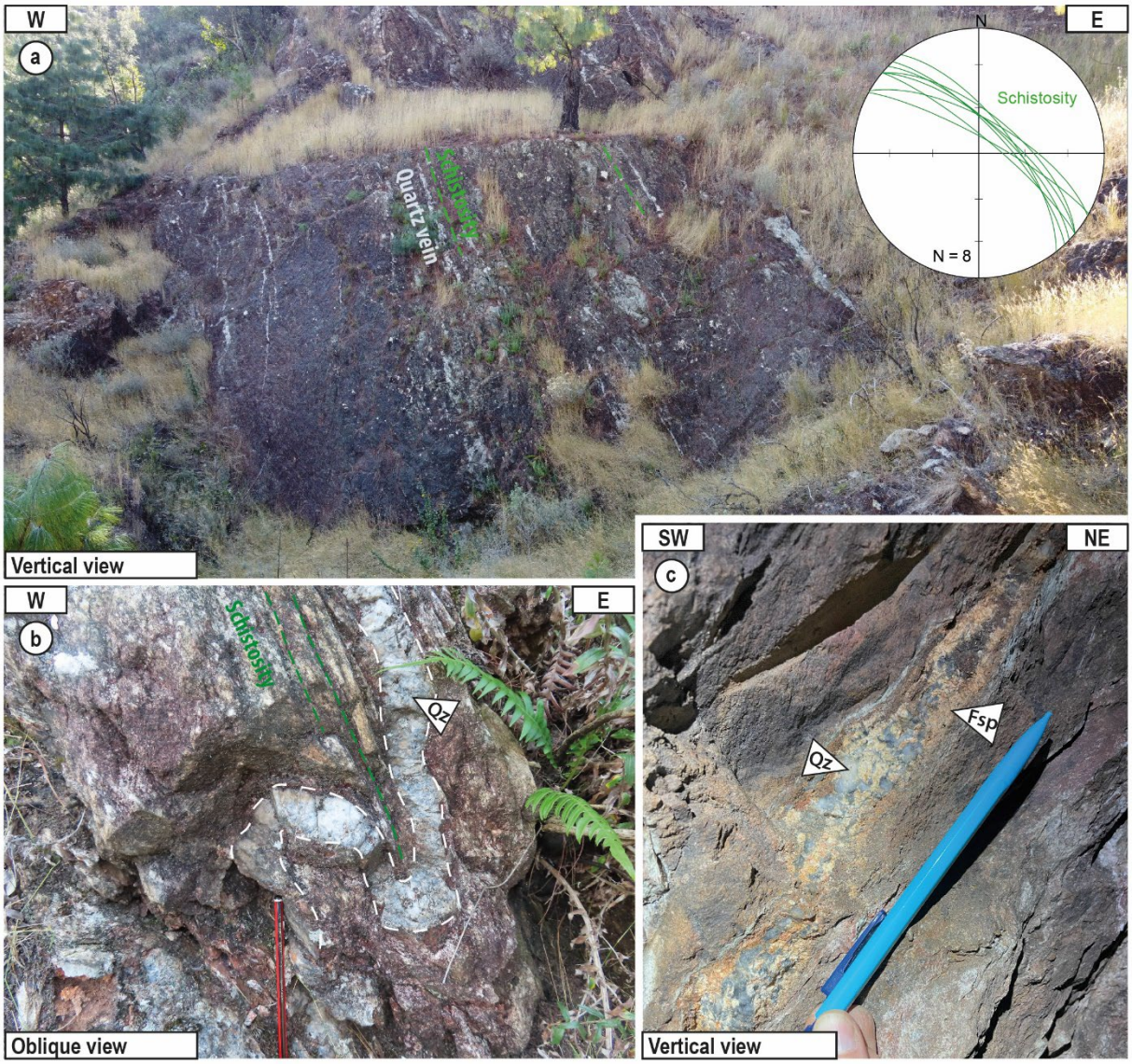

Fig. IV.13. Field observations of the Avalanche Mine. **(a)** Photo with sub-vertical NW-SE striking schistosity (green dash lines) and schistosity-parallel quartz veins; and stereonet with the NW-SE striking schistosity (Schmidt diagram, lower hemisphere). **(b)** Isoclinally folded quartz vein (white dash line), note the axial plane is parallel to the NW-SE striking schistosity (green dash line). **(c)** NW-SE striking lens composed of quartz and feldspar.

Mined quartz veins seem long and thin (cm to dm-wide) and in places affected by isoclinal folds with an NW-SE striking axial plane, parallel to the NW-SE striking schistosity (Fig. IV.13a,b). Few shallow dipping folded quartz veins cut these vertical folded veins. Lenses of quartz and milky white minerals are observed parallel to the NW-SE schistosity (Fig. IV.13c). Some rare

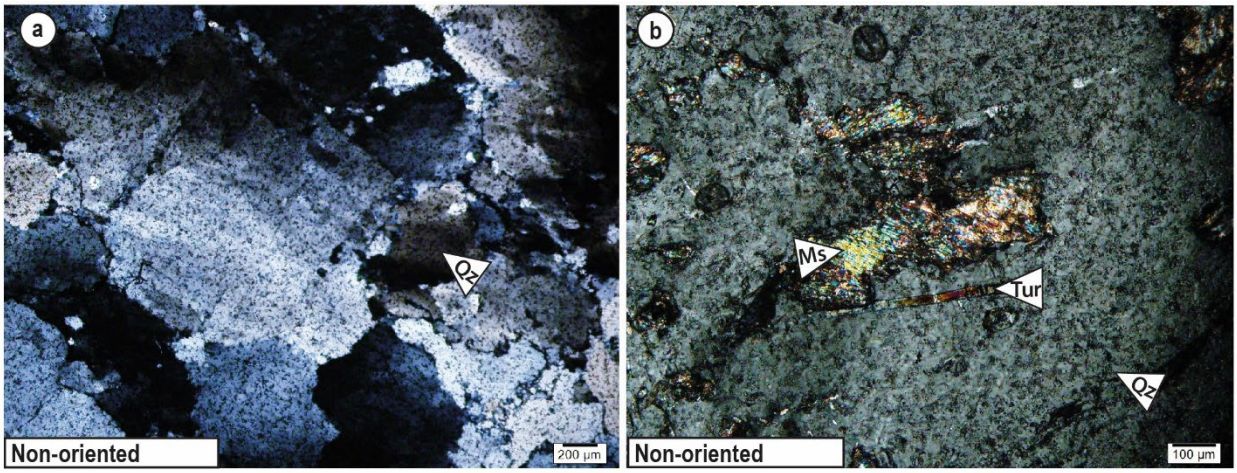

N-S striking quartz veins have been measured. The vertical and shallow dipping quartz veins are composed of quartz (Fig. IV.14a) with maybe iron-rich weathered carbonate. Schistosity-parallel lenses are composed of quartz and muscovite and numerous tourmalines (Fig. IV.14b).

Fig. IV.14. Microscopic observations of the vein in the Avalanche occurrence. **(a)** Quartz grains showing bulging (crossed polars). **(b)** Muscovite and tourmaline grain in core of the quartz vein (crossed polars).

IV.A.1.5. The Rosehill Occurrence (952)

The nº952 gold occurrences correspond to the former Rosehill Mine, straddled by numerous trenches, pits and galleries (Fig. IV.15a).

In the central part of the mine, the schistosity turns and defines a 100 m-scale fold; at the hinge of the fold, the schistosity is globally E-W striking and dip to the south (Fig. IV.15b,c,d).

This area contains numerous quartz veins, forming a large network of cm to m-wide veins, mainly NW-SE to N-S striking, with a large range of dip angles toward the southwest and the west (Fig. IV.16). All these veins are in petrographic continuity (Fig. IV.16b,c). To the south, some E-W striking, north dipping veins are observed (Fig. IV.16a).

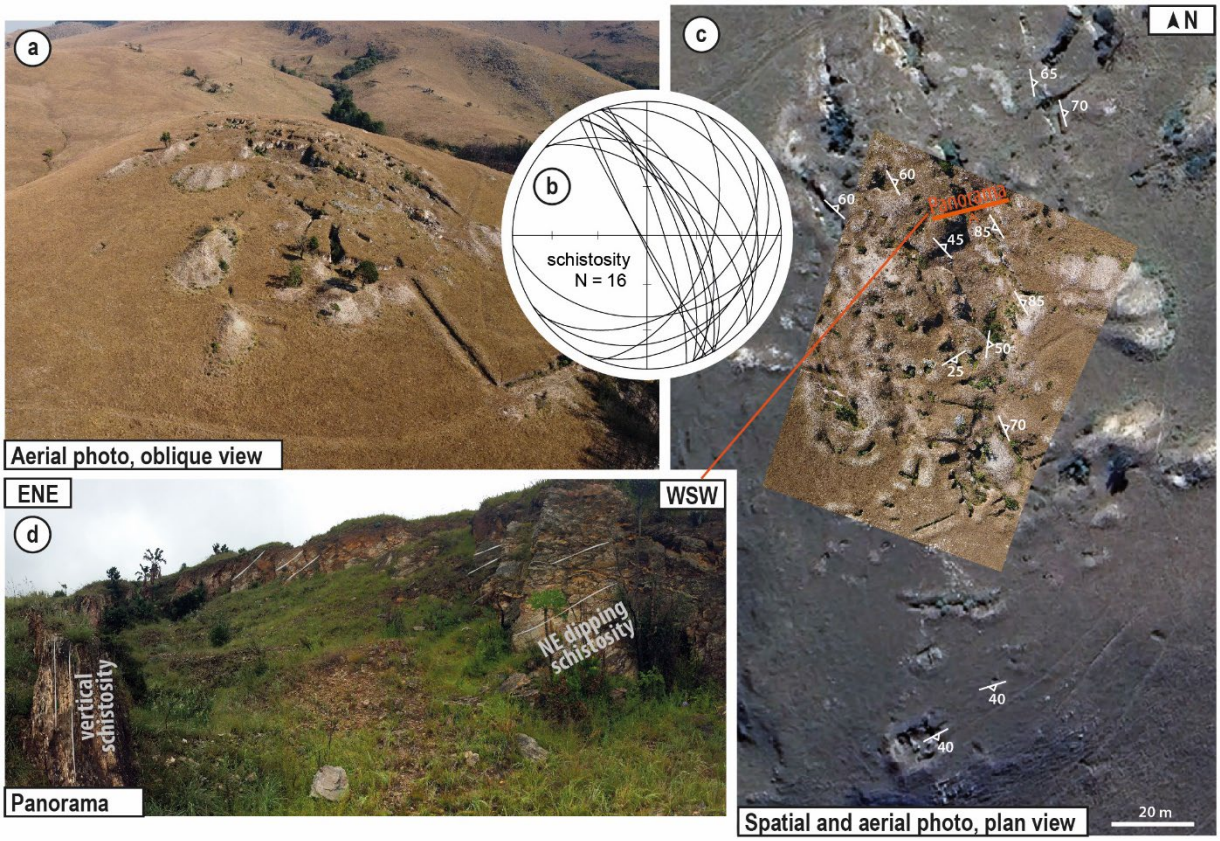

Fig. IV.15. Field observations of the country rock deformations, drone photo and Google Earth satellite image of the Rosehill occurrences. **(a)** Drone photo of the Rosehill occurrences, view to the southwest. **(b)** Stereonet of the schistosity measured in Rosehill outcrops (Schmidt diagram, lower hemisphere). **(c)** Structural map of the area with the schistosity measurements, note the change in the orientation of the schistosity, and the location of the panorama (d). **(d)** Panorama of one of the scratching areas, record the variation of dipping.

Microscopic observations reveal that the veins are composed exclusively of quartz. Within N-S striking veins, quartz is significantly recrystallised (Fig. IV.17a) whereas within the E-W striking ones, it is only recrystallised locally and in bands (Fig. IV.17b).

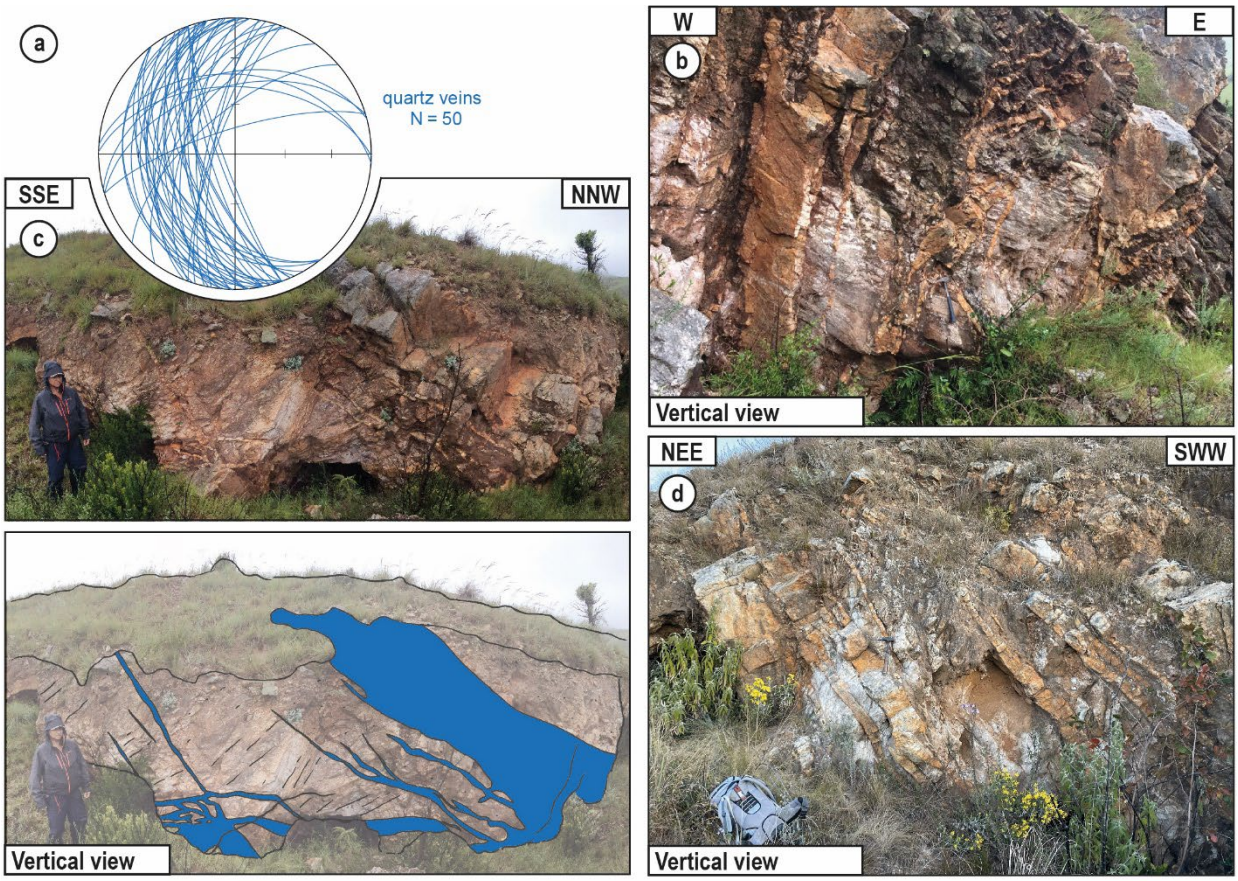

Fig. IV.16. Field observations of the hydrothermal features in the Rosehill deposit. **(a)** Stereonet of all the veins measured in the area (Schmidt diagram, lower hemisphere). **(b)** West-dipping steep veins associated to a complex network system. **(c)** Photo and sketch of coeval horizontal and west-dipping veins. **(d)** West-dipping steep planar veins.

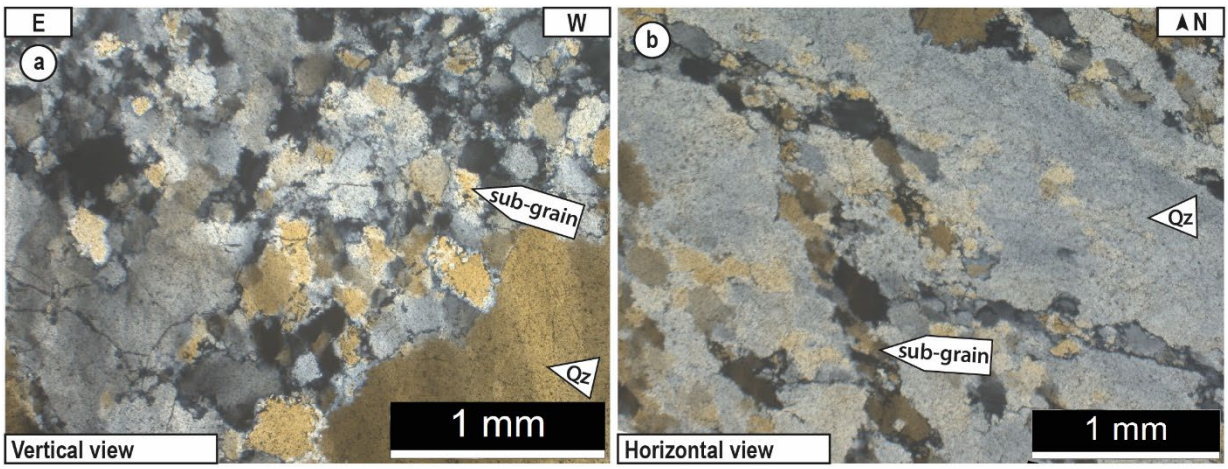

Fig. IV.17. Microscopic observations of the veins in the Rosehill occurrence. **(a)** Highly recrystallised N-S striking veins (crossed polars). **(b)** Recrystallisation locally forms sub-grain corridors in a E-W striking veins (crossed polars).

IV.A.1.6. The Primrose Occurrence (953)

The Primrose deposit (i.e., the n°953 occurrence) is composed of small galleries and scrapings and is located ca. 200 m-away south-east of the previous Rosehill occurrence.

Here, two different orientations of the schistosity have been observed: N-S striking, and weakly dipping to the east vs NW-SE steeply dipping to the NE (Fig. IV.18a,c). Unfortunately, we could not see how these two different orientations of schistosity relate to each other, no overprinting relationship has been observed. Numerous verticals and NNW-SSE striking fractures with shallow N-plunging slickenlines have also been observed (Fig. IV.18b,c).

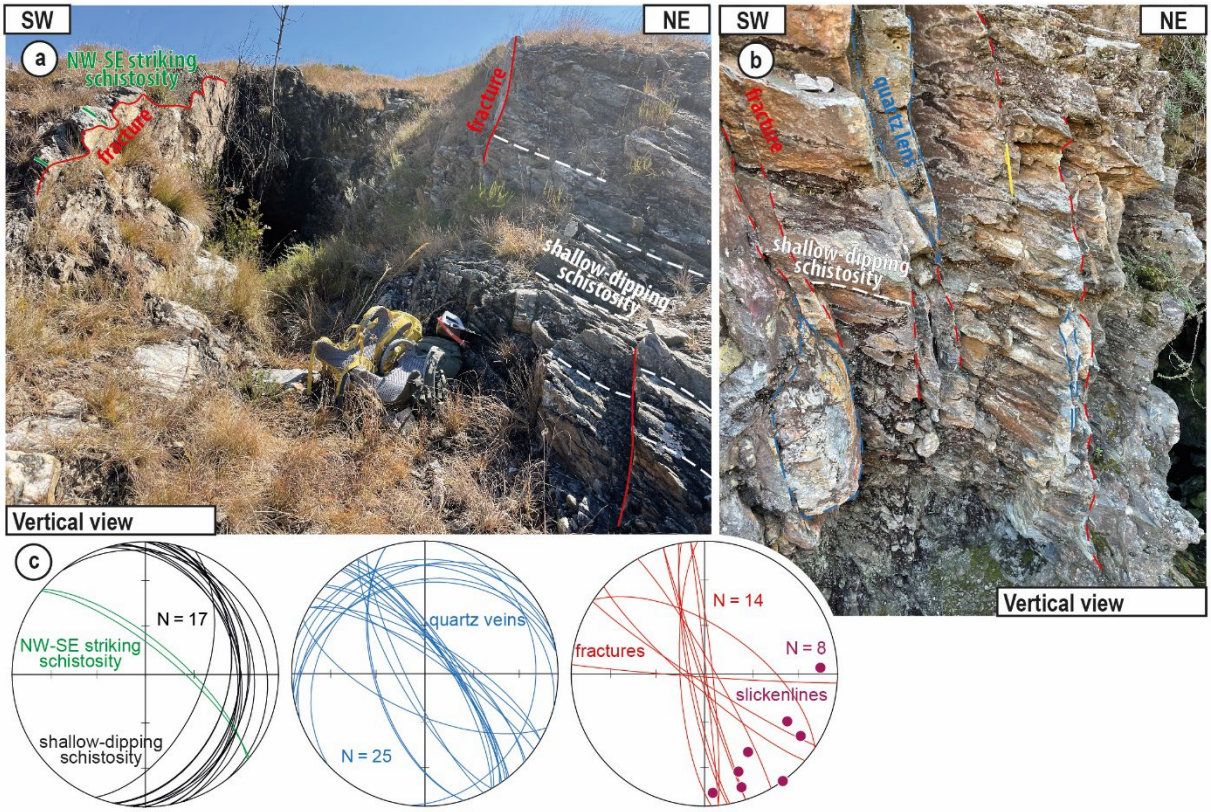

Fig. IV.18. Field observations of the country rock deformation in the Primrose occurrence. **(a)** Photo with the two schistosity orientations; at the southwestern part of the photo, the schistosity strikes to the NW-SE (green dash line) while at the northeastern part of the photo the schistosity is shallow dipping (white dash line); note the fracture plane and gallery in the zone where the schistosity orientation changes (red line). **(b)** Quartz lens (blue dash line) cutting the shallow dipping schistosity (white dash line); note the vertical fracture (red dash line). **(c)** Stereonets of the Primrose structures represented by the shallow schistosity (black great circle), the NW-SE striking schistosity (green great circle), the quartz veins (blue great circle) and the fracture plane and slickenlines (respectively red great circle and mauve dot) (Schmidt diagram, lower hemisphere).

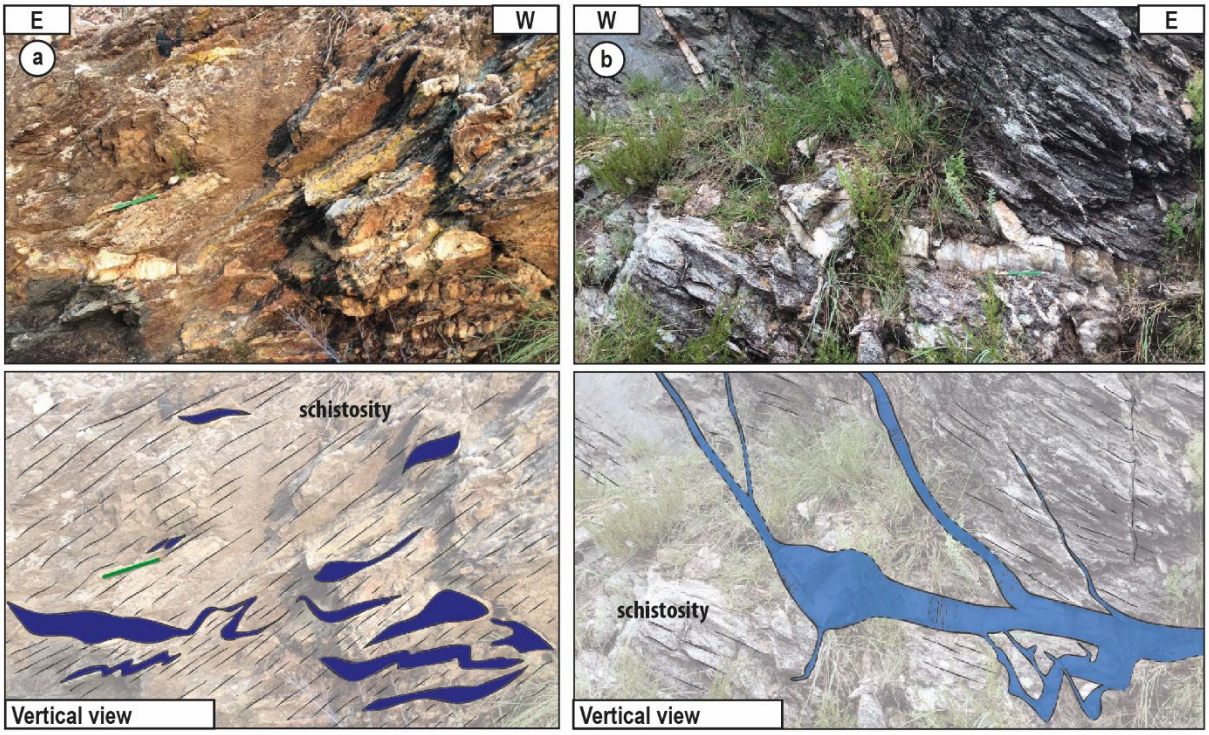

Fig. IV.19. Field observations of the three types of quartz veins at Primrose. **(a)** Photo and sketch of cm-thick quartz vein in sigmoid folded shape **(b)** Photo and sketch of sub-horizontal quartz vein coeval to steeply east-dipping quartz veins, both cutting the shallow dipping schistosity.

Three types of quartz vein geometry have been observed in this area: -i) network of cm- to dm-thick white quartz folded sigmoids (Fig. IV.19a); -ii) NW-SE to NNW-SSE striking, steeply NE-dipping, dm-scale, larger and cross-cutting the shallow dipping schistosity (Figs. IV.18b,c and IV.19b); -iii) Sub-horizontal quartz veins (Fig. IV.18c), cutting the shallow dipping schistosity (Fig. IV.19c), sometimes undulous or slightly folded.

Microscope observations show that the first vein type is formed by un-recrystallised quartz whereas the two last types are composed of quartz and Na-rich feldspar, with highly recrystallised quartz (Fig. IV.20). The two last vein types are inferred to be coeval because in petrographic continuity (Fig. IV.19b).

Fig. IV.20. Microscopic observations of the quartz veins at the Primrose occurrence. **(a)** Presence of feldspar in steep NE-dipping quartz-feldspar vein (crossed polars). **(b)** Sub-grain recrystallisation around comb quartz in a steep NE-dipping quartz vein (crossed polars).

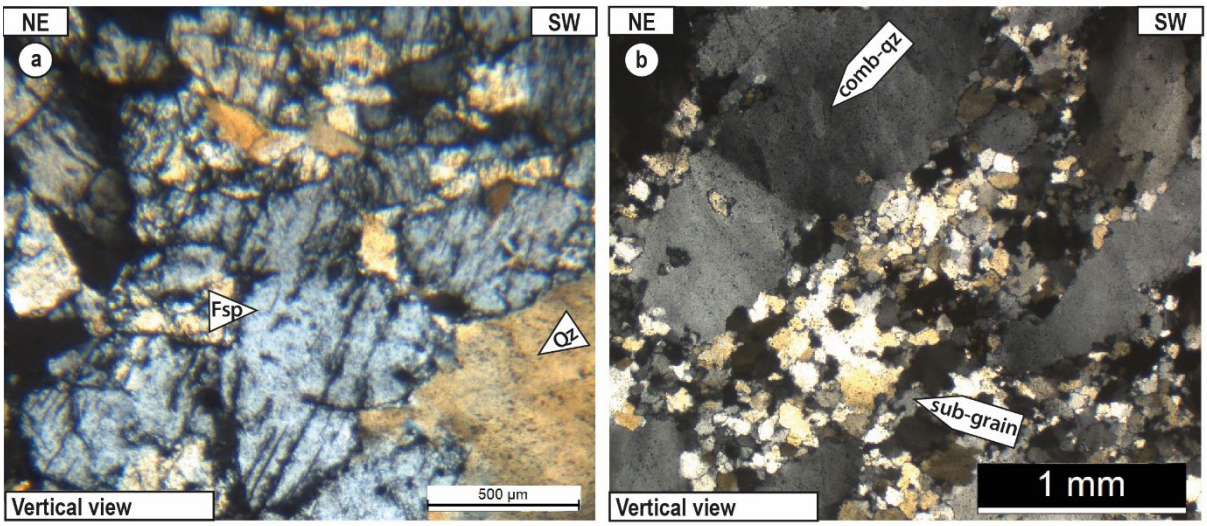

Alteration halos have been systematically observed around the NW-SE striking steep veins. This alteration is formed by a light green/white halo around the quartz veins and cm-wide grey/green alteration with tourmaline and Na-feldspars (Fig. IV.21).

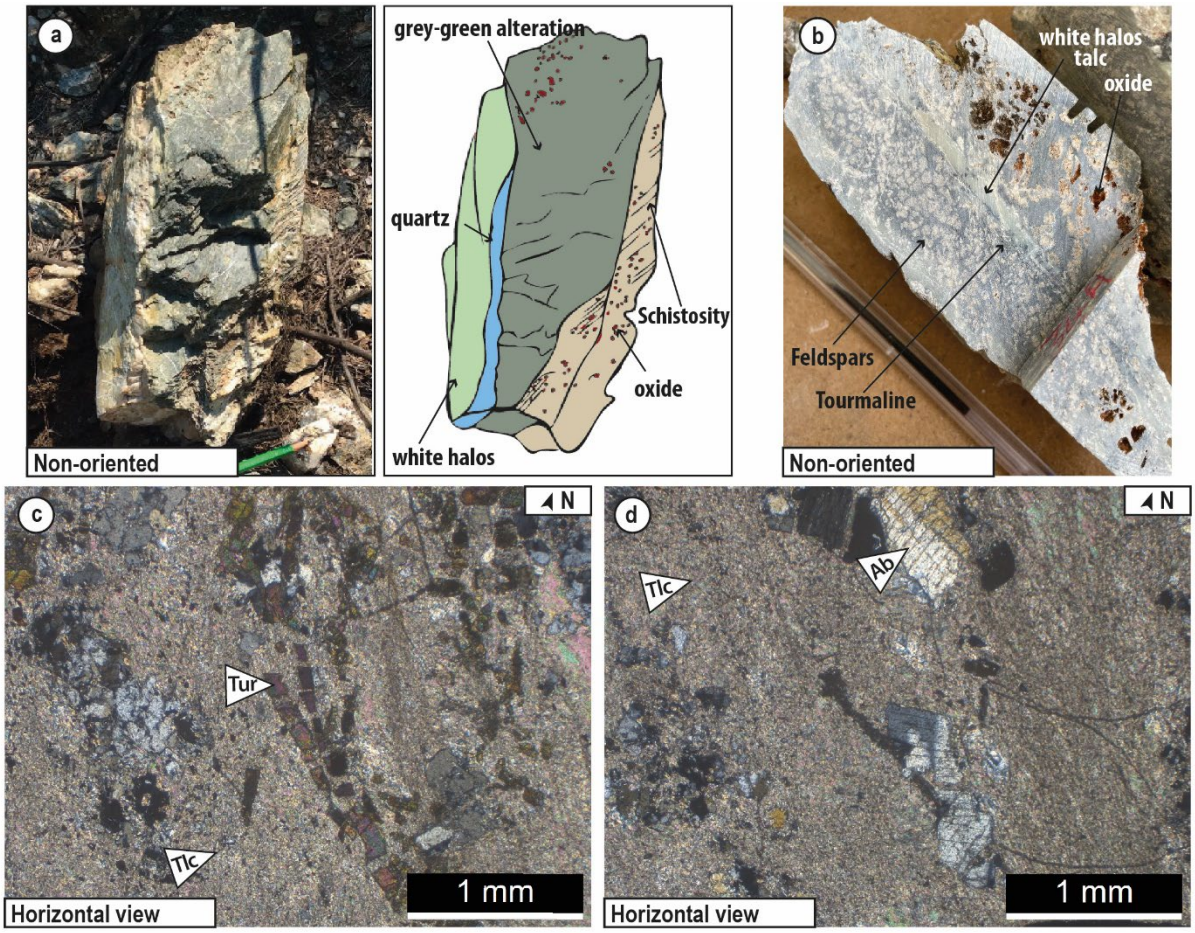

Fig. IV.21. Field and microscopic observations of the alteration in the Primrose occurrence. **(a)** Photo and sketch of cm-wide white/green alteration around the quartz vein and the dm-wide grey/green alteration around it. **(b)** Photo of a cut sample illustrates the light green plane exclusively composed of talc, and the grey part with tourmaline and feldspar. **(c)** Microscopic photo of the grey-green alteration composed of truncated tourmaline and altered albite in a talc matrix. **(d)** Microscopic photo of the grey-green alteration composed of feldspar (albite composition) in a talc matrix.

IV.A.1.7. The Welcome Occurrence (956)

Occurrence n°956, known as "Welcome", corresponds to a mining exploration zone adjacent to the Waterfall Mine. No veins or mineralised objects have been observed in this zone.

In this area, three different schistosities have been identified and classified using overprinting relationships (Fig. IV.22).

- 1) A first one, parallel to a compositional layering of mm to cm-wide carbonate bedding and thin iron-rich micas bedding, is folded in a 20 m-scale open fold.
- 2) A second schistosity is marked by micas sheets alignment oriented globally N-S striking and sub-vertical dipping.
- 3) A third one is shown by iron-rich micas alignment, strikes NW-SE, and is steeply dipping to the NE.

No quartz veins have been observed in this zone, although other hydrothermal objects have been identified such as veins filled by oxides associated with NE-SW striking leaching halos (Fig. IV.23a). Red-brown alteration part of the host rock with mm-wide tourmaline veins and alteration halos of micas and numerous rutile have been also measured NE-SW striking (Fig. IV.23b,c,d).

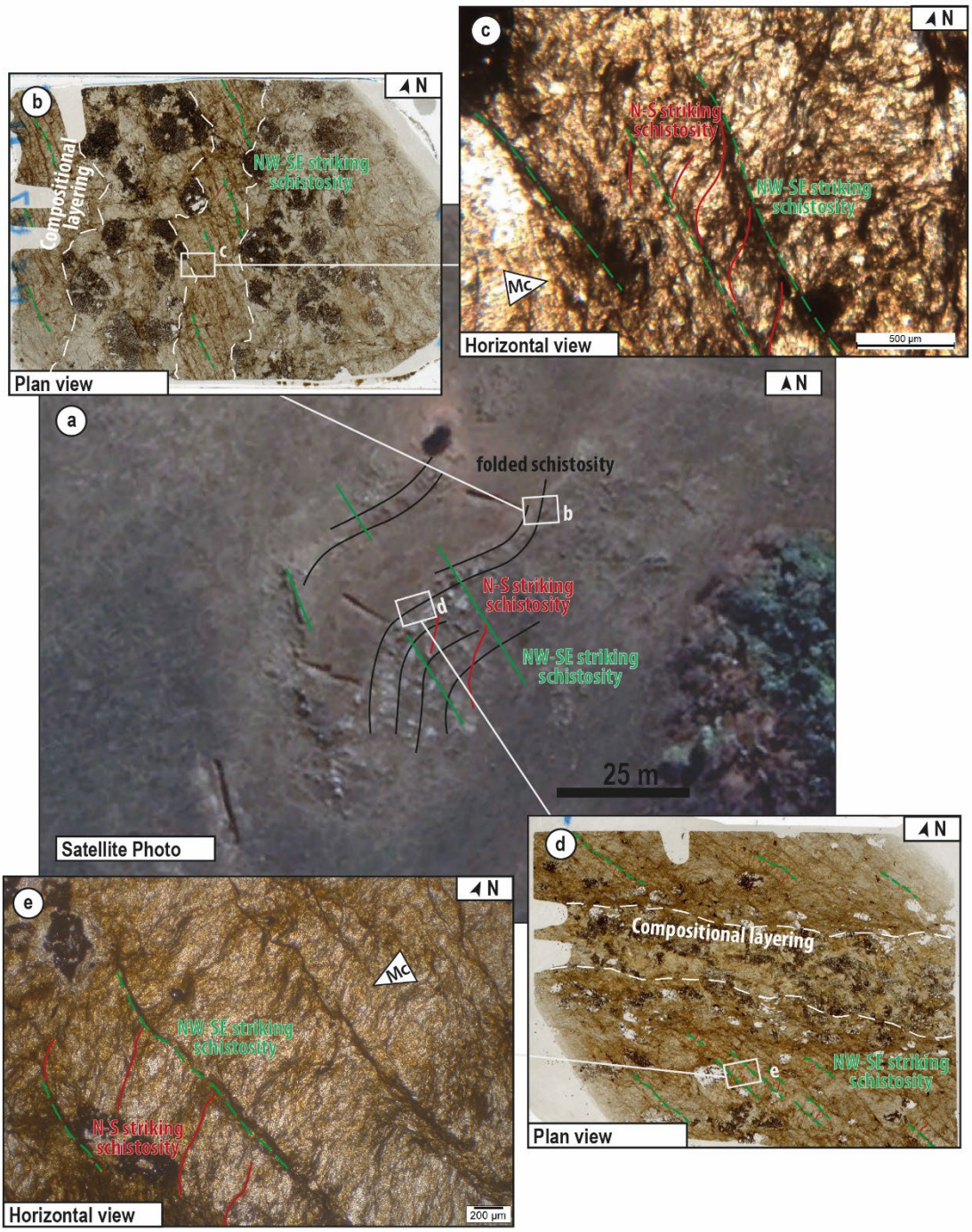

Fig. IV.22. Field and microscopic observations of the overprinting schistosities relationships in the Welcome occurrence. **(a)** Google Earth satellite image of a 100 m scale dextral fold associated with the development of an axial plane NW-SE-striking schistosity. Locations of the samples (b) and (d) are indicated. **(b)** Thin-section scan of the NNE-SSW striking limb, note the NNE-SSW striking compositional layering (white dash line) and the NW-SE striking schistosity (green dash line). Location of the image (c) is indicated. **(c)** Photomicrograph of the overprinting relations between the NW-SE striking schistosity (green dash line) and the N-S striking schistosity (red line). **(d)** Thin section scan of the ENE-WSW striking limb, note the ENE-WSW striking compositional layering (white dash line) and the NW-SE striking schistosity (green dash line). Location of the image (e) is also indicated. **(e)** Photomicrograph of the overprinting relations between the NW-SE striking schistosity (green dash line) and the N-S striking schistosity (red line). All images are observed in polarised light.

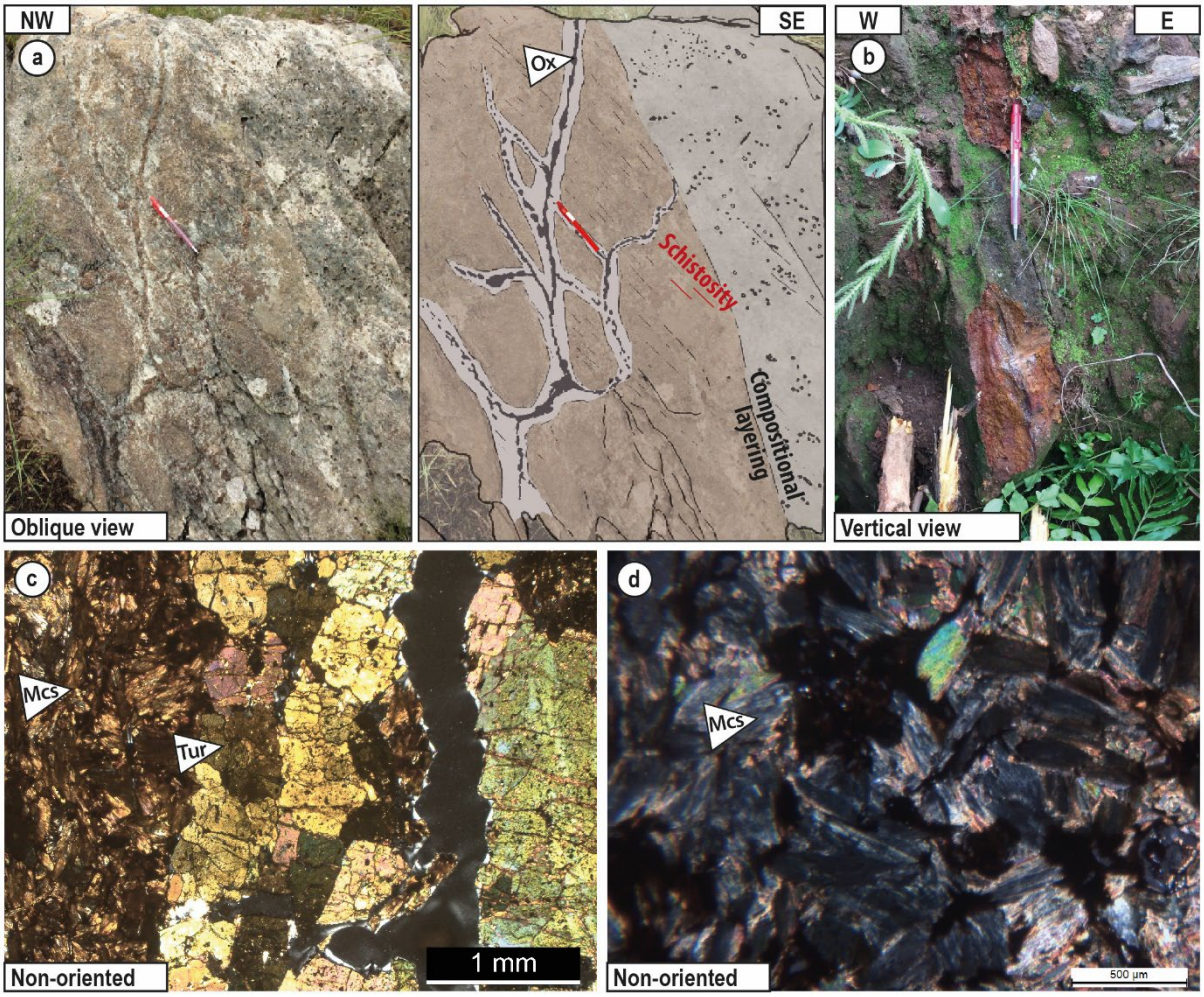

Fig. IV.23. Field and microscopic observations of the alteration in the Welcome occurrence. **(a)** Photo and sketch of oxide-rich veins and associated leaching alteration halos, note the presence of an oblique cleavage. **(b)** Photo of the red-brown alteration in the host rock with mm-wide black tourmaline veins. **(c)** Microscopic photo of the tourmaline veins with micas around it. **(d)** Microscopic photo of alteration-related white micas around the vein.

IV.A.1.8. The Waterfall Occurrence (957)

The 30 m-large former old Waterfall Mine, occurrence n°957, is collapsed; therefore, the mine area is inaccessible (Fig. IV.24) and only the surrounding rocks have been studied during our work.

Fig. IV.24. Aerial photo of the Waterfall former Mine.

Along the edge of the collapse underground mine, a cleavage defined by carbonate-rich talc-schists are ENE-WSW striking and is crenulated by folds with axial plane oriented NW-SE and steeply dipping to the SW. This schistosity carries an NNW plunging well-expressed stretching lineation. A second schistosity, parallel to the crenulation axial plane is striking WNW-ESE to NW-SE and dipping to the SW. On the XY plane, a few sigmoidal porphyroclasts filled by carbonates show ambiguous clear reverse kinematics (Fig. IV.25).

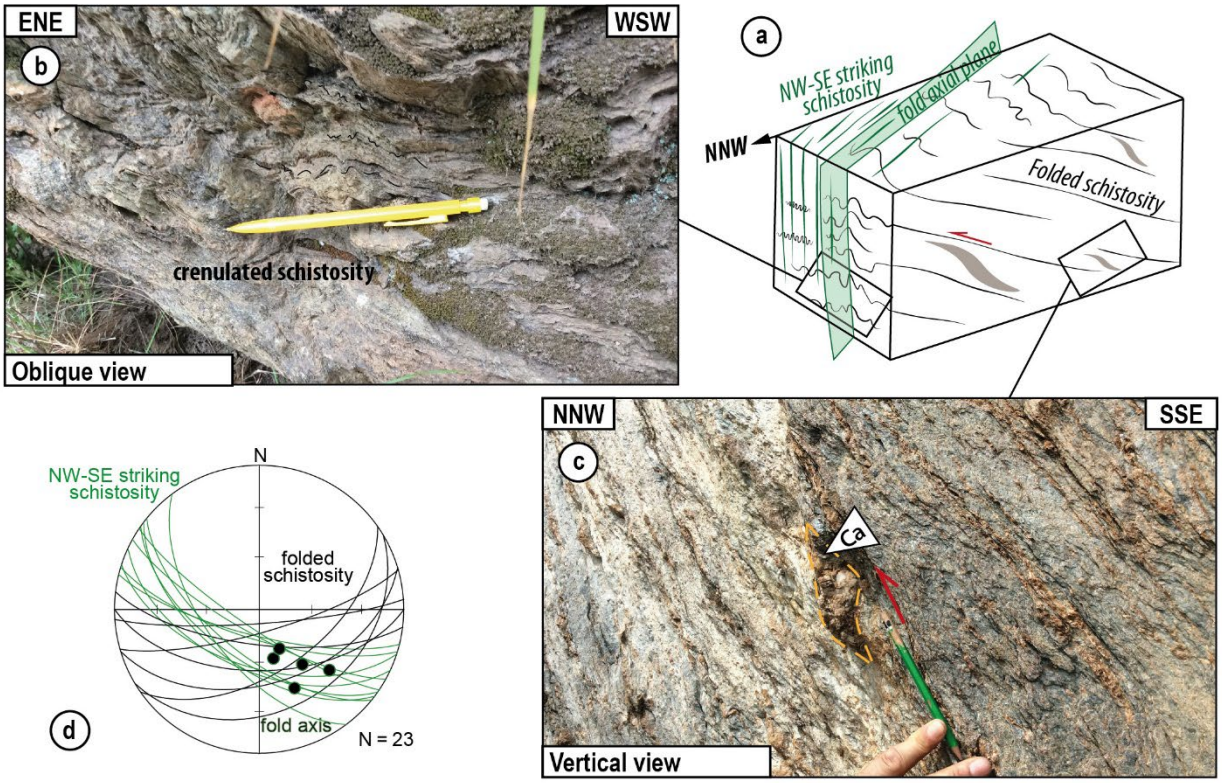

Fig. IV.25. Field observations of the country rock deformation in the Waterfall area. **(a)** Schematic 3D diagram of main structures, with the crenulated schistosity, the fold axial plane and second schistosity (in green) and the reverse carbonate-rich sigmoidal porphyroclasts (light brown). **(b)** Photo of the ENE-WSW-striking crenulated schistosity. **(c)** Photo of the carbonate sigmoid shows a reverse motion. **(d)** Stereonet of the two schistosities (black and green great circles) and the fold axes (Schmidt diagram, lower hemisphere).

To the north of the mine, ENE-WSW striking open to tightly folded schistosities, with fold axial plane NW-SE striking, also observed.

IV.A.1.9. Forbes Reef Mine (960)

The former Forbes Reef gold Mine, or n°960 occurrence, is now a collapsed mine, making access difficult and restricting observations (Fig. IV.26a).

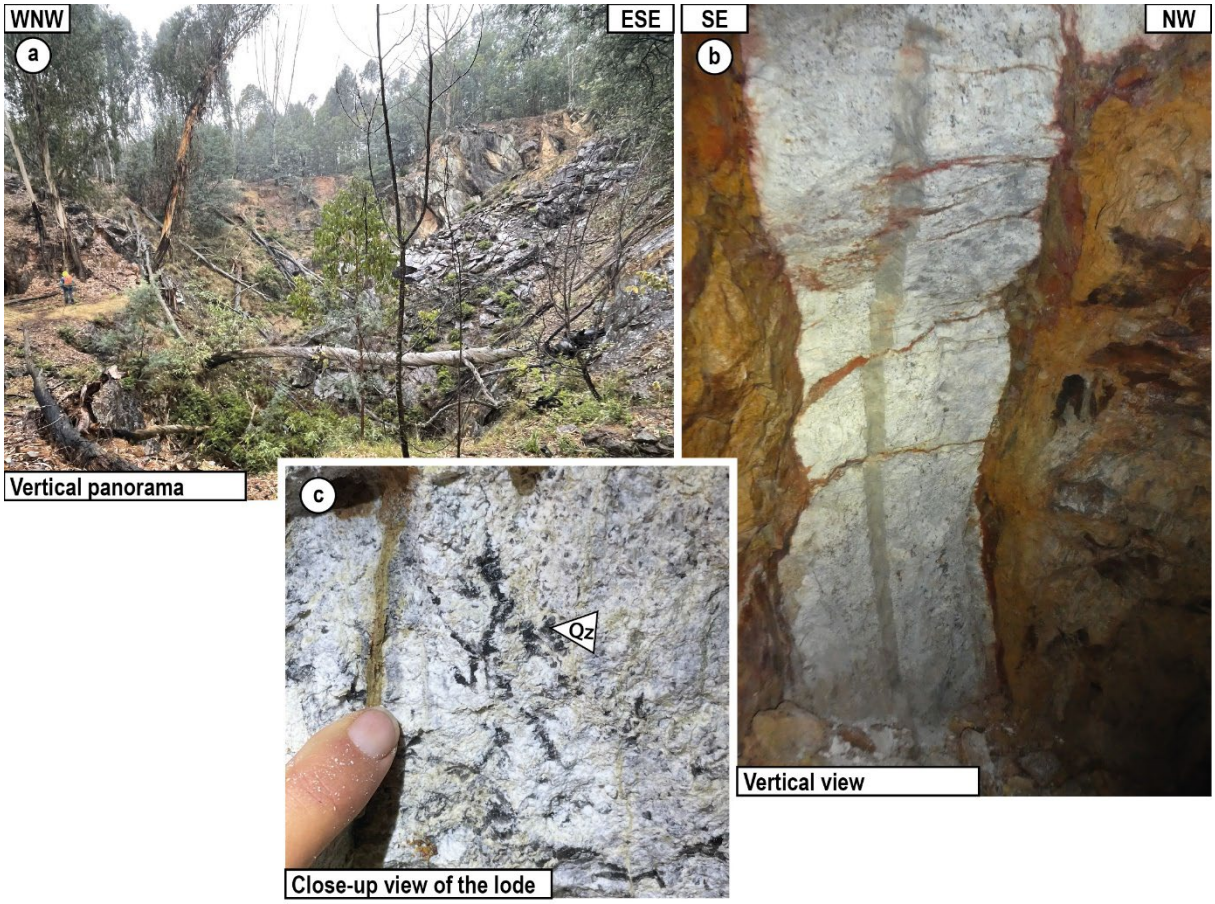

Fig. IV.26. Field observations in the Forbes Reef Mine. **(a)** Panorama of the collapsed Forbes Reef Mine. **(b)** Photo of a m-wide light grey strongly altered "magmatic" lode. **(c)** Close-up view of the lode, note the preservation of grey quartz minerals.

In the area, two different lithologies have been observed, highly altered to highly silicified schists locally magnetised (likely Onverwacht Group), and silicified sandstones (probably Moodies Group). The schistosity seems NE-SW striking and dips to the SE.

A NE-SW striking whitish-grey weathered lodes have been observed in a non-collapsed gallery, and only grey quartz grains remain (Fig. IV.26b,c). We suspect that this lode is an intensely altered leucocratic dike.

IV.A.2. Minor gold occurrences

The minor gold occurrences will not be described by zone as previously. For all outcrops, schistosity and vein measurements have been acquired, but less detailed observations have been produced in these poorly outcropping zones. To summarise the observations made, the host rock is the Onverwacht Group, which may contain m-thick chert horizon (as in Buckingham occurrence, Fig. IV.27a) and talc-schist with varying degrees of carbonate. A steep E-W to NNE-SSW striking schistosity is observed and can be affected by open to tight folds with a NNE-SSW to N-S striking axial plane, locally parallel to a vertical N-S striking schistosity, and small quartz veins (e.g. Buckingham, Fig. IV.27b; and She east occurrence, Fig. IV.28).

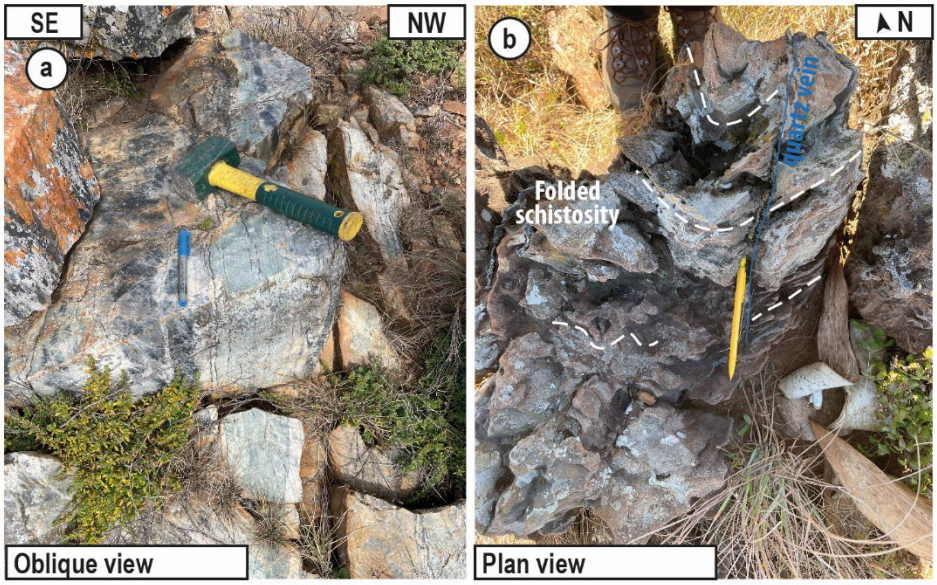

Fig. IV.27. Field observations of the Buckingham occurrence. **(a)** Black, green and white m-wide chert. **(b)** Folded schistosity (white dash line), note the quartz vein (blue line) parallel to the NNE-SSW striking axial plane.

The mineralised objects may occur in quartz veins, lenses or silicified topographic ledges (e.g., She east, Fig. IV.28a; and Hazelmere occurrence, Fig. IV.29a). Some exploited veins present localised recrystallisation in conjugate NNE-SSW and ENE-WSW striking bands (e.g., Hazelmere occurrence, Fig. IV.29a,b). Unmined quartz veins striking NE-SW, locally forming en-echelon patterns or horizontal shear veins associated with marked slickenlines quartz fibres have been observed (e.g., Evelyn occurrence, Fig. IV.30a,b). Veins composed entirely of tourmalines have also been observed, mainly in the Moodies Group (e.g., Evelyn occurrence, Fig. IV.30c).

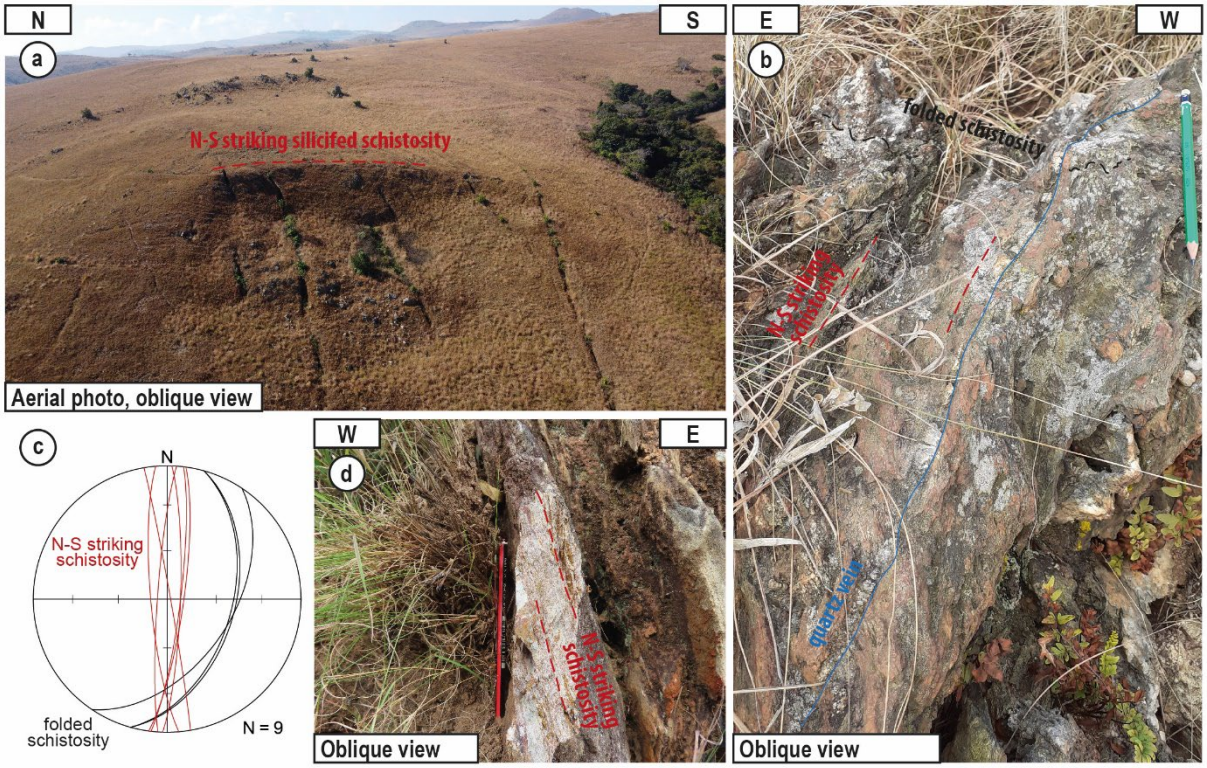

Fig. IV.28. Field observations of the She East occurrence. **(a)** Aerial photo of the N-S striking silicified gentle topographic ridge corresponding to the She east occurrence. **(b)** NE-SW striking folded schistosity (black dash line) with a N-S striking axial plane parallel to the N-S striking schistosity (red dash line) and a quartz vein (blue line). **(c)** Stereonet of the two schistosities (Schmidt diagram, lower hemisphere). **(d)** The vertical N-S striking schistosity (red dash line).

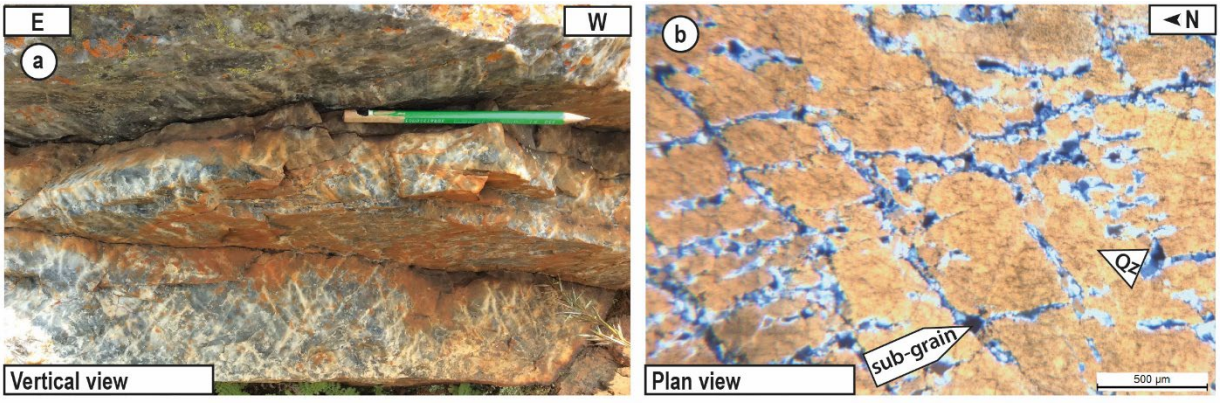

Fig. IV.29. Field and microscopic observations of the Hazelmere occurrence. **(a)** m-wide quartz vein and mm-thick white veinlets oriented in two directions. **(b)** Microscopic photo of an NNW-SSE striking quartz vein with numerous recrystallised sub-grain corridors defining conjugate bands (crossed polars).

Fig. IV.30. Field observations at the northeast of the Evelyn occurrence, in the Moodies Group. **(a)** Horizontal white quartz vein (light blue line) with strongly marked slickenlines made of quartz fibres (dark lines). **(b)** NE-SW striking en-echelon quartz vein (blue dash), and horizontal vein (light blue) with strongly marked slickenlines of quartz fibres (dark lines). **(c)** Tourmaline veins in the Moodies Group.

IV.A.3. Other geological observations

Several observations were made on quartz veins located outside from mining or explored areas in order to complete our study on all the hydrothermal features that exist in studied areas. Five of these outcrops have been the focus of detailed study in the Malolotja area. These outcrops have been labelled according to the names given during the field trips, and their locations are shown on the map in Figure IV.1.

IV.A.3.1. Outcrop Lo14

The Lo14 outcrop is located to 150 m away toward the northwest of the Rosehill occurrence. This zone is made up of highly carbonated talc-schist with N-S striking, east-dipping schistosity, locally crenulated. Dm-thick veins parallel to the schistosity with green alteration halos are observed (Fig. IV.31). Microscopically the vein is composed exclusively of quartz, and the alteration halo of talc.

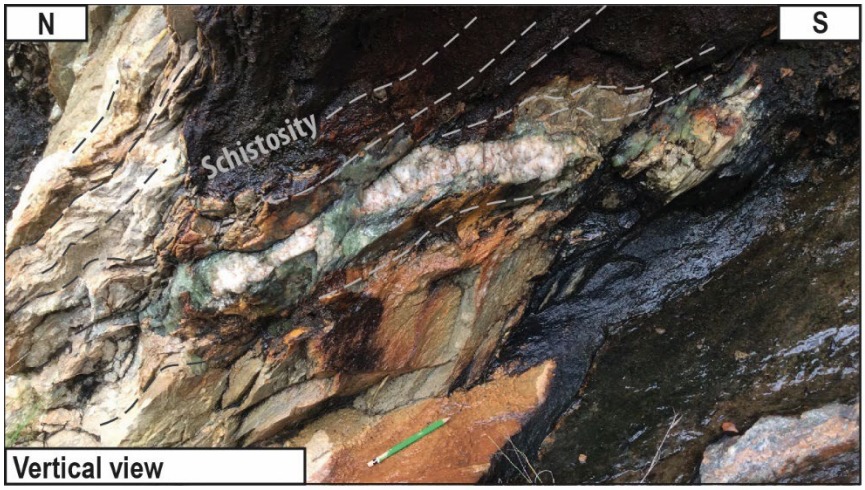

Fig. IV.31. Schistosity-parallel quartz lens with green alteration halo in Lo14 outcrop, northwest of the Rosehill occurrence.

IV.A.3.2. Outcrop Lo43

The Lo43 outcrop is located on the hill north of the Rosehill occurrence. In the core of a well-defined competent lithology trending NNW-SSE, (Fig. IV.32b), several transverse quartz veins are developed.

The carbonates in the surrounding rocks are magnesites and iron-rich carbonate which are intensively oxidised (Figs. IV.32a and IV.33a). The dm- to m-thick NE-SW-striking quartz veins dip to the southwest (Fig. IV.32e). These veins are weakly folded by open folds, with a dm-thick grey-green alteration halo (Fig. IV.32c,d). In the alteration halo, there are mm-wide tourmalines either in radial shapes (Fig. IV.32f) or in rod perpendicular to the vein edge with vein-parallel truncations (Fig. IV.32g).

Microscopic observations show that the veins are composed of quartz moderately to highly recrystallised by sub-grain rotations (Fig. IV.33b,d). The alterations halos are mainly filled by talc, Na-feldspar and tourmaline (Fig. IV.33d,e,f).

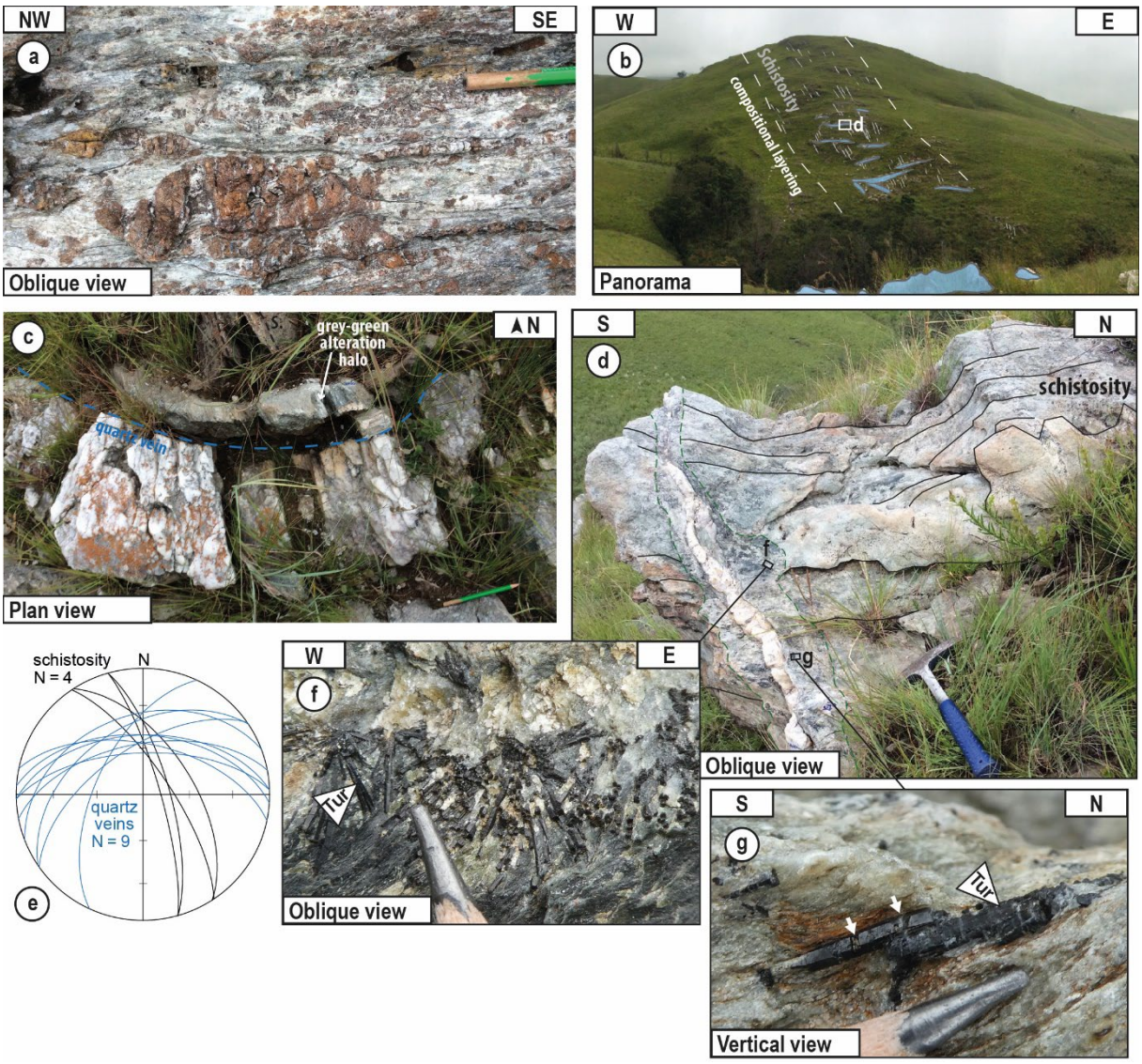

Fig. IV.32. Field observations of the Lo43 outcrop, north of the Rosehill occurrence. **(a)** Country rock composed of talc-schist with large carbonate grains. **(b)** Panorama of the Lo43 outcrop, note the schistosity parallel to the compositional layering. **(c)** Folded quartz vein, note the 10 cm-thick alteration halo in the borders of the vein. **(d)** Slightly folded NE-trending quartz vein and its greyish alteration halo, cutting the schistosity. Locations of the photo (f) and (g) are indicated. **(e)** Stereonet of the quartz veins (blue great circle) and schistosity (black great circle) measurements (Schmidt diagram, lower hemisphere). **(f)** Close-up view of the alteration halo showing radial tourmaline. **(g)** Close-up view of the truncated tourmaline rods in the alteration halo (truncation shown by white arrow).

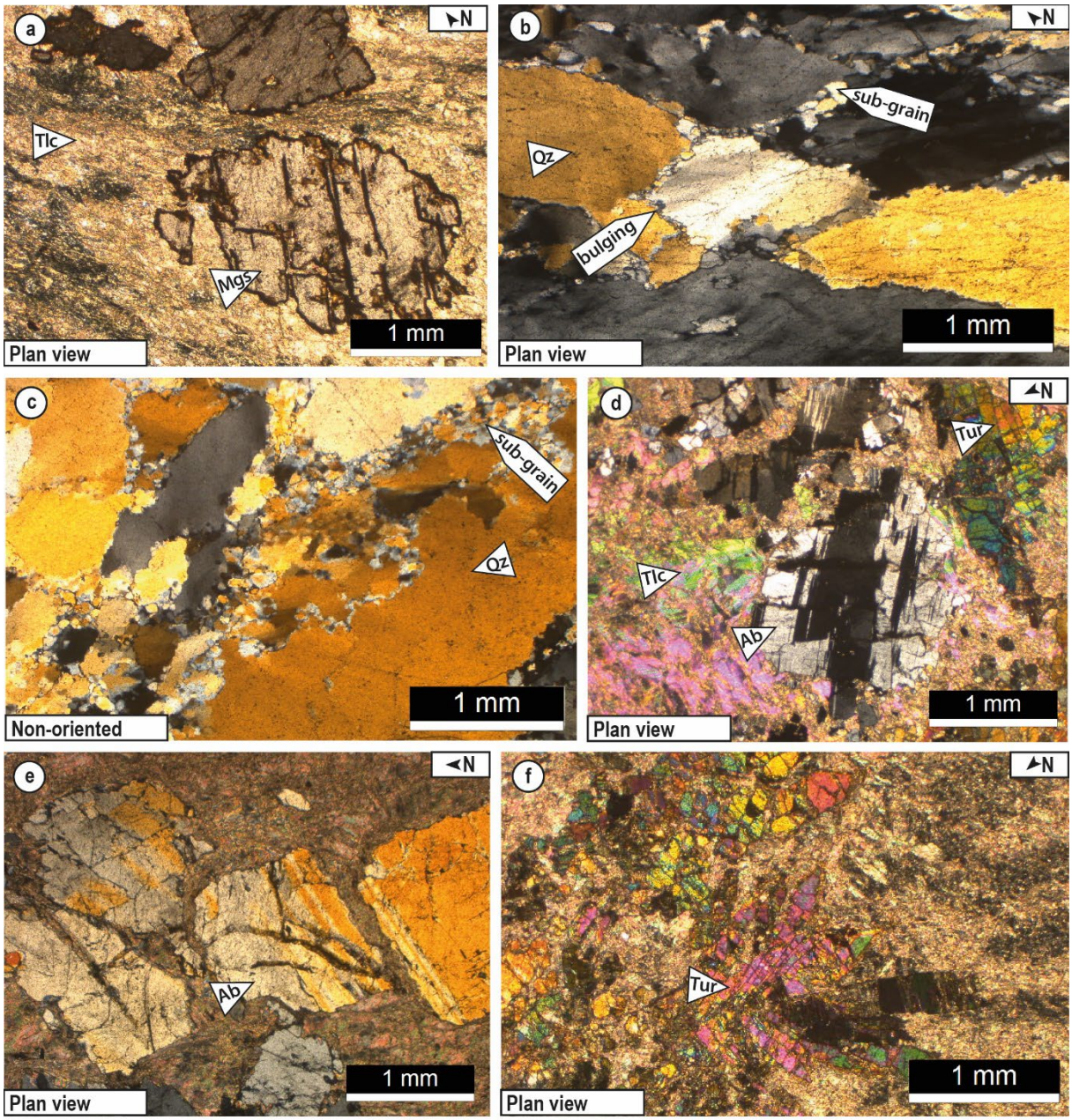

Fig. IV.33. Microscopic observations of the Lo43 outcrop, north of the Rosehill occurrence. **(a)** Country rock of the Onverwacht Group composed of talc schist and a magnesite grains (crossed polars). **(b)** NE-SW-striking quartz veins with sub-grain rotation (crossed polars). **(c)** ENE-WSW-striking quartz veins showing high recrystallisation and sub-grains formation (crossed polars). **(d)** Albite and tourmaline in the alteration halo of an NE-SW striking vein (crossed polars). **(e)** Truncated albite in the alteration halo of the NE-SW striking vein (crossed polars). **(f)** Radial tourmaline in the alteration halo of the NE-SW striking vein (crossed polars).

IV.A.3.3. Outcrop Lo37

Outcrop Lo37 is located northwest of the Forbes Reef occurrence, in the Moodies Group. The country rock is sandstone with K-, Na-feldspars and quartz grains. The bedding is N-S striking is the main part of the outcrop (Fig. IV.34) and corresponds to a limb of the large-scale Malolotja Synform. Few boudinage structures have been observed. Locally a NW-SE striking schistosity is superimposed on the bedding. NE-SW and NW-SE striking quartz veins are cutting the bedding. These veins are composed of recrystallised quartz, K and Na-feldspars (Fig. IV.35a,b,c). Few NE-SW-striking fractures filled by biotite have been identified (Fig. IV.35d).

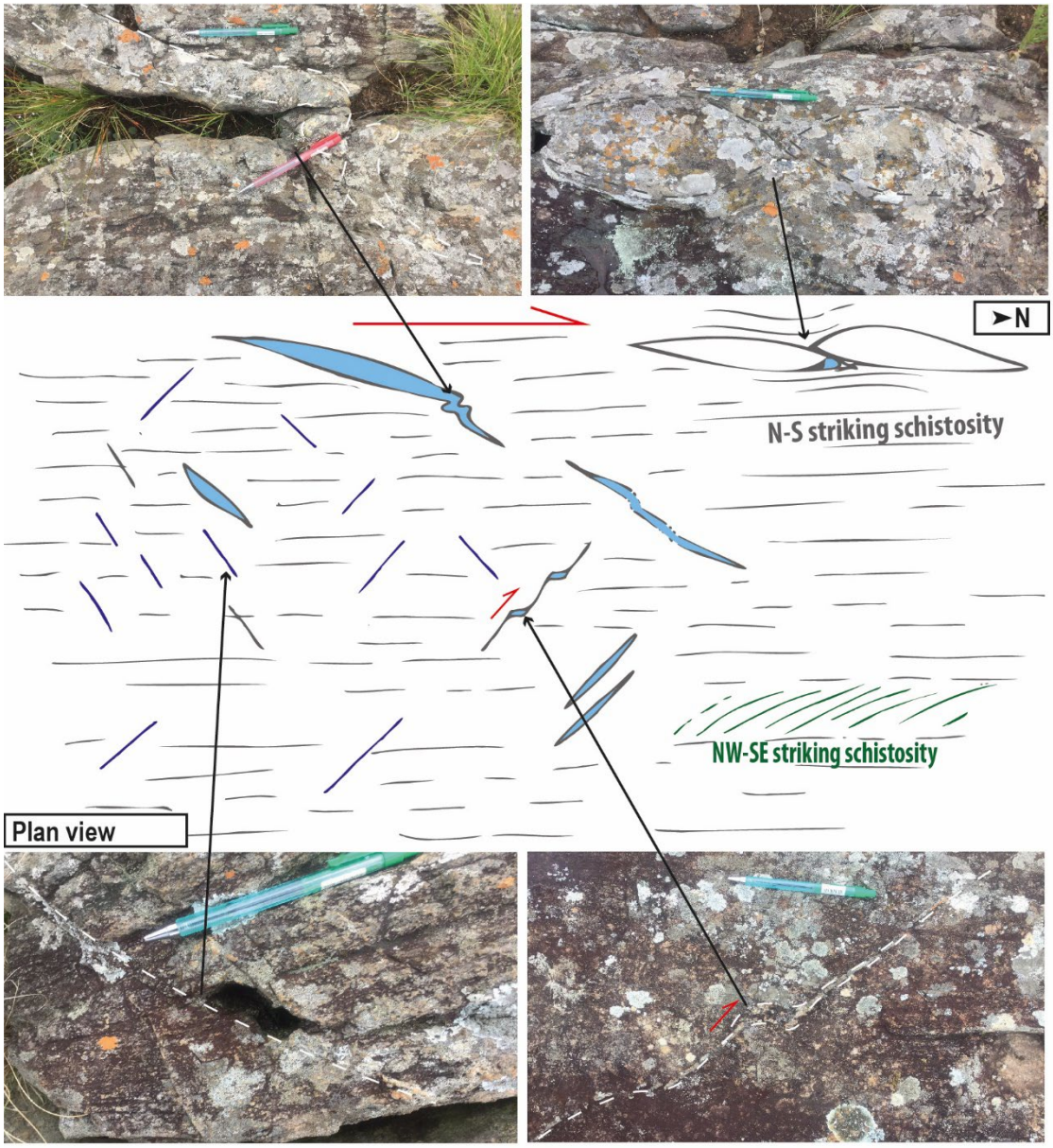

Fig. IV.34. Observations summary of Lo37 outcrop, northwest of the Forbes Reef occurrence, in the Moodies Group. Note the NE-SW striking quartz veins, and the two schistosities.

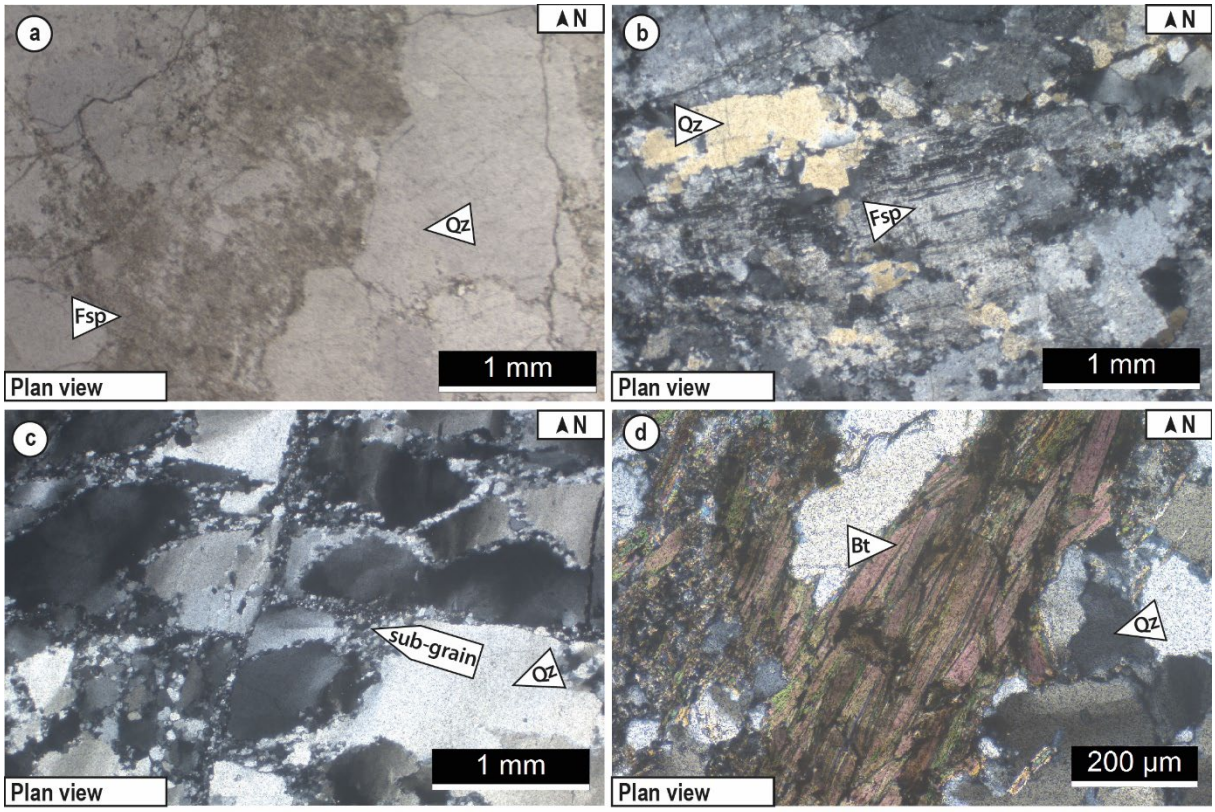

Fig. IV.35. Microscopic observations of the Lo37 outcrop, northwest of the Forbes Reef occurrence, in the Moodies Group. **(a)** NE-SW striking vein composed of quartz and feldspars (polarised light). **(b)** NE-SW striking vein composed of recrystallised quartz and feldspars (crossed polars). **(c)** NE-SW striking vein filled by quartz and sub-grain recrystallisation in band and in borders of the quartz grains (crossed polars). **(d)** Fracture filled by numerous biotite in the host rock (crossed polars).

IV.A.3.4. Outcrop Lo181

The outcrop Lo181 is located between the Welcome and the Evelyn occurrences, in the Moodies Group. Few cm-thick tourmaline veins cutting the Moodies sandstones have been measured NNE-SSW to NE-SW striking (Fig. IV.36). These veins are composed of tourmaline or quartz-tourmaline, and impregnation halos of tourmaline have been identified in the sandstone (Fig. IV.36a).

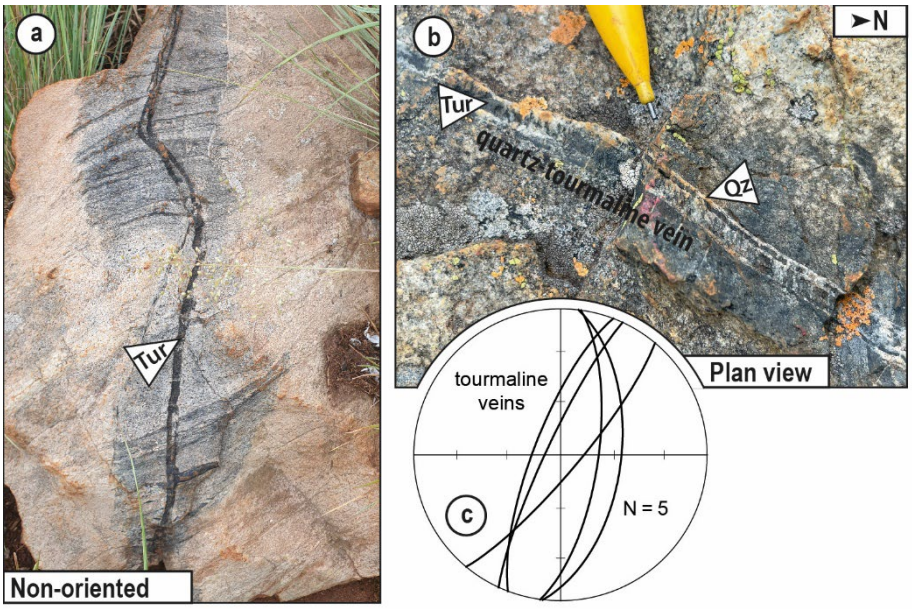

Fig. IV.36. Field observations of the Lo181 outcrop located in the Moodies Group, south of the Evelyn occurrence. **(a)** Moodies sandstone cut by a tourmaline vein and its tourmaline impregnation in the country rock. **(b)** Tourmaline-quartz vein in the Moodies group. **(c)** Stereonet showing the tourmaline veins measurements (Schmidt diagram, lower hemisphere).

IV.A.3.5. Outcrop Lo186

The outcrop Lo186 is located in the northeast part of the Malolotja Synform, in the Moodies Group. The lithology is coarse-grained and thinner layer of sandstone in which bedding is recognised (Fig. IV.37a).

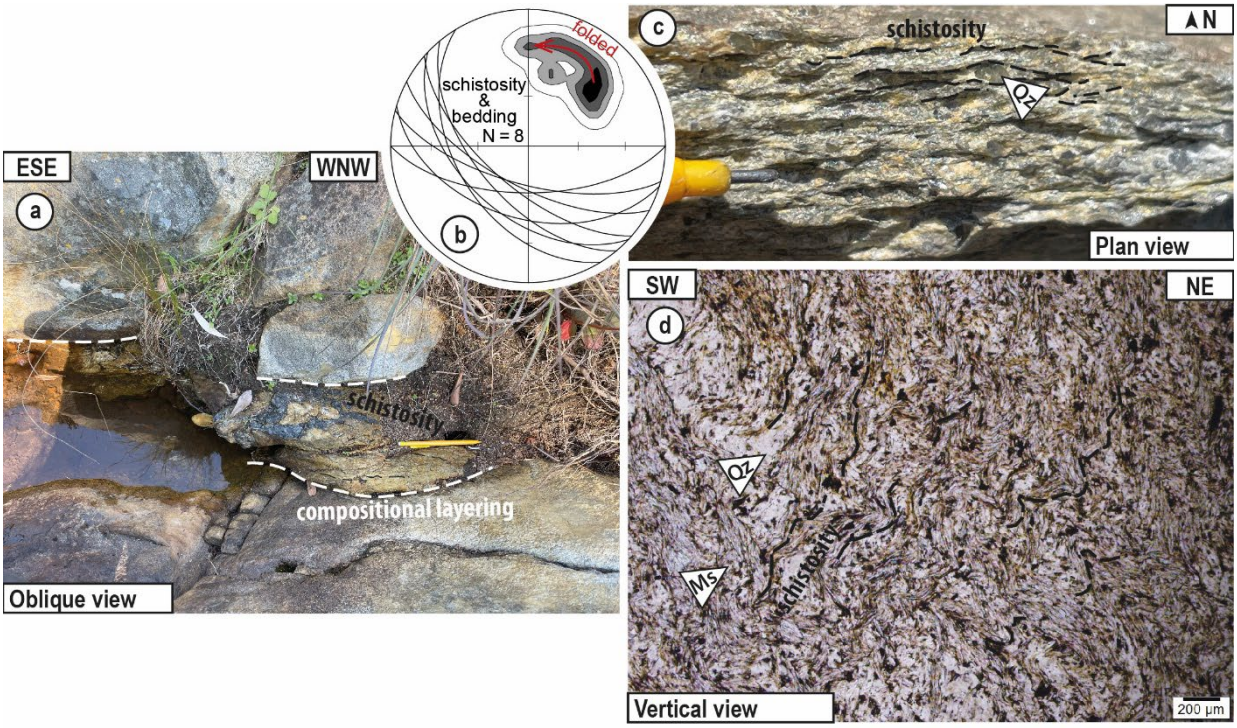

Fig. IV.37. Field and microscopic observations of the Lo186 outcrop, northeast part of the Malolotja Synform, in the Moodies Group. **(a)** Bedding in sandstone with a pelitic layer with bedding-parallel schistosity. **(b)** Stereonet of the bedding and schistosity and their pole density, note the rotation of the schistosity and bedding into E-W striking 400 m away from the Malolotja Synform (Schmidt diagram, lower hemisphere). **(c)** Schistosity in the fine-grained Moodies Group sandstone composed of quartz grains surrounded by mica sheets. **(d)** Microscopic photo of the crenulated schistosity defined by muscovite alignment in the fine-grained sandstone of the Moodies Group (polarised light).

In the thinner lithology layers, a bedding-sub-parallel NW-SE striking schistosity is also observed (Fig. IV.37a,b,c). Moving 400 m away toward the east, the bedding and the schistosity rotate, and strike E-W (Fig. IV.37b), suggesting that the bedding is folded. Muscovite sheets mark this schistosity and is locally crenulated (Fig. IV.37d).

IV.A.3.6. Outcrops in the Piggs Peak Batholith

Outcrops of the Piggs Peak granite have been observed rapidly within areas close to the Malolotja Synform. In this domain, the granite appears to have no preferential fabric and seems be formed by homogeneous grain sizes of biotite, feldspar and quartz (Fig. IV.38a). It can also show a porphyritic texture with two sizes of grains and specifically large feldspar crystals (Fig. IV.38b). Numerous aplite, pegmatite and leucogranite dikes also outcrop. They appear globally NE-SW striking although a clear orientation is difficult to identify (Fig. IV.38c,d). Locally the dikes seem to be folded at m-scale wavelengths (Fig. IV.38e).

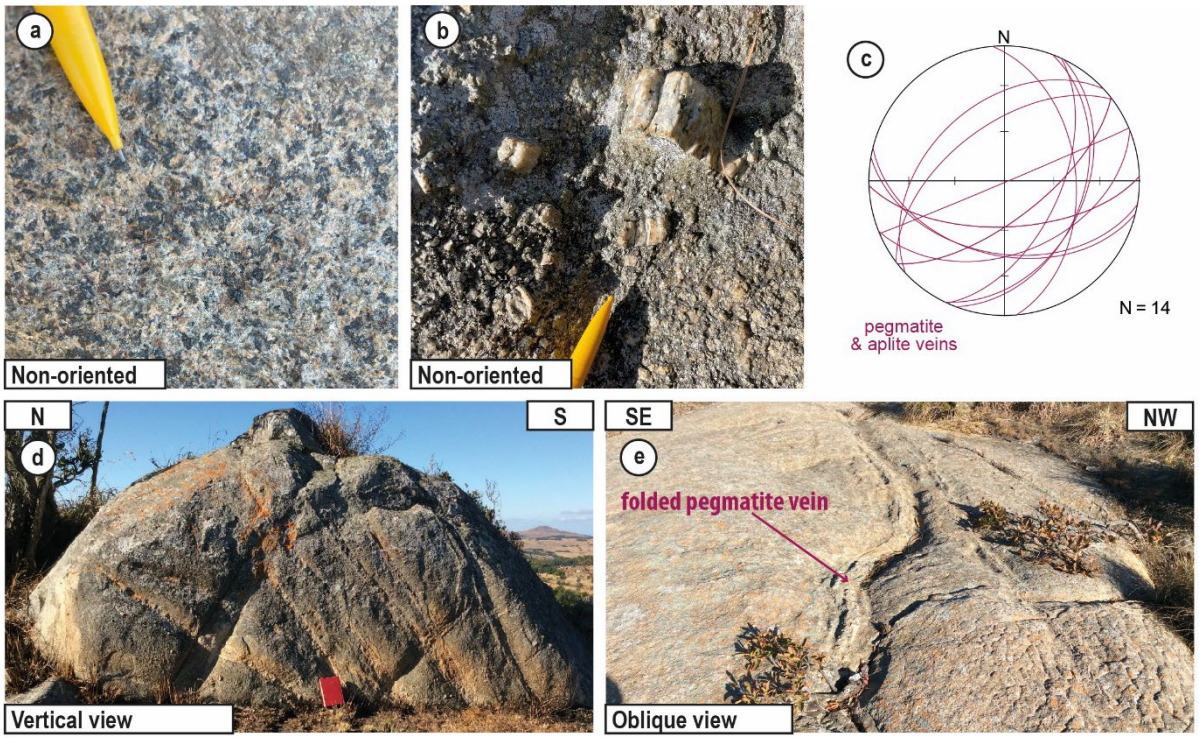

Fig. IV.38. Field observations of outcrops in the Piggs Peak batholith, east of the Malolotja regional fold. **(a)** Granite texture with mm-size quartz, feldspar, and mica grains. **(b)** Porphyritic texture of the granite with cm-size feldspars grains in a mm-large quartz, feldspars and micas matrix. **(c)** Stereonet diagram of the aplite and pegmatite veins (purple great circle) measurements (Schmidt diagram, lower hemisphere). **(d)** Numerous aplite veins cut the granite. **(e)** Folded NE-SW striking aplite vein in the Pigg Peak granite.

IV.B. The Steynsdorp area

As for Malolotja zone, the studied outcrops have been classified into three categories. However, because the Steynsdorp area is less mined than the Malolotja one, we modified slightly the classification criteria as follow: i) major occurrences, corresponding to few galleries, exploration trenches and small scrapings, well-exposed. ii) minor occurrences correspond to gold occurrences that have not been mined. iii) other outcrops which are outside gold occurrences (Fig. IV.1).

IV.B.1. Main Gold occurrences

IV.B.1.1. Occurrence n°817

The n°817 occurrences correspond to exploration-mined area, with a 20 m-long NNW-SSE striking trench. Carbonate-rich schists mark the schistosity in this area, which is vertical and N-S striking (Fig. IV.39a,b). A sub-vertical stretching lineation plunging to the NW has been measured. Numerous quartz veins are observed in this area, mainly N-S striking and mostly dipping variably to the east (Fig. IV.39a,b,c). Some 10 cm-long horizontal veins are observed with in places indicating reverse motion by an en-echelon geometry (Fig. IV.39a). The area shows numerous sub-horizontal veins (Fig. IV.39d) and these veins present locally folding. The veins are composed of quartz, carbonate, tourmaline and minor sulphides. Microscopic observations reveal that the horizontal veins are composed of vertical comb quartz (Fig. IV.40a,b), and vertical tourmalines, which are truncated and filled by quartz in the horizontal spaces (Fig. IV.40c), carbonates, and minor muscovite (Fig. IV.40d,e) and pyrite in the veins and around the veins (Fig. IV.40f). In fact, mm to cm-long thin tourmaline elongated grains are identified within all horizontal veins (Fig. IV.39d). Ankerite-pyrite alteration halo occurs around quartz veins (Fig. IV.39e).

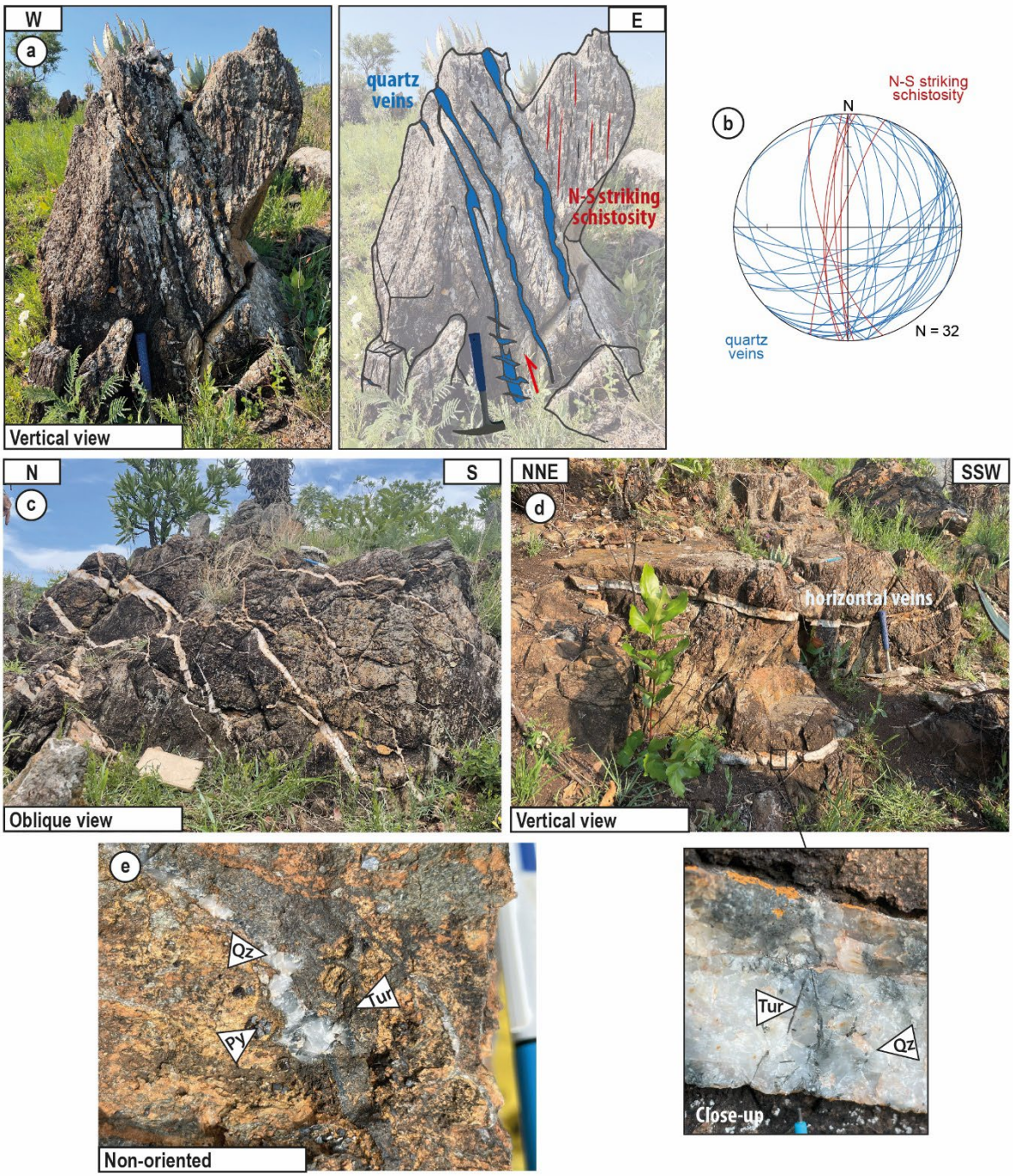

Fig. IV.39. Field observation of occurrence n°817. **(a)** Photo and sketch of a set of steeply east-dipping quartz veins cutting the N-S striking schistosity (red line), which are in turn truncated by horizontal en-echelon horizontal quartz veins. **(b)** Stereonet of the quartz veins measurements and the N-S striking schistosity in the area (Schmidt diagram, lower hemisphere). **(c)** Illustration of the association between shallow and steeply dipping quartz veins, note the petrographic continuity of all these veins. **(d)** Sub-horizontal quartz veins and close-up view of mineral assemblage in the veins. **(e)** Mm scale euhedral pyrites surrounding a quartz-tourmaline vein.

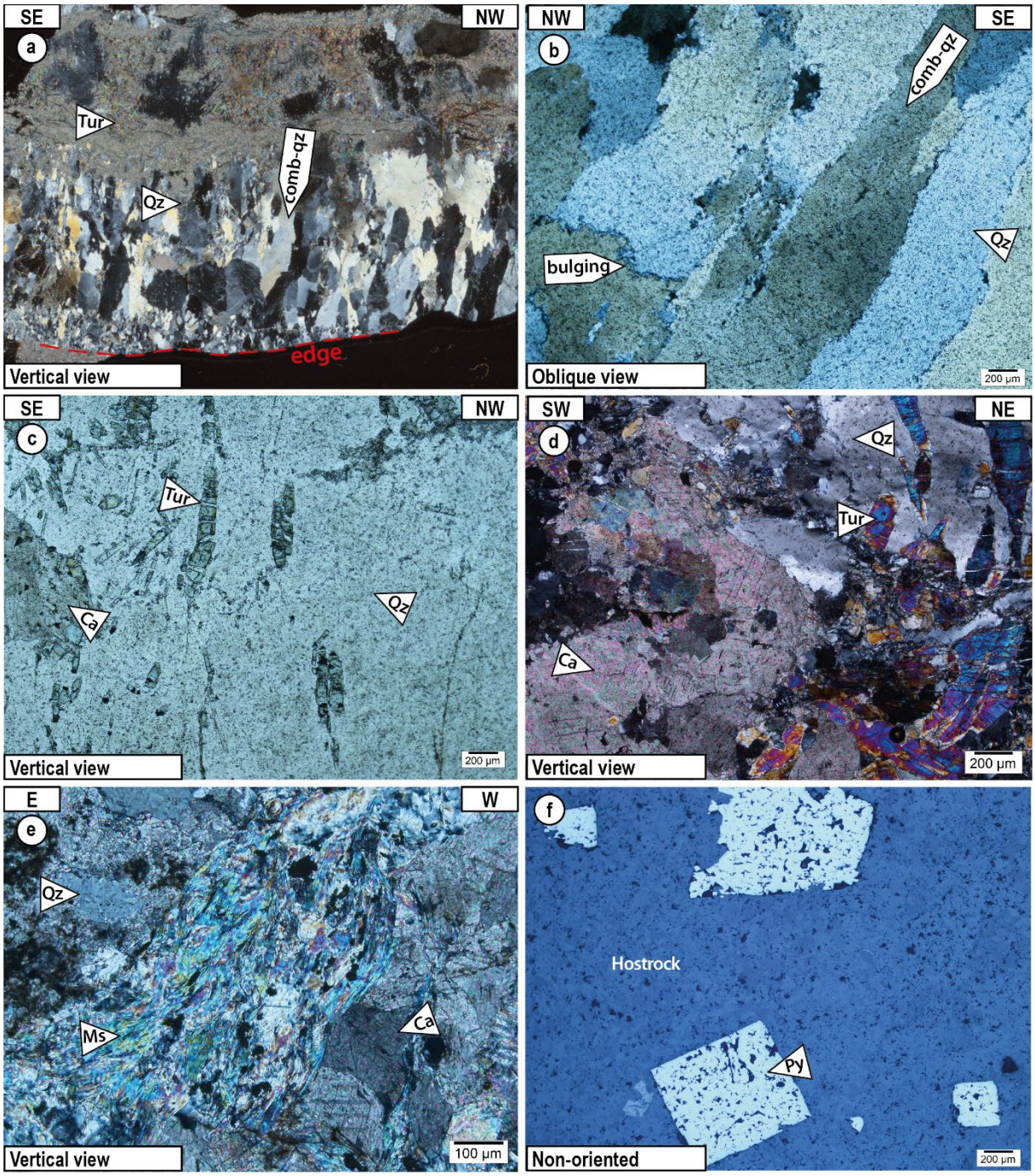

Fig. IV.40. Microscopic observations of the occurrence n°817. **(a)** Horizontal vein filled by vertical comb-quartz and tourmaline (crossed polars). **(b)** Comb quartz with incipient bulging recrystallisation (crossed polars). **(c)** Horizontal veins filled by quartz, carbonate and vertical and truncated tourmaline; the quartz-filled spaces between two adjacent truncated tourmaline segments are here parallel to the edge of the vein (polarised light). **(d)** Large carbonate, tourmaline and quartz filling a vein (crossed polars). **(e)** Carbonate, quartz and large muscovite in a quartz vein (crossed polars). **(f)** Automorphic pyrites in the host-rock at the vicinity of a quartz vein (reflected light).

IV.B.1.2. Occurrence n°818

Occurrence n°818 is a little outcrop with some diggings. The outcrop consists of altered volcanic country rock (Figs. IV.41a and IV.42a), one m-thick horizontal quartz vein (i.e., the target of the exploration trench) and satellite cm-tick horizontal veins (Fig. IV.41a,b). The upper margin of the m-wide vein bears WNW-ESE trending quartz fibre slickenlines (Fig. IV.41b,c) and has a cm-size patches of dark and beige minerals (Fig. IV.41d) and prismatic quartz in its centre (Fig. IV.41e). The cm-wide quartz veins show vertical to slightly oblique (west plunging) quartz fibre (Fig. IV.42b). Microscopically, the mm-thick quartz vein is composed of un-recrystallised quartz grains increasingly larger towards the vein centre (Fig. IV.42c,d,e); and K-feldspar between large Ca-feldspar grains, with few tourmalines (Fig. IV.42f,g).

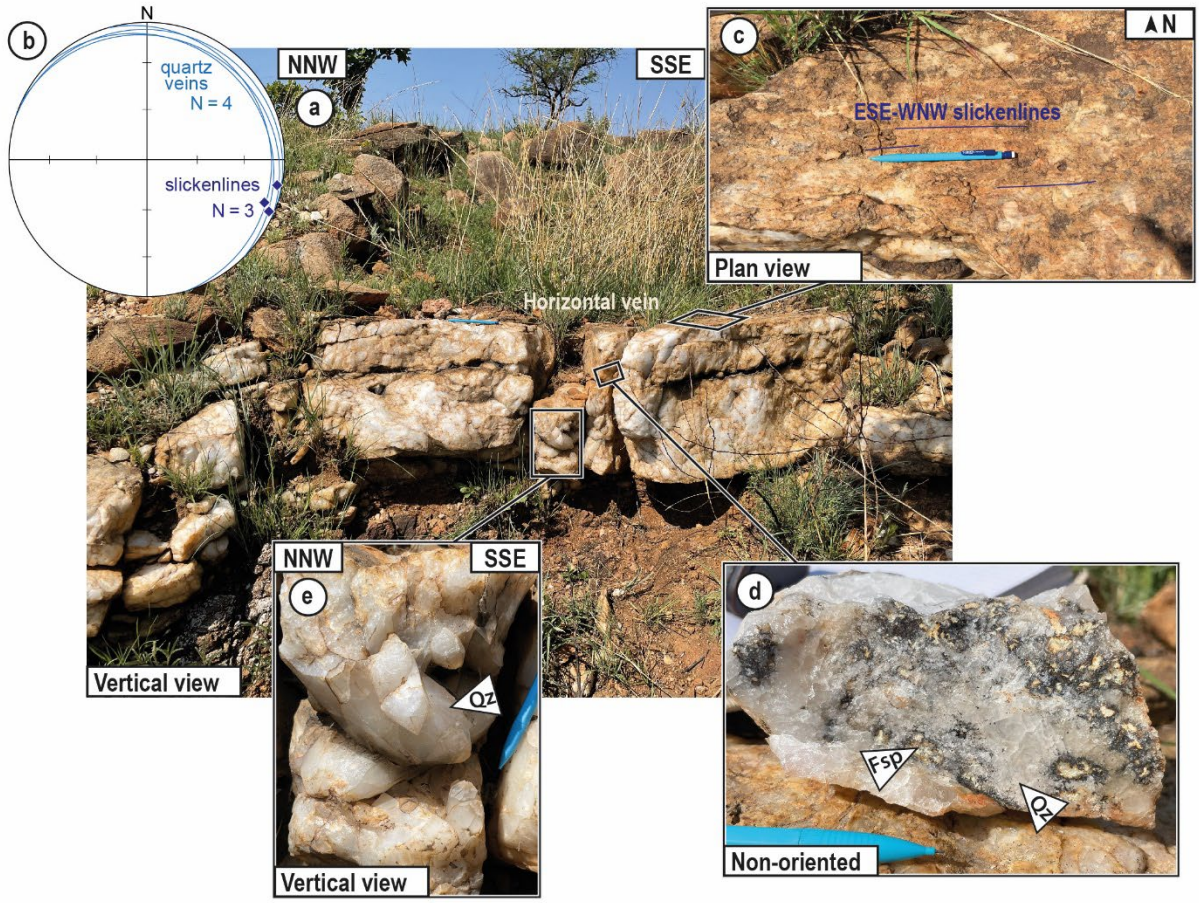

Fig. IV.41. Field observations of occurrence n°818. **(a)** Horizontal m-thick quartz vein. Locations of Photos (c), (d) and (e) are indicated. **(b)** Stereonet of veins measured in the area (blue great circle) and slickenlines (dark blue dot) on the edge of the m-thick horizontal vein (Schmidt diagram, lower hemisphere). **(c)** Photo of the slickenlines (dark blue line) on the edge of the horizontal m-thick vein. **(d)** Sample close to the upper edge of the vein containing quartz and feldspar. **(e)** Prismatic dm-long quartz in the middle of the vein.

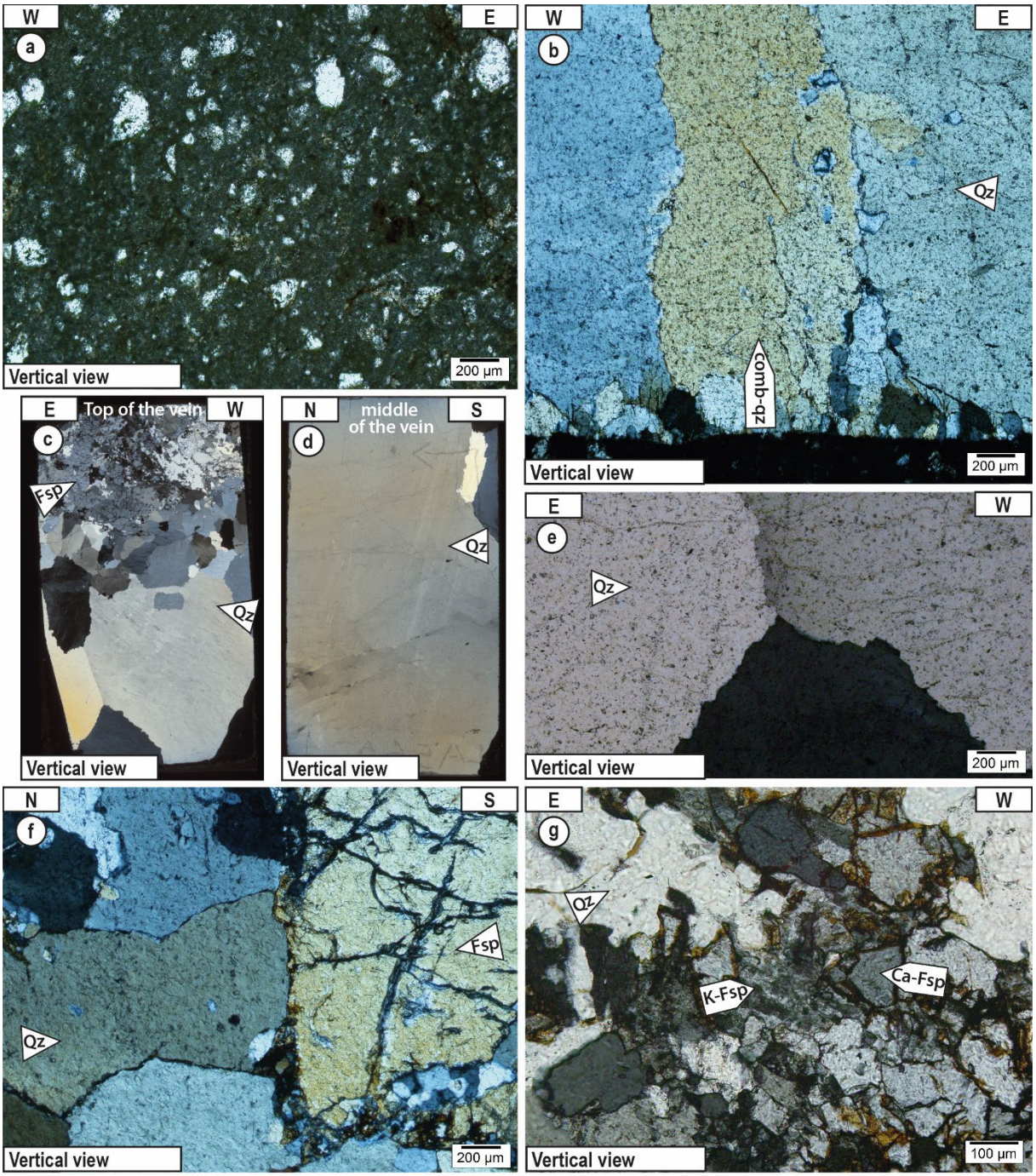

Fig. IV.42. Microscopic observations of the occurrence n°818. **(a)** Microscopic view of the volcanic host-rock (polarised light). **(b)** Vertical comb quartz at the edge of a horizontal vein (crossed polars). **(c)** Thin-section scan of a sample at the top of the m-thick horizontal vein; note the occurrence of feldspars and the increasing of grains size towards the bottom (crossed polars). **(d)** Thin-section scan of a sample in the middle of the m-thick horizontal vein, note the huge size of quartz grain (crossed polars). **(e)** Un-recrystallised quartz grains characterising the horizontal quartz veins (crossed polars). **(f)** Quartz grains and Ca-feldspar filling the m-thick horizontal vein (crossed polars). **(g)** Quartz and K-feldspars associated with Ca-feldspars grains in the m-thick horizontal vein (crossed polars).

IV.B.1.3. Occurrence n°819

The occurrence n°819 is made up of a few mine features (old trenches, scrapings, shafts). Host rocks in this area are talc-schists with a vertical N-S striking schistosity and a steeply NNW-plunging mineral lineation. E-W striking schistosity is folded with a N-S striking vertical axial plane (Fig. IV.43a). A vertical m-thick chert striking NNE-SSW can be seen on the edge of the mining area. Two quartz vein types have been identified at occurrence n°819. The first one is represented by mm to cm-wide folded quartz veins, with a N-S striking axial plane sub-vertical; and parallel to the E-W folded schistosity (Fig. IV.43a).

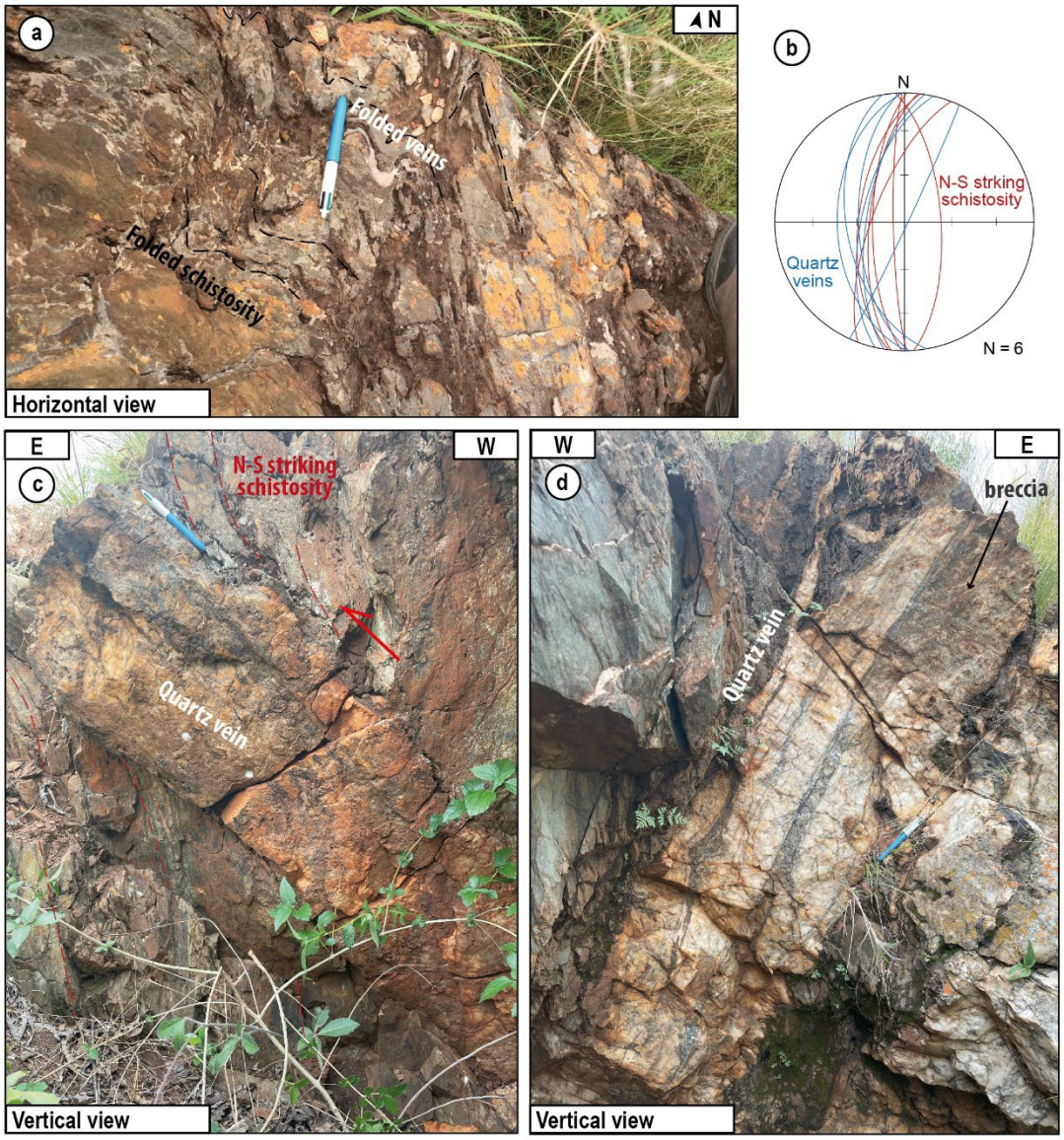

Fig. IV.43. Field observations of the occurrence n°819. **(a)** E-W striking folded schistosity (black dash line) with parallel to a cm-thick quartz vein system. **(b)** Stereonet of the steep veins (blue great circle) and N-S striking schistosity (red great circle) measurements (Schmidt diagram, lower hemisphere). **(c)** West-dipping quartz vein with drag folding of the N-S schistosity in the host-rock, attesting of a top-to-the-east reverse motion. **(d)** West-dipping array of parallel quartz veins; note the dark bands and the brecciated part of the vein.

The second one is formed by dm- to m-wide quartz veins, striking N-S and steeply dipping to the west (Fig. IV.43b). Drag folds affecting the surrounding schistosity suggest a reverse sense of shear, i.e., to the east (Fig. IV.43c). Vein texture is complex with white and grey quartz bands and in places brecciated parts (Fig. IV.43d). Observations under the microscope suggest that the early, folded veins are composed of quartz and carbonates (Fig. IV.44a). The exploited quartz veins in reverse shear zones, certainly representative of the orebodies, are composed of quartz, mm-long tourmaline, chlorite and sulphides (Fig. IV.44b,c). Quartz can be highly recrystallised as suggested by the appearance of numerous 10 µm-wide sub-grains. In the host rock numerous pyrites are observed in halo of the veins (Fig. IV.44a,d).

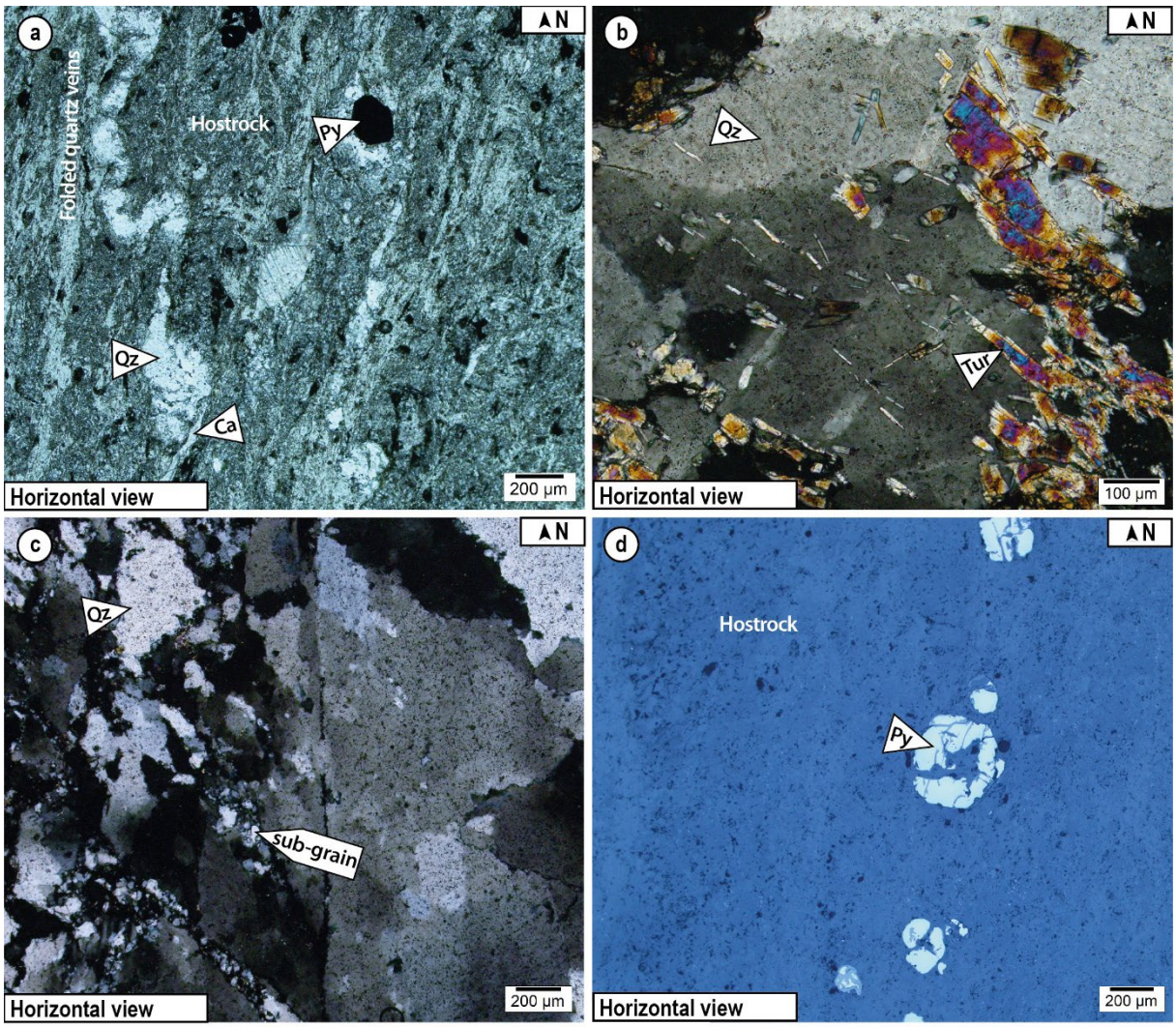

Fig. IV.44. Microscopic observations of the occurrence n°819. **(a)** Folded quartz-carbonate veins and pyrite grain within the hostrock (polarised light). **(b)** West-dipping quartz vein filled by quartz and elongated tourmaline (crossed polars). **(c)** West-dipping quartz vein with significant recrystallisation by sub-grain rotation (crossed polars). **(d)** Pyrites grains in the hostrock (reflected light).

IV.B.1.4. The Gypsy Queen occurrence (827)

Occurrence n°827 corresponds to a former small-scale mining area named Gypsy Queen (numerous trenches, galleries and tailings). The country rock of the deposit is a felsic porphyry (Fig. IV.45a,c) described by Viljoen et al. (1969) with a sub-vertical NW-SE striking foliation. 100 m-away from the mining area, a vertical N-S striking schistosity has been observed.

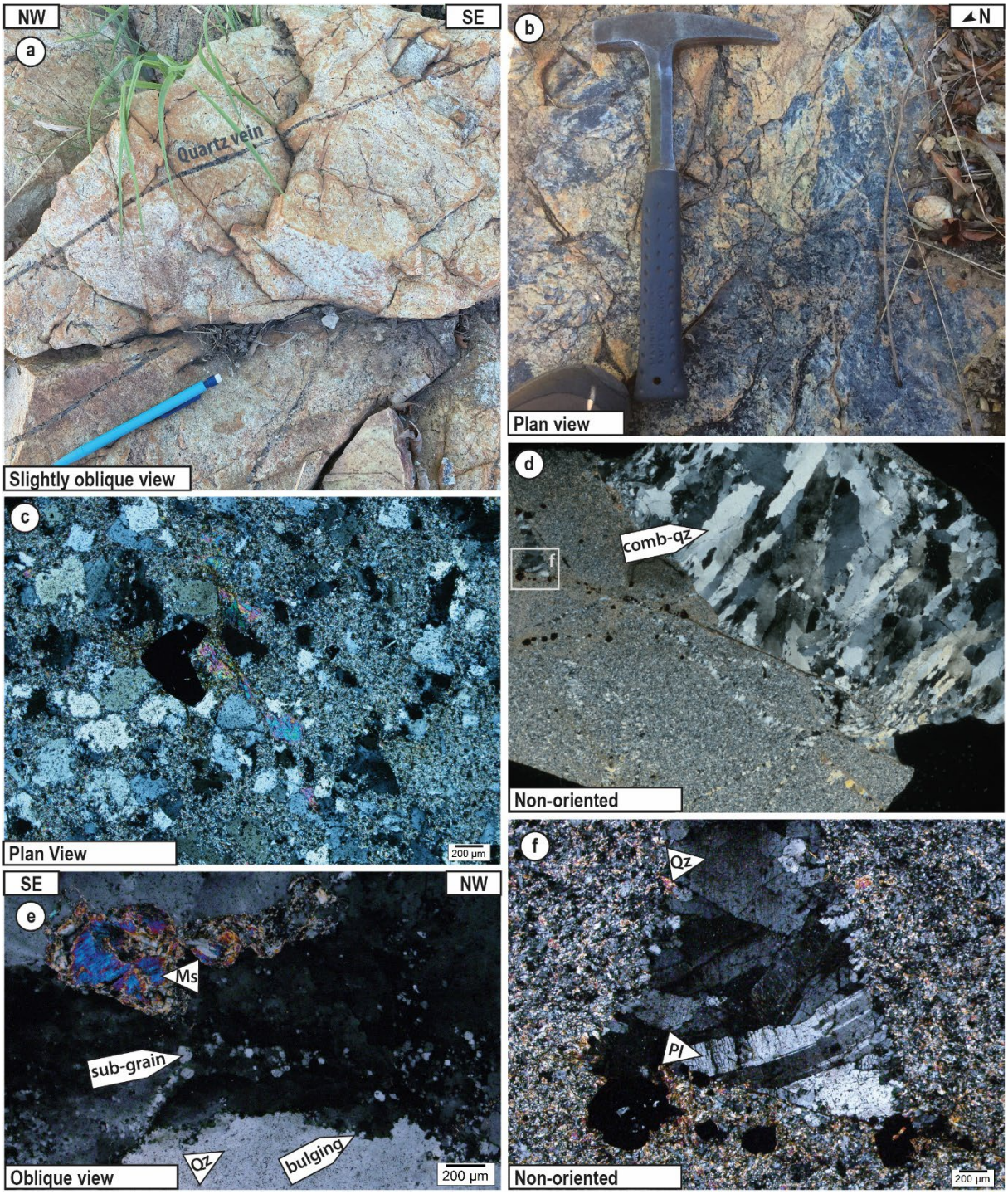

Fig. IV.45. Field and microscopic observations of the Gypsy Queen occurrence. **(a)** Felsic porphyry, note the planar dark NNW-SSE striking quartz veins. **(b)** Brecciated zone with felsic porphyry and dark quartz. **(c)** Microscopic photo of the porphyry (crossed polars). **(d)** Thin-section scan of a vein with comb quartz perpendicular to the edge of the vein, location of the microphotography (f) is indicated (crossed polars). **(e)** Muscovite and quartz filling the quarzitic part of the brecciated zone shown in b, note recrystallisation via bulging and sub-grain rotation (crossed polars). **(f)** Quartz-feldspar veins (crossed polars).

Because galleries are partly collapsed and unsafe, all observations have been made surficial outcrops. Some planar cm-thick dark quartz veins are NNW-SSE striking and steeply dip towards the ENE (Fig. IV.45a). M-thick corridors striking WNW-ESE are composed of dark quartz and green felsic host rock breccia (Fig. IV.45b).

Quartz veins are composed of recrystallised comb quartz (Fig. IV.45d), muscovite and minor feldspars (Fig. IV.45e,f). Numerous pyrites have been identified in the country rock, which can be either primary or due to an alteration halo around quartz veins. The quartz of the WNW-ESE striking corridors has a comb texture and suffers recrystallisation with sub-grains formation (Fig. IV.45e).

IV.B.1.5. The Post Office occurrence (830)

The occurrence n°830, named Post Office is made up of a few old trenches and scrapings. The country rock is talc-schist with a WNW-ESE striking, the NNE dipping schistosity, locally crenulated with fold axis plunging to the ENE. Southwards, two chert bands have been measured WNW-ESE striking and dipping to the NNE, i.e., parallel to the schistosity in the mining area.

The geometry of the veins is consistent throughout the area: all the veins are dm- to m-thick and sub-horizontal. On the wall of the veins, locally, quartz fibre slickenlines occur and are plunging to the ESE. Parallel to the veins walls they are black cm-thick gently west dipping bands composed of steeply west plunging tourmaline fibres (Fig. IV.46).

Microscopic observations reveal that the veins are composed of comb quartz with some bulging (Fig. IV.47a,b), and truncated tourmaline with pressure shadows and truncation developed in places (Fig. IV.47c). Folded tourmalines can be locally observed (Fig. IV.47d).

Fig. IV.46. One of the sub-horizontal veins observed at the Post Office occurrence, and a close-up view of the tourmaline fibres. Note that the black bands (composed of vertical tourmaline) are sub-horizontal, i.e., parallel to the edges of the vein.

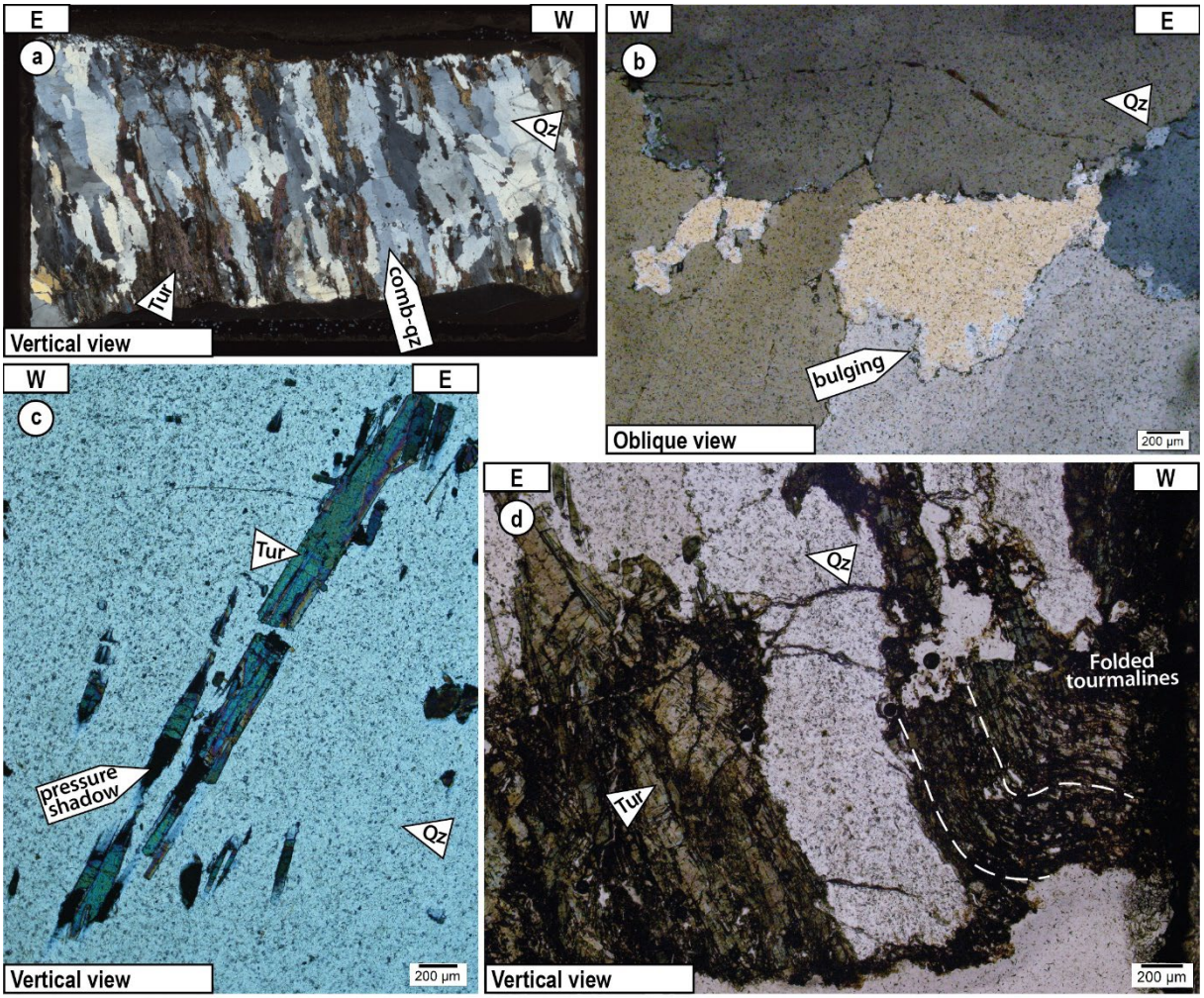

Fig. IV.47. Microscopic observations of the vein in the Post office occurrence. **(a)** Thin-section scan of the sub-horizontal vein, note the slightly oblique comb quartz and tourmalines (crossed polars). **(b)** Incipient bulging recrystallisation of the quartz in the sub-horizontal vein (crossed polars). **(c)** Steeply W-plunging tourmaline, note the truncation at the tips of the tourmaline (crossed polars). **(d)** Folded tourmaline in the sub-horizontal vein (polarised light).

IV.B.1.6. The Homestead occurrence (925)

The Homestead occurrence n°925 is a drift and a large WNW-ESE striking trenches. In this area, ENE-WSW striking locally folded schistosity is encountered; the axial planes strike WNW-ESE (Fig. IV.48a,b).

To the west, a NNE-SSW striking chert (Middle Marker) dip to the WNW. Close to the mined area, several m-thick NE-SW to ENE-WSW striking felsic tabular bodies are also observed. Felsic rocks have porphyritic texture with large feldspar crystals embedded in a fine-grained matrix (Fig. IV.48c,d). Microscopic observations show that the felsic rock is composed of large feldspar, minor chlorite, tourmaline and sulphide in a fine-grained felsic matrix (Fig. IV.49a,b,d).

Three vein geometries are observed in this area:

- i) Cleavage-parallel cm-wide quartz veins; these veins are folded together with the schistosity (Fig. IV.48b).
- ii) Cm-wide shallow dipping veins in the felsic rock. Several vertical quartz and tourmaline fibres have been reported (Fig. IV.48c,e); some veins, exclusively composed of tourmaline, act like fault planes with down-dip slickenlines; both normal and reverse motion were recognised.
- iii) Large m-wide WNW-ESE striking veins, composed of white quartz parts, brecciated zone, and dark part certainly enriched in tourmaline (Fig. IV.48f).

Microscopic observations reveal the cm-veins in the felsic rocks are composed of Na-feldspars, numerous tourmalines, rich-iron carbonate, quartz and sulphides (mostly pyrites, Fig. IV.49c,d) whereas m-thick quartz veins are formed of quartz, tourmaline, carbonate, and sulphide (Fig. IV.49e,f). Locally the carbonate and tourmaline show radial texture (Fig. IV.49f) whereas quartz is weakly recrystallised.

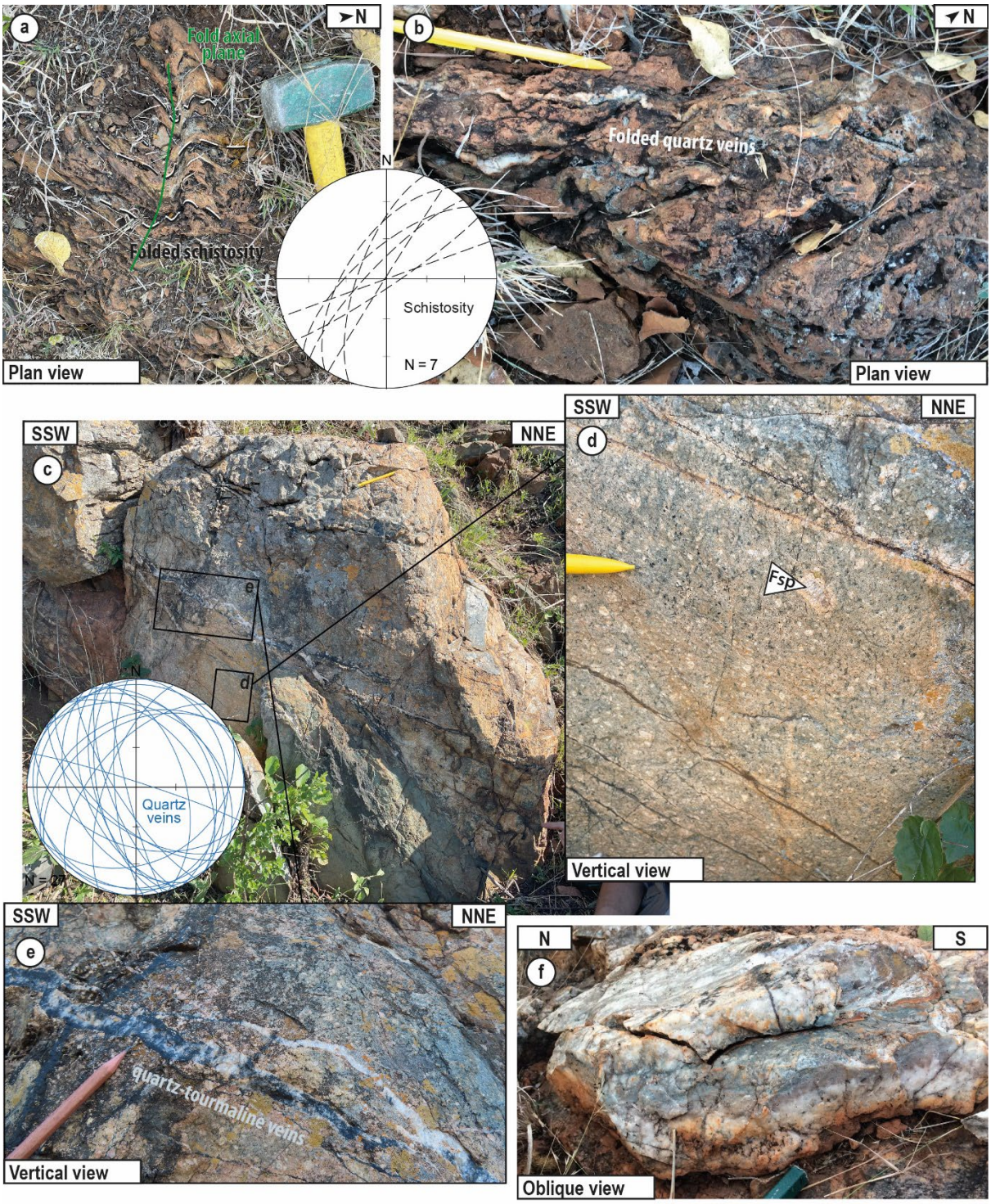

Fig. IV.48. Field observations of the Homestead occurrence and surrounding. **(a)** Folded schistosity (black dash line) and associated stereonet diagram; the axial plane is WNW-ESE striking (Schmidt diagram, lower hemisphere). **(b)** Folded schistosity and schistosity-parallel quartz veins. **(c)** Quartz veins cutting the NE-SW striking felsic rock, and stereonet diagram associated (Schmidt diagram, lower hemisphere). Locations of the photos (d) and (e) are shown. **(d)** Close-up view of the felsic rock, note the cm-size feldspars. **(e)** Quartz-tourmaline veins cutting the felsic rock, note some vertical tourmaline fibres. **(f)** Homestead mineralised feature: m-thick quartz vein, note the darker part.

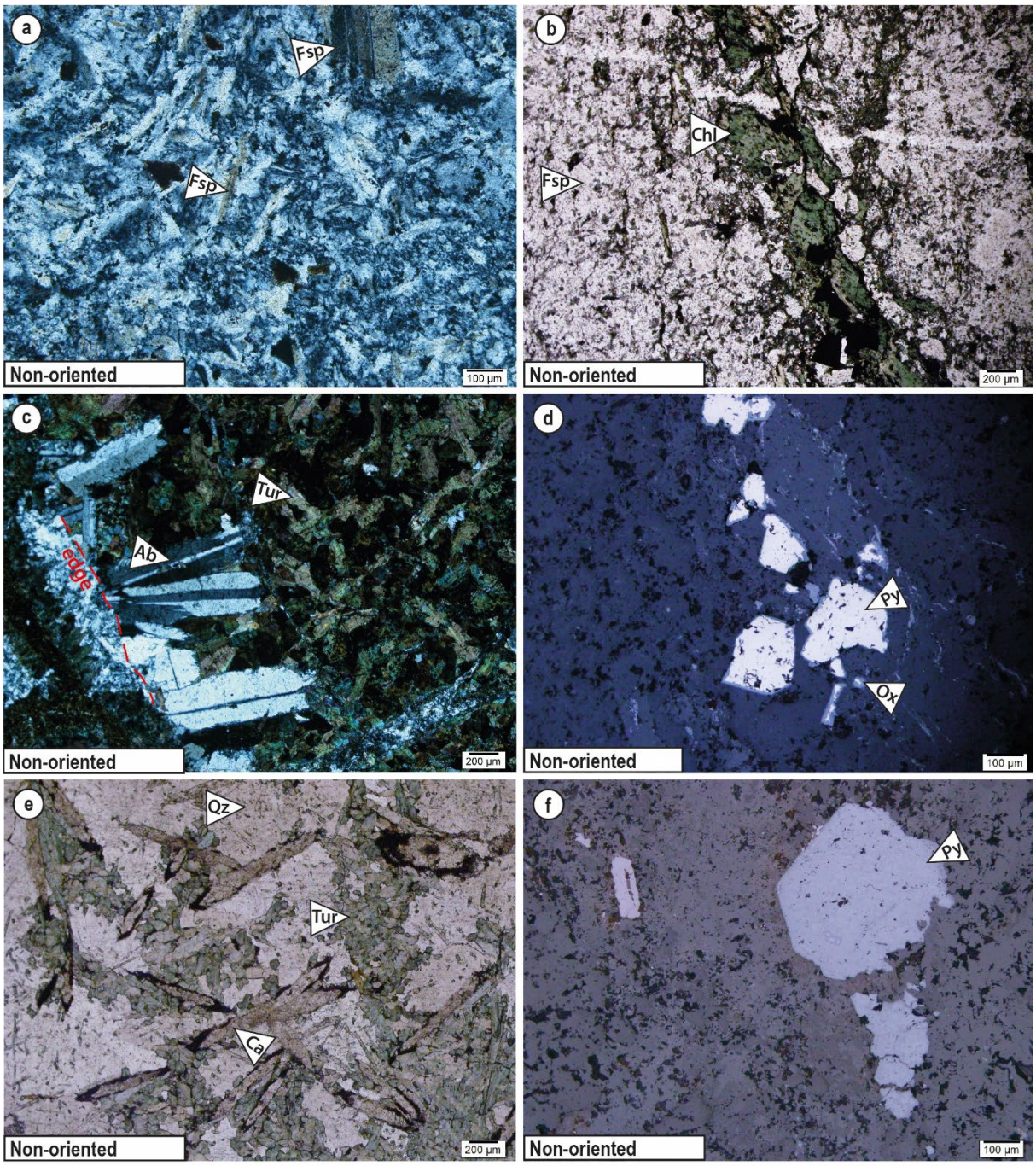

Fig. IV.49. Microscopic observations of the Homestead occurrence and surroundings. **(a)** Felsic matrix of the felsic intrusive rock composed of micro-grained feldspars, note the larger feldspars crystal on the upper right part of the photo (crossed polars). **(b)** Chlorite in the felsic rock (polarised light). **(c)** Plagioclase at the edge of a tourmaline-quartz vein cutting the felsic rock (crossed polars). **(d)** Pyrites in a tourmaline-quartz vein with oxidised rims (reflected light). **(e)** Lamellar carbonate, radial tourmaline and quartz infilling within m-thick vein (polarised light). **(f)** Pyrites in the m-thick quartz vein (reflected light).

IV.B.1.7. The Idaho occurrence (930)

The Idaho deposit, or n°930 occurrence, is composed of several galleries and trenches along a hill slope of the mountain. The country rock in this place is composed of large pillow lavas with geodic quartz inter-pillow (Fig. IV.50).

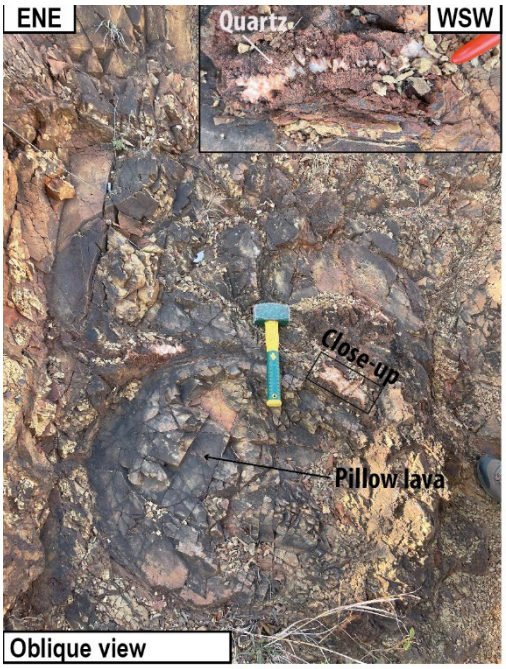

Fig. IV.50. Photo of the country rock at the Idaho occurrence, show pillow lava and inter-pillow quartz (inset).

Two different mineralised fault zones have been identified, one NE-SW striking and the other one striking ENE-WSW (Fig. IV.51a,b,d). The NE-SW striking fault zone is a vertical 10 m-large highly fractured zone with stretched pillows at the edge. Gently SW plunging slickenlines were measured, and local drag fold indicates a minor oblique sinistral motion on the fault zone (Fig. IV.51c). This fractured zone is probably enriched in sulphides as there exist numerous beige, orange and ochre oxidation traces. Fracture-parallel lenses and cm to m-wide quartz veins are inside the fault core (Fig. IV.51a,b). In the m-wide quartz veins locally layering in the veins are observed. This layering is parallel to the margins of the vein and composed of carbonate infill in the core, surrounded by well-defined prismatic quartz crystals, elongated vein-margin perpendicular quartz crystals and botryoidal quartz at the contact with host rock (Fig. IV.51e).

The second fault zone, ENE-WSW striking is also a 10 m-large, fractured zone with a parallel quartz lens inside. Strong oblique slickenlines plunging to the WSW have been measured on the fault wall, but no sense of shear information has been observed.

Microscopic observations show the vein composition, they are made of comb quartz with bulging and minor dynamic recrystallisation by bulging carbonate and rare tourmaline (Fig. IV.52).

Fig. IV.51. Field observations of the veins at the Idaho occurrence. **(a) and (b)** Fractured zone with

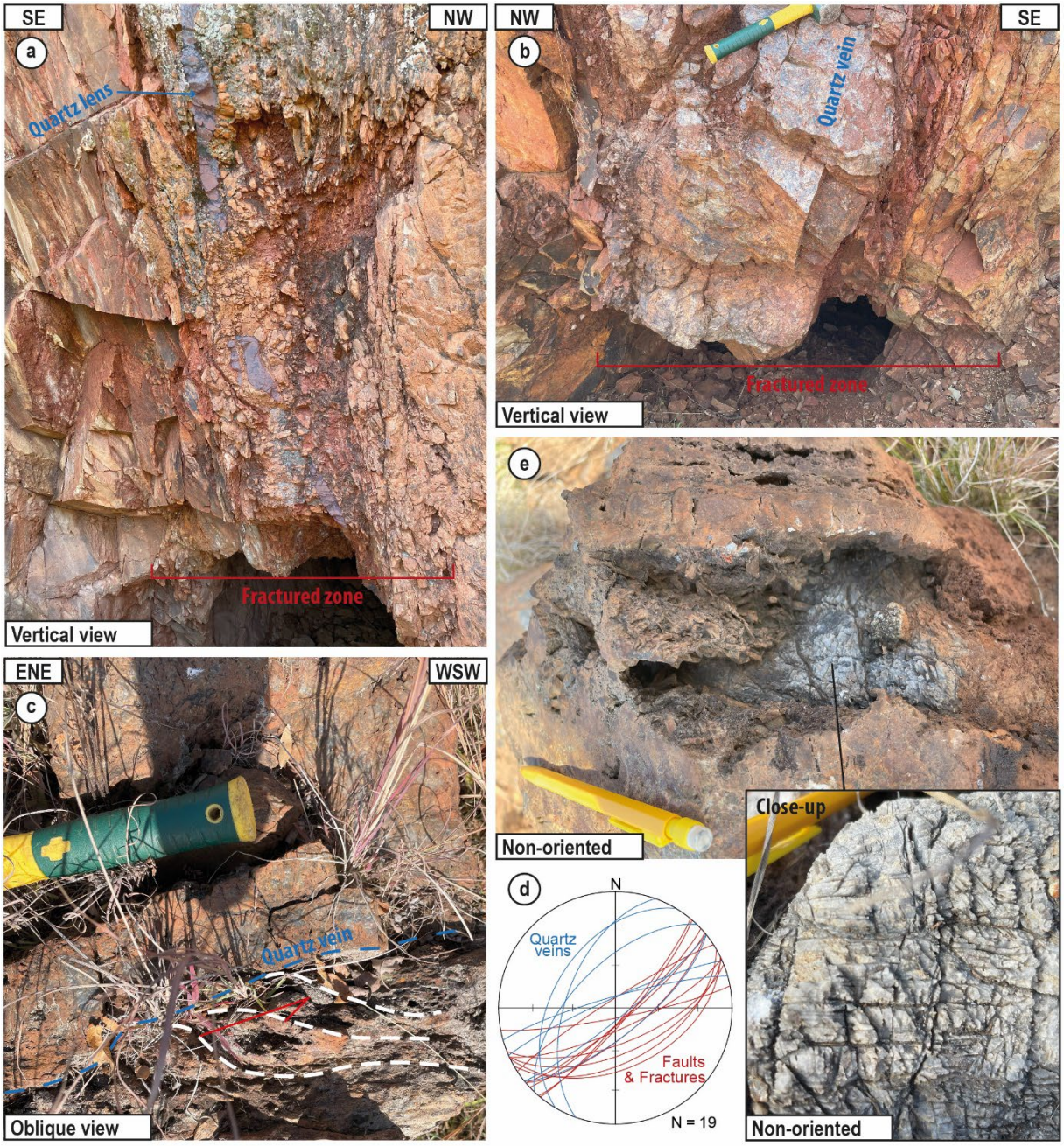

fracture-parallel quartz lens. **(c)** Drag folds (white dash line) at the edge of the quartz veins showing a potential sinistral motion. **(d)** Stereonet diagram showing the distribution of quartz veins (blue great circle), fractures and fault planes (red great circle) measured in the area (Schmidt diagram, lower hemisphere). **(e)** Internally compositionally layered, NE-SW striking vein. The layering is parallel to the margins of the vein and composed of carbonate infill in the core, surrounded by well-defined quartz crystals in geodes, elongated vein-margin perpendicular quartz crystals and botryoidal quartz at the contact with host rock. Inset: close-up view of the grey carbonate in elephant skin weathering in the middle.

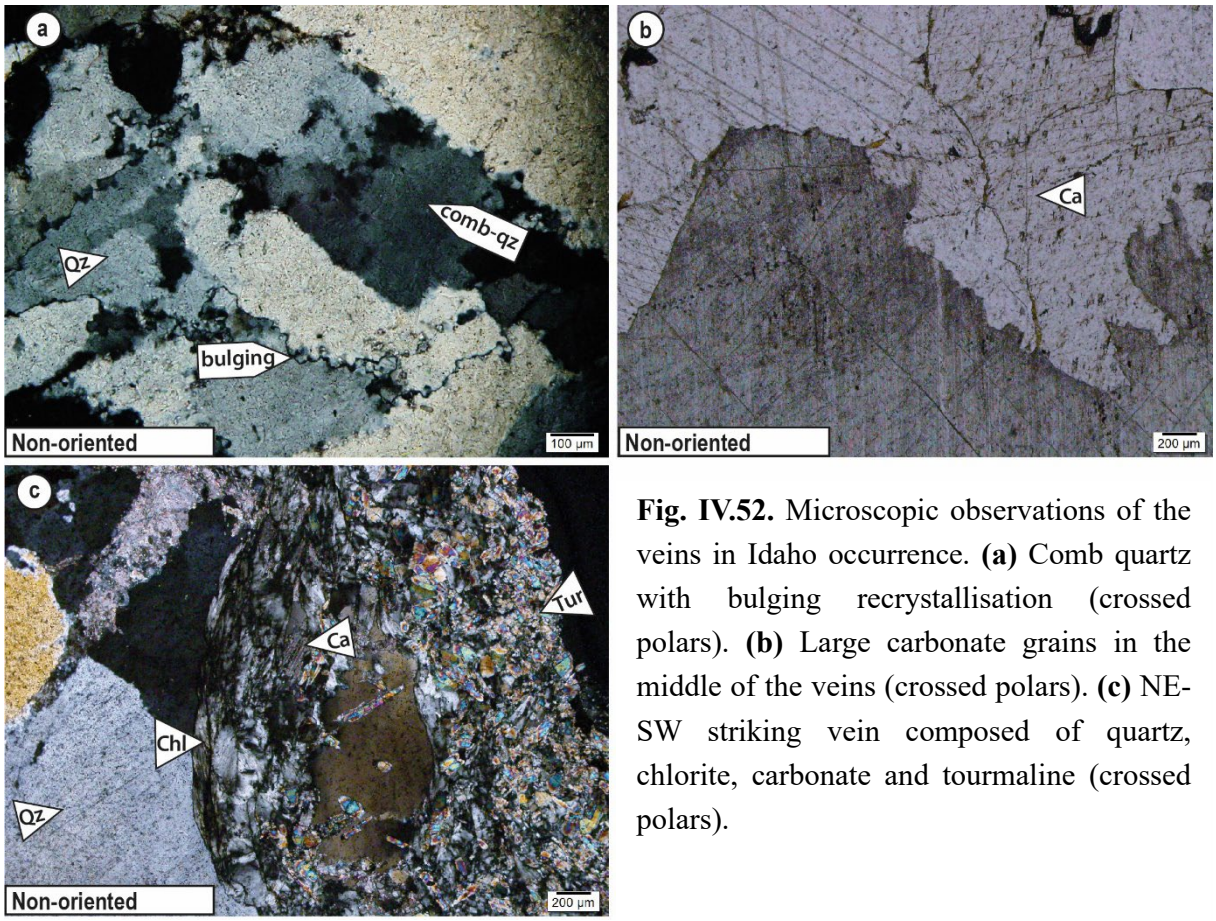

Fig. IV.52. Microscopic observations of the veins in Idaho occurrence. **(a)** Comb quartz with bulging recrystallisation (crossed polars). **(b)** Large carbonate grains in the middle of the veins (crossed polars). **(c)** NE-SW striking vein composed of quartz, chlorite, carbonate and tourmaline (crossed polars).

IV.B.1.8. The Beaconsfield occurrence (931)

In occurrence n°931 named Beaconsfield, there are three mining trenches and galleries aligned NE-SW. Two of them are inaccessible because they are covered with bushes and brambles, and the last one is an unsafe gallery.

Between these mined areas, a m-wide dark quartz vein with white quartz veinlets is aligned NE-SW and dip steeply to north-west (Fig. IV.53a).

At the entrance of the topographically lowest mined area, folded dark quartz veins were observed (Fig. IV.53b). Microscopically, veins are composed of comb quartz with dynamic recrystallisation by bulging and sub-grain rotation (Fig. IV.54).

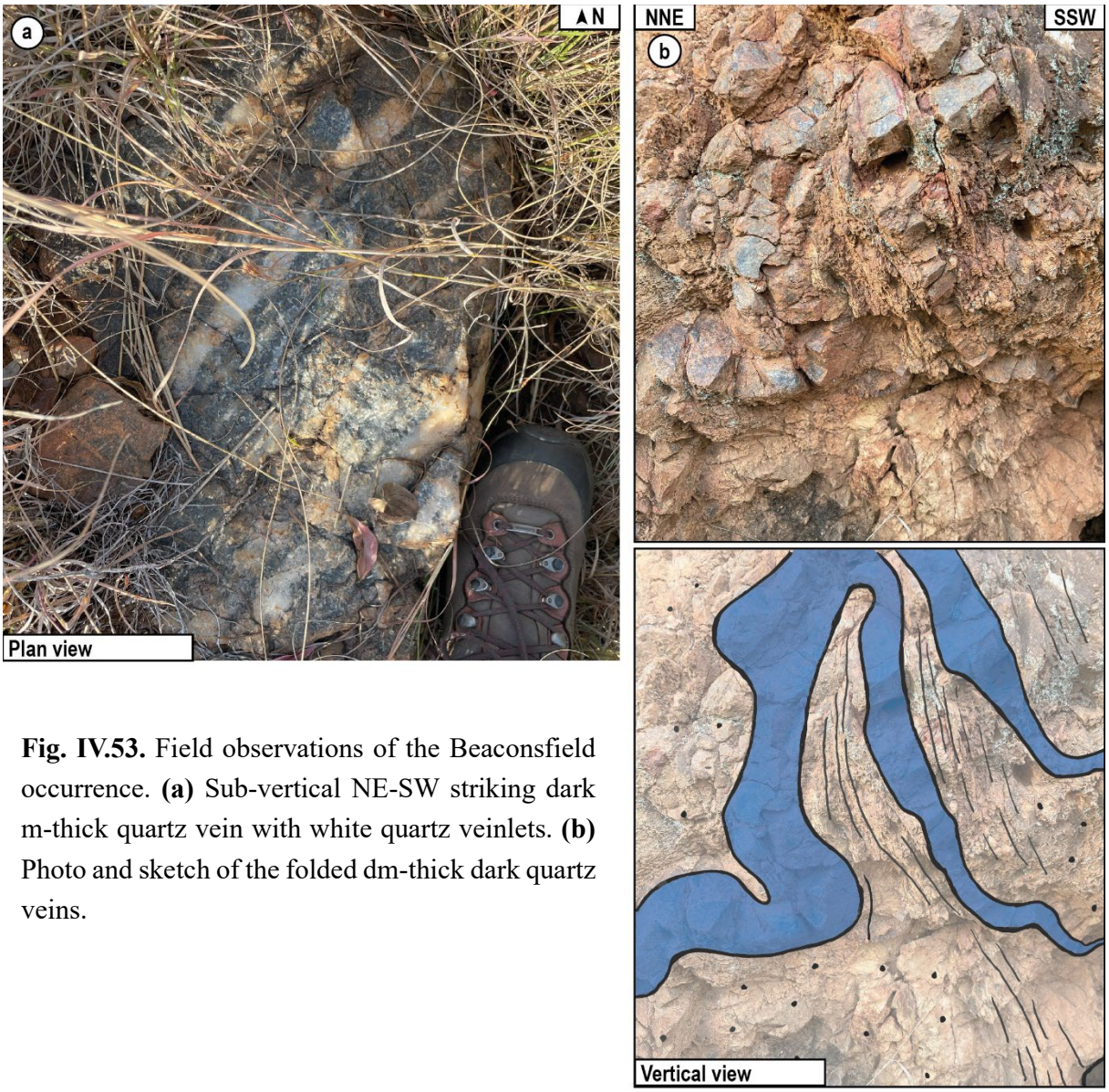

Fig. IV.53. Field observations of the Beaconsfield occurrence. **(a)** Sub-vertical NE-SW striking dark m-thick quartz vein with white quartz veinlets. **(b)** Photo and sketch of the folded dm-thick dark quartz veins.

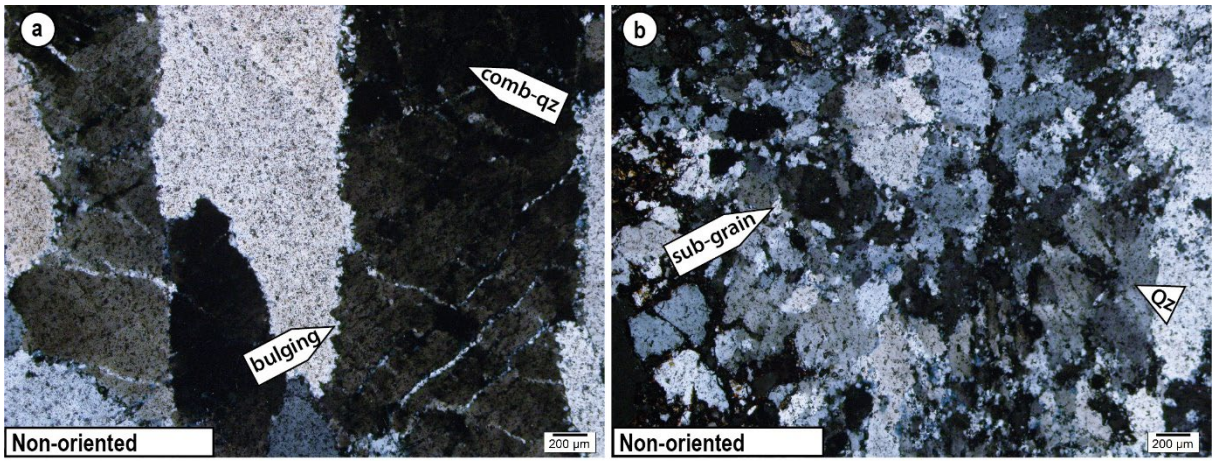

Fig. IV.54. Microscopic observations of the Beaconsfield occurrence. **(a)** Comb quartz with bulging recrystallisation at the quartz grains (crossed polars). **(b)** Sub-grain rotation of the quartz (crossed polars).

IV.B.1.9. The Unity occurrences (932&933)

The occurrences n°923 and 933 correspond to a NE-SW trench, one gallery and tailings. Close to the mine and towards the west, two different directions of schistosity have been measured: N-S and NW-SE striking, unfortunately, no overprinting relationship has been observed. Close to this zone, a m-wide white chert strikes N-S and is affected by a fault with dextral offset. To the east, the country rock is mainly composed of pillow lavas (Fig. IV55a).

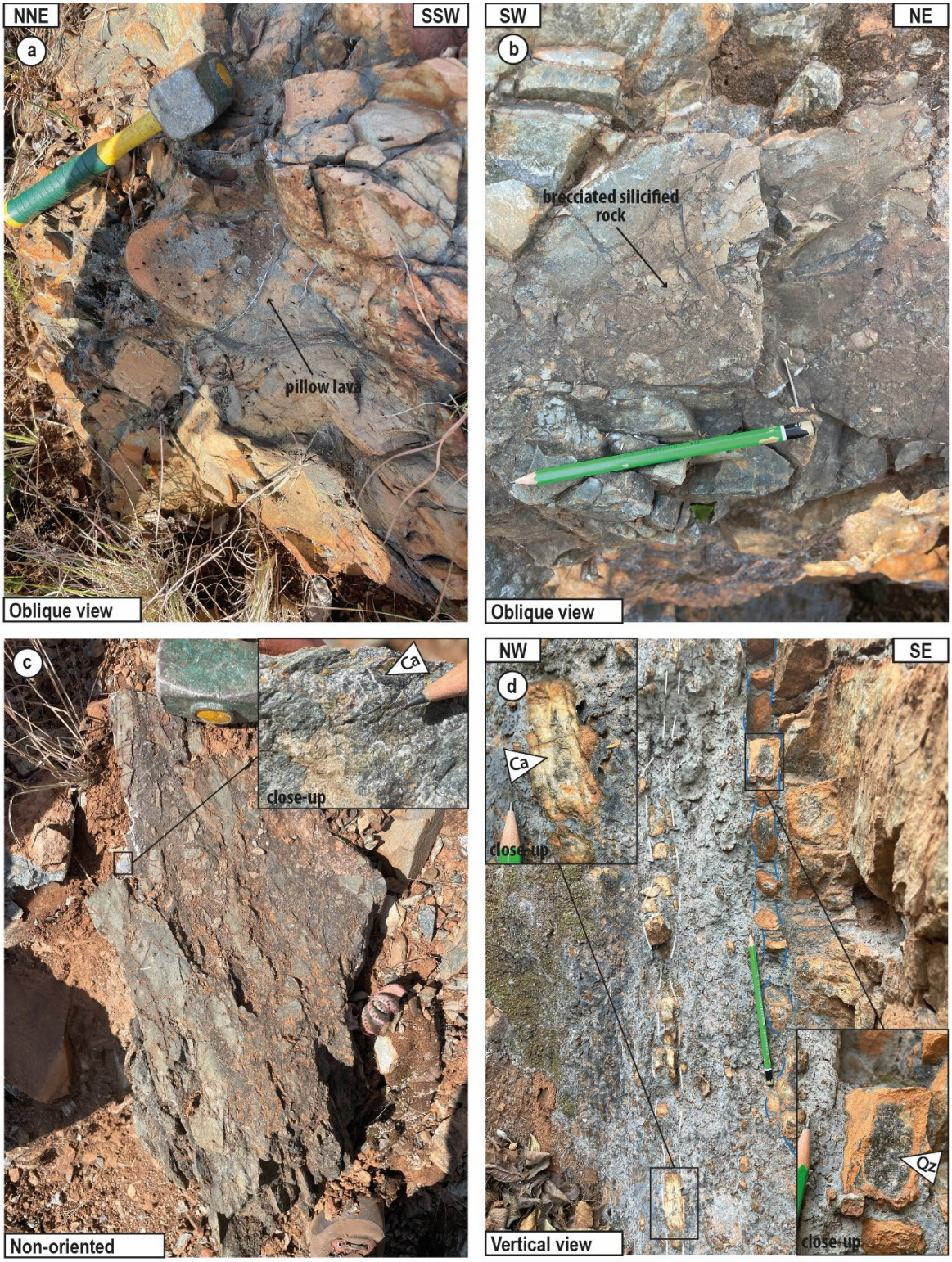

Fig. IV.55. Field observations at the Unity occurrences. **(a)** Pillow lava in the surrounding rocks of the occurrences. **(b)** Brecciated silicified rock near the fault zone. **(c)** Sample of a brecciated carbonated rock and close-up view of the carbonated rock. **(d)** Fault-parallel veins in the core fault, and close-up views of the veins. Note that white colour component in the vein is mainly composed of carbonate whereas the darker component is quartz.

The NE-SW striking mined trench is composed of a fractured corridor with breccia on the edges (Fig. IV.55b,c). Locally a schistose zone is affected by drag folding, suggesting a a dextral motion. In the trench, two parallel NE-SW striking sub-vertical dm-thick veins are observed (Figs. IV.55d and IV56a,b).

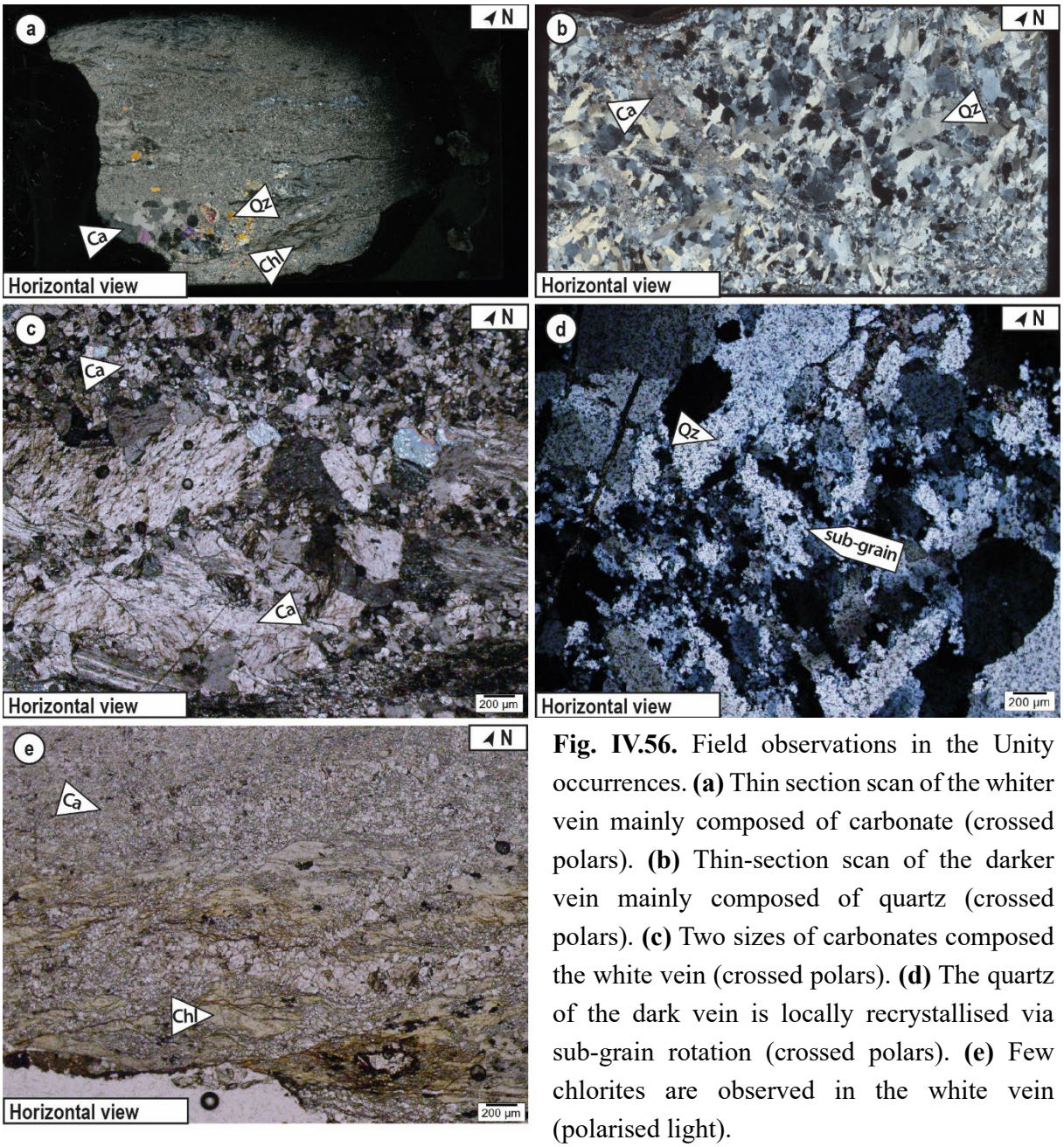

Fig. IV.56. Field observations in the Unity occurrences. **(a)** Thin section scan of the whiter vein mainly composed of carbonate (crossed polars). **(b)** Thin-section scan of the darker vein mainly composed of quartz (crossed polars). **(c)** Two sizes of carbonates composed the white vein (crossed polars). **(d)** The quartz of the dark vein is locally recrystallised via sub-grain rotation (crossed polars). **(e)** Few chlorites are observed in the white vein (polarised light).

The white vein is composed mainly of carbonate and to a less extent quartz with minor chlorite (Figs. IV.56a,c,e); and the dark vein is composed exclusively of quartz and minor carbonate (Fig. IV.56b,d).

IV.B.2. Minor Gold occurrences

Like the Malolotja gold cluster, minor gold occurrences also exist within the Steynsdorp area. To sum up, we confirm here the existence of two different schistosities. The early one is E-W striking one commonly folded by the later N-S striking schistosity. A vertical stretching lineation has also been observed mainly on the N-S schistosity (e.g., surrounding of the St George occurrence, Fig. IV.57a,b; and north of the Tug O'War occurrence, Fig. IV.58a).

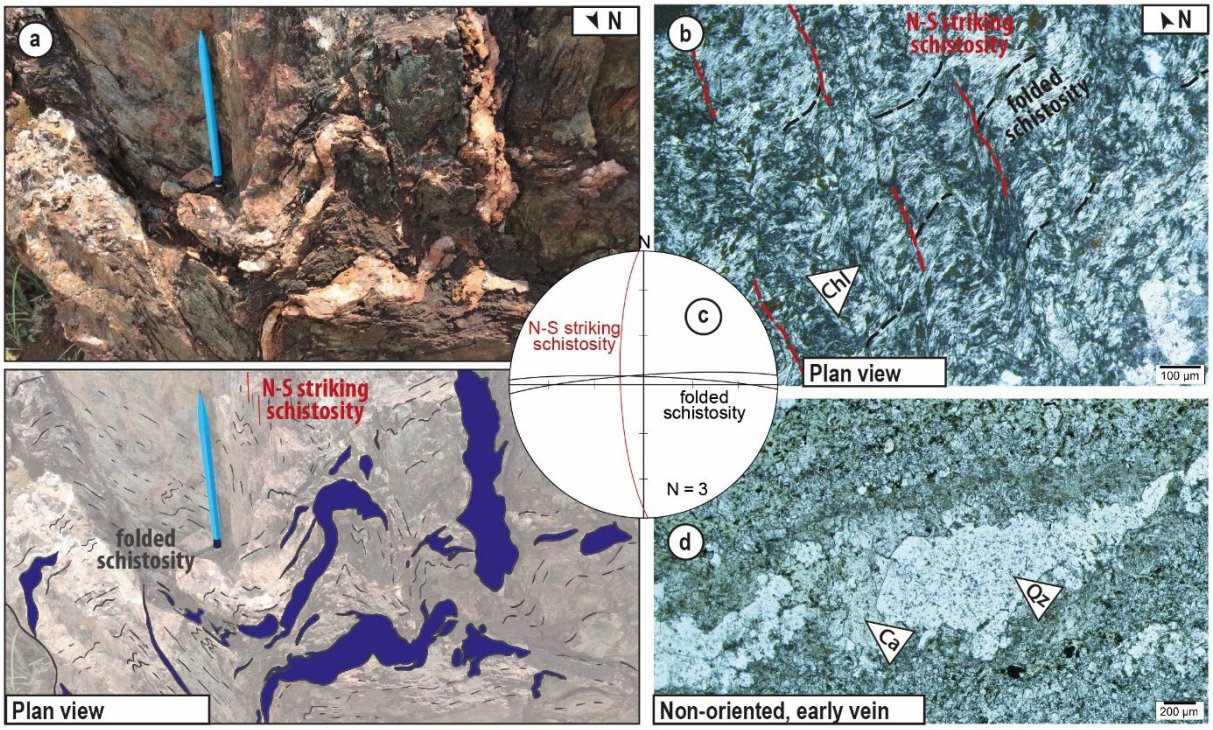

Fig. IV.57. Field and microscopic observations of the Lo.119 in the vicinity of the n°826 St George occurrence. **(a)** Photo and sketch of centimetric quartz vein sub-parallel to the E-W striking schistosity and highly folded. **(b)** Microscopic photo of crenulated E-W striking cleavage (black dash line) defined by chlorite, and the N-S striking crenulation schistosity (red dash line) (crossed polars) and **(c)** stereonet associated (Schmidt diagram, lower hemisphere). **(d)** Microscopic photo of the quartz-carbonate folded veins (polarised light).

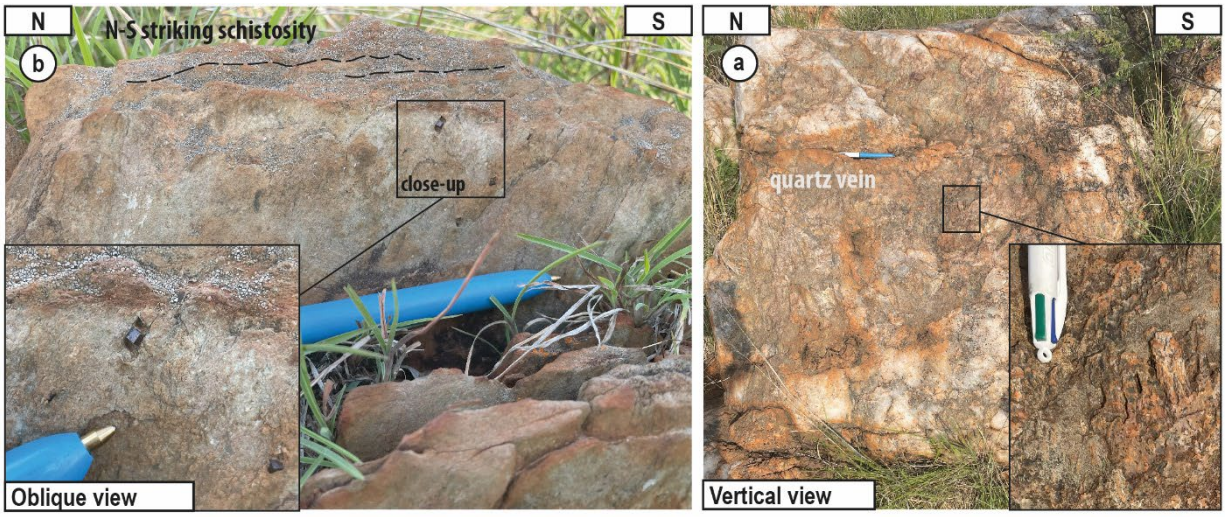

Fig. IV.58. Field observations at the north of the n°828 Tug O'War occurrence. **(a)** N-S striking schistosity (black dash line) next to the quartz vein, and close-up view of the automorphic pyrites, note that schistosity carries a vertical lineation. **(b)** N-S striking quartz veins and close-up view of the vertical quartz fibres on the edge of the vein, note the quartz fibres are parallel to the mineral lineation on the N-S striking schistosity.

Several veins have been observed, including folded cm-thick veins that appear sub-parallel to the folded schistosity, these veins are composed of quartz and carbonate (e.g., surrounding of the St George occurrence, Fig. IV.57a,c). The veins targeted by the exploration appear to be larger (m-thick) and strike approximately N-S (e.g., north of the Tug O'War, Fig. IV.58b). The surrounding country rock can show automorphic pyrites (e.g., north of the Tug O'War occurrence, Fig. IV.58a).

Locally, faults striking NE-SW to ENE-WSW have been observed in the eastern part of the Steynsdorp regional Anticline, and the brecciated surrounding rock can be seen in the fault area (e.g., Monarch occurrence, Fig. IV.59).

Fig. IV.59. Brecciated N-S striking chert (Middle Marker) in the vicinity of the n°926 Monarch occurrence.

IV.B.3. Other geological observations

IV.B.3.1. Outcrop Lo129 - Vlakplaas granodiorite

Outcrop Lo129 is located within the Vlakplaas granodiorite, northwest of the Steynsdorp gneiss. In the surrounding Onverwacht Group, the talc-chlorite magnetic schists are folded with a N-S axial plane (Fig. IV.60a). In contact with the granodiorite, the country rock appears more silicified than away from the contact. The granodiorite is not deformed, only a small (10 cm-wide), localised part may have a E-W striking foliation plane (Fig. IV.60b).

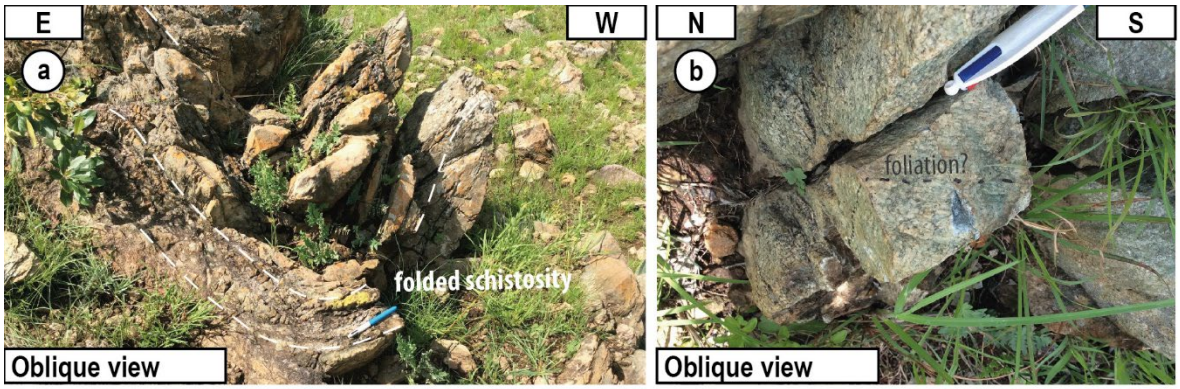

Fig. IV.60. Field observations of the outcrop Lo129, close to the Vlakplaas Granodiorite. **(a)** In the schist south of the granodiorite, the schistosity (white dash line) is folded with a N-S striking axial plane. **(b)** Photo of the granodiorite with a weak mineral planar fabric.

IV.B.3.2. Contact zone: Steynsdorp gneiss - lower Onverwacht Group rocks

The Steynsdorp gneiss is identified in the field as a north-convex half-dome in the landscape. It shows a strong metamorphic foliation marked by the alignment of quartz, biotite and feldspars. The foliation rotates from west to east of the dome and strikes ENE-WSW in the western part and NNW-SSE in the eastern part (Fig. IV.61a,b). In the foliation plane a well-expressed mineral lineation plunged to the NNE (Fig. IV.61b). Numerous aplite and pegmatite veins cut the gneiss. They are globally NE-SW striking by non-clear pattern is found (Fig. IV.61a,b). One N-S striking quartz vein with foliation drag fold is consistent with a dextral motion has been reported (Fig. IV.61c).

In contact with the Steynsdorp gneiss, the Onverwacht Group rocks are formed by layering paragneiss, amphibolite and quartzite, metamorphosed at amphibolite facies conditions. Few garnets are locally identified in the Onverwacht Group. In the area some quartz vein and amphibolitic host-rock are faulted with apparent dextral motion (Fig. IV.62a). Domino boudin structure are observed, locally the boudins are asymmetric with reverse shearing plane (Fig. IV.62b).

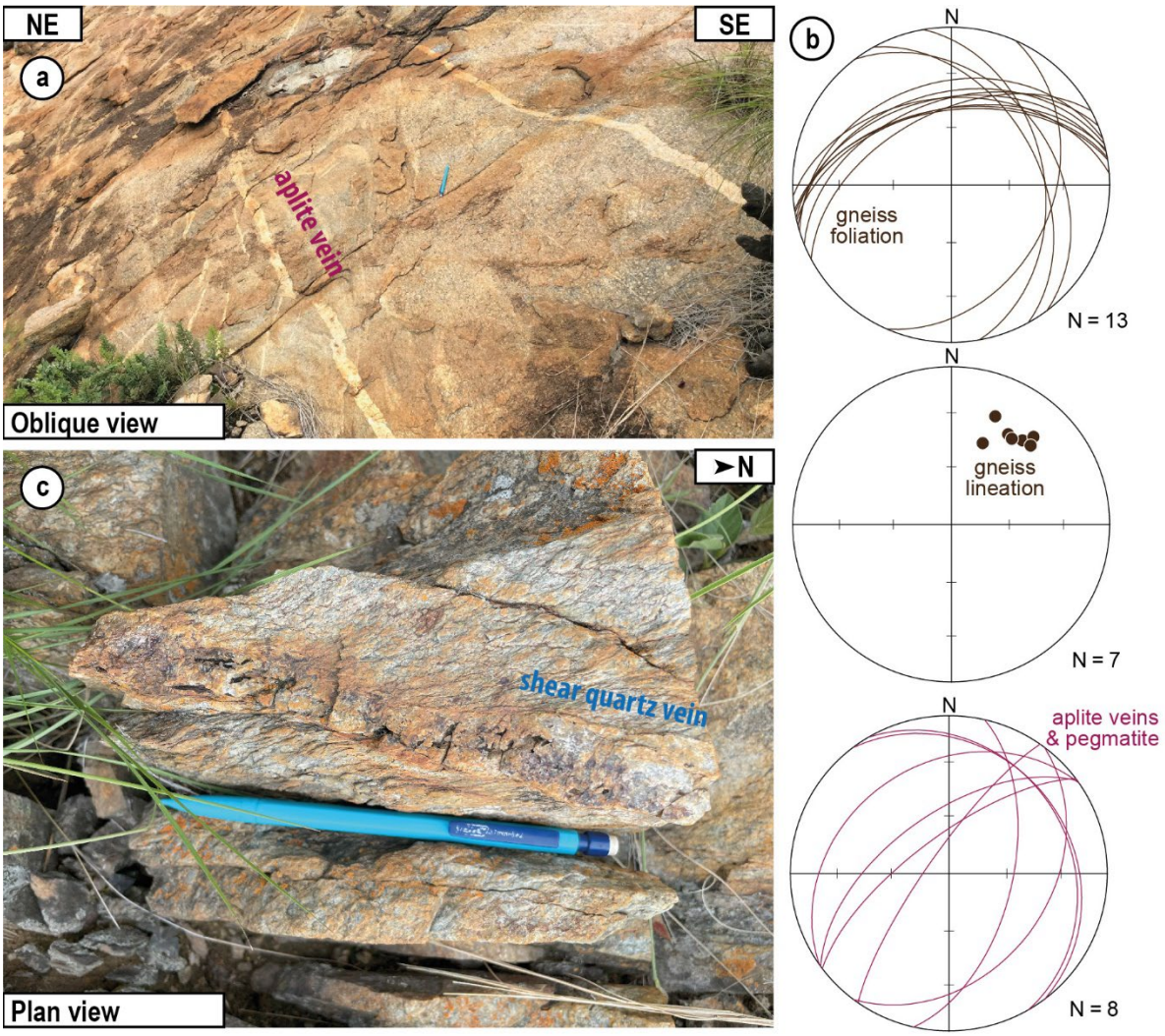

Fig. IV.61. Field observations of outcrops in the Steynsdorp gneiss northwestern part. **(a)** Numerous aplite veins cut the gneiss. **(b)** Stereonets of the gneissic foliation (brown great circle), the mineral lineation in the gneiss (brown dot) and aplite-pegmatite veins cutting the gneiss (purple great circle) (Schmidt diagram, lower hemisphere). **(c)** Vertical dextral quartz vein in the gneiss, note the drag fold of the foliation in the edge of the vein.

Away from the gneiss, the rocks are talc-schist and felsic schists. Three schistosity orientations have been reported in the talc schist. The first one is NE-SW striking and is folded in chevron folds with a steep N-S striking axial plane (Fig. IV.62c). A local N-S striking schistosity has been measured and represents the second structure. The third NW-SE striking schistosity overprints the NE-SW folded schistosity (Fig. IV.62d). In all the northwest contact, the low grade cleavage is NE-SW striking with a lineation plunging to the N or to the NNE (Fig. IV.62e). At about 1 km away from the gneiss, pillow lava metamorphosed in upper greenschist facies (presence of actinolite) are observed.

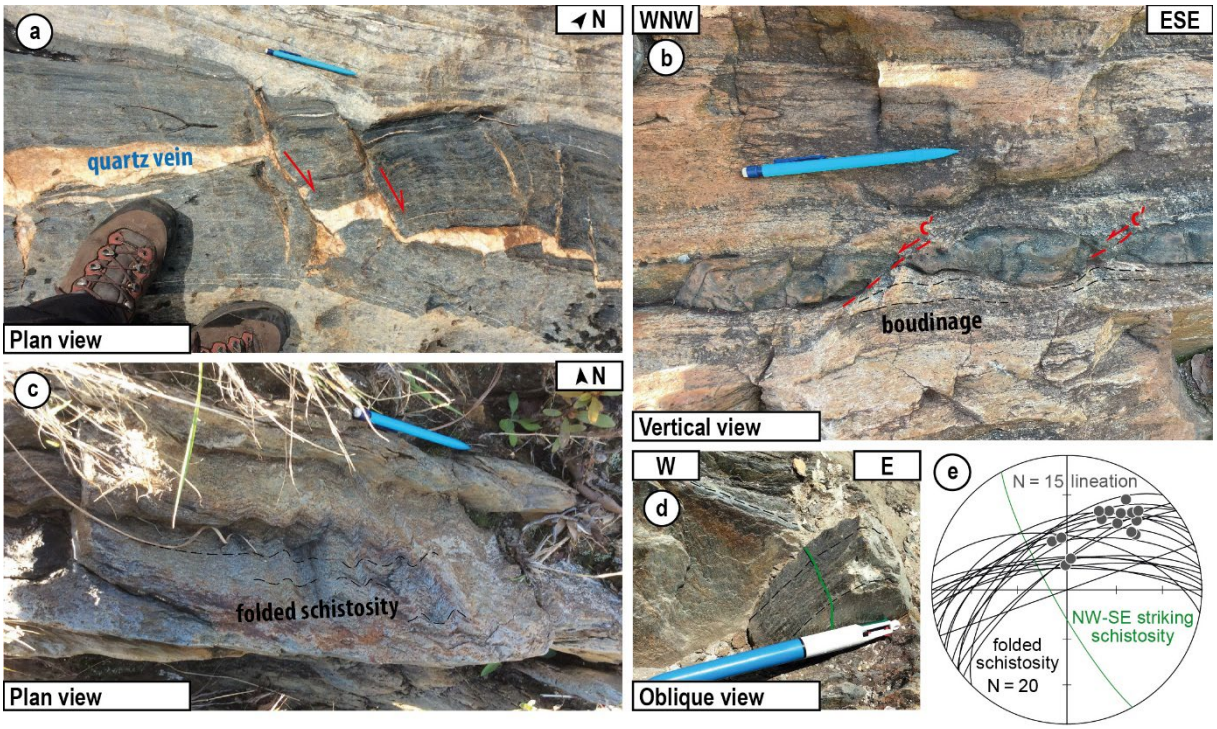

Fig. IV.62. Field observations of the Onverwacht group rock, at the northwestern contact with the Steynsdorp gneiss. **(a)** Faulted quartz vein and amphibolite, note the apparent dextral offset. **(b)** Boudinage of the Onverwacht Group rock, the observation plane is sub-parallel to the XZ plane (normal to the schistosity and parallel to the lineation), note the left-lateral shear plane. **(c)** Chevron folds of the NE-SW schistosity, note the axial plane is NNW-SSE striking. **(d)** NW-SE striking schistosity overprinting the NE-SW striking schistosity. **(e)** Stereonet of the folded schistosity (black great circle) and mineral lineation (black dot) and the NW-SE striking schistosity (green great circle) measurements (Schmidt diagram, lower hemisphere).

IV.C. Synthesis

This section is presented via the scientific article "Structure and Distribution of the Gold-Related Quartz Vein Systems in the Southwestern Part of the Barberton Greenstone Belt (South Africa, Eswatini)", by L. Travers, A. Chauvet and J. Lehmann, and published on August 1st, 2023, in Minerals, and in the section *Mineral Deposits*. The open-access version of this article is available at the following link: https://doi.org/10.3390/min13081034.

The figures in this section will be later referred to in the text as Figure IV.C.1, IV.C.2, IV.C.3, etc… IV.C.17.

minerals

MDPI

Article

Structure and Distribution of the Gold-Related Quartz Vein Systems in the Southwestern Part of the Barberton Greenstone Belt (South Africa, Eswatini)

Laurine Travers [1,2], Alain Chauvet [1,*] and Jérémie Lehmann [2]

[1] Géosciences Montpellier, CNRS (Centre National de la Recherche Scientifique), University of Montpellier, CC60 Montpellier, France; laurine.travers@umontpellier.fr
[2] Department of Geology, University of Johannesburg, Johannesburg PO Box 524, South Africa; jeremiel@uj.ac.za
* Correspondence: alain.chauvet1@umontpellier.fr

Abstract: This study investigates the structural control of the numerous gold occurrences in the southern part of the Barberton Greenstone Belt in the Malolotja and Steynsdorp areas. The gold-bearing event distribution is studied using field structural geology associated with a petrological and microstructural analysis. Three major tectonic events have been identified in quartz veins and direct country rocks. The first event (De) created a regional schistosity (Se), probably associated with an early thrusting event. The second event (Df) is related to a large-scale folding, which formed the anticline at Steynsdorp and synform at Malolotja. It resulted from a main E–W direction of shortening and is responsible for the folding of the Se schistosity. It formed a N–S-striking axial planar cleavage (Sf), observed and associated with the emplacement of the main gold-bearing veins. The mineralised system exhibits a complex vein network, in which shallow dipping veins have developed coevally with steep west- and east-dipping veins. A third deformation event (Dl) produced by NE–SW shortening is related to the late barren hydrothermal quartz vein formation. Mineralogically, the veins are filled with abundant quartz, and scarce tourmaline and feldspars. Alteration halos composed of neoformed tourmaline and plagioclase within a talc and white mica matrix developed specifically during the late Dl event. A model of regional deformation giving rise to large-scale folds and quartz vein formation formed in response to E–W and NE–SW directions of shortening globally is proposed and discussed in this paper.

Keywords: gold mineralisation; structural geology; Barberton Greenstone Belt; Archean

Citation: Travers, L.; Chauvet, A.; Lehmann, J. Structure and Distribution of the Gold-Related Quartz Vein Systems in the Southwestern Part of the Barberton Greenstone Belt (South Africa, Eswatini). *Minerals* **2023**, *13*, 1034. https://doi.org/10.3390/min13081034

Academic Editor: Liqiang Yang

Received: 05 June 2023
Revised: 25 July 2023
Accepted: 29 July 2023
Published: 1 August 2023

1. Introduction

The Archean geological record presents many singularities, which makes it distinct from the modern one. First of all, the Archean Eon is characterised by intense magmatic activity [1], with a hotter mantle [2,3] forming large continental Na-rich granite-gneissic crust of TTG (tonalite, trondhjemite, granodiorite [4]). Supracrustal rocks surrounding TTG domains, called greenstone belts, are also emblematic of the Archean Eon. They occur as elongated shapes of tight synforms and fault-bounded domains and are composed of volcano-sedimentary rocks, which were metamorphosed at greenschist to amphibolite facies conditions [5]. In addition, Archean geodynamics is inferred to differ from the modern one with a typical dome-and-keel geometry versus horizontal plate tectonics motion (e.g., [6,7]). The structural geology of greenstone belts is complicated by the fact that Archean deformation intensity seems weaker than in modern orogenic belts, with generally poorly expressed kinematic indicators [8], making it harder to unravel the tectonic evolution of Archean belts. Another particularity of the Archean domains is their metal enrichment, especially world-class gold deposits [9–11]. It is clear that, except for a

few huge Mesozoic and Cenozoic epithermal/porphyry-type gold deposits (e.g., Rocky and the Andean Mountains, Central Asian Tian Shan, and Northern Pacific Basin), most of the world-class gold deposits are Archean. Structurally controlled orebodies are excellent markers of regional deformation [12], so combining structural observation of mineralised bodies and host rock allows for a better understanding of the tectonic evolution of the Archean study area.

The Barberton Greenstone Belt (BGB) in South Africa and Eswatini is an Archean belt with an estimated production of 342 tons of gold [13] with over 350 gold deposits and occurrences, including four major operating mines (Fairview, Sheba, New Consort, and Ages mines; Figure 1). The gold deposits and occurrences are distributed nonhomogeneously throughout the belt as most of them occur in volcano-sedimentary units near the margins of plutons along major tectonic structures, such as faults and folds [14]. Indeed, most of the gold deposits are located along the Moodies, Sheba, and Barbrook faults and Ulundi, Eureka, Steynsdorp, and Malolotja folds. The gold grade also appears to be heterogeneously distributed: major mines, such as New Consort, Sheba, and Fairview, are clustered in the Eureka and Ulundi synclines in the northern part of the belt, at the junction with the Jamestown schist belt. These three mines concentrate approximately 76% of the gold produced [15]. In contrast, there are low-grade clusters, such as Steynsdorp and Malolotja (this study), in which limited quantities of gold were extracted from historical small-scale artisanal mines (gold production estimated at about 1770 kg [16]).

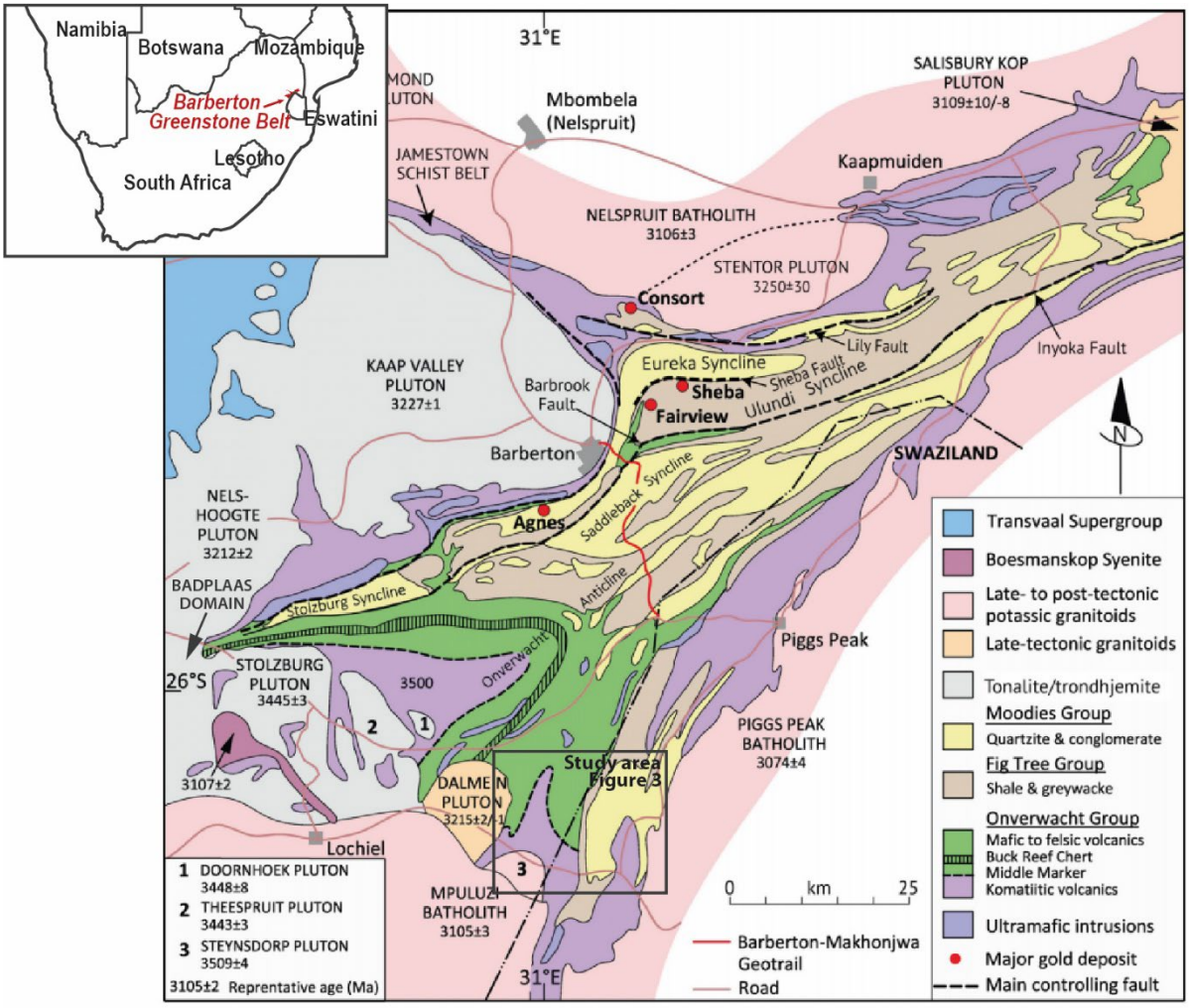

Figure 1. Geological map of the Barberton Greenstone Belt (modified from Anhaeusser [13]; published with the permission of the Geological Society of South Africa) showing the three

stratigraphic groups (Moodies, Fig Tree, and Onverwacht), the main TTGs, the late batholiths, and the four principal gold deposits. The black rectangular box depicts the location of this study area.

This spatial distribution of gold deposits and occurrences and grade in the BGB seems structurally controlled; therefore, it is likely that gold mineralisation was formed and/or affected by the regional deformation of the belt. The most studied and best-known deposits are in Fairview, Sheba, and New Consort active mines (e.g., [17–23]). However, the southern gold-bearing occurrence cluster remains poorly studied. To fill this gap, this work focuses on the structural framework of gold-related occurrences within the southern part of the Barberton Greenstone Belt, especially in the Steynsdorp anticline and Malolotja synform, which host low-grade gold occurrences. This paper aims to establish the tectono-hydrothermal model of the southern part of the Barberton Greenstone Belt by studying vein systems, their alterations, and the host-rock structures. Using new detailed field, structural, microstructural, and mineralogical analysis of the study area, we investigate the structural control of the gold-related quartz veins in the southwestern part of the Barberton Greenstone Belt.

2. Geological Setting

2.1. The Barberton Greenstone Belt and Surrounding Granitoids

The Barberton Greenstone Belt (BGB) is located along the northeastern edge of the Kaapvaal Craton, in the northeastern part of South Africa and the northwestern part of Eswatini. Measuring 120 km long and 50 km wide, this Archean belt is composed of volcano-sedimentary units surrounded by TTG rocks and intruded by numerous late potassic batholiths (Figure 1).

The stratigraphy of the BGB consists of three groups, from the oldest to the youngest—the Onverwacht, Fig Tree, and Moodies Groups [24]. The Onverwacht Group is mainly a mafic to ultramafic meta-volcano-sedimentary series [16,24,25] dated between ca. 3.55 and 3.29 Ga [26–28]. This group is composed of mafic to ultramafic volcanic units with interlayered felsic volcanic rocks and minor cherts [26,29]. The Fig Tree Group, dated at 3.28 to 3.22 Ga [26–28,30], is formed by felsic volcanic rocks and sedimentary units [26,31]. The Fig Tree Group is mainly a package of sandstones, shales, cherts, banded iron formations, and minor felsic volcanic rocks [31,32]. Last, the Moodies Group, dated from 3.22 to 3.21 Ga [33,34], represents the upper detrital series [35]. The Moodies Group is formed mainly of quartz-rich and felsic sandstones, conglomerates, and mudstones [33]. Facies and age differences between the SE and the NW parts of the BGB have been related to two distinct island arc terranes, named the southern and the northern terranes [36], or the eastern and the western domains [37].

Three main generations of TTGs were emplaced around the BGB. (i) South of the belt, the oldest one is the ca. 3.5 Ga Steynsdorp pluton [27,34], composed of highly deformed tonalite and trondhjemite [38,39]. (ii) The second generation is dated at 3440–3460 Ma and is represented by the TTGs forming the Stolzburg block [34,40], located in the southwestern part of the belt. The Stolzburg block is formed by three plutons, the Doornhoek trondhjemite, Theespruit gneiss, and Stolzburg gneiss, respectively, named from E to W. (iii) The latest generation of TTGs was formed at ca. 3.2 Ga, and they cluster mostly in two geographical domains. In the southwest part of the belt, the southwestern Badplaas domain includes the Rooihoogte pluton, the Batavia pluton, the Badplaas gneiss, and the Elandsfontein gneiss [28,41]. In the northeast part of the BGB, the Kaap Valley domain encompasses the Nelshoogte trondhjemite dated at 3236–3212 Ma [42,43] and the Kaap Valley tonalite dated at 3227 ± 1 Ma [34]. Located outside the main clusters, and to the south of the Stolzburg Block, the Dalmein pluton is the youngest TTG of the BGB. It is dated at 3215 ± 2 Ma and seems to crosscut the main NE–SW-trending structural grain of the BGB [30,34,44].

A late GMS (granite-monzogranite-syenite) suite, represented by four batholiths dated at around 3.1 Ga surrounds the BGB. The northern Nelspruit batholith is dated at 3106 ± 3 Ma [34], the eastern Pigg's Peak granite is dated at 3140 ± 4 Ma or 3074 ± 4 Ma

[43,45], and the southwestern Mpuluzi and the smallest Heerenveen batholiths are dated at 3107 + 4/−2 Ma and ca. 3110 Ma, respectively [34,46]. These large batholiths are synchronous with the Kees Zyn Doorns and Boesmanskop syenites located to the southwest of the BGB [47].

The Barberton Greenstone Belt was affected by lower greenschist facies of metamorphism [48,49], except within and in the vicinity of the Stolzburg block to the southwest [37,50–52] and around the Stentor pluton to the northeast [53] where higher grades of metamorphism were recorded. Metamorphic conditions of 650–700 °C and about 0.8–1.1 GPa [50,54] were reported within the southwestern block [37,51], while in the northeastern high-grade domain, the condition of the metamorphic peak was modelled to reach a temperature of 600–700 °C at a pressure of about 0.5 GPa [53].

The complex geological history of the Barberton Greenstone Belt led to contrasted tectonic models (e.g., [24,30,55–57]). We adopted the model classification of de Ronde and de Wit [30], which is more generalised for the belt scale (Figure 2). According to these authors, the architecture of the belt was shaped through five main tectono-metamorphic and magmatic phases:

- At ca. 3.55 Ga, the mafic to ultramafic lavas of the lower Onverwacht Group were formed, likely on top of the Ancient Gneiss Complex [58–60]. A period of intra-oceanic activity may be genetically related to these lavas [60]. The subsequent melting of a continental shield gave rise to the Steynsdorp pluton [27,39]. Around 3458 Ma, an early D0 event occurred, which involved hydrothermal alteration [30].
- At 3445–3416 Ma, an early phase of deformation D1 affected exclusively the Onverwacht Group [30]. This deformation was associated with the second generation of TTGs [30,34,39].
- At 3229–3227 Ma, a second deformation phase, D2, affected the entire belt during NW–SE shortening. D2 occurred during the intrusion of several TTG plutons (Kaap Valley, Badplaas, Nelshoogte; [30]). This tectono-magmatic event may have been caused by the subduction of the SE block under an NW block [30,44,52,61,62] or by vertical mass redistribution driven by the density inversion between the rising lighter TTGs magmas and the overlying denser upper crustal material [63]. The D2 deformation is interpreted to be coeval with the formation of the Fig Tree Group in a foreland setting [64].
- At 3226–3080 Ma, a renewed or continued NW–SE shortening accommodated by strike-slip shear zones created the D3 deformation and folded the earlier structures [30]. It marks the beginning of the collision and the suture formation between the two main NW and SE blocks [37]. In the belt, the Inyoka fault system corresponds to a large-scale thrust bringing the NW block in contact with the SE block [60]. Within the granite-gneiss block, this fault extends to a ductile deformation zone bringing in contact the Badplaas (NW) and the Stolzburg blocks (SE) [39,52]. In such a scenario, the Moodies Group sediments are interpreted as deposited in a syntectonic basin formed during the orogenic collapse that follows this event at 3.2 Ga [33].
- At ca. 3080 Ma, the fourth and last deformation event D4 is characterised by extensional or transtension tectonics [30,65]. De Ronde and de Wit [30] connected this D4 deformation with the emplacement of late GMS batholiths.

2.2. Gold Mineralisation throughout the Barberton Greenstone Belt

Barberton's gold mining history began in 1883 [15], and mining continues to this day through four main operating mines located to the northeast of the belt (see locations in Figure 1), three of which are also the most studied and best-known deposits: Fairview mine (e.g., [19,21]), Sheba mine (e.g., [17–19]) and New Consort mine (e.g., [20,22,23]). However, there are more than 300 gold occurrences in the entire Barberton Greenstone Belt [19], although most of the gold production currently comes from the four major active mines reported earlier.

The Sheba-Fairview complex is located in the northern part of the belt close to the Sheba Fault. The Sheba Fault juxtaposes the Moodies Group rocks of the Eureka syncline with the Fig Tree Group rocks of the Ulundi syncline (Figure 1). The gold mineralisation in the Sheba-Fairview complex is mainly described as a shear quartz-carbonate-sulphide lode, with sulphide dissemination in fractures or bedding parallel to shear zones [21,66], developed at greenschist facies conditions [67]. Alteration halos of fuchsite-carbonate-sericite-graphite are related to gold mineralisation [68]. The gold mineralisation occurs as refractory or micro-inclusions in sulphides (mostly in arsenopyrite and pyrite) or as free gold grains in veins and alteration halos [67,69]. Earlier work by de Ronde et al. [69] and de Ronde and de Wit [30] interpreted the gold event as the reactivation of older D2/D3

Deformation Scheme					
Tectonic event description (after De Ronde and De Wit [30])		De Ronde and De Wit [30] *Regional*	Lowe et al. [55] *South of Barberton Town*	Ramsay [56] and Anhaeusser [16] *Sheba Hills*	This study *Steynsdorp-Malolotja area*
Formation of oceanic crust; ocean floor type metamorphism (~3.55 Ga)	Deposition of Lower Onverwacht Group	D_0			
Subduction-accretion of immature island arc systems (3.55-3.45 Ga)	Deposition of Lower Onverwacht Group	D_1			
Subduction-accretion in a Cordillearan-type subduction system (3.26-3.22 Ga)	Accretion of Upper Onverwacht Group and deposition of Fig Tree Group	D_2	D_2 Folding of Onverwacht and Fig Tree rocks	D_{1s} Folding and thrusting of Onverwacht, Fig Tree and Moodies Groups	
Terrain Accretion and deposition of coarse clastics, with collisional amalgamation followed by transcurrent faulting (3.26-3.16 Ga)	Deposition of Moodies Group sediments	Early D_3	D_3 Thrusting of Moodies Group onto Fig Tree Group D_4 Folding of Moodies Group D_{5a} Upright folding		D_e Thrusting of Onverwacht Group onto Moodies Group
			D_{5b} Emplacement of Kaap Valley pluton and foliation development	D_{2s} Formation of regional cleavage with emplacement of Kaap Valley pluton	D_f Folding of Onverwacht Group and Moodies Group
Gold mineralisation; shift from transpression to transtensional deformation (~3.1 Ga)	Deposition of Moodies Group sediments	Late D_3	D_{5c} Refolding	D_{3s} Refolding Eureka syncline with with dextral thrusting on Sheba fault followed by gold mineralisation	Late D_f Gold mineralisation
Strike-slip and normal faulting; emplacement of alkaline batholiths (~3.1 Ga)		D_4		D_{4s} Formation of conjugate recumbent crenulation and chevron folds	D_l ? Folding and formation of late quartz vein

structures during late D3 NW–SE shortening. More recent research confirmed that mineralisation formed during a late stage of the D3 NW–SE shortening [68,70], although others related the gold-bearing event to the regional D4 extension tectonic event [19,71].

Figure 2. Compilation of the major tectonic evolutionary models in the literature for the Barberton Greenstone Belt compiled by Dirks et al. [19]). The structural evolution proposed in this study is added (see Section 7 Discussion for explanation).

The New Consort gold mine is located further north of the Sheba and Fairview mines (Figure 1). It is situated on a band of BGB sandwiched between the Kaap Valley tonalite and the Stentor pluton, called the Jamestown schist belt [72]. New Consort mine is associated with highly deformed host rocks metamorphosed at amphibolite facies conditions [23,72,73]. Two mineralisation phases have been described by Otto et al. [23]. Earlier mineralisation is described as disseminated sulphides with calc-silicate alteration [23]. A second phase mineralisation is defined as high-grade brittle-ductile shear zones of quartz veining with silicate alteration and abundant arsenopyrite [22]. Gold mineralisation

is associated with sulphides, mainly as native gold in arsenopyrite in veins and alteration halos [23]. The New Consort mineralisation is interpreted to be related to the de Ronde and de Wit [30] D3 event associated with diapiric emplacement of the neighbouring Nelspruit batholith or to D4 extensional shear zone network [22,73].

Several gold mineralisation ages have been published: New Consort gold mineralisation is dated at ca. 3027 ± 7 Ma [74], Golden Quarry (close to Sheba) at ca. 3009 ± 16–3017 ± 18 Ma [71], and Fairview at ca. 3084 ± 18 Ma [75]. The gold mineralisation age appears poorly constrained or shows that mineralisation took place over a long period.

Overall, there are two main theories on the interpretation of the Barberton gold mineralisation. According to different available models, it may have formed (i) either during a late phase of the NW–SE regional shortening episode, which reactivated older structures [21,66,69,70], (ii) or during a regional NW–SE extension phase, which postdated the tectonic and thermal stabilisation of the belt [23,71,74].

2.3. The Malolotja Synform and the Steynsdorp Anticline Areas and Their Gold Occurrences

The study area is located in the southwestern part of the Barberton Greenstone Belt, across the border between South Africa and Eswatini. This zone is formed of a succession of broadly NNE–SSW-trending regional folds, i.e., Kromberg antiform, Steynsdorp antiform, Ngwenya synform, Ngwenya antiform, and Malolotja synform (Figure 3; [65]). Two regional folds seem particularly well endowed with gold occurrences in this area: the Steynsdorp anticline and the Malolotja synform (Figure 3).

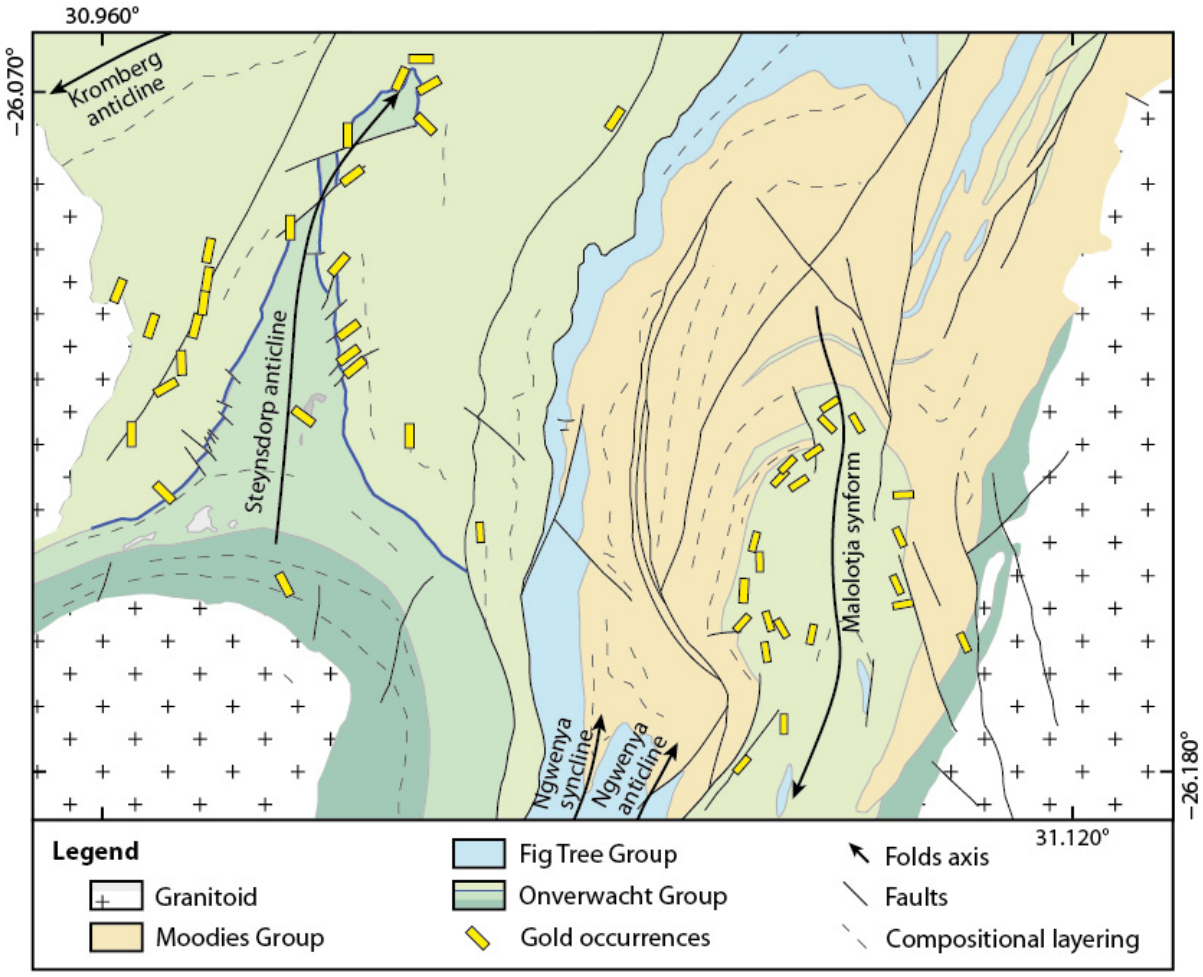

Figure 3. Geological map of the southern part of the Barberton Greenstone Belt and main gold-related occurrences (modified from Barberton Greenstone Belt metallogenic map [14] and Lana et al. [65]).

The Steynsdorp anticline is about 5 km wide and 11 km long, formed exclusively within the Onverwacht Group (Figure 3). It is located north of the BGB's oldest pluton, the 3510 Ma Steynsdorp gneiss [27]. This fold is a north-plunging anticline, with a conical fold geometry in the vicinity of the pluton and a concentric geometry in the north [38]. Stratigraphically, the Steynsdorp anticline is formed by three of the seven individual formations that formed the overall Onverwacht Group (Sandspruit, Theespruit, Komati, Hooggenoeg, Noisy, Kromberg, and Mendon complexes; [76]). The stratigraphically and structurally lowest Theespruit Formation surrounds the Steynsdorp gneiss, while the upper Komati Formation with its Middle-Marker upper horizon (blue line in Figure 3) and Hooggenoeg Formation form the concentric part of the fold [29,38]. The Steynsdorp area has been interpreted to be the result of doming effect related to the Steynsdorp pluton emplacement during the regional WNW–ESE shortening [38]. An alternative model proposes the exhumation of the Steynsdorp gneiss and subsequent extensional detachment at the contact between the Komati Formation and the Theespruit Formation during a NE–SW extension forming a dome-and-keel structure [77,78]. The Steynsdorp anticline hosts more than 25 gold-related occurrences. The gold is mostly hosted as inclusion in pyrite and, to a lesser extent, in arsenopyrite; its source is interpreted to be the mafic to ultramafic volcanic rocks of the Onverwacht Group, based on trace element analyses of gold in Steynsdorp area rocks [29].

The Malolotja synform is about 4 km wide and 12 km long, to the west and adjacent to the 3140 Ma Pigg's Peak batholith [45]. The Malolotja synform is cored by talc schists and cherts of the Onverwacht Group, which were recently correlated with Kromberg and Mendon Formations, based on new U-Pb ages [79]. The Moodies Group sandstones and minor conglomerates surround the Onverwacht Group core on the northern, western, and eastern sides of the fold, forming a tight and south-plunging synform [80]. This area has been interpreted to be refolded early NW-directed nappe of the upper Onverwacht Group over syntectonic sediments of the Moodies Group [79–81]. The Malolotja syncline hosts more than 20 gold occurrences, which are poorly documented in the available scientific literature. In the appendix of Anhaeusser [82], they are principally listed as "gold-quartz veins".

3. Lithostratigraphy

Two lithological groups (Onverwacht and Moodies) and several intrusive rocks are present in the study area. The distribution of the Onverwacht and the Moodies Groups can be easily recognised in the landscape through their geomorphological difference. In the Malolotja area, for example, rocks of the Moodies Group form high-relief topography while the Onverwacht Group mainly forms valleys and rolling hills.

The Onverwacht Group in the Malolotja syncline is composed mainly of talc schists with variable carbonate content (magnesite and dolomite-ankerite, confirmed by energy-dispersive X-ray spectroscopy analyses) in compositional layers or disseminated in talc schists (Figure 4a,b). This unit is penetratively affected by a strong cleavage marked by iron-rich micas and talc. The carbonates are commonly completely weathered, and only boxworks remain (Figure 4a). In some areas, especially near mining works, the schists are highly altered and produce alternating mm thick brown-red, ochre, and green compositional layering (Figure 4c). This unit also consists of chert beds of variable (cm to m) thickness, of white, black, and green colour.

The Moodies Group at Malolotja synform is mainly composed of medium-to-coarse-grained quartz arenites, which locally contain quartz pebbles. Clasts are mainly composed of quartz, and minor K-feldspar and plagioclase with interstitial white mica. The local matrix-supported conglomerate is interlayered in the quartz arenite. Clasts in the conglomerate are subrounded to subangular pebble-to-cobble-sized white quartz and chert. The Malolotja syncline is intruded to the east by Pigg's Peak batholith, which is granite cut by numerous pegmatite and aplitic veins.

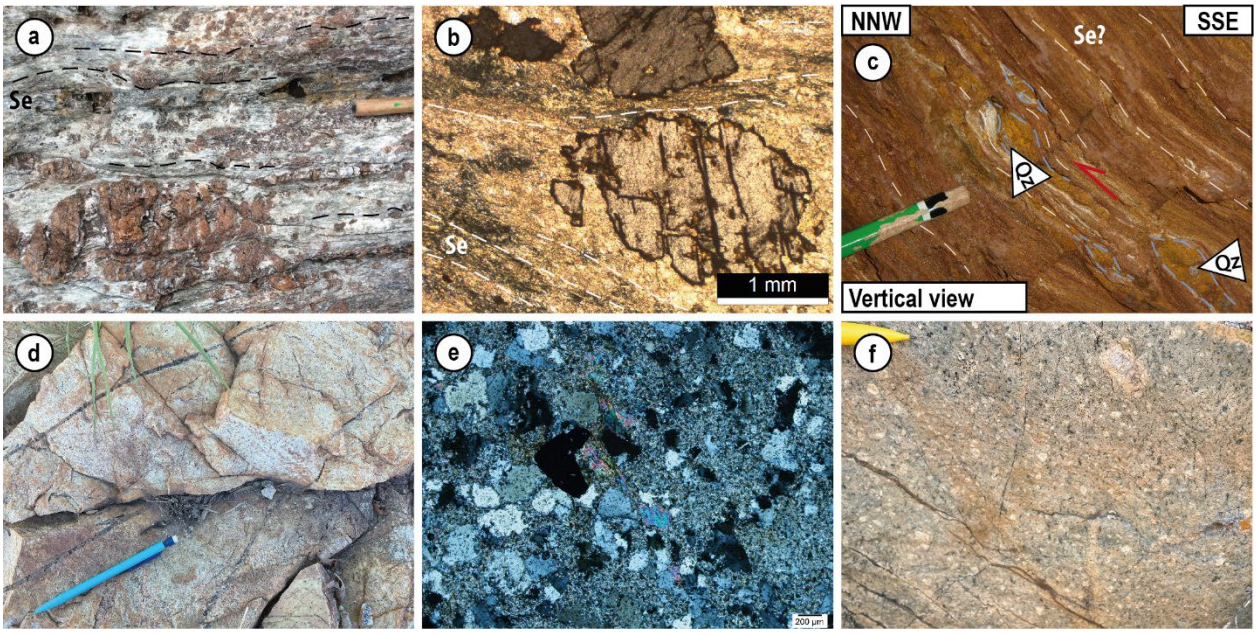

Figure 4. Field and microscopic views of the various lithologies within the Malolotja and Steynsdorp areas. (**a**) Field aspect of altered porphyritic magnesite in talc schist of the Onverwacht Group, Malolotja syncline. (**b**) Photomicrograph in plane-polarised light of iron oxide in the border of altered magnesite (note the Se cleavage), surrounded by a microcrystalline talc schist matrix, the Onverwacht Group, Malolotja syncline. (**c**) Weathered schist in She mine, with sigmoidal quartz lenses asymmetry (view parallel to stretching lineation and perpendicular to compositional layering, the Onverwacht Group), Qz = quartz. (**d**) Felsic porphyry at the old Gypsy Queen mine, east of the Steynsdorp anticline. (**e**) Microscopic view of the felsic porphyry composed of quartz, feldspar, and muscovite in a felsic microcrystalline matrix (crossed polars). (**f**) Felsic rock located in the hinge zone of the Steynsdorp antiform, showing a porphyritic texture and composed of large mm to cm size porphyritic feldspar, chlorite, and sulphides in a microcrystalline felsic groundmass.

In the Steynsdorp anticline, the lower structural unit is represented by the Steynsdorp granite-gneiss, recognisable as a north-convex half-dome in the landscape. It is a tonalite and shows a strong metamorphic foliation marked by the alignment of quartz, biotite, and feldspars. Numerous aplitic and pegmatitic veins transect the Steynsdorp granite-gneiss. The Steynsdorp gneiss and the rocks of the Onverwacht Group are separated by a tectonic contact. The Onverwacht Group stratigraphy in the Steynsdorp anticline is more varied than in the Malolotja synform. First, km thick beds of paragneiss, amphibolite, and quartzite occur, which were metamorphosed at amphibolite facies conditions. Lana et al. [77] calculated P-T conditions of metamorphism at 1.0–1.3 GPa and 640–660 °C for this unit. With increasing distance from the gneiss, the series becomes less metamorphosed with predominating talc schists and felsic schists. In the centre of the anticline, the area is covered by grass, and talc schists have been only locally observed. On both sides of the anticline, the series is composed of numerous weakly metamorphosed pillow lavas, especially in the east, and metabasalts with some iron-rich carbonate locally. These metabasalts can be foliated, visible by microcrystalline micas alignment. Rocks of the Onverwacht Group are cut by minor intrusive bodies, such as the Vlakplaats granodiorite, which is located about 1 km north of Steynsdorp gneiss (Figure 3), and shows a weak foliation. A felsic porphyry (described by Viljoen et al. [29]) is located close to the old Gypsy Queen mine (Figure 4d), east of the Steynsdorp anticline. It is formed by quartz, albite, and muscovite in a felsic microcrystalline matrix (Figure 4e). Another 10 m scale felsic porphyry, found in the hinge zone of the Steynsdorp antiform, is composed of large feldspar, chlorite, sulphides, and a feldspar matrix (Figure 4f). As everywhere in the BGB,

there are several mafic dykes that cut across the study area. They mainly have a NW–SE strike.

4. Regional Deformation

Three cleavage planes or schistosities of different orientations and significance have been observed at the Malolotja synform and Steynsdorp antiform. According to these observations and their overprinting relationships, three tectonic deformation events have been identified (Figures 5 and 6). The early deformation (De) formed the main cleavage (Se). The two other deformation phases are the main fold-related event (Df) and the late weaker deformation event (Dl). Stretching lineations are not very pronounced in the study area, except locally in the Steynsdorp gneiss and the surrounding Onverwacht Group rocks. They are metamorphosed at amphibolite facies conditions where a strong L-S tectonite exhibits a NNE plunge (this work and [77]). Another stretching lineation has been identified locally in the Malolotja zone, characterised by a SSW plunge associated with thrusting towards the NNW (e.g., Figure 4c). Because stretching lineations are poorly expressed, it has been decided to not represent them within the stereonets in Figure 5.

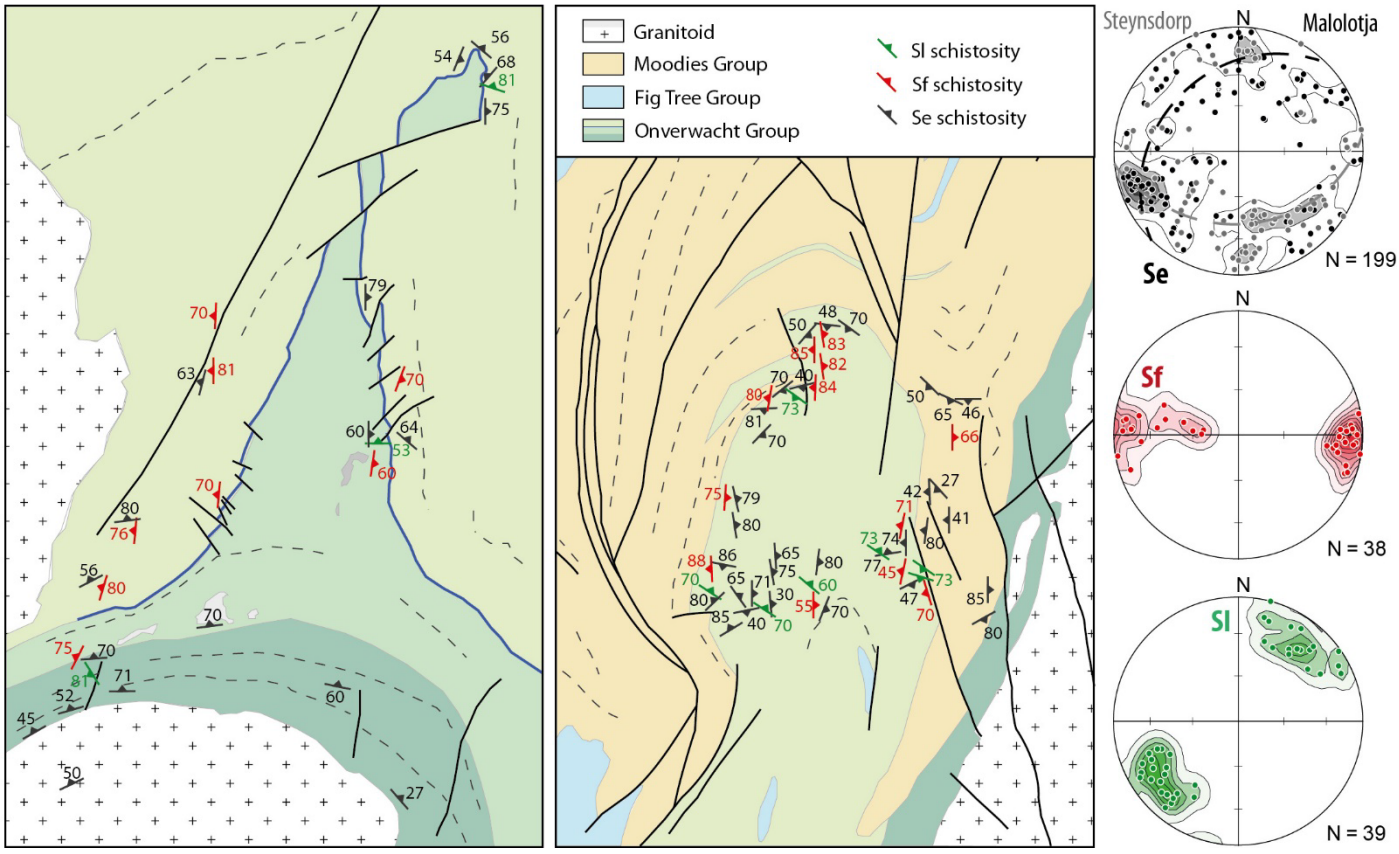

Figure 5. Structural map of the Steynsdorp antiform and the Malolotja synform with Se, Sf, and Sl cleavage distribution. Planar structural data are presented as poles to planes on equal-area lower hemisphere projections, with the associated main direction (dashed great circles). The background maps are two inset views of Figure 3 focused on the Steynsdorp (left map) and Malolotja (right map) sectors.

4.1. Early Event (De)

A regional cleavage Se affected the rocks of the Onverwacht and Moodies groups. In the Onverwacht Group talc carbonate schist, Se is marked by alignment of micas (muscovite and microcrystalline micas) and talc and is locally superimposed on compositional layering, i.e., layers varying in carbonate and pelitic content, likely representing a transposed bedding (Figure 6a,b,f,g). In carbonate-rich zones, dolomite,

ankerite or magnesite porphyroclasts locally show recrystallised tails composed of talc and white mica.

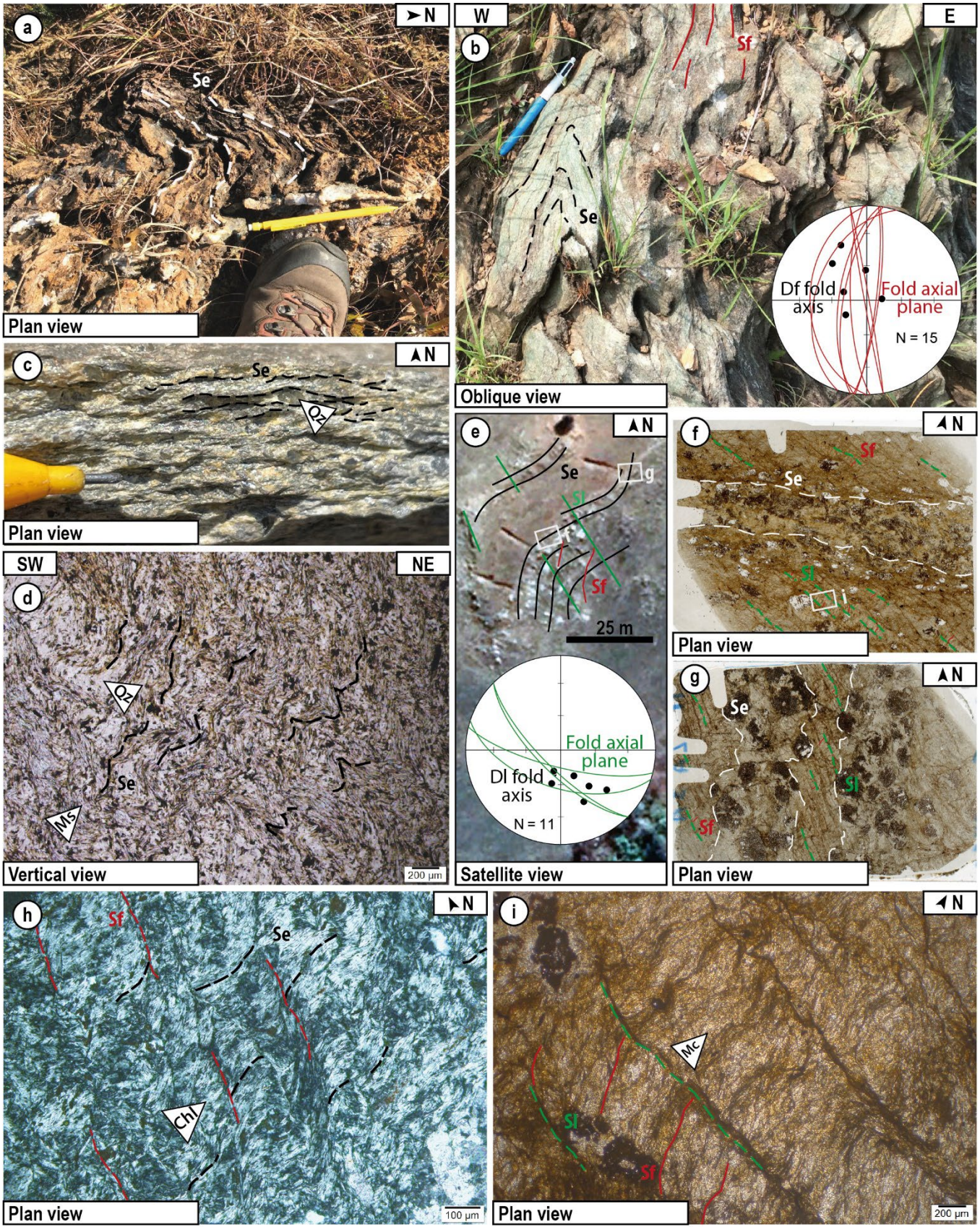

Figure 6. Field and petrographic observations documenting the three deformation events at Malolotja synform and Steynsdorp antiform. (**a**) Df-folded schistosity Se (white dashed line) west of the Malolotja synform in the Onverwacht Group rocks. (**b**) Se schistosity (black dashed line)

outlining a tight fold Ff, with a N–S-striking axial plane Sf schistosity (red line), west of the Steynsdorp antiform in the Onverwacht Group. (**Inset**) Stereonet of Ff fold axial planes (red great circle) and Ff fold axis (black dot), lower hemisphere projection. (**c**) Se schistosity (black dashed line) in the fine-grained Moodies Group sandstone (NE of the Malolotja synform) composed of mica sheets surrounding detrital quartz grains. (**d**) Photomicrograph of the Moodies Group sandstone (plane-polarised light) showing the Se cleavage defined by muscovite alignment crenulated by Dl. (**e**) East of the Malolotja synform, Google Earth satellite image of 100 m scale fold affecting Se and Sf cleavages in the Onverwacht Group rocks. Locations of the thin sections shown in (**f**,**g**) are indicated. (**Inset**) Stereonet of Fl fold axial planes (green great circles) and Fl fold axis (black dot), lower hemisphere projections. (**f**) Thin section scan of a sample collected in the NE–SW-striking limbs of the Fl fold showing relationships between Se, Sf, and Sl. Location of the sections (**i**) is indicated. (**g**) Idem within the NNE–SSW-striking limbs. Within the two images (**f**,**g**), Se (white dashed line) is parallel to the compositional layering (S0), Sf (red line) is preserved in Dl microlithons, and Sl (green dashed line) is NW–SE striking. (**h**) Photomicrograph (crossed polars) of crenulated cleavage Se defined by chlorite in the Onverwacht Group schist of the Steynsdorp antiform. Chlorite marks the axial plane of the Ff fold. (**i**) Close-up photomicrograph (plane-polarised light) of thin section scan showing the overprinting relations between Sl and Sf cleavages. All images are oriented. Arrow indicates the north in all horizontal views; all others are observed in vertical or oblique planes. The abbreviations follow Whitney and Evans [83]; Chl = chlorite, Mc = microcline, Ms = muscovite, Qz = quartz.

In the Moodies Group, Se is subparallel to bedding (Figure 6c) and mainly observed as fine-grained schistosity (Figure 6d) with mm size muscovite sheets coaxially wrapping around quartz grains. On a regional scale, Se is folded and forms the Malolotja and Steynsdorp Ff folds with a steep N–S-striking axial plane. The Se cleavage is E–W striking and steeply dipping in hinge zones of the two regional folds—Se is dipping southwards in the Malolotja synform and northwards in the Steynsdorp antiform (Figure 5). At the outcrop scale, Se is commonly folded into cm to dm scale tight N–S-striking Ff folds or open-to-tight NW–SE-striking Fl folds (see Section 4.3). The folding of Se is clearly visible in the lower-hemisphere stereonet as girdles of poles to planes (Figure 5).

4.2. Main Fold-Related Event (Df)

Both areas are characterised by large-scale folds, shaped as a synform within the Malolotja area and as an anticline at Steynsdorp (Figure 5). Because these structures are well recognisable within the two areas, we call this tectonic event a "main fold-related event". An Sf schistosity has been defined and mainly observed in the rocks of the Onverwacht Group. This schistosity is parallel to N–S striking and steep Ff fold axial planes (Figures 5 and 6b). Sf is expressed as a crenulation cleavage and by the alignment of iron-rich micas, chlorite, and talc sheets (Figure 6b,h). Ff folding ranges from crenulation to km wavelength folds, responsible for the large-scale Malolotja synform and Steynsdorp antiform. Both km scale to crenulation Ff fold axes are commonly steep to subvertical (Figure 6a,b,e).

4.3. Late Event (Dl)

A third deformation Dl is inferred from observations of NW–SE-trending open-to-tight folds and associated with steeply dipping axial planar cleavage (Figure 6e,i). Dl is common in the Malolotja syncline area and only locally observed in the Steynsdorp domain. Dl has not been observed in the Moodies Group and is only restricted to the Onverwacht lithologies. Dl is evident in the eastern limb of the Malolotja synform where it results in steep knee-shape folds of the composite compositional layering and Se cleavage (Welcome gold occurrence, Figure 6e–g). Microscale observations demonstrate that Dl also affects the Sf cleavage forming an open crenulation fold associated with crenulation cleavage Sl marked by the alignment of microcrystalline iron-rich micas and talc (Figure 6f,g,i).

5. Hydrothermal Vein System

5.1. Vein Macroscopic Study

The 3D block diagram in Figure 7 compiles the distribution of the main outcrops related to the hydrothermal vein system in the study area. Gold occurrences are almost exclusively located in the Onverwacht Group rocks (see also Figure 3). The majority of the mineralised outcrops correspond to former mining areas with small excavations (5–30 m deep), shafts, trenches, and old galleries. Thanks to the structural study of all these outcrops, we propose to classify the hydrothermal features in three distinct generations.

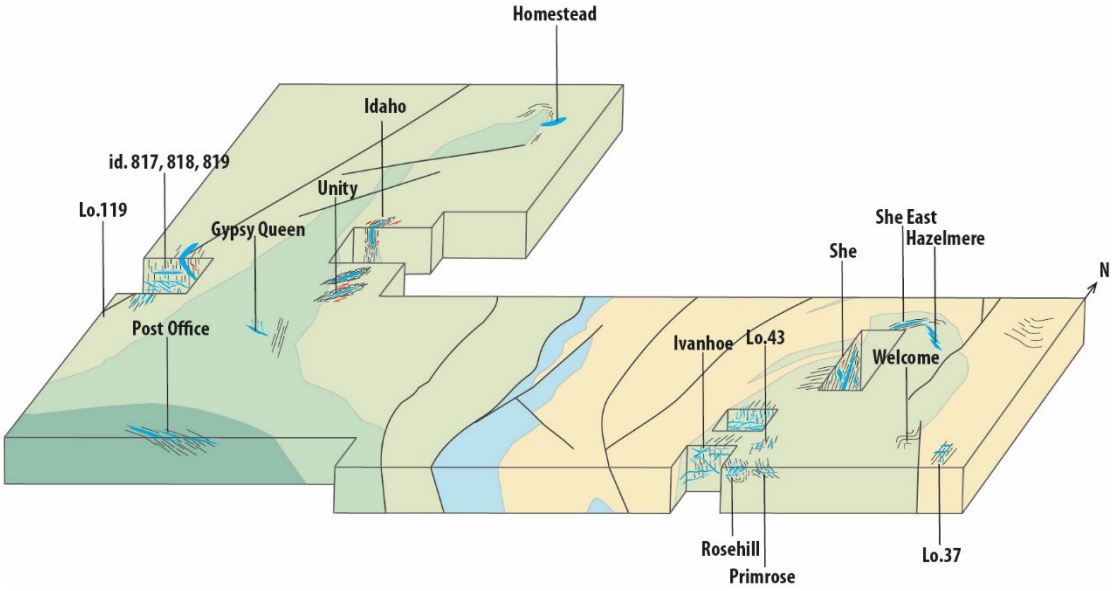

Figure 7. Simplified block diagram showing the distribution of the studied gold occurrences and outcrops within the Malolotja and Steynsdorp areas. See the text for an explanation.

5.1.1. Early Veins System

The early vein system, commonly observed and studied within the Malolotja area, is formed by a network of cm to dm thick white quartz veins, subparallel to the Se schistosity and commonly folded (Figure 8). These veins have either a sigmoid shape wrapped by the Se schistosity (Figure 8a) or a folded appearance and show acute angle relation with Se (Figure 8b). Orientation of the early veins is very variable, although most of the veins have dip angles between 20 and 50°. It is evident that early veins are highly folded (Lo 119, Primrose, Figure 8b,c, see location in Figure 7) and have a similar attitude to the cleavage Se, i.e., intensively folded.

5.1.2. Mineralised Veins System

Veins belonging to the mineralised system are here regarded as the ones occurring within or close to a mineralised occurrence indicated within the Barberton Greenstone Belt metallogenic map [14] (Figure 3). Gold occurrences in the study area correspond to small-scale former mines and mining exploration; no archival information on the gold ores has been found. Due to the proximity of the veins to the mineralised occurrence in the metallogenic map, as well as clear field evidence of historical mining activities of these veins, they are considered mineralisation-related veins even though no gold rate has been measured. Indeed, it remains impossible in such outcrops to analyse the form and the distribution of gold within such structures.

Mineralised veins always cut the schistosities Se (and in a few places the Sf, Figure 9a–c,f) and are mm to m thick. They preferentially occur in the talc schists of the

Onverwacht Group. The mineralised vein system is mainly characterised by at least three types of veins: shallow-dipping (Figure 9a–d), steeply west- or east-dipping, and subvertical (Figures 9a–c,e,f and 10). The horizontal veins are commonly folded into open-to-tight buckles (e.g., no 817 occurrence in Ivanhoe mine), with an axial plane parallel to the Sf cleavage (Figure 9b). Subvertical veins locally show reverse top-to-the-east kinematics (occurrence 819, west limb of Steynsdorp, Figure 9f). In places, the veins show varied dip angles from horizontal and west-dipping to vertical and form complex vein networks (Rosehill, Primrose, Ivanhoe; Figures 9e and 10a). In these areas, mutually

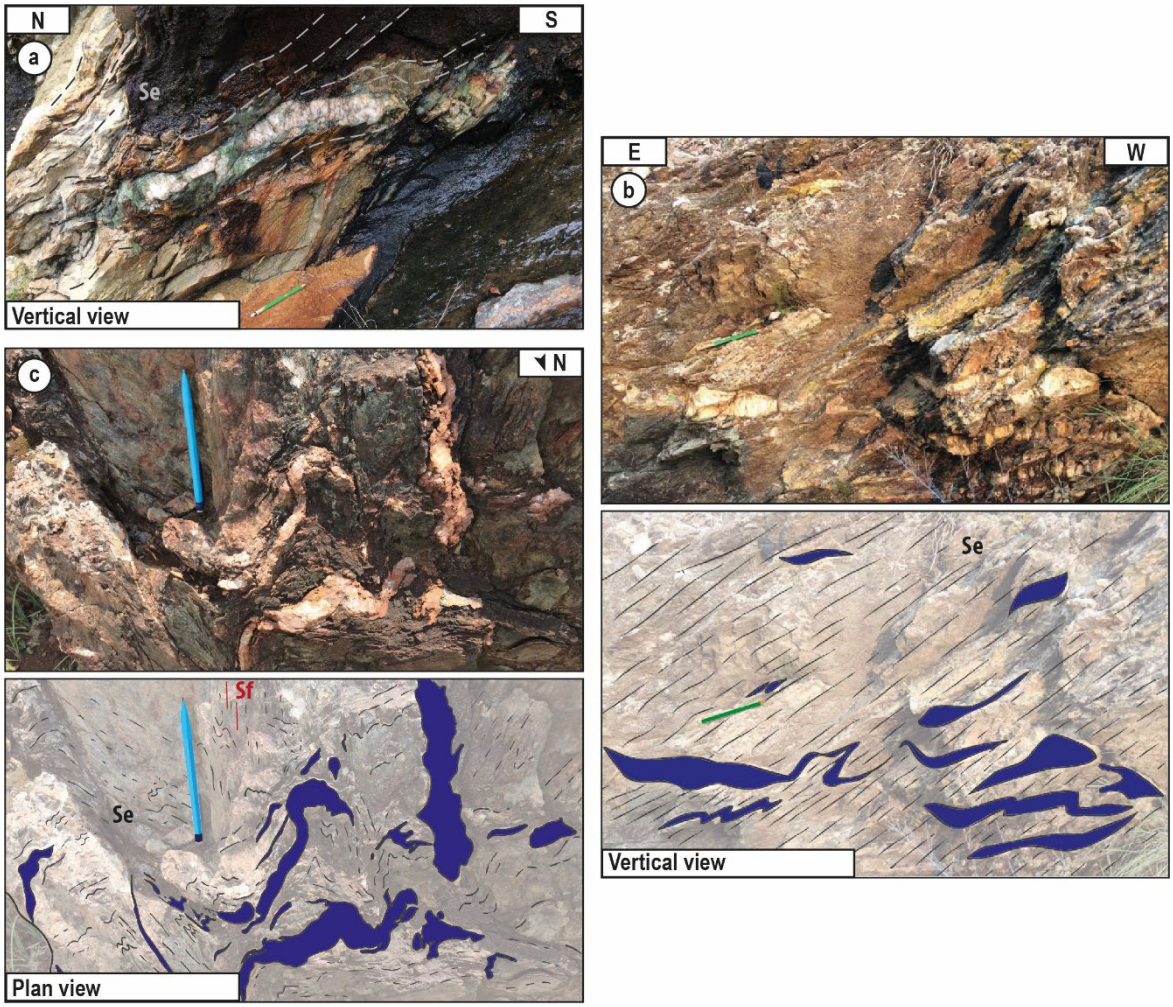

intersecting veins are generally N–S striking, dipping to the west, and exist in petrographic continuity (Figure 9b,e).

Figure 8. Field observations of the early vein system. (**a**) dm thick sigmoid quartz vein at a low angle to subparallel to the Se schistosity. Note the cm thick green talc alteration halo. (**b**) Photo and sketch of cm thick quartz vein, variably sigmoid and folded by Se (Primrose deposit). (**c**) Photo and sketch of cm thick quartz vein subparallel to the Se schistosity and highly folded in Ff folds.

In the Malolotja area, the veins are mostly N–S striking, although a small cluster of veins that strike N150 and dip steeply to the east exists in Primrose and Rosehill occurrences (Figure 10a). The Malolotja mineralisation-related vein poles form a NE–SW-striking great circle (Figure 10a). Although no clear field evidence of mineralised quartz veins folded by the late Fl folds has been reported, the great circle in Figure 10a might be interpreted to represent folded veins with a NW–SE-striking axial plane, i.e., parallel to the Fl axial planes (Figure 6e) and schistosity Sl (Figure 5). In the Steynsdorp area, veins are mainly shallowly east-dipping or steeply west-dipping and locally steeply south-dipping (Figure 10b).

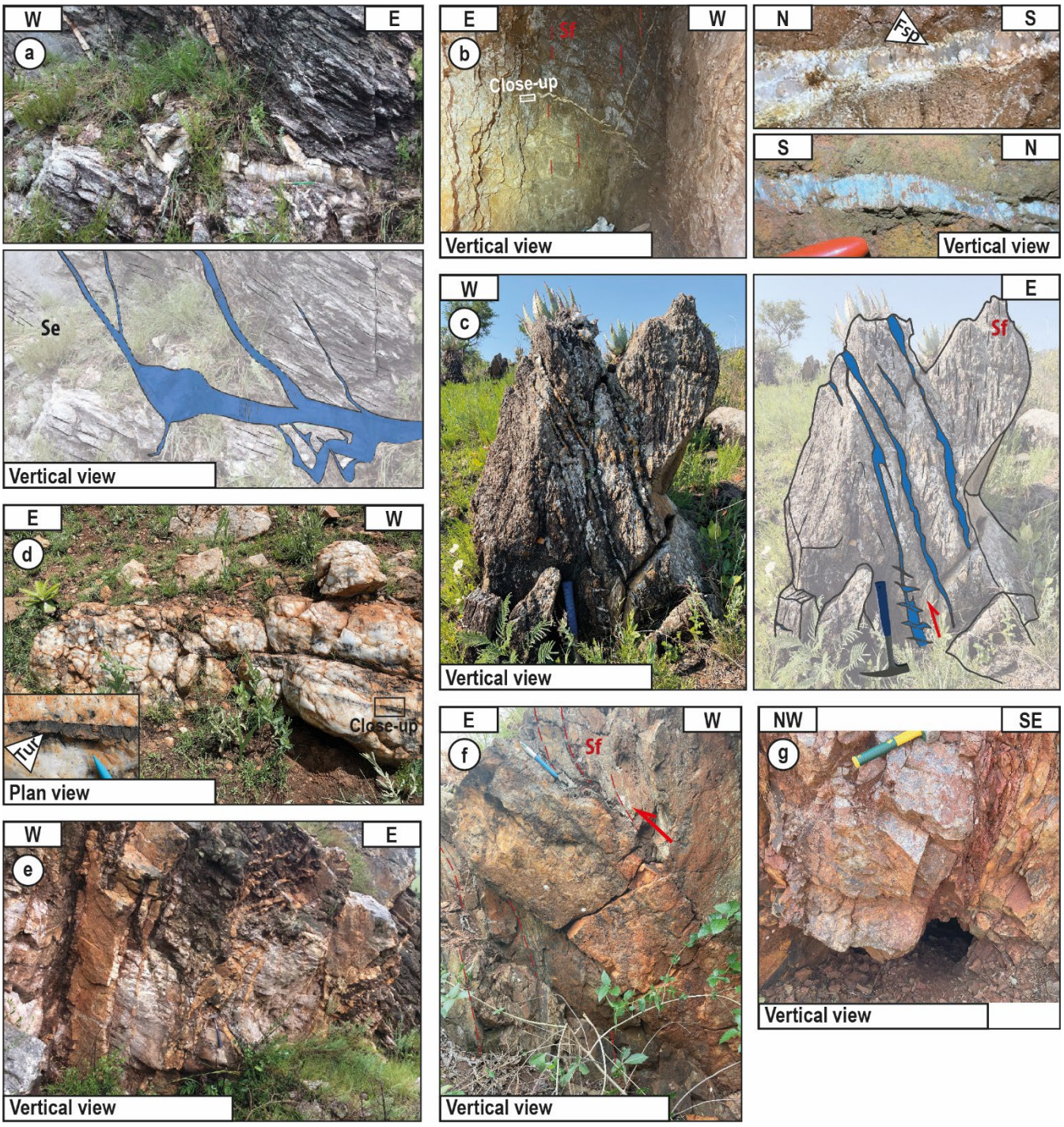

Figure 9. Field observations of the mineralised quartz vein system. (**a**) Photo and sketch of a subhorizontal quartz vein, coeval to steeply east-dipping quartz veins, both cutting the Se schistosity (Primrose mine). (**b**) Shallow-dipping folded vein coeval with steeply east-dipping quartz veins. Two close-up views of the veins show elongated feldspars grains perpendicular to the vein edge and/or comb texture of vertical quartz fibres (Ivanhoe mine). (**c**) Field photograph and sketch of a set of steep east-dipping quartz veins cutting Sf schistosity, which are in turn truncated by horizontal and echelon quartz vein (id 817 occurrences). (**d**) Horizontal quartz vein with elongated vertical tourmaline (Post office occurrence). (**e**) West-dipping steep quartz veins in a complex network system (Rosehill mine). (**f**) West-dipping quartz vein with Sf drag fold attesting reverse motion. Note that the vein is internally brecciated (id 819 occurrence). (**g**) Subvertical quartz vein parallel to a fault zone in pillow lava host rock (Idaho mine). Fsp = feldspar, tur = tourmaline.

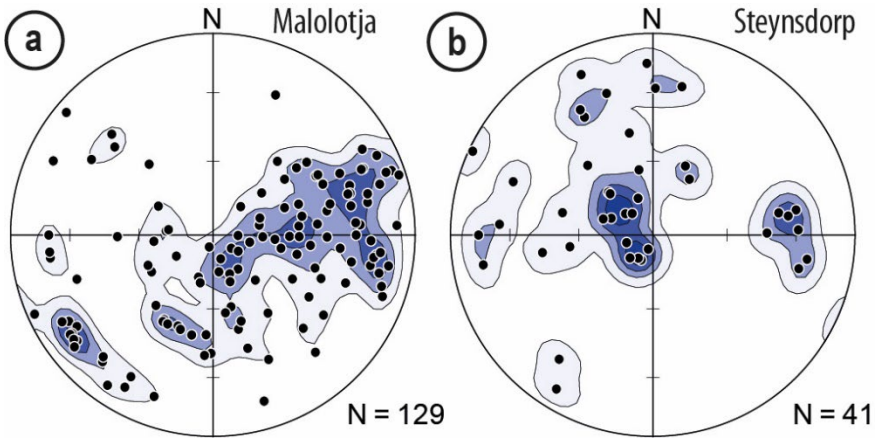

Figure 10. Stereonets of mineralised quartz veins in the study area shown as poles to planes. (**a**) Quartz veins in Primrose, Rosehill, Ivanhoe, and Waverley Reefs ancient mines in the Malolotja area. (**b**) Quartz veins in the 817, 818, 819, and Post Office gold occurrences in the Steynsdorp area.

Mineralised veins in the eastern sector of the Steynsdorp anticline do not follow the above-mentioned typology. Here, the quartz veins are located along fractured corridors that strike N40 to N70 in a pillow lava host rock (Figure 9g). Some horizontal or steeply plunging slickenlines and drag folds in the host rock have been observed in the fractured zones, associated with dextral motion in the Unity occurrence and sinistral/oblique one in the Idaho occurrence (see locations in Figure 7).

In addition to quartz, veins are composed of elongated tourmaline grains and, more rarely, K-feldspar and plagioclase (Figure 9b,d). Shallow-dipping veins exhibit, in several places, vertical comb quartz or quartz fibres and tourmalines (Figure 9b,d).

The vein system observed at the She mine does not fit with the vein generations scheme described above. In this area, the schistosity and parallel compositional layering are striking N70 and dipping 40° to the SSE, carrying a strong down-dip mineral lineation. Sigmoidal quartz and K-feldspar veins attest to a reverse sense of shear (top-to-the-NNW, Figure 4c). The mineralised quartz veins form either sigmoids wrapped by the schistosity or dm wide schistosity-parallel veins. These veins are composed of quartz-feldspar-tourmaline-chlorite-sulphides. Here, K-feldspar has been observed in the core or the sigmoidal quartz veins. The schistosity at the She mine is possibly Se, although Se elsewhere does not usually carry a lineation and is not associated with asymmetric objects showing clear kinematics. More work is needed to confidently assign the She mine schistosity to the De event.

5.1.3. Late Vein System

Some veins appear to be late and are interpreted to be unmineralised because they occur far from historical mines and diggings. Clearly, these veins have not been explored historically and are, therefore, thought to be barren. Most of them have been observed at Malolotja.

On the western limb of the Malolotja synform, numerous large metric quartz veins, slightly folded, globally strike N050–070°E (Figure 11a,b). More to the east, another complex quartz vein system is observed, representing a dextral N170°E "en échelon" system. In the Waverley Reefs area, west of Malolotja, a mineralised quartz vein system is clearly cut and displaced by subhorizontal quartz veins that are supposed to be late and barren (Figure 11e).

Even if vein systems are better expressed within the Onverwacht rocks, one outcrop in the Moodies Group in Malolotja exhibits a complex network of veins (Lo.37, Figure 12; see location in Figure 7). Two sets of cm thick white quartz veins have been observed. The first one is striking N040 and associated with dextral pull-apart and drag folds whereas the second one, less expressed, is represented by thin veins striking N100 to N140, in sinistral places (Figure 12). These observations suggest an emplacement of the veins during

a global dextral shearing, as confirmed by the observation of a weakly expressed horizontal stretching lineation on vertical Se cleavage (most likely parallel with the vertical limb of the large-scale Ff fold).

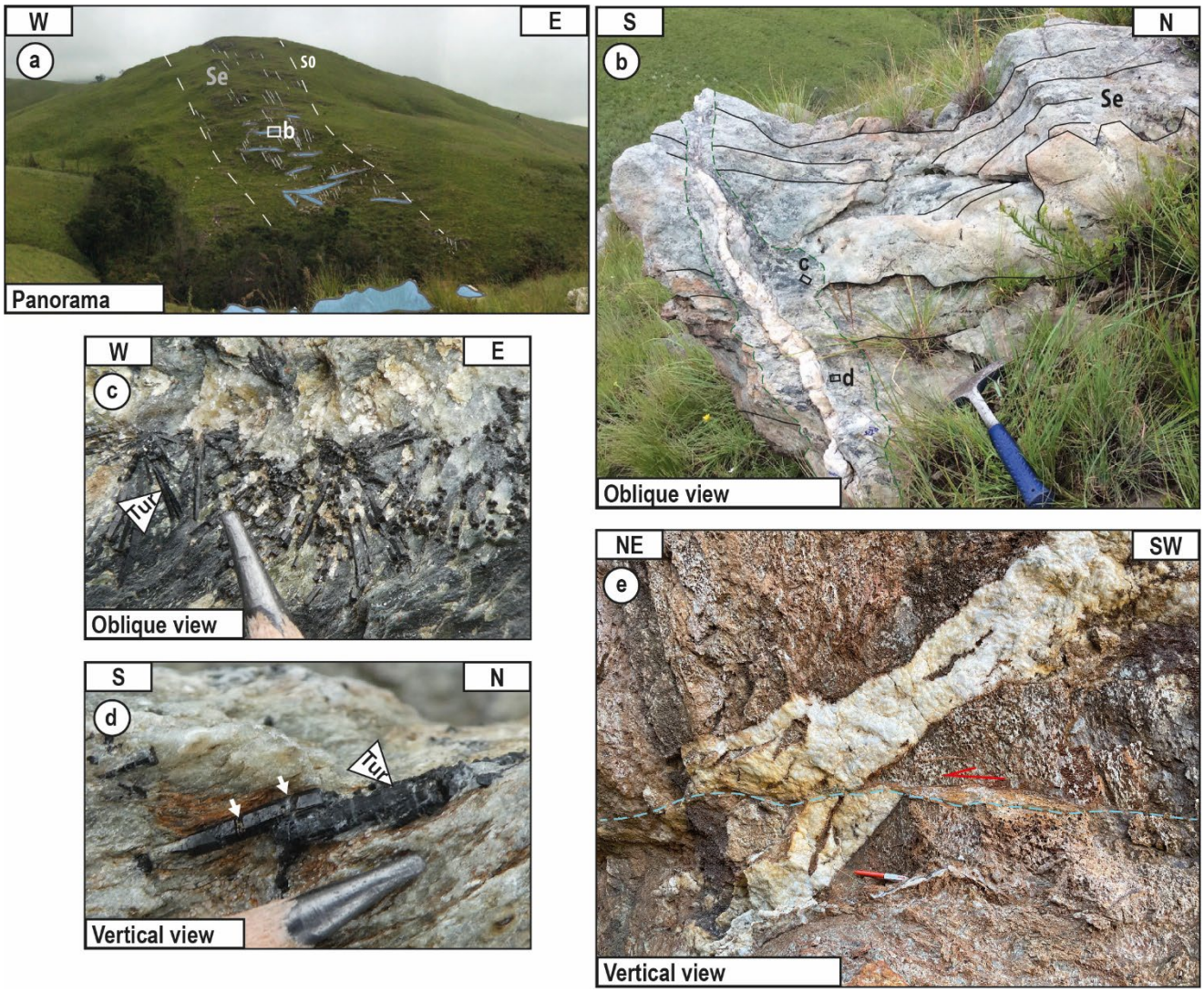

Figure 11. Field observation of the late vein system. (**a**) Panorama view of N50-striking metric quartz vein and location of the photography (**b**). Note the localisation of the vein across supposed stratigraphic bedding. (**b**) Dm thick slightly folded quartz vein and its white-greenish alteration halos, cutting the Se schistosity. Locations of the (**c**,**d**) photographs are also indicated. (**c**) Radial tourmaline rods in the alteration halos. (**d**) In the alteration halos, truncated tourmalines (truncation shown by a white arrow) are parallel to the Se schistosity. (**e**). Centimetric late quartz vein cutting and displacing a mineralised quartz vein. Tur = tourmaline.

The structural control of this late hydrothermal event is a key point of the tectono-hydrothermal evolution of the study area and will be discussed further in this work. Our preliminary suggestion is that it is controlled by a NE–SW shortening, compatible with the Dl event observed in the country rocks of the late vein system (see Section 4.3).

5.2. Vein Microscopic Study

5.2.1. Petrography

The paragenetic evolution of the vein systems in the Malolotja and Steynsdorp areas is summarised in Figure 13 and detailed here.

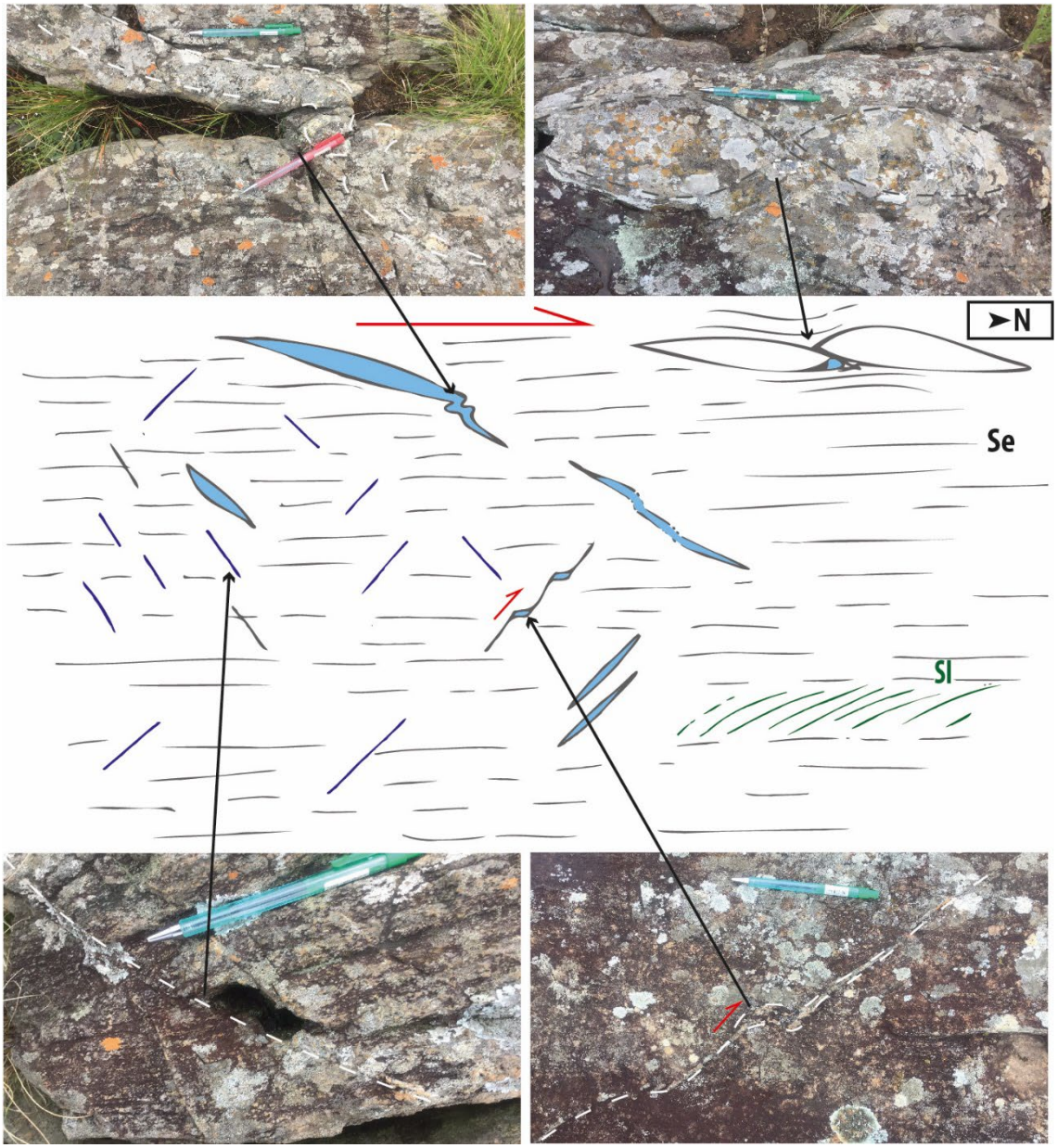

Figure 12. Sketch in map view summarising field observations pertaining to the late vein system in the Moodies Group located at Lo.37 see Figure 7.

Early veins are composed mainly of quartz and carbonates (Figure 14a). Mineralised veins are filled with quartz with Na, Ca, and K-feldspars on their edges (confirmed by energy-dispersive X-ray spectroscopy analyses that allow confirming the presence or absence of the Na, Ca, or K elements in feldspar grains). Numerous veins, especially in the Steynsdorp area, have elongated tourmalines and few carbonates, whereas others exhibit muscovite and chlorite (Figure 14b,c). Sulphides are rarely preserved and commonly replaced by iron oxides (Figure 14d). However, pyrites and some rare chalcopyrite have been recognised in this mineralised vein system (Figure 14d). The late veins are mainly composed of quartz with minor K and Na-feldspars (confirmed by energy-dispersive X-ray spectroscopy analyses allowing for the detection of the presence or absence of the Na, Ca, or K elements in feldspar grains), and μm to mm size muscovite grains.

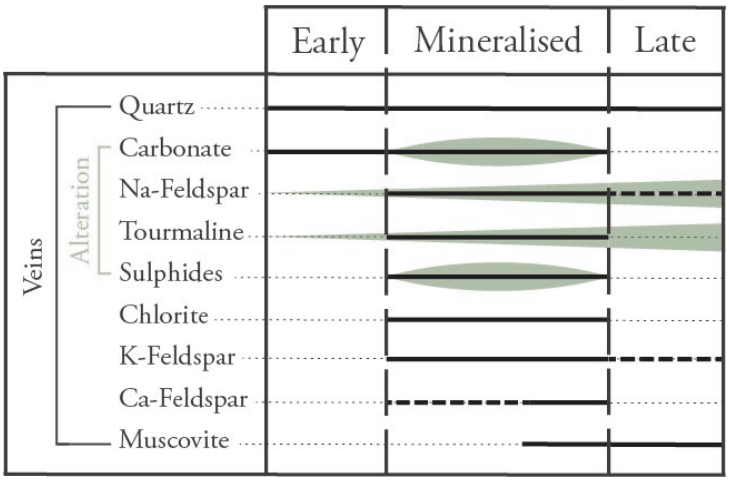

Figure 13. The paragenetic sequence of veins and alteration halos.

5.2.2. Microstructures

The early quartz vein system is mainly formed by comb quartz and anhedral carbonate infilling, which are weak or not recrystallised (Figure 14a).

In contrast, mineralised veins present a larger variety of microstructures. As already mentioned, subhorizontal or shallow-dipping veins have a comb or fibre minerals (quartz, tourmaline, feldspar) perpendicular or slightly oblique to the vein edge, clearly recording the direction of the opening (Figures 9b and 14c,e). It is common that vertical tourmalines or feldspars are truncated by horizontal fractures filled with quartz (Figure 14c). Some of the mineralised, shallow-dipping veins show moderate recrystallised quartz features, while recrystallisation is stronger in N–S-striking steep veins associated with reverse kinematics and, also, within the NE–SW-striking steep veins along fault planes in the eastern limb of the Steynsdorp anticline. All these veins exhibit quartz grains with undulatory extinction and bulging microstructures (Figure 14f). Subgrain rotation recrystallisation of previously formed comb-quartz grains is locally observed. Locally, quartz in the mineralised veins shows discrete μm wide transverse conjugate recrystallised bands (Figure 14g). The bisector of the acute angle between the conjugate bands is NE–SW trending, hence suggesting that these recrystallised bands formed during the late NE–SW shortening event.

Quartz veins of the late system are unexpectedly highly deformed, visible by more intensive subgrain rotation formation (Figure 14h). Compared with the veins associated with mineralisation, the late vein system consistently exhibits more pronounced recrystallisation microstructures, whereas they are less developed in the mineralised system. Consequently, although the mineralised system locally shows significant recrystallisation of quartz with, for example, numerous 10 μm wide subgrain formations, the late system is considered highly recrystallised due to systematic observations of subgrain rotation around quartz crystals.

5.3. Alteration

Macroscopically, several features related to alteration processes have been recognised around the three generations of vein systems and are presented here.

- Although most of the *early veins* do not show alteration features, few of them exhibit greenish-to-whitish mm to dm scale alteration halos, mainly in the Malolotja area (Figure 8a).
- At Malolotja, green alteration halos around quartz veins of the Primrose occurrence traduces the existence of alteration (Figure 15a). At Steynsdorp, mm large cubes of pyrites and ankerite crystals are found in the host rock adjacent to *mineralised quartz*

veins (Figure 15b). Brown/red leaching of the country rock is also observed in the vicinity of mining areas (e.g., She mine, Waverley Reefs, Welcome, Figure 4c).

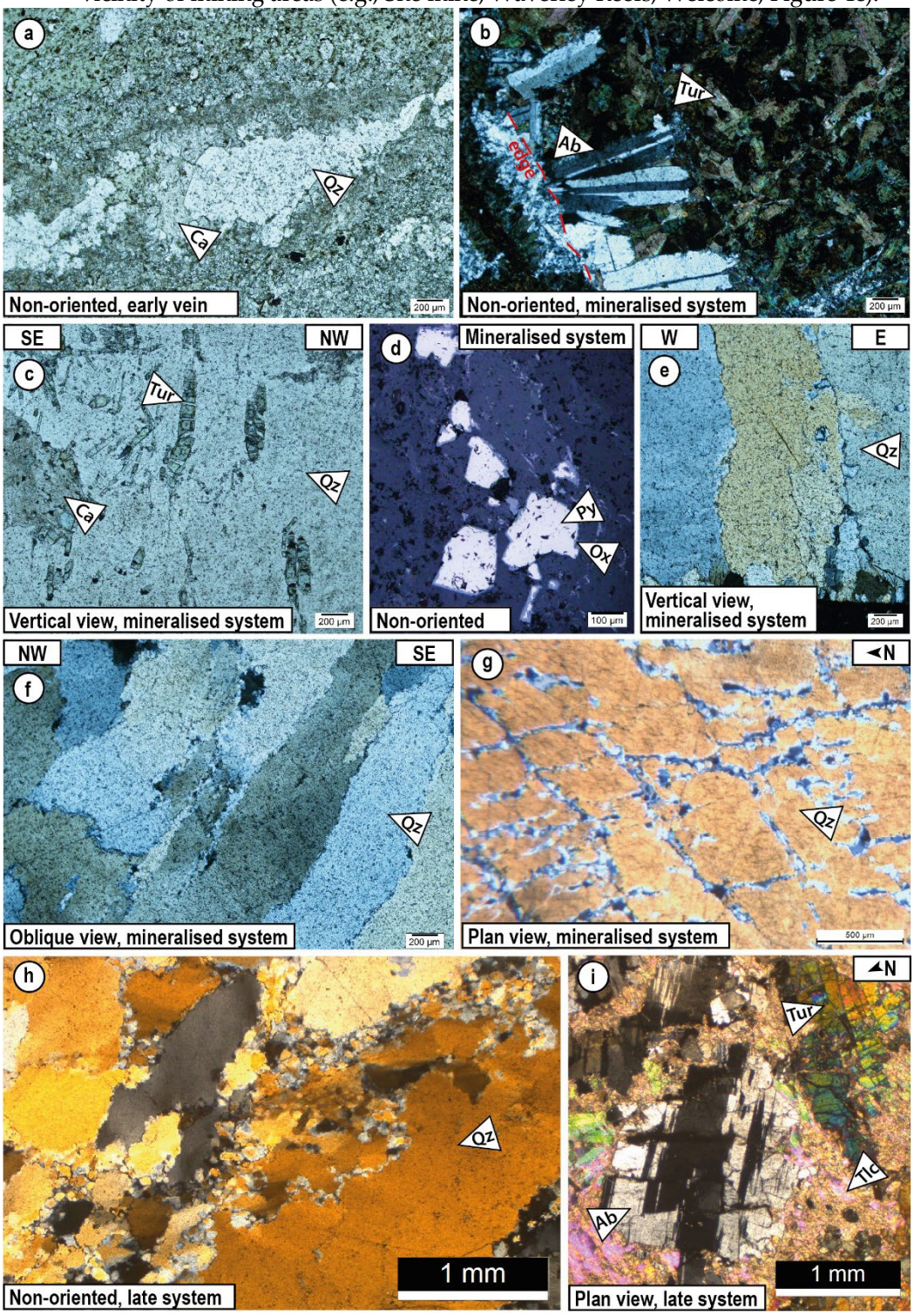

Figure 14. Microscopic observations of the three vein systems. (**a**) Early quartz-carbonate vein. (**b**) Albite at the edge of a tourmaline-quartz mineralisation-related vein (plane-polarised light). (**c**) Vertical and truncated tourmaline in a horizontal quartz-carbonate mineralisation-related vein (plane-polarised light). (**d**) Euhedral pyrites in a mineralised quartz vein with oxidised rims (reflected light). (**e**) Subvertical quartz fibres in a horizontal quartz mineralisation-related vein (crossed polars). (**f**) Comb quartz showing incipient bulging and some subgrain recrystallisation of a mineralisation-related vein (crossed polars). (**g**) Recrystallised quartz localised in conjugate bands in a quartz mineralisation-related vein (crossed polars). (**h**) Recrystallised quartz of a late vein (crossed polars). (**i**) Albite and tourmaline in an alteration halo of a late vein (crossed polars). Ab = albite, Ca = carbonate, Py= pyrite, Ox = oxide, Qz = Quartz, Tlc = talc, Tur = tourmaline.

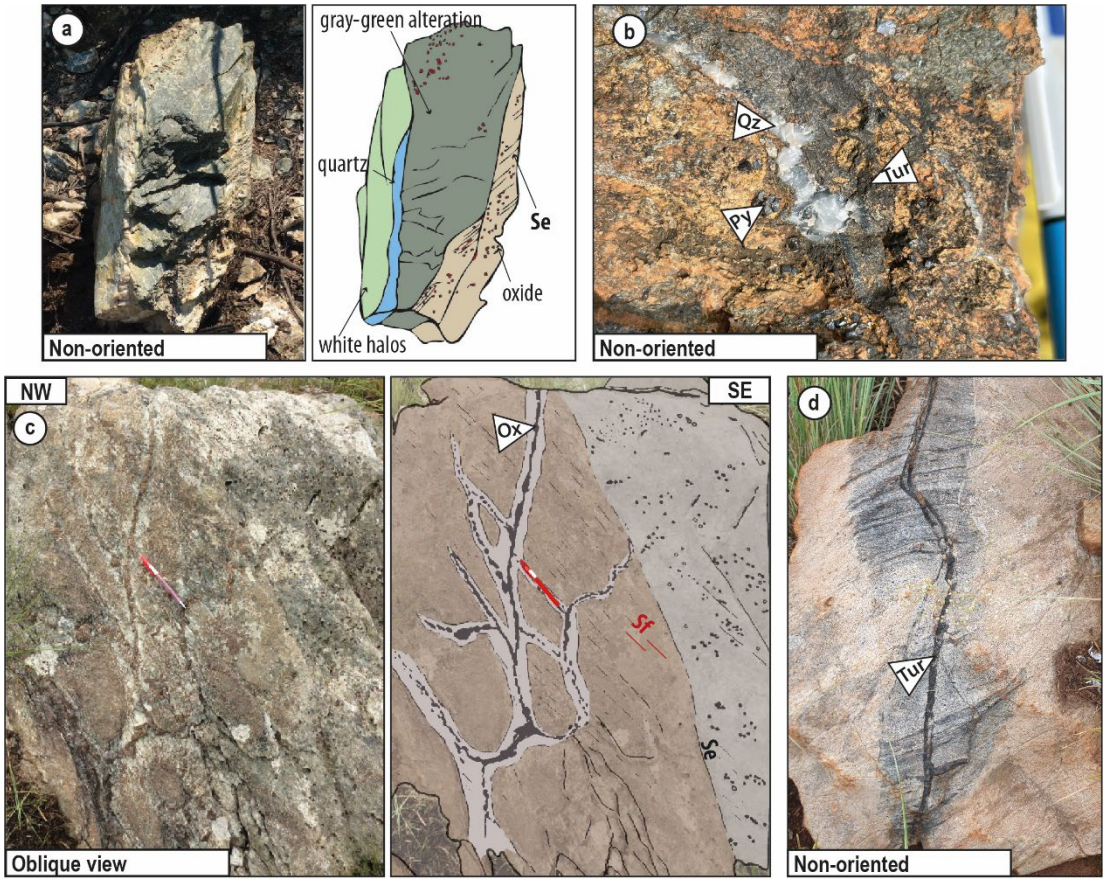

Figure 15. Field observations of the alteration features. (**a**) Field photograph and associated sketch of a vein from the Primrose occurrence showing well-developed greenish alteration halo. (**b**) Mm scale euhedral pyrites surrounding a quartz-tourmaline vein (occurrence id. 817). (**c**) Photo and sketch of oxide veins and associated white leaching alteration halos (Welcome occurrence). (**d**) Tourmaline vein surrounded by tourmaline impregnation in quartzites of the Moodies Group (close to location Lo. 37). Ox = oxide, Py = pyrite, Qz = quartz, Tur = tourmaline.

- NE–SW-striking tourmaline or oxide veins have been observed locally in the eastern limb of the Malolotja synform in both the Onverwacht and Moodies Groups (Figure 53c,d). These veins are supposed to be part of the *late barren system*. Both veins exhibit alteration effects with, respectively, leaching (Figure 15c) and/or tourmaline impregnation (Figure 15d). One of the best alteration features observed within the entire studied area is the large alteration halo present at the edge of the late vein of the outcrop Lo.43, in which mm large radial or elongated tourmaline is visible (Figure 11b–d).

Microscopically, the green and white alteration halos principally found around the veins (the three types—early, mineralised, and late) at Malolotja correspond to widespread talc, muscovite, and chlorite micrograins, in which larger albite and tourmaline grains occur. Alteration at Steynsdorp appears less developed and is represented by iron-rich carbonates and pyrite disseminations. Other alteration assemblages, including tourmalines, micas, and iron oxide impregnations, such as host rock leaching, are encountered. When oriented, these alteration-related features strike N40. As already mentioned, alteration linked to the late vein system is well expressed (Figure 11b–d) and corresponds, microscopically, to the development of large tourmaline and feldspar crystals often elongated in the core of the alteration-related talc and mica thin matrix (Figure 14i). Tourmaline can have various shapes and textures (i.e., radial, Figure 11c) but often occurs as truncated crystals (Figure 11d). This observation represents a strong argument in favour of syntectonic filling of the different vein systems.

6. Interpretation

6.1. Main Results

The new contributions of our structural and mineralogical study of the southern part of the Barberton Greenstone Belt quartz vein systems are summarised as follows:

- Three main tectonic events have been identified in the vein systems and adjacent country rocks. Three schistosities and associated folds are recognised: (i) Se cleavage (De early event), which is interpreted to be initially E–W striking and dipping to the north at Steynsdorp and to the south at Malolotja; (ii) Sf cleavage (main fold-related event) related to the large-scale N–S-trending folds; (iii) and Sl cleavage (late Dl event) N130°E striking. Stretching lineation occasionally occurs but is not well expressed in the study area.
- Similarly, three generations of veins have been established:
  - Early veins are cm to dm thick, mostly sigmoid in shape, and wrapped by Se and/or folded by Df events. Veins are mostly filled by quartz and carbonates with or without green alteration halos composed of talc, tourmaline, and albite.
  - Mineralised veins have various orientations: shallow-dipping, steeply east- and steeply west-dipping. They are the most abundant, thicker (cm to m thick), interconnected, and thus coeval (Figure 16). The steep veins have orientations varying from N–S-striking (most frequent) to N140–150-striking. The mineralogy of these veins is mainly quartz, carbonates, feldspar, tourmaline, and sulphides with alteration halos of pyrite, tourmaline, feldspar, and talc.
  - A late vein system was observed exclusively in the Malolotja area. Their geometry is variable, i.e., flat sheared veins, oblique dipping tension gashes, weakly folded N050-striking steeply dipping to the NW metric veins. These veins are composed of quartz, feldspar, and muscovite with an albite, tourmaline, and muscovite alteration halo, similar to the ones of the mineralised system, even if best-expressed.

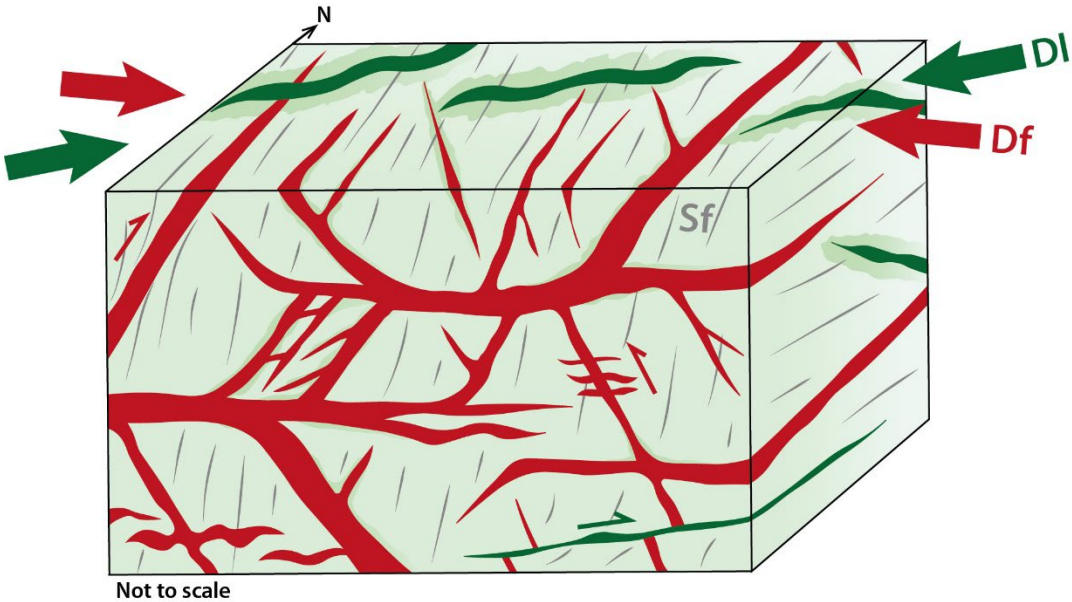

Figure 16. Synthetic sketch illustrating the distribution of the mineralised (red) and barren (green) vein system at the outcrop scale. Note the coexistence between horizontal and steeply dipping westward and eastward veins. Both have N–S and NNW–SSE strikes, although N–S veins dominate. The red and green arrows display, respectively, the Df and Dl deformations, and the grey line is the Sf schistosity.

6.2. Tectono-Hydrothermal Evolution of the Southern Barberton Greenstone Belt

A three-stage model for the tectonic evolution of the southern part of the Barberton Greenstone Belt that considers the hydrothermal events formation is proposed here (Figure 17).

a. The initial stage shows a subvertical to south-dipping Se schistosity in the Malolotja area, likely related to the Onverwacht Group overthrust on the Moodies Group rocks, as suggested by Heubeck et al. [79] and Lamb and Paris [84] (Figure 17a). At Steynsdorp, the Se schistosity is subvertical to north dipping. According to Lana et al. [65], Se formed as a response to unroofing of the Steynsdorp metamorphic core complex. Early quartz veins formed during this stage and were subsequently folded by the following events. Early quartz veins are related to this event (Figure 17a).
b. The second event, Df, results in this southern part of BGB from E–W shortening and corresponds to the formation of large-scale folds, i.e., the Steynsdorp anticline and Malolotja synform. The E–W shortening direction is obtained as normal to the Sf schistosity plane, presuming that the deformation Df is coaxial. This inference is based on consistent cleavage orientations, fold geometry (e.g., similar fold axial plane orientations and axis, Figure 6b), and lack of stretching lineation associated with Df. An associated N–S-striking axial planar schistosity Sf is created in several places (in red in Figure 17b). During this stage, most of the gold-bearing and/or gold-related hydrothermal quartz veins are emplaced, i.e., the horizontal and steep veins (Figures 16 and 17b). The association between horizontal and steep veins demonstrates their syntectonic character (see the discussion below), also confirmed by (i) upright Ff folding of the horizontal veins formed and opened in mode I character and (ii) internal texture of horizontal veins, showing vertically elongated tourmaline and quartz grains, indicative of vertical (sometimes slightly oblique) opening. In addition to the vertical tourmalines, feldspars and fibres and comb quartz are perpendicular to the vein edges (Figures 9b,d, and 14c)—the local development of elongated and/or truncated tourmaline and feldspar in alteration halo also confirms the syntectonic character (Figure 13). Generally, N–S-striking, steeply west-dipping veins formed during reverse faulting (e.g., Figures 9f and 16). The associated shallower veins (either dipping towards the west or the east) opened as shear planes in an R or R' position. The complexity of this model lies in the fact that all these veins are synchronous (e.g., Rosehill and Primrose, Figures 9a,e, and 16). Moreover, some of the flat-to-shallow-dipping veins are folded by Sf (e.g., Ivanhoe, Figures 9b and 16) or contain vertically truncated tourmalines (e.g., Figure 14c), which confirms the syntectonic character of these veins and that they formed syn in the late Df.
c. The third hydrothermal and deformation event is mainly recorded in the Malolotja area as the result of a NE–SW shortening, as determined by taking the axis parallel to the Sl poles. This deformation produced local folds and a NW–SE-striking Sl cleavage (in green in Figure 17c). In addition, this deformation controlled the emplacement of a late vein system, typified by N050-striking veins (Figures 11b, 16, and 17c) or shear veins displacing existing veins (Figure 11e). Currently, there is no indication justifying that this late vein system was associated with gold precipitation and/or concentration. Only the N050–070-striking veins of the late vein system have been represented in Figure 16.

This evolution model herein proposed considers the deformation of the host rock in parallel to the different observed vein system emplacement within the southern part of the BGB. Three deformations and hydrothermal events have been highlighted. The last two stages are significantly documented by numerous field and microstructural observations. However, several points, such as the surprising distribution of mineralisation occurrences strictly following the geometry of the first-order folds, still need to be understood. Another surprising result is the fact that late veins microscopically appear affected by intense recrystallisation processes (Figure 14h), whereas the earlier mineralised veins remain less internally deformed (Figure 14f,g). All these points will be discussed further in the text.

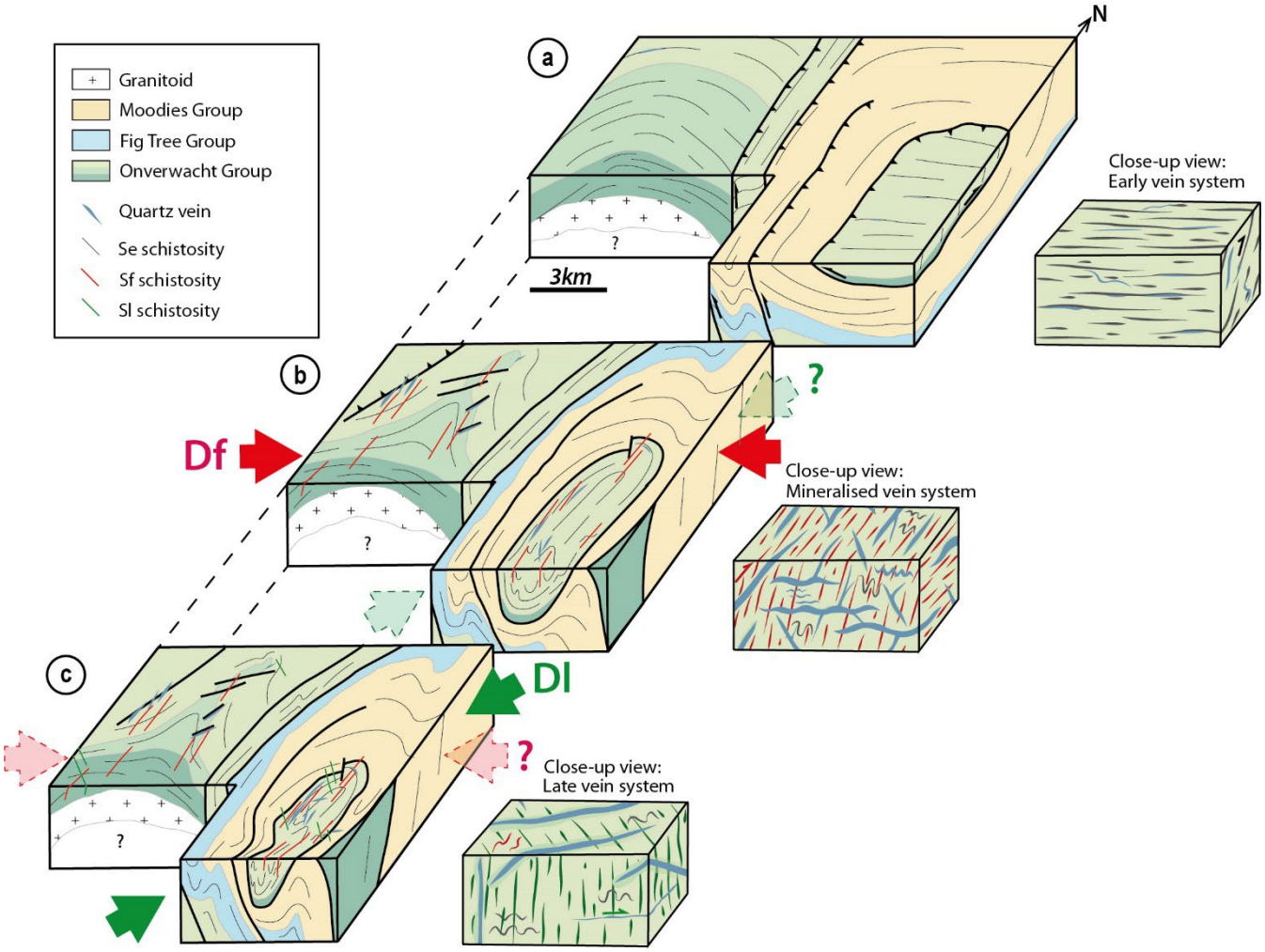

Figure 17. Three-stage tectonic evolution of the southern part of the Barberton Greenstone Belt and close-up synthetic bloc views of associated quartz vein systems, showing the structural control on the emplacement of gold-related hydrothermal features. (**a**) Early stage. (b) Main Fold-related stage. (**c**) Late stage. See the text for an explanation.

7. Discussion

7.1. Vein Formation Model

In this study, we propose a tectono-hydrothermal model in which a complex vein system, illustrated in the schematic synthetic sketch of Figure 16, controls the formation of the gold-related hydrothermal event in the southern part of the Barberton Greenstone Belt. We, therefore, suggest that a formation model of the mineralised vein system controlled by the vertical opening of horizontal veins coevals with the formation of steeper N–S-striking shear veins associated with reverse motion, which are oriented at an obtuse angle to the shortening direction of the Df deformation. (i.e., red veins in Figure 16). Additionally, another system of late barren veins opens parallel to the finite shortening axes of the Dl deformation, similar to 'en echelons' veins (i.e., green veins in Figure 16). Although this complex vein system is entirely new and undescribed in the southern part of the belt, a similar vein pattern has been described in the northern part of the belt, particularly in the Sheba/Fairview gold mines (Figure 1; i.e., [21,66,85]). The mineralised vein formation model described here, with flat vein opening in mode I and associated with steep reverse and normal veins (see above), shares similarities with the one described by Gloyn-Jones and Kisters [21] and operates in coherence with the model described by Sibson [86] that combines steeply dipping veins and low-angle folded ones. Our model

also shares some similarities with the ones by Cerda et al. [66,85]. However, three significant divergences subsist:

- The fact that all veins in our case are supposed to be coeval, in contrast to the ones described by Sheba for which a relative chronology has been defined (e.g., [66,68]).
- The orientations of the mineralised veins, which are generally striking N–S to N150 in our case, whereas they are mainly oriented NE–SW to ENE–WSW in the Sheba/Fairview systems. The structural control of the gold mineralisation is therefore interpreted with different shortening directions, i.e., E–W shortening in our case study while in the Fairview-Sheba area, they are controlled by NW–SE shortening [68,70]. The explanation of such a difference is proposed in the next chapter of the discussion. However, we note that the mineralisation-related veins are oriented perpendicular to the shortening axis direction in both models.
- It is worth noting that the Sheba/Fairview domains have been intensively exploited and are still active, whereas Malolotja/Steynsdorp areas were historically exploited with a minor gold production..

Mineralised systems showing horizontal veins associated with steep mineralised veins have been reported in several cases of gold-bearing quartz veins in Archean greenstone belts, such as the Abitibi (Canada; [87]) or the Norseman-Wiluna (Australia; [88]). Whether this specific geometry typically represents vein systems emplaced within the Archean continental crust cannot be confirmed. Such a point has been discussed by Foster and Piper [89], who clearly make a relationship between gold metallogeny, complex vein systems, and the multiplicity of tectono-thermal events that dominate during the Archean formation of the craton. Examples from the Barberton, Zimbabwe, and Tanzanian cratons have been cited.

The gold occurrences both in Malolotja and Steynsdorp areas are exclusively hosted by the Onverwacht Group rocks (Figures 3 and 7). This fact underlines that they are significantly structurally controlled and most likely linked with fold geometry and formation (see Section 6). In addition, this distribution can be also consistent with the hypothesis of Viljoen et al. [29], suggesting that the mafic to ultramafic rocks of the Onverwacht Group show substantial anomalies and, thus, are good candidates for gold sources.

7.2. Significance of the Deformation Events

The initial stage of our tectono-hydrothermal model, illustrated in Figure 17, is not well constrained by our data. In the Malolotja synform, Lamb [81] and Heubeck et al. [79] propose an early thrust towards the NW, which has been folded afterwards. The De deformation in our model may be related to this thrust event, putting the Onverwacht Group on the Moodies Group (Figure 17a). In the study area, few observations consistent with this early thrusting event have been recorded, with evidence of local reverse shear to the NNW in the hinge zone of the Malolotja synform (Figure 4c). On the contrary, the Se schistosity dips to the north at Steynsdorp. This difference in dip may be due to the doming effect related to the Steynsdorp pluton [38], which can be expressed by the NNE-plunging mineral lineation.

The Df deformation is induced by E–W shortening forming the large-scale Malolotja and Steynsdorp folds. This E–W shortening deformation visible in the southern part of the belt is interpreted as similar to the main and major NW–SE event that affected the closure of the BGB [30] but rotated locally to form the arc geometry of the belt. Indeed, the geometry of the belt and the rotation of the large-scale structures, such as faults and folds, from NE–SW to N–S striking in the south of the belt are in line with this interpretation. Because this fold-related deformation affects the Moodies Group, it probably postdates the main shortening events (i.e., D2 event [30]; Figure 2). Lamb [80] described the Malolotja syncline as D3 folds, and the Df deformation observed in this study probably corresponds to the main D3 NW–SE shortening of the belt suggested by de Ronde and de Wit ([30]; Figure 2).

A NE–SW shortening event has never been reported or described at the scale of the Barberton Greenstone Belt. The regional extent and tectonic significance of this event are therefore enigmatic. De Wit et al. [90] observed km wavelength NW–SE-striking folds to the WSW of the Stolzburg syncline that is compatible with a NE–SW shortening direction. As they refold earlier structures related to the main NW–SE shortening event, they are interpreted as late. Van Kranendonk et al. [91] also documented the existence of a NW–SE-striking, steeply dipping mylonite zone with a down-dip stretching lineation. Because a reverse motion is described, this mylonite zone is, therefore, formed by NE–SW shortening. In their work, Van Kranendonk et al. [91] noted that the mylonitic zone is along strike with the undeformed, NW–SE striking ca. 3107 Ma Kees Zyn Doorns syenite, which is coeval with the vast Mpuluzi batholith (Figure 1; [34]). Static recrystallisation of minerals related to contact metamorphism is also described. This can question a potential link between the late emplacement of the ca. 3.1 Ga batholiths and the formation of the late Dl event. No clear answer can be provided at this stage, but two facts need consideration: (i) the more recrystallised aspect of late quartz veins illustrated in Figure 14h; (ii) the persistence and maybe the increase of tourmaline, K-feldspar, and albite content both within veins and alteration halos of the late quartz vein system.

Two additional arguments can also question the chronological relationships between Dl and Df events although clear overprinting criteria are described (Figure 6i):

- Mineralogically, the two events show similar infilling and alteration halos (Figure 13).
- The mineralised vein system shows the coexistence of N–S and NW–SE-striking steep veins (Figures 10 and 16)—the fact that can be explained by simultaneous actions of Df and Dl events.

Indeed, our evolutionary model takes into account this hypothesis and proposes that earlier effects of the NE–SW shortening direction (Dl) may have occurred during the late stage of the Df deformation (Figure 17b). The final stage would be dominated by the late Dl event in continuity with the achievement of the Df folding (Figure 17c).

The shortening direction of the Df and Dl events are obtained assuming they are coaxial deformations. This suggests a regime of homogeneous strain distribution and geometric preservation. However, it cannot be excluded that the deformation can be partitioned between noncoaxial and coaxial domains as expressed by the feeling that some vein outcrops are associated with top-to-the-west verging (not illustrated here).

7.3. Timing of the Mineralisation Event

Several gold mineralisation ages have been published exclusively in the northern part of the Barberton Greenstone Belt. At Fairview mine, de Ronde et al. [75] dated a porphyry body crosscut by the mineralisation at ca. 3126 Ma (U-Pb zircon), thus representing the oldest age for mineralisation. These authors also dated a hydrothermal rutile that provides a lower bracket at ca. 3084 Ma (U-Pb). Other younger ages have been published at the New Consort mine (Figure 1) by dating a hydrothermal titanite linked to the alteration at 3027 ± 7 Ma (U-Pb [74]). The dating of a felsic dyke interpreted as coeval with the gold mineralisation at Golden Quarry (near Sheba mine) also provides ca. 3015 Ma (U-Pb zircon [71]). Overall, two periods of mineralisation seem to emerge from the literature, the first one at 3126–3084 Ma and a younger one at 3027–3015 Ma. Thus, the ages of the gold mineralisation appear to be spread over a long period of time, suggesting at least two mineralisation episodes and/or that the dating of the mineralisation is not well constrained. The first mineralisation at 3126–3084 Ma is interpreted to be controlled by the late D3 event dated at 3227–3084 Ma by de Ronde and de Wit ([30]; Figure 2), whereas the second one (3027–3015 Ma) maybe post-D3, during the stabilisation of the Kaapvaal Craton estimated around 3.1–2.7 Ga [92].

Regarding the different events proposed in the literature and summarised in Figure 2, an attempt to correlate deformation events and the two episodes of hydrothermal events of our study (Df and Dl) and, consequently, gold formation in the southern part of the BGB is discussed here. No absolute mineralisation dating is available in this part of the belt. In the model proposed in this study, the main mineralisation stage is supposed to be syn to

late Df according to Figure 17. This could be compatible with the D3 event in the de Ronde and de Wit model ([30]; Figure 2) and relatively similar to the ages obtained in the Fairview mine by de Ronde et al. [75]. If accepting the potential continuity between Df and Dl (see the discussion above) and their association with gold-related hydrothermal veins, one can suppose here that gold in the southern part of the BGB can be a long-lived event beginning during the late stage of the main shortening event (D3/Df) and ending, with a lower grade, during Dl.

8. Conclusions

Detailed field structural analysis, associated with the petrological and microstructural study of the southern part of the Barberton Greenstone Belt, straddling the international border between South Africa and Eswatini, allowed for the understanding of the structural control of the numerous quartz veins and the deformation of the host rock. The present study demonstrates that the Onverwacht and Moodies Group rocks in the southern part of the belt experienced three deformation events manifested by the development of deformation structures and associated hydrothermal veins. The first event produced a locally preserved composite foliation Se, which is E–W striking and may be related to a thrusting event. The second event is related to large-scale folding forming the Steynsdorp anticline and Malolotja synform, a N–S-striking axial planar cleavage Sf, coeval to the emplacement of a complex network of gold-related veins in response to E–W shortening. Such E–W shortening is attributed to the main regional NW–SE closure of the BGB. A third deformation event locally overprints all previous structures. It is produced by NE–SW shortening and is also related to late hydrothermal and barren quartz veins. The origin of the NE–SW shortening that formed the late veins is enigmatic. The deformation of the study area and its variations over time formed different hydrothermal vein systems. Vein and their host-rock deformation study in this part of the famous Barberton Greenstone Belt provides a good case study for a better understanding of the tectono-hydrothermal evolution of a portion of the Archean domain.

Author Contributions: conceptualization, L.T., A.C., and J.L.; fieldwork, L.T., A.C., and J.L.; formal analysis, L.T., A.C., and J.L.; investigation, L.T., A.C., and J.L.; microscopy, L.T., A.C., and J.L.; writing—original draft preparation, L.T., A.C., and J.L.; writing—review and editing, L.T., A.C., and J.L.; supervision, A.C. and J.L. All authors have read and agreed to the published version of the manuscript.

Funding: L. Travers was granted an ED GAIA scholarship to work on her doctorate project. The IRP BuCOMO also funded this research.

Data Availability Statement: The data presented in this study are available on request from the corresponding author.

Acknowledgments: This work benefited greatly from the scientific and financial support of Jean-François Moyen and the IRP BuCOMO (https://bucomo.fr/ accessed on 29 July 2023). Christoph Heubeck and Andrea Els are particularly acknowledged for their strong support and significant help during all our field trips in the Barberton area. Barberton Adventure, Astrid Christianson, Johan Eksteen (Mpumalanga Tourism & Parks Agency), Cornelius Mashaba, Teddy Dlamini (and their team from the Malolotja Nature Reserve) and Thomas Moinet are acknowledged for their assistance in the field.

Conflicts of Interest: The authors declare no conflict of interest.

References

1. Belousova, E.A.; Kostitsyn, Y.A.; Griffin, W.L.; Begg, G.C.; O'Reilly, S.Y.; Pearson, N.J. The Growth of the Continental Crust: Constraints from Zircon Hf-Isotope Data. *Lithos* **2010**, *119*, 457–466. https://doi.org/10.1016/j.lithos.2010.07.024.

2. Herzberg, C.; Condie, K.; Korenaga, J. Thermal History of the Earth and Its Petrological Expression. *Earth Planet. Sci. Lett.* **2010**, *292*, 79–88. https://doi.org/10.1016/j.epsl.2010.01.022.
3. Nisbet, E.G.; Cheadle, M.J.; Arndt, N.T.; Bickle, M.J. Constraining the Potential Temperature of the Archaean Mantle: A Review of the Evidence from Komatiites. *Lithos* **1993**, *30*, 291–307. https://doi.org/10.1016/0024-4937(93)90042-B.
4. Martin, H. Chapter 6 The Archean Grey Gneisses and the Genesis of Continental Crust. In *Developments in Precambrian Geology*; Elsevier: Amsterdam, The Netherlands, 1994; Volume 11, pp. 205–259, ISBN 978-0-444-81621-4.
5. Condie, K.C. *Archean Greenstone Belts*; Elsevier: Amsterdam, The Netherlands, 1981; ISBN 978-0-08-086902-5.
6. Gorman, B.E.; Pearce, T.H.; Birkett, T.C. On the Structure of Archean Greenstone Belts. *Precambrian Res.* **1978**, *6*, 23–41. https://doi.org/10.1016/0301-9268(78)90053-0.
7. van Hunen, J.; Moyen, J.-F. Archean Subduction: Fact or Fiction? *Annu. Rev. Earth Planet. Sci.* **2012**, *40*, 195–219. https://doi.org/10.1146/annurev-earth-042711-105255.
8. Gapais, D. Tectonics-Mineralisation Relationships within Weak Continental Lithospheres: A New Structural Framework for Precambrian Cratons. *BSGF-Earth Sci. Bull.* **2018**, *189*, 14. https://doi.org/10.1051/bsgf/2018014.
9. Barley, M.E.; Groves, D.I. Supercontinent Cycles and the Distribution of Metal Deposits through Time. *Geology* **1992**, *20*, 291. https://doi.org/10.1130/0091-7613(1992)020<0291:SCATDO>2.3.CO;2.
10. Goldfarb, R.J.; Groves, D.I.; Gardoll, S. Orogenic Gold and Geologic Time: A Global Synthesis. *Ore Geol. Rev.* **2001**, *18*, 1–75. https://doi.org/10.1016/S0169-1368(01)00016-6.
11. Groves, D.I.; Vielreicher, R.M.; Goldfarb, R.J.; Condie, K.C. Controls on the Heterogeneous Distribution of Mineral Deposits through Time. *Geol. Soc. Lond. Spec. Publ.* **2005**, *248*, 71–101. https://doi.org/10.1144/GSL.SP.2005.248.01.04.
12. Boullier, A.-M.; Robert, F. Palaeoseismic Events Recorded in Archaean Gold-Quartz Vein Networks, Val d'Or, Abitibi, Quebec, Canada. *J. Struct. Geol.* **1992**, *14*, 161–179. https://doi.org/10.1016/0191-8141(92)90054-Z.
13. Anhaeusser, C.R. The Geology and Tectonic Evolution of the Northwest Part of the Barberton Greenstone Belt, South Africa: A Review. *S. Afr. J. Geol.* **2019**, *122*, 421–454. https://doi.org/10.25131/sajg.122.0033.
14. Ward, J.H.W. *(map compiler)* Metallogenic Map of the Barberton Greenstone Belt, South Africa and Swaziland. 1:100000, Council for Geoscience, Pretoria, South Africa, 2000.
15. Pearton, T.; Viljoen, M. Gold on the Kaapvaal Craton, Outside the Witwatersrand Basin, South Africa. *S. Afr. J. Geol.* **2017**, *120*, 101–132. https://doi.org/10.25131/gssajg.120.1.101.
16. Anhaeusser, C.R. Archean Metallogeny in Southern Africa. *Econ. Geol.* **1976**, *71*, 16–43. https://doi.org/10.2113/gsecongeo.71.1.16.
17. Agangi, A.; Hofmann, A.; Przybyłowicz, W. Trace Element Zoning of Sulfides and Quartz at Sheba and Fairview Gold Mines: Clues to Mesoarchean Mineralisation in the Barberton Greenstone Belt, South Africa. *Ore Geol. Rev.* **2014**, *56*, 94–114. https://doi.org/10.1016/j.oregeorev.2013.08.016.
18. Altigani, M.A.H. Insights on Mineralogy and Chemistry of Fairview Gold Mine, Barberton Greenstone Belt, South Africa. *Indones. J. Geosci.* **2021**, *8*, 73–99. https://doi.org/10.17014/ijog.8.1.73-99.
19. Dirks, P.H.G.M.; Charlesworth, E.G.; Munyai, M.R. Cratonic Extension and Archaen Gold Mineralisation in the Sheba-Fairview Mine, Barberton Greenstone Belt, South Africa. *S. Afr. J. Geol.* **2009**, *112*, 291–316. https://doi.org/10.2113/gssajg.112.3-4.291.
20. Dziggel, A.; Otto, A.; Kisters, A.F.M.; Meyer, F.M. Chapter 5.8 Tectono-Metamorphic Controls on Archean Gold Mineralization in the Barberton Greenstone Belt, South Africa: An Example from the New Consort Gold Mine. In *Developments in Precambrian Geology*; Elsevier: Amsterdam, The Netherlands, 2007; Volume 15, pp. 699–727, ISBN 978-0-444-52810-0.
21. Gloyn-Jones, J.; Kisters, A. Ore-Shoot Formation in the Main Reef Complex of the Fairview Mine—Multiphase Gold Mineralization during Regional Folding, Barberton Greenstone Belt, South Africa. *Miner. Depos.* **2019**, *54*, 1157–1178. https://doi.org/10.1007/s00126-019-00865-9.
22. Munyai, M.R.; Dirks, P.H.G.M.; Charlesworth, E.G. Archaean Gold Mineralisation during Post-Orogenic Extension in the New Consort Gold Mine, Barberton Greenstone Belt, South Africa. *S. Afr. J. Geol.* **2011**, *114*, 121–144. https://doi.org/10.2113/gssajg.114.2.121.
23. Otto, A.; Dziggel, A.; Kisters, A.F.M.; Meyer, F.M. The New Consort Gold Mine, Barberton Greenstone Belt, South Africa: Orogenic Gold Mineralization in a Condensed Metamorphic Profile. *Miner. Depos.* **2007**, *42*, 715–735. https://doi.org/10.1007/s00126-007-0135-5.
24. Jackson, M.P.A.; Eriksson, K.A.; Harris, C.W. Early Archean Foredeep Sedimentation Related to Crustal Shortening: A Reinterpretation of the Barberton Sequence, Southern Africa. *Tectonophysics* **1987**, *136*, 197–221. https://doi.org/10.1016/0040-1951(87)90025-4.
25. Lowe, D.R.; Byerly, G.R. Ironstone Bodies of the Barberton Greenstone Belt, South Africa: Products of a Cenozoic Hydrological System, Not Archean Hydrothermal Vents! *Geol. Soc. Am. Bull.* **2007**, *119*, 65–87. https://doi.org/10.1130/B25997.1.
26. Byerly, G.R.; Kröner, A.; Lowe, D.R.; Todt, W.; Walsh, M.M. Prolonged Magmatism and Time Constraints for Sediment Deposition in the Early Archean Barberton Greenstone Belt: Evidence from the Upper Onverwacht and Fig Tree Groups. *Precambrian Res.* **1996**, *78*, 125–138. https://doi.org/10.1016/0301-9268(95)00073-9.
27. Kröner, A.; Hegner, E.; Wendt, J.I.; Byerly, G.R. The Oldest Part of the Barberton Granitoid-Greenstone Terrain, South Africa: Evidence for Crust Formation between 3.5 and 3.7 Ga. *Precambrian Res.* **1996**, *78*, 105–124. https://doi.org/10.1016/0301-9268(95)00072-0.
28. Poujol, M.; Robb, L.J.; Anhaeusser, C.R.; Gericke, B. A Review of the Geochronological Constraints on the Evolution of the Kaapvaal Craton, South Africa. *Precambrian Res.* **2003**, *127*, 181–213. https://doi.org/10.1016/S0301-9268(03)00187-6.
29. Viljoen, R.P.; Saager, R.; Viljoen, M.J. Metallogenesis and Ore Control in the Steynsdorp Goldfield, Barberton Mountain Land, South Africa. *Econ. Geol.* **1969**, *64*, 778–797. https://doi.org/10.2113/gsecongeo.64.7.778.
30. de Ronde, C.E.J.; de Wit, M.J. Tectonic History of the Barberton Greenstone Belt, South Africa: 490 Million Years of Archean Crustal Evolution. *Tectonics* **1994**, *13*, 983–1005. https://doi.org/10.1029/94TC00353.
31. Hofmann, A. The Geochemistry of Sedimentary Rocks from the Fig Tree Group, Barberton Greenstone Belt: Implications for Tectonic, Hydrothermal and Surface Processes during Mid-Archaean Times. *Precambrian Res.* **2005**, *143*, 23–49. https://doi.org/10.1016/j.precamres.2005.09.005.
32. Drabon, N.; Heubeck, C.E.; Lowe, D.R. Evolution of an Archean Fan Delta and Its Implications for the Initiation of Uplift and Deformation in the Barberton Greenstone Belt, South Africa. *J. Sediment. Res.* **2019**, *89*, 849–874. https://doi.org/10.2110/jsr.2019.46.

33. Heubeck, C.; Lowe, D.R. Depositional and Tectonic Setting of the Archean Moodies Group, Barberton Greenstone Belt, South Africa. *Precambrian Res.* **1994**, *68*, 257–290. https://doi.org/10.1016/0301-9268(94)90033-7.
34. Kamo, S.L.; Davis, D.W. Reassessment of Archean Crustal Development in the Barberton Mountain Land, South Africa, Based on U-Pb Dating. *Tectonics* **1994**, *13*, 167–192. https://doi.org/10.1029/93TC02254.
35. Heubeck, C.; Lowe, D.R. Late Syndepositional Deformation and Detachment Tectonics in the Barberton Greenstone Belt, South Africa. *Tectonics* **1994**, *13*, 1514–1536. https://doi.org/10.1029/94TC01809.
36. de Wit, M.J.; de Ronde, C.E.J.; Tredoux, M.; Roering, C.; Hart, R.J.; Armstrong, R.A.; Green, R.W.E.; Peberdy, E.; Hart, R.A. Formation of an Archaean Continent. *Nature* **1992**, *357*, 553–562. https://doi.org/10.1038/357553a0.
37. Stevens, G.; Moyen, J.-F. Chapter 5.7 Metamorphism in the Barberton Granite Greenstone Terrain: A Record of Paleoarchean Accretion. In *Developments in Precambrian Geology*; Elsevier: Amsterdam, The Netherlands, 2007; Volume 15, pp. 669–698, ISBN 978-0-444-52810-0.
38. Kisters, A.F.M.; Anhaeusser, C.R. The Structural Significance of the Steynsdorp Pluton and Anticline within the Tectonomagmatic Framework of the Barberton Mountain Land. *S. Afr. J. Geol.* **1995**, *98*, 43–51.
39. Moyen, J.-F.; Stevens, G.; Kisters, A.F.M.; Belcher, R.W. Chapter 5.6 TTG Plutons of the Barberton Granitoid-Greenstone Terrain, South Africa. In *Developments in Precambrian Geology*; Elsevier: Amsterdam, The Netherlands, 2007; Volume 15, pp. 607–667, ISBN 978-0-444-52810-0.
40. Moyen, J.-F.; Stevens, G.; Kisters, A.F.M.; Belcher, R.W.; Lemirre, B. TTG Plutons of the Barberton Granitoid-Greenstone Terrain, South Africa. In *Earth's Oldest Rocks*; Elsevier: Amsterdam, The Netherlands, 2019; pp. 615–653, ISBN 978-0-444-63901-1.
41. Kisters, A.F.M.; Belcher, R.W.; Poujol, M.; Dziggel, A. Continental Growth and Convergence-Related Arc Plutonism in the Mesoarchaean: Evidence from the Barberton Granitoid-Greenstone Terrain, South Africa. *Precambrian Res.* **2010**, *178*, 15–26. https://doi.org/10.1016/j.precamres.2010.01.002.
42. de Ronde, C.E.J.; Kamo, S.L. An Archean Arc-Arc Collisional Event: A Short-Lived (ca 3 Myr) Episode, Weltevreden Area, Barberton Greenstone Belt, South Africa. *J. Afr. Earth Sci.* **2000**, *30*, 219–248. https://doi.org/10.1016/S0899-5362(00)00017-8.
43. Robb, L.J.; Brandl, G.; Anhaeusser, C.R.; Poujol, M.; Johnson, M.R.; Thomas, R.J. Archaean Granitoid Intrusions. In *The Geology of South Africa*; Geological Society of South Africa/Council for Geoscience, Johannesburg/Pretoria, South Africa 2006; pp. 57–94.
44. Kisters, A.F.M.; Stevens, G.; Dziggel, A.; Armstrong, R.A. Extensional Detachment Faulting and Core-Complex Formation in the Southern Barberton Granite–Greenstone Terrain, South Africa: Evidence for a 3.2 Ga Orogenic Collapse. *Precambrian Res.* **2003**, *127*, 355–378. https://doi.org/10.1016/j.precamres.2003.08.002.
45. Schoene, B.; Bowring, S.A. Determining Accurate Temperature–Time Paths from U–Pb Thermochronology: An Example from the Kaapvaal Craton, Southern Africa. *Geochim. Cosmochim. Acta* **2007**, *71*, 165–185. https://doi.org/10.1016/j.gca.2006.08.029.
46. Moyen, J.-F.; Zeh, A.; Cuney, M.; Dziggel, A.; Carrouée, S. The Multiple Ways of Recycling Archaean Crust: A Case Study from the ca. 3.1 Ga Granitoids from the Barberton Greenstone Belt, South Africa. *Precambrian Res.* **2021**, *353*, 105998. https://doi.org/10.1016/j.precamres.2020.105998.
47. Anhaeusser, C.R.; Robb, L.J.; Barton, J.M.J. Mineralogy, Petrology and Origin of the Boesmanskop Syeno-Granite Complex, Barberton Mountain Land, South Africa. *Spec. Publ.-Geol. Soc. S. Afr.* **1983**, 9, 169–183.
48. Grosch, E.G.; Vidal, O.; Abu-Alam, T.; McLoughlin, N. P-T Constraints on the Metamorphic Evolution of the Paleoarchean Kromberg Type-Section, Barberton Greenstone Belt, South Africa. *J. Pet.* **2012**, *53*, 513–545. https://doi.org/10.1093/petrology/egr070.
49. Tice, M.M.; Bostick, B.C.; Lowe, D.R. Thermal History of the 3.5–3.2 Ga Onverwacht and Fig Tree Groups, Barberton Greenstone Belt, South Africa, Inferred by Raman Microspectroscopy of Carbonaceous Material. *Geology* **2004**, *32*, 37. https://doi.org/10.1130/G19915.1.
50. Cutts, K.A.; Stevens, G.; Hoffmann, J.E.; Buick, I.S.; Frei, D.; Munker, C. Paleo- to Mesoarchean Polymetamorphism in the Barberton Granite-Greenstone Belt, South Africa: Constraints from U-Pb Monazite and Lu-Hf Garnet Geochronology on the Tectonic Processes That Shaped the Belt. *Geol. Soc. Am. Bull.* **2014**, *126*, 251–270. https://doi.org/10.1130/B30807.1.
51. Diener, J.F.A.; Stevens, G.; Kisters, A.F.M.; Poujol, M. Metamorphism and Exhumation of the Basal Parts of the Barberton Greenstone Belt, South Africa: Constraining the Rates of Mesoarchaean Tectonism. *Precambrian Res.* **2005**, *143*, 87–112. https://doi.org/10.1016/j.precamres.2005.10.001.
52. Moyen, J.-F.; Stevens, G.; Kisters, A. Record of Mid-Archaean Subduction from Metamorphism in the Barberton Terrain, South Africa. *Nature* **2006**, *442*, 559–562. https://doi.org/10.1038/nature04972.
53. Dziggel, A.; Knipfer, S.; Kisters, A.F.M.; Meyer, F.M. P-T and Structural Evolution during Exhumation of High-T, Medium-P Basement Rocks in the Barberton Mountain Land, South Africa: Metamorphic Evolution, Barberton Mountain Land. *J. Metamorph. Geol.* **2006**, *24*, 535–551. https://doi.org/10.1111/j.1525-1314.2006.00653.x.
54. Dziggel, A.; Stevens, G.; Poujol, M.; Anhaeusser, C.R.; Armstrong, R.A. Metamorphism of the Granite–Greenstone Terrane South of the Barberton Greenstone Belt, South Africa: An Insight into the Tectono-Thermal Evolution of the 'Lower' Portions of the Onverwacht Group. *Precambrian Res.* **2002**, *114*, 221–247. https://doi.org/10.1016/S0301-9268(01)00225-X.
55. Lowe, D.R.; Byerly, G.R.; Heubeck, C. Structural Divisions and Development of the West-Central Part of the Barberton Greenstone Belt. In *Geologic Evolution of the Barberton Greenstone Belt, South Africa*; Lowe, D.R., Byerly, G.R., Eds.; Geological Society of America: New York, United States, 1999; Volume 329, ISBN 978-0-8137-2329-7.
56. Ramsay, J.G. Structural Investigations in the Barberton Mountian Land, Eastern Transvaal. *South Afr. J. Geol.* **1963**, *66*, 353–401.
57. Van Kranendonk, M.J. Gliding and Overthrust Nappe Tectonics of the Barberton Greenstone Belt Revisited: A Review of Deformation Styles and Processes. *S. Afr. J. Geol.* **2021**, *124*, 181–210. https://doi.org/10.25131/sajg.124.0017.
58. Anhaeusser, C.R. The Evolution of the Early Precambrian Crust of Southern Africa. *Philos. Trans. R. Soc. Lond.* **1973**, *273*, 359–388.
59. Hoffmann, J.E.; Kröner, A.; Hegner, E.; Viehmann, S.; Xie, H.; Iaccheri, L.M.; Schneider, K.P.; Hofmann, A.; Wong, J.; Geng, H.; et al. Source Composition, Fractional Crystallization and Magma Mixing Processes in the 3.48–3.43 Ga Tsawela Tonalite Suite (Ancient

Gneiss Complex, Swaziland)—Implications for Palaeoarchaean Geodynamics. *Precambrian Res.* **2016**, *276*, 43–66. https://doi.org/10.1016/j.precamres.2016.01.026.
60. Lowe, D.R. Accretionary History of the Archean Barberton Greenstone Belt (3.55–3.22 Ga), Southern Africa. *Geology* **1994**, *22*, 1099. https://doi.org/10.1130/0091-7613(1994)022<1099:AHOTAB>2.3.CO;2.
61. Armstrong, R.A.; Compston, W.; de Wit, M.J.; Williams, I.S. The Stratigraphy of the 3.5–3.2 Ga Barberton Greenstone Belt Revisited: A Single Zircon Ion Microprobe Study. *Earth Planet. Sci. Lett.* **1990**, *101*, 90–106. https://doi.org/10.1016/0012-821X(90)90127-J.
62. Kohler, E.A.; Anhaeusser, C.R. Geology and Geodynamic Setting of Archaean Silicic Metavolcaniclastic Rocks of the Bien Venue Formation, Fig Tree Group, Northeast Barberton Greenstone Belt, South Africa. *Precambrian Res.* **2002**, *116*, 199–235. https://doi.org/10.1016/S0301-9268(02)00021-9.
63. Van Kranendonk, M.J.; Kröner, A.; Hegner, E.; Connelly, J. Age, Lithology and Structural Evolution of the c. 3.53 Ga Theespruit Formation in the Tjakastad Area, Southwestern Barberton Greenstone Belt, South Africa, with Implications for Archaean Tectonics. *Chem. Geol.* **2009**, *261*, 115–139. https://doi.org/10.1016/j.chemgeo.2008.11.006.
64. Drabon, N.; Lowe, D.R. Progressive Accretion Recorded in Sedimentary Rocks of the 3.28–3.23 Ga Fig Tree Group, Barberton Greenstone Belt. *GSA Bull.* **2021**, *134*, 1258–1276. https://doi.org/10.1130/B35973.1.
65. Lana, C.; Buick, I.; Stevens, G.; Rossouw, R.; De Wet, W. 3230–3200 Ma Post-Orogenic Extension and Mid-Crustal Magmatism along the Southeastern Margin of the Barberton Greenstone Belt, South Africa. *J. Struct. Geol.* **2011**, *33*, 844–858. https://doi.org/10.1016/j.jsg.2011.03.007.
66. Cerda, L.R.P.; Jones, C.; Kisters, A. The Effects of Fault-Zone Architecture, Wall-Rock Competence and Fluid Pressure Variations on Hydrothermal Veining and Gold Mineralization along the Sheba Fault, Barberton Greenstone Belt, South Africa. *J. Afr. Earth Sci.* **2022**, *192*, 104554. https://doi.org/10.1016/j.jafrearsci.2022.104554.
67. Agangi, A.; Hofmann, A.; Eickmann, B.; Marin-Carbonne, J. Mesoarchaean Gold Mineralisation in the Barberton Greenstone Belt: A Review. In *The Archaean Geology of the Kaapvaal Craton, Southern Africa*; Kröner, A., Hofmann, A., Eds.; Regional Geology Reviews; Springer International Publishing: Cham, Switzerland, 2019; pp. 171–184, ISBN 978-3-319-78651-3.
68. Gloyn-Jones, J.; Kisters, A. Regional Folding, Low-Angle Thrusting and Permeability Networks: Structural Controls of Gold Mineralization in the Hope Reef at Fairview Mine, Barberton Greenstone Belt, South Africa. *Ore Geol. Rev.* **2018**, *102*, 585–603. https://doi.org/10.1016/j.oregeorev.2018.09.024.
69. de Ronde, C.E.J.; Spooner, E.T.C.; de Wit, M.J.; Bray, C.J. Shear Zone-Related, Au Quartz Vein Deposits in the Barberton Greenstone Belt, South Africa; Field and Petrographic Characteristics, Fluid Properties, and Light Stable Isotope Geochemistry. *Econ. Geol.* **1992**, *87*, 366–402. https://doi.org/10.2113/gsecongeo.87.2.366.
70. Jones, C.; Kisters, A. Regional and Local Controls of Hydrothermal Fluid Flow and Gold Mineralization in the Sheba and Fairview Mines, Barberton Greenstone Belt, South Africa. *Ore Geol. Rev.* **2022**, *144*, 104805. https://doi.org/10.1016/j.oregeorev.2022.104805.
71. Dirks, P.H.G.M.; Charlesworth, E.G.; Munyai, M.R.; Wormald, R. Stress Analysis, Post-Orogenic Extension and 3.01Ga Gold Mineralisation in the Barberton Greenstone Belt, South Africa. *Precambrian Res.* **2013**, *226*, 157–184. https://doi.org/10.1016/j.precamres.2012.12.007.
72. Anhaeusser, C.R. The Geology of the Jamestown Hills Area of the Barberton Mountain Land, South Africa. *S. Afr. J. Geol.* **1972**, *75*, 225–263.
73. Viljoen, M.J. The Geology of the Lily Syncline and Portion of the Eureka Syncline Between the Consort Mine and Joe's Luck Siding, Barberton Mountain Land. Master's Thesis, University of the Witwatersrand, Johannesburg, South Africa, 1963.
74. Dziggel, A.; Poujol, M.; Otto, A.; Kisters, A.F.M.; Trieloff, M.; Schwarz, W.H.; Meyer, F.M. New U–Pb and 40Ar/39Ar Ages from the Northern Margin of the Barberton Greenstone Belt, South Africa: Implications for the Formation of Mesoarchaean Gold Deposits. *Precambrian Res.* **2010**, *179*, 206–220. https://doi.org/10.1016/j.precamres.2010.03.006.
75. de Ronde, C.E.J.; Kamo, S.; Davis, D.W.; De Wit, M.J.; Spooner, E.T.C. Field, Geochemical and U-Pb Isotopic Constraints from Hypabyssal Felsic Intrusions within the Barberton Greenstone Belt, South Africa: Implications for Tectonics and the Timing of Gold Mineralization. *Precambrian Res.* **1991**, *49*, 261–280. https://doi.org/10.1016/0301-9268(91)90037-B.
76. Furnes, H.; de Wit, M.; Robins, B. A Review of New Interpretations of the Tectonostratigraphy, Geochemistry and Evolution of the Onverwacht Suite, Barberton Greenstone Belt, South Africa. *Gondwana Res.* **2013**, *23*, 403–428. https://doi.org/10.1016/j.gr.2012.05.007.
77. Lana, C.; Kisters, A.; Stevens, G. Exhumation of Mesoarchean TTG Gneisses from the Middle Crust: Insights from the Steynsdorp Core Complex, Barberton Granitoid-Greenstone Terrain, South Africa. *Geol. Soc. Am. Bull.* **2010**, *122*, 183–197. https://doi.org/10.1130/B26580.1.
78. Lana, C.; Tohver, E.; Cawood, P. Quantifying Rates of Dome-and-Keel Formation in the Barberton Granitoid-Greenstone Belt, South Africa. *Precambrian Res.* **2010**, *177*, 199–211. https://doi.org/10.1016/j.precamres.2009.12.001.
79. Heubeck, C.; Thomsen, T.B.; Heredia, B.D.; Zeh, A.; Balling, P. The Malolotsha Klippe: Large-Scale Subhorizontal Tectonics Along the Southern Margin of the Archean Barberton Greenstone Belt, Eswatini. *Tectonics* **2023**, *42*, e2022TC007359. https://doi.org/10.1029/2022TC007359.
80. Lamb, S. Archean Synsedimentary Tectonic Deformation—A Comparison with the Quaternary. *Geology* **1987**, *15*, 565. https://doi.org/10.1130/0091-7613(1987)15<565:ASTDCW>2.0.CO;2.
81. Lamb, S.H. Structures on the Eastern Margin of the Archaean Barberton Greenstone Belt, Northwest Swaziland. In *Precambrian Tectonics Illustrated*; E. Schweizerbart'sche: Stuttgart, Germany, 1984; pp. 19–39.
82. Anhaeusser, C.R. Archaean Gold Mineralization in the Baberton Mountain Land. *Miner. Depos. South. Afr.* **1986**, *I&II*, 113–154.
83. Whitney, D.L.; Evans, B.W. Abbreviations for Names of Rock-Forming Minerals. *Am. Mineral.* **2010**, *95*, 185–187. https://doi.org/10.2138/am.2010.3371.
84. Lamb, S.; Paris, I. Post-Onverwacht Group Stratigraphy in the SE Part of the Archaean Barbeton Greenstone Belt. *J. Afr. Earth Sci.* **1988**, *7*, 285–306. https://doi.org/10.1016/0899-5362(88)90074-7.
85. Cerda, L.R.P.; Jones, C.; Kisters, A. Multi-Stage Alteration, Rheological Switches and High-Grade Gold Mineralization at Sheba Mine, Barberton Greenstone Belt, South Africa. *Ore Geol. Rev.* **2020**, *127*, 103852. https://doi.org/10.1016/j.oregeorev.2020.103852.
86. Sibson, R.H. Earthquake Faulting as a Structural Process. *J. Struct. Geol.* **1989**, *11*, 1–14. https://doi.org/10.1016/0191-8141(89)90032-1.

87. Robert, F.; Boullier, A.-M.; Firdaous, K. Gold-Quartz Veins in Metamorphic Terranes and Their Bearing on the Role of Fluids in Faulting. *J. Geophys. Res.* **1995**, *100*, 12861–12879. https://doi.org/10.1029/95JB00190.
88. Nguyen, P.T.; Harris, L.B.; Powell, C.M.; Cox, S.F. Fault-Valve Behaviour in Optimally Oriented Shear Zones: An Example at the Revenge Gold Mine, Kambalda, Western Australia. *J. Struct. Geol.* **1998**, *20*, 1625–1640. https://doi.org/10.1016/S0191-8141(98)00054-6.
89. Foster, R.P.; Piper, D.P. Archaean Lode Gold Deposits in Africa: Crustal Setting, Metallogenesis and Cratonization. *Ore Geol. Rev.* **1993**, *8*, 303–347. https://doi.org/10.1016/0169-1368(93)90021-P.
90. de Wit, M.J.; Fripp, R.E.P.; Stanistreet, I.G. Tectonic, and Stratigraphic Implications of New Field Observations along the Southern Part of the Barberton Greenstone Belt. *Spec. Publ.-Geol. Soc. S. Afr.* **1983**, 9, 21–29.
91. Van Kranendonk, M.J.; Kröner, A.; Hoffmann, J.E.; Nagel, T.; Anhaeusser, C.R. Just Another Drip: Re-Analysis of a Proposed Mesoarchean Suture from the Barberton Mountain Land, South Africa. *Precambrian Res.* **2014**, *254*, 19–35. https://doi.org/10.1016/j.precamres.2014.07.022.
92. Schoene, B.; Dudas, F.O.L.; Bowring, S.A.; de Wit, M. Sm-Nd Isotopic Mapping of Lithospheric Growth and Stabilization in the Eastern Kaapvaal Craton. *Terra Nova* **2009**, *21*, 219–228. https://doi.org/10.1111/j.1365-3121.2009.00877.

Chapter V: Northern Gold Provinces

The spatial analysis *(Chapter III)* has revealed two clusters of gold occurrences in the northern part of the BGB, bounded to the south by the Inyoka, Saddleback, and Barbrook faults (Fig. III.15). One of these clusters, situated in proximity to the Barbrook fault zone near the Shiyalongubo dam, will be designated here as the Shiyalongubo area. The other cluster forms an east-convex crescent-shaped map pattern around the town of Barberton, rimming the margin of the Kaap Valley pluton.

The Shiyalongubo area cluster encompasses over 15 gold occurrences, which are mainly historical gold mines. On the other hand, the cluster around the town of Barberton hosts more than 90 gold occurrences and four active mines: Agnes, Sheba, Fairview, and New Consort. All occurrences in these two clusters are predominantly concentrated within shear zones and veins, and a smaller portion is present in the form of stockwork. The gold occurrences and deposits of the Barberton cluster are mostly located along the Sheba fault and in the inner and outer arcs of the Eureka and Ulundi large-scale synclines, respectively (Fig. V.1).

The gold occurrence cluster encompassing the town of Barberton covers a wide area (i.e., over 240 km^2) with a heterogeneous spatial distribution of occurrences and deposits (Figs. III.13 and III.14) and has therefore been categorised into multiple distinct zones (Fig. V.1).

- Toward the western part of the Barberton cluster a multitude of gold occurrences and the active Agnes Mine are located near the Moodies and Sheba fault network. In this zone, the orientation of faults and folds is ENE-WSW, the area has been labelled as the Agnes sector. The striking direction of the gold mineralised structures seems parallel to the main structures in this area, i.e., approximately ENE-WSW striking.
- Further to the southeast, a former gold mine known as Svengali classified as a stockwork in the metallogenic map occurs and, because it is spatially disconnected with the other zones, it forms a sector on its own, the Svengali sector.
- In the vicinity of Barberton, the orientation of folds and faults varies from ENE-WSW to the SW to NE-SW-striking to the NE and hosts several gold occurrences. This region will be identified as the Barberton sector. Note that the orientation of the gold-hosting

structures rotates in agreement with the rotation of the folds and faults in the host rocks and are roughly NE-SW striking.

- Lastly, within the area characterised by the re-folding of the Eureka and Ulundi synclines, a zone containing substantial deposits is identified; it is termed the Sheba-Fairview sector. Two directions of mineralised structures have been identified, a first parallel to the main folded structures, and a second one, oblique, NW-SE to NNW-SSE striking.

The Fairview, Sheba and New Consort deposits within the northern part of the belt, are currently operational and have received extensive scientific research attention and abundant literature (Dziggel et al., 2007; Otto et al., 2007; Dirks et al., 2009; Munyai et al., 2011; Agangi et al., 2014; Gloyn-Jones and Kisters, 2018; Altigani, 2021). However, a significant number of gold occurrences and deposits situated in this region have not been thoroughly investigated, those mentioned in this chapter have been indicated in bold in the map of Figure V.1. This chapter aims to bridge this gap by studying the structural framework of most of the gold-related quartz veins in the northern gold provinces of the Barberton Greenstone Belt.

V.A. Regional Deformation

V.A.1. Bedding

The northern part of the Barberton Greenstone Belt is revealing the bedding of the three main stratigraphic groups, visible by clear compositional layering. In the Agnes sector, bedding generally strikes in the NE-SW direction and is sub-vertical (Fig. V.1, stereonet with the black poles in the Agnes sector). In the vicinity of the Svengali pit, the bedding is NE-SW to ENE-WSW striking and steeply dipping SE to SSE. Surprisingly, the Barberton area deviates from the NE-SW striking pattern, as its bedding orientation is NW-SE striking, possibly indicative of an over-representation of bedding measurements in a hinge unlike the other measurements that appear to correspond with limbs. In the Shiyalongubo area, bedding is approximately NE-SW striking and steeply dipping NW.

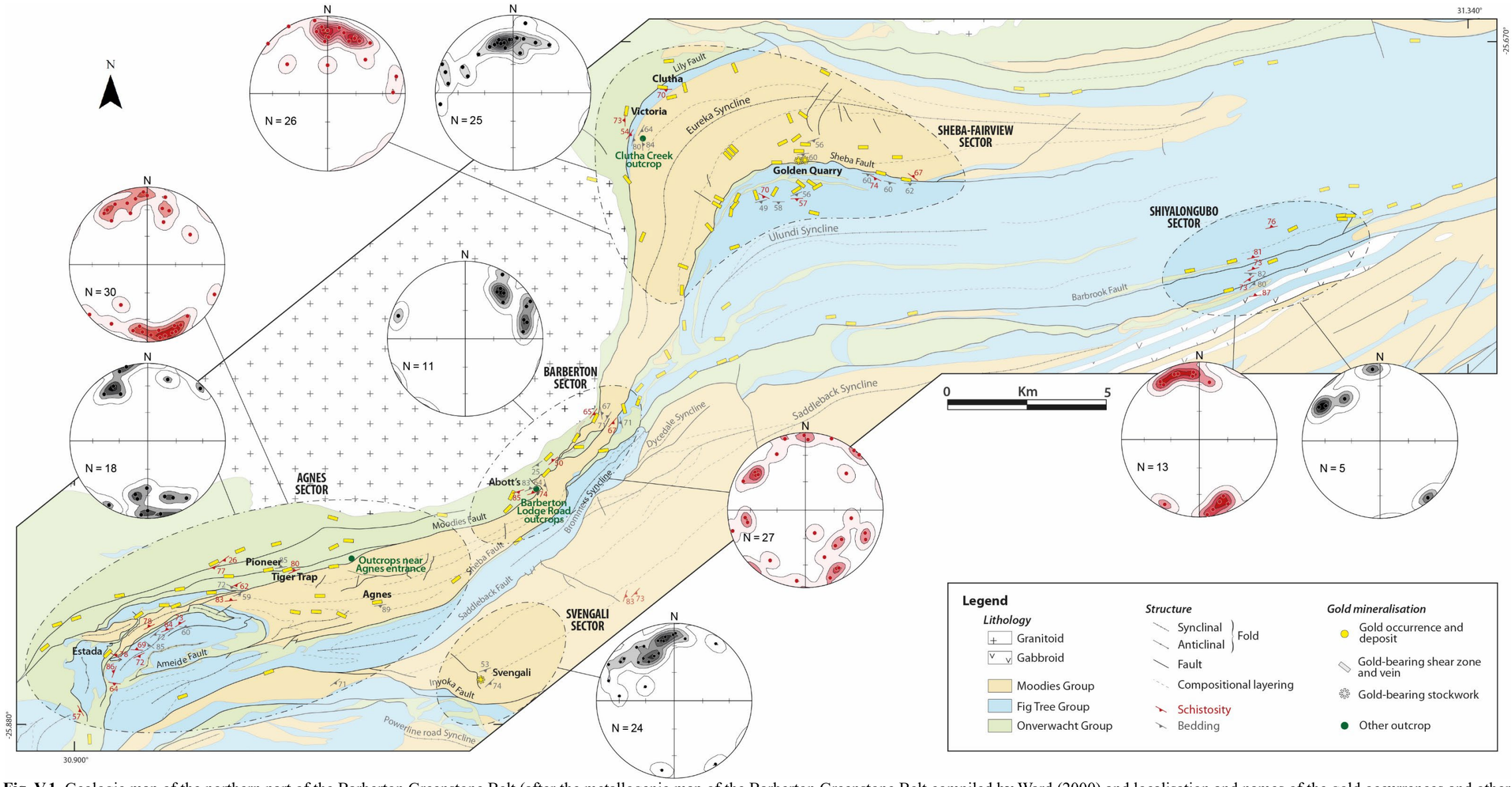

Fig. V.1. Geologic map of the northern part of the Barberton Greenstone Belt (after the metallogenic map of the Barberton Greenstone Belt compiled by Ward (2000) and localisation and names of the gold occurrences and other studied outcrops. Stereonets (lower-hemisphere equal area) in pole-to-plane of the bedding (black poles) and schistosity (red poles) are indicated for each sector herein defined.

Into the Sheba-Fairview sector, the bedding is clearly folded, which is visible by the km-wide large arcuate shape of this sector, characterised by a axial plane striking NW-SE (Fig. V.1). Globally the bedding is ENE-WSW striking and dipping NNW in the overall area (Fig. V.2a).

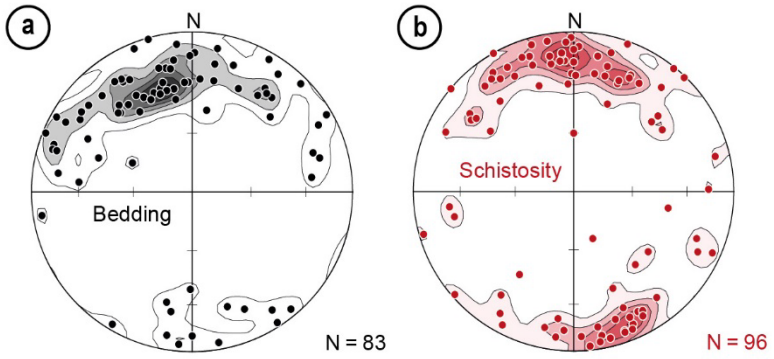

Fig. V.2. Stereonets of all the bedding and schistosity measurements in the northern part of the BGB **(a)** shows bedding plane density distribution and **(b)** shows schistosity density. Both are represented in poles to planes, Schmidt diagram, lower hemisphere.

V.A.2. Main Folds

The northern portion of the Barberton Greenstone Belt displays km-scale (e.g., Ulundi, Eureka, Saddleback, Dycedale, Brommers synclines; Figs. V.1 and V.3) and cm to m-scales folds (Fig. V.4). Folding is particularly pronounced in the shales and Banded Iron Formation (BIF) rocks of the Fig Tree Group (Fig. V.4a,b). The axial planes of these folds predominantly strike NE-SW to E-W (Fig. V.4c).

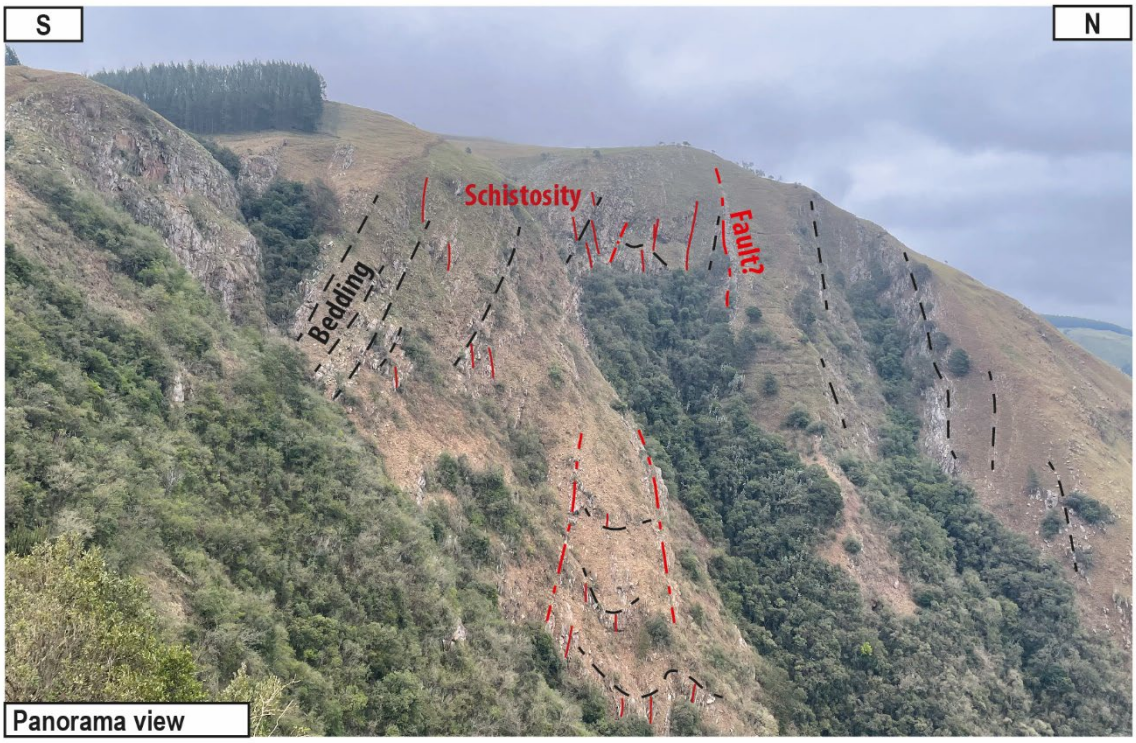

Fig. V.3. Panoramic view to the west of Mount Morgan, illustrating the large-scale folding of the northern part of the Barberton Greenstone Belt.

Within the Sheba-Fairview region, the presence of local non-cylindrical folds in Fig Tree Group cherts, characterised by axes that range from steep to shallow plunging (Fig. V.4d,e), has been identified. The non-cylindricity is observed on a scale of 10 metres and the axial plane of the folds is stable and NE-SW striking and sub-vertical.

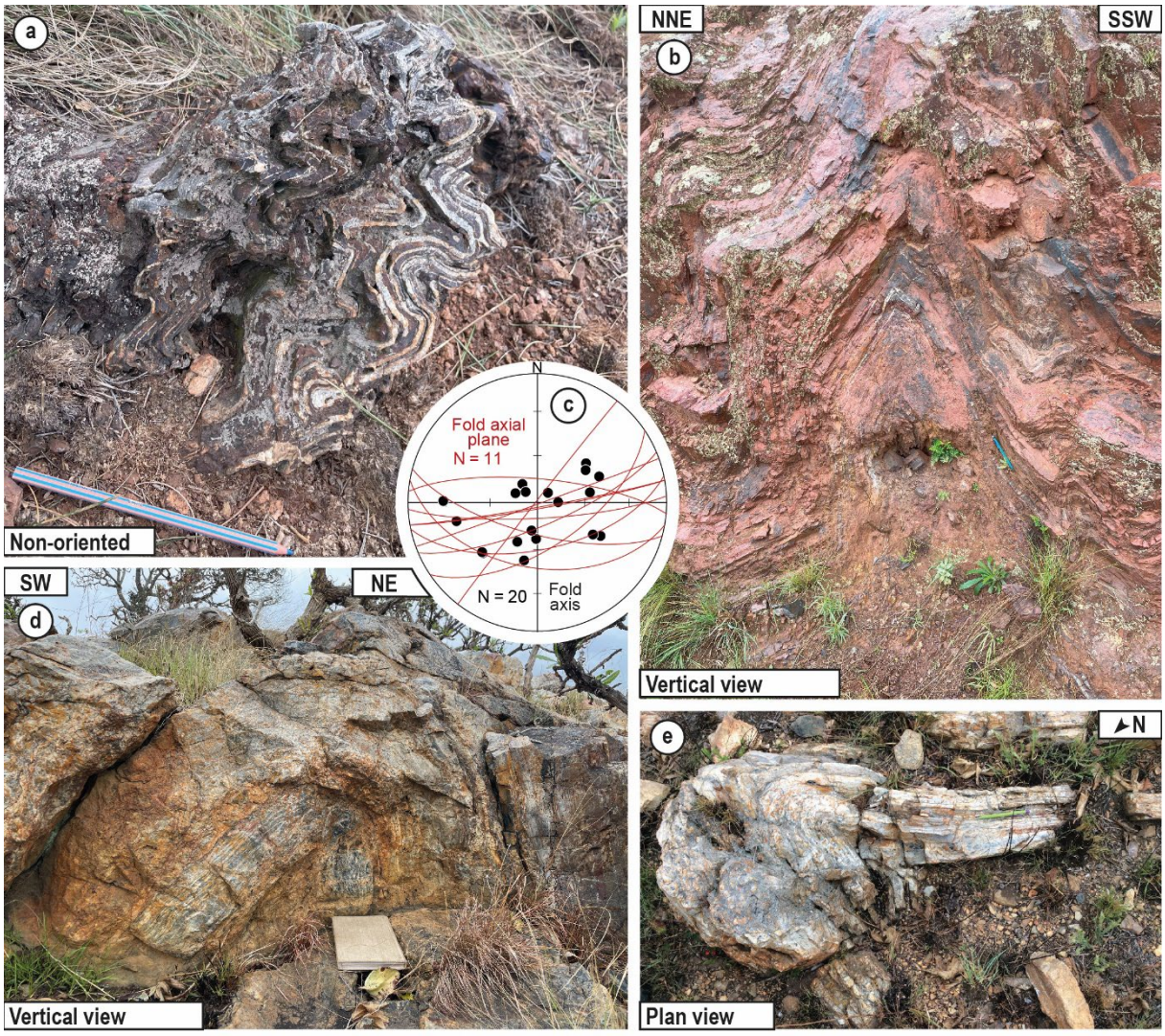

Fig. V.4. Field observations documenting the folded bedding. **(a)** Folded BIF of the Fig Tree Group situated in the Agnes area. **(b)** Folded iron-rich shales folded and located in the Shiyalongubo area, Fig Tree Group. **(c)** Stereonet of axial planes of the folded bedding (red great circles) and fold axes (black dots) (Schmidt diagram, lower hemisphere). **(d)** Folded chert of the Fig Tree Group with a vertical fold axial plane and a shallow plunging fold axis located in the Sheba-Fairview area. **(e)** Folded chert with a vertical axial plane and a steeply plunging to the SW fold axis located in the Sheba-Fairview area.

V.A.3. Schistosities

The schistosity in the northern part of the belt, has a small angular difference with the bedding (Fig. V.5). Indeed, the laminated lithologies develop a, predominantly NE-SW to E-W striking schistosity (Fig. V.5a,b) which is sub-vertical (Fig. V.5c,d). Because this angle is constant within the entire belt, schistosity can be oriented NE-SW to E-W (Figs. V.4b and V.6a). Like the bedding, the schistosity seems to rotate on a large scale, as in the Agnes and Shiyalongubo areas where the schistosity is broadly NE-SW to ENE-WSW striking. In the Barberton and Sheba-Fairview areas the schistosity has a more variable N-S to E-W strike.

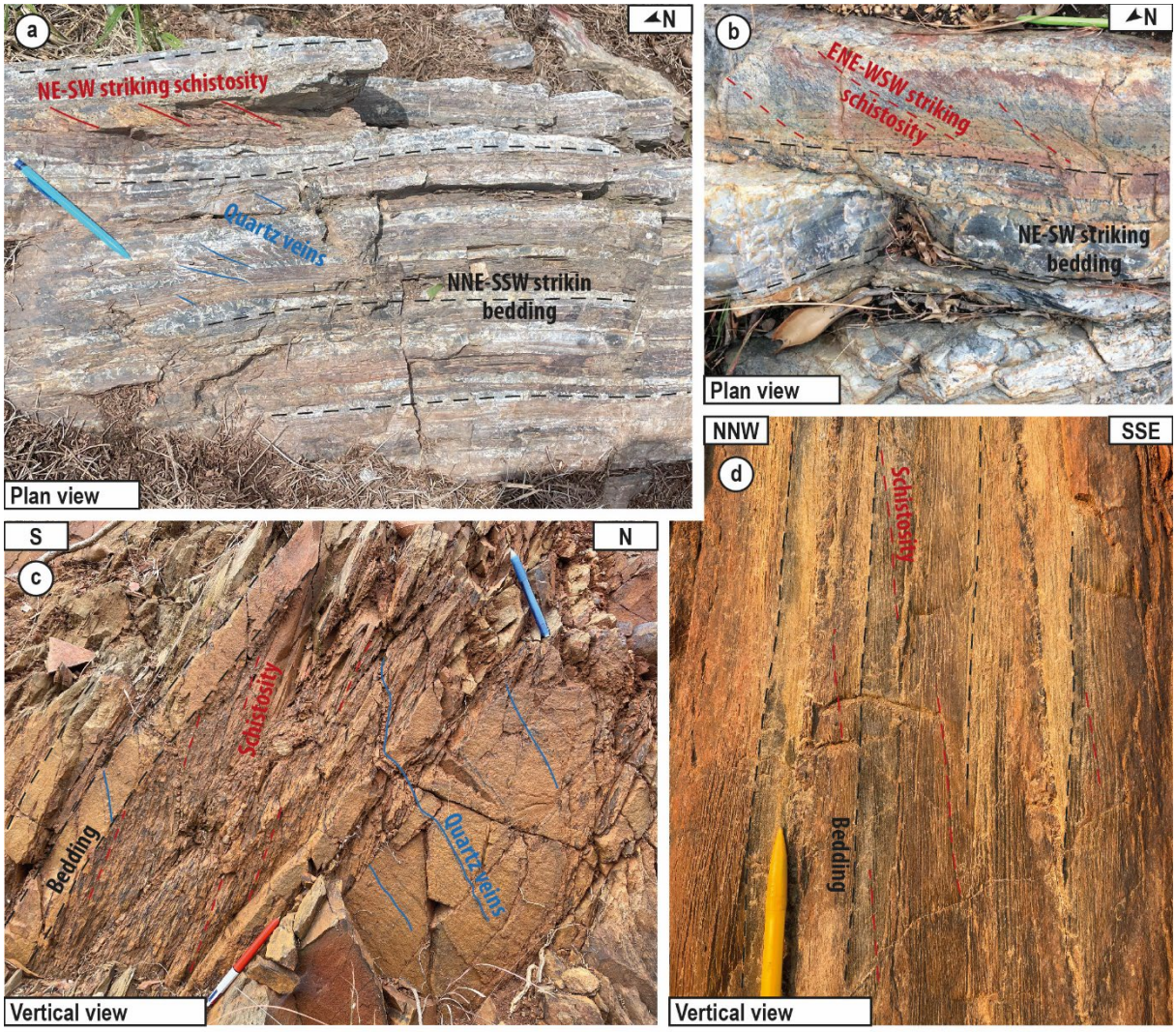

Fig. V.5. Field observations of the NE-SW to E-W striking schistosity developed in laminated lithologies, where bedding-cleavage acute angle relations are observed. **(a)** Finely layered intercalation of Fig Tree chert exhibits a NE-SW striking schistosity developed in the finer shale layer in the Agnes area. Note the quartz vein array that is parallel to the schistosity. **(b)** NNE-SSW striking Fig Tree chert exhibits a NE-SW striking schistosity in the Sheba-Fairview area (west limb of the re-folded Ulundi Syncline). **(c)** Fig Tree shales exhibit a steeply dipping schistosity in the

finer grained layers, in the Sheba-Fairview area (eastern limb of the re-folded Ulundi Syncline). Note that the orientation of the quartz veins is refracted between the shale-dominated and sand-dominated beds. **(d)** Fig Tree shales exhibit a steeply dipping NE-SW striking schistosity in the finer grained layers (Shiyalongubo area).

One can note that schistosity can also be affected by smaller-scale folds; observed with a NE-SW to E-W striking axial plane (Fig. V.6b).

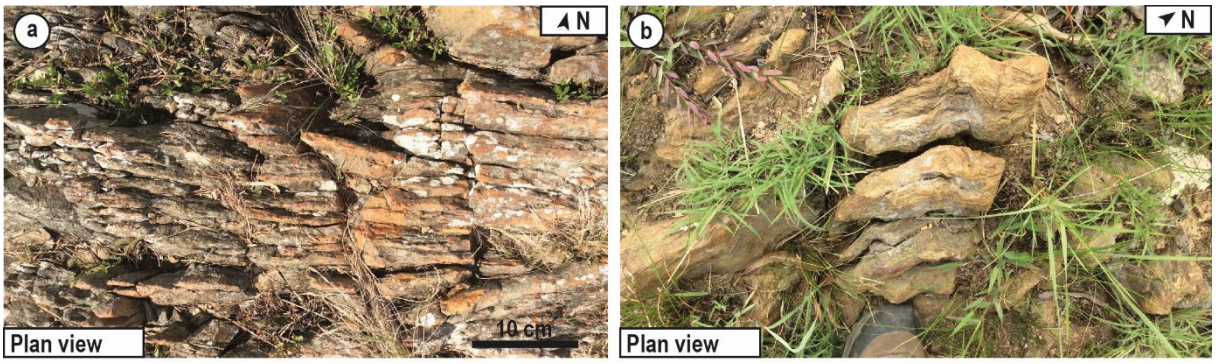

Fig. V.6. Field observations of the schistosity in the northern part of the Barberton Greenstone Belt. **(a)** ENE-WSW striking schistosity in the Agnes area in the schists of the Onverwacht Group. **(b)** Folded NE-SW striking schistosity in the talc-schist of the Onverwacht Group in the Barberton area. The fold axial plane strikes about E-W.

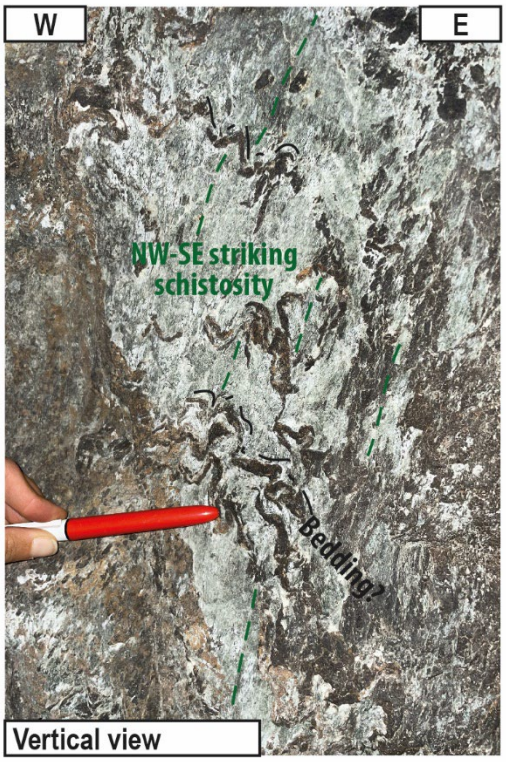

Within the Victoria Mine area, which is located in the western limb of the re-folded Eureka Syncline, the main schistosity is parallel to compositional layering S0 and exhibits a predominant sub-vertical N-S orientation, suggesting that it rotated by at least 60 degrees about a steep axis from its orientation at Agnes and Barberton sectors. However, locally, a NW-SE striking schistosity, steeply dipping to the SW was also observed at this mine (Fig. V.7), which is folding the compositional layering and perhaps the N-S striking schistosity as well. Observations of this local schistosity raise the question of whether it corresponds to another late schistosity, or if it represents a locally folded segment of the N-S-striking schistosity within the zone.

Fig. V.7. Field observations of the local, axial planar NW-SE striking schistosity in the Victoria Mine.

V.A.4. Other Local Folds

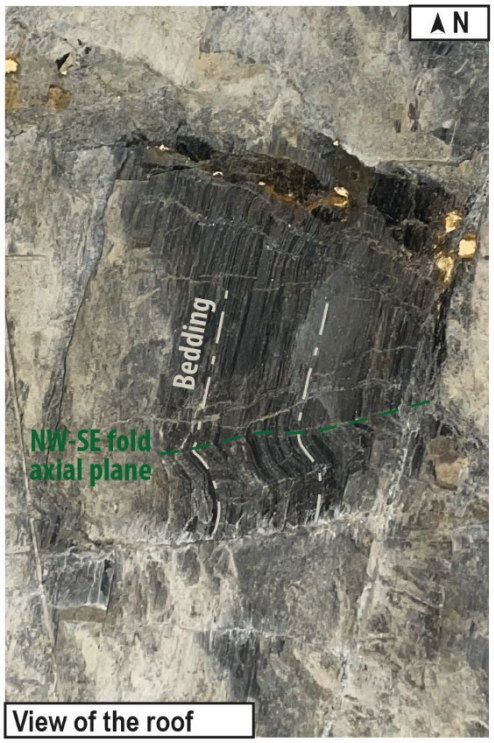

Locally a few other folds have been observed which do not appear to be part of the same system as the main folding events.

In Clutha Mine at the hinge of the Sheba-Fairview sector, local conjugate kink-bands are identified (Fig. V.8). These local folds carry a fold axial plane sub-vertical, NW-SE striking and fold steep NE-SW striking bedding planes.

Fig. V.8. Field observations of conjugate contractional kink-bands affecting bedding planes in Clutha Mine, Fairview-Sheba sector, with a NW-SE striking mirror surface.

Another folding affects locally the bedding and the schistosity within the northern part of the Barberton Greenstone Belt. Chevron folds with horizontal axial planes (Fig. V.9) were reported in vicinity of the Barberton Mountain Lodge private road.

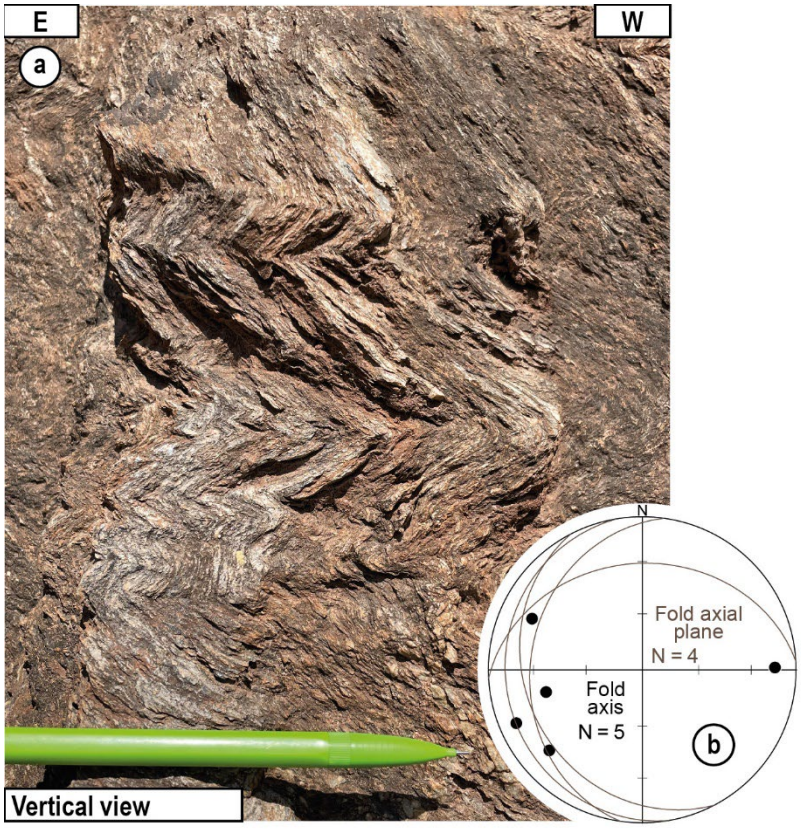

Fig. V.9. Field observations of recumbent chevron folds affecting the schistosity in the Barberton area. **(a)** Chevron fold associated with sub-horizontal axial planes. **(b)** Stereonet of the sub-horizontal axial planes of the chevrons folds (brown great circles) and fold axis (black dots) (Schmidt diagram, lower hemisphere).

V.A.5. Faults

In addition, the rocks within the northern part of the belt are transected by numerous main and secondary faults (Figs. V.1, V.3, V.10 and V.11a). These faults are mainly exhibiting thrusting motion and are NE-SW, NW-SE and E-W striking (Fig. V.11b). The map in Figure V.1 clearly shows that the main faults rotate in the Sheba-Fairview area, and therefore suggest that they were affected by the re-folding of the Eureka and Ulundi large-scale folding.

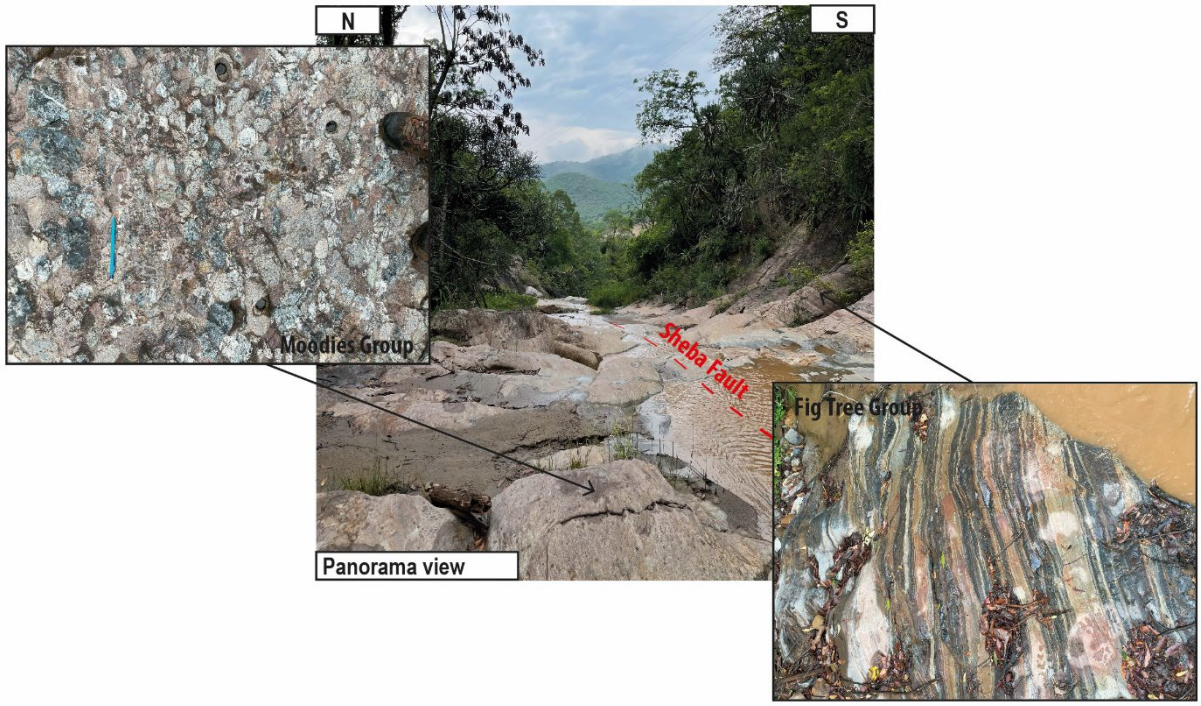

Fig. V.10. Panorama view of the Sheba Fault putting in contact the conglomerate of the Moddies Group with the shales of the Fig Tree Group. Insets are close-up views of the two different lithostratigraphic groups. This outcrop is located in the Sheba-Fairview area, in Sheba Creek.

Other faults are also identified but with strike-slip motion. For example, in the Barberton Mountains Lodge private road, numerous NE-SW striking and minor N-S and E-W striking secondary faults are observed with sub-horizontal slickenlines showing sinistral motion.

In summary, several folding, schistosity and faulting observations have been made in the northern part of the Barberton Greenstone Belt.

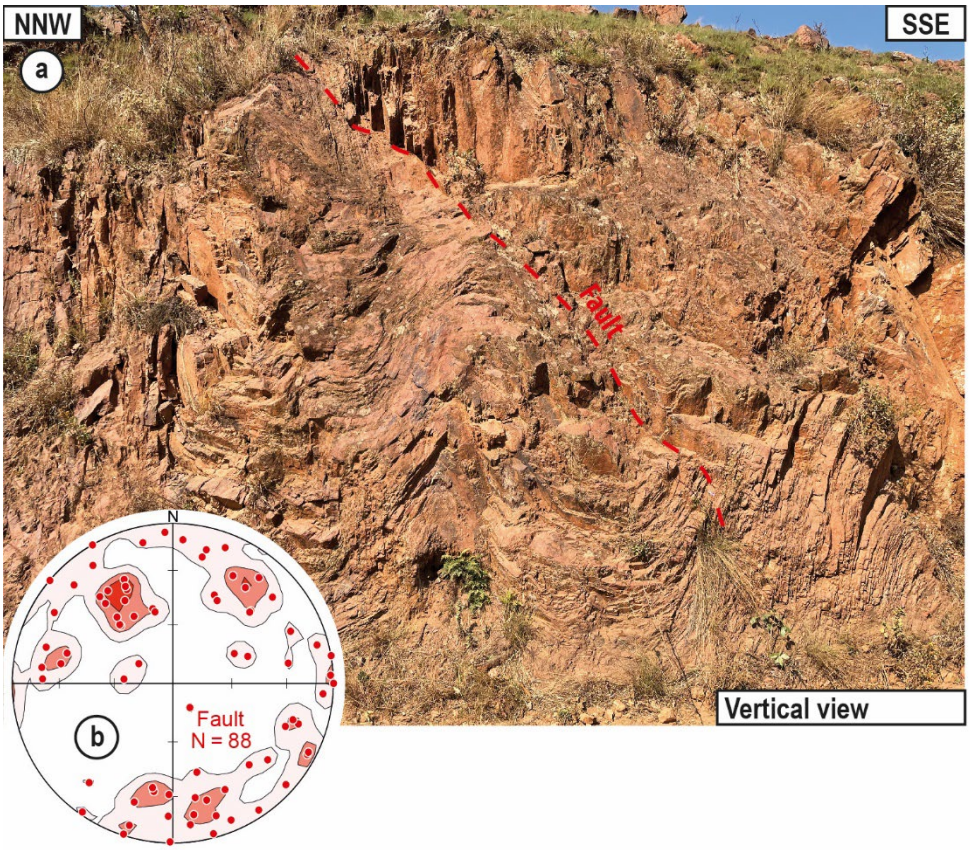

Fig. V.11. Field observations of a fault zone in the northern part of the Barberton Greenstone Belt. **(a)** ENE-WSW striking fault cutting folded rock of the Fig Tree Group in the Shiyalongubo area, this fault belongs to the Barbrook fault network. **(b)** Stereonet showing all the fault measurements in the northern part of the Barberton Greenstone Belt. The planes are represented in poles to planes with density distribution (Schmidt diagram, lower hemisphere).

V.B. Mineralised quartz vein system

The northern region of the Barberton Greenstone Belt hosts over a hundred gold occurrences, and four active mines. A significant portion of these occurrences correspond to former mines that have since been abandoned. The map in Figure V.1 shows the distribution of these occurrences and active mining sites that are predominantly clustered along the Moodies (also known as Lily), Sheba, and Barbrook faults, as well as within the Eureka and Ulundi synclines (Fig. V.1).

Veins described as mineralised are defined as those either situated within or in close proximity to a designated mineralised occurrence, as depicted on the Barberton Greenstone Belt's metallogenic map. These veins, owing to their spatial proximity with the mineralised occurrence and the visible historical mining activity around them, are classified as mineralisation-associated veins, even in the absence of quantifiable gold content.

V.B.1. Field macroscopy study

The diverse types of occurrences and quartz vein settings examined in this region will be illustrated through the example of seven historical significant mines or galleries, each serving as a noteworthy representation of distinct quartz vein network configurations prevalent across the northern part of the belt. These illustrative examples are spread across the Agnes, Sheba-Fairview, and Shiyalongubo areas, offering insights into the varied manifestations of quartz veins within the broader context.

V.B.1.1. Tiger Trap and Pioneer mines

In the Agnes area, situated in the northwestern part of the Barberton Greenstone Belt (Fig. V.1), the former Tiger Trap and Pioneer mines are closely positioned (they are located at ca. 600 m from each other), exhibiting similar gold-mineralisation patterns. Within these mines, decimetre to meter-wide quartz-carbonate veins, roughly oriented along the ENE-WSW striking direction and sub-vertical, have been actively exploited (Fig. V.12a).

Within this zone, a multitude of veins striking ENE-WSW (sometimes E-W) and dipping steeply towards the NNW is observed, characterised by reverse movement towards the south. This is discernible through the presence of down-dip lineations within the host rock and the presence of numerous drag folds in the surrounding country rock (Fig. V.12b,c). The ENE-WSW striking direction is sub-parallel with the regional schistosity and regional fault striking direction.

Furthermore, shallower dipping veins or horizontal ones are also present (Figs. V.12d and V.13), exhibiting a geometry ranging from undulation to folding (Figs. V.12d and V.13b). Notably, some of these veins exhibit horizontal en-echelon arrangements, showing a southward-directed reverse motion (Fig. V.13c).

In each of these zones, the veins consist of quartz-carbonate composition (Fig. V.14a). Some of them are brecciated (Fig. V.14b).

Most rocks of the Pioneer/Tiger trap area are intensively affected by fuchsite-related alteration, with abundant pyrite dissemination at the vein periphery and a scattering of pyrite within the veins (Fig. V.15a); or in proximity to the breccia zones (Fig. V.15b).

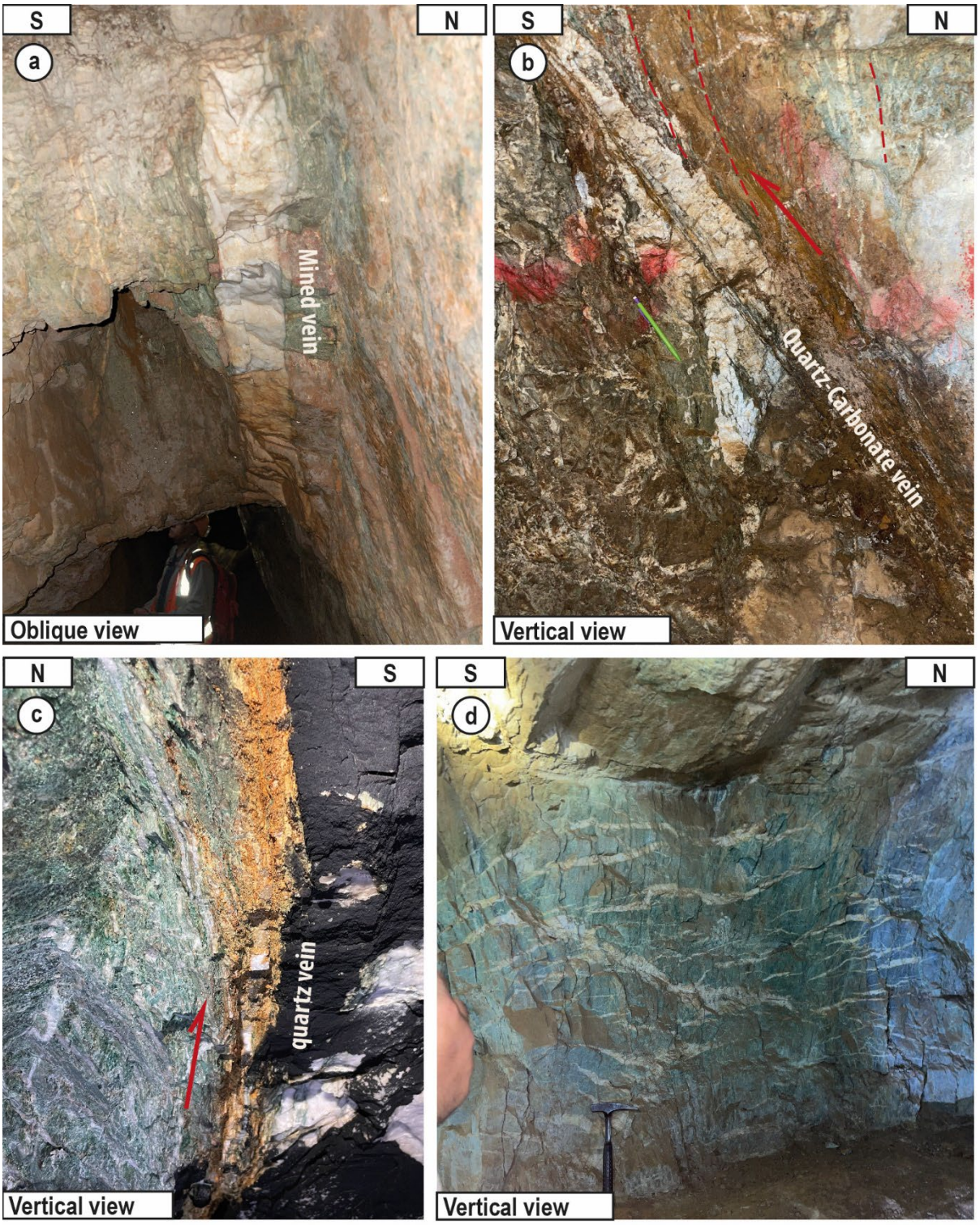

Fig. V.12. Field observations of E-W striking mineralised veins at Pioneer and Tiger Trap mines. **(a)** Major mined quartz vein within Pioneer Mine. **(b)** North-dipping and E-W striking quartz vein displaying reverse motion (Tiger Trap Mine). **(c)** Drag folds in host rock surrounding a quartz vein depicting a reverse sense of shear in the lineation-parallel plan (Tiger Trap Mine). **(d)** Quartz veins array comprising north-dipping quartz veins and gently undulating shallow-dipping quartz veins (Pioneer Mine).

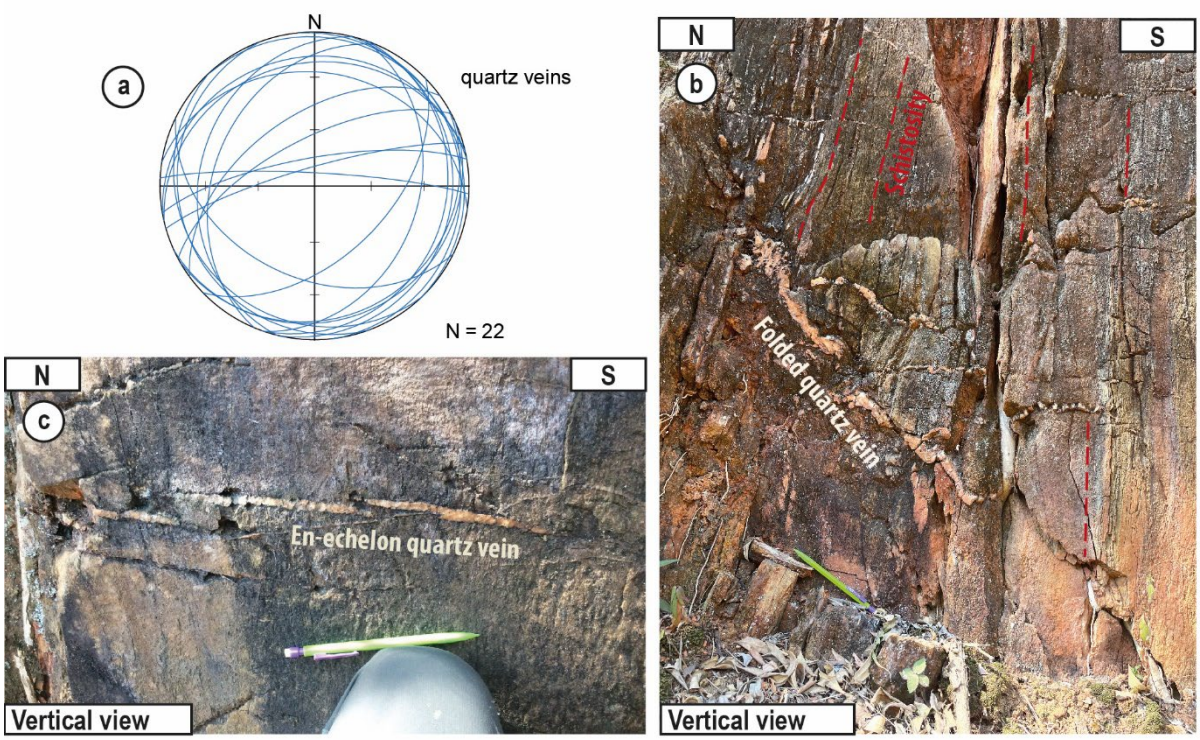

Fig. V.13. Field observations of shallow-dipping quartz veins in the Pioneer/Tiger trap area. **(a)** Stereonet representing all the quartz-carbonate veins (Schmidt diagram, lower hemisphere). **(b)** Folded shallow dipping veins alongside steeper veins. **(c)** En-echelon arrangement of horizontal veins.

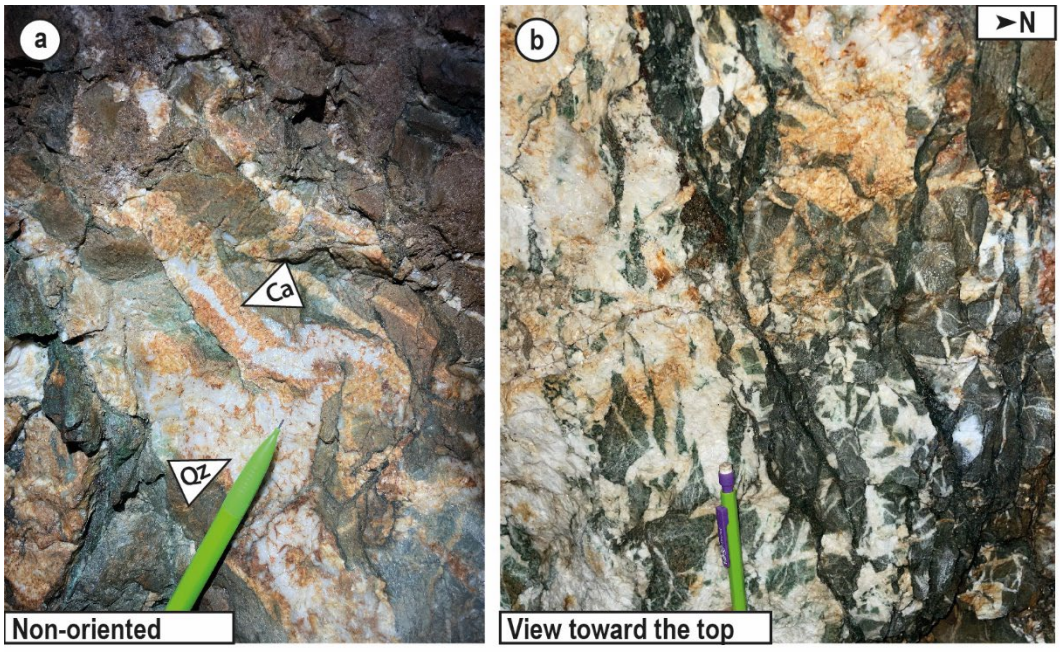

Fig. V.14. Field observations of various vein types in the Pioneer/Tiger trap area. **(a)** Folded quartz-carbonate veins (Tiger Trap Mine). **(b)** Breccia zone showing sharp-shaped quartz-carbonate fragments (Tiger Trap Mine).

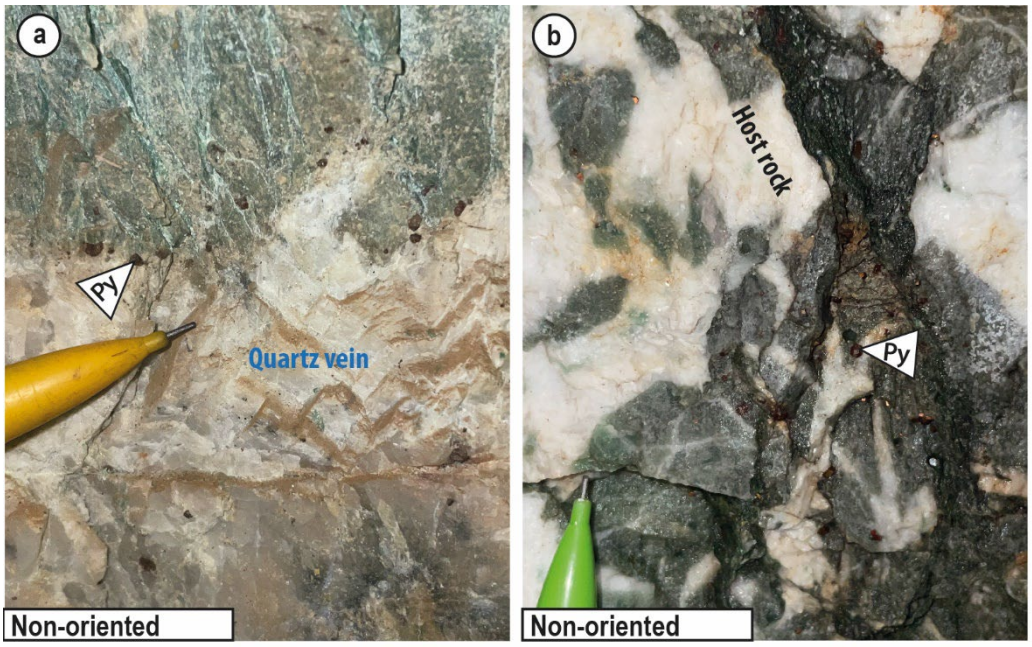

Fig. V.15. Field observations of the sulphide distribution at Pioneer and Tiger Trap mines. **(a)** The abundance of pyrite near the quartz vein and sparse within the vein (Tiger Trap Mine). **(b)** Presence of pyrite within a brecciated zone (Tiger Trap Mine).

V.B.1.2. The Agnes Mine

The Agnes Mine, an operational site situated in the northwestern region of the belt, was investigated during this work and specifically the abandoned level number 17 serves as subject of a detailed analysis here.

Within this zone, both bedding and veins exhibit a regular ENE-WSW striking orientation and display vertical dipping. Notably, all veins run parallel to the bedding, as illustrated in Figure V.16. These veins vary in thickness from mm to cm-thick, occasionally forming lens-like shapes, and are predominantly composed of carbonate and quartz minerals.

Symmetrical boudins have been documented in this area. These boudins affect competent layers (Fig. V.17a), and carbonate-quartz veins (Fig. V.17a,b). These observations are particularly evident when examining vertical observational planes.

This entire zone exhibits high abundance of mm-wide euhedral pyrites dispersed within bedding planes (Fig. V.18a) or aligned along layers (Fig. V.18b). Notably, their concentration tends to be more pronounced in proximity to carbonate-quartz veins (Fig. V.18b).

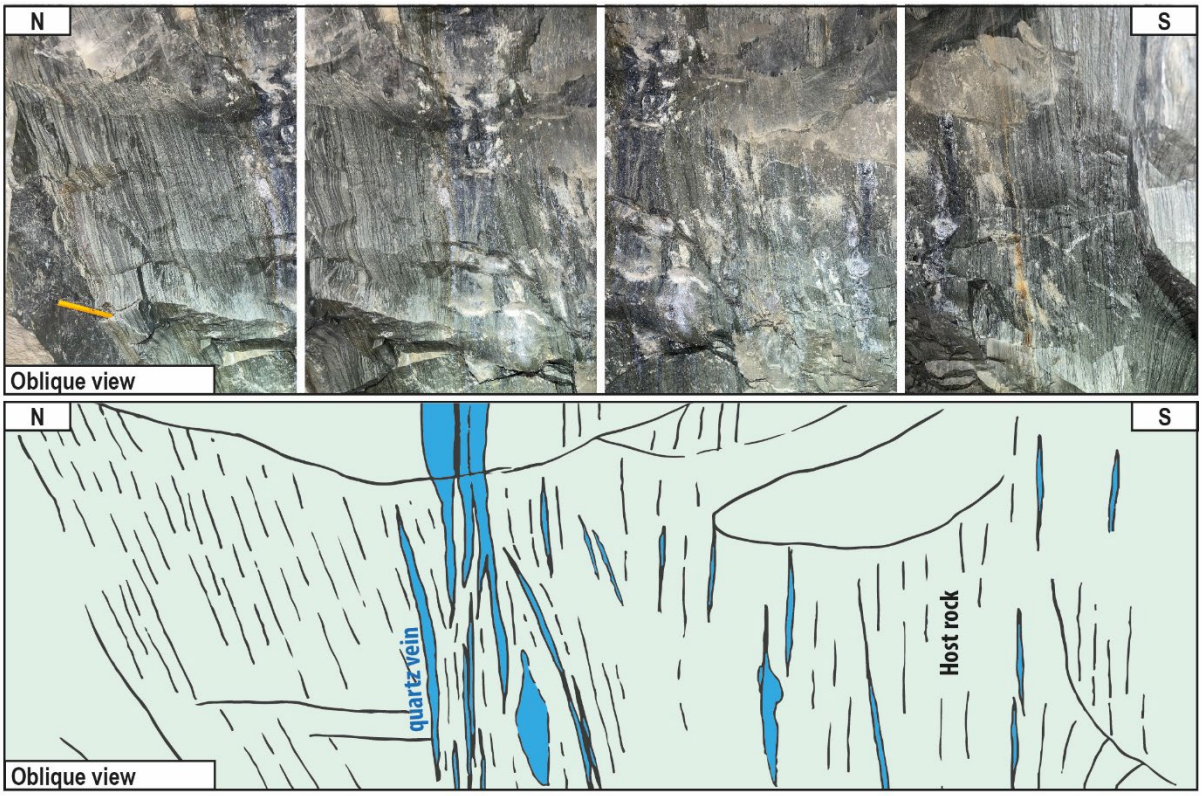

Fig. V.16. Frontal cross-section of one Agnes Mine tunnel photographs progressing from west to east, accompanied by corresponding panoramic sketch, reveal steeply bedding-parallel tabular veins and lenses.

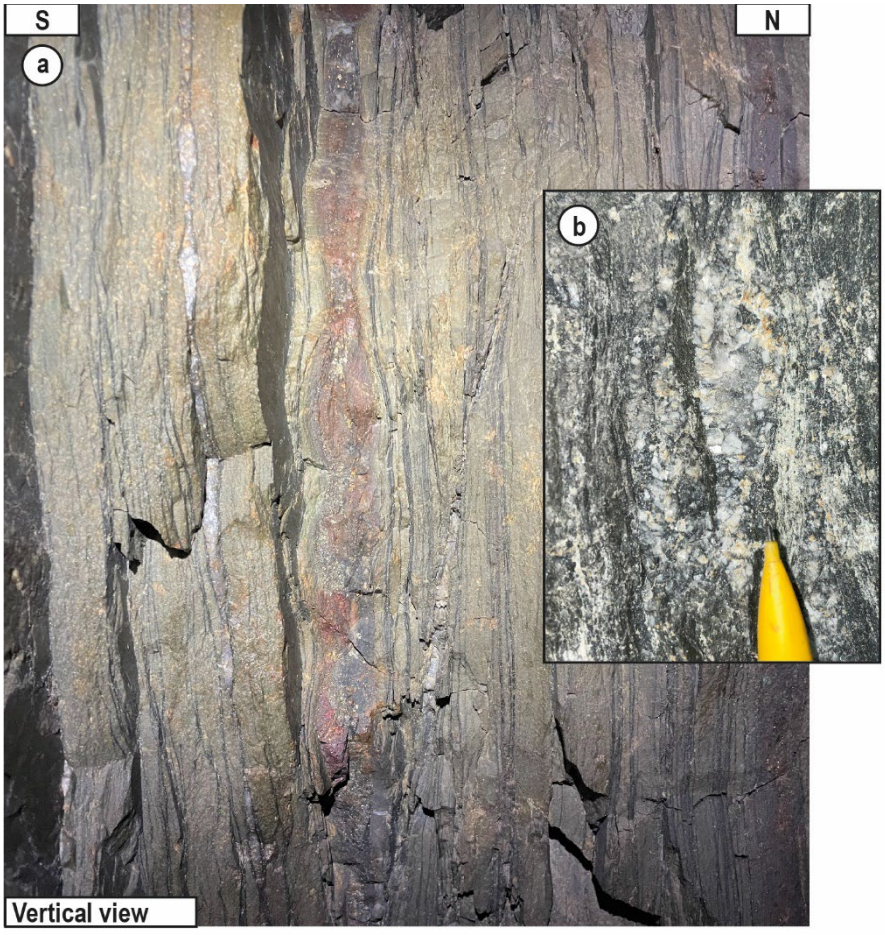

Fig. V.17. Field observations of boudinage structures in Agnes Mine. **(a)** Bedding-parallel veins and host rock show boudinage. **(b)** Inset of a quartz-carbonate lens.

Furthermore, the host rock and bedding-parallel veins are cross-cut by quartz-filled faults, which exhibit a top-to-the-south reverse motion (Fig. V.19). The quartz-filled faults bear down-dip striations. This sense of shear is depicted by the presence of drag folds of country rock and veins around the fault planes. These reverse veins have similar attitude than the mineralised veins observed at the Tiger Trap and Pioneer mines.

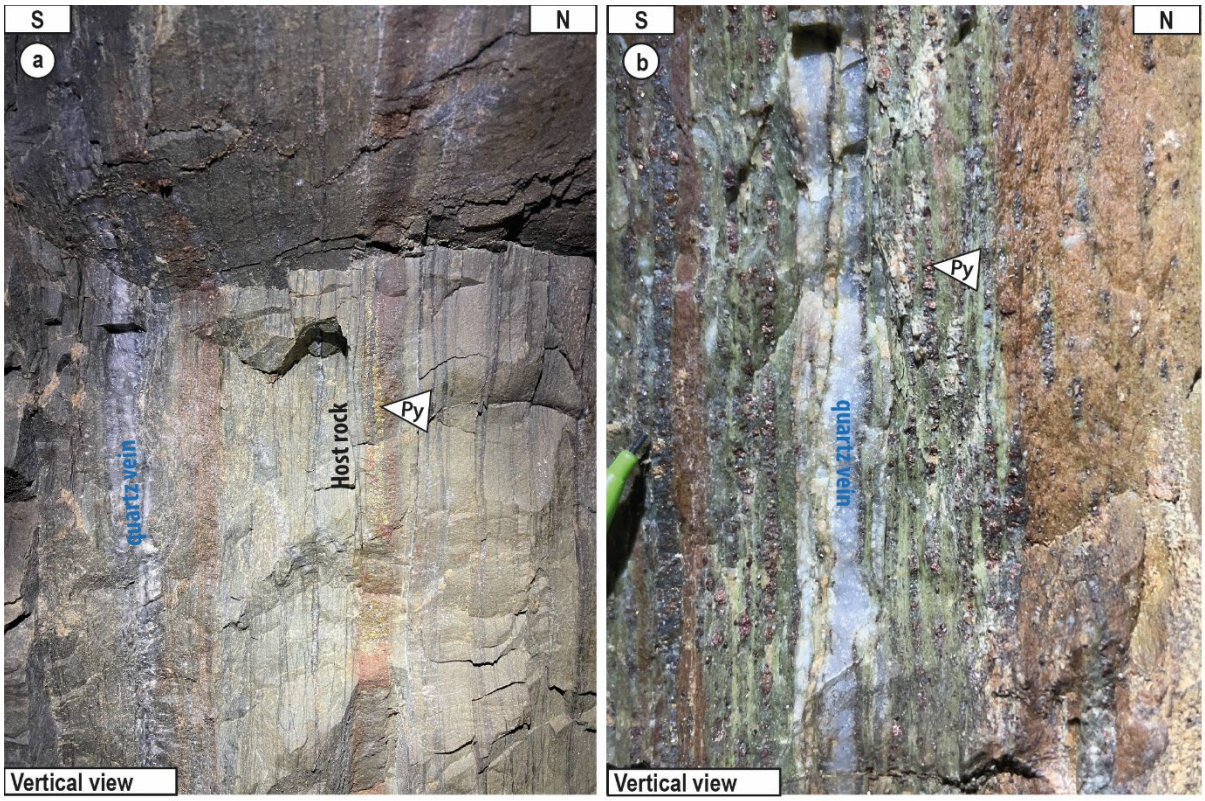

Fig. V.18. Field observations of the sulphide distribution. **(a)** Bedding parallel pyrite veins. **(b)** Numerous pyrites are observed in the vicinity of the veins, they are aligned along bedding planes.

Fig. V.19. Photo of a fault plane with reverse sense of shear. The fault is filled with quartz.

V.B.1.3. Victoria Mine

The former Victoria Mine is situated along the western flank of the re-folded Sheba-Fairview area, positioned to the north of the Lily fault (see Figure V.1). Within this structural domain, the schistosity is N-S striking and dips sub-vertically.

Notably, this area is marked by cm to m-thick quartz veins that strike N-S and exhibit a steep westward dip (Figs. V.20 and V.21). These veins display downdip slickenlines along their edges. Furthermore, the drag folds of the schistosity around the veins reveal a reverse sense of shear, with top movement towards the East (Fig. V.21).

In proximity to these veins, are shallow-dipping veins ranging from cm to dm in thickness. These veins exhibit in some places a petrographic continuity with the steeper veins (Fig. V.21). This whole system is consistent with an eastward thrust motion.

Fig. V.20. Photo depicting a m-thick quartz vein with a N-S striking orientation. Slickenlines associated with drag folds of adjacent schistosity attest of top to the east reverse sense of shear.

Some veins run parallel to the schistosity, occasionally displaying "chocolate tablet" boudinage, i.e., boudinage in two directions (horizontally and vertically, see Figure V.22 for visual representation).

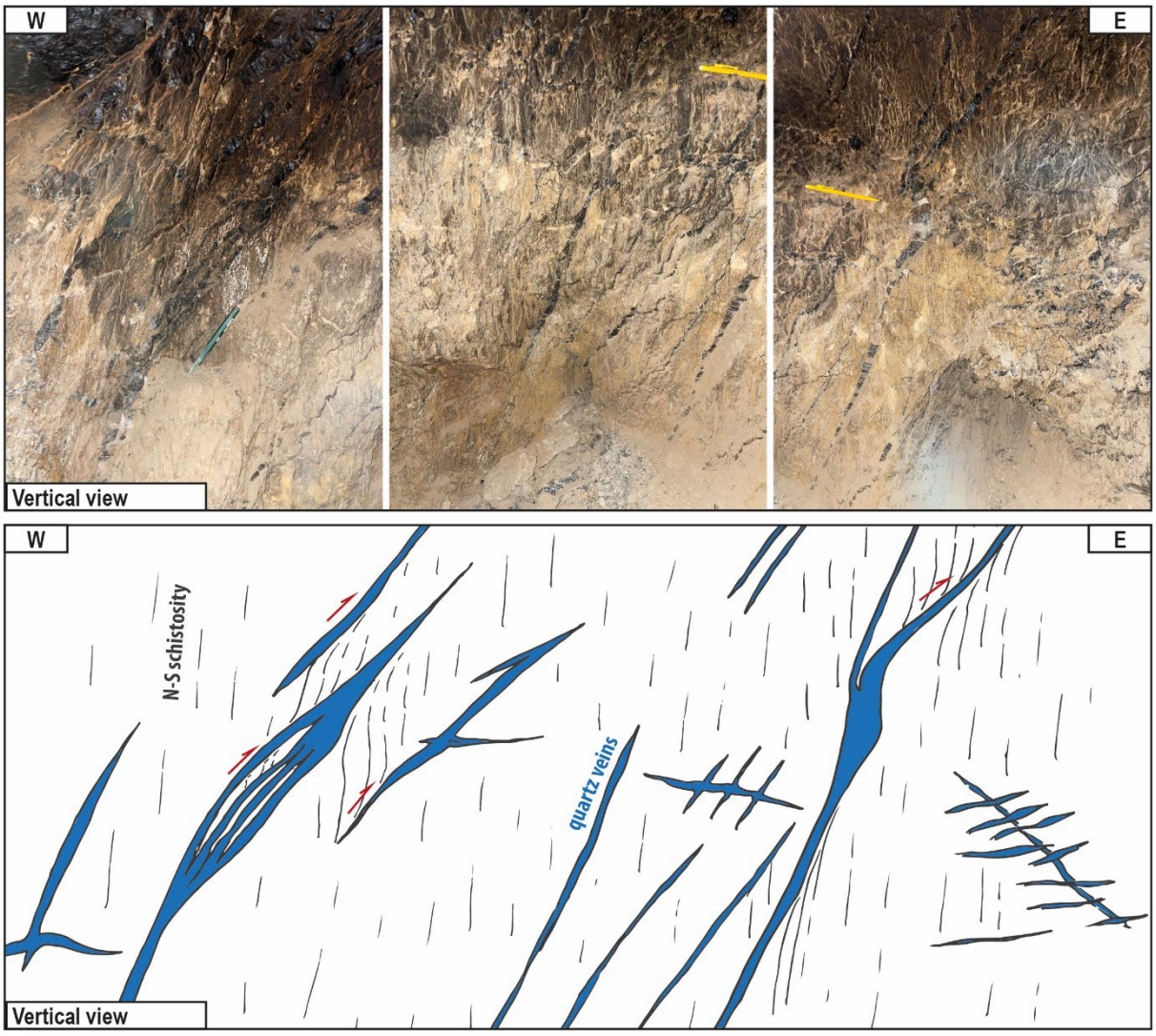

Fig. V.21. Tunnel face photographs progressing from west to east, accompanied by corresponding panoramic sketch, reveal dominant steeply dipping quartz veins to the west and minor shallow-dipping ones. Drag fold of schistosity attests of a reverse motion along the steeper veins.

However, slickenlines observed in the edge of the boudinage veins suggested a dominant reverse sense of shear.

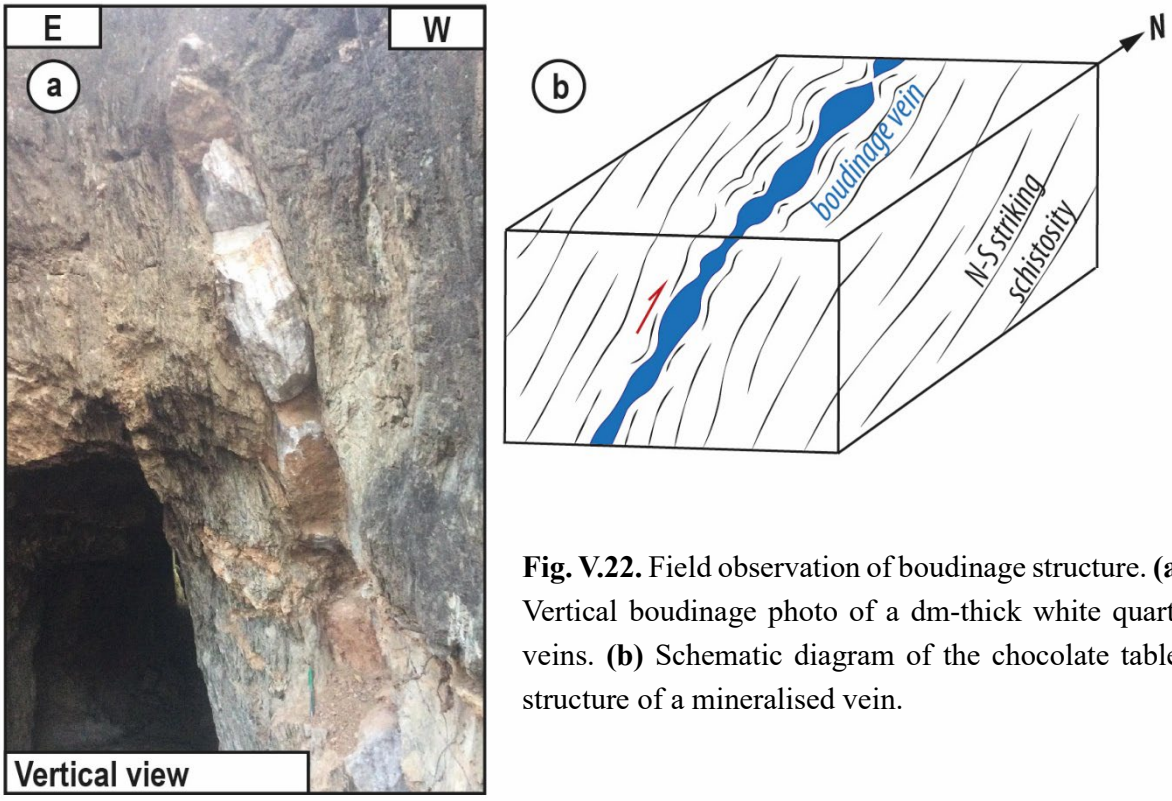

Fig. V.22. Field observation of boudinage structure. **(a)** Vertical boudinage photo of a dm-thick white quartz veins. **(b)** Schematic diagram of the chocolate tablet structure of a mineralised vein.

To sum up, the vein striking direction is parallel to the host rock schistosity, although with some minor variations in dip present in certain areas (Fig. V.21). All these findings strongly suggest a structural control of the mineralised system at Victoria by a top-to-the-east thrusting event.

V.B.1.3. Clutha Mine

The Clutha Mine is an abandoned site situated adjacent to the southern side of the Lily fault, in close proximity to the refolded hinge of the Eureka Syncline. In this area, the bedding is globally NE-SW steeply dipping to the SE.

The mine consists of a main drift NNW-SSE and NW-SE trending, which is approximately 1.2 km long (Fig. V.23). This main drift is accompanied by several subsidiary galleries that follow the mineralised veins. The overall layout of the mine is succinctly depicted in the plan illustrated in Figure V.23, highlighting the galleries studied in this research and in blue the visible orebodies.

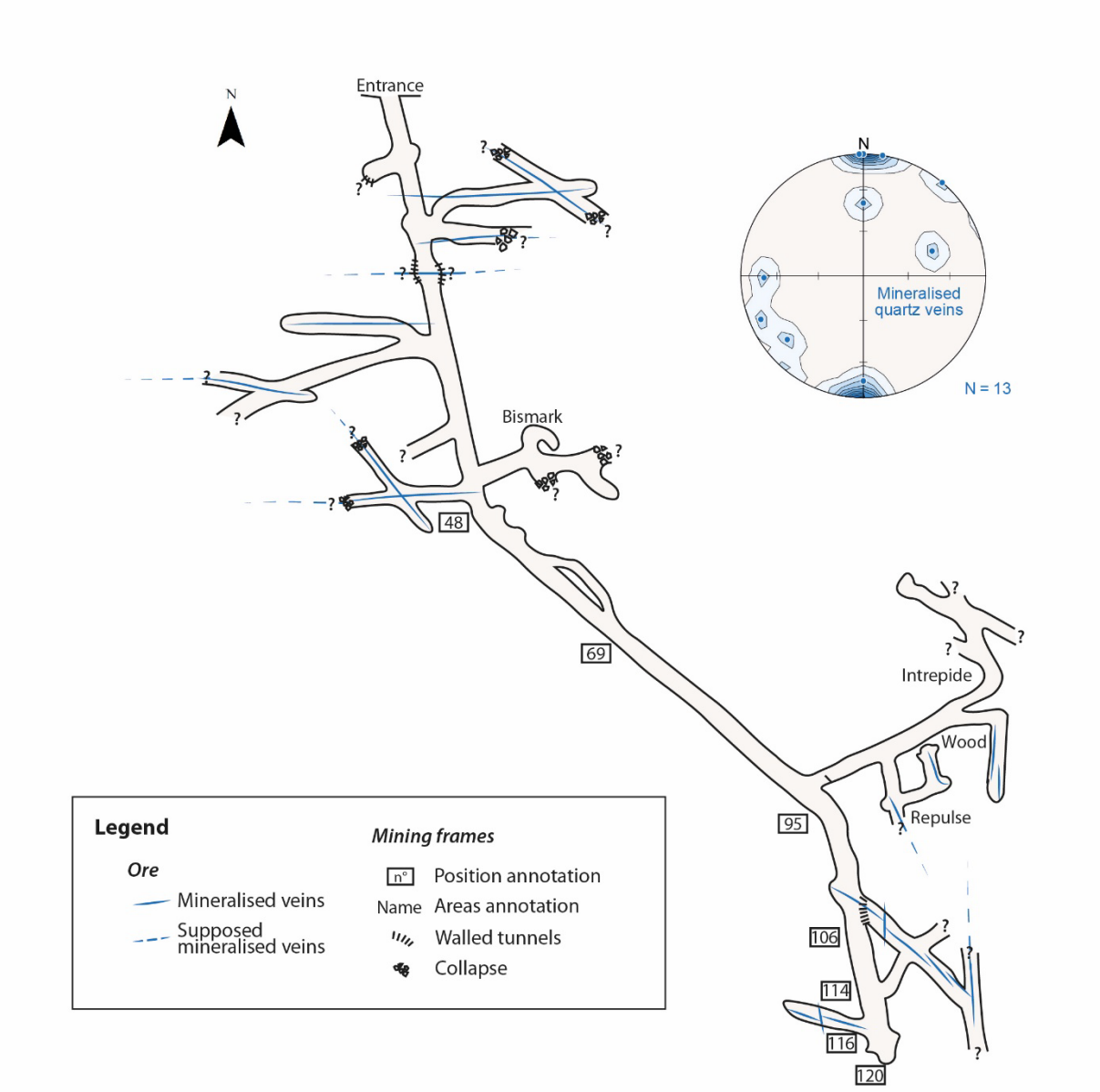

Fig. V.23. Schematic diagram of the studied galleries, view from the top, with mined quartz vein shown in blue. The stereonet depicts the m-thick mineralised quartz veins in pole-to-plane representation (Schmidt diagram, lower hemisphere).

Notably, instances of elongated, straight cm-thick quartz veins were observed in several locations (Fig. V.24). These veins are shallow dipping and seem to be cut by the steep NW-SE veins (Fig. V.24a) or associated with satellite ENE-WSW striking, steep quartz veins (Fig. V.24b).

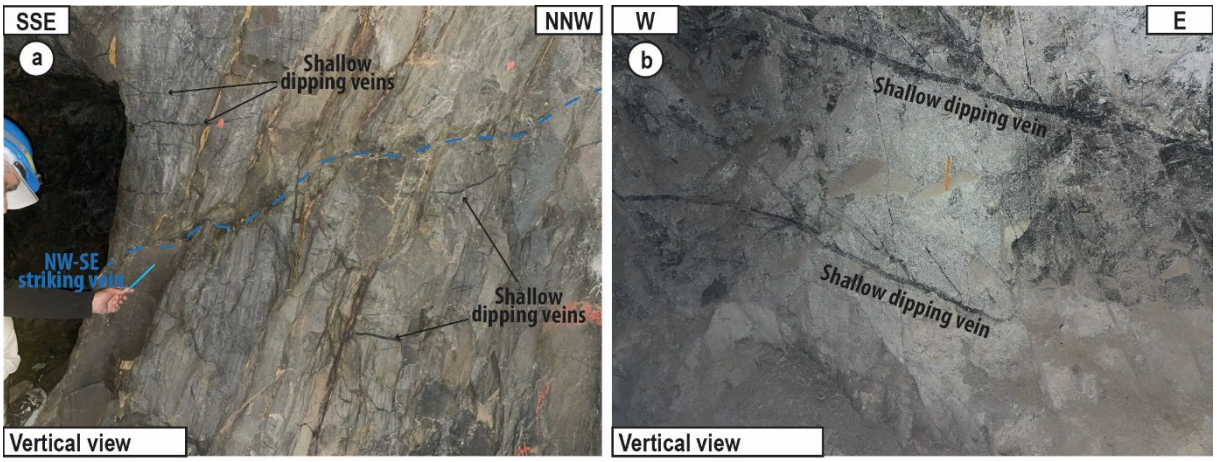

Fig. V.24. Field observations of the shallow dipping veins. **(a)** Shallow dipping veins crosscut by NW-SE striking veins; this photo is taken in the vicinity of the position annotation n°118 in Figure V.23. **(b)** Shallow dipping veins in textural continuity with steeper satellite veins, this photo is located near the Intrepide annotation in Figure V.23.

On large-scale, the veins closest to the mine entrance are E-W striking and sub-vertical (Figs. V.23 and V.25a,b). A total of six E-W striking mineralised lodes were measured at the entrance of the mine, revealing a spatial distribution suggesting an en-echelon pattern (Fig. V.23). A plethora of structural features, such as drag folds, pull-apart veins, and transtensional zones, strongly indicate a dextral strike-slip movement associated with these veins (Fig. V.25a,c,d). These veins seem to be in petrographic continuity with NW-SE striking veins. And in addition, on a smaller scale, the alignment of NW-SE striking en-echelon veins formed an E-W striking vein (Fig. V.25c), suggesting that both directions of veins are contemporaneous.

In the southern part of the mine, a new type of mineralised veins emerges – the sub-vertical to steeply E-dipping N-S striking veins. These veins appear to intersect and offset the previously mentioned E-W striking veins (Fig. V.26a). Locally, down-dip slickenlines and drag folds of bedding planes suggest the possibility of reverse motion top to the west (Fig. V.26b).

In this mine, numerous euhedral pyrites crystals were observed especially in the vicinity of N-S, E-W and NW-SE striking veins, while fewer are identified within the veins (Fig. V.27). Few pyrites seem to occur around the shallow-dipping veins.

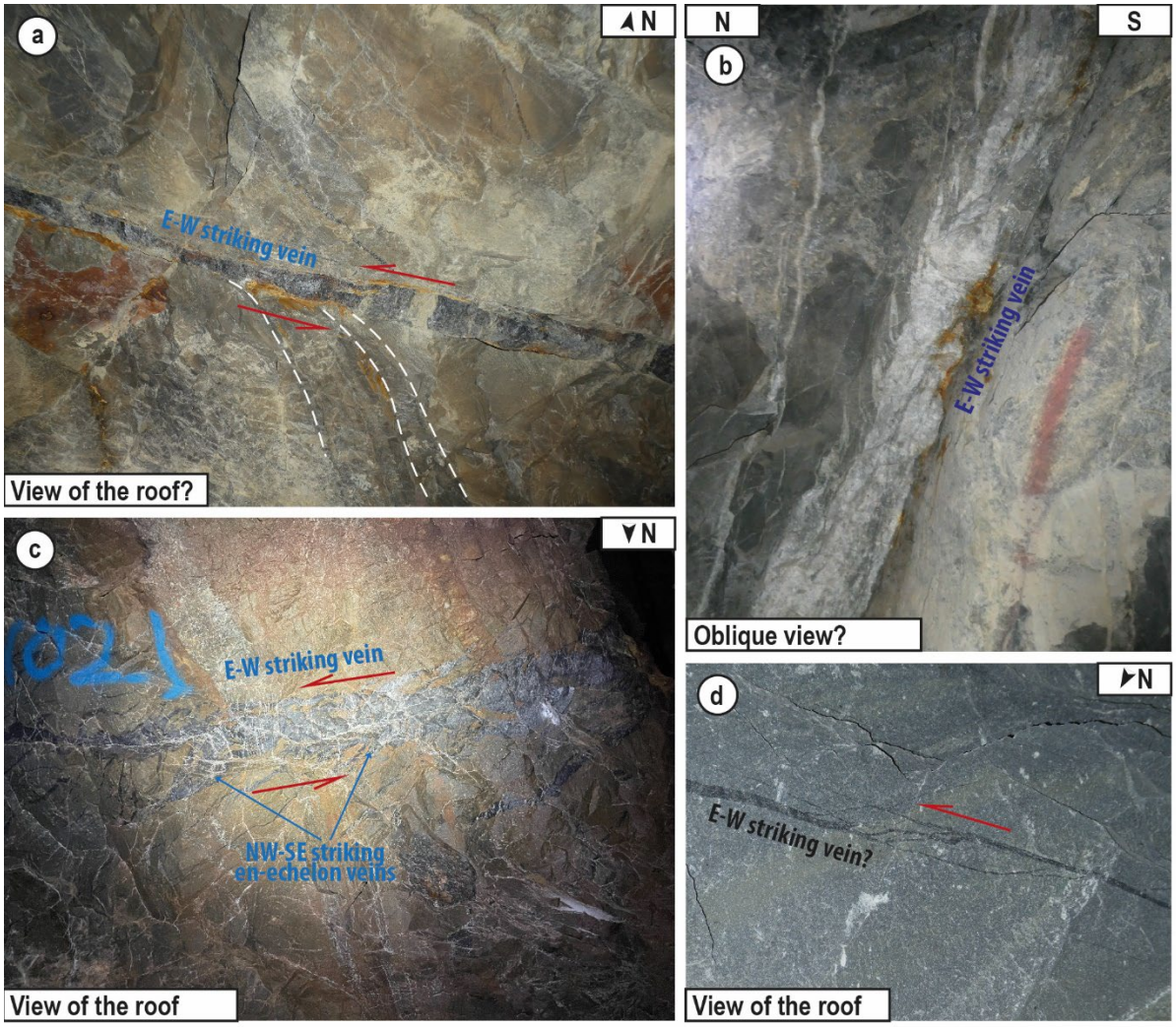

Fig. V.25. Field observation of E-W and NW-SE striking veins. **(a)** E-W striking dm-wide vein which show dextral drag folds, this vein is situated near the entrance of the mine. **(b)** E-W striking and sub-vertical dm-thick white quartz vein, near the position annotation n°48. **(c)** NW-SE striking en-echelon quartz veins aligned and formed a E-W striking vein. This photo is taken in vicinity of the position annotation n°116. **(d)** E-W striking cm-thick veins with a transtensional zone between them illustrated by a dextral motion. Note that all the photos with the roof view, i.e., (a), (c) and (d), show apparent sinistral movements that are in reality dextral projections.

Numerous small and thin east-dipping white quartz veins are also observed, particularly between the annotations n°48 and 69. No sulphides are visible in this area, raising the possibility that these veins might not be mineralised. No cross-cutting relationship with the mineralised veins above described is observed.

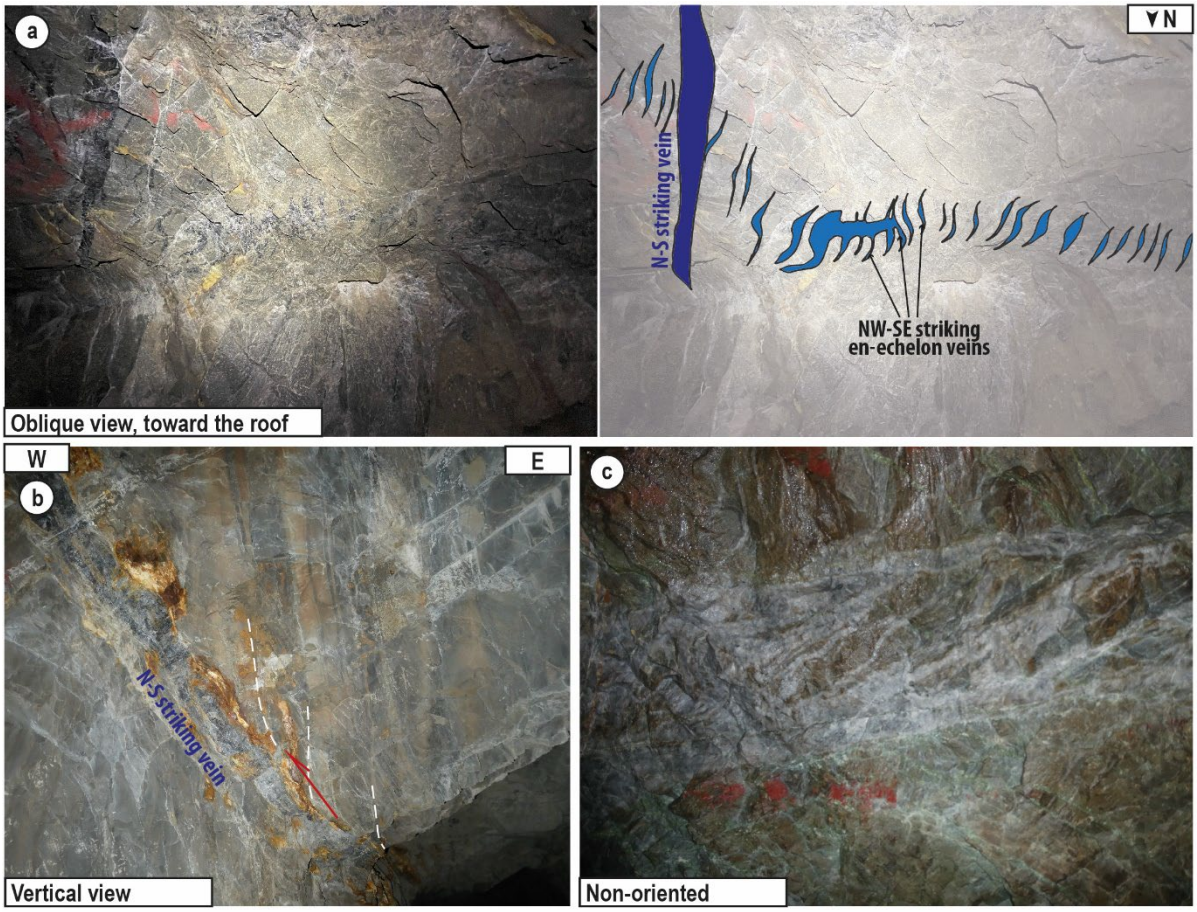

Fig. V.26. N-S striking mineralised vein observations **(a)** Photo and associated sketch of a N-S striking vein cut and offset a E-W striking vein and its NW-SE striking en-echelon veins. This photo is located in vicinity of the position annotation n°116. **(b)** N-S striking and steeply dipping to the east vein. The bedding formed drag folds on the edge of the vein, representing a reverse motion toward the west. This vein is situated near the Wood annotation. **(c)** N-S striking vein in the vicinity of the Repulse annotation.

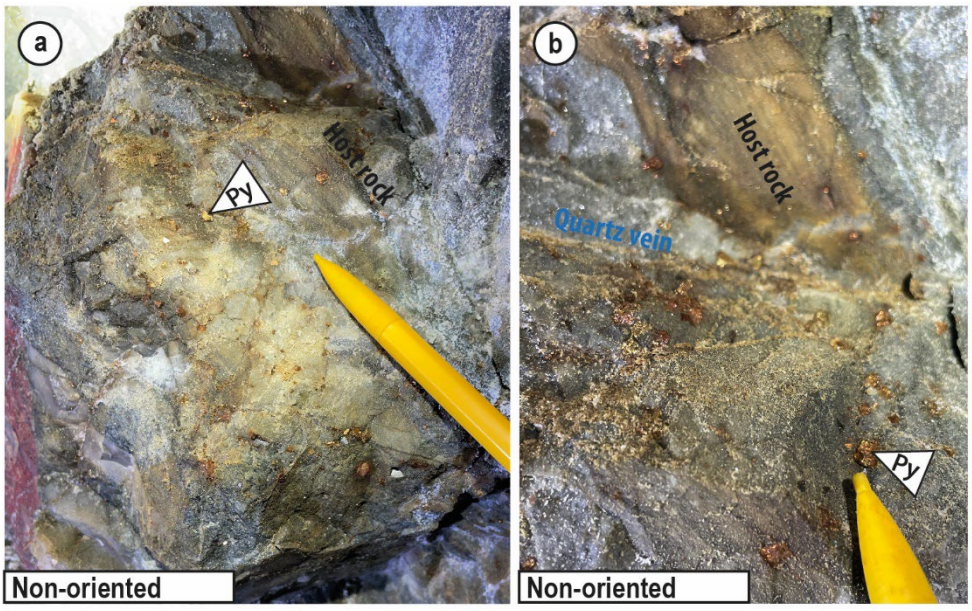

Fig. V.27. Field observations of the sulphide distribution. **(a)** Numerous pyrites were observed near a quartz vein. **(b)** The abundance of pyrite near the quartz vein and sparse within the vein.

To summarise, several types of veins were documented at Clutha Mine and illustrated within Figure V.28. Shallow dipping veins, which may have possibly formed early in the hydrothermal history (Fig. V.28a), precede or are possibly linked to synchronous E-W and NW-SE veins (Fig. V.28b). These synchronous veins distinctly showcase a pronounced dextral motion, notably visible in E-W striking veins (Fig. V.28b). Subsequently, mineralised N-S striking veins, intersecting the previous assemblage, may carry a potentially implying a reverse motion towards the east (Fig. V.28c). The presence of an additional hydrothermal event is suggested by the formation of non-mineralised white veins, possibly postdating the entire sequence (Fig. V.28d).

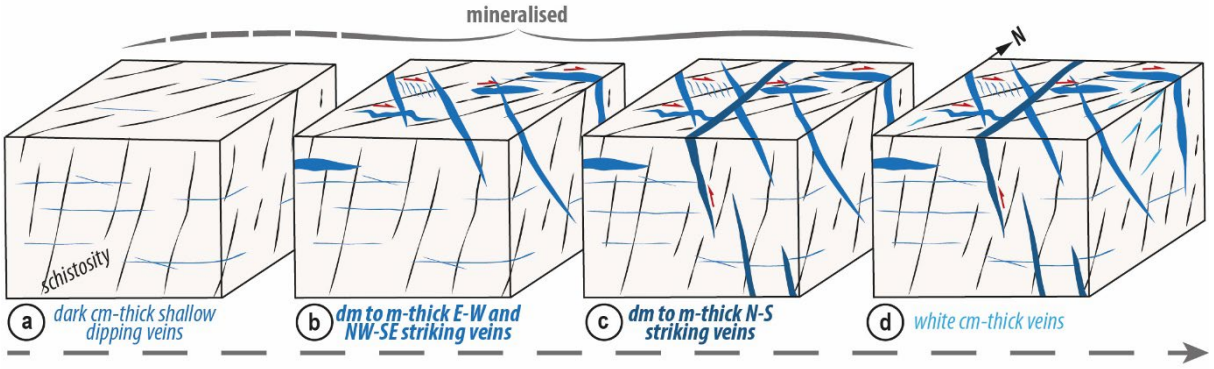

Fig. V.28. Synthetic diagram of the quartz vein chronology in the Clutha Mine. **(a)** Shallow dipping veins may have formed earlier than the E-W and NW-SE striking veins. **(b)** E-W striking veins emplaced during dextral transcurrent shearing contemporaneously with NW-SE striking veins. **(c)** N-S striking veins crosscut the previous vein systems. **(d)** Cm-thick white veins, there are non-mineralised.

V.B.1.3. Golden Quarry

The historic Golden Quarry was once actively worked for its abundant gold-rich stockwork. Golden Quarry is located in the Sheba-Fairview area, north wall of the Sheba fault (Fig. V.1).

Within several hundred meters area, an exceptionally dense network of veins is underlined, thus forming the so-called stockwork. This stockwork is distinctly characterised by mm to cm-wide quartz veins that have various orientations (Fig. V.29).

Within the stockwork area, bedding and/or cleavage display m-scale folding with gently ENE-plunging hinge line; however, this folding seems to have occurred prior to vein formation, as it does not impact the veins themselves (see shallow veins in Figure V.30).

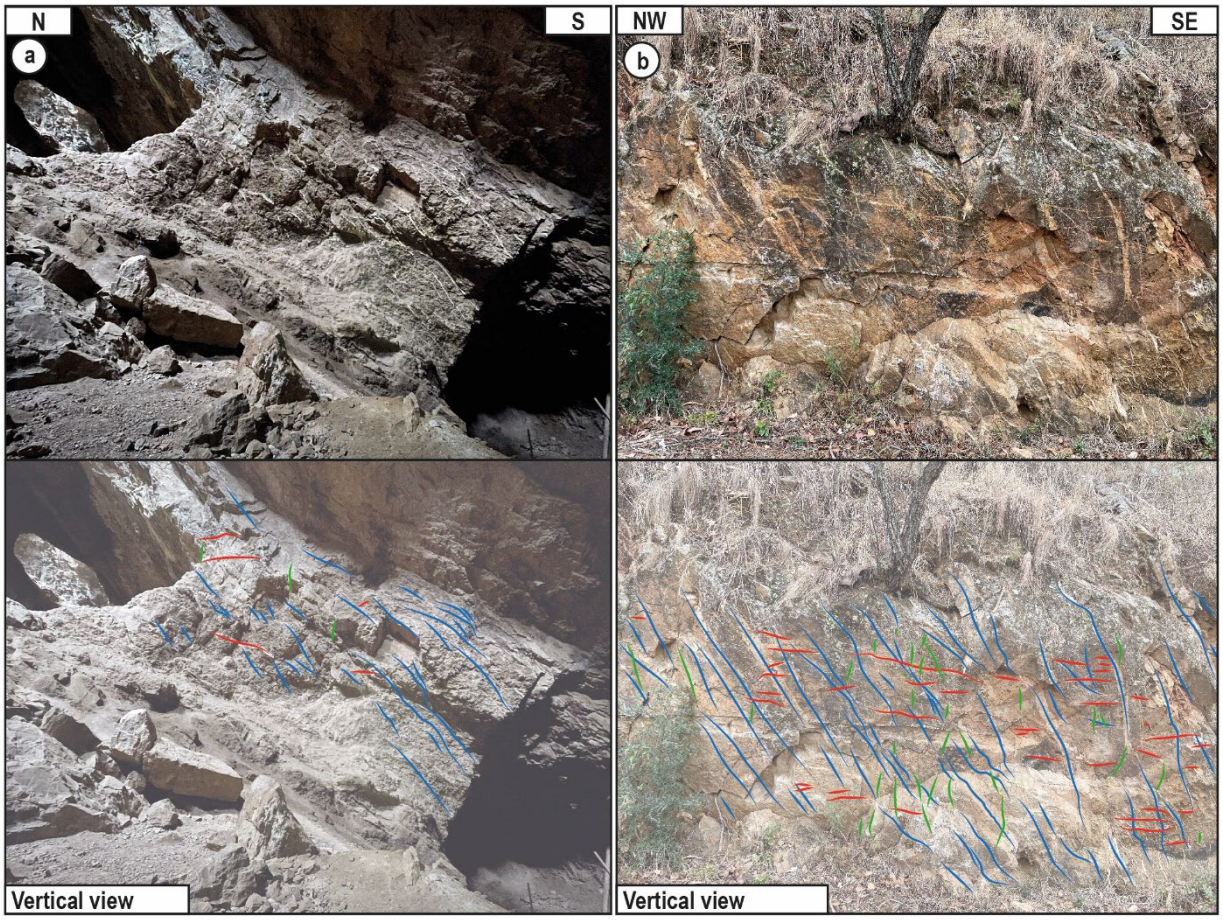

Fig. V.29. Wide shots of the Golden Quarry stockwork. **(a)** Photo and associated sketch inside the mine, prominent vein orientation is depicted, the veins predominantly dipping towards the south. **(b)** Photo and associated sketch outside the mine illustrate steep south-eastward dipping veins and shallower dipping prominent veins.

Fig. V.30. Photo and corresponding sketch of the folded bedding with sub-vertical veins, shallow dipping veins and NE-dipping veins.

These veins exhibit discernible preferred orientations, with three principal directions documented and illustrated in Figure V.31a. The predominant trend is an NE-SW strike, dipping to the southeast (Figs. V.29, V.30 and V.31b), accompanied by a multitude of sub-vertical veins striking NNW-SSE (Figs. V.29b, V.30 and V.31b). Additionally, relatively less steep veins are evident, oriented in the NE-SW striking direction and dipping towards the northwest (Figs. V.29b, V.30 and V.31b).

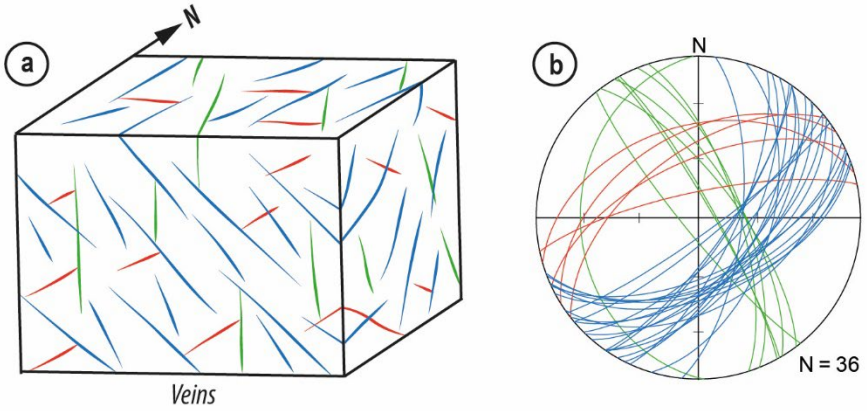

Fig. V.31. Visualisation of stockwork veins at Golden Quarry categorised by orientation. **(a)** Schematic block diagram showcasing distinct veins delineated by varying colours. **(b)** Stereonets presenting measurements of all veins within the Golden Quarry deposit, with colours matching those depicted in the previous diagram.

V.B.1.4. Shiyalongubo

The abandoned mines within the Shiyalongubo area remain inaccessible due to safety concerns. Consequently, our examination of this region was centred on roadside exposures allowing a N-S trending cross-section, where cm to dm-scale quartz veins served as proximal indicators with respect to the mine. In all this area, bedding and schistosity are broadly NE-SW striking with various dips to the SE.

Towards the southern extremity of the cross-section, two distinct vein types are observed. N-S striking veins, dipping eastwards, nearly perpendicular to the host rock's schistosity (Fig. V.32a) whereas shallow-dipping veins hosting sub-vertical mm-sized tourmalines are also prominently occurring (Fig. V.32b).

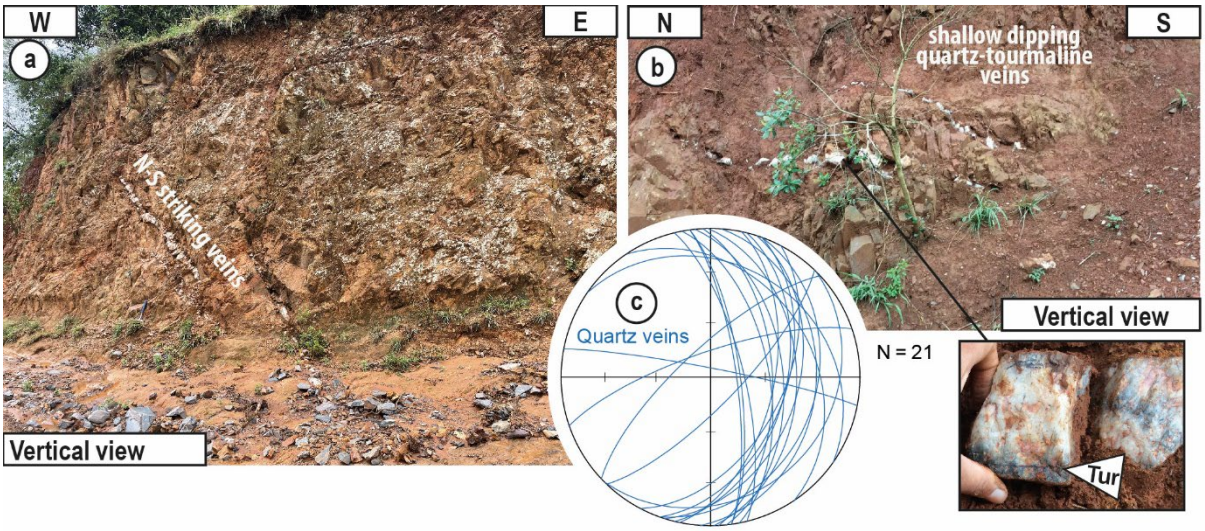

Fig. V.32. Field observations of hydrothermal quartz veins in the southern part of the cross-section of the Shiyalongubo area. **(a)** N-S striking and steeply dipping to the east quartz veins. **(b)** Shallow dipping quartz-tourmaline veins and inset with a close-up view of a vein with sub-vertical tourmaline. **(c)** Stereonets of all the veins measured in the Shiyalongubo area (Schmidt diagram, lower hemisphere).

In the central part of the cross-section, there are still shallow dipping veins cut by ENE-WSW striking and NNW-dipping small faults. Vertical WNW-ESE striking veins cut the bedding and schistosity; vertical striations have been observed on these veins.

Within the central portion of the cross-section, a series of shallow-dipping veins (Fig. V.32c) are crosscut and offset by minor ENE-WSW striking and dipping toward the NNW faults (Fig. V.33). Vertically oriented WNW-ESE striking veins (Fig. V.33) cut across the bedding and schistosity, where discernible striations are observed on the edge.

In the northernmost segment of the section, veins are parallel to the bedding and both veins and bedding appear at a slight angle to the schistosity (Fig. V.34a). Additionally, quartz pod with schistosity wrapping around it are observed (Fig. V.34b).

To summarise our observations, four vein types are discerned within the Shiyalongubo domain: i) veins perpendicular to the schistosity (N-S striking, with a E-dipping, Fig. V.32a); ii) shallow-dipping veins (Figs. V.32b,c and V.33); iii) sub-vertical WNW-ESE striking veins (Fig. V.33); and iv) bedding-parallel veins (Fig. V.34a). This various vein assemblage underscores the complexity of the geological setting.

Fig. V.33. Panorama view and associated sketch of hydrothermal quartz veins in the middle part of the cross section of the Shiyalongubo area.

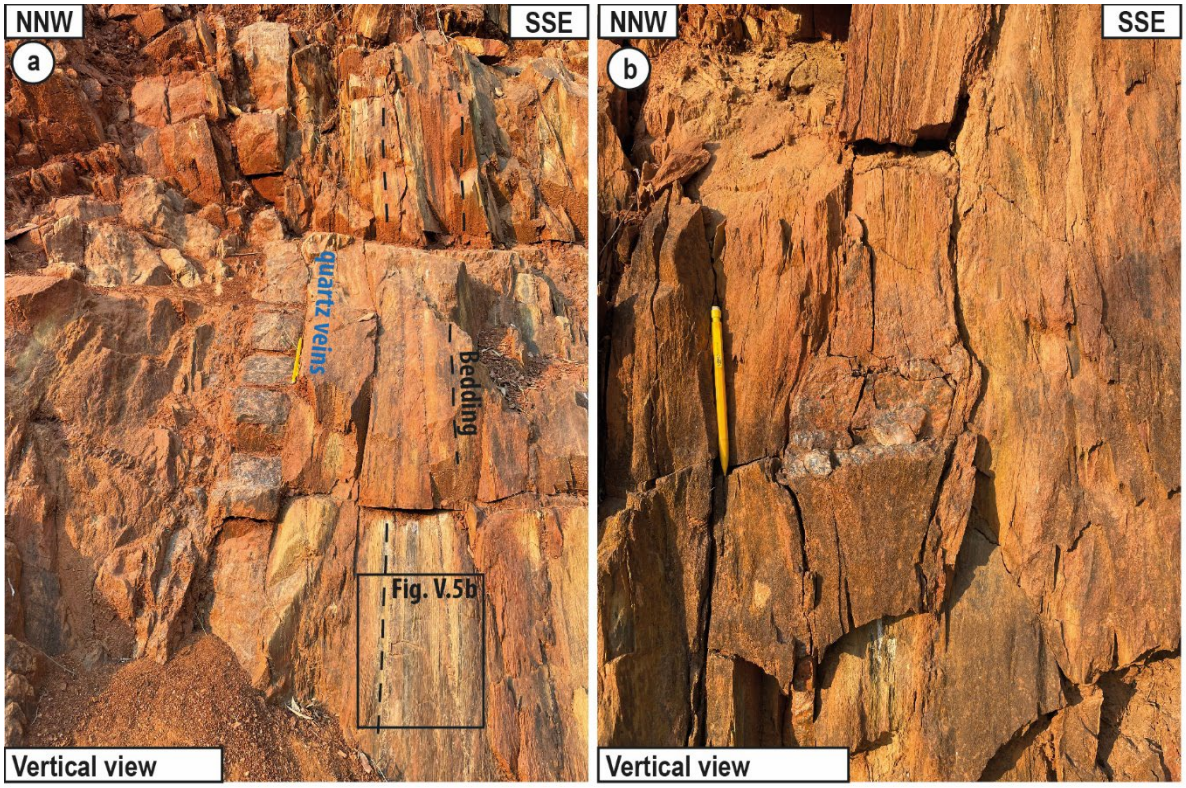

Fig. V.34. Field observations of hydrothermal quartz veins in the northern segment of the Shiyalongubo cross-section. **(a)** Bedding-parallel quartz vein. The localisation of Figure V.5d in the *Regional Deformation* section is identified. **(b)** Quartz pod with schistosity wrapping around it.

V.B.1.5. Synthesis

The northern part of the Barberton Greenstone Belt presents a diverse array of mineralised veins across various mining sites. To synthesise six gold-related quartz vein types are identified:

- **The bedding-parallel veins:** Notably present in the Agnes Mine, Victoria Mine and the Shiyalongubo area, these veins are aligned with the stratification of the host rock and can show boudinage structure. Similar structures were also identified in the Estada former Mine, in the western part of the Agnes sector, with bedding-parallel cm-thick quartz lenses.
- **Thrusting veins:** Tiger Trap, Pioneer, and Victoria mines unveil reverse veins with thrusting motion towards respectively the SSE and the E. These veins are sub-parallel to the major structural framework of the belt and seem to be more in a back-thrusting position. Comparable veins appear to have occurred at the former Estada Mine (western section of the Agnes sector) but not in a back-thrusting position: NE-SW striking, and SE-dipping quartz veins have been identified, exhibiting a reverse motion towards the NW.
- **Shallow dipping veins:** Widespread, shallow dipping veins, though abundant, often take a secondary role in mining operations. They are identified across Tiger Trap, Victoria, Clutha mines, and the Shiyalongubo area.
- **Dextral motion vertical veins:** These veins are observed exclusively in the Clutha Mine.
- **Schistosity-perpendicular steep veins:** These veins are encountered in the Clutha Mine and in the Shiyalongubo area. In contrast to bedding-parallel veins, this type seems to open perpendicular to the major structure.
- **Stockwork network or brecciated zone:** Golden Quarry exhibits these complex features characterised by a high density of quartz, likely influenced by structural control. Another stockwork system was also observed in the former Svengali Mine.

V.B.2. Microscopy study

V.B.2.1. Petrography

The mineralisation-related vein in the northern part of the Barberton Greenstone Belt is mainly composed of quartz, carbonate and sulphides, occasionally featuring rare occurrences of feldspars and tourmaline (Fig. V.35).

Although carbonates are observed in all the mineralised area, their abundance is especially pronounced within the Agnes area, and notably in the Tiger Trap, Pioneer, and Agnes mines (Fig. V.35a). In lesser abundance, the Sheba-Fairview area, the mineralised veins reveal carbonates (Fig. V.35b). The Shiyalongubo area shows quite small quantities of carbonates.

Felspars, predominantly plagioclase, have been observed in the Sheba-Fairview zone, particularly in the E-W striking veins at Clutha Mine and N-S striking veins in Victoria Mine (Fig. V.35c,d). Feldspars are also observed within a mineralised vein of the Abott's gold occurrence in the Barberton area. However, these feldspars generally show intense marks of alteration (Fig. V.35d).

Albeit in small amounts, tourmalines have been identified in the Clutha Mine (Fig. V.35e). In contrast, numerous and large tourmalines have been observed in shallow dipping veins in the Shiyalongubo area (Fig. V.35f), an indicator of the opening direction of the vein. Sulphides have been observed in almost all the mined veins but are more frequent within vein halos and will be described in the *V.B.2.3 Metallogeny* section.

V.B.2.2. Microstructures

The mineralisation-related veins exhibit a large variety of microstructures reflecting the occurrence of late to synchronous deformation events.

Numerous veins exhibit a distinctive comb and fibre texture, generally composed of quartz crystals, providing evidence of the vein formation opening dynamics (Fig. V.36a,b). Alongside these combs, secondary minerals can be encountered, including carbonates – particularly prevalent in the Agnes and Sheba-Fairview zones (Fig. V.36c,d); plagioclase – mainly within the Sheba-Fairview zone and the Barberton area (Fig. V.36e); and tourmalines – only identified in the Shiyalongubo area (Fig. V.36f). These tourmalines are accompanied by pressure shadows (see inset in Figure V.36f).

Various additional microstructures have been identified, further enhancing the complexity of the observations. Notably, asymmetrical quartz sigmoids have been documented at the Victoria Mine, revealing reverse movements top to westward (Fig. V.37a). Additionally, symmetrical quartz sigmoids are found at the Agnes Mine, indicating pure shear dominated strain (Fig. V.37b). In the Agnes zone, large-carbonate sub-vertical veins are perpendicularly and horizontally truncated, and these open fractures (Fig. V.37c) are filled by smaller carbonates and quartz fibres, underscoring a perpendicular opening pattern (Fig. V.37d,e).

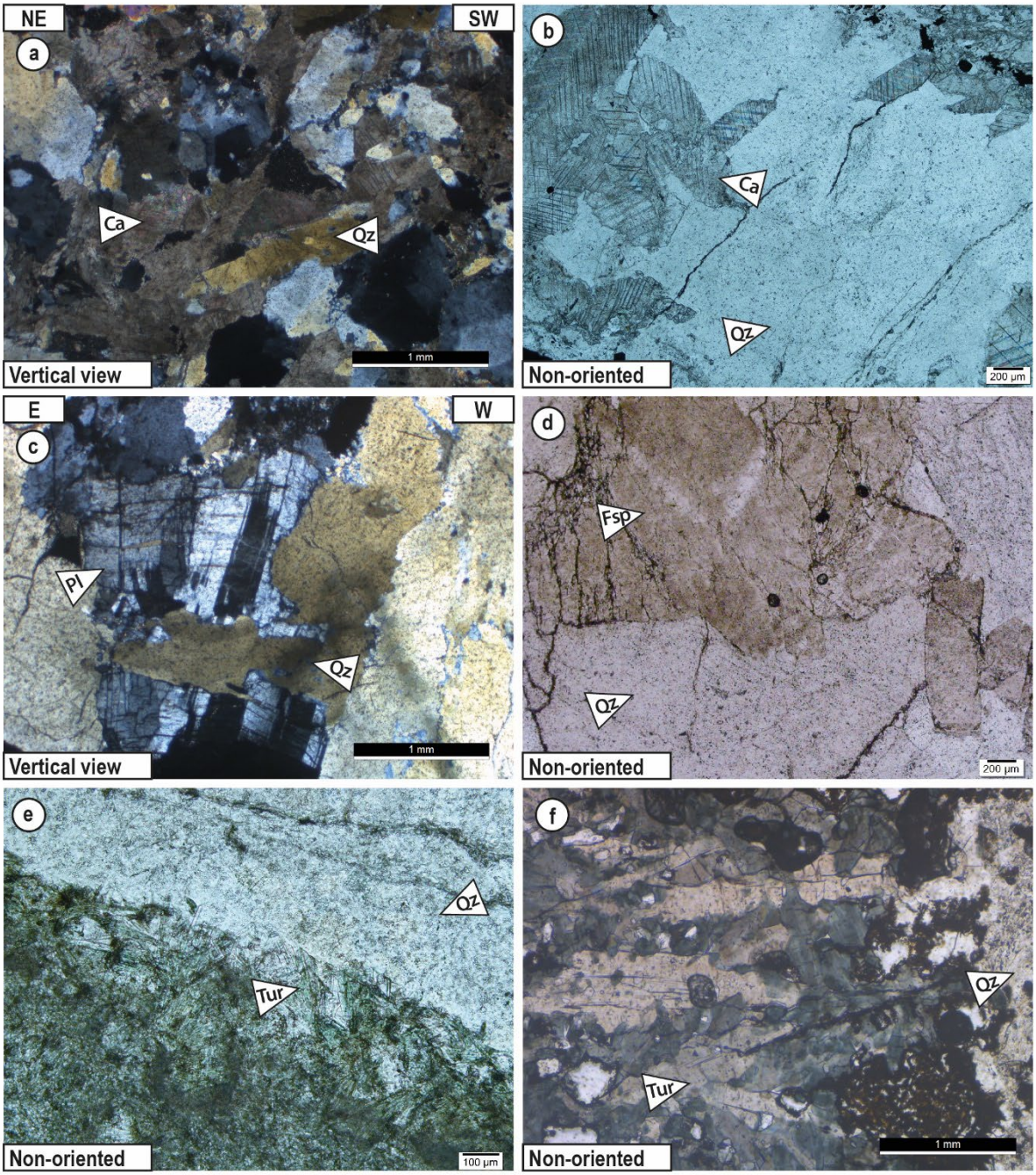

Fig. V.35. Microscopic observations of the mineralised system mineralogy in the northern part of the belt. **(a)** A vein in the Tiger Trap Mine is composed of quartz and carbonate (crossed polars). **(b)** NW-SE striking vein in Clutha Mine exhibits quartz and carbonate crystals (plane-polarised light). **(c)** Fractured plagioclase filled by quartz in a Victoria Mine vein (crossed polars). **(d)** Altered feldspars within a E-W striking vein in Clutha Mine (plane-polarised light). **(e)** Fine-grained tourmalines located in a vein edge of a NW-SE striking vein, Clutha Mine (plane-polarised light). **(f)** Shallow dipping vein composed of large, elongated tourmalines in the Shiyalongubo area (plane-polarised light).

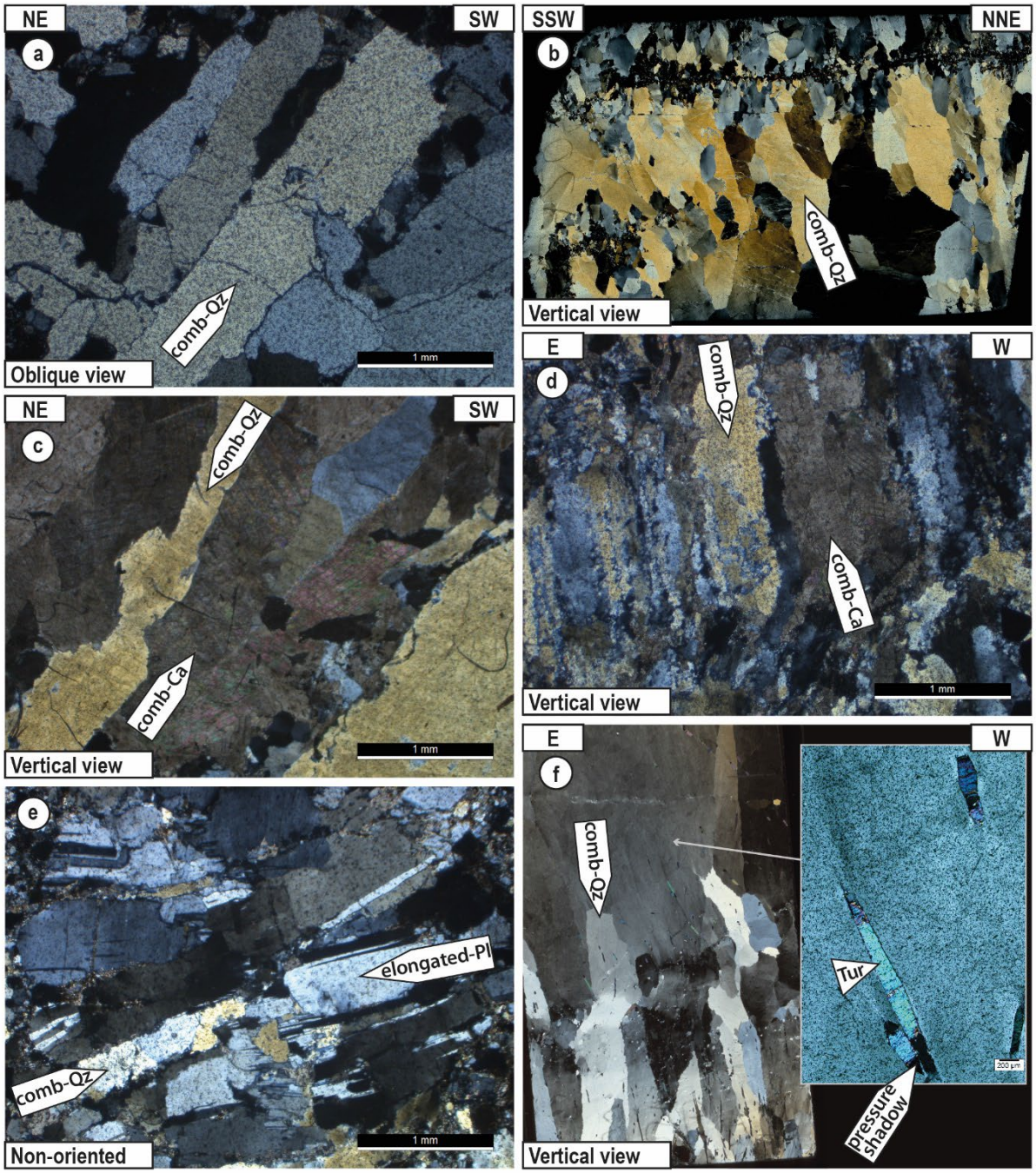

Fig. V.36. Comb texture observations of the mineralised system of the northern part of the belt. **(a)** Comb quartz in a NW-SE striking and steeply SW-dipping quartz vein in the vicinity of the Royal Sheba gold occurrence, Sheba-Fairview area, (crossed polars). **(b)** Thin-section scan of a comb quartz texture in a shallow dipping vein in the Shiyalongubo area (crossed polars). **(c)** Comb texture of quartz and carbonate crystals in a Tiger Trap steeply N-dipping vein (crossed polars). **(d)** Mineralised shallow dipping vein in Clutha Mine showing quartz and carbonate fibres (crossed polars). **(e)** Plagioclases with elongation axis parallel to comb quartz, located in the Abott's gold occurrence (crossed polars). **(f)** Thin section scan of a shallow dipping quartz-tourmaline vein in the Shiyalongubo area, showing sub-vertical comb quartz and vertically elongated tourmaline. Inset of a sub-vertical tourmaline with pressure shadow (crossed polars).

Moreover, smaller mm-thick quartz or carbonate veins with antitaxial fibres have been observed in the host-rock, exhibiting a growth trajectory aligned with the vein opening; these display a reverse motion towards the north at Tiger Trap Mine (Fig. V.37f) and towards the south at Agnes Mine (Fig. V.37g).

Quartz recrystallisation microstructure exhibits considerable variability within the observed zones. Some areas display minimal or no recrystallisation (Fig. V.38a,b,c), with local dynamic recrystallisation features as bulging of quartz (Fig. V.38d). Dynamic recrystallisation is more pronounced in specific areas, giving rise to sub-grain rotations (Fig. V.38d,e). Notably, a concentration of recrystallised planes is observed along conjugate fracture bands (Fig. V.38f,g). These fractures seem responding to sub-horizontal NE-SW trending maximum principal stress within vertical veins (Fig. V.38f) and sub-horizontal NNE-SSW trending maximum principal stress within horizontal veins (Fig. V.38g).

V.B.2.3. Metallogeny

Sulphides are notably present within the mineralisation-related veins, though they are more abundant in the vicinity of the veins themselves.

These sulphides mainly consist of euhedral pyrites, often occurring as cubes or truncated cubes (Fig. V.39a,b). There are also minor anhedral chalcopyrite and pyrrhotite that are present around the pyrites (Fig. V.39c,d). Some pyrites exhibit oxidations, visible through the presence of iron oxide halos (Fig. V.39e).

In the Agnes zone, it is relatively common for sulphides to feature fringes composed of quartz and carbonate fibres, these fringes are predominantly found in pressure shadows (Fig. V.39f).

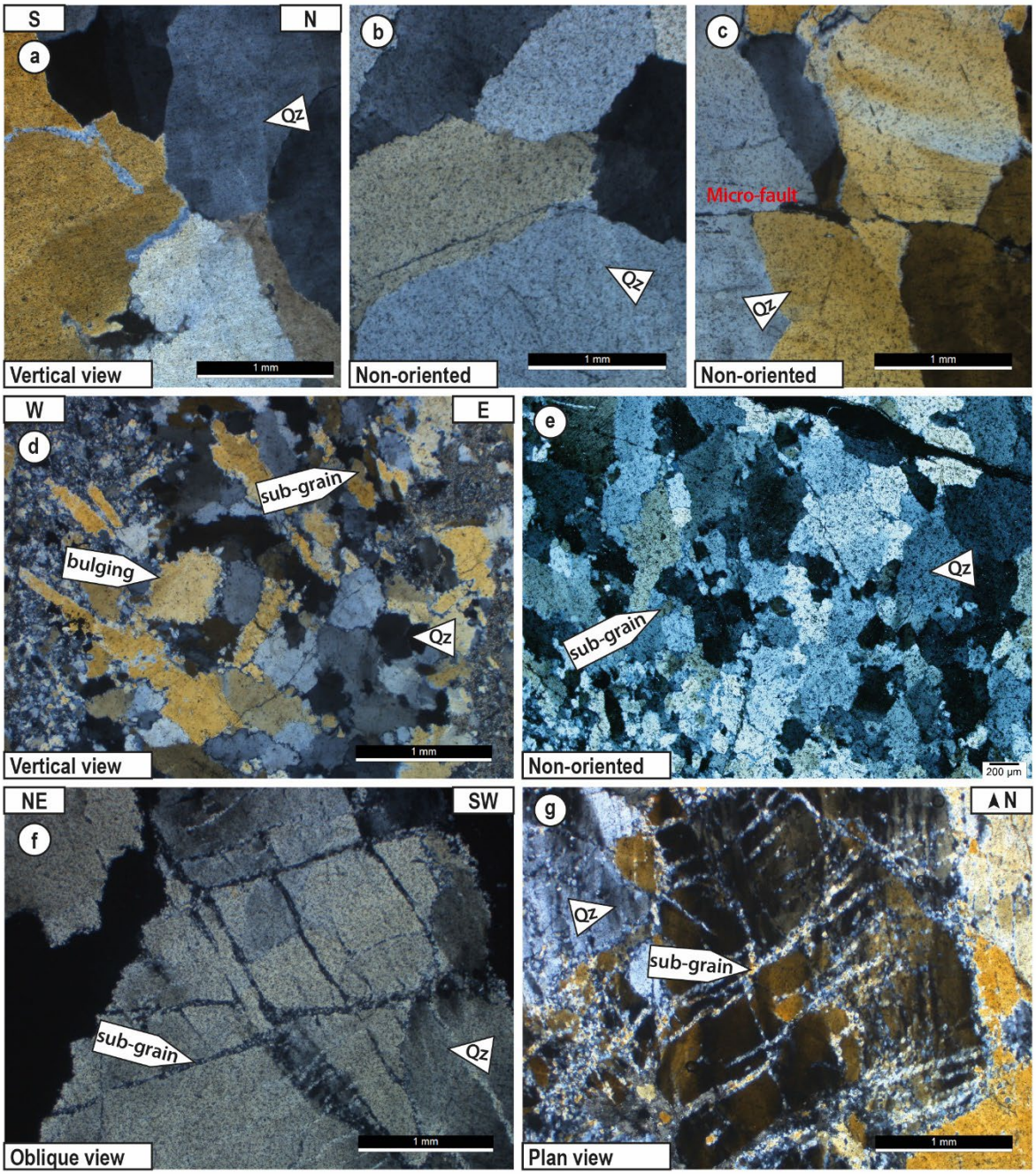

Fig. V.37. Microstructural observations of the mineralised system of the northern part of the belt. **(a)** Asymmetric quartz sigmoids indicate a reverse motion towards the west, Victoria Mine (plane-polarised light). **(b)** Symmetric carbonate clast parallel to the sub-vertical E-W striking bedding plane in the Agnes Mine (plane-polarised light). **(c)** Thin-section scan of bedding-parallel vein in Agnes Mine. This vein is fractured sub-horizontally and sub-perpendicular to its edge and the fractures are filled by quartz and carbonate (crossed polars). **(d)** Microphotograph of an open fracture filled by carbonate on edge and quartz in the central part, Agnes Mine (crossed polars). **(e)** Microphotograph of a fracture filled by comb-carbonate on edge and comb-quartz in the middle, Tiger Trap Mine (crossed polars). **(f)** Carbonate vein in Tiger Trap Mine with antitaxial carbonate fibre growth, indicating a reverse motion during the opening trajectory (crossed polars). **(g)** Antiaxial quartz fibres in an Agnes Mine vein, expressing the growth opening trajectory in reverse motion to the south (crossed polars).

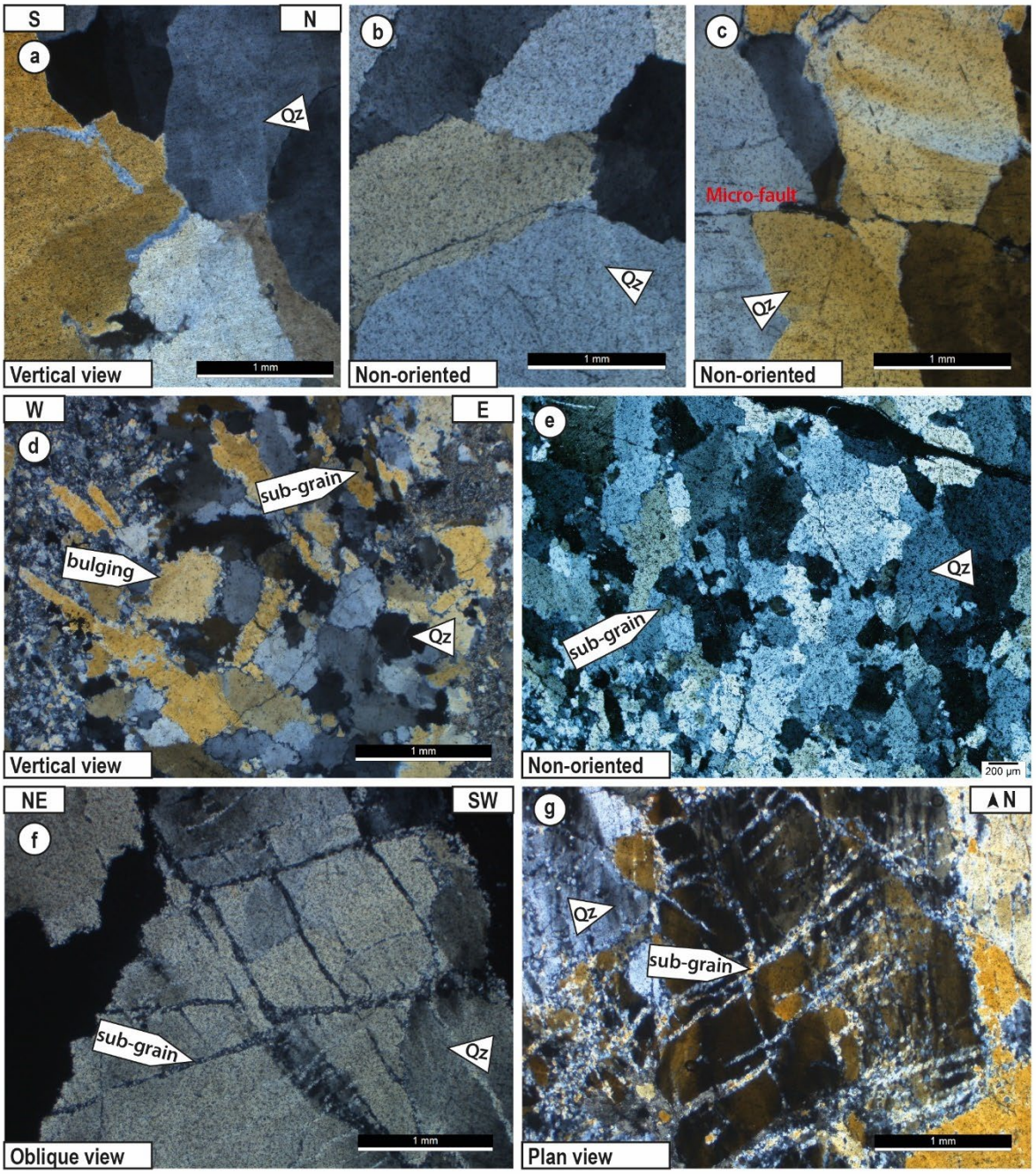

Fig. V.38. Microscopic observations of the quartz recrystallisation in the mineralised system of the northern part of the belt. **(a)** Large quartz grain unrecrystallised in a mineralised Tiger Trap E-W striking and steep vein (crossed polars). **(b)** Large quartz grain unrecrystallised in a mineralised vein in the Barberton area, Abott's gold occurrence (crossed polars). **(c)** Large unrecrystallised quartz grain offset by a micro-fault in a shallow dipping vein in the Shiyalongubo area (crossed polars). **(d)** Quartz grains with bulging and minor sub-grain rotation of quartz in a N-S striking steep vein in Clutha Mine (crossed polars). **(e)** Quartz recrystallisation feature illustrated by sub-grain rotation of quartz in a E-W striking vertical vein in Clutha Mine (crossed polars). **(f)** Recrystallised quartz forming conjugate bands in a vein of Victoria Mine, view in sub-vertical plan (crossed polars). **(g)** Recrystallised quartz located in conjugate bands in a vein of Victoria Mine, plan view (crossed polars).

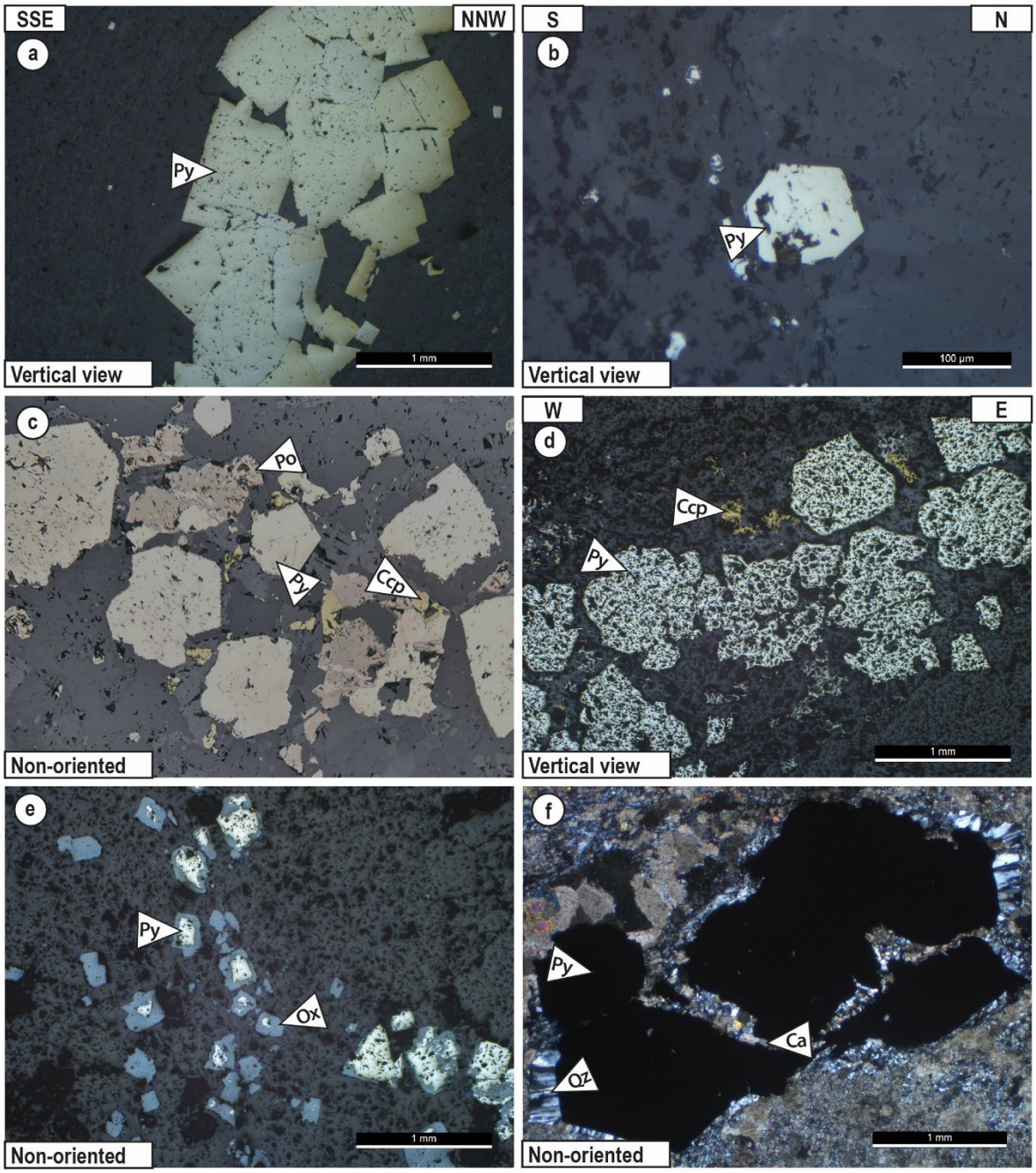

Fig. V.39. Microscopic observation of the metallogeny of the mineralised veins and surrounding in the northern part of the belt. **(a)** Bedding-parallel pyrites vein in Agnes Mine, the pyrites are euhedral and cubic in shape (reflected light). **(b)** The edge of a mineralised E-W striking steep vein in Tiger Trap Mine shows two sizes of pyrites in truncated cubic shape (reflected light). **(c)** NW-SE striking vein in Clutha Mine carrying several types of sulphides. Numerous pyrites with sparse chalcopyrite and pyrrhotite are identified (reflected light). **(d)** Mm-large pyrites and rare chalcopyrite are observed in the country rock of a E-W striking vein near the annotation n°119 in Clutha Mine (reflected light); see Figure V.23 for location. **(e)** Pyrites with an oxide halo, Abott's gold occurrence, Barberton area (reflected light). **(f)** Quartz and carbonate fringes in the pressure shadow of pyrites (crossed polars).

V.C. Late quartz vein system

Another hydrothermal vein system has been identified within the northern part of the Barberton Greenstone Belt. They are categorised as the late quartz vein system, as they appear to be controlled by another deformation event from that of the mineralised system. No indications of associated mineralisation have been detected within this system, which, therefore, appears barren. Additionally, cross-cutting relationships with the mineralisation-related system suggest that these veins are late.

V.C.1. Field macroscopy study

Three distinct categories of late-stage quartz vein systems have been discerned based on their morphological characteristics: i) en-echelon sub-horizontal veins; ii) shallow shearing veins; iii) complex quartz vein networks.

V.C.1.1. En-echelon veins

Late barren en-echelon vein morphology has been frequently identified (Figs. V.40, V.41 and V.42). These en-echelon veins are gently dipping to the north and aligned in shallow dipping to the north plane (Figs V.40 and V.41). Quartz fibres plunging to the south have been reported, perpendicular to the veins edge (Fig. V.40a). This type of vein is well exposed in Clutha Creek outcrop, situated within the Sheba-Fairview area, close to the Victoria Mine (Figs. V.40 and V.41).

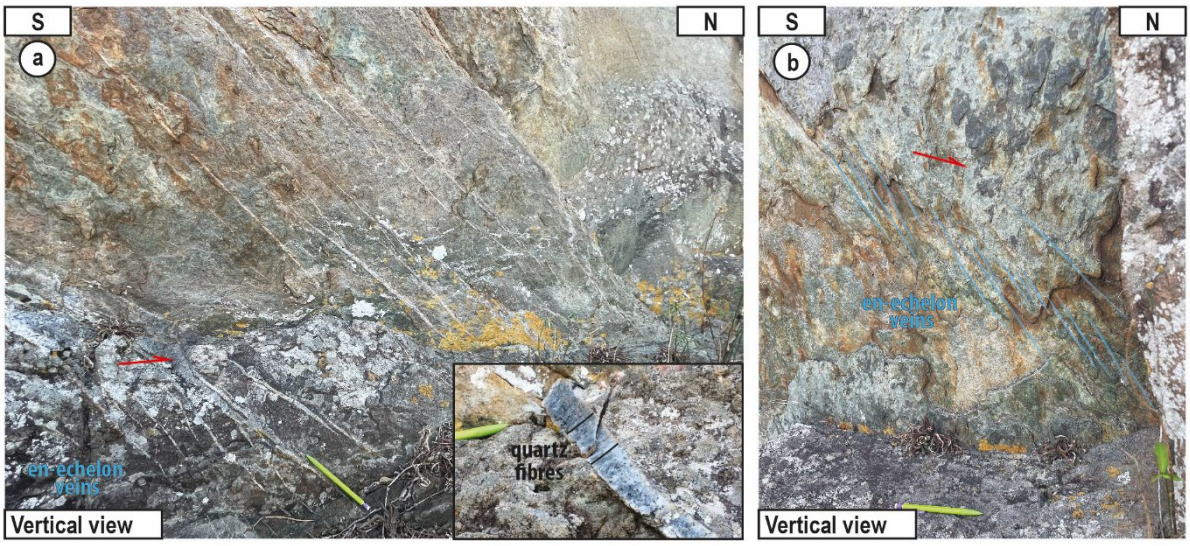

Fig. V.40. Field observations of en-echelon veins in the Clutha Creek outcrop, Sheba-Fairview area, northern part of the belt. **(a)** Photo of the en-echelon vein system and inset of a close-up view of the quartz fibres. **(b)** Photo of en-echelon veins highlighted by the blue lines.

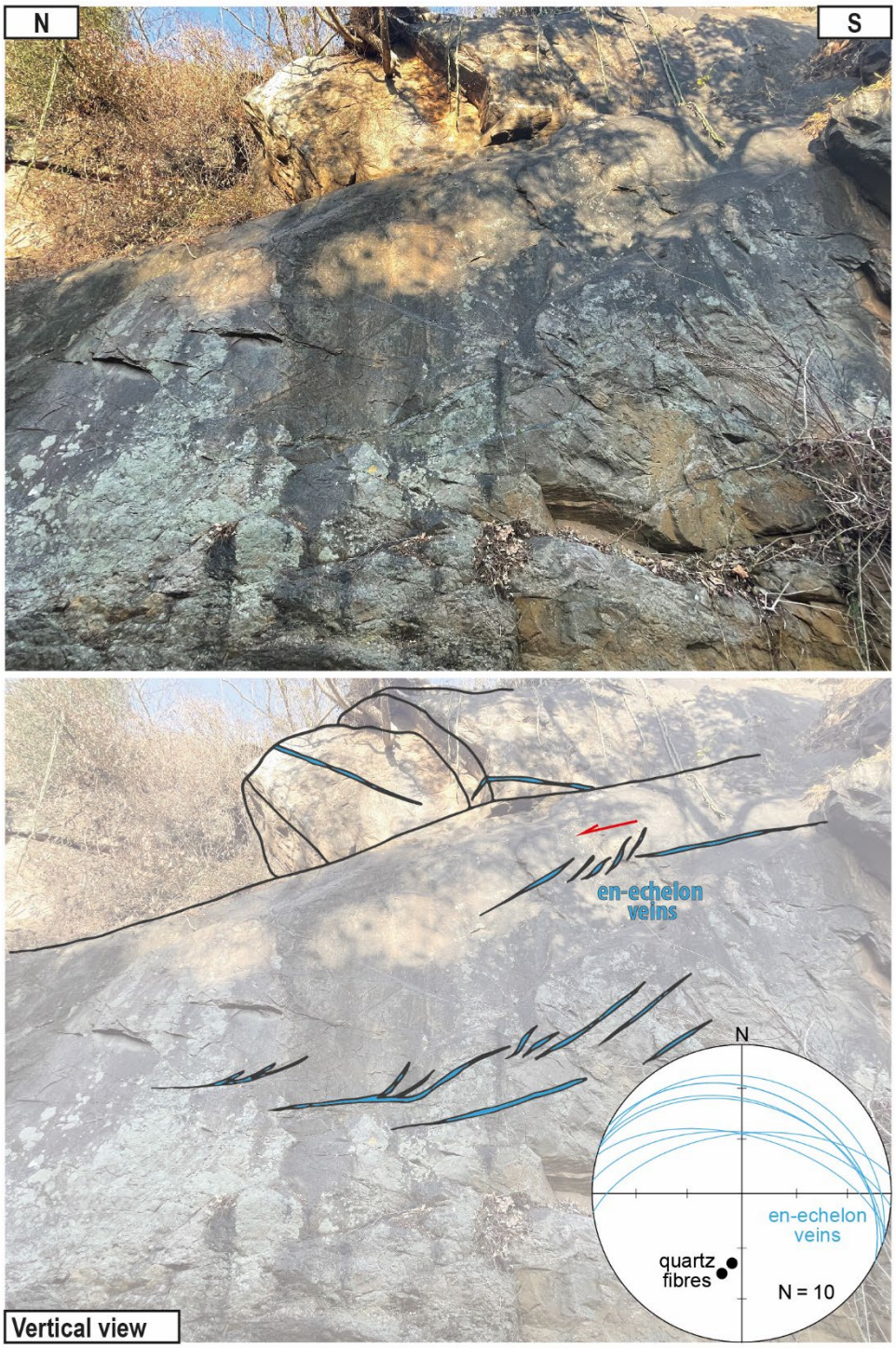

Fig. V.41. Photo and associated sketch of en-echelon veins of the late vein system in Clutha creek, Sheba-Fairview area, northern part of the Barberton Greenstone Belt. Stereonet representation of all the en-echelon vein measurements in this outcrop (blue great circles); quartz fibres orientation is also indicated (black dots) in Schmidt diagram, lower hemisphere.

Fig. V.42. Panorama and associated sketch of en-echelon veins of the late vein system near Agnes Mine, northern part of the Barberton Greenstone Belt.

It is important to highlight that these en-echelon veins differ from those observed in mineralised systems (e.g., as depicted in Tiger Trap Mine in Figure V.13c) for several reasons. First, the veins observed here lack indications of mineralisation and are thus classified as barren. Additionally, the veins observed within mineralised systems are characterised by sub-horizontal orientation with predominantly vertical fibres. In contrast, these veins dip northwards and their fibres plunge southwards, and therefore do not respond to the same stress field as the mineralised vein system.

These en-echelon veins are aligned in shallow dipping planes, which can be filled by quartz. Therefore, numerous shallow dipping veins are observed near en-echelon veins (Figs. V.41 and V.42). The white cm-thick shallow dipping veins observed in the Clutha Mine may belong to this system (e.g., Fig. V.28d).

V.C.1.2. Shallow-dipping shear veins

Several late shallow-dipping veins exhibiting a reverse motion have been documented. These veins crosscut the host rock schistosity, displaying reverse motion with top-to-SW-W shearing in places indicated by drag fold structures. They are mainly narrow (cm-thick), shallow dipping to the north/northeast and filled with quartz. Two notable outcrops exemplify this vein system.

The first is situated near the Abott's Mine (see location in Figure V.1), intersecting the N-S striking sub-vertical veins. Here, the schistosity, striking ENE-WSW and dipping south-southeast, exhibits a strong shallow NE-plunging stretching lineation. Note that this schistosity is also folded with a shallow-dipping axial plane (Figs. V.9 and V.43; see section *Regional Deformation*). A set of N-S striking vertical veins is observed within this outcrop (Fig. V.43), cutting the schistosity. A shallow NE-dipping vein cut and drag fold the schistosity, suggesting a reverse motion toward the southwest (Fig. V.43).

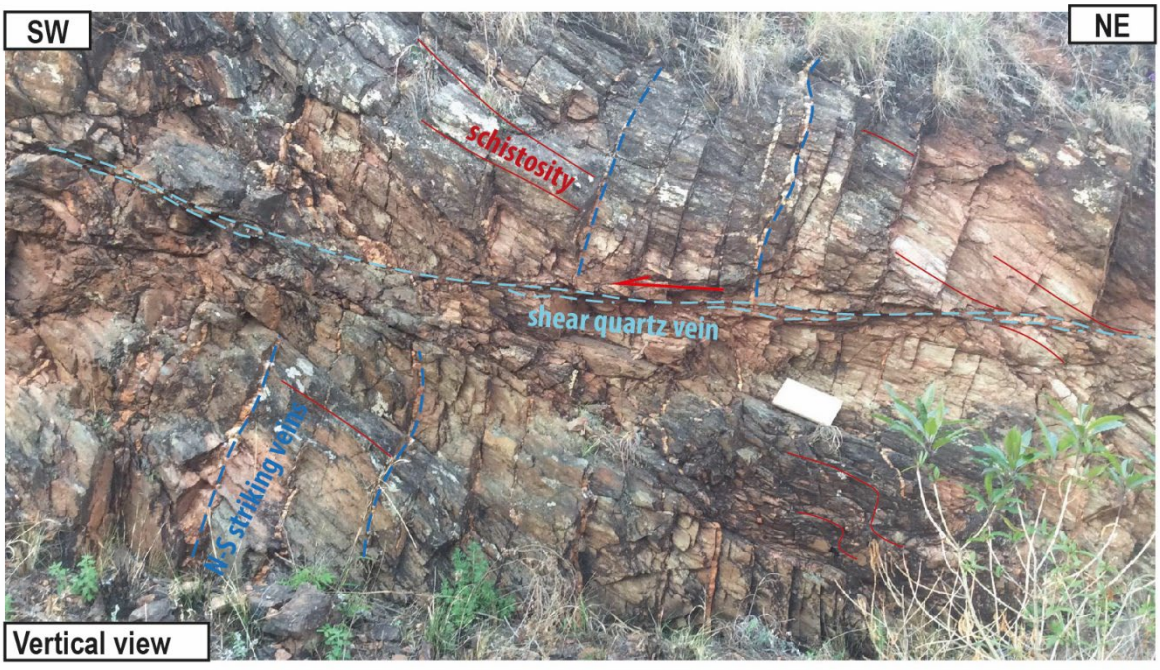

Fig. V.43. Illustration of the shear vein near the Abott's occurrence, in the Barberton area. The shearing vein (dashed light blue line) cut and created drag folds in the schistosity (red line), representing a reverse motion top to the SW. Note that the schistosity is folded with a shallow-dipping axial fold plane (visible in the bottom right corner). The shear quartz vein crosscut the steep veins of the complex vein network (blue dashed line).

The second significant outcrop is located within the Svengali Mine. In this area, the mineralisation style is similar to the Golden Quarry stockwork (see section *Golden Quarry*) according to the metallogenic map and field observations. However, a shallow E-dipping vein cutting the mineralisation-related stockwork vein system displays two distinct orientations of horizontal quartz fibres, one trending E-W to ENE-WSW, and the other trending N-S (Fig. V.44a). In the plane parallel to the E-W striking fibres, the NE-SW striking sub-vertical schistosity is drag-folded by the vein, indicating reverse motion directed westward (Fig. V.44b).

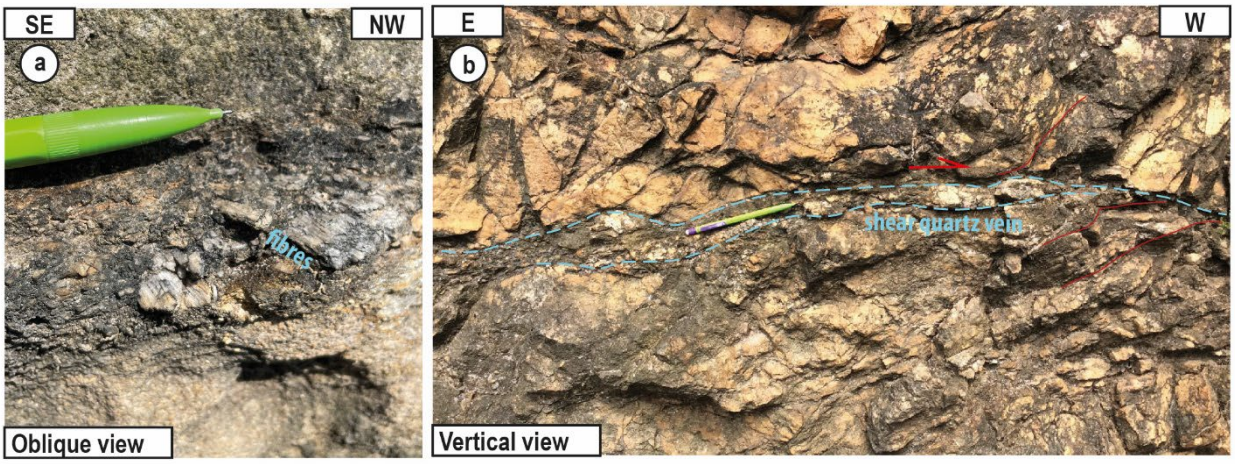

Fig. V.44. Field observations of a shearing vein in Svengali Mine. **(a)** Macrophotography of the south plunging quartz fibres. Note that everywhere else the fibres are mainly E-W striking. **(b)** The shallow E-dipping vein (blue dashed line) cut and drag-folded the schistosity (red line), displaying reverse motion top to the west.

The shallow-dipping veins observed in the mineralised system exhibit sub-vertical to steep comb and fibre quartz (see Figure V.36b,d,f of the M*ineralised Microstructures* section). In contrast, these shallow veins display sub-horizontal fibres and show reverse motion globally top to the WSW (Figs. V.43 and V.44) these veins do not therefore seem to belong to the mineralised system. Additionally, these veins are classified as late-stage phenomena, as they intersect the mineralised system (cutting and offsetting the stockwork in Svengali Mine).

V.C.1.3. Complex quartz vein network

The third type of late veins is characterised by the development of complex quartz vein networks. This type is observed in close proximity (< 100 m far) to major faults and is formed by a multitude of cm- to dm-thick veins confined within a zone making hundred to two hundred meters long (Fig. V.45). Within this region of high vein density, there are no indications of mineralisation, thus classifying these veins as barren.

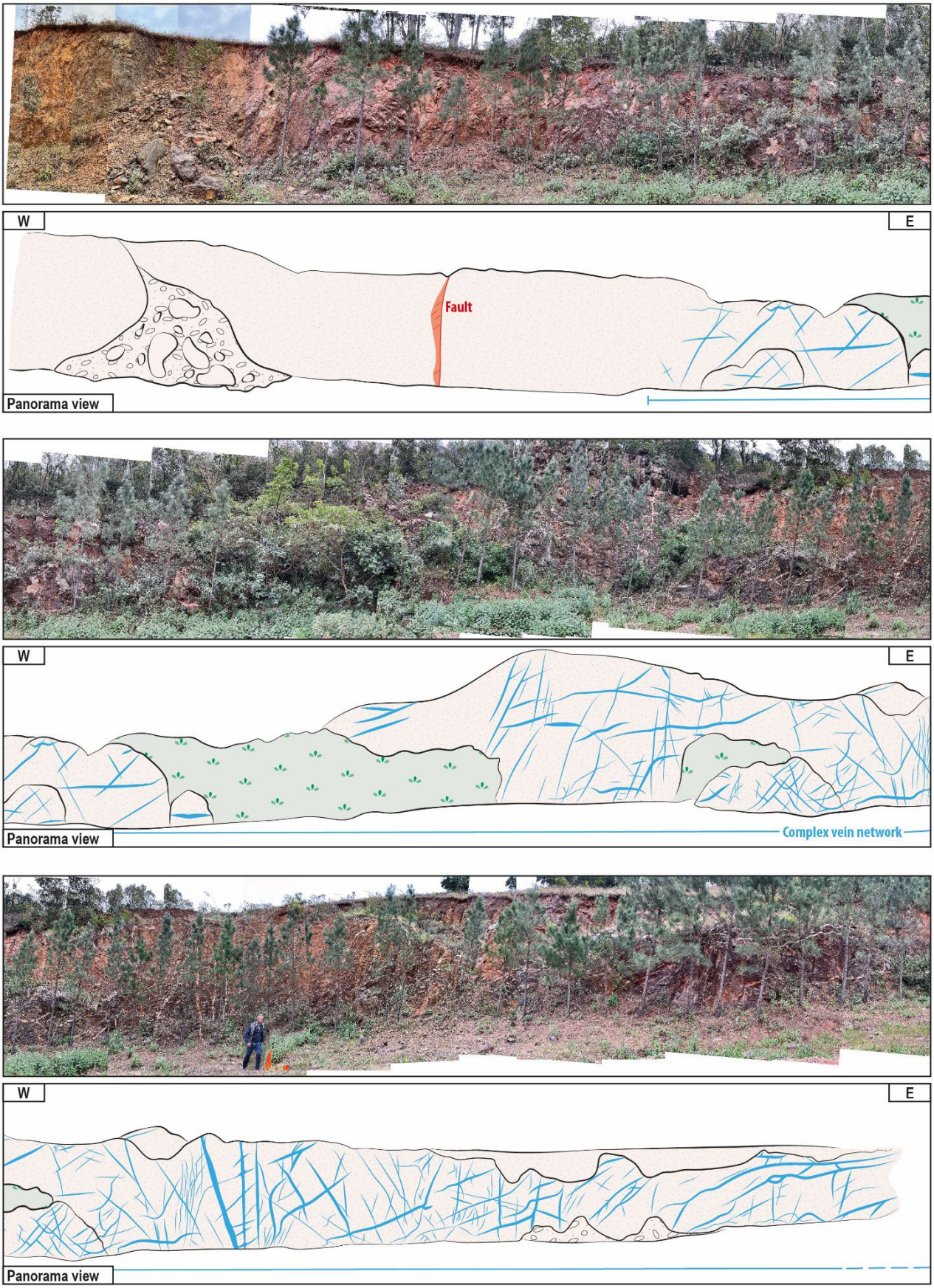

Fig. V.45. Photo mosaics depicting the west-east cross-section of the complex vein network near to Agnes Mine, and corresponding sketches.

Two principal outcrops serve as illustrative examples of this vein system, with one situated in the Agnes area and the other in the Barberton region.

The first outcrop is located near the Agnes Mine (Fig. V.1), in proximity to the Moodies fault—a prominent fault accompanied by several associated minor faults with horizontal slickenlines. Over approximately 200 meters along a E-W direction, numerous cm- to dm-thick veins of varying orientations were observed (Fig. V.45). While these veins exhibit multiple directions, three primary orientations can be discerned (Figs. V.45 and V.46a): i) sub-vertical NNE-SSW striking veins; ii) veins with a gentle dip towards the northwest, these veins are predominant; and iii) few veins displaying a gentle dip towards the southeast (Fig. V.46a). These veins often share petrological continuity or intersect with one another, making it challenging to establish a precise chronological relationship between them.

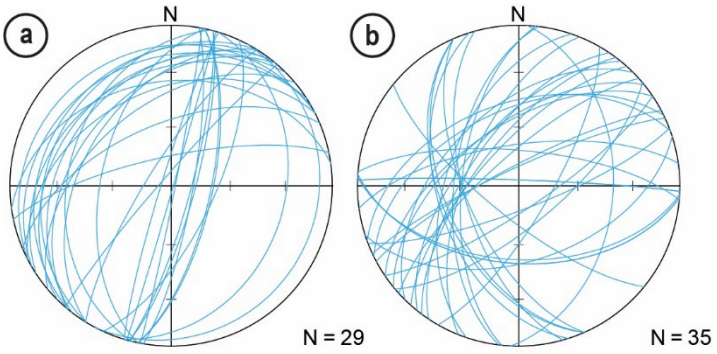

Fig. V.46. Stereonets of late quartz vein measurements in complex vein network, in the northern part of the belt, (Schmidt diagram, lower hemisphere). **(a)** Late complex vein network near Agnes Mine. **(b)** Late complex vein network on the road of the Barberton Mountains Lodge.

Another illustrative outcrop is identified along the Barberton Mountains Lodge private road, close to the Abott's gold occurrence (Fig. V.1). Once again, this site is situated within a fault relay zone where the Moodies fault is displaced by an NW-SE striking fault following the map of Lowe et al. (2012), see location in Figure V.1. Within this zone, an array of cm- to dm-thick quartz veins are observed, alongside larger m-thick sub-vertical quartz veins (Fig. V.47). The composition of these veins mainly consists of quartz and carbonate. By considering their orientations, several distinct vein types can be identified: i) sub-vertical NE-SW striking m-thick veins, with horizontal slickenlines of quartz on their edges; ii) cm-thick NNW-SSE striking veins that are steeply dipping to the west and display folding with a horizontal axial plane; iii) cm to dm-thick NE-SW striking veins with a dip towards the northwest; and iv) rare E-W striking veins (Fig. V.46b).

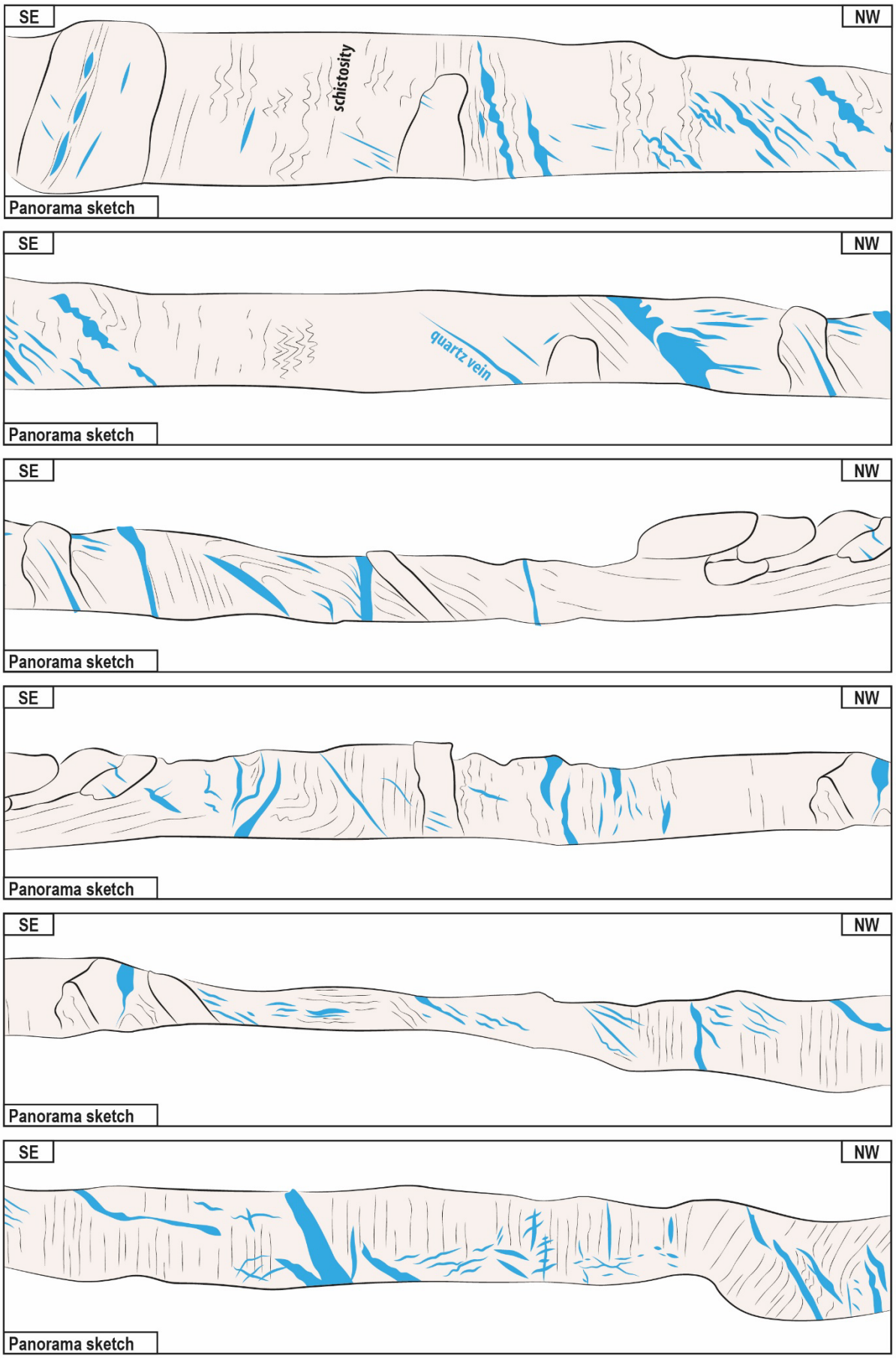
SE
NW
schistosity
Panorama sketch
SE
NW
quartz vein
Panorama sketch
SE
NW
Panorama sketch
SE
NW
Panorama sketch
SE
NW
Panorama sketch
SE
NW
Panorama sketch

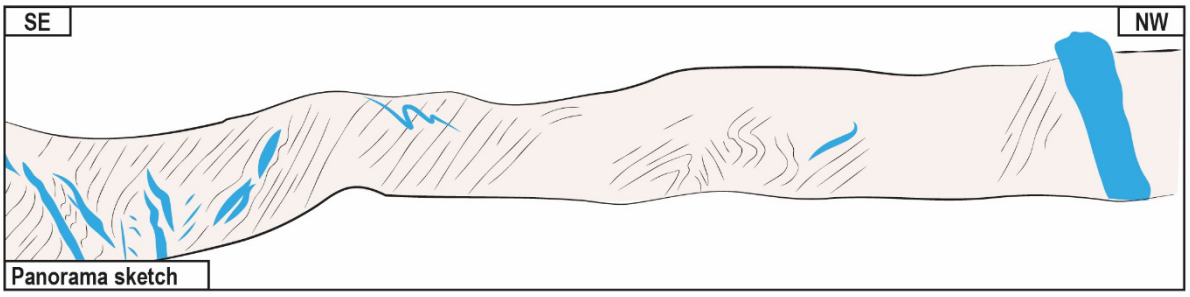

Fig V.47. Sketch of the Southeast-Northwest cross-section of the complex vein network along the Barberton Mountains Lodge private road.

Locally, E-W striking quartz-filled faults are identified, exhibiting horizontal slickensides that describe sinistral movement. In this area, they probably are bedding-parallel veins and thrusting top to the SE veins (Fig. V.47), which belong to the 'mineralised vein system' described above in section *V.B Mineralised quartz vein system*.

These complex quartz vein networks seem associated with the late system because of few characteristics. Here, the m-thick veins display horizontal sinistral motion, whereas mineralised veins in the surrounding depict reverse motion, moreover they are not mineralised.

V.C.2. Microscopy study

V.C.2.1. Petrography

The mineralogy of the late-stage system veins closely resembles the mineralisation-related system. The main distinction lies in the scarcity or absence of sulphides in the late system in contrast to the mineralised veins which are well endowed with pyrites (see section *V.B.2.3 Metallogeny*).

The veins are predominantly composed of quartz, carbonate, and feldspars (Fig. V.48a,b,c). Feldspars are notably more abundant, occasionally forming veins that are nearly exclusively composed of plagioclase (Fig. V.48d).

V.C.2.2. Microstructures

Like the mineralisation-related system, late veins display a large variety of microstructures.

In several local zones, weakly deformed quartz can be observed, often accompanied by minimal bulging at the edge of mm-large quartz grains (Fig. V.49a), or recrystallisation occurring along distinct bands (Fig. V.49b).

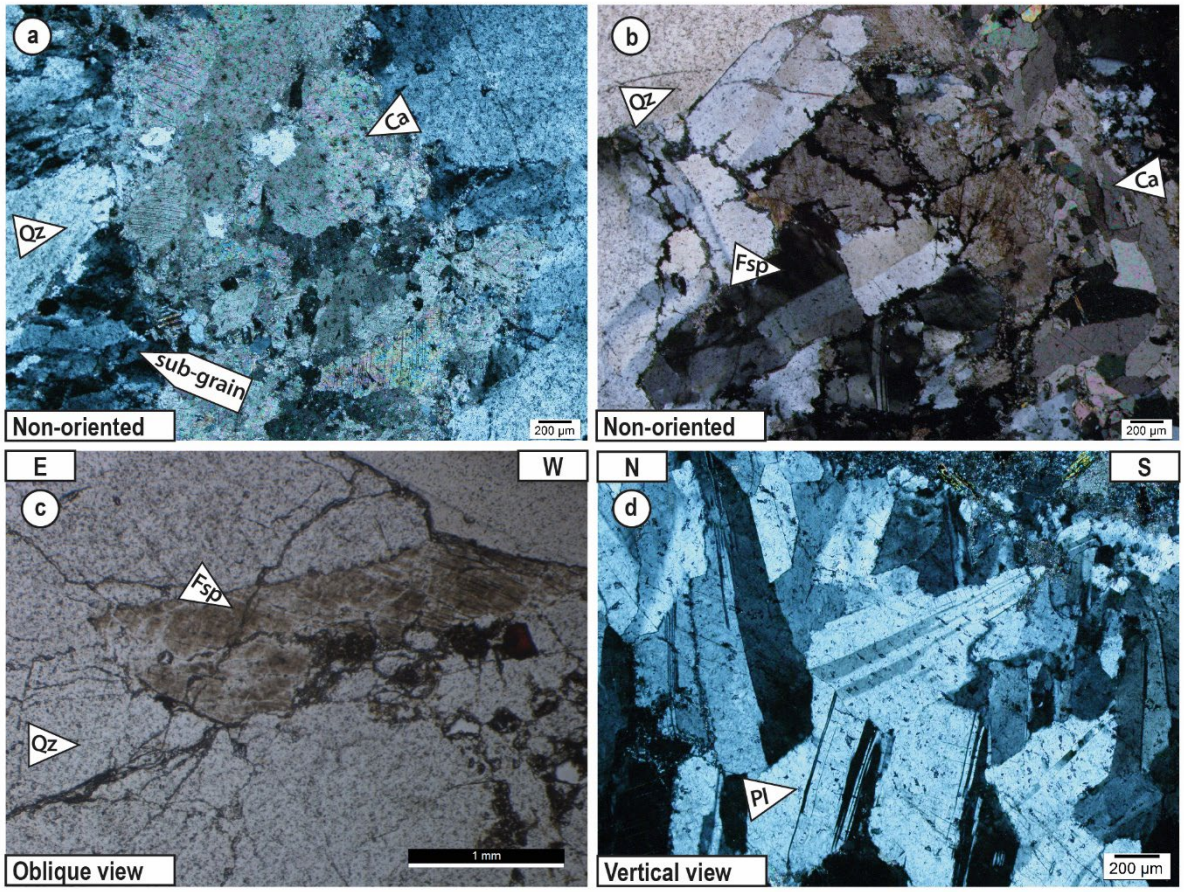

Fig. V.48. Microscopic observations of the late system mineralogy in the northern part of the belt. **(a)** A vein in a complex vein network in the Barberton area composed of quartz and carbonate. Locally the quartz is recrystallised by sub-grain rotation (crossed polars). **(b)** Another vein of the complex vein network in the Barberton area exhibits quartz, feldspars and carbonate crystals (crossed polars). **(c)** Altered feldspars within an en-echelon vein in Clutha Creek, Sheba-Fairview area (plane-polarised light). **(d)** White shallow dipping vein in the Clutha Mine composed mainly by plagioclase, with few quartz and carbonate (crossed polars).

However, in a broader context, these veins predominantly feature fibrous or comb-quartz texture, frequently carrying numerous sub-rotated grains interspersed among the pre-existing quartz grains (Fig. V.49c,d).

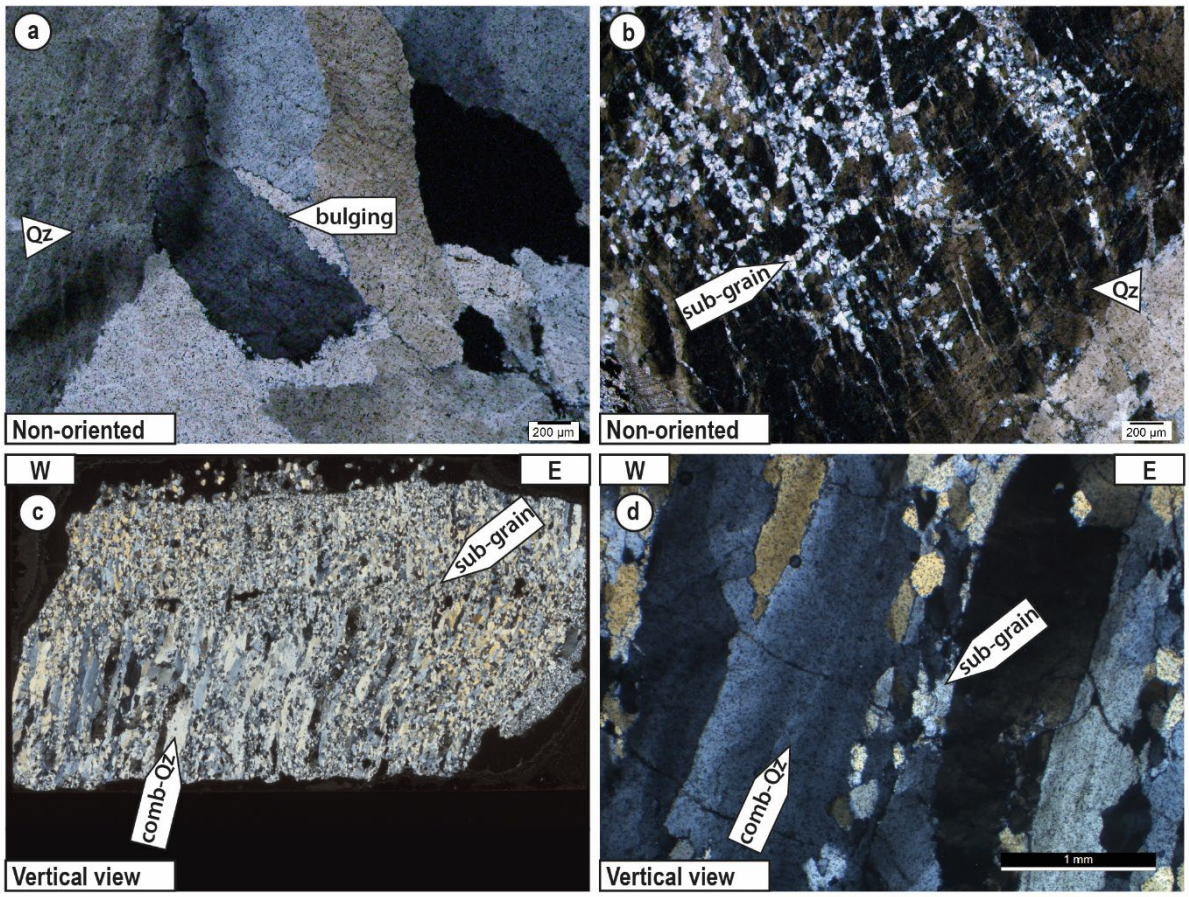

Fig. V.49. Microstructure observations of the quartz in the late system of the northern part of the belt. **(a)** Large quartz grains displaying bulging on edge, sample of the complex vein network in the Barberton area (crossed polars). **(b)** Recrystallised quartz located in conjugate bands in a vein of the complex vein network in the Barberton area (crossed polars). **(c)** Thin-section scan of an en-echelon vein in Clutha creek, Sheba-Fairview are, showing sub-vertical comb quartz and a large amounts of sub-grain rotation (crossed polars). **(d)** Close-up view of the thin section displayed in *(c)*. Sub-grain rotation occurs along comb quartz grains (crossed polars).

V.D. Interpretation

V.D.1. Main Results

The structural, microstructural, and mineralogy studies of the gold-related quartz veins in the northern part of the Barberton Greenstone Belt have uncovered several findings, which can be summarised as following:

- Deformation events have been recorded within the host rock. The bedding has been affected by a major folding event, which produced tight folds with an ENE-WSW striking axial plane (Fig. V.4c). These folds are particularly well-expressed in the Fig Tree Group rocks (Fig. V.4). With an acute angle with the bedding, a vertical NE-SW to

ENE-WSW striking schistosity has been identified (Fig. V.5). The bedding and schistosity planes are arcuate in the Sheba-Fairview area (Fig. V.1). This schistosity and the bedding occasionally display boudinage structures and folding (Figs. V.6a, V.9 and V.17). The entire area is cut by several faults, which are predominantly vertical and NE-SW striking (Figs. V.10 and V.11). Additionally, a late folding event has been observed near Barberton town, characterised by recumbent folds (Fig. V.9) and also identified by Anhaeusser (1984).

- The mineralisation-related veins exhibit various geometries, which we have illustrated through six deposit examples: Tiger Trap/Pioneer, Agnes, Victoria, Clutha, Golden Quarry, and the Shiyalongubo area.
    - Tiger Trap and Pioneer former mines are situated in the western part of the study area, north of the Moodies fault in the Onverwacht Group host-rocks. In this area, large steep ENE-WSW striking veins were mined in the past (Fig. V.12a). These steep veins show thrusting top to the south-southeast criteria, in a back thrust position with respect to the overall NW vergence of the belt. Despite sharing the same striking orientation as the country rock, these veins are commonly shallower than the bedding and schistosity in the host rocks. Additionally, several smaller sub-horizontal undulating veins have been identified (Figs. V.12d and V.13b). Mineralogically, both the thrust-related and sub-horizontal veins are composed mainly of carbonate and quartz within a fuchsitised country-rock hosting numerous disseminated pyrites in veins vicinity (Figs. V.15 and V.39b). Sub-horizontal veins exhibit microscopically sub-vertical comb quartz and carbonate perpendicular to the vein edges.
    - Agnes Mine is situated in Moodies Hill rocks between the Sheba and Moodies faults. The mineralisation-related vein system at Agnes is formed of bedding-parallel veins and lenses, oriented vertically and ENE-WSW striking. These veins exhibit symmetric boudinage structures and the lenses show symmetrical sigmoids (Figs. V.17 and V.37b). Mineralogically, the veins are composed mainly of carbonates with quartz, and the ore is surely hosted by the numerous pyrites aligned in the host rocks. However, gold not observed. Microscopically, the bedding-parallel veins show sub-horizontal truncation filled by perpendicular elongated quartz and carbonate crystals.
    - In the former Victoria Mine, located in the N-S striking, western limb of the Sheba-Fairview regional refolded fold, the schistosity is oriented about N-S

striking and is dipping steeply to the west. The vein system is formed by N-S striking steeply dipping to the west dm-thick veins, showing evidence of thrusting with top to the east motion (Fig. V.21). Other veins are also observed which are smaller sub-horizontal veins. Mineralogically veins are composed of quartz-carbonate with few plagioclase grains.

- Clutha Mine is located north of the Sheba-Fairview area, in the vicinity of the regional refolded fold hinge. In this mine, the quartz vein system is complex and expressed through sub-vertical gold-related quartz veins with three main directions: E-W, NW-SE and the N-S (Fig. V.23). The E-W striking veins exhibit clear dextral motion (Fig. V.25) and seem to be synchronous to the NW-SE striking veins. The NW-SE striking veins do not show clear motion. The N-S striking veins locally show vertical reverse motion and cut the two first vein systems (E-W and NW-SE striking veins, Fig. V.28). A set of two cm-thick sub-horizontal veins are also observed. Somes are associated with the mineralisation-related veins (Fig. V.24), and others are shallow-dipping white veins gently dipping to the west and seem barren (Fig. V.28). All of gold-related veins (i.e., exploited) exhibit a similar composition with quartz, carbonate, numerous sulphides and few plagioclase (Figs. V.35b,d and V.39c). The barren shallow dipping veins are composed of quartz-carbonate with numerous K and Na-feldspars (Fig. V.48d).
- The Golden Quarry is a former stockwork mining operation in the Sheba-Fairview area, situated north to the Sheba Fault, in the Eureka Syncline. Although this area contains several cm-thick veins, three main systematic directions were identified: i) NE-SW striking and steeply dipping to the southeast, ii) NE-SW striking and dipping to the northwest, and iii) NW-SE striking and vertical veins (Fig. V.31). All these veins are composed of quartz and carbonates.
- The Shiyalongubo area is located along the Barbrook fault (Fig. V.1) in the eastern part of the study area, numerous deposits and occurrences are on site. The strike of the schistosity and bedding in the area is ENE-WSW, similar to Agnes ones. In this area, sub-horizontal veins, bedding-parallel veins and schistosity-perpendicular veins are identified (Figs. V.32, V.33 and V.34). Mineralogically the veins are composed of quartz with rare carbonate, and the

sub-vertical veins show vertical tourmaline and comb-quartz (Figs. V.35f and V.36b,f).

- In addition to the mineralised system, a system of late veins has been identified. The veins show three different morphologies: i) shallow-dipping veins - en-echelons veins (Figs. V.40, V.41 and V.42); ii) shallow-dipping veins with shear motion top to the southwest (Figs. V.43 and V.44); and iii) complex vein systems (Figs. V.45 and V.47) located in proximity to major faults and minor sinistral faults. All these vein systems locally intersect the mineralised veins and are therefore considered late. Moreover, these veins do not seem to be related to the gold mineralisation (i.e., there is no sign of mining activity in their vicinity) and are therefore considered barren.

All these observations collectively provide valuable insights for establishing the different structural controls that have affected gold mineralisation and other veins in the northern part of the Barberton Greenstone Belt.

V.D.2. Vein formation model for the northern domain

The country rock deformation features within the northern part of the Barberton Greenstone Belt suggest the existence of a NW-SE to NNW-SSE shortening event, as classically described in the literature (see the section *II.B.3 The tectonic models* in the *Geological Setting* chapter). This shortening event forms the tight folds of the bedding and a NE-SW to ENE-WSW striking regional schistosity. From a structural point of view, this deformation is the cause of large kilometre-wide folds, similar to our Df deformation event in the southern part of the BGB (see Chapter IV *Southern gold provinces*). In the literature, authors agree that there are several successive episodes of this shortening event (e.g., de Ronde and de Wit, 1994; Lowe, 1994; Dziggel and Kisters, 2019). Different episodes of Df (Df1, Df2, Df3…) would therefore interact for forming the final architecture of the northern part of the belt. The NE-SW to ENE-WSW striking structures are folded in the Sheba-Fairview area with a global NW-SE axial plane (the Fairview-Sheba regional refolded fold). In the literature, this folding event is interpreted as a late episode of the NW-SE striking regional shortening causing the rocks of the belt to curve against adjacent TTG bodies, creating this regional refolded fold. Another late, local folding event is recorded in this study (Fig. V.9), with a horizontal axial plane, and is attributed to local extension.

The different deposits have been divided into four main types of veins, which are formed by different mechanisms (Fig. V.50):

- **Thrust-related- veins and associated sub-horizontal veins** were observed in Pioneer, Tiger Trap and Victoria. These veins generally cut the bedding and the schistosity planes and exhibit drag-fold on their edge. The thrust-related veins strike parallel to the closest fault, (i.e., at Pioneer and Tiger Trap ENE-WSW and at Victoria N-S Fig.V.1. Surprisingly, back thrusts are frequent to dominant (top to the SSE at Pioneer-Tiger Trap, and to the East at Victoria). These veins are therefore consistent with a NW-SE to NNW-SSE shortening at Tiger Trap-Pioneer and E-W one at Victoria. However, if we unfold the structures of the Victoria zone about a steep axis corresponding to the intersection of the eastern and western limb with the NW-SE-striking steep axial plane of the regional reclined, refolded fold train, they can be interpreted to have formed by the same NW-SE to NNW-SSE shortening event. In the vicinity of these thrust-related veins, numerous sub-horizontal veins, sometimes undulating, have been observed. Microscopically, the sub-horizontal veins exhibit sub-vertical elongated quartz, carbonate and tourmalines, perpendicular to the vein edges (Fig. V.36b,d,f). Therefore, these sub-horizontal veins are interpreted as mode I opening veins, formed during horizontal shortening. The combo of steep thrusting veins and mode I opening sub-horizontal veins is a strong argument in favour of a structural control guided by a NW-SE to NNW-SSE horizontal shortening.
- **Bedding-parallel veins** were identified in the northern part of the Barberton Greenstone Belt. They are often observed deformed in the host rocks, frequently affected by boudinage (Agnes and Victoria mines, Shiyalongubo area; Figs. V.17, V.22 and V.34). Indeed, the boudinage features and sigmoidal lenses are often symmetrical, related to pure shear strain. The orientation of the boudins is observed in both orthogonal planes, suggesting chocolate-tablet boudinage globally in the ENE-WSW striking plane. The bedding-parallel veins are therefore interpreted to have formed during coeval vertical and NNW-SSE striking horizontal extension compatible with a NNW-SSE striking horizontal shortening event, normal to the boudins. Sub-horizontal intra-vein fractures are also observed with sub-vertical quartz and carbonate filling, perpendicular to the vein edge (Fig. V.37c,d,e). These filled fractures support an interpretation of vertical extension, opening similar to the sub-horizontal veins previously addressed.

- **Stockwork zones** are observed in vicinity of regional faults (high fluid flow area?). In these areas, numerous cm-thick veins with 3 main orientations occur (Fig. V.31). At Golden Quarry, the more represented orientation is NE-SW striking and steeply dipping to the southeast, while numerous NE-SW-striking veins, dipping to the northwest are subsidiary. These two directions can correspond to conjugate veins formed during a NW-SE shortening event. A third set of veins is vertical and NW-SE striking. These veins are perpendicular to the structure, similar to the NW-SE striking veins of the Clutha complex and can correspond to accommodation fracture veins or tension gashes formed during the ongoing NW-SE shortening and shearing.

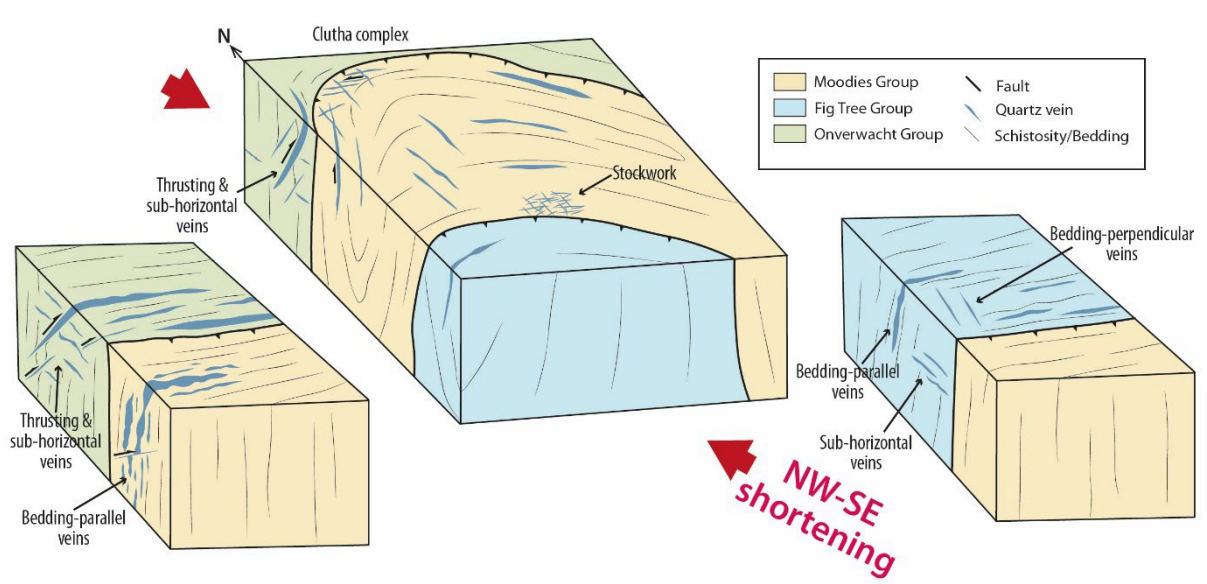

Fig. V.50. Schematic block models illustrating the different types of gold-related quartz veins and their location in the northern part of the Barberton Greenstone Belt. Note the diagram is only for schematic representation, is not to scale.

- **Clutha Mine Complex** hosts several gold-related veins different, in term of orientation, from those previously presented. In the galleries, we observed mineralised veins E-W, NW-SE, and N-S striking, all steep (Fig. V.23). The E-W veins exhibit clear dextral motion which can be formed during a shortening striking WNW-ESE to NNW-SSE. The NW-SE striking veins form small-scale en-echelon tension gashes, perpendicular to the main structures of the belt and are interpreted to have formed during NW-SE shortening. The N-S veins show reverse motion and appears late to the two first sets of veins. The tectonic event responsible for these N-S veins is less obvious to characterise, but it can also be compatible with the NW-SE shortening event.

All these gold-related veins of the northern part of the Barberton Greenstone Belt show different morphologies and orientations. However, they all seem to be formed under a NNW-SSE to NW-SE horizontal shortening corresponding to what we call here the Df deformation in the southern part of the belt, i.e., the one responsible for the main regional shortening and major fold/thrust formation (Travers et al., 2023).

Another system was observed, considering late and barren in this study. Several types of veins have been classified in this system.

- The en-echelon veins system shows shallow dipping veins oriented globally WNW-ESE to E-W, presenting vertical fibre (Figs. V.40a and V.49c). These veins are interpreted as the result of a horizontal shortening, and the echelons indicate reverse motion to the north-northeast, which cannot be associated to the main NW-SE horizontal shortening. Parallel to the alignment of the en-echelon veins, shallow-dipping veins are also observed but do not show any motion.
- Another system of shallow dipping veins was identified, exhibiting horizontal shearing motion top to the southeast and to the east characterised by the gently east-dipping quartz fibres in the veins or northeast-directed lineation in the host rock. If lineation in the host rocks may be associated with a NE-SW directed shearing or to stretching lineation parallel to recumbent folds occurring in the area remains in discussion. However, the occurrence of drag-folding of the host rock in reverse motion against the veins favour the first hypothesis, i.e., NE to SW verging shearing (Figs. V.43 and V.44). These veins and motion can be formed by a NE-SW shortening event.
- The last type of veins in the late and barren system is the complex vein networks, located in the vicinity of major and second-order faults. The second-order faults exhibit sub-horizontal striations and sinistral motion. The complex vein networks are formed by numerous veins with a NW-dipping and NE-SW striking orientation that comes out (Fig. V.46). Locally, quartz fibers were observed on these steep NE-SW striking veins, indicating a horizontal motion. We interpreted these vein complex networks as controlled by the faults that border them and that can open in sinister movement. This movement is also compatible with a NE-SW shortening. However, and because some of the veins in the network vein complex may show reverse criteria (Fig. V.47), a control by the Df event cannot be entirely excluded and, in this case, veins can be reactivated during the second NE-SW shortening. This late and barren system looks, therefore and at contrary to the mineralised systems which are controlled mainly by thrusting with

predominantly vertical movement, more associated with predominant horizontal movement (Fig. V.51). If these strike-slip motions result from transpression or transtension remains difficult to decide even if the apparent dominance of reverse motion can favour transpression.

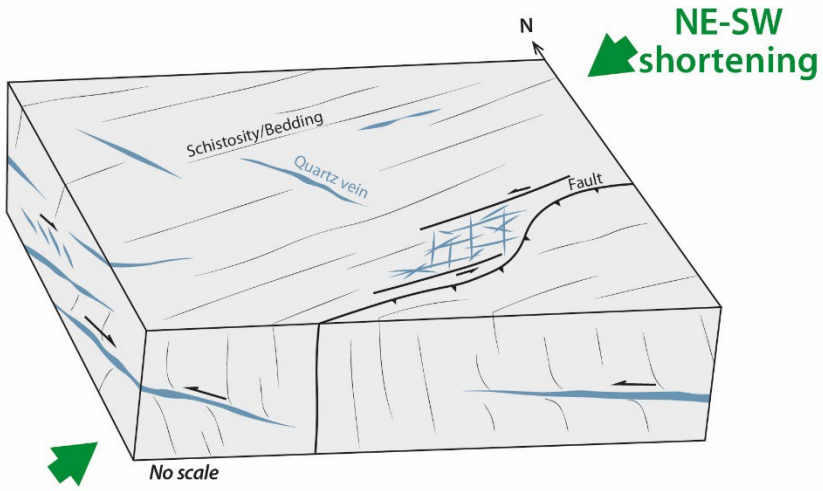

Fig. V.51. Illustrative diagram of the overall structures of the late and barren system.

These proposed structural controls of the different vein systems consider both the deformation inventory of the host rocks and of the vein systems within the northern part of the Barberton Greenstone Belt. Two main hydrothermal systems have been highlighted, documented by numerous field and microstructural observations. However, several points, such as the high concentration of high-grade mineralisation deposits in the Sheba-Fairview area and the weak observation of NE-SW shortening records in the surrounding rocks, still need to be understood. All these points will be discussed further in the general discussion of this PhD.

V.E. Discussion

V.E.1. Structural control of the gold mineralisation

In the previous section, we propose an interpretation of the structural control of the hydrothermal systems of the northern part of the Barberton Greenstone Belt. We suggest that the gold-related vein system is formed during a NW-SE to WNW-ESE horizontal shortening event, which produces several different vein morphologies. Another late and barren hydrothermal system is also identified and is formed during a NE-SW shortening event. Previous works on the northern part of the Barberton Greenstone Belt suggest that the gold mineralisation occurs during an extensional event after the craton stabilisation (Otto et al., 2007;

Dirks et al., 2009, 2013). Our extensive field, structural, and microstructural investigation of the mineralisation-related veins and textural findings of gold-related features do not support an extensional setting. Instead, other authors proposed that gold mineralisation may have formed during a late phase of the regional NW–SE regional shortening (de Ronde et al., 1992; Gloyn-Jones and Kisters, 2019; Jones and Kisters, 2022; Pintos Cerda et al., 2022). This late phase involved the reactivation of older geological structures, providing a fluid path for the deposition of gold (Jones and Kisters, 2022; Pintos Cerda et al., 2022). Although some of their observed mineralisation morphologies differ from those shown in this study, our findings seem consistent with their interpretation (see below).

We characterise several morphologies in the gold-related vein system via the example of six deposit areas which shows: bedding-parallel veins (Agnes, Victoria mines), steep thrusting veins associated with sub-horizontal veins (Tigger, Pioneer, Victoria mines), stockwork areas (Golden Quarry), schistosity-perpendicular veins are dextral motion veins (Clutha Mine). Gloyn-Jones and Kisters (2019) observed bedding-parallel veins with boudinage structure and sub-horizontal filled fractures characterised as mineralised boudin necks in the Fairview Mine. Jones and Kisters (2022) also observed bedding-parallel veins and bedding-parallel concentrations of sulphides in Fairview and Thomas deposits. These structures are similar to our observed bedding-parallel veins. Quite a few articles mentioned large shallow dipping to the southeast shear mineralised veins with thrusting motion top to the northwest in Sheba and Fairview mines (Gloyn-Jones and Kisters, 2018, 2019; Pintos Cerda et al., 2020, 2022). Those morphologies differ from our observation even if we also observed thrusting shear veins, but they are either steeply dipping to the northwest or carried reverse motion top to the southeast, in back-thrust position. Their observations were made in active and intensive mined areas with high-grade mineralisation, which raises the question of whether our observed steep shearing veins are second-order veins of these large shallow highly-mineralised shear areas. The sub-horizontal mode I, referred as ‘extensional veins’ are also observed (Gloyn-Jones and Kisters, 2019; Pintos Cerda et al., 2020, 2022), although Pintos Cerda et al. (2020) identified several sets of these veins. The schistosity-perpendicular veins, which are developed at Clutha and in the Shiyalongubo area are not frequently described in the literature except Jones and Kisters (2022) that mentioned such type of vein and associated them also with a NW-SE shortening event.

Many of the vein morphologies observed in this study bear similarities to some of the active veins described in the Sheba-Fairview complex, but there are still some differences remaining. Anyway, gold mineralisation in the northern part of Barberton appears to be controlled by a global NW-SE horizontal shortening, consistent with interpretations made at the Sheba and Fairview mines.

V.E.2. Significance and timing of deformation event

We characterised the structural control of the gold mineralisation as a NW-SE shortening relative to the Df event already defined in the southern part of the Barberton belt (Travers et al., 2023). The Df deformation corresponds to several successive or continuous episodes of NW-SE shortening (see the first paragraph of the section '*V.D.2 Vein formation model for the northern domain*'). The gold-related veins crosscut the schistosity in several areas (e.g., Figs V.12, V.21, V.25, V.26, V.30 and V.33) and do not seem to be affected by intense folding (e.g., Fig. V.30). Indeed, folding in the host-rocks is always tighter than in the adjacent veins. Therefore, it appears that the gold mineralisation occurred late in the history of Df. Moreover, the steep thrusting veins are frequently represented in back-thrust position, and generally back-thrusts orogenic domains are in general qualified as being fairly late in the tectonic history.

In the Clutha area, we observed dextral sub-horizontal motion associated with NW-SE shortening. Similar motions were also identified in the Sheba-Fairview area (Gloyn-Jones and Kisters, 2018; Pintos Cerda et al., 2022). This dextral motion can be related to strike-slip reactivation caused by the flexural slip of the regional refolded fold, which is described as a late event during NW-SE shortening (Anhaeusser, 1976, 2019; Jones and Kisters, 2022), thus confirming the coeval formation of a part of the mineralisation and the Sheba-Fairview regional refolded fold. However, the mineralisation-related vein system in the Victoria deposits raises doubts about their formation during late stage. Because the steep thrusting mineralised veins are, in this deposit, N-S striking and therefore cannot be related to regional NW-SE shortening. Indeed, an oblique reverse/sinistral movement on N-S-striking veins should have been observed to be structurally controlled by the NW-SE shortening., they surely have been rotated by the formation of the regional refolded fold. Is there a folding of veins initially oriented ENE-WSW into N-S striking? Or is there a local rotation of stresses? Bedding-parallel veins have undergone boudinage and sub-horizontal fracturing (Fig. V.37c,d,e), they are probably deformed by the NW-SE shortening, Jones and Kisters (2022) interpret these veins as drains for fluids during flexural slip.

The late and barren vein system is interpreted as formed under a NE-SW shortening event. This deformation has never been described in the northern part of the Barberton Greenstone Belt, and no clear evidence of this deformation has been observed in the country rock during study of the northern part of the belt. Dirks et al. (2009) observed sinistral motion, described as normal and formed during an extension event related to the gold mineralisation. Sinistral motions were also identified in this study, we can therefore wonder whether these sinistral movements are the same? However, the sinistral motion observed here is associated with NE-SW shortening linked with horizontal displacement and the late barren vein system. Reverse motion observed in the shallow-dipping veins can be tricky to observe due to the shallow dip of these veins; however the en-echelon veins bearing the sub-vertical comb quartz (Fig. V.40a) leaves the doubt and allows us to confirm the horizontal compressive nature of this system. Dirks et al. (2009) also say that they observed several times more than one lineation on the measured surfaces. This raises the question of whether there has been a tectonic inversion from a transpressive to a transtensive regime, or vice versa, and constant re-using and reactivation of structures as frequently occurring.

V.F. Conclusions

A detailed field structural analysis, combined with petrological and microstructural investigations in the northern region of the Barberton Greenstone Belt, has facilitated the comprehension of the structural controls governing numerous quartz veins and the deformation processes affecting the host rock. This research has uncovered the presence of two distinct vein events. The first event is associated with gold mineralisation and was formed during a period of NW-SE horizontal shortening. It is manifested through a variety of vein morphologies, including thrusting veins, bedding parallel veins, stockwork formations, dextral shearing veins, and veins oriented perpendicular to the structural framework. The second vein system is regarded as late and barren, interpreted as formed during horizontal motion and possibly associated with sinistral transpressional forces during an NE-SW shortening episode.

Chapter VI: General Interpretation and Discussion

V.I.A. Main Findings

This first part of the discussion is a review of the main results obtained from the spatial analysis, field, structural, microstructural and mineralogical study of most of the gold occurrences and deposits in the Barberton Greenstone Belt. This summary will provide a basis for discussion of the various deformations herein characterised, their significance, the gold mineralisation formation model and its genetic classification.

VI.A.1. Gold Distribution

The spatial analysis conducted here offers valuable insights into quantifying the links and relationships between various factors and gold occurrences within the Barberton Greenstone Belt. Several potential controls for gold mineralisation parameters have been studied, such as the favourability of the lithology group, the structural objects, and the spatial statistical distribution of gold occurrences and deposits.

- According to the Weight of Evidence (WoE) method, the most favourable geological layers for hosting gold occurrences would be the dolomitic metasomatite, the Banded Iron Formation (BIF), and the rocks of the Onverwacht Group. Because the two first lithologies are mapped as sub-units belonging to various groups within the belt, their favourability assessment is distorted. Indeed, it is important to exercise caution when interpreting these results and finally, it doesn't appear to exist a clear lithological control on the distribution of gold occurrences (Fig. III.7).
- Gold occurrences and deposits seem to be structurally controlled, with most of them exhibiting a strike ranging from NE-SW to E-W, with an isolated peak close to NW-SE striking (Fig. III.8). The majority of them are found in proximity to folds and faults (respectively < 3 km of a fold axial surface and < 500 m of a fault), and their orientations are similar to the closest folds or faults (Figs. II.10 and II.12). However, establishing a precise relationship between these occurrences and nearby structural features is challenging due to the varying styles of fracturing within fold and fault zones.

Additionally, several major belt structures respond to NW-SE shortening, making it difficult to establish temporal links between these structures and gold occurrences.

- Gold-bearing occurrences are primarily concentrated within the belt's boundaries. A notable variation in gold grades is observed between the northern and southern parts of the belt (Fig. III.13). Higher-grade areas are predominantly located in the northern section, and principally in the vicinity of the Sheba-Fairview complex.
- The spatial distribution analysis has identified four main clusters of high occurrence-density areas (Fig. III.14). Two clusters are situated in the southern zone, encompassing the Malolotja and Steynsdorp large-scale folds. The other two clusters are found in the northern zone, one near the town of Barberton, including the Sheba-Fairview area, and the other near the Shiyalongubo dam along the Barbrook fault.

It is crucial to interpret these findings with caution, they are based entirely on the quality of the input data, here it corresponds to the Metallogenic map of the Barberton Greenstone Belt compiled by Ward (2000).

While lithology doesn't seem to exert a strong control over mineralisation, the spatial link with faults and folds appears clear and demonstrated, although it is difficult to establish the genetic nature of these relationships. The identification of clusters and the differences in gold grades between the northern and southern regions provide valuable insights for further fieldwork and exploration activities in the area. This type of study is very useful first quantification step before starting a field survey to target the fieldwork activities as effectively as possible and can be applied elsewhere.

VI.A.2. Southern Domain

Regarding the Southern part of the Barberton Greenstone Belt, this study presents new structural, microstructural, and mineralogical information on quartz veins associated with gold mineralisation and their alteration. Detailed observations centred around the Steynsdorp Anticline and the Malolotja Synform lead us to propose a three-stage model outlining the tectonic evolution and associated hydrothermal features.

- The initial stage is characterised by a sub-vertical Se schistosity. In the Malolotja sector, this schistosity is interpreted to result from the overthrusting of Onverwacht Group onto Moodies Group rocks, as suggested by previous researchers (Lamb, 1986; Lamb and Paris, 1988; Heubeck et al., 2023). The Se schistosity orientation undergoes variations

in different locations, such as becoming sub-vertical to north-dipping at Steynsdorp. This phase gave rise to the formation of early quartz veins, which are associated with the Se schistosity and are apparently barren in gold.

- The second event, labelled Df is predominant in the southern part of BGB and is characterised by E-W shortening. This tectonic episode gives rise to the development of large-scale folds (Df), exemplified by the Steynsdorp Anticline and the Malolotja Synform. A vertical N-S striking schistosity, Sf, is also associated, parallel, in Malolotja, to Se in fold limbs. During this stage, the majority of gold-bearing and/or gold-related hydrothermal quartz veins are emplaced, including both horizontal and steep veins. The syntectonic character of these veins is substantiated by various lines of evidence such as the upright Ff folding of horizontal veins formed in a mode I opening character, such as internal vein textures revealing vertical (in places slightly oblique) opening associated with synchronous steeper veins, mostly N-S striking, and that exhibiting reverse motion.
- The third hydrothermal and deformation event is attributed to NE-SW shortening. This event results in localised folding and the development of a NW-SE-striking Sl schistosity. Furthermore, it controls the emplacement of a late vein system, characterised by NE-SW striking veins or shallow-dipping shear veins.

The proposed three-stage model explicates the complex tectonic evolution and associated hydrothermal events in the Southern part of the Barberton Greenstone Belt.

VI.A.3. Northern Domain

Within the northern part of the Barberton Greenstone Belt, the study focus on the structural, microstructural, and mineralogical analyses of quartz veins linked to gold mineralisation. By studying six critical, distinct deposits and areas, namely Tiger Trap/Pioneer, Agnes, Victoria, Clutha, Golden Quarry, the Shiyalongubo region and other key outcrops, we reveal the presence of two distinct hydrothermal vein systems.

- In the northern part of the Barberton Greenstone Belt, a significant NW-SE to NNW-SSE shortening event has left its mark on the landscape. This event has generated tight folds and a NE-SW to ENE-WSW striking foliation, resembling the Df deformation features seen in the southern part of the belt. These structures are rotated in the Sheba-Fairview area. This event is attributed to a late episode of NW-SE shortening and formation of an regional refolding fold (Jones and Kisters, 2022).

- Four main types of veins are identified within different deposits: thrusting and sub-horizontal veins, bedding-parallel veins, stockwork network, complex vein systems. All of these veins are formed during the Df event, of a NNW-SSE to NW-SE horizontal shortening (see *Chapter V* for more detail).
- A late and barren vein system is also observed, exhibiting various vein types with distinct characteristics. These include en-echelon veins, veins with vertical fibres, shallow dipping shear veins and complex vein networks. The are all controlled by a NE-SW shortening.

This study highlights the presence of two distinct deformations linked to hydrothermal events within the northern part of the Barberton Greenstone Belt.

VI.B. Discussion

Detailed interpretation and discussion on the structural control and formation model of the hydrothermal features and deformation events are exposed n *Chapiter IV* and *Chapiter V*. We discuss here the general interpretations and contribution of our findings to the overall understanding of the Barberton Greenstone Belt.

VI.B.1. The Deformation Events and their Significance

In our structural analyses of the southern region of the Barberton Greenstone Belt, we have discerned three distinct deformation events labelled as De (early deformation), Df (main fold/thrust-related deformation), and Dl (late deformation). These events are closely associated with the formation of hydrothermal vein features.

De deformation is not precisely constrained by our available data. This deformation, pre-dating the regional folding Df at Steynsdorp and Malolotja areas, had dramatic contrasting effects on the rocks. Indeed, at Malolotja, it formed a nappe leading to the overthrusting of upper Onverwacht Group rocks on top of Moodies quartzites as recently suggested by Heubeck et al. (2023) and older literature (Lamb, 1984). Instead, at Steynsdorp, early deformation produced an arcuate belt of gneissic foliation at amphibolite facies condition, surrounding the Steynsdorp Pluton and developed across the intrusive contact with the Theespruit Formation schist (Kisters and Anhaeusser, 1995). Such contrasted pre-Df structural record suggest that early, complex, unresolved tectonics operated in the southern part of the BGB, and that a major decoupling interface could have localised in the belts between the Steynsdorp and Malolotja sectors. The

Df event is responsible for the large-scale folding and the development of the vertical N-S striking Sf schistosity. Finally, Dl formed localised folds and a vertical NW–SE-striking Sl cleavage mostly in the southern part of the Barberton Greenstone Belt.

In contrast, in the northern part of the Barberton Greenstone Belt, only the Df event is well characterised. No and weak evidence of the De and Dl deformation features was found within the internal deformational structures of the country rock. In this region, Df formed km-scale large folds, established a generally vertical ENE-WSW striking schistosity, and generated major thrust faults. In the junction with the Jamestown schist belt, particularly in the Fairview-Sheba area, these structures exhibit rotation, with an axial plane striking approximately NW-SE striking. Df is interpreted as a horizontal shortening event with a prevailing NW-SE to NNW-SSE striking orientation.

At large scale, the axial planes, the Sf schistosity, and the major faults display rotation between the northern and southern portions of the belt, as illustrated in maps and structural measurements (Figs. IV.C.5, V.1 and VI.1). The Df shortening deformation, described as E-W striking in the south, rotates to a NW-SE to NNW-SSE orientation towards the north (Fig. VI.1). Such a geometry defines an arcuate fold-thrust belt that is not uncommon within other types of orogenic belt, i.e., the Alps, the Balkans, etc Curved fold and thrust belts are typical of progressive orocline, which that are commonly convex-shape thrusts in map view towards the main direction of movement (e.g., Johnston et al., 2013), which is in the BGB towards the NW, although this study revealed the importance of back-thrusting in the northern BGB. However, one can question here if this specific geometry was not the result of the pre-existence of competent or hard crystalline massifs that surrounded the metasediments and could have controlled the geometry of the subsequent deformational events. The Onverwacht Anticline could be a potential candidate. It lies between these two zones and is described as a vertically plunging anticline (Schmitz and Heubeck, 2021), forming an arcuate half-elliptical shape seemingly weakly affected by late major faults. It is questionable whether this anticline forms as a sufficiently rigid body around which the southern part of the belt could have rotated during overall NW-SE shortening, similar to the dynamics observed in the Fairview-Sheba area, with the help of the Kaapvaal and Stentor plutons. Another candidate might be the Piggs Peak pluton in Swaziland – its NW margin with BGB is arcuate, with a similar shape as the arcuate BGB belt. This would imply that some of the Df deformation is post-3.1 Ga, which is the emplacement age of this batholith.

These two rigid bodies might have operated in tandem to shape the deformation of the BGB. More structural work should focus on testing whether they have acted as indenters, deflecting deformation structures in surrounding softer BGB around their envelopes.

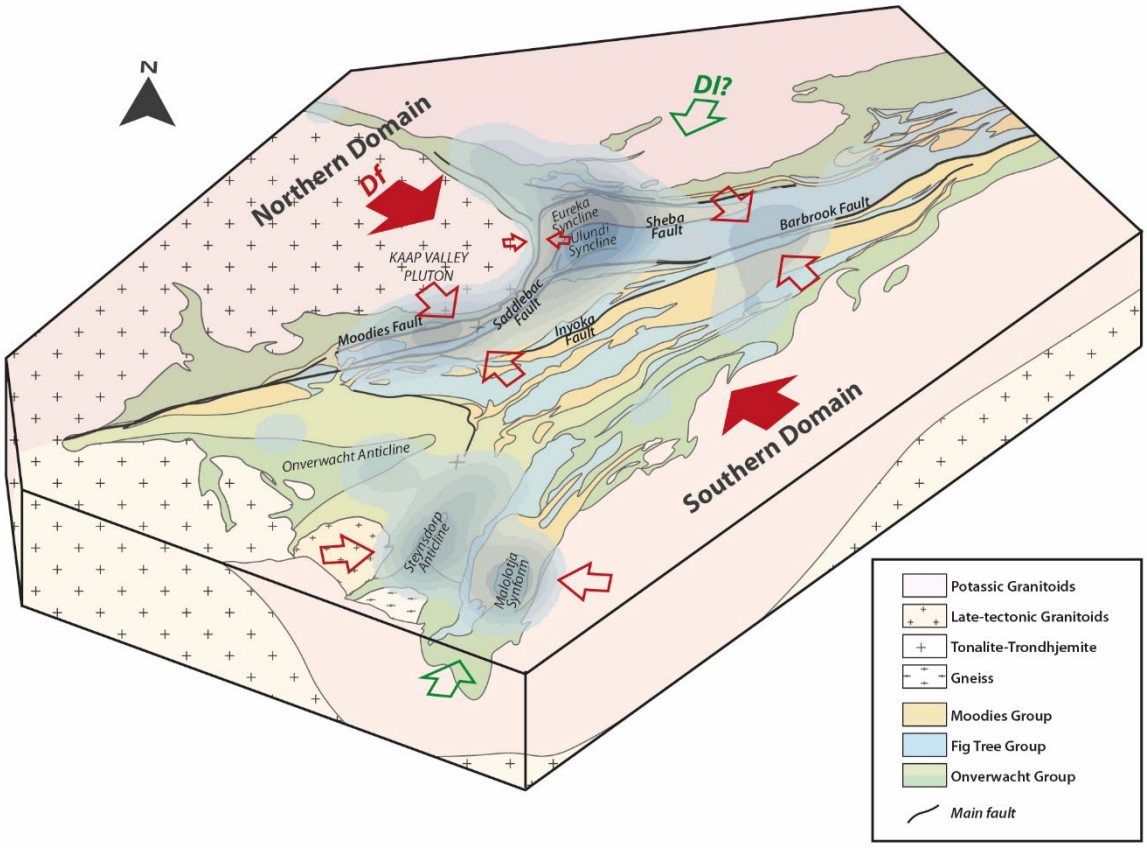

Fig. VI.1. Synthetic bloc diagram illustrates the rotation of the Df shortening event in the Barberton Greenstone Belt. Diagram inspired by Jackson et al. (1987).

The Dl deformation event corresponds to NE-SW shortening throughout the Barberton Greenstone Belt and represents an uncharacterised tectonic phenomenon within the existing literature on the Barberton Greenstone Belt. This enigmatic deformation event is mostly documented within the country rock of the Malolotja area, resulting in the development of a Sl schistosity associated with local folding. In all other regions, the Dl event is predominantly observed through the formation of late and barren veins. The age and tectonic significance of this event are unknown. From a mineralogical perspective, the late vein system is characterised by quartz, feldspars (both Na and K), and the development of tourmaline and albite alteration (even if tourmaline and feldspar can also be represented, but minor, within vein of the mineralised system). The composition bears similarities to magmatic-hydrothermal mineralogy (Thompson et al., 1999; Lang and Baker, 2001). Given that the Barberton Greenstone Belt is surrounded by late potassic batholiths, one may speculate about a potential link between the

late vein system and these intrusions. However, further research is necessary to comprehensively understand the nature and implications of the Dl deformation.

VI.B.2. The Structural Control of the Gold Mineralisation

The gold-related vein system within the southern part of the Barberton Greenstone Belt has been described as steep thrusting veins associated with mode I opening horizontal veins (Travers et al., 2023). This system corresponds to the "thrusting veins, and sub-horizontal" association also observed in the northern part of the belt. However, a notable directional disparity exists between the two domains - the steep veins strike approximately N-S due to E-W shortening, whereas in the northern section, the steep veins are generally oriented ENE-WSW striking, resulting from NNW-SSE shortening.

Thus, in agreement with the deformation record of the host-rocks, we demonstrate a rotation of the Df shortening directions through the structural analyses of quartz hydrothermal features; surely formed during the predominant NW-SE shortening. This rotation is then also recorded in the veins associated with the gold mineralisation, confirming a strong and significant structural control. It is also demonstrated that Df, as a deformation event, not only gave rise to fold and thrust structures but also appears, likely a late phase of the NW-SE shortening, as a fundamental actor of the structural emplacement of gold mineralisation. Spatial analysis underscores a clear spatial link between the proximity and orientation of gold occurrences and these folds and faults. This link is surely due to the fact that all these structures are formed by the same deformation.

Furthermore, utilising IDW interpolation on the size of deposits and occurrences allow for the distinction of two distinct domains within the Barberton Greenstone Belt, each characterised by differing gold grades. The northern sector, delineated by major faults such as Inyoka, Barbrook, and Saddleback, exhibits a higher gold content compared to the southern one (Figs. III.13 and III.15). Consistently, our field studies have identified more morphologies of gold-related veins in the northern domain, suggesting that greater complexity could be a potential explanation for elevated gold content. Furthermore, it is worth noting that existing literature recognises tectono-stratigraphic differences between the southern and northern domains. (de Wit et al., 1992; Lowe, 1994) which may contribute to the gold enrichment observed in the northern part. However, it is important to note that no clear lithological control on gold occurrences was highlighted from the spatial analysis of lithology in this study. Recent structural scientific research on the Sheba-Fairview complex has unveiled intricate mineralised structures (Gloyn-Jones and Kisters, 2018,

2019; Dziggel and Kisters, 2019; Pintos Cerda et al., 2020, 2022; Jones and Kisters, 2022), similar to some of those proposed in the northern part of this study (see *Chapter V*). This raises the question of whether complex vein architecture is a characteristic feature of more advanced systems rich in gold.

In several places, these veins are cut across the Sf schistosity. Regarding the timing of vein formation with respect to the episodes of deformation shaping the Barberton Greenstone Belt, they appear to occur during a relative late episode of the main Df deformation marked by NW-SE regional shortening. Multiple gold mineralisation ages have been reported in the northern part of the Barberton Greenstone Belt, with two distinct periods emerging from the literature: an earlier phase dating to 3126–3084 Ma (de Ronde et al., 1991) and a younger phase at 3027–3015 Ma (Dziggel et al., 2010; Dirks et al., 2013), Consequently, the ages of gold mineralisation appear to span an extended timeframe.

However, the mineralised vein system suffers two successive rotations in time: one first at large scale with the formation of the large-scale arc geometry of the entire BGB; and the second, at more local scale, with the late formation of the refolded fold of the Sheba-Fairview complex, associated with the most important gold deposits. This prompts the question of whether main huge mineralisations formed first and are subsequently rotated, or if they are the result of the system maturation during ongoing NW-SE shortening event and then formation of the main deposit later, within and during the formation of the most arcuate part of the belt as suggested by Jones and Kisters 2022. In addition, one can question if the formation of the two-scales observed arcuate systems, the larger one at entire belt scale and the smaller one at Sheba-Fairview refolded area one, can also be assisted by the occurrence of the unknown, late, regional NE-SW horizontal shortening, identified in this work. Indeed, the role of the neighbouring crystalline bodies (i.e., the Kaap Valley and Stolzburg complexes), as relative competent bodies that can have a passive role during ongoing deformation of the belt but also the role of the late batholith emplacement such as the Nelspruit and Mpuluzi one in the development of the late NE-SW event need to be questioned. However, body forces effects from pluton emplacement (e.g., ballooning or diapirism) on the deformation of the host rocks would be localised at the margins of plutons, and decrease away from the plutons (e.g., Paterson et al., 1998; Johnson et al., 2003). Such a strain gradients are not observed in this study, and Dl structures appear to have no spatial correlation with the geometry and proximity of exposed plutons. Thus, more work is required to unravel the potential impact of body forces on the deformation of the BGB supracrustal sequences.

This long period, associated to specific rheological-control deformation (with two perpendicular events affecting a zone composed by numerous rigid blocks) might be linked to the characteristics of Archean domains, which tend to exhibit more distributed deformation and lower differential stresses, potentially enabling prolonged deformation owing to their warmer and less rigid crust (Sleep, 1992; Gapais et al., 2009; Gapais, 2018).

VI.B.3. Typology of the mineralisation

Gold mineralisation in the Barberton Greenstone Belt has been traditionally characterised as orogenic gold (de Ronde and de Wit, 1994; Otto et al., 2007; Dziggel et al., 2010; Agangi et al., 2014; Altigani, 2021). It is typically interpreted as a product of a late event within the accretional history of the domains metamorphosed at greenschist facies (de Ronde and de Wit, 1994; Otto et al., 2007; Pintos Cerda et al., 2020). Our findings agree with this interpretation, as we have observed gold-related veins resulting from a strong compressive structural control and mostly concentrated at the vicinity of major faults (in the northern part), two characteristic features commonly associated with the global context described for orogenic gold (Groves et al., 1998, 2018; Deng et al., 2015; Wang et al., 2022).

Alternative viewpoint, suggesting that gold may have formed during an extensive event after the stabilisation of the craton have also been proposed (Dirks et al., 2009, 2013; Munyai et al., 2011). While our study did not uncover any extensional deformation event related to mineralisation, the debate continues regarding whether gold can be unequivocally labelled as orogenic in this context. Indeed, an intriguing aspect of the gold-related veins in the Barberton Greenstone Belt is the consistent presence of K-feldspars. This raises questions about the potential existence of a magmatic component in the mineralisation process. Additionally, in the Forbes Reef Mine of the Malolotja area, we have observed grey weathered lodes, likely of magmatic origin (Fig. IV.26). This mine is also described as close to granitoid intrusions (Anhaeusser, 1986). Similarly, in the Steynsdorp area, the Gypsy Queen gold occurrence has been classified as associated with intrusive porphyry (Viljoen et al., 1969) and numerous feldspar-rich magmatic bodies surely comparable to felsic intrusions have also been found in several areas of our study area, i.e., Homestead (Fig. IV.48). Furthermore, a pegmatite intrusion in the New Consort Mine, in the northern part of the Barberton Greenstone Belt, has been interpreted as syn-gold mineralisation (Dziggel et al., 2010). Moreover, de Ronde et al. (1992) characterised fluid related to the mineralisation as likely originating from a source outside the belt. We can then reasonably wonder whether the gold mineralisation of the Barberton

Greenstone Belt has a mixed typology between orogenic and intrusion related, encompassing elements of both processes. In an increasing number of deposits classified as orogenic gold, magmatic-hydrothermal processes are being identified (Aliyari et al., 2012; Doublier et al., 2014; Wu et al., 2021). This suggests that orogenic gold may not be entirely disconnected from intrusion-related processes, although this aspect remains a topic of ongoing debate in the gold mineralisation research (Goldfarb and Pitcairn, 2023).

Conclusions

In summary, the comprehensive analysis of the Barberton Greenstone Belt, including the spatial distribution of gold-related occurrences both within its southern and northern regions provides several significant insights into the geological and structural characteristics of the area.

The spatial distribution analysis reveals that gold occurrences in the Barberton Greenstone Belt are not uniformly distributed. Instead, they cluster in four main areas: Barberton, Steynsdorp, Malolotja, and Shiyalongubo. An inverse distance weighting (IDW) interpolation map highlights a higher tonnage of deposits along the northern flank of the belt.

The southern part of the belt, has experienced three deformation events, leading to the formation of different hydrothermal vein systems. The first event is related to thrusting and the development of a composite foliation, while the second event is characterised by large-scale folding and the emplacement of gold-related veins due to a local E-W shortening. The third event, associated with NE-SW shortening, overprints previous structures and is linked to late hydrothermal and barren quartz veins. The northern region of the belt has also been subject of polyphase deformation during which two distinct vein events are distinguished. The first event, associated with gold mineralisation, occurred during NW-SE to NNW-SEE horizontal shortening and resulted in various vein morphologies. The second vein system is considered late and barren, formed during NE-SW shortening.

On a regional scale, two main tectonic events are involved in the formation of hydrothermal features within the Barberton Greenstone Belt. Firstly, a significant deformation event associated with large-scale folding and thrust faults structurally controls the emplacement of gold-bearing veins. This deformation event is characterised by a single, prolonged (~ 100 Myr) or pulsed NW-SE shortening at regional scale in the Barberton Greenstone Belt. Veins associated with gold mineralisation exhibit diverse morphologies, including steep thrusting veins coupled with sub-horizontal veins, bedding parallel veins, and more complex vein systems. Secondly, there is evidence of a late deformation event in the region, marked by an enigmatic NE-SW shortening, which is also closely linked to the formation of late-stage hydrothermal quartz veins. This late deformation event introduces an additional layer of complexity to the geological history of the Barberton Greenstone Belt.

In conclusion, the combined findings of structural analysis, petrological studies, microstructural investigations and spatial distribution analysis provide valuable insights into the geological and tectonic history of the Barberton Greenstone Belt. These findings contribute to our understanding of the complex processes that have shaped this Archean domain and are essential for targeting fieldwork activities and resource exploration in the region.

References

Agangi, A., Hofmann, A., Eickmann, B., Marin-Carbonne, J., 2019. Mesoarchaean Gold Mineralisation in the Barberton Greenstone Belt: A Review. In: Kröner, A., Hofmann, A. (Eds.), The Archaean Geology of the Kaapvaal Craton, Southern Africa, Regional Geology Reviews. Springer International Publishing, Cham, 171–184. https://doi.org/10.1007/978-3-319-78652-0_7

Agangi, A., Hofmann, A., Eickmann, B., Marin-Carbonne, J., Reddy, S.M., 2016. An atmospheric source of S in Mesoarchaean structurally-controlled gold mineralisation of the Barberton Greenstone Belt. Precambrian Research 285, 10–20. https://doi.org/10.1016/j.precamres.2016.09.004

Agangi, A., Hofmann, A., Przybyłowicz, W., 2014. Trace element zoning of sulfides and quartz at Sheba and Fairview gold mines: Clues to Mesoarchean mineralisation in the Barberton Greenstone Belt, South Africa. Ore Geology Reviews 56, 94–114. https://doi.org/10.1016/j.oregeorev.2013.08.016

Agterberg, F.P., Bonham-Carter, G.F., Wright, D.F., 1990. Statistical Pattern Integration for Mineral Exploration. Computer Applications in Resource Estimation. Elsevier, 1–21. https://doi.org/10.1016/B978-0-08-037245-7.50006-8

Aliyari, F., Rastad, E., Mohajjel, M., 2012. Gold Deposits in the Sanandaj–Sirjan Zone: Orogenic Gold Deposits or Intrusion-Related Gold Systems? Resource Geology 62, 296–315. https://doi.org/10.1111/j.1751-3928.2012.00196.x

Altigani, M.A.H., 2021. Insights on Mineralogy and Chemistry of Fairview Gold Mine, Barberton Greenstone Belt, South Africa. Indonesian Journal on Geoscience 8, 73–99. https://doi.org/10.17014/ijog.8.1.73-99

Altigani, M.A.H., Merkle, R.K.W., Dixon, R.D., 2016. Geochemical identification of episodes of gold mineralisation in the Barberton Greenstone Belt, South Africa. Ore Geology Reviews 75, 186–205. https://doi.org/10.1016/j.oregeorev.2015.12.016

Anhaeusser, C.R., 2019. The geology and tectonic evolution of the northwest part of the Barberton Greenstone Belt, South Africa: A review. South African Journal of Geology 122, 421–454. https://doi.org/10.25131/sajg.122.0033

Anhaeusser, C.R., 2001. The anatomy of an extrusive-intrusive Archaean mafic-ultramafic sequence: the Nelshoogte Schist Belt and Stolzburg Layered Ultramafic Complex, Barberton Greenstone Belt, South Africa. South African Journal of Geology 104, 167–204. https://doi.org/10.2113/1040167

Anhaeusser, C.R., 1986. Archaean Gold Mineralization in the Baberton Mountain Land. In: Maske, S. (Ed.), Mineral Deposits of Southern Africa I&II, 113–154.

Anhaeusser, C.R., 1984. Structural elements of Archaen granite-greenstone terranes as examplified by the Baberton Mountain Land, Southern Africa. In: Kröner, A., Greiling, R. (Eds.), Precambrian Tectonics Illustrated. E. Schweizerbart'sche, Stuttgart, 57–78.

Anhaeusser, C.R., 1981. Chapter 6 Geotectonic Evolution of the Archaean Successions in the Barberton Mountain Land, South Africa. Developments in Precambrian Geology. Elsevier, 137–160. https://doi.org/10.1016/S0166-2635(08)70011-2

Anhaeusser, C.R., 1976a. Archean metallogeny in southern Africa. Economic Geology 71, 16–43. https://doi.org/10.2113/gsecongeo.71.1.16

Anhaeusser, C.R., 1976b. The geology of the Sheba Hills area of the Barberton Mountain Land, South Africa, with particular reference to the Eureka Syncline. South African Journal of Geology 79, 253–280.

Anhaeusser, C.R., 1973. The evolution of the early Precambrian crust of southern Africa. Phil. Trans. Roy. Soc. Lond. 273, 359–388.

Anhaeusser, C.R., 1972. The geology of the Jamestown hills area of the Barberton Mountain Land, South Africa. South African Journal of Geology 75, 225–263.

Anhaeusser, C.R., 1971. Cyclic volcanicity and sedimentation in the evolutionary development of Archaean greenstone belts of shield areas. Spec. Publ. Geol. Soc. Aust. 3, 57–70.

Anhaeusser, C.R., Robb, L.J., Barton, J.M.J., 1983. Mineralogy, petrology and origin of the Boesmanskop syeno-granite complex, Barberton Mountain land, South Africa. Spec. Pub. Geol. Soc. S. Afr 169–183.

Argapadmi, W., Toth, E.R., Fehr, M.A., Schönbächler, M., Heinrich, C.A., 2018. Silver Isotopes as a Source and Transport Tracer for Gold: A Reconnaissance Study at the Sheba and New Consort Gold Mines in the Barberton Greenstone Belt, Kaapvaal Craton, South Africa☼. Economic Geology 113, 1553–1570. https://doi.org/10.5382/econgeo.2018.4602

Armstrong, R.A., Compston, W., de Wit, M.J., Williams, I.S., 1990. The stratigraphy of the 3.5-3.2 Ga Barberton Greenstone Belt revisited: A single zircon ion microprobe study. Earth and Planetary Science Letters 101, 90–106. https://doi.org/10.1016/0012-821X(90)90127-J

Barley, M.E., Groves, D.I., 1992. Supercontinent cycles and the distribution of metal deposits through time. Geology 20, 291. https://doi.org/10.1130/0091-7613(1992)020<0291:SCATDO>2.3.CO;2

Bartier, P.M., Keller, C.P., 1996. Multivariate interpolation to incorporate thematic surface data using inverse distance weighting (IDW). Computers & Geosciences 22, 795–799. https://doi.org/10.1016/0098-3004(96)00021-0

Bekker, A., Barley, M.E., Fiorentini, M.L., Rouxel, O.J., Rumble, D., Beresford, S.W., 2009. Atmospheric Sulfur in Archean Komatiite-Hosted Nickel Deposits. Science 326, 1086–1089. https://doi.org/10.1126/science.1177742

Belcher, R.W., Kisters, A.F.M., 2006. Progressive adjustments of ascent and emplacement controls during incremental construction of the 3.1Ga Heerenveen batholith, South Africa. Journal of Structural Geology 28, 1406–1421. https://doi.org/10.1016/j.jsg.2006.05.001

Belousova, E.A., Kostitsyn, Y.A., Griffin, W.L., Begg, G.C., O'Reilly, S.Y., Pearson, N.J., 2010. The growth of the continental crust: Constraints from zircon Hf-isotope data. Lithos 119, 457–466. https://doi.org/10.1016/j.lithos.2010.07.024

Bonham-Carter, G.F., Agterberg, F.P., 1990. Application of a Microcomputer-based Geographic Information System to Mineral-Potential Mapping. Microcomputer Applications in Geology 2. Elsevier, 49–74. https://doi.org/10.1016/B978-0-08-040261-1.50012-X

Bouhallier, H., 1994. Evolution structurale et métamorphique de la croûte continentale archéenne (craton de Dherwar, Inde du Sud). PhD Thesis. Université Rennes.

Bouhallier, H., Chardon, D., Choukroune, P., 1995. Strain patterns in Archaean dome-and-basin structures: The Dharwar craton (Karnataka, South India). Earth and Planetary Science Letters 135, 57–75. https://doi.org/10.1016/0012-821X(95)00144-2

Boullier, A.-M., Robert, F., 1992. Palaeoseismic events recorded in Archaean gold-quartz vein networks, Val d'Or, Abitibi, Quebec, Canada. Journal of Structural Geology 14, 161–179. https://doi.org/10.1016/0191-8141(92)90054-Z

Brown, M., 2015. Paleo- to Mesoarchean polymetamorphism in the Barberton Granite-Greenstone Belt, South Africa: Constraints from U-Pb monazite and Lu-Hf garnet geochronology on the tectonic processes that shaped the belt: Discussion. Geological Society of America Bulletin 127, 1550–1557. https://doi.org/10.1130/B31198.1

Brown, M., 2007. Metamorphic Conditions in Orogenic Belts: A Record of Secular Change. International Geology Review 49, 193–234. https://doi.org/10.2747/0020-6814.49.3.193

Brown, M., Johnson, T., Gardiner, N.J., 2020. Plate Tectonics and the Archean Earth. Annual Review of Earth and Planetary Sciences 48, 291–320. https://doi.org/10.1146/annurev-earth-081619-052705

Byerly, G.R., 1999. Komatiites of the Mendon Formation: Late-stage ultramafic volcanism in the Barberton Greenstone Belt. Geologic Evolution of the Barberton Greenstone Belt, South Africa. Geological Society of America. https://doi.org/10.1130/0-8137-2329-9.189

Byerly, G.R., Kröner, A., Lowe, D.R., Todt, W., Walsh, M.M., 1996. Prolonged magmatism and time constraints for sediment deposition in the early Archean Barberton greenstone belt: evidence from the Upper Onverwacht and Fig Tree groups. Precambrian Research 78, 125–138. https://doi.org/10.1016/0301-9268(95)00073-9

Cagnard, F., Brun, J.-P., Gapais, D., 2006. Modes of thickening of analogue weak lithospheres. Tectonophysics 421, 145–160. https://doi.org/10.1016/j.tecto.2006.04.016

Capitanio, F.A., Nebel, O., Cawood, P.A., Weinberg, R.F., Clos, F., 2019. Lithosphere differentiation in the early Earth controls Archean tectonics. Earth and Planetary Science Letters 525, 115755. https://doi.org/10.1016/j.epsl.2019.115755

Catuneanu, O., Eriksson, P.G., 1999. The sequence stratigraphic concept and the Precambrian rock record: an example from the 2.7–2.1 Ga Transvaal Supergroup, Kaapvaal craton. Precambrian Research 97, 215–251. https://doi.org/10.1016/S0301-9268(99)00033-9

Cawood, P.A., Kröner, A., Pisarevsky, S., 2006. Precambrian plate tectonics: Criteria and evidence. GSA Today 16, 4. https://doi.org/10.1130/GSAT01607.1

Chardon, D., Gapais, D., Cagnard, F., 2009. Flow of ultra-hot orogens: A view from the Precambrian, clues for the Phanerozoic. Tectonophysics 477, 105–118. https://doi.org/10.1016/j.tecto.2009.03.008

Chardon, D., Peucat, J.-J., Jayananda, M., Choukroune, P., Fanning, C.M., 2002. Archean granite-greenstone tectonics at Kolar (South India): Interplay of diapirism and bulk inhomogeneous contraction during juvenile magmatic accretion: ARCHEAN GRANITE-GREENSTONE TECTONICS, KOLAR, INDIA. Tectonics 21, 7-1-7–17. https://doi.org/10.1029/2001TC901032

Chen, C.-W., Rondenay, S., Evans, Rob.L., Snyder, D.B., 2009. Geophysical Detection of Relict Metasomatism from an Archean (~3.5 Ga) Subduction Zone. Science 326, 1089–1091. https://doi.org/10.1126/science.1178477

Clemens, J.D., Belcher, R.W., Kisters, A., 2010. The Heerenveen Batholith, Barberton Mountain Land, South Africa: Mesoarchaean, Potassic, Felsic Magmas Formed by Melting of an Ancient Subduction Complex. Journal of Petrology 51, 1099–1120. https://doi.org/10.1093/petrology/egq014

Collins, W.J., Van Kranendonk, M.J., Teyssier, C., 1998. Partial convective overturn of Archaean crust in the east Pilbara Craton, Western Australia: driving mechanisms and tectonic implications. Journal of Structural Geology 20, 1405–1424. https://doi.org/10.1016/S0191-8141(98)00073-X

Condie, K.C., 2014. Growth of continental crust: a balance between preservation and recycling. Mineralogical Magazine 78, 623–637. https://doi.org/10.1180/minmag.2014.078.3.11

Condie, K.C., 1981. Archean Greenstone Belts. Elsevier.

Condie, K.C., Benn, K., 2006. Archean geodynamics: Similar to or different from modern geodynamics? In: Benn, K., Mareschal, J.-C., Condie, K.C. (Eds.), Geophysical Monograph Series. American Geophysical Union, Washington, D. C., 47–59. https://doi.org/10.1029/164GM05

Condie, K.C., Macke, J.E., Reimer, T.O., 1970. Petrology and Geochemistry of Early Precambrian Graywackes from the Fig Tree Group, South Africa. Geological Society of America Bulletin 81, 2759. https://doi.org/10.1130/0016-7606(1970)81[2759:PAGOEP]2.0.CO;2

Cutts, K.A., Stevens, G., Hoffmann, J.E., Buick, I.S., Frei, D., Munker, C., 2014. Paleo- to Mesoarchean polymetamorphism in the Barberton Granite-Greenstone Belt, South Africa: Constraints from U-Pb monazite and Lu-Hf garnet geochronology on the tectonic processes that shaped the belt. Geological Society of America Bulletin 126, 251–270. https://doi.org/10.1130/B30807.1

de Ronde, C.E.J., de Wit, M.J., 1994. Tectonic history of the Barberton greenstone belt, South Africa: 490 million years of Archean crustal evolution. Tectonics 13, 983–1005. https://doi.org/10.1029/94TC00353

de Ronde, C.E.J., Kamo, S., Davis, D.W., De Wit, M.J., Spooner, E.T.C., 1991. Field, geochemical and U-Pb isotopic constraints from hypabyssal felsic intrusions within the Barberton greenstone belt, South Africa: Implications for tectonics and the timing of gold mineralization. Precambrian Research 49, 261–280. https://doi.org/10.1016/0301-9268(91)90037-B

de Ronde, C.E.J., Kamo, S.L., 2000. An Archean arc-arc collisional event: a short-lived (ca 3 Myr) episode, Weltevreden area, Barberton greenstone belt, South Africa. Journal of African Earth Sciences 30, 219–248. https://doi.org/10.1016/S0899-5362(00)00017-8

de Ronde, C.E.J., Spooner, E.T.C., de Wit, M.J., Bray, C.J., 1992. Shear zone-related, Au quartz vein deposits in the Barberton greenstone belt, South Africa; field and petrographic characteristics, fluid properties, and light stable isotope geochemistry. Economic Geology 87, 366–402. https://doi.org/10.2113/gsecongeo.87.2.366

de Wit, M.J., de Ronde, C.E.J., Tredoux, M., Roering, C., Hart, R.J., Armstrong, R.A., Green, R.W.E., Peberdy, E., Hart, R.A., 1992. Formation of an Archaean continent. Nature 357, 553–562. https://doi.org/10.1038/357553a0

de Wit, M.J., Fripp, R.E.P., Stanistreet, I.G., 1983. Tectonic, and stratigraphic implications of new field observations along the southern part of the Barberton greenstone belt.

Tectonic, and Stratigraphic Implications of New Field Observations along the Southern Part of the Barberton Greenstone Belt 21–29.

de Wit, M.J., Furnes, H., MacLennan, S., Doucouré, M., Schoene, B., Weckmann, U., Martinez, U., Bowring, S., 2018. Paleoarchean bedrock lithologies across the Makhonjwa Mountains of South Africa and Swaziland linked to geochemical, magnetic and tectonic data reveal early plate tectonic genes flanking subduction margins. Geoscience Frontiers 9, 603–665. https://doi.org/10.1016/j.gsf.2017.10.005

de Wit, M.J., Furnes, H., Robins, B., 2011. Geology and tectonostratigraphy of the Onverwacht Suite, Barberton Greenstone Belt, South Africa. Precambrian Research 186, 1–27. https://doi.org/10.1016/j.precamres.2010.12.007

de Wit, M.J., Hart, R.A., 1993. Earth's earliest continental lithosphere, hydrothermal flux and crustal recycling. Lithos 30, 309–335. https://doi.org/10.1016/0024-4937(93)90043-C

de Wit, M.J., Hart, R.A., Hart, R.J., 1987. The Jamestown Ophiolite Complex, Barberton mountain belt: a section through 3.5 Ga oceanic crust. Journal of African Earth Sciences (1983) 6, 681–730. https://doi.org/10.1016/0899-5362(87)90007-8

Deng, J., Wang, Q., Li, G., Zhao, Y., 2015. Structural control and genesis of the Oligocene Zhenyuan orogenic gold deposit, SW China. Ore Geology Reviews 65, 42–54. https://doi.org/10.1016/j.oregeorev.2014.08.002

Deveaud, S., Gumiaux, C., Gloaguen, E., Branquet, Y., 2013. Spatial statistical analysis applied to rare-element LCT-type pegmatite fields: an original approach to constrain faults-pegmatites-granites relationships. Journal of Geosciences 163–182. https://doi.org/10.3190/jgeosci.141

Dewey, J.F., Pitman, W.C., Ryan, W.B.F., Bonnin, J., 1973. Plate Tectonics and the Evolution of the Alpine System. Geological Society of America Bulletin 84, 3137. https://doi.org/10.1130/0016-7606(1973)84<3137:PTATEO>2.0.CO;2

Dewey, J.F., Windley, B.F., 1997. Growth and differentiation of the continental crust. Philosophical Transactions of the Royal Society of London. Series A, Mathematical and Physical Sciences 301, 189–206. https://doi.org/10.1098/rsta.1981.0105

Diener, J.F.A., Stevens, G., Kisters, A.F.M., Poujol, M., 2005. Metamorphism and exhumation of the basal parts of the Barberton greenstone belt, South Africa: Constraining the rates of Mesoarchaean tectonism. Precambrian Research 143, 87–112. https://doi.org/10.1016/j.precamres.2005.10.001

Dirks, P.H.G.M., Charlesworth, E.G., Munyai, M.R., 2009. Cratonic Extension and Archaen Gold Mineralisation in the Sheba-Fairview Mine, Barberton Greenstone Belt, South Africa. South African Journal of Geology 112, 291–316. https://doi.org/10.2113/gssajg.112.3-4.291

Dirks, P.H.G.M., Charlesworth, E.G., Munyai, M.R., Wormald, R., 2013. Stress analysis, post-orogenic extension and 3.01Ga gold mineralisation in the Barberton Greenstone Belt, South Africa. Precambrian Research 226, 157–184. https://doi.org/10.1016/j.precamres.2012.12.007

Dodd, M.S., Wang, H., Li, C., Towner, M., Thomson, A.R., Slack, J.F., Wan, Y., Pirajno, F., Manikyamba, C., Wang, Q., Papineau, D., 2022. Abiotic anoxic iron oxidation, formation of Archean banded iron formations, and the oxidation of early Earth. Earth and Planetary Science Letters 584, 117469. https://doi.org/10.1016/j.epsl.2022.117469

Doublier, M.P., Thébaud, N., Wingate, M.T.D., Romano, S.S., Kirkland, C.L., Gessner, K., Mole, D.R., Evans, N., 2014. Structure and timing of Neoarchean gold mineralization in the Southern Cross district (Yilgarn Craton, Western Australia) suggest leading role of late Low-Ca I-type granite intrusions. Journal of Structural Geology 67, 205–221. https://doi.org/10.1016/j.jsg.2014.02.009

Drabon, N., Heubeck, C.E., Lowe, D.R., 2019. Evolution of an Archean fan delta and its implications for the initiation of uplift and deformation in the Barberton greenstone belt, South Africa. Journal of Sedimentary Research 89, 849–874. https://doi.org/10.2110/jsr.2019.46

Drabon, N., Lowe, D.R., 2021. Progressive accretion recorded in sedimentary rocks of the 3.28–3.23 Ga Fig Tree Group, Barberton Greenstone Belt. GSA Bulletin 134, 1258–1276. https://doi.org/10.1130/B35973.1

Drummond, M.S., Defant, M.J., 1990. A model for Trondhjemite-Tonalite-Dacite Genesis and crustal growth via slab melting: Archean to modern comparisons. Journal of Geophysical Research: Solid Earth 95, 21503–21521. https://doi.org/10.1029/JB095iB13p21503

Dziggel, A., Kisters, A.F.M., 2019. Tectonometamorphic Controls on Archaean Gold Mineralization in the Barberton Greenstone Belt, South Africa. Earth's Oldest Rocks. Elsevier, 655–674. https://doi.org/10.1016/B978-0-444-63901-1.00026-5

Dziggel, A., Knipfer, S., Kisters, A.F.M., Meyer, F.M., 2006. P-T and structural evolution during exhumation of high-T, medium-P basement rocks in the Barberton Mountain Land, South Africa: Metamorphic Evolution, Barberton Mountain Land. Journal of Metamorphic Geology 24, 535–551. https://doi.org/10.1111/j.1525-1314.2006.00653.x

Dziggel, A., Otto, A., Kisters, A.F.M., Meyer, F.M., 2007. Chapter 5.8 Tectono-Metamorphic Controls on Archean Gold Mineralization in the Barberton Greenstone Belt, South Africa: An Example from the New Consort Gold Mine. Developments in Precambrian Geology. Elsevier, 699–727. https://doi.org/10.1016/S0166-2635(07)15058-1

Dziggel, A., Poujol, M., Otto, A., Kisters, A.F.M., Trieloff, M., Schwarz, W.H., Meyer, F.M., 2010. New U–Pb and 40Ar/39Ar ages from the northern margin of the Barberton greenstone belt, South Africa: Implications for the formation of Mesoarchaean gold deposits. Precambrian Research 179, 206–220. https://doi.org/10.1016/j.precamres.2010.03.006

Dziggel, A., Stevens, G., Poujol, M., Anhaeusser, C.R., Armstrong, R.A., 2002. Metamorphism of the granite–greenstone terrane south of the Barberton greenstone belt, South Africa: an insight into the tectono-thermal evolution of the 'lower' portions of the Onverwacht Group. Precambrian Research 114, 221–247. https://doi.org/10.1016/S0301-9268(01)00225-X

Eriksson, P.G., Altermann, W., 1998. An overview of the geology of the Transvaal Supergroup dolomites (South Africa). Environmental Geology 36, 179–188. https://doi.org/10.1007/s002540050334

Evans, R.L., Jones, A.G., Garcia, X., Muller, M., Hamilton, M., Evans, S., Fourie, C.J.S., Spratt, J., Webb, S., Jelsma, H., Hutchins, D., 2011. Electrical lithosphere beneath the Kaapvaal craton, southern Africa. Journal of Geophysical Research: Solid Earth 116. https://doi.org/10.1029/2010JB007883

Foster, R.P., Piper, D.P., 1993. Archaean lode gold deposits in Africa: Crustal setting, metallogenesis and cratonization. Ore Geology Reviews 8, 303–347. https://doi.org/10.1016/0169-1368(93)90021-P

Frimmel, H.E., 2008. Earth's continental crustal gold endowment. Earth and Planetary Science Letters 267, 45–55. https://doi.org/10.1016/j.epsl.2007.11.022

Furnes, H., de Wit, M., Dilek, Y., 2014. Four billion years of ophiolites reveal secular trends in oceanic crust formation. Geoscience Frontiers 5, 571–603. https://doi.org/10.1016/j.gsf.2014.02.002

Furnes, H., de Wit, M., Robins, B., 2013. A review of new interpretations of the tectonostratigraphy, geochemistry and evolution of the Onverwacht Suite, Barberton Greenstone Belt, South Africa. Gondwana Research 23, 403–428. https://doi.org/10.1016/j.gr.2012.05.007

Gao, S., Luo, T.-C., Zhang, B.-R., Zhang, H.-F., Han, Y., Zhao, Z.-D., Hu, Y.-K., 1998. Chemical composition of the continental crust as revealed by studies in East China. Geochimica et Cosmochimica Acta 62, 1959–1975. https://doi.org/10.1016/S0016-7037(98)00121-5

Gapais, D., 2018. Tectonics-mineralisation relationships within weak continental lithospheres: a new structural framework for Precambrian cratons. BSGF - Earth Sciences Bulletin 189, 14. https://doi.org/10.1051/bsgf/2018014

Gapais, D., Cagnard, F., Gueydan, F., Barbey, P., Ballèvre, M., 2009. Mountain building and exhumation processes through time: inferences from nature and models. Terra Nova 21, 188–194. https://doi.org/10.1111/j.1365-3121.2009.00873.x

Gloyn-Jones, J., Kisters, A., 2019. Ore-shoot formation in the Main Reef Complex of the Fairview Mine—multiphase gold mineralization during regional folding, Barberton Greenstone Belt, South Africa. Mineralium Deposita 54, 1157–1178. https://doi.org/10.1007/s00126-019-00865-9

Gloyn-Jones, J., Kisters, A., 2018. Regional folding, low-angle thrusting and permeability networks: Structural controls of gold mineralization in the Hope reef at Fairview Mine, Barberton Greenstone Belt, South Africa. Ore Geology Reviews 102, 585–603. https://doi.org/10.1016/j.oregeorev.2018.09.024

Goldfarb, R.J., Groves, D.I., Gardoll, S., 2001. Orogenic gold and geologic time: a global synthesis. Ore Geology Reviews 18, 1–75. https://doi.org/10.1016/S0169-1368(01)00016-6

Goldfarb, R.J., Pitcairn, I., 2023. Orogenic gold: is a genetic association with magmatism realistic? Mineralium Deposita 58, 5–35. https://doi.org/10.1007/s00126-022-01146-8

Goodwin, A.M., 1996. Principles of Precambrian Geology. Elsevier.

Gorman, B.E., Pearce, T.H., Birkett, T.C., 1978. On the structure of Archean greenstone belts. Precambrian Research 6, 23–41. https://doi.org/10.1016/0301-9268(78)90053-0

Grosch, E.G., Vidal, O., Abu-Alam, T., McLoughlin, N., 2012. P-T Constraints on the Metamorphic Evolution of the Paleoarchean Kromberg Type-Section, Barberton Greenstone Belt, South Africa. Journal of Petrology 53, 513–545. https://doi.org/10.1093/petrology/egr070

Groves, D.I., Goldfarb, R.J., Gebre-Mariam, M., Hagemann, S.G., Robert, F., 1998a. Orogenic gold deposits: A proposed classification in the context of their crustal distribution and

relationship to other gold deposit types. Ore Geology Reviews 13, 7–27. https://doi.org/10.1016/S0169-1368(97)00012-7

Groves, D.I., Goldfarb, R.J., Gebre-Mariam, M., Hagemann, S.G., Robert, F., 1998b. Orogenic gold deposits: A proposed classification in the context of their crustal distribution and relationship to other gold deposit types. Ore Geology Reviews 13, 7–27. https://doi.org/10.1016/S0169-1368(97)00012-7

Groves, D.I., Santosh, M., Goldfarb, R.J., Zhang, L., 2018. Structural geometry of orogenic gold deposits: Implications for exploration of world-class and giant deposits. Geoscience Frontiers 9, 1163–1177. https://doi.org/10.1016/j.gsf.2018.01.006

Groves, D.I., Vielreicher, R.M., Goldfarb, R.J., Condie, K.C., 2005. Controls on the heterogeneous distribution of mineral deposits through time. Geological Society, London, Special Publications 248, 71–101. https://doi.org/10.1144/GSL.SP.2005.248.01.04

Gumsley, A., Stamsnijder, J., Larsson, E., Söderlund, U., Naeraa, T., de Kock, M., Sałacińska, A., Gawęda, A., Humbert, F., Ernst, R., 2020. Neoarchean large igneous provinces on the Kaapvaal Craton in southern Africa re-define the formation of the Ventersdorp Supergroup and its temporal equivalents. GSA Bulletin 132, 1829–1844. https://doi.org/10.1130/B35237.1

Hagemann, S.G., Angerer, T., Duuring, P., Rosière, C.A., Figueiredo e Silva, R.C., Lobato, L., Hensler, A.S., Walde, D.H.G., 2016. BIF-hosted iron mineral system: A review. Ore Geology Reviews 76, 317–359. https://doi.org/10.1016/j.oregeorev.2015.11.004

Hamilton, W.B., 1998. Archean magmatism and deformation were not products of plate tectonics. Precambrian Research 91, 143–179. https://doi.org/10.1016/S0301-9268(98)00042-4

Herzberg, C., Condie, K., Korenaga, J., 2010. Thermal history of the Earth and its petrological expression. Earth and Planetary Science Letters 292, 79–88. https://doi.org/10.1016/j.epsl.2010.01.022

Heubeck, C., Lowe, D.R., 1994a. Late syndepositional deformation and detachment tectonics in the Barberton Greenstone Belt, South Africa. Tectonics 13, 1514–1536. https://doi.org/10.1029/94TC01809

Heubeck, C., Lowe, D.R., 1994b. Depositional and tectonic setting of the Archean Moodies Group, Barberton Greenstone Belt, South Africa. Precambrian Research 68, 257–290. https://doi.org/10.1016/0301-9268(94)90033-7

Heubeck, C., Thomsen, T.B., Heredia, B.D., Zeh, A., Balling, P., 2023. The Malolotsha Klippe: Large-Scale Subhorizontal Tectonics Along the Southern Margin of the Archean Barberton Greenstone Belt, Eswatini. Tectonics 42. https://doi.org/10.1029/2022TC007359

Heubeck, C., Wendt, J.I., Toulkeridis, T., Kröner, A., Lowe, D.R., 1993. Timing of deformation of the Archaean Barberton Greenstone Belt, South Africa: constraints from zircon dating of the Salisbury Kop Pluton. South African Journal of Geology 1–8.

Hoatson, D.M., Jaireth, S., Jaques, A.L., 2006. Nickel sulfide deposits in Australia: Characteristics, resources, and potential. Ore Geology Reviews 29, 177–241. https://doi.org/10.1016/j.oregeorev.2006.05.002

Hoffmann, J.E., Kröner, A., Hegner, E., Viehmann, S., Xie, H., Iaccheri, L.M., Schneider, K.P., Hofmann, A., Wong, J., Geng, H., Yang, J., 2016. Source composition, fractional

crystallization and magma mixing processes in the 3.48–3.43Ga Tsawela tonalite suite (Ancient Gneiss Complex, Swaziland) – Implications for Palaeoarchaean geodynamics. Precambrian Research 276, 43–66. https://doi.org/10.1016/j.precamres.2016.01.026

Hofmann, A., 2005. The geochemistry of sedimentary rocks from the Fig Tree Group, Barberton greenstone belt: Implications for tectonic, hydrothermal and surface processes during mid-Archaean times. Precambrian Research 143, 23–49. https://doi.org/10.1016/j.precamres.2005.09.005

Hofmann, A., Pitcairn, I., Wilson, A., 2017. Gold mobility during Palaeoarchaean submarine alteration. Earth and Planetary Science Letters 462, 47–54. https://doi.org/10.1016/j.epsl.2017.01.008

Hofmann, A., Uwe Reimold, W., Koeberl, C., 2006. Archean spherule layers in the Barberton greenstone belt, South Africa: A discussion of problems related to the impact interpretation. Processes on the Early Earth. Geological Society of America. https://doi.org/10.1130/2006.2405(03)

Hunter, D.R., 1991. Crustal processes during Archaean evolution of the southeastern Kaapvaal province. Journal of African Earth Sciences (and the Middle East) 13, 13–25. https://doi.org/10.1016/0899-5362(91)90041-V

Hunter, D.R., 1970. The ancient Gneiss complex in Swaziland. South African Journal of Geology 73, 107–150.

Jackson, M.P.A., Eriksson, K.A., Harris, C.W., 1987. Early Archean foredeep sedimentation related to crustal shortening: a reinterpretation of the Barberton Sequence, Southern Africa. Tectonophysics 136, 197–221. https://doi.org/10.1016/0040-1951(87)90025-4

Jenner, F.E., Bennett, V.C., Nutman, A.P., Friend, C.R.L., Norman, M.D., Yaxley, G., 2009. Evidence for subduction at 3.8 Ga: Geochemistry of arc-like metabasalts from the southern edge of the Isua Supracrustal Belt. Chemical Geology 261, 83–98. https://doi.org/10.1016/j.chemgeo.2008.09.016

Johnson, S.E., Fletcher, J.M., Fanning, C.M., Vernon, R.H., Paterson, S.R., Tate, M.C., 2003. Structure, emplacement and lateral expansion of the San José tonalite pluton, Peninsular Ranges batholith, Baja California, México. Journal of Structural Geology 25, 1933–1957. https://doi.org/10.1016/S0191-8141(03)00015-4

Johnston, S.T., Weil, A.B., Gutierrez-Alonso, G., 2013. Oroclines: Thick and thin. Geological Society of America Bulletin 125, 643–663. https://doi.org/10.1130/B30765.1

Jones, C., Kisters, A., 2022. Regional and local controls of hydrothermal fluid flow and gold mineralization in the Sheba and Fairview mines, Barberton Greenstone Belt, South Africa. Ore Geology Reviews 144, 104805. https://doi.org/10.1016/j.oregeorev.2022.104805

Kamo, S.L., Davis, D.W., 1994. Reassessment of Archean crustal development in the Barberton Mountain Land, South Africa, based on U-Pb dating. Tectonics 13, 167–192. https://doi.org/10.1029/93TC02254

Karato, S., 2010. Rheology of the deep upper mantle and its implications for the preservation of the continental roots: A review. Tectonophysics 481, 82–98. https://doi.org/10.1016/j.tecto.2009.04.011

Kgaswane, E.M., Rathod, G.W., Saunders, I., 2018. Tectonic History of the Kaapvaal Craton: Constraints From Rheological Modeling. Journal of Geophysical Research: Solid Earth. https://doi.org/10.1029/2018JB015631

Kisters, A.F.M., Anhaeusser, C.R., 1995a. Emplacement features of Archaean TTG plutons along the southern margin of the Barberton greenstone belt, South Africa. Precambrian Research 75, 1–15. https://doi.org/10.1016/0301-9268(95)00003-N

Kisters, A.F.M., Anhaeusser, C.R., 1995b. The structural significance of the Steynsdorp pluton and anticline within the tectonomagmatic framework of the Barberton Mountain Land. South African Journal of Geology 98, 43–51.

Kisters, A.F.M., Belcher, R.W., Poujol, M., Dziggel, A., 2010. Continental growth and convergence-related arc plutonism in the Mesoarchaean: Evidence from the Barberton granitoid-greenstone terrain, South Africa. Precambrian Research 178, 15–26. https://doi.org/10.1016/j.precamres.2010.01.002

Kisters, A.F.M., Stevens, G., Dziggel, A., Armstrong, R.A., 2003. Extensional detachment faulting and core-complex formation in the southern Barberton granite–greenstone terrain, South Africa: evidence for a 3.2 Ga orogenic collapse. Precambrian Research 127, 355–378. https://doi.org/10.1016/j.precamres.2003.08.002

Kohler, E.A., Anhaeusser, C.R., 2002. Geology and geodynamic setting of Archaean silicic metavolcaniclastic rocks of the Bien Venue Formation, Fig Tree Group, northeast Barberton greenstone belt, South Africa. Precambrian Research 116, 199–235. https://doi.org/10.1016/S0301-9268(02)00021-9

Korenaga, J., 2006. Archean geodynamics and the thermal evolution of Earth. In: Benn, K., Mareschal, J.-C., Condie, K.C. (Eds.), Geophysical Monograph Series. American Geophysical Union, Washington, D. C., 7–32. https://doi.org/10.1029/164GM03

Kröner, A., Hegner, E., Wendt, J.I., Byerly, G.R., 1996. The oldest part of the Barberton granitoid-greenstone terrain, South Africa: evidence for crust formation between 3.5 and 3.7 Ga. Precambrian Research 78, 105–124. https://doi.org/10.1016/0301-9268(95)00072-0

Kröner, A., Hoffmann, J.E., Wong, J.M., Geng, H.-Y., Schneider, K.P., Xie, H., Yang, J.-H., Nhleko, N., 2019. Archaean Crystalline Rocks of the Eastern Kaapvaal Craton. In: Kröner, A., Hofmann, A. (Eds.), The Archaean Geology of the Kaapvaal Craton, Southern Africa, Regional Geology Reviews. Springer International Publishing, Cham, 1–32. https://doi.org/10.1007/978-3-319-78652-0_1

Lamb, S., 1987. Archean synsedimentary tectonic deformation—A comparison with the Quaternary. Geology 15, 565. https://doi.org/10.1130/0091-7613(1987)15<565:ASTDCW>2.0.CO;2

Lamb, S., Paris, I., 1988. Post-onverwacht group stratigraphy in the SE part of the Archaean Barbeton greenstone belt. Journal of African Earth Sciences (and the Middle East) 7, 285–306. https://doi.org/10.1016/0899-5362(88)90074-7

Lamb, S.H., 1986. Synsedimentary deformation and thrusting on the eatern margin of the Barberton Greenstone belt, Swaziland.

Lamb, S.H., 1984. Structures on the eastern margin of the Archaean Barberton greenstone belt, northwest Swaziland. Precambrian Tectonics Illustrated. 19–39.

Lana, C., Buick, I., Stevens, G., Rossouw, R., De Wet, W., 2011. 3230–3200 Ma post-orogenic extension and mid-crustal magmatism along the southeastern margin of the Barberton Greenstone Belt, South Africa. Journal of Structural Geology 33, 844–858. https://doi.org/10.1016/j.jsg.2011.03.007

Lana, C., Kisters, A., Stevens, G., 2010. Exhumation of Mesoarchean TTG gneisses from the middle crust: Insights from the Steynsdorp core complex, Barberton granitoid-greenstone terrain, South Africa. Geological Society of America Bulletin 122, 183–197. https://doi.org/10.1130/B26580.1

Lana, Cristiano, Tohver, E., Cawood, P., 2010. Quantifying rates of dome-and-keel formation in the Barberton granitoid-greenstone belt, South Africa. Precambrian Research 177, 199–211. https://doi.org/10.1016/j.precamres.2009.12.001

Lang, J., Baker, T., 2001. Intrusion-related gold systems: the present level of understanding. Mineralium Deposita 36, 477–489. https://doi.org/10.1007/s001260100184

Laurent, O., Björnsen, J., Wotzlaw, J.-F., Bretscher, S., Pimenta Silva, M., Moyen, J.-F., Ulmer, P., Bachmann, O., 2020. Earth's earliest granitoids are crystal-rich magma reservoirs tapped by silicic eruptions. Nature Geoscience 13, 163–169. https://doi.org/10.1038/s41561-019-0520-6

Ledevin, M., 2019. Archean Cherts. Earth's Oldest Rocks. Elsevier, 913–944. https://doi.org/10.1016/B978-0-444-63901-1.00037-X

Li, H., Zhang, Zengjie, Li, L., Zhang, Zhaochong, Chen, J., Yao, T., 2014. Types and general characteristics of the BIF-related iron deposits in China. Ore Geology Reviews 57, 264–287. https://doi.org/10.1016/j.oregeorev.2013.09.014

Lin, S., Parks, J., Heaman, L.M., Simonetti, A., Corkery, M.T., 2013. Diapirism and sagduction as a mechanism for deposition and burial of "Timiskaming-type" sedimentary sequences, Superior Province: Evidence from detrital zircon geochronology and implications for the Borden Lake conglomerate in the exposed middle to lower crust in the Kapuskasing uplift. Precambrian Research 238, 148–157. https://doi.org/10.1016/j.precamres.2013.09.012

Lowe, D.R., 1994. Accretionary history of the Archean Barberton Greenstone Belt (3.55-3.22 Ga), southern Africa. Geology 22, 1099. https://doi.org/10.1130/0091-7613(1994)022<1099:AHOTAB>2.3.CO;2

Lowe, D.R., 1980. Archean Sedimentation. Annual Review of Earth and Planetary Sciences 8, 145–167. https://doi.org/10.1146/annurev.ea.08.050180.001045

Lowe, D.R., Byerly, G.R., 2007a. Ironstone bodies of the Barberton greenstone belt, South Africa: Products of a Cenozoic hydrological system, not Archean hydrothermal vents! Geological Society of America Bulletin 119, 65–87. https://doi.org/10.1130/B25997.1

Lowe, D.R., Byerly, G.R., 2007b. Chapter 5.3 An Overview of the Geology of the Barberton Greenstone Belt and Vicinity: Implications for Early Crustal Development. Developments in Precambrian Geology. Elsevier, 481–526. https://doi.org/10.1016/S0166-2635(07)15053-2

Lowe, D.R., Byerly, G.R., Heubeck, C., 2012. Geologic map of the west-central Barberton Greenstone Belt, South Africa., scale 1:25000, Geological Society of America, Map and Chart Series No. 103. ed.

Lowe, D.R., Byerly, G.R., Heubeck, C., 1999. Structural divisions and development of the west-central part of the Barberton Greenstone Belt. In: Lowe, D.R., Byerly, G.R. (Eds.), Geologic Evolution of the Barberton Greenstone Belt, South Africa. Geological Society of America, 0. https://doi.org/10.1130/0-8137-2329-9.37

Martin, H., 2005. Genesis and Evolution of the Primitive Earth Continental Crust. In: Gargaud, M., Barbier, B., Martin, H., Reisse, J. (Eds.), Lectures in Astrobiology, Advances in

Astrobiology and Biogeophysics. Springer Berlin Heidelberg, Berlin, Heidelberg, 113–163. https://doi.org/10.1007/10913406_5

Martin, H., 1994. Chapter 6 The Archean Grey Gneisses and the Genesis of Continental Crust. Developments in Precambrian Geology. Elsevier, 205–259. https://doi.org/10.1016/S0166-2635(08)70224-X

Moyen, J.-F., Martin, H., 2012. Forty years of TTG research. Lithos 148, 312–336. https://doi.org/10.1016/j.lithos.2012.06.010

Moyen, J.-F., Stevens, G., Kisters, A., 2006. Record of mid-Archaean subduction from metamorphism in the Barberton terrain, South Africa. Nature 442, 559–562. https://doi.org/10.1038/nature04972

Moyen, J.-F., Stevens, G., Kisters, A.F.M., Belcher, R.W., 2007. Chapter 5.6 TTG Plutons of the Barberton Granitoid-Greenstone Terrain, South Africa. Developments in Precambrian Geology. Elsevier, 607–667. https://doi.org/10.1016/S0166-2635(07)15056-8

Moyen, J.-F., Stevens, G., Kisters, A.F.M., Belcher, R.W., Lemirre, B., 2019. TTG Plutons of the Barberton Granitoid-Greenstone Terrain, South Africa. Earth's Oldest Rocks. Elsevier, 615–653. https://doi.org/10.1016/B978-0-444-63901-1.00025-3

Moyen, J.-F., Zeh, A., Cuney, M., Dziggel, A., Carrouée, S., 2021. The multiple ways of recycling Archaean crust: A case study from the ca. 3.1 Ga granitoids from the Barberton Greenstone Belt, South Africa. Precambrian Research 353, 105998. https://doi.org/10.1016/j.precamres.2020.105998

Muntean, J.L., Frimmel, H.E., Phillips, N., Law, J., Myers, R., 2005. Controversies on the Origin of World-Class Gold Deposits, Part II: Witwatersrand Gold Deposits. SEG Discovery 7–19. https://doi.org/10.5382/SEGnews.2005-60.fea

Munyai, M.R., Dirks, P.H.G.M., Charlesworth, E.G., 2011. Archaean Gold Mineralisation during Post-orogenic Extension in the New Consort Gold Mine, Barberton Greenstone Belt, South Africa. South African Journal of Geology 114, 121–144. https://doi.org/10.2113/gssajg.114.2.121

Murphy, R.C.L., 2022. Stabilising a craton: the origin and emplacement of the 3.1 Ga Mpuluzi Batholith. thesis. Macquarie University. https://doi.org/10.25949/19442867.v1

Nguyen, P.T., Harris, L.B., Powell, C.M., Cox, S.F., 1998. Fault-valve behaviour in optimally oriented shear zones: an example at the Revenge gold mine, Kambalda, Western Australia. Journal of Structural Geology 20, 1625–1640. https://doi.org/10.1016/S0191-8141(98)00054-6

Nisbet, E.G., Cheadle, M.J., Arndt, N.T., Bickle, M.J., 1993. Constraining the potential temperature of the Archaean mantle: A review of the evidence from komatiites. Lithos 30, 291–307. https://doi.org/10.1016/0024-4937(93)90042-B

Otto, A., Dziggel, A., Kisters, A.F.M., Meyer, F.M., 2007. The New Consort Gold Mine, Barberton greenstone belt, South Africa: orogenic gold mineralization in a condensed metamorphic profile. Mineralium Deposita 42, 715–735. https://doi.org/10.1007/s00126-007-0135-5

Palme, H., O'Neill, H.St.C., 2007. 2.01 - Cosmochemical Estimates of Mantle Composition. In: Holland, H.D., Turekian, K.K. (Eds.), Treatise on Geochemistry. Pergamon, Oxford, 1–38. https://doi.org/10.1016/B0-08-043751-6/02177-0

Paterson, S.R., Fowler, T.K., Schmidt, K.L., Yoshinobu, A.S., Yuan, E.S., Miller, R.B., 1998. Interpreting magmatic fabric patterns in plutons. Lithos 44, 53–82. https://doi.org/10.1016/S0024-4937(98)00022-X

Pearton, T., Viljoen, M., 2017. Gold on the Kaapvaal Craton, outside the Witwatersrand Basin, South Africa. South African Journal of Geology 120, 101–132. https://doi.org/10.25131/gssajg.120.1.101

Pintos Cerda, L.R., Jones, C., Kisters, A.F.M., 2022. The effects of fault-zone architecture, wall-rock competence and fluid pressure variations on hydrothermal veining and gold mineralization along the Sheba Fault, Barberton Greenstone Belt, South Africa. Journal of African Earth Sciences 192, 104554. https://doi.org/10.1016/j.jafrearsci.2022.104554

Pintos Cerda, L.R., Jones, C., Kisters, A.F.M., 2020. Multi-stage alteration, rheological switches and high-grade gold mineralization at Sheba Mine, Barberton Greenstone Belt, South Africa. Ore Geology Reviews 127, 103852. https://doi.org/10.1016/j.oregeorev.2020.103852

Porwal, A., González-Álvarez, I., Markwitz, V., McCuaig, T.C., Mamuse, A., 2010. Weights-of-evidence and logistic regression modeling of magmatic nickel sulfide prospectivity in the Yilgarn Craton, Western Australia. Ore Geology Reviews 38, 184–196. https://doi.org/10.1016/j.oregeorev.2010.04.002

Poujol, M., Robb, L.J., Anhaeusser, C.R., Gericke, B., 2003. A review of the geochronological constraints on the evolution of the Kaapvaal Craton, South Africa. Precambrian Research 127, 181–213. https://doi.org/10.1016/S0301-9268(03)00187-6

Ramsay, J.G., 1963. Structural investigations in the Barberton Mountian land, Eastern Transvaal. South African Journal of Geology 66, 353–401.

Robb, L.J., Brandl, G., Anhaeusser, C.R., Poujol, M., Johnson, M.R., Thomas, R.J., 2006. Archaean granitoid intrusions. The Geology of South Africa. Geological Society of South Africa, Johannesburg/Council for Geoscience Pretoria, Johannesburg, South Africa, 57–94.

Robert, F., Boullier, A.-M., Firdaous, K., 1995. Gold-quartz veins in metamorphic terranes and their bearing on the role of fluids in faulting. Journal of Geophysical Research: Solid Earth 100, 12861–12879. https://doi.org/10.1029/95JB00190

Robin, C., 2011. Pétrogenèse des komatiites de Barberton (Afrique du Sud). PhD Thesis. Université de Grenoble.

Salvo, M.D., Gadais, M., Roche-Woillez, G., 2005. L'estimation de la densité par la méthode du noyau: méthode et outils. Note méthodologique et technique. Rapport de recherche. Centre d'études sur les réseaux, les transports, l'urbanisme et les constructions publiques (CERTU).

Savage, H.M., Brodsky, E.E., 2011. Collateral damage: Evolution with displacement of fracture distribution and secondary fault strands in fault damage zones. Journal of Geophysical Research 116, B03405. https://doi.org/10.1029/2010JB007665

Schmitz, M., Heubeck, C., 2021. Constraints on deformation mechanisms of the Barberton Greenstone Belt from regional stratigraphic and structural data of the synorogenic Moodies Group. Precambrian Research 362, 106177. https://doi.org/10.1016/j.precamres.2021.106177

Schmitz, M.D., Bowring, S.A., de Wit, M.J., Gartz, V., 2004. Subduction and terrane collision stabilize the western Kaapvaal craton tectosphere 2.9 billion years ago. Earth and Planetary Science Letters 222, 363–376. https://doi.org/10.1016/j.epsl.2004.03.036

Schoene, B., Bowring, S.A., 2010. Rates and mechanisms of Mesoarchean magmatic arc construction, eastern Kaapvaal craton, Swaziland. Geological Society of America Bulletin 122, 408–429. https://doi.org/10.1130/B26501.1

Schoene, B., Bowring, S.A., 2007. Determining accurate temperature–time paths from U–Pb thermochronology: An example from the Kaapvaal craton, southern Africa. Geochimica et Cosmochimica Acta 71, 165–185. https://doi.org/10.1016/j.gca.2006.08.029

Schoene, B., de Wit, M.J., Bowring, S.A., 2008. Mesoarchean assembly and stabilization of the eastern Kaapvaal craton: A structural-thermochronological perspective: EVOLUTION OF EAST KAAPVAAL CRATON. Tectonics 27, n/a-n/a. https://doi.org/10.1029/2008TC002267

Schoene, B., Dudas, F.O.L., Bowring, S.A., de Wit, M., 2009. Sm-Nd isotopic mapping of lithospheric growth and stabilization in the eastern Kaapvaal craton. Terra Nova 21, 219–228. https://doi.org/10.1111/j.1365-3121.2009.00877.x

Schouwstra, R.P., 1995. Wall-rock alteration as a guide to gold-bearing fracture zones in the Zwartkoppie Section, Sheba Gold Mine, South Africa. 16.

Scoates, J.S., Friedman, R.M., 2008. Precise Age of the Platiniferous Merensky Reef, Bushveld Complex, South Africa, by the U-Pb Zircon Chemical Abrasion ID-TIMS Technique. Economic Geology 103, 465–471. https://doi.org/10.2113/gsecongeo.103.3.465

Setianto, A., Triandini, T., 2015. Comparaison of Kriging and Inerse Distance Weighted (IDW) Interpolation Methods in lineament Extraction and Analysis. Journal of Applied Geology 5. https://doi.org/10.22146/jag.7204

Sibson, R.H., 1989. Earthquake faulting as a structural process. Journal of Structural Geology 11, 1–14. https://doi.org/10.1016/0191-8141(89)90032-1

Silverman, B.W., 1986. Density Estimation for Statistics and Data Analysis. CRC Press.

Sleep, N.H., 1992. Archean plate tectonics: what can be learned from continental geology? Canadian Journal of Earth Sciences 29, 2066–2071. https://doi.org/10.1139/e92-164

Sleep, N.H., Windley, B.F., 1982. Archean Plate Tectonics: Constraints and Inferences. The Journal of Geology. https://doi.org/10.1086/628691

Solum, J.G., Huisman, B.A.H., 2017. Toward the creation of models to predict static and dynamic fault-seal potential in carbonates. Petroleum Geoscience 23, 70–91. https://doi.org/10.1144/petgeo2016-044

Spatial Analyst toolbox | Documentation [WWW Document], n.d. An overview of the Spatial Analyst toolbox—ArcGIS Pro | Documentation. URL https://pro.arcgis.com/en/pro-app/latest/tool-reference/spatial-analyst/an-overview-of-the-spatial-analyst-toolbox.htm (accessed 7.11.23).

Spencer, C.J., Roberts, N.M.W., Santosh, M., 2017. Growth, destruction, and preservation of Earth's continental crust. Earth-Science Reviews 172, 87–106. https://doi.org/10.1016/j.earscirev.2017.07.013

Stevens, G., Moyen, J.-F., 2007. Chapter 5.7 Metamorphism in the Barberton Granite Greenstone Terrain: A Record of Paleoarchean Accretion. Developments in

Precambrian Geology. Elsevier, 669–698. https://doi.org/10.1016/S0166-2635(07)15057-X

Thompson, J.F.H., Sillitoe, R.H., Baker, T., Lang, J.R., Mortensen, J.K., 1999. Intrusion-related gold deposits associated with tungsten-tin provinces. Mineralium Deposita 34, 323–334. https://doi.org/10.1007/s001260050207

Thompson Stiegler, M., Cooper, M., Byerly, G.R., Lowe, D.R., 2012. Geochemistry and petrology of komatiites of the Pioneer Ultramafic Complex of the 3.3 Ga Weltevreden Formation, Barberton greenstone belt, South Africa. Precambrian Research 212–213, 1–12. https://doi.org/10.1016/j.precamres.2012.04.017

Tice, M.M., Bostick, B.C., Lowe, D.R., 2004. Thermal history of the 3.5–3.2 Ga Onverwacht and Fig Tree Groups, Barberton greenstone belt, South Africa, inferred by Raman microspectroscopy of carbonaceous material. Geology 32, 37. https://doi.org/10.1130/G19915.1

Torabi, A., Berg, S.S., 2011. Scaling of fault attributes: A review. Marine and Petroleum Geology 28, 1444–1460. https://doi.org/10.1016/j.marpetgeo.2011.04.003

Travers, L., Chauvet, A., Lehmann, J., 2023. Structure and Distribution of the Gold-Related Quartz Vein Systems in the Southwestern Part of the Barberton Greenstone Belt (South Africa, Eswatini). Minerals 13, 1034. https://doi.org/10.3390/min13081034

Tucker, R.F., Viljoen, R.P., Viljoen, M.J., 2016. A Review of the Witwatersrand Basin - The World's Greatest Goldfield. Episodes 39, 104–133. https://doi.org/10.18814/epiiugs/2016/v39i2/95771

Van der Westhuizen, W.A., De Bruiyn, H., Meintjes, P.G., 1991. The Ventersdorp supergroup: an overview. Journal of African Earth Sciences (and the Middle East) 13, 83–105. https://doi.org/10.1016/0899-5362(91)90045-Z

van Hunen, J., Moyen, J.-F., 2012. Archean Subduction: Fact or Fiction? Annual Review of Earth and Planetary Sciences 40, 195–219. https://doi.org/10.1146/annurev-earth-042711-105255

van Hunen, J., van den Berg, A.P., 2008. Plate tectonics on the early Earth: Limitations imposed by strength and buoyancy of subducted lithosphere. Lithos 103, 217–235. https://doi.org/10.1016/j.lithos.2007.09.016

Van Kranendonk, M.J., 2021. Gliding and overthrust nappe tectonics of the Barberton Greenstone Belt revisited: A review of deformation styles and processes. South African Journal of Geology 124, 181–210. https://doi.org/10.25131/sajg.124.0017

Van Kranendonk, M.J., 2011. Cool greenstone drips and the role of partial convective overturn in Barberton greenstone belt evolution. Journal of African Earth Sciences 60, 346–352. https://doi.org/10.1016/j.jafrearsci.2011.03.012

Van Kranendonk, M.J., Kröner, A., Hegner, E., Connelly, J., 2009. Age, lithology and structural evolution of the c. 3.53 Ga Theespruit Formation in the Tjakastad area, southwestern Barberton Greenstone Belt, South Africa, with implications for Archaean tectonics. Chemical Geology 261, 115–139. https://doi.org/10.1016/j.chemgeo.2008.11.006

Van Kranendonk, M.J., Kröner, A., Hoffmann, J.E., Nagel, T., Anhaeusser, C.R., 2014. Just another drip: Re-analysis of a proposed Mesoarchean suture from the Barberton Mountain Land, South Africa. Precambrian Research 254, 19–35. https://doi.org/10.1016/j.precamres.2014.07.022

Van Reenen, D.D., Barton, J.M., Roering, C., Smith, C.A., Van Schalkwyk, J.F., 1987. Deep crystal response to continental collision: The Limpopo belt of southern Africa. Geology 15, 11. https://doi.org/10.1130/0091-7613(1987)15<11:DCRTCC>2.0.CO;2

Viljoen, M.J., 1963. The Geology of the Lily Syncline and Portion of the Eureka Syncline Between the Consort Mine and Joe's Luck Siding, Barberton Mountain Land. MSc Thesis. University of the Witwatersrand, Johannesburg, South Africa.

Viljoen, M.J., Viljoen, R.P., 1969. An introduction to the geology of the Barberton granite-greenstone terrain. Spec. Publ. Geol. Soc. S. Afr. 2, 9–27.

Viljoen, R.P., Saager, R., Viljoen, M.J., 1969. Metallogenesis and ore control in the Steynsdorp goldfield, Barberton mountain land, South Africa. Economic Geology 64, 778–797. https://doi.org/10.2113/gsecongeo.64.7.778

Visser, D.J.L., 1956. The geology of the Barberton area. Union of South Africa, Department of Mines.

Wang, Q., Yang, Lin, Zhao, H., Groves, D.I., Weng, W., Xue, S., Li, H., Dong, C., Yang, Liqiang, Li, D., Deng, J., 2022. Towards a universal model for orogenic gold systems: A perspective based on Chinese examples with geodynamic, temporal, and deposit-scale structural and geochemical diversity. Earth-Science Reviews 224, 103861. https://doi.org/10.1016/j.earscirev.2021.103861

Ward, J.H.W., 2000. Metallogenic map of the Barberton Greenstone Belt, South Africa and Swaziland., scale 1:100000, Council for Geoscience. ed.

Weed, D.L., 2005. Weight of Evidence: A Review of Concept and Methods. Risk Analysis 25, 1545–1557. https://doi.org/10.1111/j.1539-6924.2005.00699.x

Westraat, JanusD., Kisters, AlexanderF.M., Poujol, M., Stevens, G., 2005. Transcurrent shearing, granite sheeting and the incremental construction of the tabular 3.1 Ga Mpuluzi batholith, Barberton granite–greenstone terrane, South Africa. Journal of the Geological Society 162, 373–388. https://doi.org/10.1144/0016-764904-026

Whitney, D.L., Evans, B.W., 2010. Abbreviations for names of rock-forming minerals. American Mineralogist 95, 185–187. https://doi.org/10.2138/am.2010.3371

Wu, J., Zeng, Q., Santosh, M., Fan, H., Wei, Z., Yang, K., Zhang, Z., Li, X., Liang, G., 2021. Intrusion-related orogenic gold deposit in the East Kunlun belt, NW China: A multiproxy investigation. Ore Geology Reviews 139, 104550. https://doi.org/10.1016/j.oregeorev.2021.104550

Yeend, W.E., Shawe, D., R., 1989. Gold in Placer Deposits. U.S. Geological Survey Bulletin.

Yin, A., Harrison, T.M., 2000. Geologic Evolution of the Himalayan-Tibetan Orogen. Annual Review of Earth and Planetary Sciences 28, 211–280. https://doi.org/10.1146/annurev.earth.28.1.211

Annexes

Annexe 1:

Table 1. List of Minerals Abbreviations

Many of the mineral abbreviations come from Whitney and Evans (2010).

Abbreviated Term	Mineral Name
Ab	Albite
Bt	Biotite
Ca	Carbonate (indeterminate)
Ccp	Chalcopyrite
Chl	Chlorite
Fsp	Feldspar
Qz	Quartz
Mc	Microcline
Mcs	Micas (indeterminate)
Mgs	Magnesite
Mlc	Malachite
Ms	Muscovite
Ox	Oxide
Pl	Plagioclase
Po	Pyrrhotite
Py	Pyrite
Tlc	Talc
Tur	Tourmaline

Annexe 2:

Table 2. List of Gold Occurrences and Deposit

After the Metallogenic Map of the Barberton Greenstone Belt compiled by Ward (2000).

N°	Name	Commodity	Morphology	WGS84_X	WGS84_Y
707		Gold	Mineralised shear zone	31,3123817	-25,7646813
283	ROSE REEF	Gold	Vein	31,09196378	-25,73934182
281	KIMBERLEY SHEBA	Gold	Vein	31,10044101	-25,72737947
277	BLUE ROCK REEF	Gold	Vein	31,1028403	-25,7202857
276	KIDSON	Gold	Vein	31,10340542	-25,71832265
256	THOMAS	Gold	Vein	31,12588239	-25,6938542
251	GOLDEN VALLEY	Gold	Vein	31,10849454	-25,67819194
941	HAZELMERE	Gold	Mineralised shear zone	31,08612926	-26,12261869
940		Gold	Mineralised shear zone	31,08131085	-26,12273767
943	OBAN	Gold	Mineralised shear zone	31,07470785	-26,12975708
947	WAVERLEY REEFS	Gold	Mineralised shear zone	31,06929874	-26,14286679
948	INVANHOE	Gold	Mineralised shear zone	31,07015535	-26,14581732
950		Gold	Mineralised shear zone	31,06758553	-26,1507666
952		Gold	Mineralised shear zone	31,0716782	-26,15552552
955	PRIMROSE	Gold	Mineralised shear zone	31,07120231	-26,16085551
956	WELCOME	Gold	Mineralised shear zone	31,09308146	-26,14945789
963	ART UNION	Gold	Mineralised shear zone	31,07410525	-26,17265764
964	ART UNION EXTENSION	Gold	Mineralised shear zone	31,06708584	-26,17985551
966	RED REEFS	Gold	Mineralised shear zone	31,08011339	-26,19484611
968	MOTJANE	Gold	Mineralised shear zone	31,02611979	-26,23164029
828	TUG O' WAR	Gold	Mineralised shear zone	30,97124111	-26,13448791
826	ST GEORGE	Gold	Mineralised shear zone	30,96564462	-26,12466549
827	GYPSY QUEEN	Gold	Mineralised shear zone	30,99436947	-26,1214675
935	MOTHER OF ALL	Gold	Mineralised shear zone	31,01195845	-26,12455128
937	CONQUEROR'S WAY	Gold	Mineralised shear zone	31,02360829	-26,14054126
933	UNITY	Gold	Mineralised shear zone	31,00257386	-26,11347965
932	BOARSHEAD	Gold	Mineralised shear zone	31,00166014	-26,11256593
931	BEACONSFIELD	Gold	Mineralised shear zone	31,00126039	-26,10845423
930	IDAHO	Gold	Mineralised shear zone	31,00000404	-26,09651885
821	COMSTOCK	Gold	Mineralised shear zone	30,99206616	-26,08943757
928	WAVE	Gold	Mineralised shear zone	31,00166014	-26,08349844
927	ATLAS	Gold	Mineralised shear zone	31,0014222	-26,07637909
926	MONARCH	Gold	Mineralised shear zone	31,0150803	-26,07342856
925	HOMESTEAD	Gold	Mineralised shear zone	31,01541343	-26,06743232
924	NEVADA	Gold	Mineralised shear zone	31,01170147	-26,06648053
923	CONTRACTORS	Gold	Mineralised shear zone	31,01384298	-26,06253063
929	HAMILTON	Gold	Mineralised shear zone	31,04620365	-26,07247678
819	BEHIND THE SCENES	Gold	Mineralised shear zone	30,97834618	-26,09859184
816		Gold	Mineralised shear zone	30,9687522	-26,10652972
818		Gold	Mineralised shear zone	30,97783222	-26,10247512
817	CORONELLA	Gold	Mineralised shear zone	30,97623322	-26,1063584
823	ROCHFORD	Gold	Mineralised shear zone	30,97377762	-26,11349678
904		Gold	Mineralised shear zone	31,02647217	-26,03141455
903	OVERBERG	Gold	Mineralised shear zone	31,0206857	-26,02745976
902	INDEPENDENT	Gold	Mineralised shear zone	31,01452456	-26,02754302

901	DICK'S LUCK	Gold	Mineralised shear zone	31,01531552	-26,02342172
907		Gold	Mineralised shear zone	31,03275819	-26,0243792
908	THISTLE	Gold	Mineralised shear zone	31,03513106	-26,02350498
909	DURBAN SYNDICATE	Gold	Mineralised shear zone	31,05016628	-26,03147909
910	MOGUL	Gold	Mineralised shear zone	31,06848813	-26,03461997
814		Gold	Mineralised shear zone	30,98828377	-26,03440482
808		Gold	Mineralised shear zone	30,93940488	-26,01741928
805		Gold	Mineralised shear zone	30,92684133	-26,00736843
804		Gold	Mineralised shear zone	30,9210164	-26,00851057
802	KOMATI LILY	Gold	Mineralised shear zone	30,90788178	-26,01947513
801		Gold	Mineralised shear zone	30,90187543	-26,01536243
556	ONVERWACHT	Gold	Mineralised shear zone	30,92017189	-25,98642818
555	VIOLET	Gold	Mineralised shear zone	30,84198566	-25,96236755
549		Gold	Mineralised shear zone	30,97642657	-25,84554274
547	SHEBANG	Gold	Mineralised shear zone	30,98433828	-25,84658375
545	GOLDEN HILL	Gold	Mineralised shear zone	30,98173277	-25,83151938
543	CUADRO	Gold	Mineralised shear zone	30,98647305	-25,82353907
606	DAISY	Gold	Mineralised shear zone	31,0496725	-25,79788285
607		Gold	Mineralised shear zone	31,05909516	-25,79488473
608	RIMERS	Gold	Mineralised shear zone	31,05825046	-25,79192706
614	ALBERTHA	Gold	Mineralised shear zone	31,08503563	-25,77262947
616	CHEVAL DE COURSE	Gold	Mineralised shear zone	31,08729612	-25,76650236
615	TRUE BLUE	Gold	Mineralised shear zone	31,09505911	-25,77265921
664	BLACK DIAMOND CREEK	Gold	Mineralised shear zone	31,22392847	-25,90366488
619	ALFSTROM	Gold	Mineralised shear zone	31,10363504	-25,76154219
279		Gold	Mineralised shear zone	31,10850025	-25,72036978
280		Gold	Mineralised shear zone	31,10735811	-25,72240422
275		Gold	Mineralised shear zone	31,11514192	-25,71724277
274		Gold	Mineralised shear zone	31,1209597	-25,71642186
273		Gold	Mineralised shear zone	31,12791962	-25,71585079
271		Gold	Mineralised shear zone	31,13250294	-25,7137621
272		Gold	Mineralised shear zone	31,12896944	-25,71372641
240	CALEDONIAN	Gold	Mineralised shear zone	31,0633677	-25,71256047
241	MAZEPPA	Gold	Mineralised shear zone	31,07453927	-25,71256047
245		Gold	Mineralised shear zone	31,08841586	-25,68722557
246		Gold	Mineralised shear zone	31,0926394	-25,68425124
247	WOODSTOCK	Gold	Mineralised shear zone	31,08731535	-25,6762503
622	CONDOR	Gold	Mineralised shear zone	31,13861095	-25,7547988
340	MARTIN'S REEF	Gold	Mineralised shear zone	31,30017476	-25,72470175
342	BROWN'S	Gold	Mineralised shear zone	31,30814596	-25,72267921
348	GORDON	Gold	Mineralised shear zone	31,4082782	-25,7466744
330	ROSE'S FORTUNE	Gold	Mineralised shear zone	31,27824812	-25,67662555
347	BON ACCORD	Gold	Mineralised shear zone	31,40511949	-25,66648251
328	WEENEN COUNTRY	Gold	Mineralised shear zone	31,35313124	-25,6495813
326	ADAMANDA	Gold	Mineralised shear zone	31,37989423	-25,63750077
325	SCOTSMAN	Gold	Mineralised shear zone	31,41166817	-25,62657064
416	EXILE	Gold	Mineralised shear zone	31,59192285	-25,5957123
409	SUSSEX	Gold	Mineralised shear zone	31,5329186	-25,53276282
402	FIGARO	Gold	Mineralised shear zone	31,60590985	-25,47648857
111	HESTER	Gold	Mineralised shear zone	30,77781315	-25,56634346
117	OPHIR	Gold	Mineralised shear zone	30,79858585	-25,56423763
120	NORTH SHEBA	Gold	Mineralised shear zone	30,87101968	-25,5682193
121	CONDOR	Gold	Mineralised shear zone	30,88565337	-25,57517923
122	ALPEDOR	Gold	Mineralised shear zone	30,90399901	-25,57239526
126	LANCASHIRE	Gold	Mineralised shear zone	30,94144489	-25,5963136

129	KAFFIRS LIMITED	Gold	Mineralised shear zone	30,96724419	-25,60832988
131	MARY HOPE	Gold	Mineralised shear zone	30,98887379	-25,61824477
133	NEW INDEPENDENT	Gold	Mineralised shear zone	30,97745238	-25,63427044
134	BONNY DUNDEE	Gold	Mineralised shear zone	30,98869533	-25,63330676
138	JUMBO	Gold	Mineralised shear zone	30,99082019	-25,64533732
204	GEM	Gold	Mineralised shear zone	31,0064691	-25,6211831
214	OLGA	Gold	Mineralised shear zone	31,01664586	-25,64745136
220		Gold	Mineralised shear zone	31,03057998	-25,6583588
222	VERDITE	Gold	Mineralised shear zone	31,03482732	-25,65942956
267	NIL DESPERANDUM	Gold	Mineralised shear zone	31,121648	-25,70737509
253		Gold	Mineralised shear zone	31,1062291	-25,70528116
255		Gold	Mineralised shear zone	31,10822784	-25,70328242
264		Gold	Mineralised shear zone	31,12345639	-25,70137885
263	EUREKA	Gold	Mineralised shear zone	31,1278346	-25,6998084
265	MAMBA	Gold	Mineralised shear zone	31,13083272	-25,70180715
266		Gold	Mineralised shear zone	31,12864362	-25,7038059
322	OVERTON	Gold	Mineralised shear zone	31,26576753	-25,62171211
286	GREAT SHE	Gold	Mineralised shear zone	31,15486184	-25,71070078
288	LOCHIEL	Gold	Mineralised shear zone	31,15975164	-25,70570391
290	CLEOPATRA	Gold	Mineralised shear zone	31,20606219	-25,68673842
250	MAJAJA	Gold	Mineralised shear zone	31,13575509	-25,66175624
249	BULLION	Gold	Mineralised shear zone	31,11815184	-25,65515562
248	GERRO DE PASCO	Gold	Mineralised shear zone	31,10876486	-25,64812431
239	BRIAN BORU	Gold	Mineralised shear zone	31,05557096	-25,69343837
225	DUDLEY	Gold	Mineralised shear zone	31,04403533	-25,68864137
232		Gold	Mineralised shear zone	31,09446526	-25,6451229
231		Gold	Mineralised shear zone	31,08975393	-25,64412353
229		Gold	Mineralised shear zone	31,07983157	-25,64223185
228		Gold	Mineralised shear zone	31,06787478	-25,64851363
234		Gold	Mineralised shear zone	31,07344272	-25,65147606
258	THISTLE	Gold	Mineralised shear zone	31,13694222	-25,67974216
825	FULLARTON	Gold	Placer (alluvial)	30,97234994	-26,1185222
662	OLD ENGLAND	Gold	Mineralised shear zone	31,21942403	-25,93882963
919		Gold	Mineralised shear zone	31,16325988	-26,0039147
656	NOTTINGHAM HILL	Gold	Mineralised shear zone	31,16741204	-25,96385648
939	SHE EAST	Gold	Mineralised shear zone	31,08202469	-26,11958488
945	JIM'S LUCK	Gold	Mineralised shear zone	31,07634195	-26,13287305
946	KENILWORTH	Gold	Mineralised shear zone	31,09414032	-26,13458626
949	EVELYN	Gold	Mineralised shear zone	31,09328371	-26,14162947
953		Gold	Mineralised shear zone	31,07358177	-26,15666766
954	GITSHAMS	Gold	Mineralised shear zone	31,07872141	-26,15761945
967	ALBINO	Gold	Mineralised shear zone	31,0920107	-26,19674968
830	POST OFFICE	Gold	Mineralised shear zone	30,99122859	-26,14944996
820	GLENEFFER	Gold	Mineralised shear zone	30,97874593	-26,09453724
815		Gold	Mineralised shear zone	30,96349835	-26,10030505
824		Gold	Mineralised shear zone	30,97177887	-26,11652345
944	BUCKINGHAM	Gold	Mineralised shear zone	31,07375473	-26,1316629
813	SHEBA QUEEN	Gold	Mineralised shear zone	30,98438145	-26,03854508
812		Gold	Mineralised shear zone	30,9788611	-26,03949687
806		Gold	Mineralised shear zone	30,92998221	-26,01142303
807		Gold	Mineralised shear zone	30,93649242	-26,00845347
803		Gold	Mineralised shear zone	30,91239324	-26,01342178
554		Gold	Mineralised shear zone	30,81434584	-25,96134676
553		Gold	Mineralised shear zone	30,80449487	-25,97276817
552		Gold	Mineralised shear zone	30,79350176	-25,95834864
551		Gold	Mineralised shear zone	30,7827466	-25,96630794

502		Gold	Mineralised shear zone	30,71778969	-25,94134977
518	GREMLIN	Gold	Mineralised shear zone	30,86890388	-25,87740661
522		Gold	Mineralised shear zone	30,9003257	-25,84757912
526		Gold	Mineralised shear zone	30,91410754	-25,84054211
527		Gold	Mineralised shear zone	30,92027034	-25,84651455
532		Gold	Mineralised shear zone	30,92821775	-25,84354023
534		Gold	Mineralised shear zone	30,93299689	-25,83854633
535		Gold	Mineralised shear zone	30,94305904	-25,83948622
550	IVY PIONEER	Gold	Mineralised shear zone	30,97737835	-25,84048638
536		Gold	Mineralised shear zone	30,94858212	-25,83458651
537		Gold	Mineralised shear zone	30,94387079	-25,83058901
538		Gold	Mineralised shear zone	30,95225839	-25,82655583
541		Gold	Mineralised shear zone	30,96355963	-25,82457175
544		Gold	Mineralised shear zone	30,98177441	-25,82557113
542		Gold	Mineralised shear zone	30,98142732	-25,81659693
626	GREAT DE KAAP	Gold	Mineralised shear zone	31,02040622	-25,83553366
625	NOTTINGHAM CLAIMS	Gold	Mineralised shear zone	31,03998958	-25,82369108
611		Gold	Mineralised shear zone	31,07334653	-25,78295038
613	MYSIDORA	Gold	Mineralised shear zone	31,07834339	-25,77661506
655	EMLEMBE	Gold	Mineralised shear zone	31,12091722	-25,95154074
711	MHLEKWA	Gold	Mineralised shear zone	31,30675115	-25,85466851
701	LUFATA SOUTH	Gold	Mineralised shear zone	31,26214458	-25,81763061
702	LUFATA CENTRAL	Gold	Mineralised shear zone	31,27495798	-25,81266943
710	LOMATI EXTENSION	Gold	Mineralised shear zone	31,29719404	-25,81263374
703	LUFATA NORTH	Gold	Mineralised shear zone	31,29275635	-25,80267284
706		Gold	Mineralised shear zone	31,3129088	-25,78662774
618	HOTTENTOT	Gold	Mineralised shear zone	31,10570517	-25,75144137
282	WAGGON ROAD	Gold	Mineralised shear zone	31,10845344	-25,73348834
324	GREAT AMERICAN	Gold	Mineralised shear zone	31,37536532	-25,61460163
412	BIG BUFFALO	Gold	Mineralised shear zone	31,51234386	-25,59963543
408	ROGOFF'S	Gold	Mineralised shear zone	31,54048528	-25,52671899
407	BEACON	Gold	Mineralised shear zone	31,55219223	-25,51972338
405	COULTER	Gold	Mineralised shear zone	31,56954802	-25,51064811
404	HORSESHOE	Gold	Mineralised shear zone	31,57731101	-25,50353947
403	THORNHILL	Gold	Mineralised shear zone	31,5912499	-25,48991468
113	MAIZIE	Gold	Mineralised shear zone	30,78869918	-25,56727145
119	KOFFIEKULTUUR	Gold	Mineralised shear zone	30,82113902	-25,56436125
208		Gold	Mineralised shear zone	31,00272959	-25,6282632
201		Gold	Mineralised shear zone	31,02380942	-25,61330113
291	HONEYBIRD	Gold	Mineralised shear zone	31,21659131	-25,68566766
289	MEXICAN	Gold	Mineralised shear zone	31,19824566	-25,68470398
822		Gold	Placer (alluvial)	30,97920279	-26,10938507
942		Gold	Mineralised shear zone	31,0791607	-26,12765338
951	AVALANCHE	Gold	Mineralised shear zone	31,06768071	-26,15581106
957	WATERFALL	Gold	Mineralised shear zone	31,0942117	-26,15272965
906	VON BRANDIS	Gold	Mineralised shear zone	31,03817379	-26,02848096
517	BELVUE	Gold	Mineralised shear zone	30,84788333	-25,88943875
520	SATISFIED	Gold	Mineralised shear zone	30,89033807	-25,85640192
520	WELTEVREDEN	Gold	Mineralised shear zone	30,89427845	-25,84943485
533	MOUNT MORGAN	Gold	Mineralised shear zone	30,93189639	-25,8435432
528	ESTADA	Gold	Mineralised shear zone	30,91022248	-25,85852191
540	TIGER TRAP	Gold	Mineralised shear zone	30,96717761	-25,83258776
603	GREAT SCOT	Gold	Mineralised shear zone	31,03694823	-25,81373661
604	ABBOTT'S	Gold	Mineralised shear zone	31,03794761	-25,80973911
609	CASTALIAN	Gold	Mineralised shear zone	31,06684983	-25,79589854

610	GOLDEN CRESCENT	Gold	Mineralised shear zone	31,06442355	-25,78592471
612	MAY	Gold	Mineralised shear zone	31,07804596	-25,78066015
658	DEVIL'S REEF	Gold	Mineralised shear zone	31,17074283	-25,93871624
639	KOBOLONBO	Gold	Mineralised shear zone	31,19943737	-25,89175022
708	WYLDSDALE	Gold	Mineralised shear zone	31,28520156	-25,81566755
709	LOMATI	Gold	Mineralised shear zone	31,29391039	-25,81466818
620	DEVONIAN	Gold	Mineralised shear zone	31,1042418	-25,76864488
621	FLORENCE	Gold	Mineralised shear zone	31,10806083	-25,7676455
617	NEW ORATAVA	Gold	Mineralised shear zone	31,09235639	-25,75758038
284	NORTH STAR	Gold	Mineralised shear zone	31,09171394	-25,74644451
285	ULUNDI	Gold	Mineralised shear zone	31,13366602	-25,7228821
623	OLD ORATAVA	Gold	Mineralised shear zone	31,14503549	-25,75682134
333	CASCADE	Gold	Mineralised shear zone	31,26539656	-25,73770098
335	IMPERIAL	Gold	Mineralised shear zone	31,27821591	-25,73770098
336	VESUVIUS	Gold	Mineralised shear zone	31,28463212	-25,72768345
343	CLIFFORD SCOTT	Gold	Mineralised shear zone	31,31591489	-25,72046234
345	CROWN	Gold	Mineralised shear zone	31,33646749	-25,71466241
349	DAISY	Gold	Mineralised shear zone	31,41325127	-25,74262932
346	AURORA	Gold	Mineralised shear zone	31,37644253	-25,70054132
329	KIMBERLEY IMPERIAL	Gold	Mineralised shear zone	31,32319911	-25,66991785
221	ALBION	Gold	Mineralised shear zone	31,02727699	-25,66147887
627	SVENGALI	Gold	Stockwork	31,02812076	-25,86646559
960	FORBES REEF	Gold	Mineralised shear zone	31,1043839	-26,15927317
519	MONTROSE	Gold	Mineralised shear zone	30,90465925	-25,88450319
529	MAID OF THE MOUNTAIN	Gold	Mineralised shear zone	30,93418598	-25,87139712
539	PIONEER	Gold	Mineralised shear zone	30,96107429	-25,83255207
602	ROSETTA	Gold	Mineralised shear zone	31,01603277	-25,81566397
661	PIGG'S PEAK	Gold	Mineralised shear zone	31,21171985	-25,94773249
252	BELFAST	Gold	Mineralised shear zone	31,07918052	-25,73027646
242	VICTORIA	Gold	Mineralised shear zone	31,07420452	-25,69156808
243	CLUTHA	Gold	Mineralised shear zone	31,08553076	-25,68425124
624	EAGLE'S NEST	Gold	Mineralised shear zone	31,16448758	-25,75384701
334	MAKONJWA	Gold	Mineralised shear zone	31,2643258	-25,74665371
332	BARBROOK	Gold	Mineralised shear zone	31,25198235	-25,74064557
337	BUSHBUCK	Gold	Mineralised shear zone	31,29465679	-25,71567193
338	DAYLIGHT	Gold	Mineralised shear zone	31,30388553	-25,71466423
339	TAYLOR'S	Gold	Mineralised shear zone	31,2997881	-25,72366073
341	FRENCH BOB'S	Gold	Mineralised shear zone	31,30294088	-25,72366073
344	MAID OF THE MIST	Gold	Mineralised shear zone	31,32349943	-25,72073003
331	LILY	Gold	Mineralised shear zone	31,26736803	-25,67658213
327	THREE SISTERS	Gold	Mineralised shear zone	31,37373143	-25,64259282
132	WORCESTER	Gold	Mineralised shear zone	30,97652439	-25,62420532
253	VICTORY HILL	Gold	Mineralised shear zone	31,10713329	-25,7042342
262	BONANZA	Gold	Mineralised shear zone	31,14900229	-25,70277797
257	JOE'S LUCK	Gold	Mineralised shear zone	31,13002265	-25,69275964
287	ROYAL SHEBA	Gold	Mineralised shear zone	31,1625713	-25,71262814
269	GOLDEN QUARRY	Gold	Stockwork	31,13035683	-25,70675643
546	AGNES	Gold	Mineralised shear zone	30,99538493	-25,84249108
278	FAIRVIEW	Gold	Mineralised shear zone	31,10910463	-25,71828062
270	SHEBA	Gold	Mineralised shear zone	31,1344303	-25,71479717
233	NEW CONSORT	Gold	Mineralised shear zone	31,08049782	-25,65007932
530	PRINCETON	Gold	Mineralised shear zone	30,96122449	-25,86417552
548	ALPINE	Gold	Mineralised shear zone	30,96963222	-25,84551299
605	FORTUNA	Gold	Mineralised shear zone	31,04885159	-25,80291541

Annexe 3:

Table 3. SEM Analysis of feldspars.

Malolotja SEM-EDS feldspars analysis

Type	Sample Name	electron image nu.	sp nu.	Element abundance (± standard deviation) (weight %)										
				O	Si	Al	C	Na	K	Ca	Fe	Mg	Ti	Ba
Mineralised vein	LA5A	elec. im. 12	sp. 85	56,0 (± 1,9)	22,8 (± 4,8)	7,2 (± 3,7)	6,9 (± 0,8)	0,2 (± 0,1)	6,5 (± 3,4)	0,1 (± 0,0)	0,1 (± 0,0)	0,0 (± 0,0)	0,2 (± 0,1)	-
Mineralised vein	LA5A	elec. im. 12	sp. 86	56,7 (± 1,9)	23,3 (± 4,8)	7,4 (± 3,7)	5,6 (± 0,8)	0,3 (± 0,1)	6,4 (± 3,4)	0,0 (± 0,0)	0,0 (± 0,0)	0,0 (± 0,0)	0,2 (± 0,1)	-
Mineralised vein	LA5A	elec. im. 12	sp. 87	56,1 (± 1,9)	24,2 (± 4,8)	6,8 (± 3,7)	6,1 (± 0,8)	0,2 (± 0,1)	6,5 (± 3,4)	0,0 (± 0,0)	0,0 (± 0,0)	0,0 (± 0,0)	0,0 (± 0,1)	-
Mineralised alteration	LA34D2	elec. im. 13	sp. 90	53,5 (± 3,1)	20,9 (± 10,5)	6,7 (± 4,1)	12,6 (± 6,4)	6,2 (± 2,9)	0,0 (± 0,0)	0,0 (± 0,0)	0,0 (± 0,0)	0,0 (± 0,0)	0,0 (± 0,0)	-
Mineralised alteration	LA34D2	elec. im. 13	sp. 91	54,2 (± 3,1)	20,6 (± 10,5)	6,5 (± 4,1)	11,6 (± 6,4)	6,2 (± 2,9)	0,0 (± 0,0)	0,0 (± 0,0)	0,0 (± 0,0)	0,0 (± 0,0)	0,0 (± 0,0)	-
Late vein	LA37B	elec. im. 1	sp. 1	56,6 (± 0,3)	23,0 (± 0,3)	7,7 (± 0,1)	5,4 (± 0,4)	0,7 (± 2,7)	6,5 (± 2,9)	0,1 (± 0,1)	0,0 (± 0,0)	0,0 (± 0,0)	0,1 (± 0,0)	-
Late vein	LA37B	elec. im. 1	sp. 2	57,0 (± 0,3)	23,1 (± 0,3)	7,8 (± 0,1)	4,6 (± 0,4)	0,8 (± 2,7)	6,7 (± 2,9)	0,0 (± 0,1)	0,0 (± 0,0)	0,0 (± 0,0)	0,0 (± 0,0)	-
Late vein	LA37B	elec. im. 1	sp. 3	57,0 (± 0,3)	22,6 (± 0,3)	7,6 (± 0,1)	5,7 (± 0,4)	6,1 (± 2,7)	0,8 (± 2,9)	0,1 (± 0,1)	0,0 (± 0,0)	0,0 (± 0,0)	0,0 (± 0,0)	-
Late vein	LA37B	elec. im. 1	sp. 4	57,1 (± 0,3)	22,8 (± 0,3)	7,9 (± 0,1)	4,9 (± 0,4)	6,0 (± 2,7)	0,9 (± 2,9)	0,2 (± 0,1)	0,0 (± 0,0)	0,0 (± 0,0)	0,0 (± 0,0)	-
Late vein	LA37B	elec. im. 1	sp. 5	56,9 (± 0,3)	22,5 (± 0,3)	7,6 (± 0,1)	5,4 (± 0,4)	5,9 (± 2,7)	1,1 (± 2,9)	0,2 (± 0,1)	0,0 (± 0,0)	0,0 (± 0,0)	0,0 (± 0,0)	-
Late vein	LA37B	elec. im. 1	sp. 6	56,4 (± 0,3)	22,4 (± 0,3)	7,6 (± 0,1)	4,7 (± 0,4)	5,8 (± 2,7)	1,0 (± 2,9)	0,2 (± 0,1)	0,1 (± 0,0)	0,0 (± 0,0)	0,0 (± 0,0)	-
Late vein	LA37B	elec. im. 2	sp. 7	56,0 (± 4,6)	23,4 (± 5,6)	7,9 (± 2,9)	4,8 (± 4,6)	0,8 (± 2,3)	6,9 (± 2,8)	0,1 (± 0,5)	0,0 (± 0,1)	0,0 (± 0,0)	0,0 (± 0,3)	-
Late vein	LA37B	elec. im. 2	sp. 8	56,0 (± 4,6)	22,9 (± 5,6)	7,9 (± 2,9)	6,1 (± 4,6)	0,7 (± 2,3)	6,7 (± 2,8)	0,1 (± 0,5)	0,0 (± 0,1)	0,0 (± 0,0)	0,0 (± 0,3)	-
Late vein	LA37B	elec. im. 2	sp. 9	54,8 (± 4,6)	21,9 (± 5,6)	7,4 (± 2,9)	9,1 (± 4,6)	6,2 (± 2,3)	0,4 (± 2,8)	0,2 (± 0,5)	0,0 (± 0,1)	0,0 (± 0,0)	0,0 (± 0,3)	-
Late vein	LA37B	elec. im. 2	sp. 10	56,0 (± 4,3)	23,2 (± 5,6)	7,8 (± 2,9)	5,9 (± 4,6)	5,7 (± 2,3)	1,2 (± 2,8)	0,2 (± 0,5)	0,0 (± 0,1)	0,0 (± 0,0)	0,0 (± 0,3)	-
Late vein	LA37B	elec. im. 3	sp. 15	56,1 (± 10,3)	24,1 (± 8,9)	7,2 (± 3,3)	5,4 (± 3,5)	0,8 (± 1,9)	6,2 (± 3,1)	0,1 (± 0,9)	0,0 (± 1,5)	0,0 (± 0,2)	0,0 (± 0,1)	-
Late vein	LA37B	elec. im. 3	sp. 16	56,5 (± 10,3)	24,4 (± 8,9)	7,3 (± 3,3)	4,7 (± 3,5)	0,6 (± 1,9)	6,3 (± 3,1)	0,0 (± 0,9)	0,0 (± 1,5)	0,0 (± 0,2)	0,0 (± 0,1)	-
Late vein	LA37B	elec. im. 3	sp. 17	56,5 (± 10,3)	23,9 (± 8,9)	7,2 (± 3,3)	5,3 (± 3,5)	0,5 (± 1,9)	6,5 (± 3,1)	0,1 (± 0,9)	0,0 (± 1,5)	0,0 (± 0,2)	0,0 (± 0,1)	-
Late vein	LA37B	elec. im. 3	sp. 19	57,5 (± 10,3)	23,1 (± 8,9)	7,8 (± 3,3)	4,4 (± 3,5)	6,5 (± 1,9)	0,3 (± 3,1)	0,3 (± 0,9)	0,0 (± 1,5)	0,0 (± 0,2)	0,0 (± 0,1)	-
Late vein	LA37B	elec. im. 4	sp. 24	57,2 (± 6,9)	24,1 (± 5,1)	7,1 (± 5,6)	4,8 (± 6,5)	0,7 (± 1,8)	5,9 (± 2,1)	0,1 (± 1,3)	0,0 (± 1,6)	0,0 (± 0,1)	0,0 (± 0,3)	-
Late vein	LA37B	elec. im. 4	sp. 25	57,4 (± 6,9)	23,0 (± 5,1)	7,6 (± 5,6)	5,4 (± 6,5)	5,8 (± 1,8)	0,3 (± 2,1)	0,4 (± 1,3)	0,0 (± 1,6)	0,0 (± 0,1)	0,0 (± 0,3)	-
Late vein	LA37B	elec. im. 5	sp. 33	55,4 (± 13,1)	22,4 (± 9,3)	7,3 (± 2,6)	7,2 (± 10,0)	0,5 (± 0,2)	6,0 (± 2,4)	0,1 (± 0,4)	0,4 (± 0,3)	0,3 (± 0,2)	0,1 (± 0,6)	-
Late vein	LA37B	elec. im. 5	sp. 38	58,0 (± 13,1)	20,3 (± 9,3)	6,5 (± 2,6)	7,2 (± 10,0)	0,4 (± 0,2)	5,1 (± 2,4)	0,1 (± 0,4)	0,4 (± 0,3)	0,5 (± 0,2)	0,1 (± 0,6)	-
Late vein	LA37B	elec. im. 6	sp. 39	55,9 (± 2,1)	23,1 (± 4,9)	7,6 (± 0,5)	5,8 (± 1,4)	0,8 (± 1,9)	6,3 (± 2,4)	0,1 (± 0,1)	0,2 (± 2,2)	0,2 (± 3,4)	0,0 (± 0,1)	-
Late vein	LA37B	elec. im. 6	sp. 40	56,7 (± 2,1)	22,6 (± 4,9)	7,8 (± 0,5)	5,3 (± 1,4)	6,2 (± 1,9)	0,4 (± 2,4)	0,4 (± 0,1)	0,2 (± 2,2)	0,2 (± 3,4)	0,0 (± 0,1)	-
Late vein	LA37B	elec. im. 6	sp. 42	56,5 (± 2,1)	23,4 (± 4,9)	7,7 (± 0,5)	4,6 (± 1,4)	0,8 (± 1,9)	6,3 (± 2,4)	0,0 (± 0,1)	0,3 (± 2,2)	0,3 (± 3,4)	0,0 (± 0,1)	-
Late vein	LA37B	elec. im. 7	sp. 49	56,3 (± 2,0)	21,6 (± 7,5)	9,0 (± 4,0)	5,6 (± 2,2)	4,4 (± 1,3)	0,5 (± 1,7)	1,8 (± 2,6)	0,3 (± 1,5)	0,3 (± 2,3)	0,0 (± 2,1)	-
Late vein	LA37B	elec. im. 7	sp. 50	57,5 (± 2,0)	18,5 (± 7,5)	11,2 (± 4,0)	5,3 (± 2,2)	0,3 (± 1,3)	4,2 (± 1,7)	0,1 (± 2,6)	1,0 (± 1,5)	1,7 (± 2,3)	0,0 (± 2,1)	-
Late vein	LA37B	elec. im. 8	sp. 58	56,4 (± 1,3)	22,1 (± 2,8)	7,5 (± 1,8)	6,5 (± 0,8)	6,0 (± 2,0)	0,4 (± 1,6)	0,2 (± 3,8)	0,3 (± 1,8)	0,4 (± 2,8)	0,0 (± 3,0)	-
Late alteration	LA43A	elec. im. 7	sp. 36	64,1 (± 6,7)	14,6 (± 5,5)	5,5 (± 3,7)	4,1 (± 13,2)	7,2 (± 2,9)	0,0 (± 0,0)	0,0 (± 0,0)	0 (± 0,2)	0,1 (± 4,8)	0,0 (± 0,0)	-
Late alteration	LA43A	elec. im. 9	sp. 45	62,5 (± 0,7)	15,9 (± 2,2)	6,9 (± 3,8)	7,7 (± 1,1)	4,1 (± 1,8)	0,3 (± 0,1)	1,1 (± 0,5)	0,4 (± 0,3)	1,1 (± 5,2)	0,0 (± 0,0)	-
Late alteration	LA43A	elec. im. 11	sp. 58	62,8 (± 8,4)	16,1 (± 6,2)	6,0 (± 2,7)	4,6 (± 19,2)	7,2 (± 4,2)	0,0 (± 0,0)	0,0 (± 0,0)	0,0 (± 0,3)	0,0 (± 5,4)	0,0 (± 0,0)	-
Late alteration	LA43A	elec. im. 11	sp. 61	64,9 (± 8,4)	16,4 (± 6,2)	6,1 (± 2,7)	4,3 (± 19,2)	7,6 (± 4,2)	0,0 (± 0,0)	0,0 (± 0,0)	0,0 (± 0,3)	0,0 (± 5,4)	0,0 (± 0,0)	-
Late alteration	LA43E	elec. im. 13	sp. 85	56,5 (± 0,2)	22,6 (± 1,6)	7,6 (± 4,0)	5,6 (± 2,1)	7,1 (± 3,6)	0,0 (± 0,0)	0,0 (± 0,0)	0,1 (± 0,5)	0,3 (± 6,7)	0,0 (± 0,0)	-
Late alteration	LA43E	elec. im. 13	sp. 86	56,2 (± 0,2)	23,5 (± 1,6)	6,6 (± 4,0)	6,7 (± 2,1)	5,9 (± 3,6)	0,0 (± 0,0)	0,1 (± 0,0)	0,0 (± 0,5)	0,4 (± 6,7)	0,0 (± 0,0)	-

Steynsdorp SEM-EDS feldspars analysis

Type	Sample Name	electron image nu.	sp nu.	Element abundance (± standard deviation) (weight %)										
				O	Si	Al	C	Na	K	Ca	Fe	Mg	Ti	Ba
Mineralised vein	LA136A	elec. im. 3	sp. 7	38,9 (± 0,3)	17,4 (± 0,1)	8,5 (± 0,1)	15,4 (± 0,4)	-	-	12,6 (± 0,1)	4,5 (± 0,1)	1,2 (± 0,0)	-	-
Mineralised vein	LA136A	elec. im. 3	sp. 8	39,0 (± 0,4)	17,5 (± 0,2)	8,5 (± 0,1)	15,0 (± 0,6)	0,0 (± 0,0)	0,0 (± 0,0)	12,6 (± 0,1)	4,6 (± 0,1)	1,2 (± 0,0)	-	-
Mineralised vein	LA136A	elec. im. 3	sp. 9	38,3 (± 0,4)	26,1 (± 0,3)	8,5 (± 0,1)	14,7 (± 0,7)	-	11,8 (± 0,1)	-	0,2 (± 0,1)	-	-	0,4 (± 0,1)
Mineralised vein	LA136A	elec. im. 3	sp. 10	38,2 (± 0,4)	25,9 (± 0,3)	8,6 (± 0,1)	15,4 (± 0,7)	-	11,9 (± 0,1)	-	-	-	-	-
Mineralised vein	LA136A	elec. im. 5	sp. 22	34,6 (± 0,4)	23,3 (± 0,2)	7,7 (± 0,1)	23,5 (± 0,7)	-	10,8 (± 0,1)	-	-	-	-	-
Mineralised vein	LA136A	elec. im. 5	sp. 23	38,5 (± 0,4)	25,4 (± 0,3)	8,3 (± 0,1)	16,4 (± 0,7)	-	11,5 (± 0,1)	-	-	-	-	-
Mineralised vein	LA136A	elec. im. 5	sp. 24	45,2 (± 0,4)	16,4 (± 0,2)	8,3 (± 0,1)	14,5 (± 0,6)	-	0,3 (± 0,0)	9,6 (± 0,1)	3,3 (± 0,1)	1,1 (± 0,0)	-	-
Mineralised vein	LA136A	elec. im. 5	sp. 26	39,1 (± 0,3)	17,4 (± 0,1)	8,4 (± 0,1)	15,6 (± 0,4)	-	-	12,3 (± 0,1)	4,0 (± 0,1)	1,0 (± 0,0)	-	-
Mineralised vein	LA136A	elec. im. 5	sp. 27	39,6 (± 0,3)	17,3 (± 0,1)	8,4 (± 0,1)	15,3 (± 0,4)	-	-	12,3 (± 0,1)	3,7 (± 0,1)	1,1 (± 0,0)	-	-
Mineralised vein	LA136A	elec. im. 6	sp. 31	42,3 (± 0,3)	32,4 (± 0,2)	10,4 (± 0,1)	-	-	14,8 (± 0,1)	-	-	-	-	-
Mineralised vein	LA136A	elec. im. 6	sp. 32	39,1 (± 0,4)	26,7 (± 0,3)	8,6 (± 0,1)	13,2 (± 0,7)	-	12,4 (± 0,1)	-	-	-	-	-
Mineralised vein	LA136A	elec. im. 6	sp. 33	39,3 (± 0,4)	27,4 (± 0,3)	8,9 (± 0,1)	12,0 (± 0,7)	-	12,3 (± 0,1)	-	-	-	-	-
Mineralised vein	LA136A	elec. im. 6	sp. 35	39,9 (± 0,3)	18,2 (± 0,1)	8,8 (± 0,1)	12,9 (± 0,4)	-	-	13,1 (± 0,1)	4,3 (± 0,1)	1,5 (± 0,0)	-	-
Mineralised vein	LA136A	elec. im. 6	sp. 36	40,1 (± 0,3)	18,2 (± 0,1)	8,8 (± 0,1)	12,7 (± 0,4)	-	-	13,0 (± 0,1)	4,6 (± 0,1)	1,4 (± 0,0)	-	-
Mineralised vein	LA136A	elec. im. 7	sp. 40	43,5 (± 0,3)	21,8 (± 0,2)	10,4 (± 0,1)	-	-	-	15,1 (± 0,1)	5,1 (± 0,1)	1,2 (± 0,1)	-	-
Mineralised vein	LA136A	elec. im. 7	sp. 41	44 (± 0,3)	21,8 (± 0,2)	10,5 (± 0,1)	-	-	-	15,4 (± 0,1)	-	1,7 (± 0,1)	-	-
Mineralised vein	LA136A	elec. im. 7	sp. 42	43,5 (± 0,3)	32,1 (± 0,2)	10,2 (± 0,1)	-	-	14,3 (± 0,1)	-	-	-	-	-
Mineralised vein	LA136A	elec. im. 7	sp. 43	38,8 (± 0,3)	17,5 (± 0,1)	8,4 (± 0,1)	15,7 (± 0,4)	-	-	12,4 (± 0,1)	4,8 (± 0,1)	1,2 (± 0,0)	-	-
Mineralised vein	LA136A	elec. im. 8	sp. 46	38,0 (± 0,4)	26,1 (± 0,3)	8,6 (± 0,1)	15,4 (± 0,7)	-	12,0 (± 0,1)	-	-	-	-	-
Mineralised vein	LA136A	elec. im. 8	sp. 47	38,6 (± 0,4)	26,2 (± 0,3)	8,5 (± 0,1)	14,7 (± 0,7)	-	12,1 (± 0,1)	-	-	-	-	-
Mineralised vein	LA136A	elec. im. 8	sp. 48	38,5 (± 0,4)	26,4 (± 0,3)	8,8 (± 0,1)	14,5 (± 0,7)	-	11,9 (± 0,1)	-	-	-	-	-
Mineralised vein	LA136A	elec. im. 8	sp. 52	38,8 (± 0,3)	17,4 (± 0,1)	8,6 (± 0,1)	15,6 (± 0,4)	-	-	12,6 (± 0,1)	4,3 (± 0,1)	1,4 (± 0,0)	-	-
Mineralised vein	LA136A	elec. im. 8	sp. 53	38,8 (± 0,3)	17,5 (± 0,1)	8,4 (± 0,1)	15,7 (± 0,4)	-	-	12,4 (± 0,1)	4,8 (± 0,1)	1,2 (± 0,0)	-	-
Mineralised vein	LA60C	elec. im. 2	sp. 1	43,2 (± 0,3)	24,9 (± 0,2)	8,4 (± 0,1)	16,3 (± 0,4)	7,2 (± 0,1)	-	-	-	-	-	-
Mineralised vein	LA60C	elec. im. 2	sp. 2	43,1 (± 0,3)	24,4 (± 0,2)	8,2 (± 0,1)	17,2 (± 0,4)	7,1 (± 0,1)	-	-	-	-	-	-
Mineralised vein	LA60C	elec. im. 3	sp. 11	44,0 (± 0,3)	31,0 (± 0,2)	4,0 (± 0,1)	17,5 (± 0,4)	3,4 (± 0,1)	-	-	-	-	-	-
Mineralised vein	LA60C	elec. im. 3	sp. 12	43,2 (± 0,3)	24,2 (± 0,2)	8,1 (± 0,1)	17,4 (± 0,4)	7,1 (± 0,1)	-	-	-	-	-	-
Mineralised vein	LA60C	elec. im. 3	sp. 13	43,6 (± 0,3)	24,1 (± 0,2)	8,1 (± 0,1)	17,1 (± 0,4)	7,2 (± 0,1)	-	-	-	-	-	-
Mineralised vein	LA60C	elec. im. 3	sp. 14	43,6 (± 0,3)	24,3 (± 0,2)	8,2 (± 0,1)	16,8 (± 0,4)	7,1 (± 0,1)	-	-	-	-	-	-
Mineralised vein	LA60C	elec. im. 4	sp. 27	43 (± 0,3)	24,7 (± 0,2)	8,0 (± 0,1)	17,4 (± 0,4)	7,0 (± 0,1)	-	-	-	-	-	-
Mineralised vein	LA60C	elec. im. 4	sp. 28	42,8 (± 0,3)	24,2 (± 0,2)	8,1 (± 0,1)	17,7 (± 0,4)	7,1 (± 0,1)	-	0,1 (± 0,0)	-	-	-	-
Mineralised vein	LA60C	elec. im. 5	sp. 34	44,3 (± 0,3)	28,5 (± 0,2)	5,4 (± 0,1)	17,9 (± 0,4)	4,0 (± 0,1)	-	-	-	-	-	-
Mineralised vein	LA60C	elec. im. 5	sp. 37	43,0 (± 0,3)	24,5 (± 0,2)	8,2 (± 0,1)	17,1 (± 0,4)	7,2 (± 0,1)	-	-	-	-	-	-
Mineralised vein	LA60C	elec. im. 7	sp. 54	43,1 (± 0,3)	25,7 (± 0,2)	8,6 (± 0,1)	13,7 (± 0,4)	7,3 (± 0,1)	-	-	1,5 (± 0,1)	-	-	-
Mineralised vein	LA60C	elec. im. 7	sp. 55	42,2 (± 0,3)	19,2 (± 0,1)	6,3 (± 0,1)	13,5 (± 0,4)	5,3 (± 0,1)	-	0,2 (± 0,0)	12,4 (± 0,2)	-	-	-
Mineralised vein	LA60C	elec. im. 11	sp. 71	46,1 (± 0,2)	33,9 (± 0,2)	11,0 (± 0,1)	-	9,1 (± 0,1)	-	-	-	-	-	-
Mineralised vein	LA60C	elec. im. 11	sp. 72	46,0 (± 0,2)	33,9 (± 0,2)	11,1 (± 0,1)	-	9,0 (± 0,1)	-	-	-	-	-	-

Annexe 4 : Analyse Microsonde

Lames Minces Sélectionnées

6 lames minces ont été sélectionnées pour analyser ponctuellement (LA2A, LA3E, LA14, LA34A1, LA43E et LA43F2) dont 3 ont été utiliser pour faire des cartes chimiques (LA2A, LA34A1 et LA43E).

1. Lame mince LA2A

La lame LA2A provient d'un échantillon de l'affleurement Waterfall de l'unité Onverwacht. Cet affleurement correspond à une ancienne mine, où l'on peut voir des schistes cisaillés avec des zones à altération noire. L'échantillon provient d'un schiste carbonaté cisaillé sans altération *(fig. 1)*.

Figure 1 : Photographie de l'affleurement avec l'échantillon LA2A.

Au microscope la lame présente des carbonates de tailles variables avec un plan de cisaillement

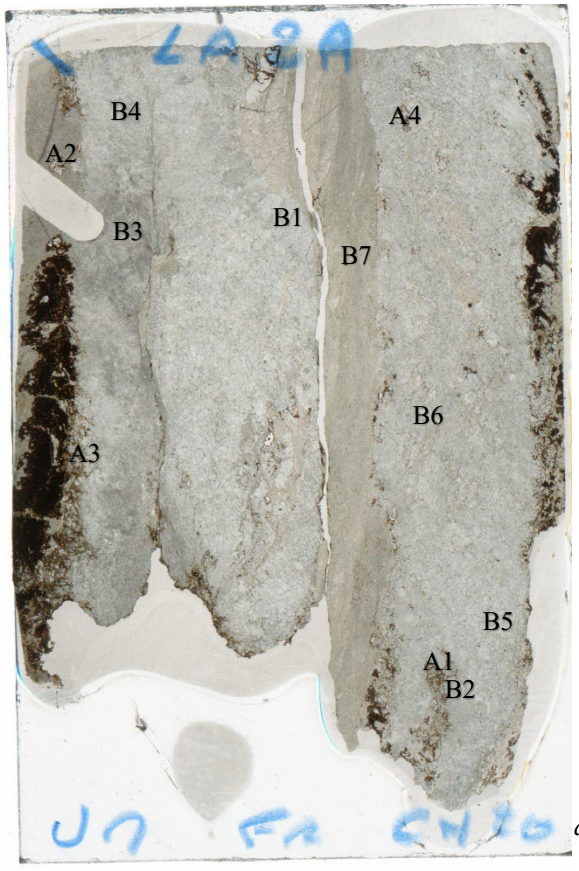

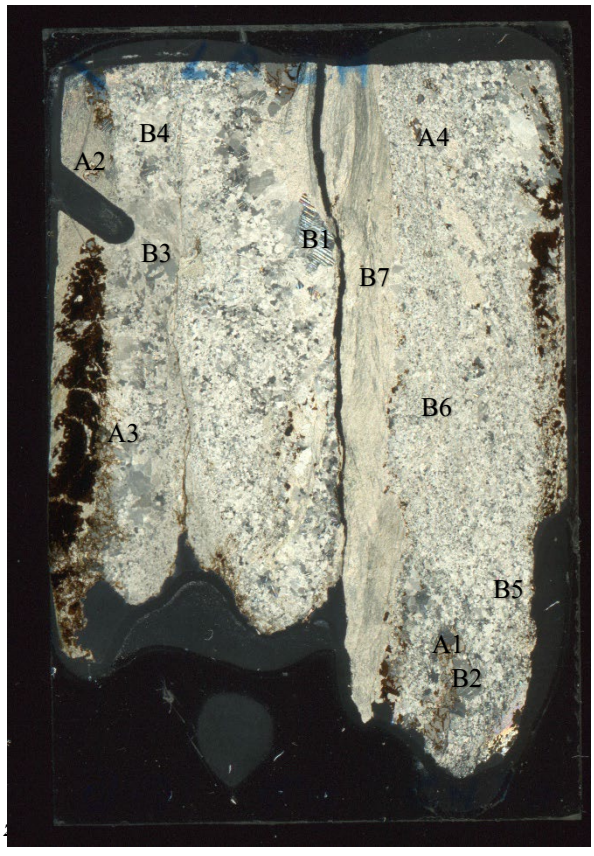

des

composé de matériel beaucoup plus fin. Sur les bords des oxydes sont alignés formant des lentilles fracturées *(fig.2)*.

L'analyse chimique au MEB, a montré que les zones à grains grossiers possèdent de grosses dolomites et des magnésites (?), le plan de cisaillement est composé de mica et de talc (à vérifier). Et les oxydes sont des oxydes de fer avec la présence de quelques petites pyrites.

Une analyse à la microsonde a été réalisée sur cette lame mince pour affirmer la présence de magnésite (ou de brucite), pour préciser l'histoire des carbonates et pour examiner la nature de la zone cisaillée. Des zones d'étude ont été repérées au microscope, ces zones sont détaillées dans le rapport *Préparation Microsonde* et localisées sur la *figure 2.*

2. Lame mince LA3E

Vers l'indice d'or de Welcome, à l'est du synforme dans l'unité Onverwacht l'échantillon LA3E a été prélevé dans une tranchée qui possède une altération rouge/brune *(fig. 3)*.

Figure 3 : Photo de l'échantillon LA3E.

Au microscope, l'échantillon est composé d'une veine de tourmalines (et quelques tourmalines hors de la veine), des gros micas sombres ainsi que beaucoup d'oxydes et des rutiles orientés en positions S2 (ou non) et présentant quelques fois une auréole blanche.

Les analyses chimiques au MEB ont démontré la présence de rutiles, de tourmalines, de micas, de quartz, de talc, d'oxydes de fer de quelques pyrites et peut-être de kaolinite.

À la microsonde, il est envisagé de comparer les tourmalines de la veine avec celles de l'encaissant (mais aussi avec les zones d'altérations des échantillons LA14, LA34A1 et LA43E). La nature des micas a été analysée ainsi que la zone blanchie autour des rutiles. Les rutiles vont aussi être étudiés pour voir s'il existe une différence chimique entre les rutiles en position S2 ou et ceux hors cette position. Des zones d'étude ont été repérées au microscope, ces zones sont détaillées dans le rapport *Préparation Microsonde* et localisées sur la *figure 4.*

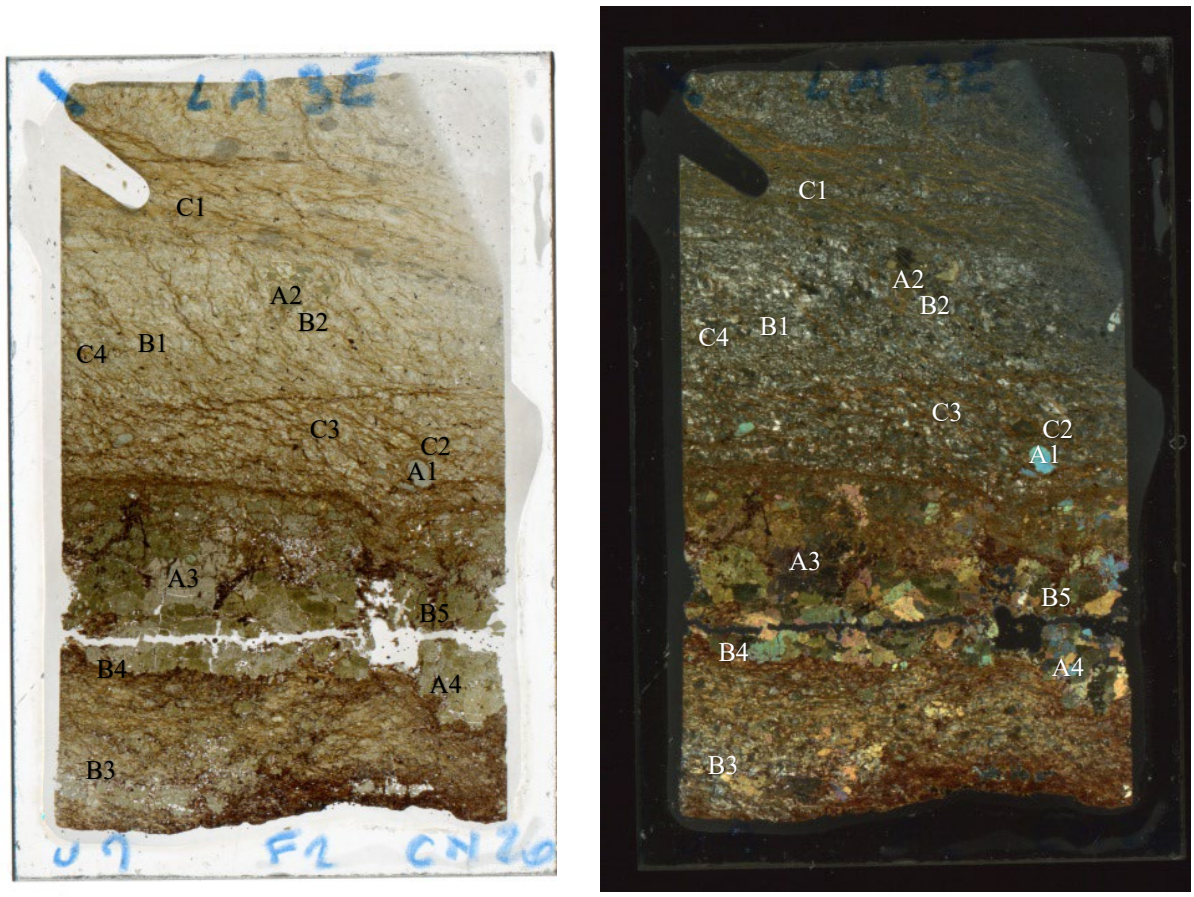

Figure 4 : Scans de la lame LA3E avec la localisation zones à observer, à gauche scan en lumière naturelle, à droite en lumière polarisée analysée

3. Lame mince LA14

L'échantillon LA14 provient d'une veine de quartz avec un halo d'altération vert décimétrique *(fig. 5)* au Nord-Ouest de l'indice d'or Rosehill, en direction de l'indice Avalanche dans l'unité Onverwacht. La veine de quartz est parallèle à la schistosité de l'encaissant.

Figure 5 : Photographie de la veine de quartz et de son altération à l'affleurement.

Au microscope le quartz est peu déformé, il présente de la fracturation remplie par des micas/talc semblables à l'altération *(fig. 6)*. L'altération est composée d'une matrice de micas/talc fins avec des feldspaths parallèles à la veine et présentant un tronçonnement ainsi que quelques tourmalines. Aucune analyse MEB n'a encore été réalisée à ce jour.

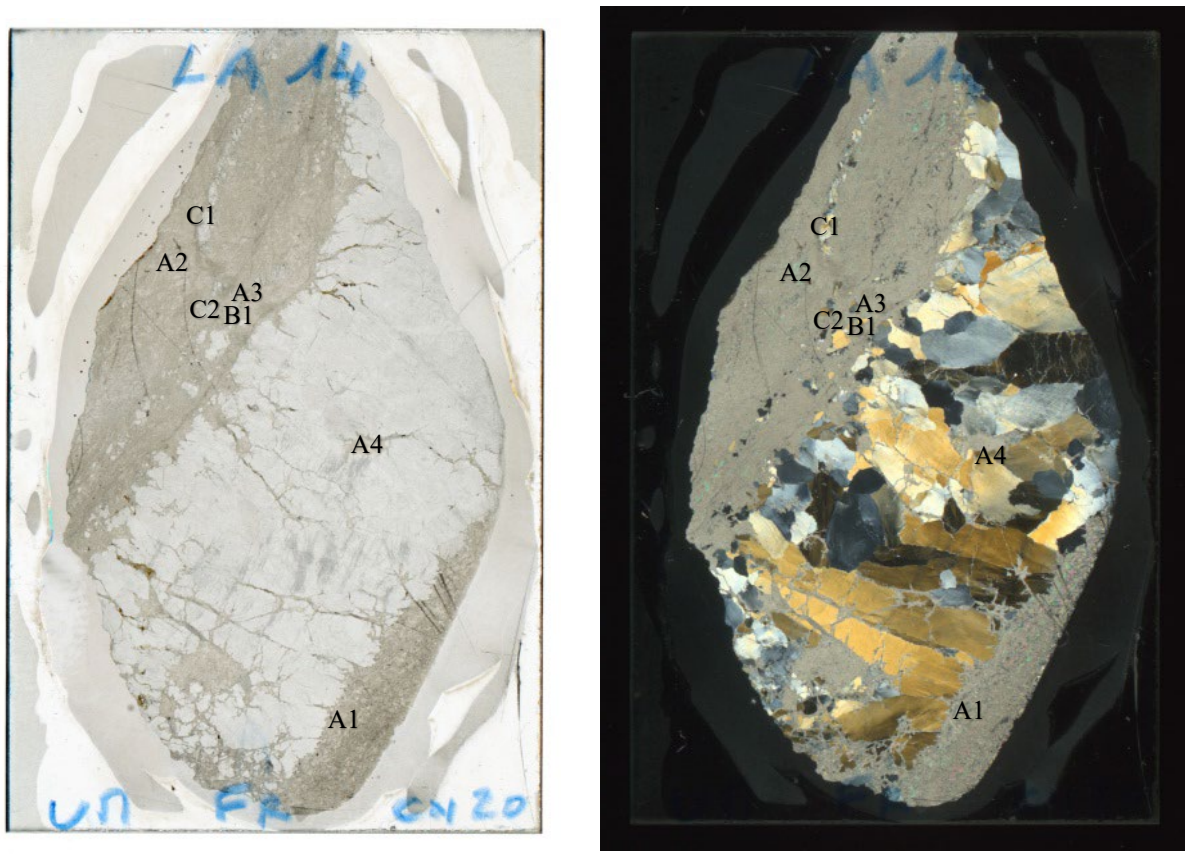

Figure 6 : Scans de la lame LA14 avec l'emplacement des zones d'intérêt, à gauche observation en lumière naturelle, à droite observation à la lumière polarisée analysée.

Le but de l'analyse à la microsonde, sur cette lame, est de caractériser la nature de l'altération verte, de comparer les tourmalines et les albites à celles rencontrer dans les autres lames. Les zones analysées sont localisées sur la *figure 6*.

4. Lame mince LA34A1

L'affleurement LA34 correspond à la partie Sud de l'indice d'or Primrose, dans l'unité Onverwacht. L'échantillon LA34A est composé de schiste de l'encaissant *(fig. 7)*, compris entre deux fractures qui sont localement remplies par du quartz. Cet échantillon est donc marqué par la schistosité S0/S1 cisaillé par les plans de fracture qui peuvent être remplis par du quartz et possède un plaquage vert.

Figure 7 : Photographie de l'échantillon LA34A sur l'affleurement.

Au microscope, sur la lame LA34A1, les plans de cisaillement (parallèles à la fracturation remplie de quartz) sont composés d'une matrice microcristalline de mica/talc. La zone avec la schistosité S0/S1 possède des tourmalines tronçonnées ainsi que des albites, cette schistosité est cisaillée par les plans de cisaillement *(fig. 8).* Aucune analyse MEB n'a été réalisée sur cette lame mince.

La microsonde va permettre de caractériser la nature des veines vertes qui jouent le rôle de plans de cisaillement. Puis de comparer les tourmalines et les albites avec les autres altérations. Les micas de l'encaissant et du tronçonnement vont être comparés. Les zones ciblées pour l'analyse au MEB sont localisées sur la *figure 8* (ces zones sont détaillées dans le rapport *Préparation Microsonde*).

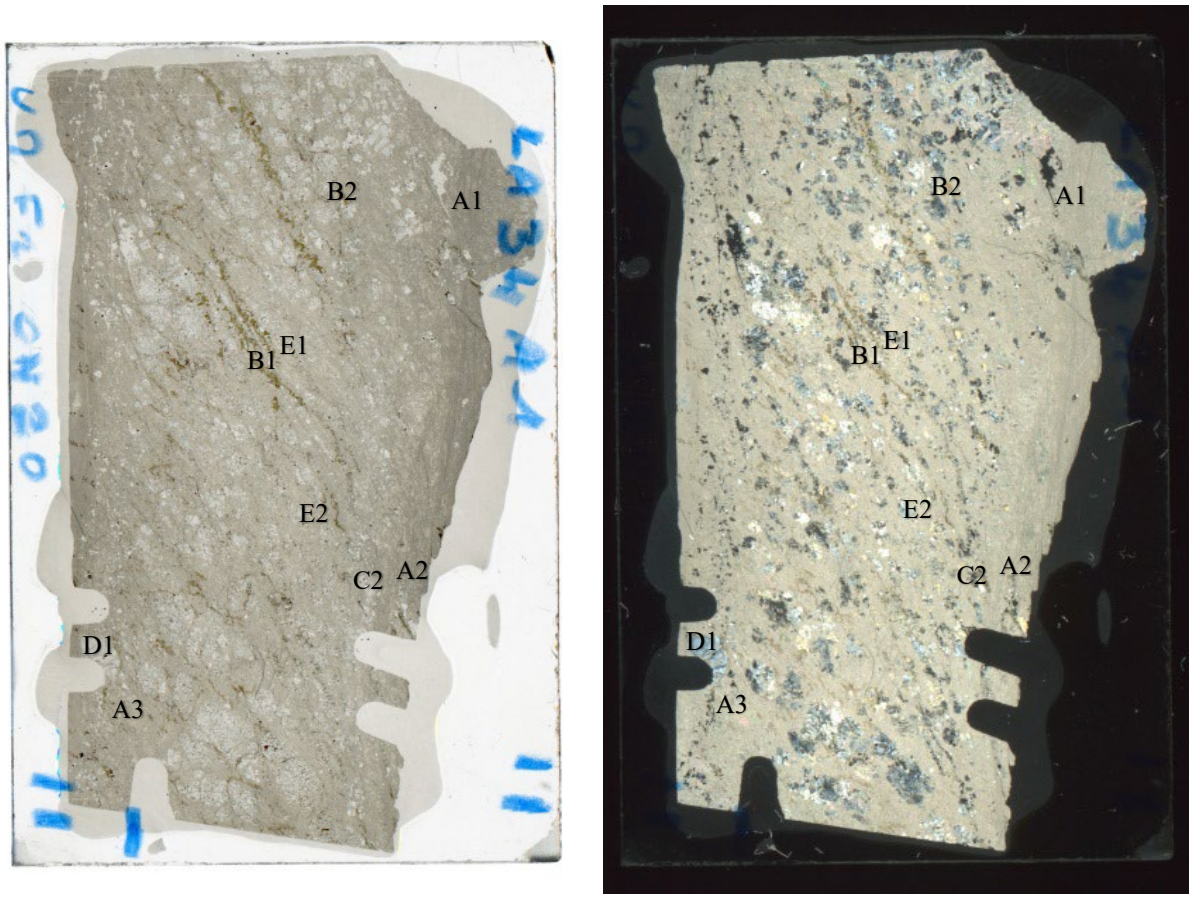

Figure 8 : Scans de la lame LA34A1 avec les secteurs localisés, à gauche en lumière naturelle, à droite en lumière polarisée analysée

5. Lame mince LA43E

L'affleurement LA43 correspond à la colline au nord de Primrose dans l'unité Onverwacht. Les veines de quartz de cet affleurement sont globalement E-W, plissées avec des axes de plis parallèles à la schistosité S0/S1. Ces veines ont des auréoles d'altération gris-vert décimétrique, l'échantillon LA43E correspond à l'une d'elles *(fig. 9)*.

Au microscope, on peut apercevoir la coupe entre l'altération proche de la veine de quartz (en bas) et l'encaissant (en haut). Proche de la veine de quartz, l'altération est composée de micas/talc clairs et microcristallins. Au-dessus de cette altération, on peut voir des albites (parallèles à la veine de quartz ou parallèles à la schistosité S0/S1), un peu plus loin on observe des tourmalines plissées (parallèles à la veine ou parallèles à la schistosité). À la limite entre l'altération et l'encaissant, des micas/talc plus sombres apparaissent *(fig. 10)*. Aucune analyse MEB n'a été effectuée sur cet échantillon.

Figure 9 : Photographie de l'échantillon LA43E sur l'affleurement, juste au-dessus d'une veine de quartz plissée.

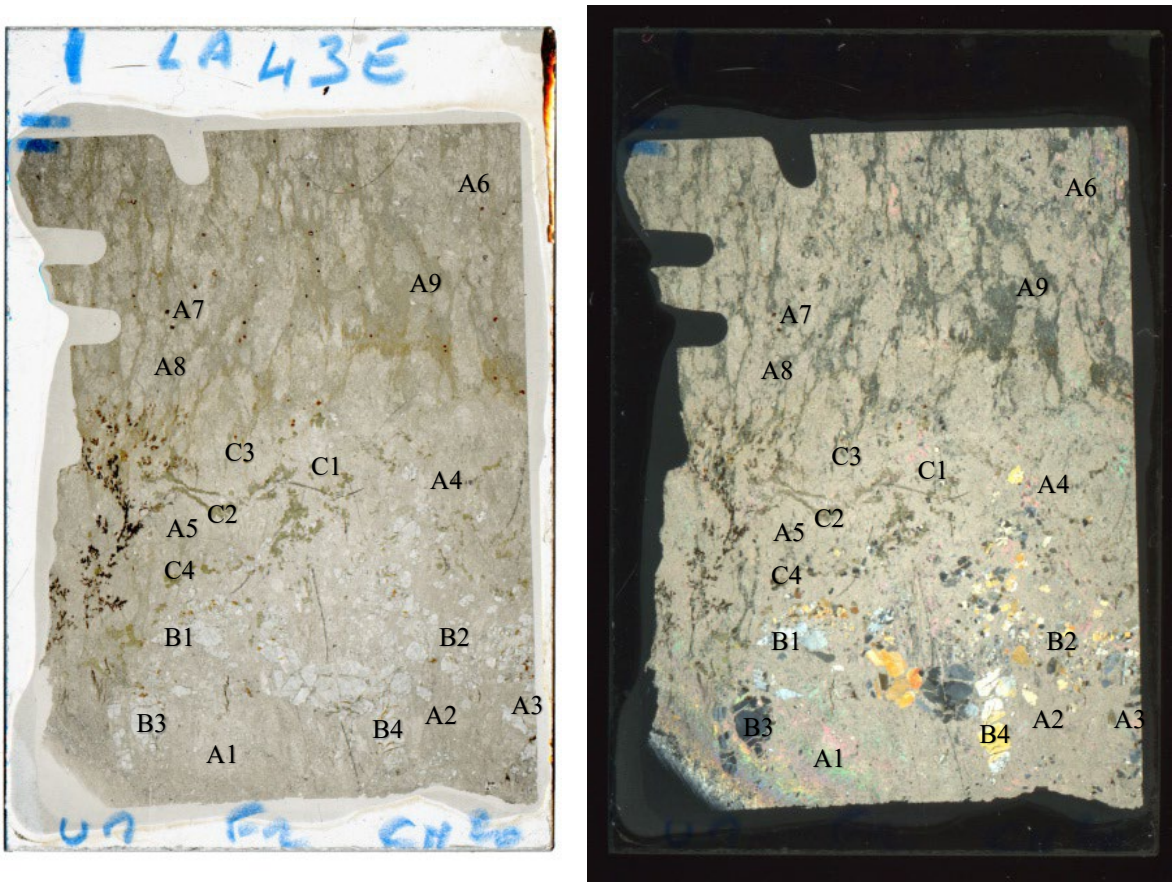

Figure 10 : Scans de la lame LA43E avec les secteurs localisés, à gauche scan en lumière naturelle, à droite en lumière polarisée analysée

À la microsonde, les analyses ont été réalisées dans le but de comparer les tourmalines et albites avec les autres échantillons mais aussi sur les mêmes minéraux de cette lame selon leurs orientations (parallèles à la veine ou à la schistosité). Les micas/talc vont être analysés en fonction de leur emplacement (zone grise, encaissant, dans le tronçonnement, proche de la veine).

6. Lame mince LA43F2

Cet échantillon correspond à l'encaissant de l'affleurement précédant *(fig. 11)*. Au microscope, on observe des gros minéraux automorphes (magnésites?) tronçonnés, des dolomites ainsi que des micas microcristallins dont des zones plus sombres *(fig. 12)*.

Figure 11 : Photographie de l'encaissant à l'endroit où l'échantillon LA43F a été prélevé.

Au MEB, ces minéraux ont des compositions similaires à de la magnésite (entourée par des oxydes de fer), de la dolomite, du talc, des micas et quelques rutiles.

L'analyse à la microsonde a permis de préciser la nature des minéraux automorphes avec des oxydes (magnésites ou des brucites), d'avoir la composition des dolomites ainsi que de caractériser les différents micas/talc (zone sombre, zone claire, mica dans le tronçonnement). Les zones analysées sont localisées sur la *figure 12*.

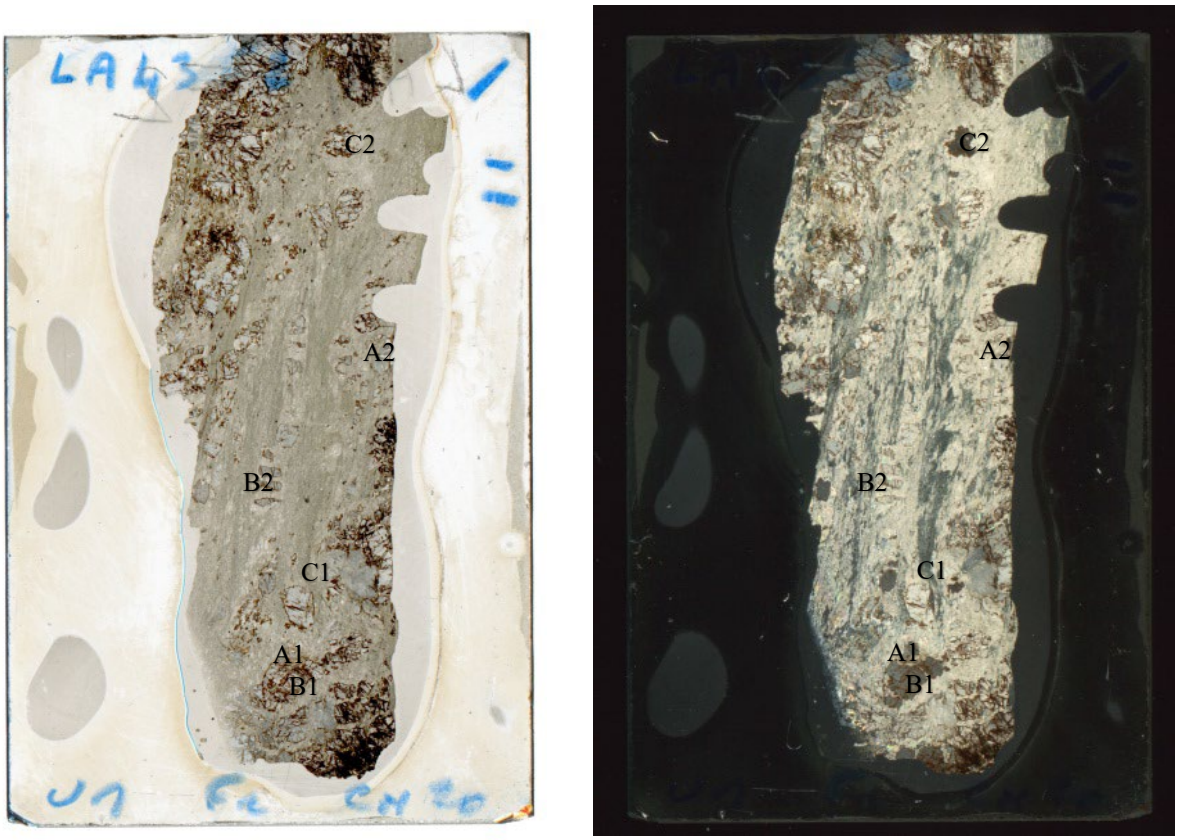

Figure 12 : Scans de la lame LA43F2 avec les zones d'analyses, à gauche en lumière naturelle, à droite en lumière polarisée analysée

Analyses chimiques

1. Acquisition

L'analyse à la microsonde CAMECA SX-100 du service Microsonde de la plateforme MAGE du laboratoire Géosciences s'est déroulée sur 3 jours (22, 23 et 26 juillet 2021). En milieu de séance du 23 juillet, les standards ont été remplacés pour mieux correspondre avec les minéraux à analyser, les analyses du 22 juillet et une partie des analyses du 23 juillet sont donc possiblement inexactes.

Les conditions d'utilisation sont accessibles sur les données brutes des analyses.

2. Analyse des Tourmalines

TOURMALINE ANALYSES

Samples	LA34A1				LA43E				LA14			LA3E			
N° analysis	B2-02-220721	B2-05-220721	B2-02-260721	B2-05-260721	C4-25-230721	C4-26-230721	C2-29-230721	C2-30-230721	B1-30-260721	B1-31-260721	B1-32-260721	A4-38-260721	A4-38-260721	A1-42-260721	A1-43-260721
SiO_2	37,55	37,44	37,28	37,42	38,08	37,52	37,91	38,24	38,12	70,04	37,96	37,37	36,95	37,27	37,43
TiO_2	0,34	0,88	0,58	0,98	0,22	0,52	0,11	0,08	0,63	0,02	0,62	1,00	1,11	0,52	0,54
Al_2O_3	29,06	27,72	28,45	27,91	32,12	31,29	30,86	30,82	31,57	19,90	30,21	29,90	21,27	30,43	30,47
FeO	3,18	4,28	3,66	4,30	3,26	3,20	1,68	1,67	2,66	0,03	2,07	5,37	6,80	6,49	6,45
MnO	0,00	0,01	0,00	0,01	0,00	0,00	0,00	0,01	0,00	0,01	0,01	0,06	0,00	0,01	0,01
MgO	9,58	8,98	9,65	9,59	10,68	10,85	9,74	10,51	10,93	0,00	9,75	9,16	9,10	9,57	9,29
CaO	0,27	0,37	0,36	0,34	0,14	0,36	0,08	0,06	0,13	0,06	0,21	1,15	1,19	1,25	1,19
Na_2O	2,62	2,71	2,68	2,73	2,95	2,81	2,66	2,19	2,73	12,06	2,69	2,34	2,29	2,25	2,32
K_2O	0,00	0,00	0,00	0,00	0,00	0,00	0,00	0,01	0,00	0,02	0,00	0,01	0,01	0,00	0,00
F	0,00	0,04	0,00	0,06	0,00	0,00	0,02	0,00	0,00	0,02	0,00	0,00	0,00	0,04	0,05
BaO	0,00	0,02	0,00	0,01	0,00	0,00	0,00	0,00	0,00	0,00	0,00	0,00	0,01	0,00	0,00
Total	82,61	82,45	82,67	83,36	87,45	86,56	83,07	83,58	86,78	102,16	83,53	88,15	87,35	87,83	87,75
										X (albite)					

Tableau 1 : Tableau des résultats d'analyse des tourmalines à la microsonde. Les résultats sont donnés en pourcentage oxyde, la colonne grisée corresponde à une analyse qui ne correspond pas à la chimie des tourmalines.

Les résultats des analyses à la microsonde sont reportés sur le *Tableau 1*. Chaque point analysé à la microsonde est visible sur la planche photo de la *figure 13*, les zones d'analyse (B2, C4, C2 etc..) sont localisées sur les scans de leurs lames associées au chapitre *Rappel sur les lames minces sélectionnées* et leurs coordonnées sont écrites dans le rapport *Préparation Microsonde*. Les pourcentages d'oxyde sont globalement similaires sur toutes les analyses, surtout sur une même lame. Les valeurs d'Al2O3 et de FeO sont les taux les plus variables.

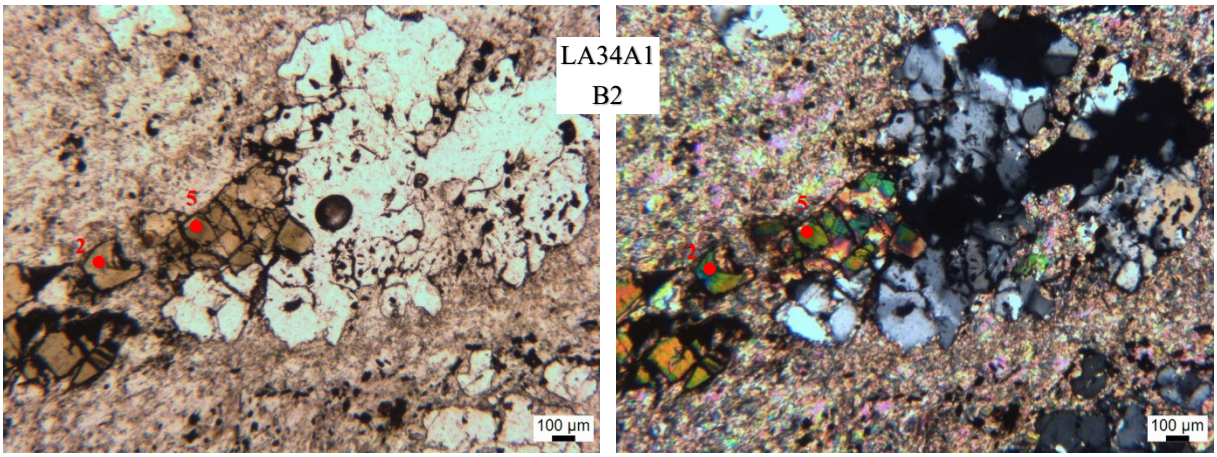
LA34A1
B2
5
2
100 µm
5
2
100 µm

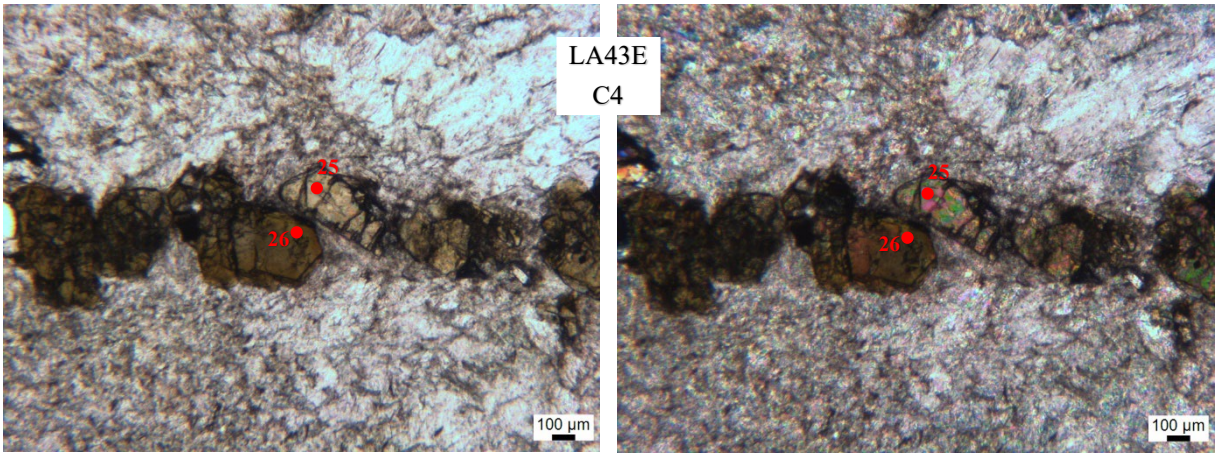
LA43E
C4
25
26
100 µm
25
26
100 µm

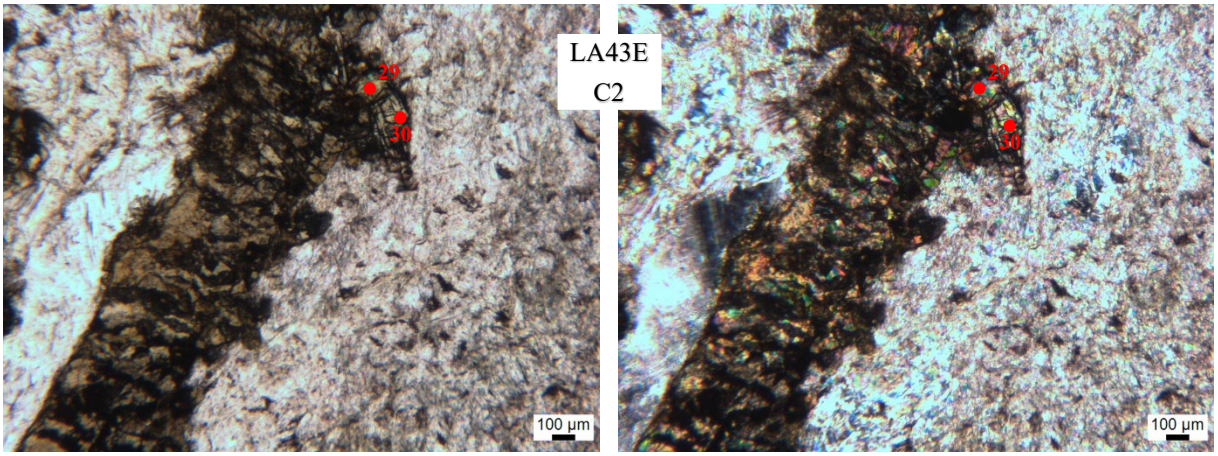
LA43E
C2
29
30
100 µm
29
30
100 µm

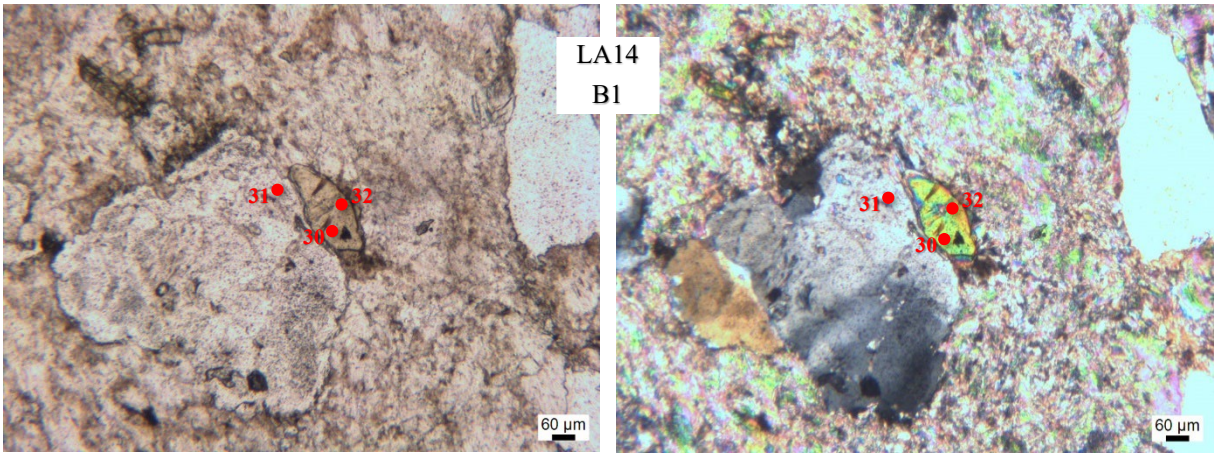
LA14
B1
31
32
30
60 µm
31
32
30
60 µm

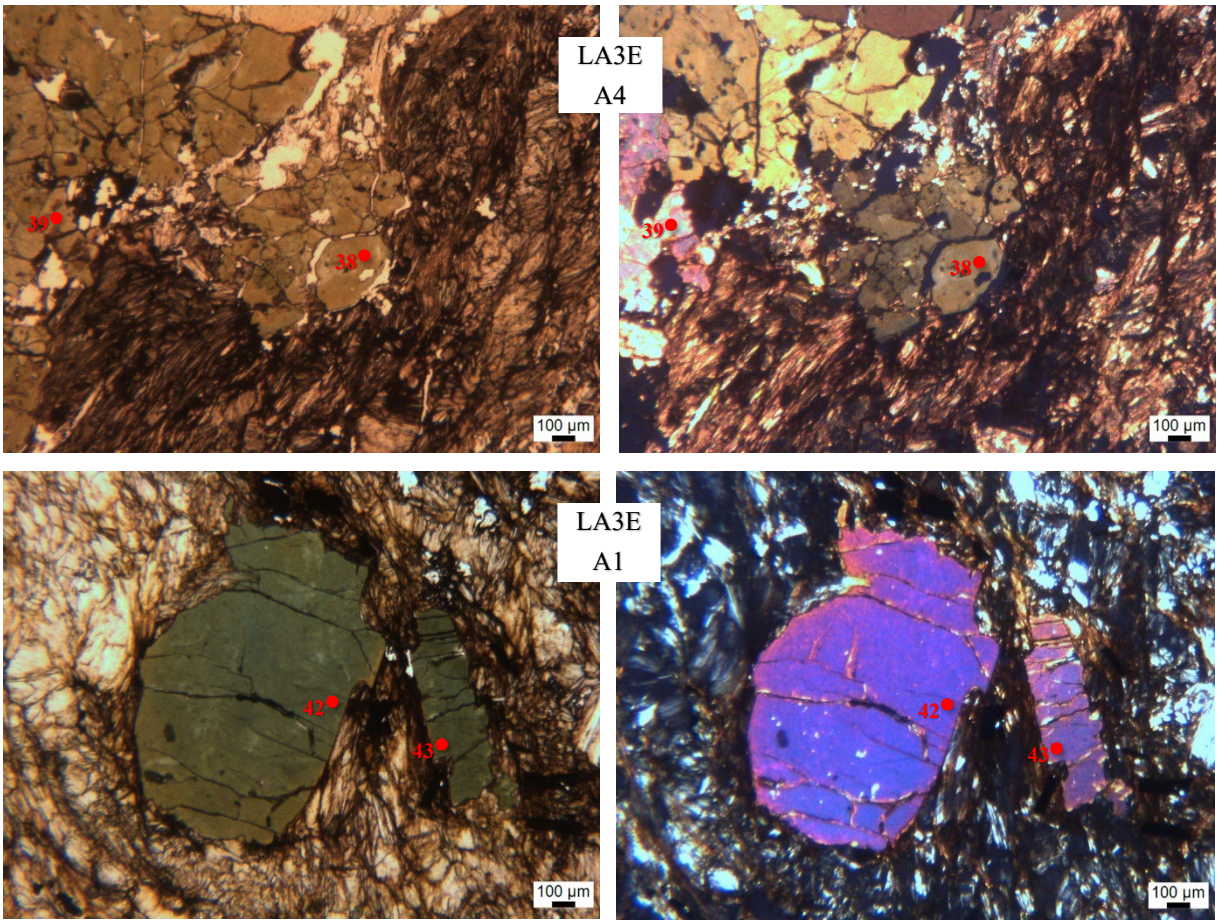

Figure 13 : Planche photographique des zones d'analysées à la microsonde pour les tourmalines avec la localisation des points d'analyse en rouge. A droite photographie en lumière polarisée, à gauche photographie en lumière polarisée analysée.

3. Analyse des Albites

Les résultats des analyses sur les albites sont visibles sur le *Tableau 2*. Chaque point analysé à la microsonde est localisé sur la planche photo de la *figure 14*, les zones d'analyse sur les lames sont reportées sur les scans des lames au chapitre *Rappel sur les lames minces sélectionnées* et leurs coordonnées sont écrites dans le rapport *Préparation Microsonde*. Les analyses sont globalement toutes homogènes, cependant de nombreuses analyses ont un pourcentage total supérieur à 100% (dont certaines non écrit dans le *Tableau 2*). La calibration et le choix des standards ont donc été changés au cours de la journée du 23 juillet. Mais de nombreuses analyses de la journée du 26 juillet ont aussi un pourcentage largement supérieur à 100%, toutes les analyses reportées dans ce rapport sont donc possiblement biaisées.

ALBITE ANALYSES

Samples	LA34A1						LA43E									
N° analysis	B2-01-220721	B2-06-220721	B2-07-220721	B2-01-260721	B2-06-260721	B2-07-260721	B3-02-230721	B3-05-230721	B3-09-230721	B3-11-230721	B3-12-230721	B3-13-230721	B1-21-230721	B1-39-230721	B4-01-260721	B4-02-260721
SiO_2	69,03	0,10	68,82	0,17	69,06	69,11	68,33	68,43	69,50	69,89	69,29	68,49	68,13	70,18	68,72	70,38
TiO_2	0,00	0,00	0,01	0,00	0,01	0,00	0,01	0,00	0,03	0,03	0,00	0,00	0,03	0,00	0,00	0,00
Al_2O_3	19,99	0,01	20,23	0,00	19,81	19,86	19,81	19,65	19,90	20,07	20,18	19,71	19,86	19,89	19,84	19,79
FeO	0,04	0,01	0,00	0,03	0,02	0,09	0,02	0,01	0,03	0,04	0,00	0,02	0,03	0,04	0,02	0,00
MgO	0,00	0,01	0,00	0,03	0,00	0,00	0,00	0,00	0,00	0,00	0,00	0,01	0,02	0,00	0,00	0,00
CaO	0,20	0,00	0,39	0,01	0,19	0,14	0,07	0,03	0,07	0,05	0,08	0,12	0,14	0,02	0,06	0,05
Na_2O	11,86	0,01	11,68	0,01	11,78	11,66	11,83	11,72	11,69	11,84	11,66	11,78	11,73	11,98	11,73	11,61
K_2O	0,00	0,00	0,01	0,00	0,01	0,01	0,00	0,00	0,02	0,01	0,00	0,00	0,00	0,01	0,01	0,01
MnO	0,00	0,00	0,00	0,00	0,00	0,00	0,01	0,00	0,00	0,02	0,00	0,01	0,00	0,00	0,01	0,01
F	0,00	0,03	0,02	0,00	0,00	0,00	0,00	0,00	0,00	0,02	0,00	0,08	0,03	0,02	0,00	0,00
BaO	0,00	0,00	0,00	0,00	0,00	0,00	0,00	0,00	0,00	0,00	0,00	0,00	0,00	0,00	0,00	0,00
Total	101,13	0,17	101,14	0,26	100,87	100,87	100,09	99,85	101,23	101,96	101,22	100,23	99,98	102,14	100,38	101,84
		X (vide)		X (vide)										X		

Rq: analyses de 1 à 13 avec beaucoup d'analyse >102% non écrit dans ce tableau

Samples	LA14							
N° analysis	C2-14-230721	C2-15-230721	C2-16-230721	C2-17-230721	C2-18-230721	C1-03-260721	C1-04-260721	B1-31-260721
SiO_2	70,76	71,20	68,95	68,54	69,15	69,75	69,93	70,04
TiO_2	0,00	0,03	0,02	0,02	0,00	0,00	0,00	0,02
Al_2O_3	20,10	20,07	19,84	19,64	19,86	19,95	19,85	19,90
FeO	0,02	0,00	0,01	0,04	0,02	0,01	0,00	0,03
MgO	0,00	0,01	0,00	0,00	0,00	0,01	0,00	0,00
CaO	0,10	0,02	0,02	0,05	0,02	0,02	0,08	0,06
Na_2O	11,87	11,86	11,94	11,87	11,92	11,76	11,88	12,06
K_2O	0,00	0,01	0,01	0,01	0,01	0,01	0,01	0,02
MnO	0,00	0,00	0,00	0,00	0,00	0,00	0,00	0,01
F	0,00	0,06	0,00	0,02	0,04	0,04	0,04	0,02
BaO	0,00	0,00	0,00	0,00	0,00	0,00	0,00	0,00
Total	102,85	103,25	100,79	100,19	101,01	101,55	101,78	102,16
	X	X						X

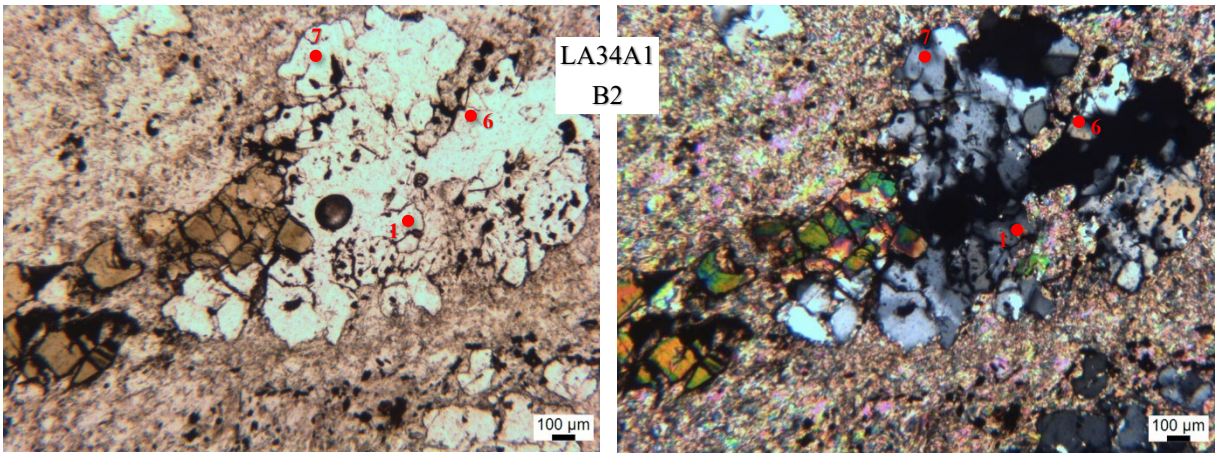

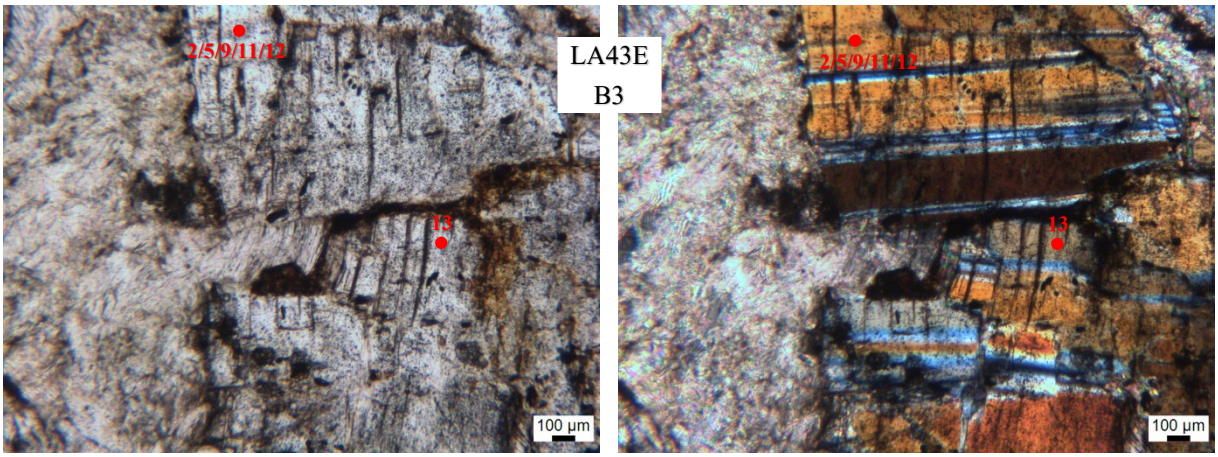

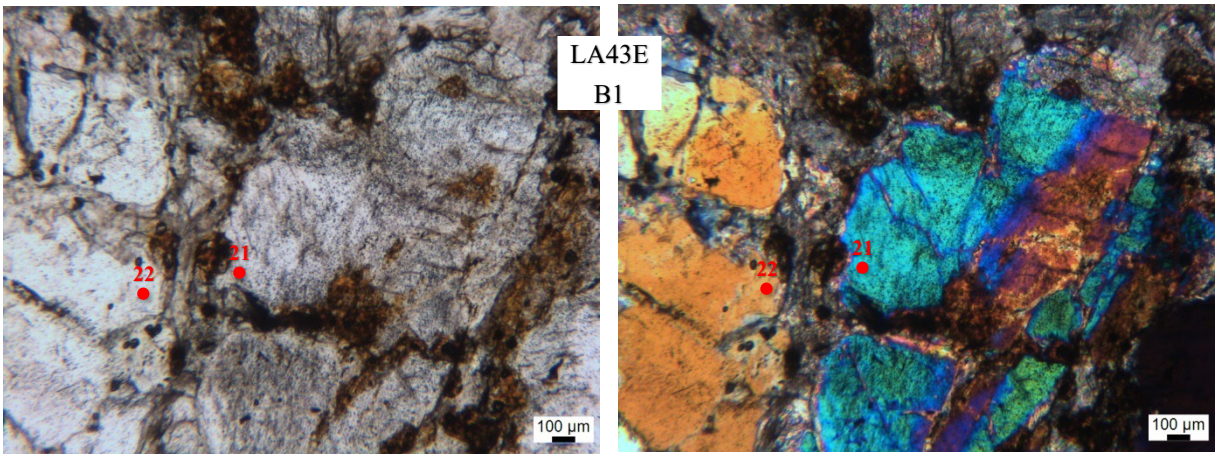
LA43E
B1
22
21
100 µm
22
21
100 µm

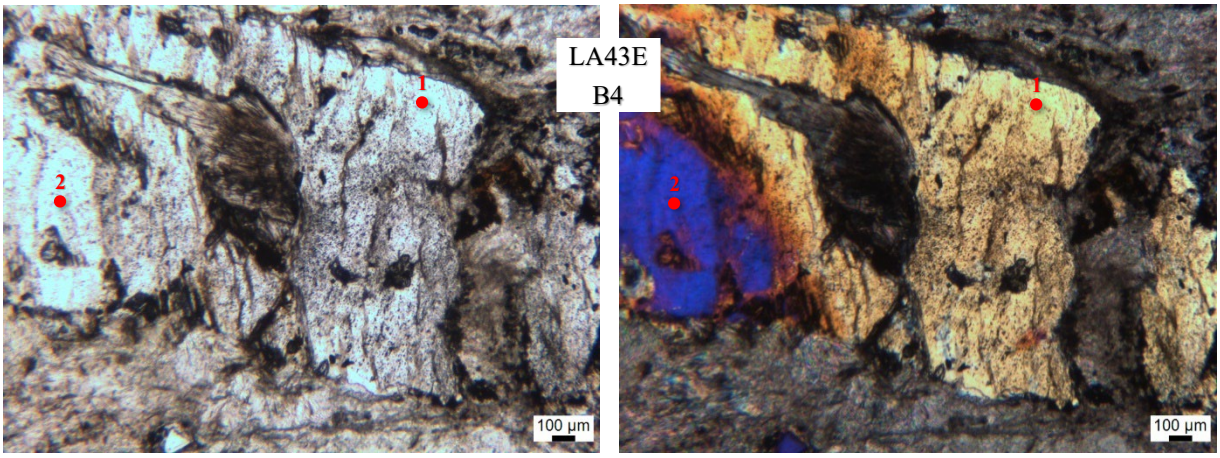
LA43E
B4
1
2
100 µm
1
2
100 µm

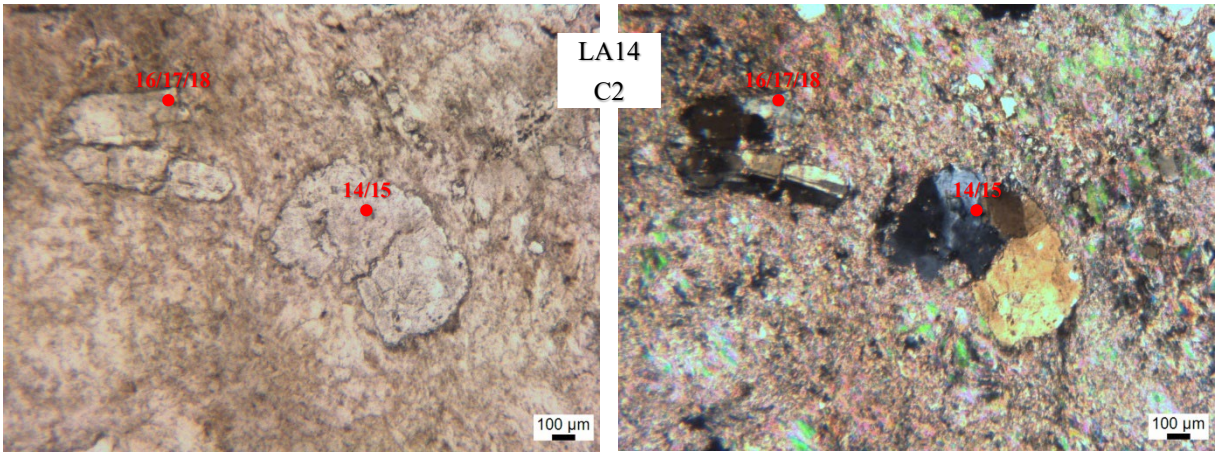
LA14
C2
16/17/18
14/15
100 µm
16/17/18
14/15
100 µm

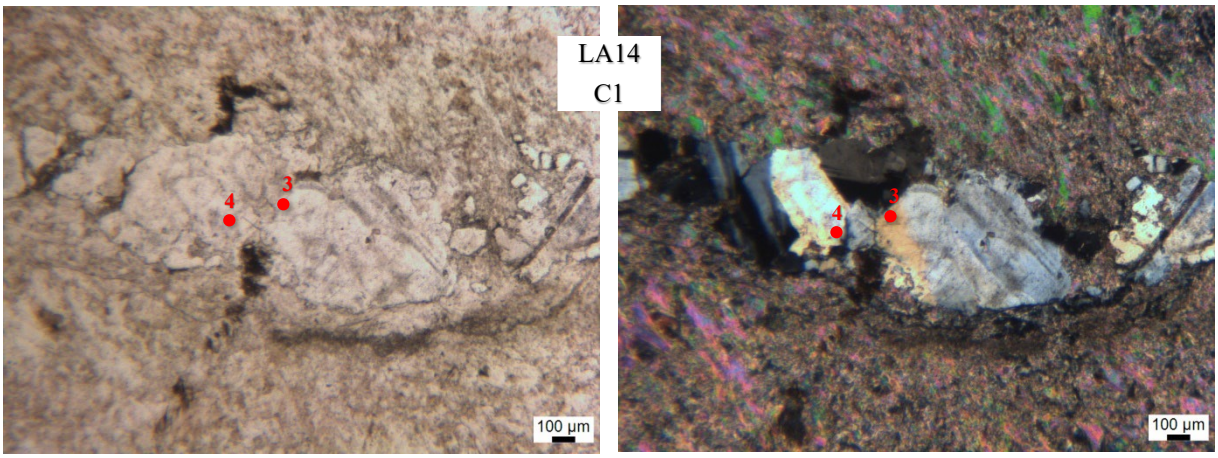
LA14
C1
4
3
100 µm
4
3
100 µm

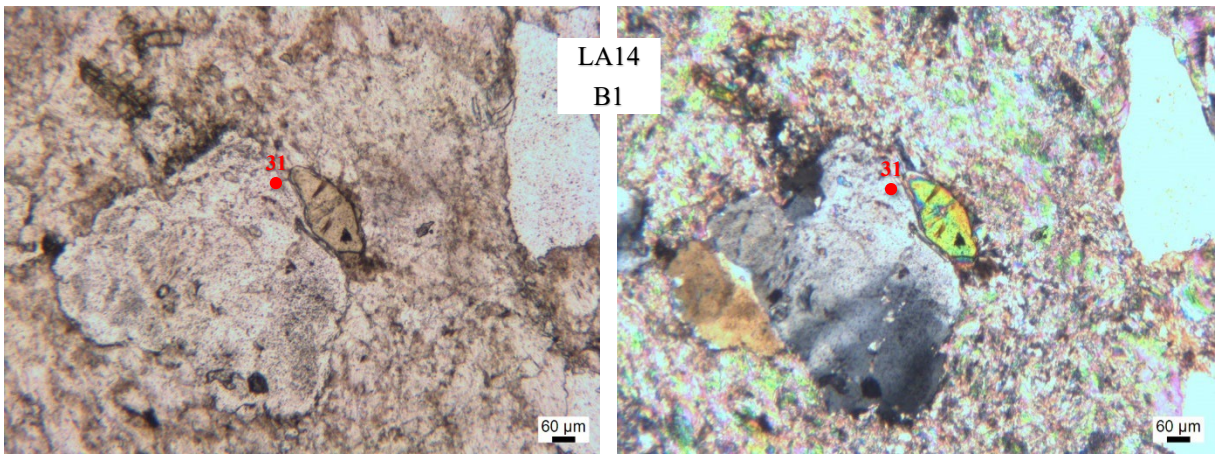

Figure 14 : Planche photographique des zones d'analysées à la microsonde pour les albites avec la localisation des points d'analyse en rouge. A droite photographie en lumière polarisée, à gauche photographie en lumière polarisée analysée.

4. Analyse des Magnésites

MAGNESITE ANALYSES

Samples	LA2A				LA43F2				
N° analysis	A2-15-220721	A2-16-220721	A2-15-260721	A2-16-260721	B1-11-260721	B1-12-260721	B2-17-260721	A1-09-260721	A1-10-260721
FeO	14,43	12,90	15,35	13,72	16,23	14,59	17,08	15,90	13,15
MnO	0,18	0,56	0,26	0,46	0,03	0,15	1,42	0,19	0,09
MgO	37,06	39,72	40,06	41,19	39,40	40,49	38,08	39,85	39,85
CaO	0,09	0,23	0,20	0,17	0,11	0,47	0,09	0,14	0,08
SiO_2	5,03	0,00	0,03	0,00	0,02	0,00	0,02	0,02	0,01
TiO_2	0,00	0,00	0,00	0,01	0,01	0,02	0,00	0,00	0,01
Al_2O_3	0,00	0,00	0,03	0,00	0,01	0,01	0,01	0,00	0,00
Na_2O	0,01	0,00	0,00	0,00	0,01	0,00	0,01	0,01	0,00
K_2O	0,00	0,00	0,00	0,00	0,00	0,00	0,00	0,00	0,00
F	0,02	0,03	0,02	0,00	0,01	0,03	0,00	0,00	0,00
BaO	0,00	0,00	0,00	0,00	0,00	0,00	0,00	0,00	0,00
Total	56,83	53,44	55,95	55,55	55,83	55,76	56,70	56,11	55,31
								Ajout	Ajout

Tableau 3 : Tableau d'analyse des magnésites à la microsonde. Les résultats sont donnés en pourcentage oxyde.

Les résultats des analyses chimiques réalisées sur les magnésites sont visibles sur le *Tableau 3*. Chaque point d'analyse à la microsonde est localisé sur la planche photo de la *figure 15*, les zones visées sur les lames sont reportées sur les scans des lames au chapitre *Rappel sur les lames minces sélectionnées* (et leurs coordonnées sur le rapport *Préparation Microsonde*). Les pourcentages d'oxydes sont globalement similaires mais les taux de FeO et de MgO peuvent varier de quelques pourcents.

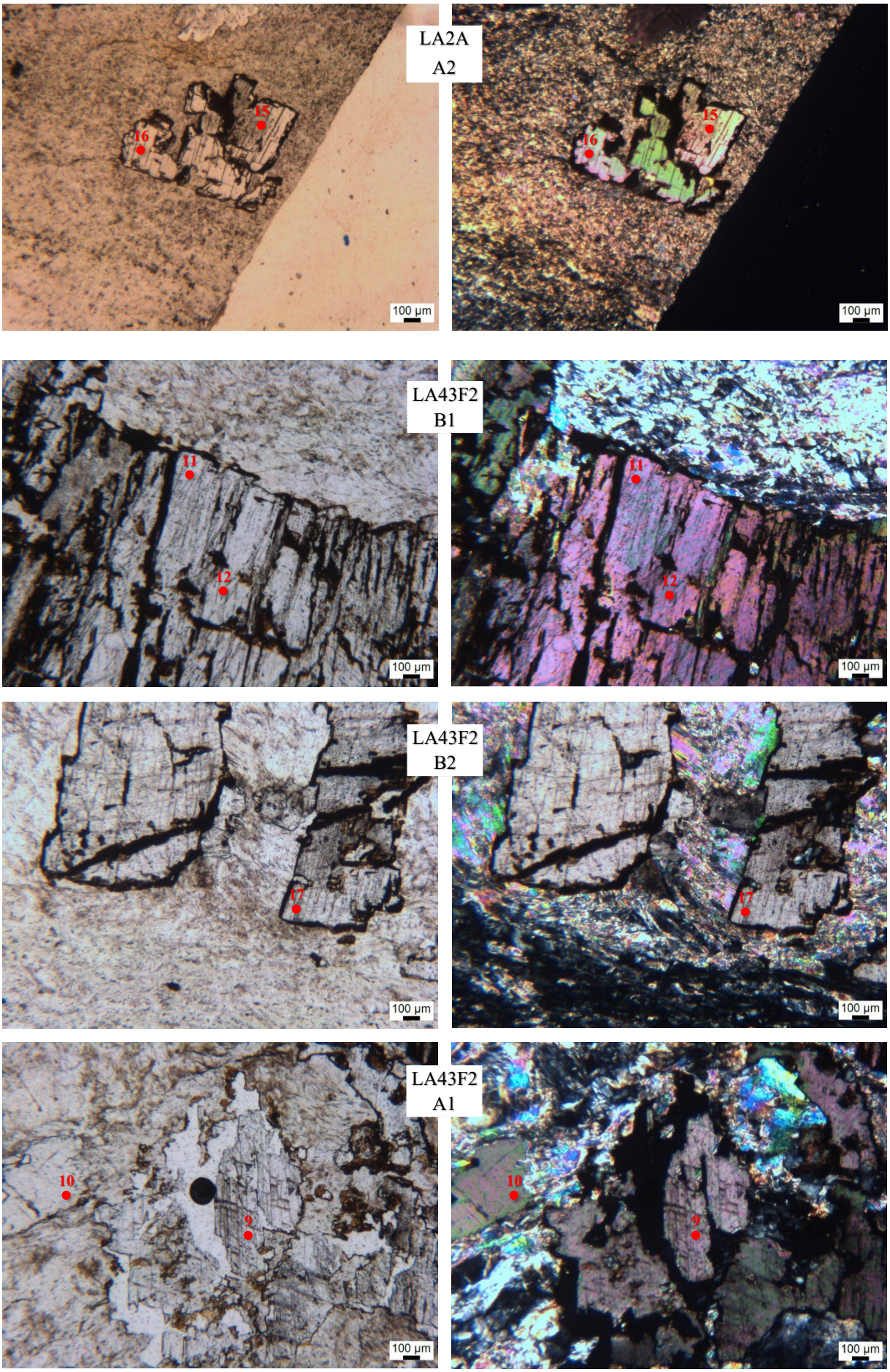

Figure 15 : Planche photographique des zones d'analysées à la microsonde pour les magnésites avec la localisation des points d'analyse en rouge.

5. Analyse des Dolomites

DOLOMITE ANALYSES

Samples	LA43F2					
N° analysis	A1-09-260721	A1-10-260721	A2-24-260721	A2-25-260721	B1-13-260721	B1-14-260721
FeO	15,90	13,15	3,25	3,76	5,40	4,82
MnO	0,19	0,09	0,89	0,66	0,51	0,34
MgO	39,85	39,85	20,57	21,13	20,39	21,55
CaO	0,14	0,08	30,25	29,93	29,02	29,25
SiO_2	0,02	0,01	0,07	1,60	0,01	0,01
TiO_2	0,00	0,01	0,00	0,02	0,04	0,00
Al_2O_3	0,00	0,00	0,02	0,18	0,00	0,00
Na_2O	0,01	0,00	0,00	0,00	0,01	0,01
K_2O	0,00	0,00	0,00	0,00	0,00	0,00
F	0,00	0,00	0,02	0,02	0,00	0,00
BaO	0,00	0,00	0,00	0,00	0,00	0,00
Total	56,11	55,31	55,07	57,29	55,37	55,97
	X	X Magnésite			Ajout	Ajout

Tableau 4 : Tableau des résultats des analyses microsonde des dolomites. Les résultats sont donnés en pourcentage oxyde, les colonnes grisées correspondent à des analyses qui ne représentent pas de la dolomite.

Les analyses à la microsonde des dolomites sont reportées sur le *Tableau 4*. Chaque point analysé à la microsonde est localisé sur la planche photo de la *figure 16*, les zones d'analyse sur les lames sont localisées sur les scans des lames au chapitre *Rappel sur les lames minces sélectionnées* et leurs coordonnées sont écrites dans le rapport *Préparation Microsonde*. Les résultats des analyses des dolomites sont globalement homogènes, hormis pour le FeO qui a des taux plus variables.

Sur l'échantillon LA43F2, sur l'emplacement B1 on peut noter que la dolomite est dans des interstices de magnésite. Cette dolomite peut donc être liée à la cristallisation de la magnésite ou bien cristallisée dans les fractures post-magnésite.

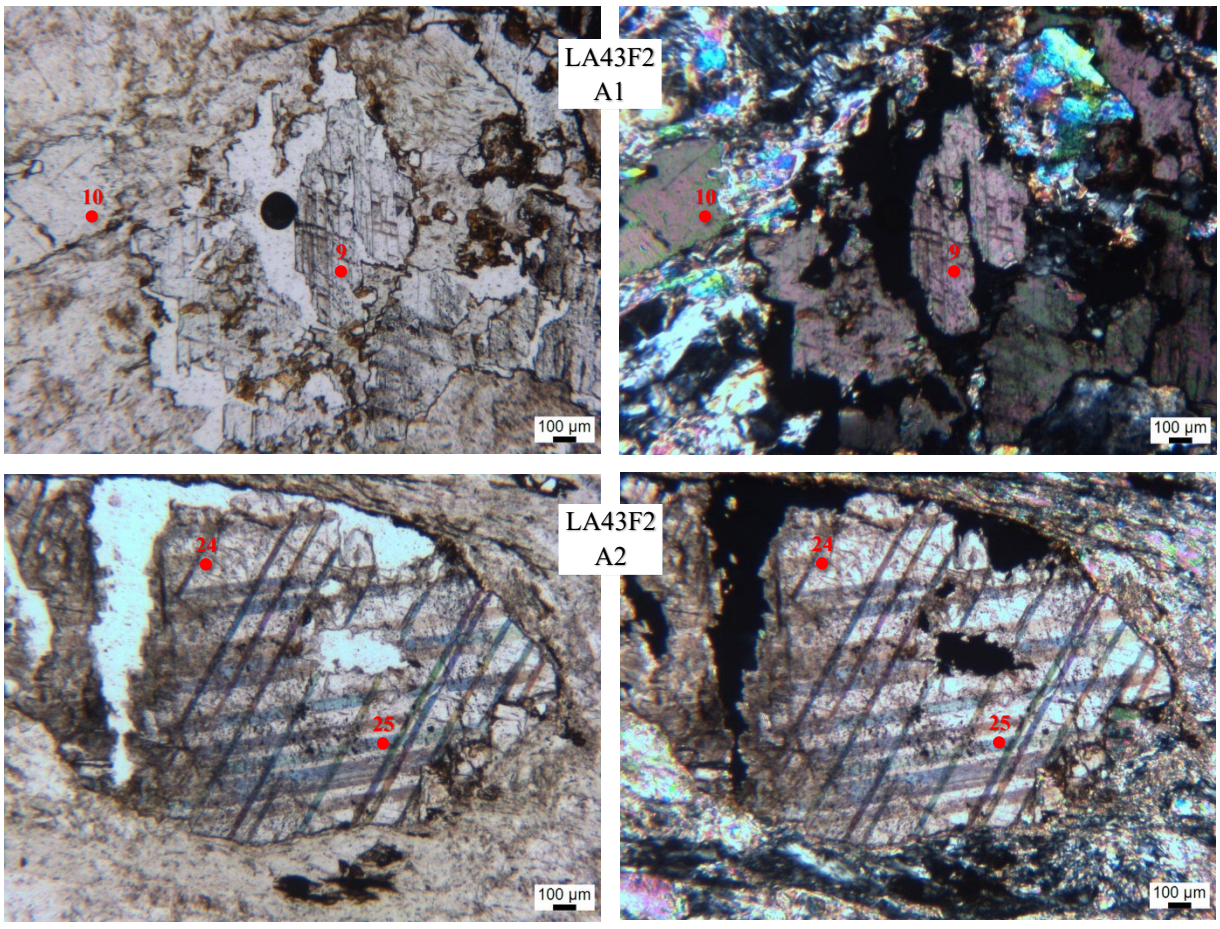

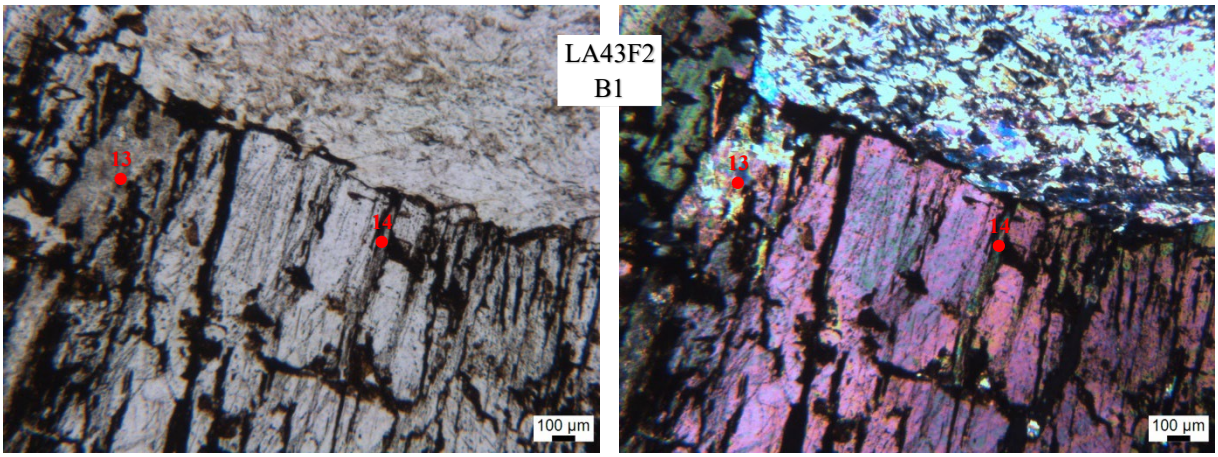

Figure 16 : Planche photographique des zones d'analysées à la microsonde pour les dolomites avec la localisation des points d'analyse en rouge. A droite photographie en lumière polarisée, à gauche photographie en lumière polarisée analysée.

6. Analyse des Rutiles

RUTILE ANALYSES

Samples	LA3E			
N° analysis	C2-46-260721	C2-47-260721	C3-48-260721	C3-52-260721
SiO_2	28,72	0,43	0,02	0,01
TiO_2	0,33	54,23	56,31	55,40
Al_2O_3	21,69	0,17	0,00	0,01
FeO	15,23	42,51	42,54	43,17
MnO	0,13	3,55	3,76	3,50
MgO	23,52	0,28	0,05	0,04
CaO	0,02	0,05	0,00	0,00
Na_2O	0,00	0,00	0,00	0,01
K_2O	0,00	0,01	0,00	0,00
F	0,10	0,00	0,00	0,03
BaO	0,00	1,84	1,75	1,77
Total	89,75	103,07	104,43	103,93
	X (mica) X		X	X

Tableau 5 : Tableau d'analyses des dolomites à la microsonde. Les résultats sont donnés en pourcentage oxyde, les colonnes grisées correspondent à des analyses qui ne représentent pas de la dolomite ou des pourcentages totaux supérieurs à 102%.

Les analyses à la microsonde des rutiles sont reportées sur le *Tableau 5*. Chaque point analysé à la microsonde est localisé sur la planche photo de la *figure 17* (les secteurs d'analyse sur les lames sont placés au chapitre *Rappel sur les lames minces sélectionnées* et leurs coordonnées sont écrites dans le rapport *Préparation Microsonde*). Les résultats des analyses des rutiles sont tous faux ou supérieur à 102%. Les analyses des rutiles ont été effectuées le 26 juillet, après le changement de standards. Cependant ces pourcentages, largement supérieurs à 100%, laissent penser que ce changement n'a pas suffi à corriger la calibration.

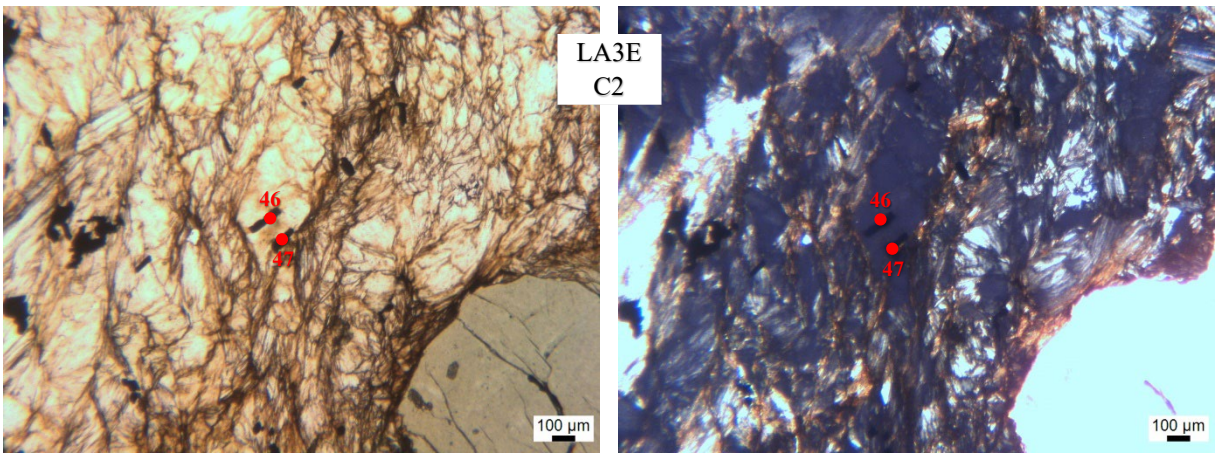

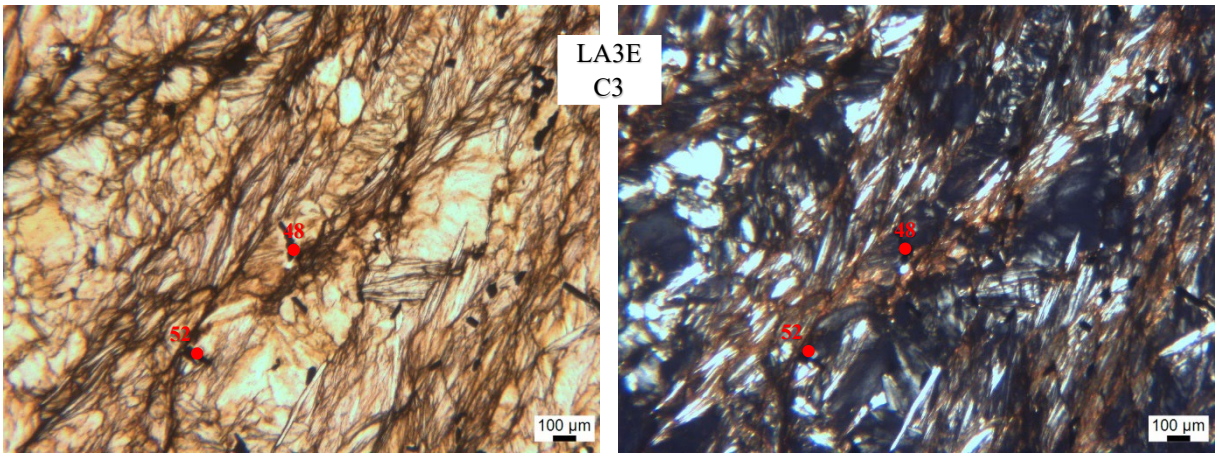

Figure 17 : Planche photographique des zones d'analysées à la microsonde pour les rutiles avec la localisation des points d'analyse en rouge. A droite photographie en lumière polarisée, à gauche photographie en lumière polarisée analysée.

7. Analyse des Micas/Talc

Encaissant clair ANALYSES

Samples	LA34A1		LA43E						LA43F2				LA3E			
N° analysis	E1-14-220721	E1-14-260721	A1-19-230721	A1-20-230721	A4-27-230721	A4-28-230721	A7-07-260721	A7-08-260721	B1-15-260721	B1-16-260721	B2-20-260721	B2-21-260721	A4-36-260721	A4-37-260721	A1-44-260721	A1-45-260721
SiO_2	62,42	62,17	62,42	63,07	62,91	62,82	63,33	62,72	63,60	62,68	29,68	29,53	28,97	18,45	28,13	29,39
TiO_2	0,02	0,07	0,00	0,01	0,00	0,01	0,06	0,04	0,00	0,05	0,03	0,06	0,06	0,06	0,08	0,07
Al_2O_3	0,20	0,56	0,18	0,12	0,31	0,19	0,31	0,51	0,07	0,49	19,58	19,74	23,60	14,27	21,15	22,47
FeO	4,76	4,96	4,98	4,13	4,14	4,24	3,48	3,51	3,70	3,86	10,76	10,69	15,43	9,19	15,52	14,63
MnO	0,00	0,00	0,02	0,03	0,02	0,01	0,02	0,02	0,00	0,01	0,06	0,05	0,14	3,35	0,19	0,15
MgO	27,74	29,18	29,52	29,94	30,10	29,32	30,04	30,19	29,18	29,78	26,92	27,06	12,15	11,44	23,79	22,06
CaO	0,00	0,03	0,02	0,01	0,01	0,02	0,00	0,02	0,06	0,01	0,04	0,07	0,10	0,14	0,03	0,03
Na_2O	0,02	0,12	0,03	0,02	0,03	0,02	0,07	0,09	0,02	0,10	0,03	0,03	0,03	0,08	0,01	0,02
K_2O	0,00	0,00	0,00	0,01	0,00	0,01	0,00	0,00	0,02	0,00	0,02	0,02	0,01	0,03	0,01	0,01
F	0,00	0,00	0,00	0,04	0,00	0,11	0,00	0,05	0,01	0,01	0,06	0,02	0,00	0,05	0,00	0,03
BaO	0,00	0,00	0,00	0,00	0,00	0,00	0,00	0,00	0,00	0,00	0,00	0,00	0,00	0,00	0,00	0,00
Total	95,16	97,10	97,18	97,37	97,53	96,75	97,31	97,15	96,64	96,99	87,19	87,28	80,48	57,05	88,90	88,87
														X		

Samples	LA3E		
N° analysis	C3-50-260721	C3-51-260721	C2-46-260721
SiO_2	28,74	28,31	28,72
TiO_2	0,09	0,06	0,33
Al_2O_3	21,79	21,52	21,69
FeO	15,64	15,21	15,23
MnO	0,16	0,14	0,13
MgO	21,23	22,99	23,52
CaO	0,04	0,06	0,02
Na_2O	0,02	0,00	0,00
K_2O	0,00	0,01	0,00
F	0,01	0,00	0,10
BaO	0,00	0,00	0,00
Total	87,72	88,31	89,75
			Ajout

Tableau 6 : Tableau d'analyses de l'encaissant clair à la microsonde. Les résultats sont donnés en pourcentage oxyde, les colonnes grisées correspondent à des analyses qui ne représentent pas des valeurs similaires à la chimie des talcs ou micas.

Les résultats, des analyses chimiques à la microsonde, de l'encaissant clair sont reportées sur le *Tableau 6*. Chaque point analysé à la microsonde est localisé sur la planche photo de la *figure 18*, les zones d'analyse sur les lames sont localisées sur les scans des lames au chapitre *Rappel sur les lames minces sélectionnées* et leurs coordonnées sont écrites dans le rapport *Préparation Microsonde*.

Ces analyses montrent que l'encaissant est constitué de Talc avec une composition très proche d'une analyse à l'autre (LA34A1, LA43E et LA43F2) et/ou de micas avec des compositions plus variables (LA43F2, LA3E).

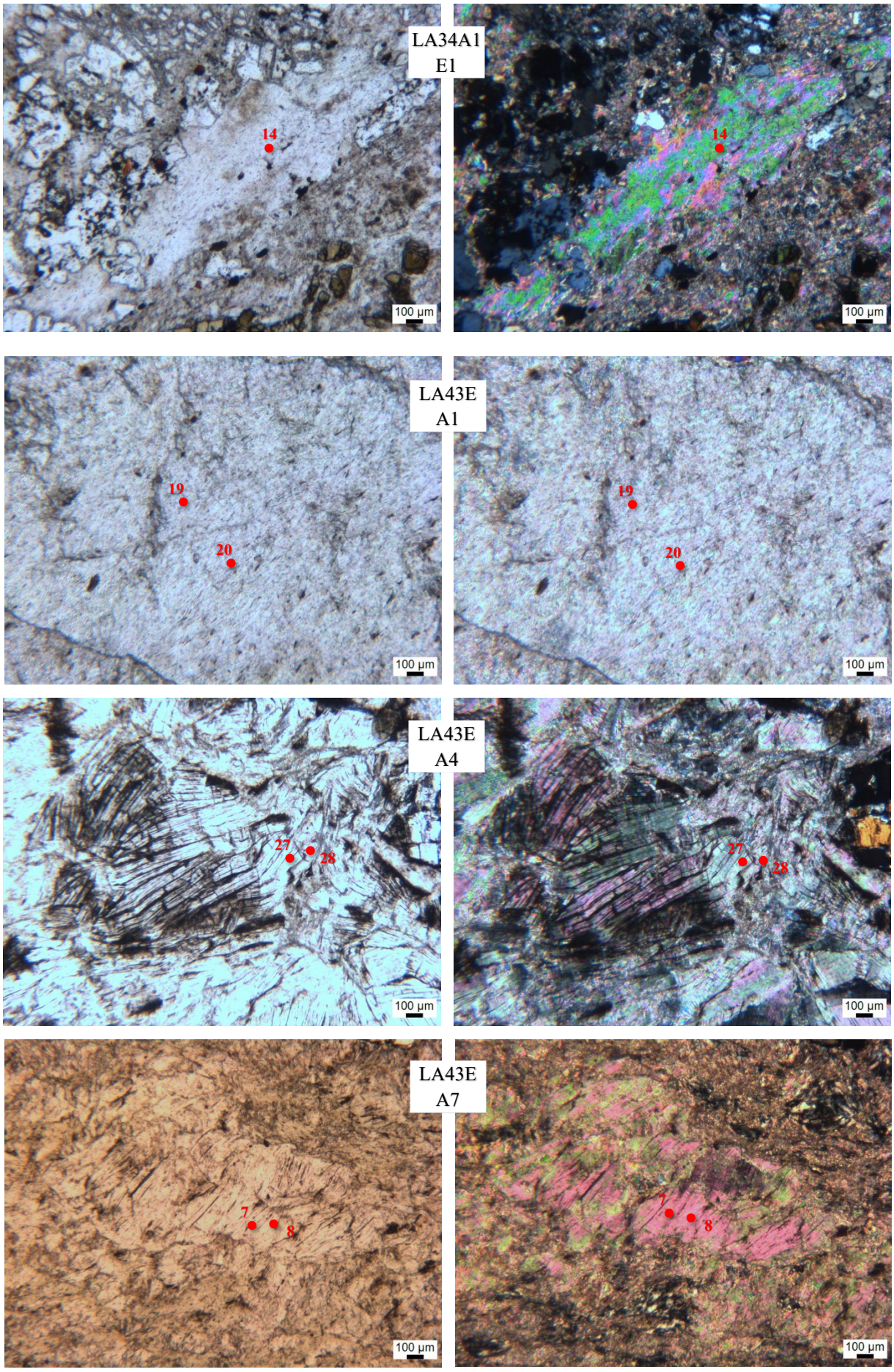
LA34A1
E1
14
14
100 µm
100 µm
LA43E
A1
19
20
19
20
100 µm
100 µm
LA43E
A4
27
28
27
28
100 µm
100 µm
LA43E
A7
7
8
7
8
100 µm
100 µm

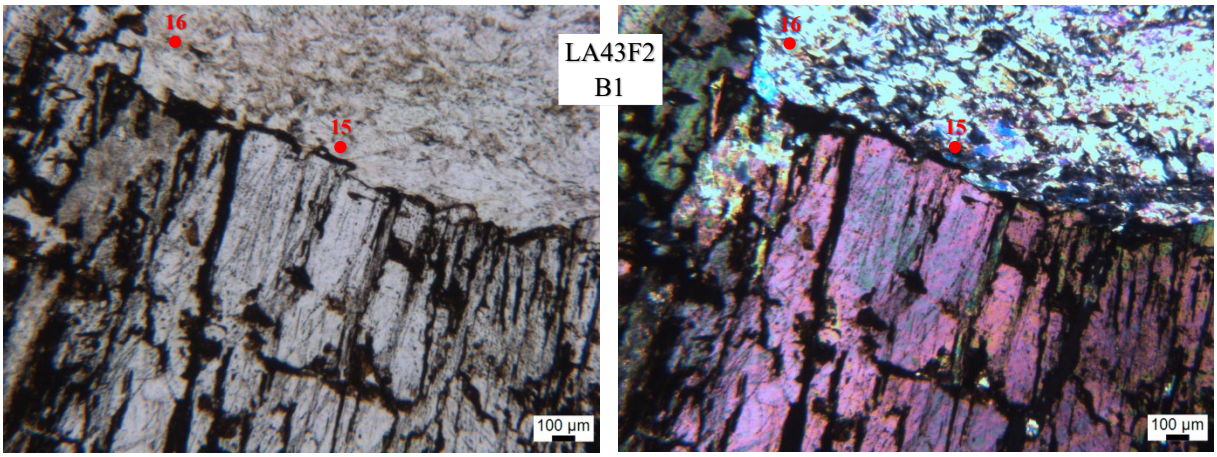
LA43F2
B1
16
15
16
15
100 µm
100 µm

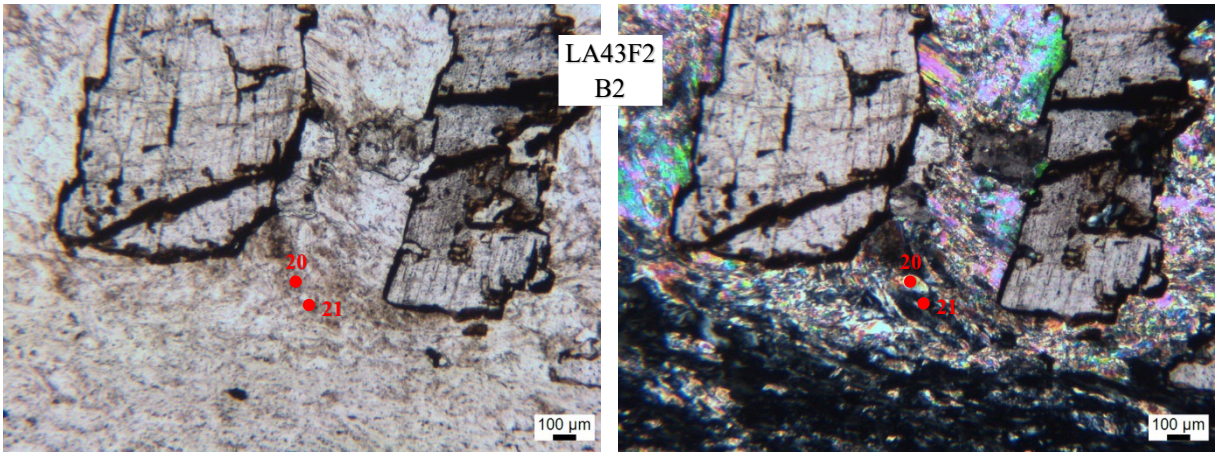
LA43F2
B2
20
21
20
21
100 µm
100 µm

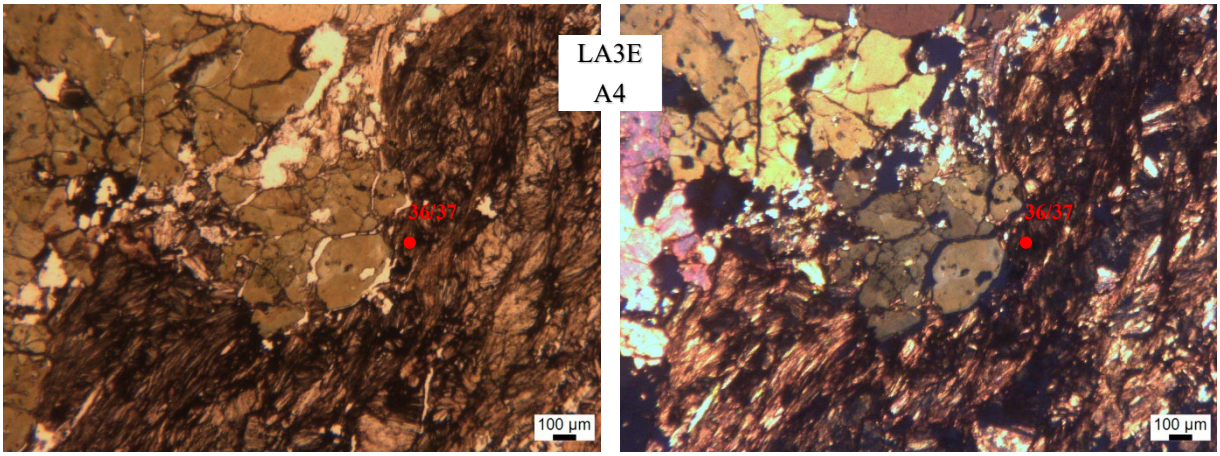
LA3E
A4
36/37
36/37
100 µm
100 µm

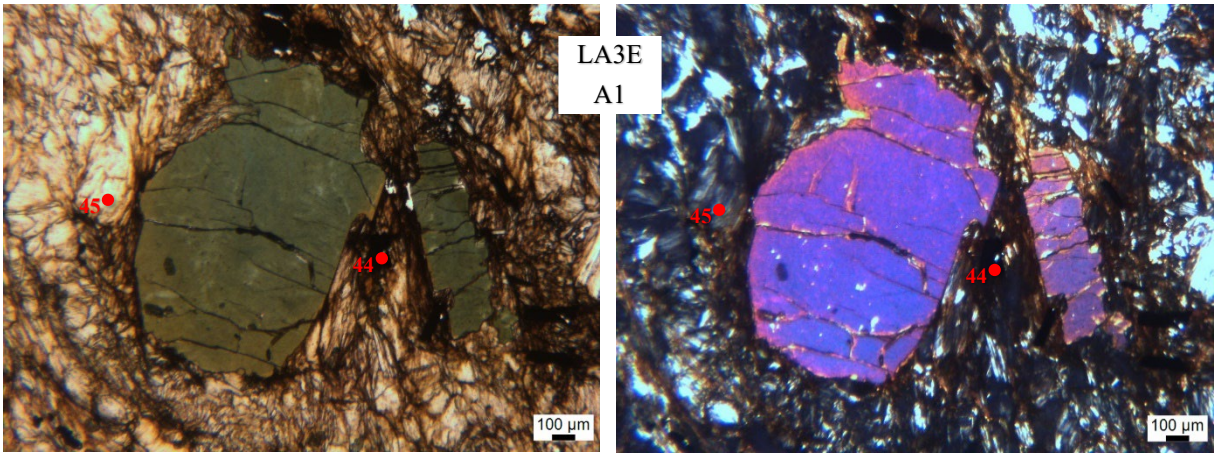
LA3E
A1
45
44
45
44
100 µm
100 µm

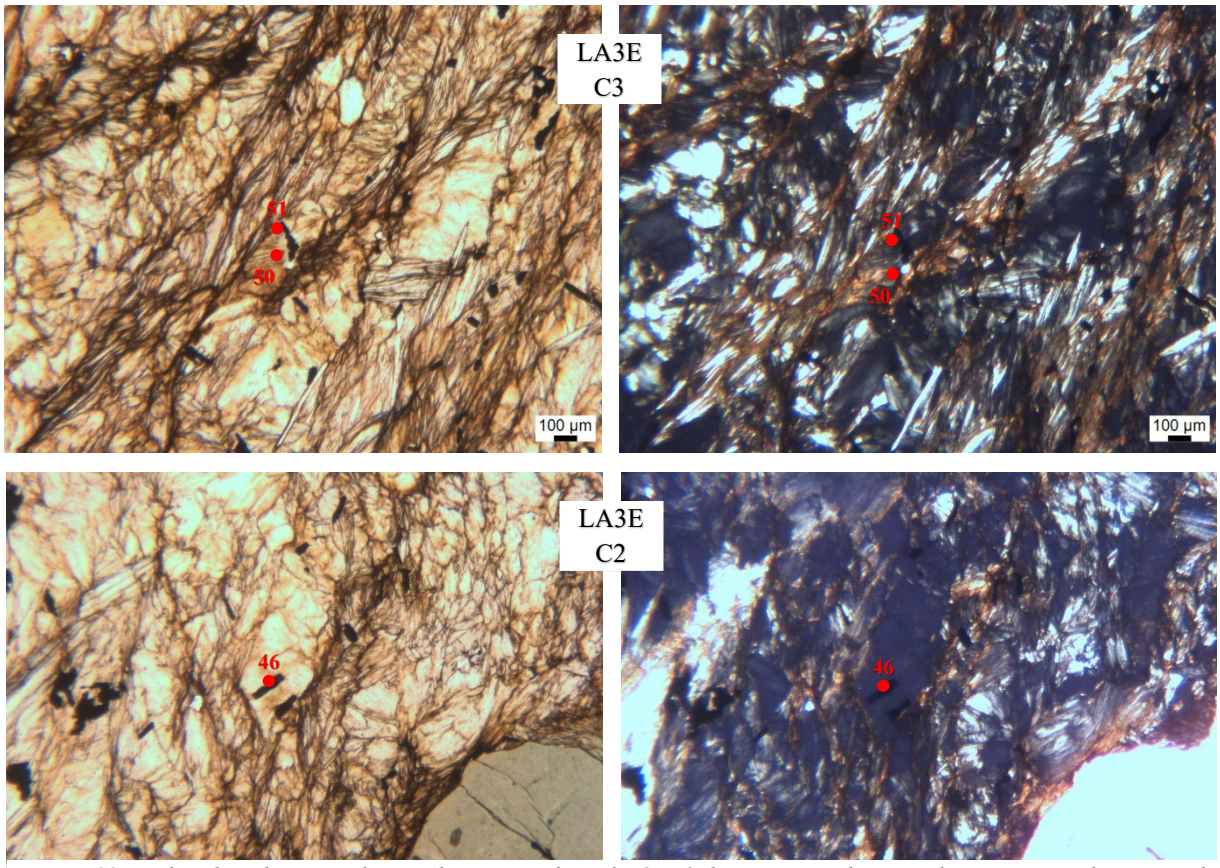

Figure 18 : Planche photographique des zones d'analysées à la microsonde pour l'encaissant clair avec la localisation des points d'analyse en rouge. A droite photographie en lumière polarisée, à gauche photographie en lumière polarisée analysée.

Encaissant sombre ANALYSES

Samples	LA43E		LA43F2	
N° analysis	A8-05-260721	A8-06-260721	B2-22-260721	B2-23-260721
SiO_2	43,57	29,32	42,73	29,10
TiO_2	0,08	0,02	0,02	0,04
Al_2O_3	11,84	20,13	11,44	19,37
FeO	7,90	9,91	7,83	10,72
MnO	0,04	0,06	0,06	0,06
MgO	28,20	27,61	28,42	27,39
CaO	0,05	0,01	0,04	0,04
Na_2O	0,03	0,03	0,04	0,02
K_2O	0,00	0,00	0,01	0,02
F	0,03	0,01	0,07	0,04
BaO	0,00	0,00	0,00	0,00
Total	91,73	87,10	90,64	86,81

Tableau 7 : Tableau d'analyses de l'encaissant sombre à la microsonde. Les résultats sont donnés en pourcentage oxyde.

Les zones où l'encaissant est plus sombre ont été analysées, les résultats de ces analyses sont reportés sur le *Tableau 7*. Les points d'analyses sont localisés sur les secteurs d'intérêt sur la planche photo de *figure 19* (les secteurs d'intérêt sont situés sur les lames au chapitre *Rappel sur les lames minces sélectionnées*).

Les zones sombres de l'encaissant sont composées de mica riche en Fer, les analyses dévoilent des compositions variables d'un point à l'autre.

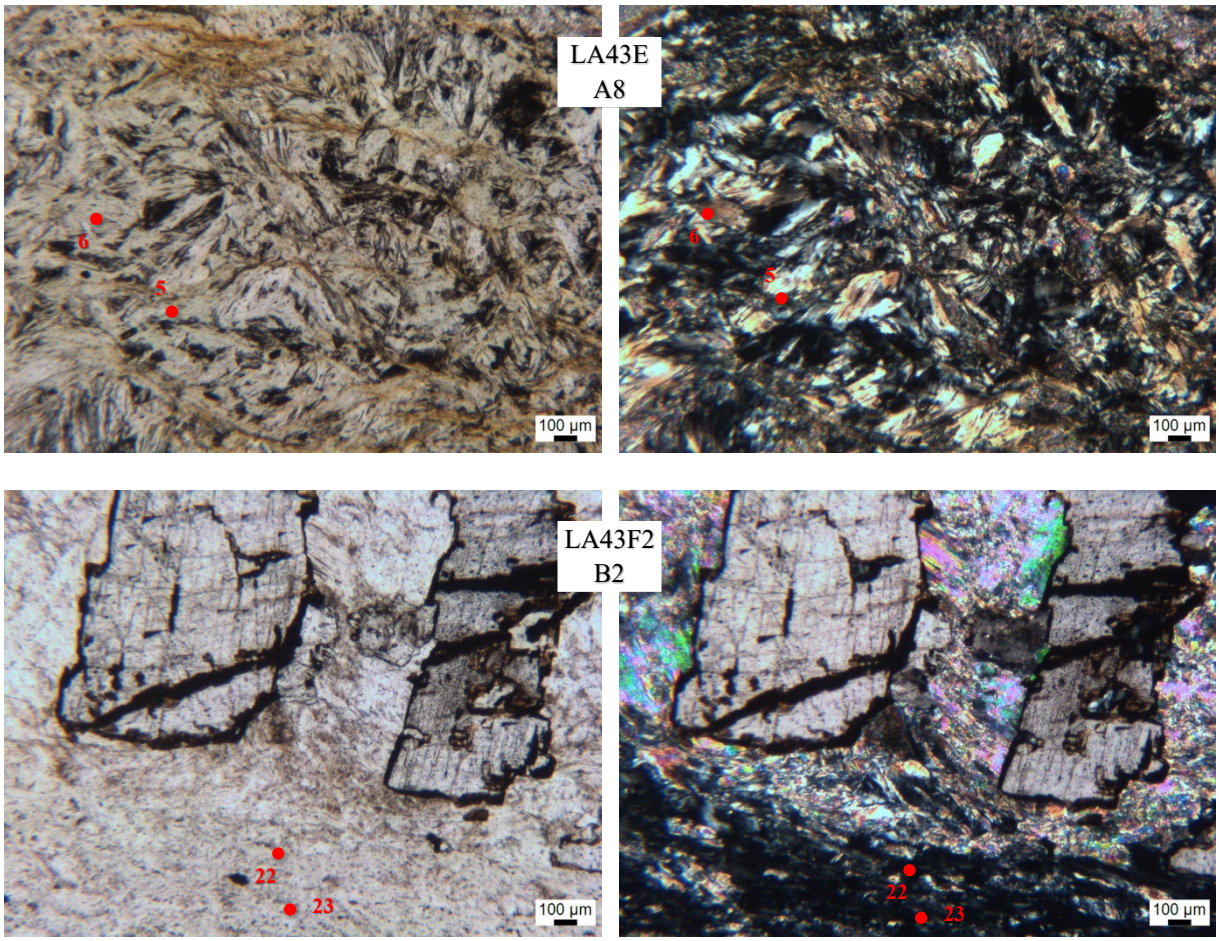

Figure 19 : Planche photographique des zones d'analysées à la microsonde pour l'encaissant clair avec la localisation des points d'analyse en rouge. A droite photographie en lumière polarisée, à gauche photographie en lumière polarisée analysée.

Alteration ANALYSES

Samples	LA43E		LA34A1						LA14			
N° analysis	A1-19-230721	A1-20-230721	A1-08-220721	A1-09-220721	A1-10-220721	A1-11-220721	A1-12-220721	A1-13-220721	A2-26-260721	A2-27-260721	A3-28-260721	A3-29-260721
SiO_2	62,42	63,07	62,20	61,86	62,16	61,16	62,63	61,64	63,58	63,99	63,14	62,68
TiO_2	0,00	0,01	0,01	0,02	0,02	0,02	0,00	0,01	0,00	0,00	0,00	0,00
Al_2O_3	0,18	0,12	0,18	0,13	0,16	1,43	0,97	0,51	0,16	0,17	0,12	0,46
FeO	4,98	4,13	5,49	5,69	5,47	4,63	4,79	4,93	2,46	1,91	2,09	2,64
MnO	0,02	0,03	0,01	0,02	0,03	0,02	0,01	0,00	0,03	0,00	0,00	0,05
MgO	29,52	29,94	27,26	25,97	27,24	26,38	26,88	23,98	30,61	31,11	30,74	30,12
CaO	0,02	0,01	0,05	0,11	0,03	0,08	0,02	0,24	0,00	0,00	0,01	0,03
Na_2O	0,03	0,02	0,04	0,03	0,02	0,03	0,03	0,03	0,01	0,02	0,01	0,05
K_2O	0,00	0,01	0,00	0,01	0,00	0,02	0,00	0,01	0,00	0,01	0,00	0,01
F	0,00	0,04	0,03	0,04	0,02	0,02	0,06	0,06	0,03	0,00	0,00	0,00
BaO	0,00	0,00	0,00	0,00	0,00	0,00	0,00	0,00	0,00	0,00	0,00	0,00
Total	97,18	97,37	95,27	93,87	95,16	93,78	95,39	91,41	96,89	97,21	96,11	96,05

Tableau 8 : Tableau des résultats d'analyse de l'altération verte à la microsonde.

Les résultats sont donnés en pourcentage oxyde.

L'altération verte visible à proximité des veines de quartz a été analysée à la microsonde, les résultats de ces analyses sont donnés sur le *Tableau 8*. Les points analysés ainsi que les photographies des secteurs sélectionnés sont visibles sur la planche photo de la *figure 20*. La localisation des points d'analyse n° 08 à 13, sur la lame LA34A1, représentent une ligne horizontale sur la zone A1, ces points ne sont pas localisés sur la *figure 20*.

L’altération verte est composée exclusivement de Talc plus ou moins ferreux.

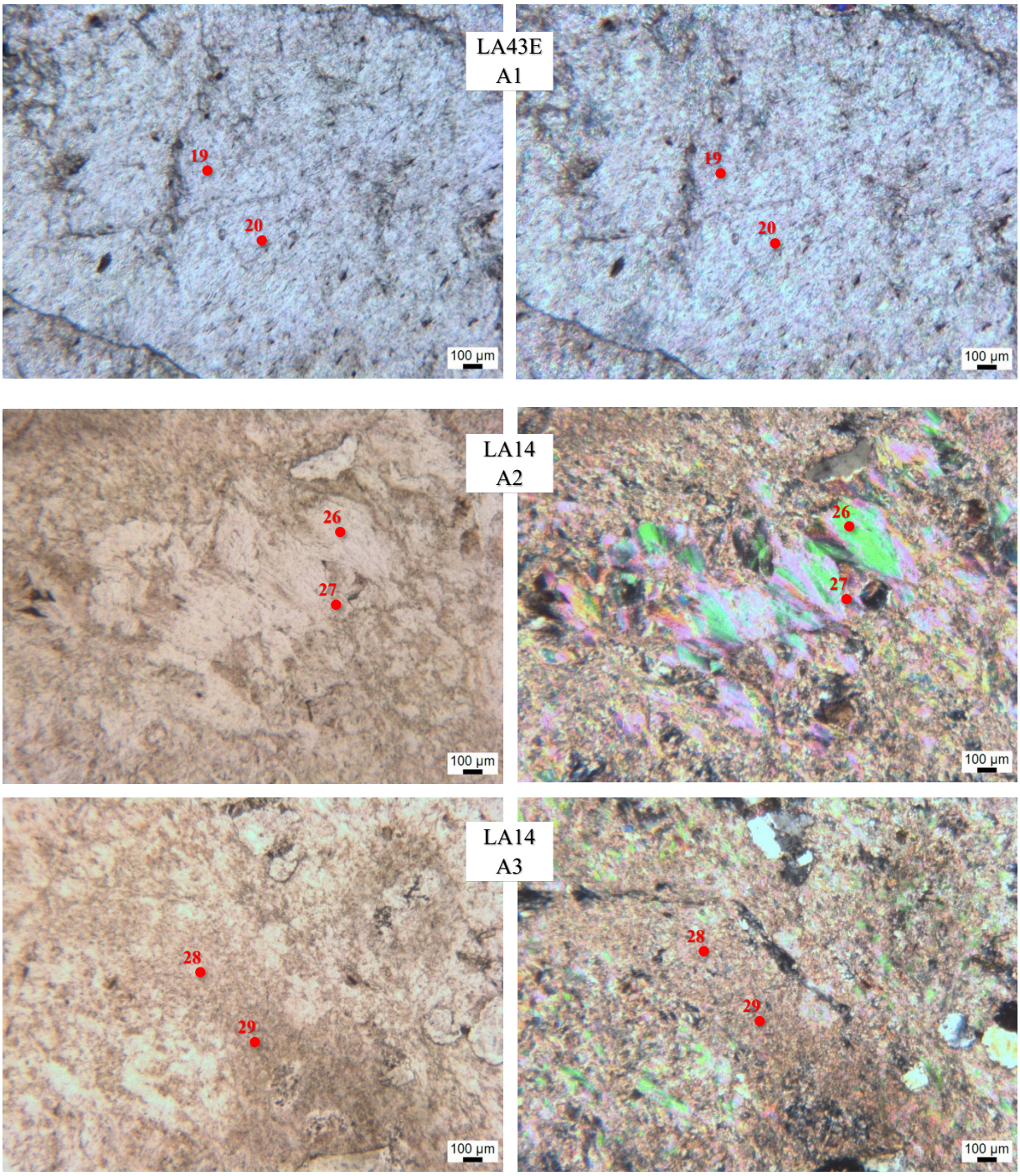

Figure 20 : Planche photographique des zones d’analysées à la microsonde pour l’altération verte avec la localisation des points d’analyse en rouge. A droite photographie en lumière polarisée, à gauche photographie en lumière polarisée analysée.

Fracture ANALYSES

Samples	LA3E		LA43F2				LA34A1				LA43E		LA14	
N° analysis	B5-40-260721	B5-41-260721	B1-13-260721	B1-14-260721	B2-18-260721	B2-19-260721	B2-03-220721	B2-04-220721	B2-03-260721	B2-04-260721	B1-23-230721	B1-24-230721	A4-33-260721	A4-33-260721
SiO_2	30,87	62,30	0,01	0,01	62,71	63,38	60,12	62,66	61,79	63,05	62,42	63,07	63,00	64,08
TiO_2	0,08	0,02	0,04	0,00	0,00	0,00	0,00	0,01	0,00	0,03	0,00	0,01	0,00	0,01
Al_2O_3	21,27	0,65	0,00	0,00	0,10	0,03	0,11	0,47	0,22	0,12	0,18	0,12	0,30	0,21
FeO	12,86	6,65	5,40	4,82	3,67	3,80	4,72	4,82	4,81	4,67	4,98	4,13	2,73	2,36
MnO	0,28	0,14	0,51	0,34	0,00	0,04	0,01	0,04	0,03	0,01	0,02	0,03	0,01	0,02
MgO	14,12	26,48	20,39	21,55	30,48	29,97	27,15	27,79	29,18	29,07	29,52	29,94	30,76	30,39
CaO	0,10	0,13	29,02	29,25	0,00	0,04	0,17	0,06	0,11	0,06	0,02	0,01	0,02	0,04
Na_2O	0,04	0,06	0,01	0,01	0,02	0,04	0,01	0,02	0,05	0,02	0,03	0,02	0,06	0,03
K_2O	0,04	0,00	0,00	0,00	0,01	0,02	0,01	0,01	0,00	0,01	0,00	0,01	0,00	0,00
F	0,00	0,17	0,00	0,00	0,00	0,00	0,04	0,00	0,02	0,04	0,00	0,04	0,00	0,05
BaO	0,00	0,00	0,00	0,00	0,00	0,00	0,00	0,00	0,00	0,00	0,00	0,00	0,00	0,00
Total	79,66	96,60	55,37	55,97	97,00	97,31	92,34	95,87	96,21	97,08	97,18	97,37	96,90	97,20
			X	X dolomite										

Tableau 9 : Tableau d'analyses des remplissages des fractures à la microsonde. Les résultats sont donnés en pourcentage oxyde, les colonnes grisées correspondent à des analyses qui n'ont pas la chimie des micas/talc.

Lors des séances à la microsonde, le remplissage des fractures par des micas et/ou talcs a été analysé chimiquement (*Tableau 9*). La localisation de ces analyses est visible sur la *figure 21*.

La majorité des fractures analysées est remplie par du Talc plus ou moins ferreux, on retrouve sur une fracture un mica (LA3E zone B5, analyse 40). Dans la zone B1 de l'échantillon LA43F2, des dolomites sont entre les interstices d'une magnésite, cette analyse a été ajoutée au tableau des dolomites (voir partie *Analyse des Dolomites*).

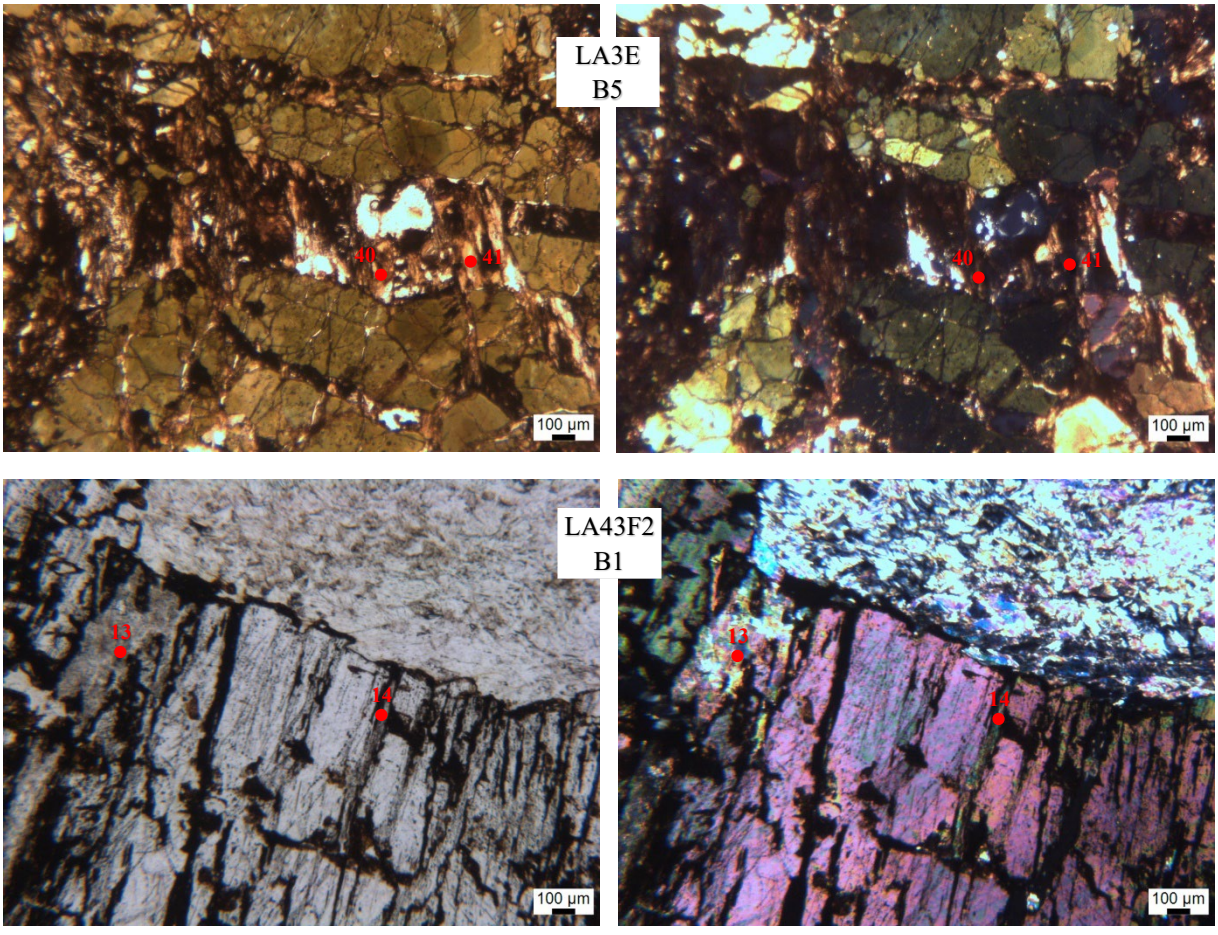

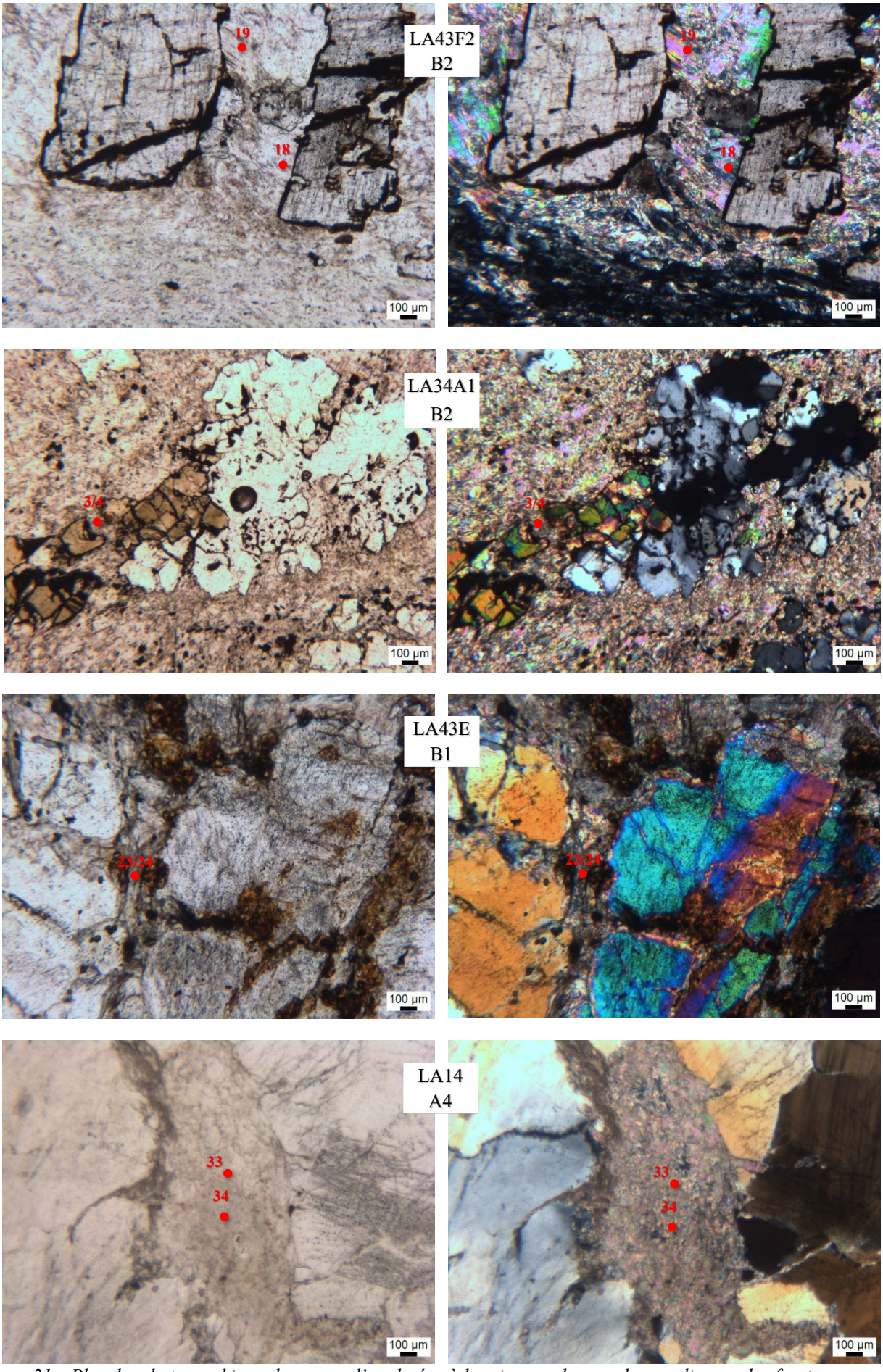

Figure 21 : Planche photographique des zones d'analysées à la microsonde pour le remplissage des fractures avec la localisation des points d'analyse en rouge.

Cartographie

Trois lames ont fait l'objet d'une cartographie chimique à la microsonde, la lame LA2A, LA34A1 et 43E. L'emplacement des parties de lames analysées pour les cartes chimiques est localisé sur la *figure 22*. Pour chaque lame, des cartes chimiques des éléments Al, Mg, Fe, Ca et K ont été réalisées.

Figure 22 : Scans des lames minces sélectionnées pour réaliser des cartes chimiques, avec l'emplacement des cadres des cartes en bleu. Respectivement de gauche à droite : LA2A, LA34A1 et LA43E.

1. Cartographie chimique de la lame LA2A

Les cartes chimiques de la lame LA2A sont compilées sur la *figure 23*. Ces cartes montrent que le plan de cisaillement à grains fins au milieu de la lame est composé majoritairement de micas (présence d'Al) avec quelques minéraux de talc (absence d'Al). De plus sur ce même plan de cisaillement on peut distinguer des figures de mouvement (surtout sur les cartes d'Al et de Mg). La lentille noire à gauche de la lame est composée d'oxydes de Fer, le tronçonnement de cette lentille est rempli par du Talc (pic de Mg et absence d'Al). La lame est composée majoritairement de dolomite (beaucoup de Ca et de Mg) avec quelques bandes de magnésites (absence de Ca et pic de Mg).

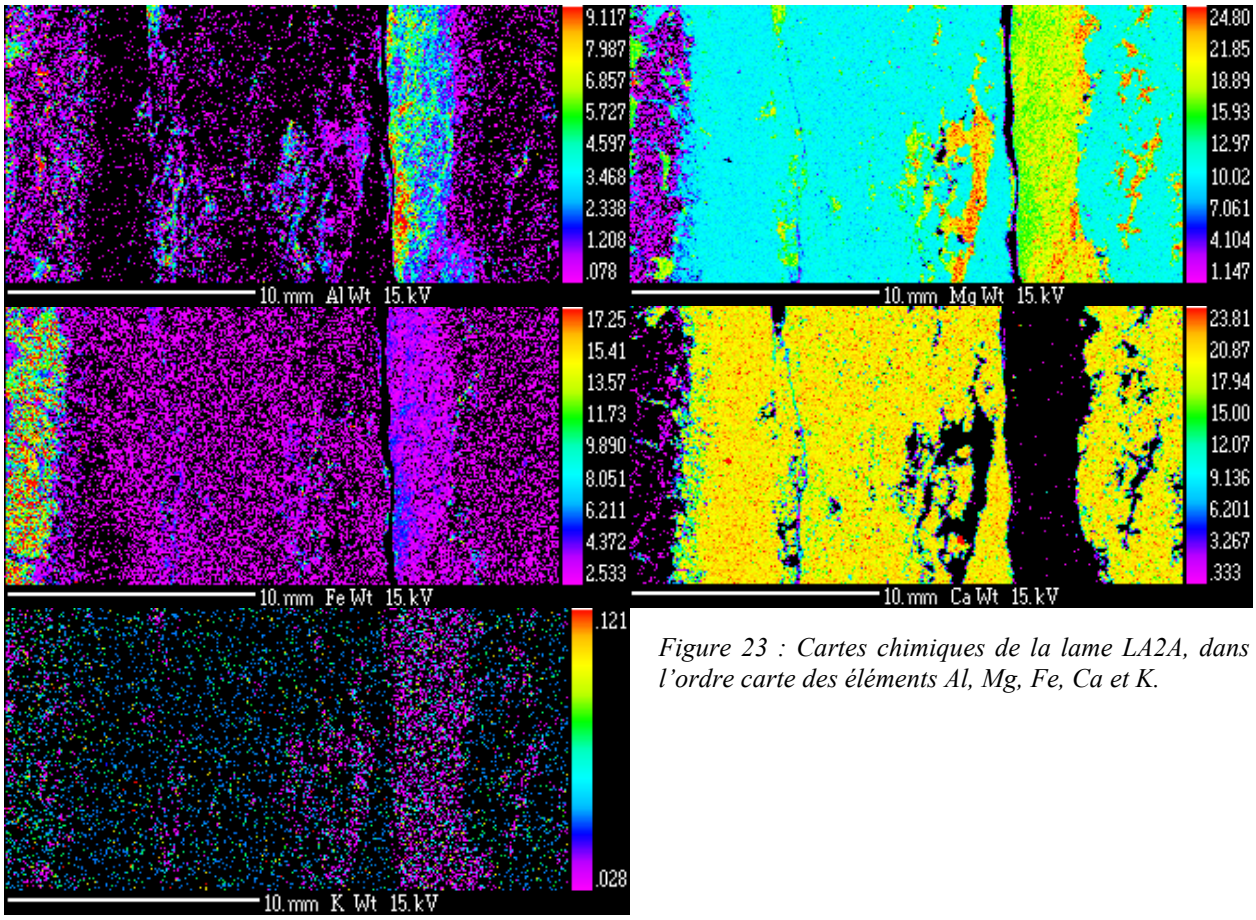

Figure 23 : Cartes chimiques de la lame LA2A, dans l'ordre carte des éléments Al, Mg, Fe, Ca et K.

2. Cartographie chimique de la lame LA34A1

Les cartes chimiques de la lame LA34A1 sont compilées sur la *figure 24*. Le plan de cisaillement (en bas à droite des cartes) est composé, tout comme le reste de la matrice, de Talc (absence d'Al, beaucoup de Mg). Cependant on peut noter sur le bord de ce plan un enrichissement en Fer (et un déficit d'Al ?). Les principaux minéraux visibles, plutôt sur la partie gauche des cartes, sont composés d'Al et sont appauvris en Mg et Fe par rapport à la matrice. Ces minéraux peuvent correspondre à la chimie des albites.

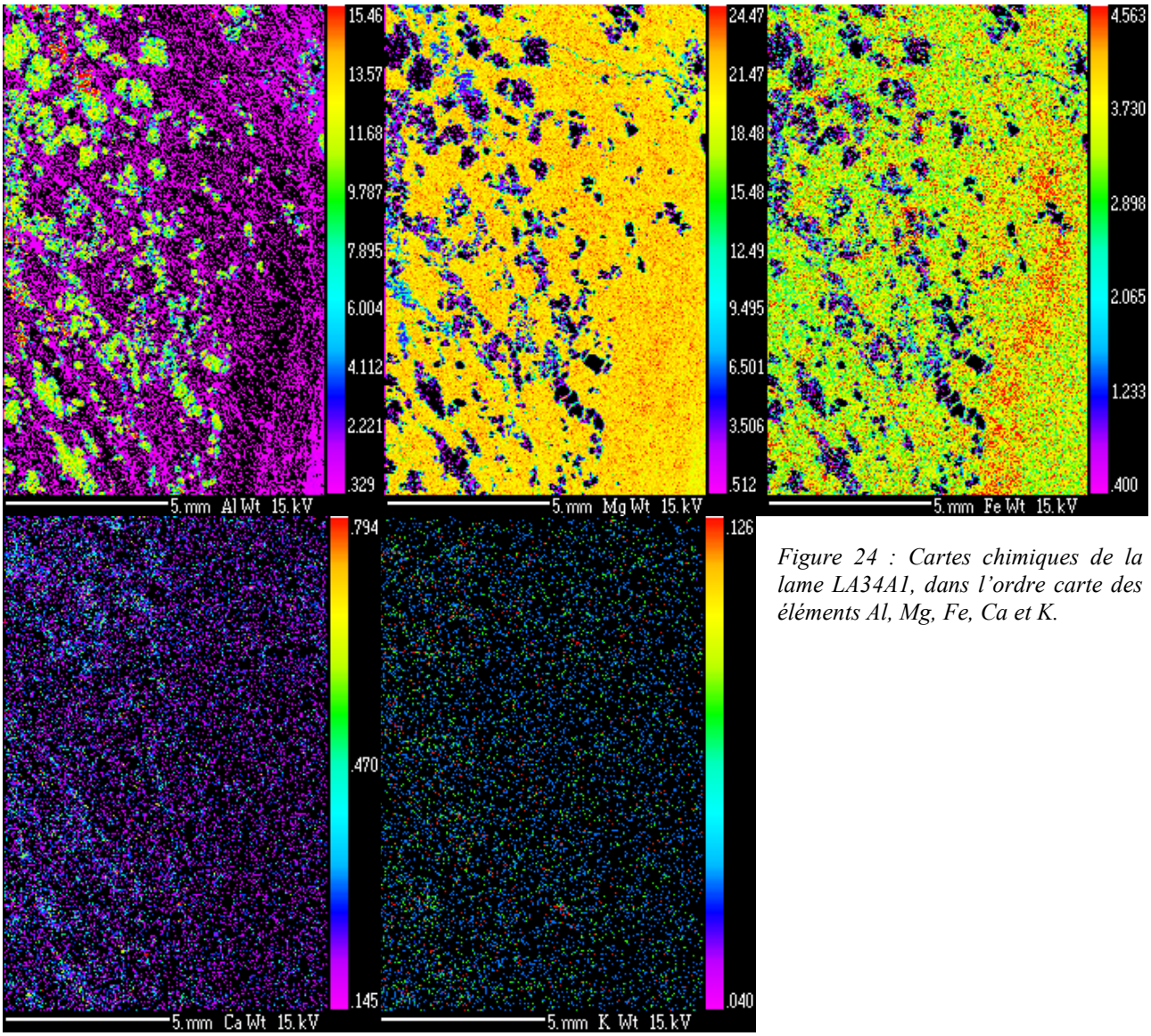

Figure 24 : Cartes chimiques de la lame LA34A1, dans l'ordre carte des éléments Al, Mg, Fe, Ca et K.

3. Cartographie chimique de la lame LA43E

Les cartes chimiques de la lame LA34A1 sont compilées sur la *figure 25*. Les cartes chimiques de la lame 43E sont très intéressantes, on peut tout d'abord remarquer 5 taux d'Al distincts sur la carte des Al. Dans un premier temps, on voit un grand minéral qui renvoie une chimie d'Al moyenne (verte, 9156), ce minéral est très pauvre en Mg et en Fer, ce qui correspond à la chimie des albites.

On peut aussi noter la présence d'un minéral qui est lieu très enrichi en Al (rouge, 1436). Ce minéral est lui aussi appauvri en Mg et en Fer mais dans une moindre mesure. Cette chimie coïncide à celle des Tourmalines. On voit très clairement ici le plissement de ce minéral.

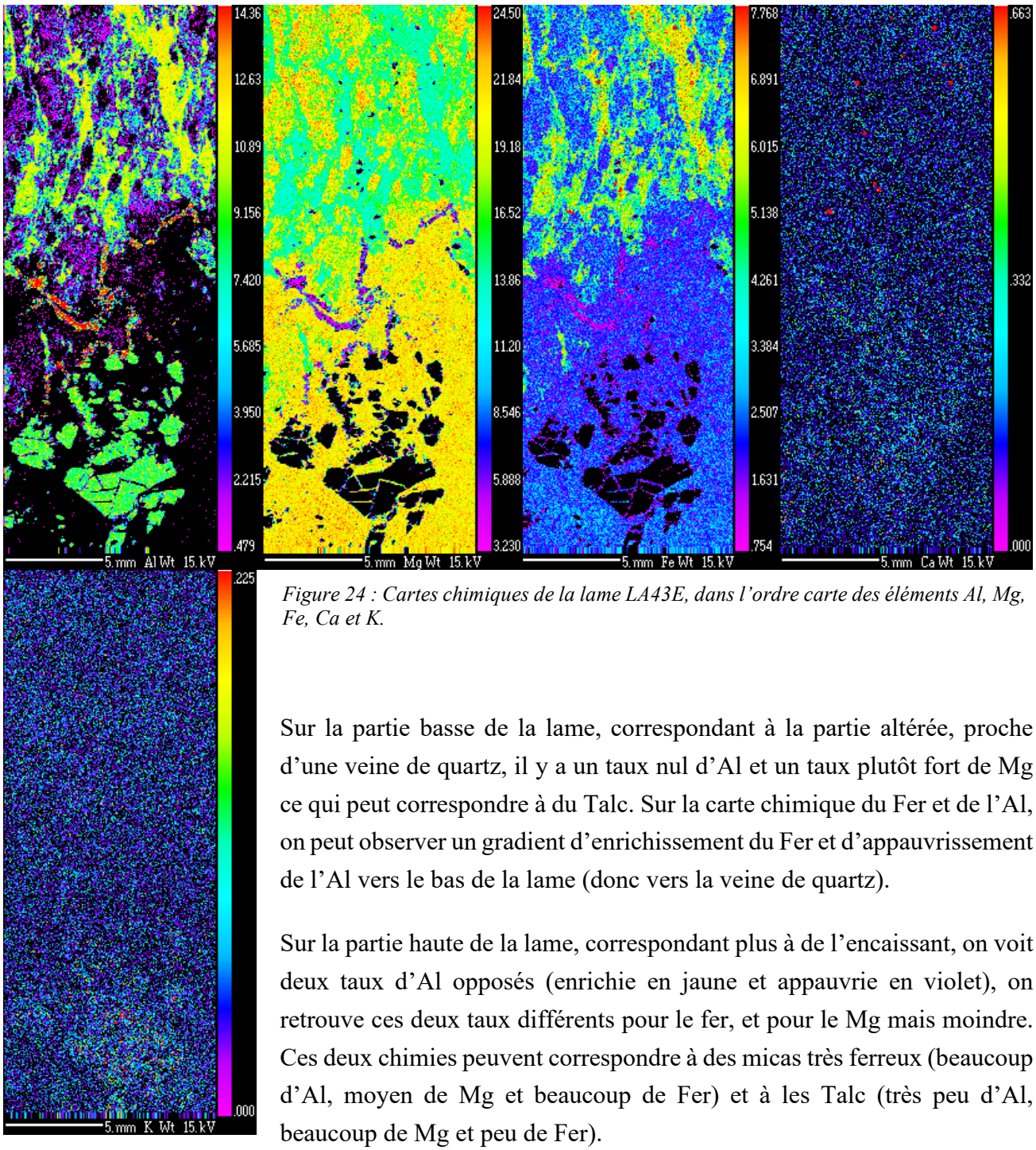

Figure 24 : Cartes chimiques de la lame LA43E, dans l'ordre carte des éléments Al, Mg, Fe, Ca et K.

Sur la partie basse de la lame, correspondant à la partie altérée, proche d'une veine de quartz, il y a un taux nul d'Al et un taux plutôt fort de Mg ce qui peut correspondre à du Talc. Sur la carte chimique du Fer et de l'Al, on peut observer un gradient d'enrichissement du Fer et d'appauvrissement de l'Al vers le bas de la lame (donc vers la veine de quartz).

Sur la partie haute de la lame, correspondant plus à de l'encaissant, on voit deux taux d'Al opposés (enrichie en jaune et appauvrie en violet), on retrouve ces deux taux différents pour le fer, et pour le Mg mais moindre. Ces deux chimies peuvent correspondre à des micas très ferreux (beaucoup d'Al, moyen de Mg et beaucoup de Fer) et à les Talc (très peu d'Al, beaucoup de Mg et peu de Fer).

On peut aussi noter la présence de « points » à forte concentration de Ca qui sont peut-être des dolomites de l'encaissant.

Annexe 5:

Preliminary result of microthermometry of inclusion fluids:

Sample	name	FI	Type	size (um)	V%	Tff	sTff	Tm(hh)	sTfm	Tm	sTm	Th	sTh
LA77B	#Azone5-incl1	2 - green	V+LH2O	13,5	40	-50,6	0,3			-11,8	2,5	215,8	0,2
LA77B	#Azone5b-incl2	1 - blue	V+LH2O	11	10	-45,4	0,3			-10,4	0,9	217,5	0,1
LA77B	#Azone5b-incl3	1 - blue	V+LH2O	13	15	-46,6	0,3			-10,5	0,4	234,7	0,9
LA77B	#Azone5b-incl4	1 - blue	V+LH2O	18,5	10	-44,5	0,5			-8,8	0,7	223,0	0,3
LA77B	#Azone5b-incl5	2 - green	V+LH2O	14	15	-44,2	0,5			-8,9	0,2	215,0	1,5
LA77B	#Azone5b-incl6	2 - green	V+LH2O	12	10	-44,8	0,8			-8,6	0,5	221,5	0,3
LA77B	#Azone5b-incl7	1 - blue	V+LH2O	13,5	10	-43,5	0,7			-8,6	0,4	nd	nd
LA77B	#Azone5b-incl8	2 - green	V+LH2O	16,5	30	-42,8	1,0			-8,0	0,3	215,2	25,7
LA77B	#Azone5b-incl9	1 - blue	V+LH2O	10	30	-44,2	0,5			-9,1	0,4	231,6	1,8
LA77B	#Azone5b-incl10	2 - green	V+LH2O	10,5	10	-43,8	0,3			-8,2	0,3	216,5	0,4
LA77B	#Azone5b-incl11	other	V+LH2O	12,5	30	-43,7	0,6			-8,1	0,6	grise	nd
LA77B	#Bzone4-incl1	2 - green	V+LH2O	25	10	-44,3	0,3			-8,3	0,2	cs	cs
LA77B	#Bzone4-incl2	2 - green	V+LH2O	18,5	15	-44,4	0,5			-8,5	0,1	cs	cs
LA77B	#Bzone4-incl3	2 - green	V+LH2O	12	10	-43,5	0,8			-8,0	0,7	cs	cs
LA77B	#Bzone4-incl4	1 - blue	V+LH2O	23	10	-45,4	0,3			-8,4	0,2	cs	cs
LA77B	#Bzone4-incl5	1 - blue	V+LH2O	8	15	-44,9	0,5			-9,2	0,5	cs	cs
LA77B	#Bzone4-incl6	other	V+LH2O	40	35	-42,6	0,3			-7,4	0,0	cs	cs
LA77B	#Bzone4-incl7	2 - green	V+LH2O	11,5	10	-46,0	0,9			-9,8	0,5	cs	cs
LA77B	#Bzone4-incl8	other	V+LH2O	28	20	-47,2	0,4			-10,5	0,3	cs	cs
LA77B	#Bzone4-incl9	2 - green	V+LH2O	12	15	-43,5	0,3			-7,8	0,2	cs	cs
LA77B	#Bzone4-incl10	1 - blue	V+LH2O	11,5	20	-44,4	0,7			-8,9	0,3	cs	cs
		Blue	***Average$_b$***	***13,6***	***15,0***	***-44,9***	***0,5***			***-9,2***	***0,5***	***226,7***	***0,8***
		Green	***Average$_g$***	***14,6***	***16,5***	***-44,8***	***0,6***			***-8,8***	***0,5***	***216,8***	***5,6***
			Average$_{tot}$:	***15,9***	***17,6***	***-44,8***	***0,5***			***-8,9***	***0,5***	***221,2***	***3,4***

Sample	name	FI	Type	size (um)	V%	Tff	sTff	Tm(hh)	sTfm	Tm	sTm	Th	sTh
LA95B	#Azone4-incl5	FIA1	V+LH2O	12	10	-42,4	1,3	nd	nd	-9,0	0,7	grise	nd
LA95B	#Azone4-incl6		V+LH2O	22,5	15	-40,5	0,3	nd	nd	-6,4	0,2	235,9	1,4
LA95B	#Azone4-incl7	FIA1	V+LH2O	22	10	-42,6	1,6	nd	nd	-7,7	0,6	239,4	18,2
LA95B	#Azone4-incl8	FIA1	V+LH2O	12,5	20	-43,8	0,3	nd	nd	-7,7	0,1	grise	nd
LA95B	#Azone4-incl9	FIA1	V+C02+H20?	17	10	-43,6	1,1	nd	nd	-8,2	0,8	247,2	1,4
LA95B	#Azone4-incl10		V+LH2O	8	25	-44,2	3,2	nd	nd	-10,7	1,9	211,2	2,6
LA95B	#Azone4-incl11	FIA1	V+LH2O	12,5	35	-44,3	1,1	nd	nd	-8,1	1,8	grise	nd
LA95B	#Bzone3-incl4		V+LH2O	13	20	-49,0	2,0	nd	nd	-12,7	0,5	nd	nd
LA95B	#Bzone3-incl8		V+LH2O	11,5	25	-49,2	0,4	nd	nd	-13,7	1,3	nd	nd
LA95B	#Bzone3-incl9	FIA1	V+LH2O	13	25	-48,2	0,4	nd	nd	-8,2	nd	nd	nd

Sample	name	FI	Type	Tff	sTff	Tm(hh)	sTfm	Tm	sTm	Th	sTh
LA56A	#Azone1-incl1	FIA2	V+LH2O	-41,5	0,2	-22,4	1,5	-5,4	0,0	219,0	2,7
LA56A	#Azone1-incl2	FIA2	V+LH2O	-50,8	0,9	-11,7	0,9	-4,5	0,1	169,3	13,8
LA56A	#Azone1-incl3	other	V+LH2O	-52,5	0,2	-25,1	1,5	-10,6	0,6	nd	nd
LA56A	#Azone1-incl4	FIA2	V+LH2O	-43,8	0,3	-20,1	2,2	-5,1	0,1	nd	nd
LA56A	#Azone1-incl5	FIA2	V+LH2O	-44,3	7,0	-23,9	1,2	-5,3	0,4	215,9	nd
LA56A	#Azone1-incl6	FIA2	V+LH2O	-54,6	0,4	-21,7	4,1	-4,3	0,8	nd	nd
				-47,0	**1,7**	**-19,9**	**2,0**	**-4,9**	**0,3**	nd	nd

Sample	name	FI	Type	Tff	sTff	Tm(hh)	sTfm	Tm	sTm	Th	sTh
LA153A	#Azone4-incl5		V+LH2O	-81,7	7,7	nd	nd	-13,3	0,4	299,6	14,4
LA153A	#Azone4-incl6	FIA3	V+LH2O	-71,0	1,4	-28,5	nd	-20,1	4,2	grise	nd
LA153A	#Azone4-incl7	FIA3	V+LH2O	-76,9	0,8	nd	nd	-25,1	2,7	182,1	15,2
LA153A	#Azone4-incl8	FIA3	V+LH2O	-94,1	1,0	nd	nd	-20,1	0,2	117,0	nd

Sample	name	FI	Type	Tff	sTff	Tm(hh)	sTfm	Tm	sTm	Th	sTh
LA83F	#Azone5-incl1	FIA4	V+LH2O+sels	-75,9	12,8	-34,6	1,4	-28,2	4,1	>300	nd
LA83F	#Azone5-incl2	FIA4	V+LH2O+sels	-67,2	8,9	-33,6	4,1	-30,3	nd	>300	nd
LA83F	#Azone5-incl3	FIA4	V+LH2O+sels	-69,9	17,5	-33,8	0,3	-29,7	nd	grise	nd
LA83F	#Azone5-incl4	FIA4	V+LH2O+sels	-74,5	0,7	-31,0	1,4	-17,8	1,8	282,2	11,5
LA83F	#Bzone6-incl1	FIA1	V+LH2O	-41,5	0,5	nd	nd	-9,0	0,2	nd	nd
LA83F	#Bzone6-incl2	FIA1	V+LH2O	-43,5	2,2	nd	nd	-9,5	0,1	nd	nd
LA83F	#Bzone6-incl3	FIA1	V+LH2O	-44,7	0,4	nd	nd	-9,1	0,9	nd	nd
LA83F	#Bzone6-incl4	FIA1	V+LH2O	-46,5	0,7	nd	nd	-7,2	1,4	nd	nd
LA83F	#Bzone6-incl5	FIA1	V+LH2O	-44,3	nd	nd	nd	-7,7	1,9	nd	nd
LA83F	#Bzone6-incl6	FIA1	V+LH2O	-45,9	0,8	nd	nd	-7,9	1,5	nd	nd

Sample	name	FI	Type	size (um)	V%	Tff	sTff	TmCO2	sTmCO2	Tmcl	sTmcl	ThCO2	sThCO2	Th	sTh
LA95B	#Azone4-incl1		V+C02+H20	14	25	-118,7	0,4	-65,2	0,2	7,5	0,2	26,7	0,7	nd	nd
LA95B	#Azone4-incl2		V+C02+H20	19	20	-118,9	0,1	-65,2	0,2	nd	nd	nd	nd	nd	nd
LA95B	#Azone4-incl3		V+C02+H20	22	10	nd	nd	nd	nd	nd	nd	nd	nd	>300	nd
LA95B	#Azone4-incl4		V+C02+H20	20	20	-118,4	nd	-65,1	0,1	8,3	0,8	nd	nd	>300	nd
LA95B	#Bzone3-incl1		V+C02+H20	15	60	-112,6	1,3	-63,6	0,4	nd	nd	13,3	0,4	nd	nd
LA95B	#Bzone3-incl2		V+C02	13	80	-111,5	1,1	-64,0	0,1	nd	nd	13,0	0,2	nd	nd
LA95B	#Bzone3-incl3		V+C02+H20	15	20	-112,9	1,6	-64,7	0,3	nd	nd	20,7	0,3	nd	nd
LA95B	#Bzone3-incl5		V+C02+H20	10,5	50	-112,9	0,3	-64,3	0,1	nd	nd	15,6	0,1	nd	nd
LA95B	#Bzone3-incl6		V+C02+H20	15	50	-112,9	0,3	-64,3	0,1	nd	nd	15,6	0,1	nd	nd
LA95B	#Bzone3-incl7		V+C02	14	100	-109,3	0,6	-63,8	0,2	nd	nd	7,8	0,1	nd	nd

Sample	name	FI	Type	Tff	sTff	TmCO2	sTmCO2	Tmcl	sTmcl	ThCO2	sThCO2	Th	sTh
LA153A	#Azone4-incl1		V+C02+H20	-110,8	4,9	-65,7	0,2	5,0	nd	28,2	0,6	grise	nd
LA153A	#Azone4-incl2		V+C02+H20	-115,2	0,7	-66,4	1,4	nd	nd	28,2	0,5	grise	nd
LA153A	#Azone4-incl3		V+C02+H20	-111,4	0,7	-65,7	0,2	nd	nd	28,1	0,5	grise	nd
LA153A	#Azone4-incl4		V+C02+H20	-115,0	0,6	-65,9	0,5	6,4	nd	28,3	0,1	grise	nd
LA153A	#Bzone2-incl1		V+C02+H20	-120,9	0,5	-66,8	0,1	8,0	0,3	34,3	1,0	294,7	4,0
LA153A	#Bzone2-incl2		V+C02+H20	-121,4	0,3	-66,9	0,3	7,9	0,1	34,4	1,0	310,9	0,7
LA153A	#Bzone2-incl3		V+C02+H20	-120,1	1,8	-66,7	nd	7,8	nd	33,6	0,1	304,8	9,4
LA153A	#Bzone2-incl4		V+C02+H20	-119,2	0,9	-67,1	0,2	7,9	0,1	33,4	1,1	264,0	45,3
LA153A	#Bzone2-incl5		V+C02+H20	-120,3	0,7	-67,1	0,1	8,0	0,4	nd	nd	grise	nd

Sample	name	FI	Type	Tff	sTff	TmCO2	sTmCO2	Tmcl	sTmcl	ThCO2	sThCO2	Th	sTh
LA83F	#Bzone6-incl6vide		C02(+V?)	-112,1	1,0	-67,3	0,5	nd	nd	12,1	0,3	nd	nd
LA83F	#Bzone6-incl7		C02(+V?)	-110,1	0,6	-67,3	0,5	nd	nd	9,9	0,4	nd	nd
LA83F	#Bzone6-incl8		C02(+V?)	-103,7	6,8	-67,5	0,2	nd	nd	11,5	0,2	nd	nd
LA83F	#Bzone6-incl9		C02(+V?)	-97,9	1,4	-67,3	0,3	nd	nd	11,2	0,3	nd	nd
LA83F	#Czone4-incl1		V+C02+H20	-114,6	0,9	-65,5	0,3	-15,3	5,8	31,3	1,1	>400	nd
LA83F	#Czone4-incl2		V+C02+H20	-94,9	0,8	-65,1	0,3	-15,6	14,2	31,9	0,1	>400	nd
LA83F	#Czone4-incl3		V+C02+H20	-116,0	0,5	-65,7	0,0	nd	nd	30,5	0,3	>400	nd
LA83F	#Czone4-incl4		V+C02+H20	-104,2	1,7	-66,2	0,0	-13,3	4,6	6,5	0,4	>400	nd

UNIVERSITÉ DE MONTPELLIER

UNIVERSITY OF JOHANNESBURG

CONVENTION
DE COTUTELLE INTERNATIONALE DE THESE

INTERNATIONAL JOINT DOCTORATE CONVENTION

Cette convention réglemente les relations entre :
L'Université de Montpellier, ci-après désignée "UM", représentée par son Président.
This convention regulates the relations between:
The Université de Montpellier hereafter referred to as "UM", represented by its President.

et

L'Université de Johannesburg, ci-après désignée "UJ" représentée par son vice-recteur
The University of Johannesburg, hereafter referred to as "UJ", represented by its Vice Chancellor.

pour la thèse préparée en cotutelle par:
for the international joint doctorate prepared by:

Mme Nom *Mrs Name* **TRAVERS**
Prénom / *First Name* : **Laurine**
née le /***born on*** 9 Mars / ***March, 1996*** à/*in* Valognes (France)
Nationalité /***Nationality:*** Française / ***French***
Ecole doctorale à Montpellier / *Doctoral School in Montpellier*: GAIA
Secteur de Formation/ ***Field of Research*** : Géologie, Sciences de la Terre / ***Geology, Earth Sciences***
Titre ou sujet de la thèse / ***Title or subject of the dissertation*** : Caractérisation et distribution de l'hydrothermalisme dans la ceinture de roches vertes de Barberton (Afrique du Sud) – Approche multi-échelle, implications sur les minéralisations aurifères et sur la géodynamique archéeenne. / ***Characterization and distribution of the hydrothermal event within the Barberton Greenstone Belt (South Africa) – Multi-scale approach and implications on gold mineralization formation and Archean geodynamics.***

L'UM et l'UJ sont ci-après désignées individuellement la « Partie » et collectivement les « Parties ».
The UM and the UJ are hereinafter referred to individually as "Party" and collectively as the "Parties".

pp

PREAMBULE
PREAMBLE

Pour la partie française :

- Vu le code de l'éducation
- Vu l'arrêté du 25 mai 2016 fixant le cadre national de la formation et les modalités conduisant à la délivrance du diplôme national de doctorat

For the French Party:

Considering the French code of Education
Considering the decree of the 25th of May 2016 setting out the national framework for doctoral education and the procedures leading to the award of the national PhD degree.

Pour la partie sud-africaine:

Considérant que l'Université de Johannesburg est une entité juridique établie en vertu de la loi 101 de 1997 (telle que modifiée),
Considérant le cadre politique pour l'internationalisation de l'enseignement supérieur (2019 tel que déterminé aux termes de l'article 3 de la loi de 1997 sur l'enseignement supérieur (loi 101 de 1997), telle que modifiée,
Considérant la politique de l'UJ sur les diplômes collaboratifs et de maîtrise et de doctorat avec les établissements d'enseignement supérieur partenaires et la politique relative aux diplômes supérieurs. L'échange de toute information personnelle concernant les personnes concernées, y compris les étudiants, se fera avec le consentement et conformément à toute législation sur la protection de la vie privée et des données, y compris, mais sans s'y limiter, le RGPD et la loi de 2013 sur la protection des informations personnelles.

For the South African Party:

Considering that the University of Johannesburg is a juristic entity established in terms of the Higher Education Act 101 of 1997 (as amended);
Considering the Policy Framework for Internationalisation of Higher Education (2019 as determined in terms of Section 3 of the Higher Education Act, 1997 (Act 101 of 1997) as amended ;
Considering the UJ Policy on Collaborative Masters and Doctoral Degrees with partner Higher Education Institutions (2013, amended 2018);
Considering the UJ Academic Regulations (2020, updated annually);
Considering the UJ Higher Degrees Policy (2009, amended 2016), and considering the exchange of any personal information regarding any data subjects, including students, will be with the consent and in accordance with the privacy and data protection legislation in South Africa and France, including but not limited to the GDPR and the Protection of Personal Information Act, 2013.

pp

IL EST CONVENU CE QUI SUIT :
IT IS AGREED AS FOLLOWS:

TITRE I : MODALITES ADMINISTRATIVES
SECTION I: ADMINISTRATIVE CLAUSES

Article 1 : Durée de la thèse
Article 1: Duration of the PhD dissertation

Afin de mettre en place une codirection, la demande en cotutelle est effectuée auprès des deux établissements la même année universitaire. Un délai courant éventuellement jusqu'au 30 avril de l'année d'inscription est autorisé à l'Université de Montpellier pour permettre au doctorant de finaliser sa codirection dans l'établissement partenaire.
In order to set up a real joint supervision, the registration for the international joint supervision of a PhD is done in the two contracting universities the same year. To give the candidate the possibility to finalize her joint supervision, the registration may be authorised until the 30th of April of the year of the registration at the University of Montpellier.

À l'Université de Montpellier, la première inscription en doctorat de Mme Laurine TRAVERS, spécialité : Géosciences est prise à compter de la rentrée universitaire 2020/2021.
At the University of Montpellier, the first enrolment of Mrs Laurine TRAVERS for a PhD, specialty: Geosciences is registered from the beginning of the French academic year 2020/2021.

A l'Université de Johannesburg, la première inscription en doctorat de Mme Laurine TRAVERS, spécialité : Géologie est prise à compter de janvier 2021.
At the University of Johannesburg, the first enrolment of Mrs Laurine TRAVERS for a PhD, specialty Geology is registered from January 2021.

La durée des travaux de recherche prévue est de trois (3) années universitaires consécutives à partir de cette première inscription.
En Afrique du Sud, la durée maximale autorisée pour l'achèvement d'une thèse est de quatre (4) ans.
The duration of the research studies should last three (3) consecutive academic years starting from the first enrolment.
In South Africa, the maximum duration permitted for completion of a doctoral study is four (4) years.

Le travail de recherche pourra être prolongé par un accord spécifique entre les deux établissements, sur proposition des deux directeurs de thèse et après avis du comité de suivi individuel et du directeur de l'école doctorale, sur demande motivée du doctorant. La réinscription en 4ème année de doctorat, devra faire l'objet d'une demande d'inscription dérogatoire auprès de l'Université de Montpellier.
Toute autre demande de prolongation annuelle pourrait être accordée à titre dérogatoire par le chef d'établissement sur demande motivée du doctorant.
The thesis may be extended by a specific agreement between both institutions by the proposal of both thesis supervisors and after the opinion of the individual monitoring committee and the director of the doctoral school, on request of the PhD student. For the enrollment in 4th year of doctorate or more, a derogatory application for registration will be mandatory at the University of Montpellier.
Any other request for an annual extension may be granted as an exception by the head of the institution upon request from the doctoral student.

pp

À l'Université de Johannesburg, les prolongations des périodes stipulées ci-dessus nécessitent une recommandation des co-superviseurs et du chef de département ainsi que l'approbation du comité des diplômes supérieurs de la faculté et du doyen exécutif. Les prolongations ne seront accordées que dans des circonstances exceptionnelles et seront en général limitées à 24 mois pour un doctorat.
At the University of Johannesburg, extensions to the periods stipulated above require a recommendation by the co-supervisors and HoD (Head of Department) and approval by the Faculty Higher Degrees Committee and Executive Dean. Extensions will only be granted in exceptional circumstances and will in general be limited to 24 months for a doctoral study.

Pour chaque année supplémentaire, une demande d'inscription dérogatoire sera obligatoire à l'Université de Montpellier.
For each additional year, a derogatory application for registration will be mandatory at the University of Montpellier.

Sous réserve d'une approbation dans des circonstances exceptionnelles, l'étudiant est tenu de s'inscrire simultanément à l'Université de Johannesburg pour chaque année supplémentaire. Des frais d'inscription pour les années supplémentaires peuvent être appliqués dans les cas où la durée totale dépasse le nombre maximal d'années autorisé (quatre ans).
Subject to approval in exceptional circumstances, the student is required to register concurrently at the University of Johannesburg for each additional year. Registration fees for additional years may be applied in cases where the total duration exceeds the maximum allowable number of years (four years).

La thèse est préparée par périodes alternées d'un an dans chacun des deux laboratoires d'accueil selon un équilibre de séjour désigné ci-dessous :

1 - Septembre 2020 - Septembre 2021 : Université de Montpellier
2 - Octobre 2021 - Septembre 2022 : Université de Johannesburg
3 - Octobre 2022 - Septembre 2023 : Université de Montpellier
4 - Octobre 2023 - Septembre 2024 : Université de Johannesburg

Le présent Accord prendra effet à la date de sa signature par les deux parties et restera en vigueur pendant une période initiale de trois ans.

The dissertation will be prepared in alternate periods of one year spent in each of the two designated laboratories according to the balance as follows :

1 - September 2020 - September 2021: University of Montpellier
2 - October 2021 – September 2022: University of Johannesburg
3 - October 2022 – September 2023: University of Montpellier
4 - October 2023 – September 2024: University of Johannesburg

This Agreement will commence on the beginning of the academic year 2020-2021 and shall remain in force for a period of four years.

La résiliation peut avoir lieu conformément à la clause de résiliation évoqué dans l'article 1 du Titre IV.
Termination may take place in accordance with the Termination clause mentioned in the article 1 – section IV.

pp

Article 2 : Inscription
Article 2: Registration

La doctorante s'inscrit administrativement dans les deux établissements partenaires pour chaque année de préparation de la thèse. Elle règle le montant annuel des droits de scolarité dans un seul des établissements. L'établissement partenaire l'exonère de droits de scolarité.
The PhD student should register administratively in the two partner institutions for each year of the preparation of her dissertation. She pays the annual tuition fees in one of the institutions only. The other contracting university waives its fees.

Année universitaire Academic year	**Paiement des droits de scolarité Registrations fees paid to**
2020/2021	Université de Montpellier
2021/2022	University of Johannesburg
2022/2023	Université de Montpellier
2023/2024	University of Johannesburg

Article 3 : Couverture sociale, assurances, hébergement et aides financières
Article 3: Social insurances, lodging and financial ressources

A son arrivée dans l'université partenaire, la doctorante devra justifier être couverte par une assurance santé (carte européenne d'assurance maladie pour les citoyens EU, ou une autre attestation d'assurance équivalente pour les citoyens extra-communautaires).
En complément, la doctorante devra être en mesure de présenter une attestation d'assurance responsabilité civile.
The PhD student, at the beginning of the activities at the Partner University, will prove to be in possession of health insurance (the European Health Insurance Card for EU citizens, or another equivalent insurance certification for non-EU citizens).
In addition, the student may also be required to sign of a liability insurance policy.

Le doctorant doit également disposer de moyens financiers suffisants pour financer ses périodes de recherche en France (cas du doctorant étranger) ou à l'étranger (cas du doctorant français).
The PhD student must also have sufficient financial means to finance his/her research periods in France (in the case of foreign PhD students) or abroad (in the case of French PhD students).

Organisme financeur	Université de Montpellier
Programme de financement	Contrat doctoral
Date de début – date de fin	Du 01/10/2020 au 30/09/2023
Montant mensuel	1768.55€
Statut BGF / BGE	non

Funding Body	***University of Montpellier***
Funding Programme	***PhD contract***
Start - end	***From 01/10/2020 to 30/09/2023***
Monthly amount	***1768.55€***
BGF / BGE status	***no***

A l'Université de Montpellier, la doctorante doit se conformer aux règles en vigueur définies par la convention individuelle de formation, la charte du doctorat et de son école doctorale.
A l'Université de Johannesburg le doctorant doit se conformer aux règles en vigueur du département de Géologie et de l'Université de Johannesburg en général.

pp

At the University of Montpellier, the PhD student must comply with the rules defined by the individual training agreement, the doctoral charter and his/her doctoral school.
At the University of Johannesburg, the PhD student must comply with the rules applicable of the Department of Geology and the University of Johannesburg generally.

La doctorante sera chargée de prendre les dispositions nécessaires pour satisfaire aux exigences en matière d'immigration (par exemple, un permis d'études). L'université d'accueil s'engage à apporter son aide, si nécessaire, pour la demande de visas. Les exigences d'immigration pour les visas étudiant en Afrique du Sud exigent que l'étudiant soit enregistré auprès d'une assurance maladie sud-africaine. La couverture médicale doit être enregistrée auprès du Council for Medical Aid Schemes (CMS) https://www.medicalschemes.com/MedicalSchemes.aspx.
The PhD student will be responsible for arranging the necessary relevant immigration requirements (e.g. a study permit). The host university agrees to assist where necessary with the application of visas. Immigration requirements for student visas in South Africa requires that the student be registered with a South African medical aid provider. The medical aid cover must be registered in terms of the Council for Medical Aid Schemes (CMS) https://www.medicalschemes.com/MedicalSchemes.aspx.

Le doctorant est responsable des frais d'hébergement, de voyages internationaux et locaux dans le pays d'accueil, des livres, de l'équipement, de l'assurance maladie et des autres dépenses découlant du diplôme conjoint
The PhD student is responsible for costs of accommodation, international and local travel in host country, books, equipment, health insurance and other expenses arising out of the joint degree.

Article 4 : Règlements applicables
Article 4: Applicable regulations

Le doctorant devra respecter le règlement intérieur ainsi que toutes les règles générales ou particulières d'hygiène et de sécurité en vigueur sur le lieu d'accueil. Le doctorant sera soumis à l'autorité hiérarchique du responsable du laboratoire d'accueil.
The PhD student will have to respect the internal regulations and all general or specific health and safety regulations applicable at the host institution. The PhD student will be subject to the hierarchical authority of the host laboratory manager.

TITRE II : MODALITES PEDAGOGIQUES
SECTION II: ACADEMIC CLAUSES

Article 1 : Directeurs de thèse
Article 1 : Thesis supervisors

	Université de Montpellier	University of Johannesburg
Unité / Unit	Géosciences Montpellier	Department of Geology
Directeur d'Unité / Director of Department	Benoit IIDEFONSE	Michiel DE KOCK
Directeur de thèse / Thesis Supervisor	Alain CHAUVET	Jérémie LEHMANN

Les deux directeurs de thèse s'engagent à exercer pleinement leurs fonctions d'encadrement en collaboration l'un avec l'autre (art.16, art. 22 de l'arrêté du 25 mai 2016).

pp

Both supervisors undertake to fully exercise of their supervisory functions in collaboration with each other (art.16, art. 22 of the decree of the 25 of may 2016).

Un descriptif (de 1-2 pages) de la thèse est joint en Annexe 1 « Descriptif détaillé de la thèse ».
A detailed description of the thesis (1-2 pages) is given in Annex 1 "Detailed description of the thesis".

Article 2 : Modus operandi de la soutenance de thèse
Article 2: Modus operandi for the defense of the thesis

La thèse donne lieu à une soutenance unique reconnue par les deux universités.
The thesis is subjected to a single defense presentation recognized by both universities.

Lieu de soutenance de la thèse (université / ville / pays) ***Place of the thesis defense (university / city / country)***	Université de Montpellier, Montpellier, France
Langue dans laquelle la thèse est rédigée et soutenue ***Language in which the thesis is written and defended***	Anglais English
Langue du résumé oral et écrit ***Language of the written oral summary***	Français et anglais French and English

En France, conformément à l'article 17 de l'arrêté du 25 mai 2016, la soutenance n'a lieu qu'après avis favorable des rapporteurs.
In France, according to the article 17 of the decree of May 25, 2016, the presentation will take place after a positive notification by the referees.

Rapporteurs:
Referees:
Les rapporteurs sont des personnes extérieures aux universités partenaires et à leurs écoles doctorales. Ils doivent être au nombre de deux au moins, et sont désignés conjointement par les universités.
En Afrique du Sud, les rapporteurs (examinateurs externes) doivent être au moins trois.
The referees should not belong to the two partner universities and to their doctoral schools. At least, two referees should be jointly proposed by the universities.
In South Africa, the referees (external examiners) must be at least three.

Membres du jury:
Members of the jury:
Les présidents des deux universités désignent conjointement les membres du jury à répartition égale entre les deux établissements.

En France, conformément à l'article 18 de l'arrêté du 25 mai 2016 relatif à la formation doctorale, le nombre des membres du jury est compris entre 4 et 8.
La moitié, au moins, des membres du jury doit être composée de Professeurs ou assimilés.
Le jury comprend au moins deux membres extérieurs aux Établissements et aux Écoles Doctorales d'inscription du doctorant.

A l'Université de Johannesburg, le processus d'examen doit inclure au moins 3 examinateurs externes qui fournissent un rapport écrit et un avis relatif à l'attribution du diplôme. Le résultat positif des rapports écrits constituera les conditions d'obtention du diplôme de l'Université de Johannesburg. Quand le consensus concernant l'attribution du diplôme est établi, deux des trois examinateurs de l'UJ seront invités au jury conjoint.

pp

Par conséquent, le jury devra inclure au moins 2 membres extérieurs aux Établissements et aux Écoles Doctorales d'inscription du doctorant.
NB : Les directeurs de thèse participent au jury mais ne prennent pas part à la décision.

Les membres du jury désignent parmi eux un président et le cas échéant, un rapporteur de soutenance. Le président doit être un professeur ou assimilé ou un enseignant de rang équivalent au sens de l'alinéa précédent. Les directeurs de thèse ne peuvent être choisis comme président du jury.

En France, conformément à l'article 19 de l'arrêté du 25 mai 2016, l'admission ou l'ajournement est prononcé à l'issue des délibérations des membres du jury.

The presidents of the two universities shall appoint the members of the jury, equally between the two institutions.

In France, according to the article 18 of the decree of the 25th of May 2016 relative to the doctoral studies, the jury must be composed of a minimum of 4 members and a maximum of 8 members.
At least, half of the members of the jury should be Professors or equivalent positions.
The jury should be composed at least two evaluators external to the partner universities and doctoral schools where the candidate is registered.

At the University of Johannesburg, the examination process must include at least 3 external examinators who provide a written report and recommendation on awarding the degree. The positive outcome of the written reports will be constitute the requirements of fulfilment of the degree awarding requirements at the University of Johannesburg. When a consensus on the awarding of the degree is reached, two out of the three examiners at UJ will be invited to the joint jury.
Therefore, the jury will be composed at least of a minimum of 2 evaluators external to the partner universities and doctoral schools where the candidate is registered.
NB: Thesis supervisors participate in the jury but cannot take part in the decision.

The jury members will appoint a chairperson and, where applicable, a secretary. The chairperson must be a professor or equivalent rank as detailed in the previous paragraph. Thesis supervisors cannot be designated as the chairperson of the jury.

In France, according to the article 19 of the decree of 25th of May 2016, admission or adjournment is pronounced after the deliberations of the jury members.

Article 3 : Délivrance des diplômes
Article 3: Awarding of diplomas

Les deux établissements décident que le diplôme de docteur sera délivré par chaque université sur proposition conforme du jury.
The two universities decide that the doctoral degree is awarded by each university based on the recommendation of the jury.

Sur le diplôme français, figurent la spécialité doctorale, le nom de l'école doctorale, le titre de la thèse, ainsi que les noms et titres des membres du jury et l'indication d'une cotutelle internationale de thèse. Le nom de l'University of Johannesburg sera traduit en français sur le diplôme français. Il sera donc écrit « Université de Johannesbourg » sur le diplôme français.
On the French diploma, the doctoral specialty, the name of the doctoral school, the title of the thesis, as well as the names and titles of the jury members and the indication of

pp

an international co-supervision of the thesis will be indicated. The name of the University of Johannesburg will be translated in French on the French diploma. So, it will be written "Université de Johannesbourg" on the French diploma.

Pour le diplôme sud-africain, figurent une indication de spécialité ou de discipline, le titre de la thèse ou l'intitulé des principaux travaux, la mention de la cotutelle internationale, les noms et titres des membres du jury et la date de soutenance les signatures originales du vice-chancelier et du registraire (ou équivalent).
For the South African diploma, an indication of the specialty or the discipline, the title of the dissertation or the heading of principal studies, the mention of the international joint supervision of PhD dissertation, the names and titles of the jury members, the date of graduation and the original signatures of both the Vice-Chancellor and Registrar (or equivalent) will be indicated on the South African diploma.

Article 4 : Modalités de dépôt, signalement, de diffusion et d'archivage des thèses
Article 4: Registration, signaling, reproduction of the dissertation:

Pour la France, les modalités de dépôt, signalement, de diffusion et d'archivages des thèses sont régies par l'arrêté du 25 mai 2016.
For France, the modalities of registration, announcement, publication, diffusion and archives of the dissertation are regulated by the decree of the 25th of May 2016.

Pour l'Afrique du Sud, les modalités de dépôt, signalement, de diffusion et d'archivages des thèses sont régies par la Politique et l'Administration des diplômes supérieurs et administration des diplômes supérieurs.
For South Africa, the modalities of submission, announcement, publication and archives of the dissertation are regulated by Higher Degrees Policy and Higher Degrees Administration.

TITRE III : PROPRIETE INTELLECTUELLE – CONFIDENTIALITE – PUBLICATIONS
SECTION III: INTELLECTUAL PROPERTY - CONFIDENTIALITY - PUBLICATIONS

Article 1 : Propriété intellectuelle
Article 1: Intellectual Property

Connaissances Propres : ce terme désigne les informations et connaissances techniques et/ou scientifiques et/ou tout autre type d'informations, sous quelque forme qu'elles soient, brevetables ou non et/ou brevetées ou non, ainsi que tous les droits y afférents, appartenant à une Partie ou détenue par elle avant la date d'entrée en vigueur du Contrat et/ou développées ou acquises par elle en dehors de l'objet de thèse.
Own Knowledge: this term refers to the technical and / or scientific information and / or any other type of information, in whatsoever form, patentable and / or patented or not, as well as all related rights, owned by a Party before the date on which the contract comes into force and / or developed or acquired by this Party outside the thesis.

Les Connaissances Propres des Parties restent leurs propriétés respectives.
Une Partie ne reçoit aucun droit sur les Connaissances Propres de l'autre Partie du fait du contrat.
The Parties Own Knowledge shall remain their exclusive property.
The other Party shall receive no rights, under this agreement, over the own knowledge of the other party.

Chaque université accorde à l'autre une licence gratuite, non exclusive et non transférable pour l'utilisation de ses propres connaissances (à l'exclusion du droit d'accorder des sous-licences) à des fins non commerciales, et dans la mesure où cette licence est strictement requise par cette autre partie pour remplir toute obligation qu'elle pourrait avoir en relation avec les études et pour aider, superviser, guider et permettre la conduite des études par l'étudiant.
Both universities respectively each grant to the other, a free of charge, non-exclusive and non-transferable licence to use its Own Knowledge, (excluding the right to grant sub-licenses), for non-commercial purposes, and to the extent that such licence is strictly required by such other party to perform any obligation it may have in relation to the Studies and to assist, supervise, guide and enable the conduct of the Studies by the Student.

Résultats : ce terme désigne toutes les informations et connaissances techniques et/ou scientifiques, brevetées ou non, brevetables ou non, y compris les savoir-faire, les plans, schémas, dessins, formules ou tout autre type d'information, sous quelque forme qu'elle soit, et tous les droits y afférents, développées dans le cadre de la thèse.
Results: this term refers to all technical and / or scientific information and knowledge, patented or not, patentable or not, including know-how, plans, diagrams, drawings, formulas or any other type of information, in whatsoever form, and all related rights, developed during the thesis.

A défaut d'accord complémentaire spécifique conclu entre les Parties, les dispositions suivantes s'appliqueront aux Résultats.
Unless otherwise agreed in a specific agreement concluded by the Parties, the following provisions shall apply to the Results.

Les Résultats sont répartis entre les Parties, proportionnellement à leurs contributions matérielles, financières et humaines. A cet effet, chaque Partie s'engage à fournir ses meilleurs efforts pour obtenir de son personnel et/ou toute autre personne susceptible d'intervenir dans le projet de thèse pour son compte, et en particulier le doctorant, l'ensemble des cessions nécessaires à donner plein effet aux obligations qui lui incombent au titre de la présente convention et à garantir l'autre Partie la plénitude de ses droits de propriété intellectuelle sur les Résultats.
The Results are shared between the Parties in proportion to their material, financial and human contributions. To this extent, each Party commits to obtain from its staff and/or anyone else who may get involved in the thesis project on its behalf, notably the PhD student, all the rights necessary to give full effect to its obligations under the present agreement and to ensure that the other Party can fully enjoy its intellectual property rights over the Results.

Article 2 : Exploitation
Article 2: Exploitation

Chaque Partie peut utiliser librement et gratuitement les Résultats pour ses besoins propres de recherche et dans le cadre de collaborations de recherche avec des tiers, à l'exclusion de toute utilisation, directe et/ou indirecte, à des fins industrielles et/ou commerciales.

Les Parties copropriétaires des Résultats précisent leurs modalités d'exploitation dans le cadre d'un accord de valorisation avant toute exploitation industrielle et commerciale et/ou, dans l'hypothèse de brevets nouveaux.

Each Party can freely and free of charge, use the Results for its own internal research needs and within the framework of research collaborations with third parties, excluding any direct and/or indirect commercial and/or industrial use.

pp

The co-owners of Results shall specify their operating conditions in a joint ownership agreement prior to any industrial and/or commercial use or in the case of new patents.

Article 3 : Confidentialité
Article 3: Confidentiality

Dans le cadre de la convention, les informations (données, documents, méthodes, savoir-faire, etc.), leur objet, leur support, leur mode de transmission, leur origine, qu'elles soient protégées ou non par un titre ou un droit de propriété intellectuelle, communiquées pendant la durée de la convention entre les Parties sont des informations confidentielles (ci-après désignées les « Informations Confidentielles »).

Les Parties s'engagent expressément pendant la durée de la convention et pendant un délai de cinq (5) ans à compter de l'échéance ou de la résiliation anticipée de la convention, à ce que les Informations Confidentielles :
a) soient gardées strictement confidentielles et soient traitées avec le même degré de protection qu'elles accordent à leurs propres Informations Confidentielles ;
b) soient gardées dans un lieu sécurisé et non accessible à tous ;
c) ne soient communiquées qu'aux seuls membres de leur personnel ayant à les connaître et pour qui la divulgation est essentielle à la réalisation des objectifs poursuivis par les Parties. A ce titre, les Parties s'engagent à prendre toutes mesures raisonnables auprès de ceux-ci pour garantir le respect de la convention ;
d) ne soient communiquées qu'aux tiers (sous-traitants, filiales ou autres) ayant à les connaître et après autorisation écrite de la Partie qui les a communiquées. Les Parties s'engagent à faire signer aux tiers ayant accès aux Informations Confidentielles, un accord de confidentialité reprenant les stipulations de la convention;
e) ne soient utilisées qu'aux seules fins d'exécution de la convention, toute autre utilisation des Informations Confidentielles impliquant le consentement préalable et écrit de la Partie qui les a communiquées ;
f) ne soient copiées qu'après l'autorisation préalable et écrite de la Partie qui les a communiquées ;
g) ne soient pas publiées sans le consentement des deux parties

Pursuant to this agreement, any information (data, documents, methods, know-how, etc.), their purpose, support, mode of transmission, origin, protected or not by an intellectual property right, which are disclosed between the parties during the period covered by this agreement, are considered to be confidential information (hereinafter referred to as the « Confidential Information »).

The Parties explicitly undertake to ensure that, for the entire duration of the agreement and for the further five (5) years following its expiry, any Confidential Information :
a) is kept strictly confidential and are treated with the same high standards of confidentiality as their own confidential information
b) is kept in a secure space with a restricted access
c) is only disclosed to staff members who need to know the information and from whom the disclosure is strictly necessary to achieve goals pursued by the Parties. As such, the parties commit to take any reasonable measures regarding the staff concerned to ensure compliance with the agreement.
d) is only provided to third parties (subcontractors, subsidiaries or others) which have to be familiar therewith and subject to a written agreement of the disclosing Party. The Parties undertake to sign a non-disclosure agreement based on the terms of this agreement with the third parties with access to confidential information.
e) is used for the sole purpose of performing the agreement. Any other use of Confidential Information imply the prior written consent of the disclosing Party
f) is reproduced only after prior written consent of the disclosing Party

pp

g) is not published without the consent of both parties.

Exceptions

Ne sont pas considérées comme des Informations Confidentielles, les informations dont les Parties peuvent apporter la preuve :

- qu'elles étaient disponibles publiquement en l'absence de toute faute qui leur soit imputable ;
- qu'elles ont été reçues d'un tiers de manière licite ;
- qu'elles étaient déjà en sa possession avant la conclusion de la convention ;
- qu'elles ont été développées de manière indépendante et de bonne foi par des membres de leur personnel n'ayant pas eu accès à ces Informations Confidentielles ;
- qu'elles ont été divulguées en vertu d'une décision judiciaire ;
- qu'elles ont été divulguées par la Partie dont elles émanent ;
- qu'elles ont été utilisées ou divulguées avec l'autorisation écrite de la Partie dont elles émanent.

Toute autre communication ou utilisation des Informations Confidentielles transmises exige le consentement écrit et préalable de la Partie qui les a divulguées.

Le présent article ne pourra pas faire obstacle à la soutenance de la thèse du doctorant, cette soutenance devant être organisée chaque fois de façon à garantir, tout en respectant la réglementation universitaire en vigueur, la confidentialité de certains Résultats.

Information is not considered to be confidential when the parties can prove that this information:

- was publicly available in the absence of fault of their own;
- had been lawfully received from a third party;
- was already in its possession before the execution of the agreement;
- had been developed independently and in good faith by its employees without prior access to information of the other Party;
- had been communicated according to a court decision;
- was published by the disclosing Party;
- had been used or disclosed with a written consent of the disclosing Party;

Any other use or disclosure of the Confidential Information requires the prior written consent of the Party who make disclosures.

The present article shall not prevent the thesis defence of the PhD student. This thesis defence should be organised in compliance with the academic regulations and the confidentiality rules about the Results.

Article 4 : Publications
Article 4 : Publications

Chaque Partie s'engage à ne pas publier, de quelque façon que ce soit, les Connaissances Propres des autres Parties, sauf autorisation préalable et écrite.
Each Party commits to not publish, in any way whatsoever, the Own Knowledge of the other Parties, unless prior written permission.

pp

Tout projet de publication ou communication d'information relative au Projet ou aux Résultats par l'une des Parties, devra recevoir, pendant la durée de l'Accord et les deux (2) ans qui suivent son expiration ou sa résiliation, l'accord préalable écrit des Parties.

Any proposition of publication or communication about information relating to the Project or the Results during the term of the Agreement and within two (2) years following its expiry or termination must receive the written agreement of each Party beforehand.

Les Parties feront connaître leur décision dans un délai maximum d'un (1) mois à compter de la date de notification de la demande, cette décision pouvant consister : (i) à accepter sans réserve le projet de communication et/ou de publication ; (ii) à demander des modifications, en particulier si certaines informations contenues dans le projet sont de nature à porter préjudice à l'exploitation industrielle et commerciale des Connaissances Antérieures et/ou des Résultats. De telles suppressions ou modifications ne devront pas porter atteinte à la valeur scientifique de la publication ; (iii) à demander à ce que la publication ou communication soit différée si des causes réelles et sérieuses lui paraissent l'exiger, en particulier si des informations contenues dans le projet de publication ou de communication doivent faire l'objet d'une protection au titre de la propriété industrielle.
En l'absence de réponse d'une Partie à l'issue de ce délai, l'accord de cette Partie sera réputé acquis.

The Parties will notify their decision within a maximum of one (1) month from the date of the request notification, which may involve: (i) accepting without reservation the draft of the communication and / or publication; (ii) asking for changes, in particular if some information in the project may damage the industrial and commercial utilization of the Prior Knowledge and / or Results. Such deletions or modifications shall not affect the scientific value of the publication; (iii) request to postpone the publication or communication if there are real and serious causes to require it, in particular if there are some information in the publication or communication draft which require to be protected by virtue of the industrial property.
If one of the Party doesn't reply at the end of this deadline, its agreement would be taken for granted.

Si des informations contenues dans la publication ou communication doivent faire l'objet d'une protection au titre de la propriété industrielle, une des Parties pourra retarder la publication ou la communication pour une période maximale de dix-huit (18) mois à compter de la demande de publication ou communication de l'autre Partie.

If there are any information in the publication or the communication which are subject to industrial property protection, one of the Parties may delay the publication or communication for a maximum period of eighteen (18) months from the request for publication of the other Party.

Ces publications et/ou communications devront mentionner le concours apporté par chacune des Parties à la réalisation des activités de recherche.

Pour l'Université de Montpellier, la signature des publications sera libellée comme suit :

[Acronyme de l'unité ou libellé court], Univ Montpellier, [tutelle(s) principale(s)], [employeur si différent de(s) tutelle(s) principales], [ville de l'unité de recherche], France

Pour l'Université de Johannesburg, la signature des publications sera libellée comme suit :
Department of Geology, University of Johannesburg, Auckland Park, P.O. Box 524, Johannesburg 2006, South Africa.

pp

These publications and/or communications shall refer to the contribution made by each Party to the realization of research activities.

For the University of Montpellier, the signature of publications shall be worded as follows:

[Unit acronym or short name], Univ Montpellier, [main supervisor(s)], [employer if different from main supervisor(s)], [city of the research unit], France
For the University of Johannesburg, the signature of publications shall be worded as follows:

Department of Geology, University of Johannesburg, Auckland Park, P.O. Box 524, Johannesburg 2006, South Africa.

FORCE MAJEURE

Si l'une des parties est empêchée, en tout ou en partie, d'exercer l'un de ses devoirs, fonctions ou obligations au titre du présent accord, que ce soit de manière ponctuelle ou définitive, en raison d'un cas de force majeure (ce qui, aux fins des présentes, signifie toute épidémie, pandémie, guerre, émeutes politiques, troubles civils, insurrection, sabotage,), alors ce manquement ne constituera pas une violation au titre du présent document, et l'obligation d'exécution sera suspendue pendant la durée de cette prévention, à condition que la partie concernée fasse tout son possible pour réduire au minimum tout retard occasionné par ce manquement.
If either party is prevented, whether in whole or in part, from performing any of its duties, functions or obligations under this agreement, whether timeously or at all, due to an act of God (which for the purposes hereof shall mean any epidemic, pandemic, war, political riots, civil commotions, insurrection, sabotage, legal prohibitions or restrictions), then such failure shall not constitute a breach under this document, and the obligation to perform shall be suspended to the extent and during the continuance of such prevention provided that the affected party shall use its best endeavours to minimise any delay occasioned thereby.

Malgré toute disposition contraire contenue ou implicite dans la présente clause, si un tel retard devait durer pendant une période de 3 (trois) mois ou plus, la partie lésée sera en droit, mais non dans l'obligation, d'annuler cet accord sur notification écrite à l'autre partie à cet effet et cette partie n'aura aucune réclamation contre la partie lésée à ce sujet.
Notwithstanding anything to the contrary contained or implied in this clause, should such delay endure for a period of 3 (three) months or more, then the aggrieved party shall be entitled, but not obliged, to cancel this agreement on written notice to the other party to such effect and that party shall not have any claim against the aggrieved party arising there from.

À tout moment, le meilleur intérêt de tous les membres du personnel et des étudiants sera de la plus haute importance. En cas de risques sanitaires identifiés ou d'apparition d'une épidémie ou d'une pandémie, les deux parties évalueront la situation et s'entendront sur la meilleure voie à suivre. Un tel événement de force majeure peut entraîner la suspension temporaire de tout programme d'échange. Une fois que les deux parties ont évalué les risques pertinents, une décision doit être prise pour renvoyer les étudiants ou le personnel en visite dans leur pays d'origine.
At all times the best interest of any staff and students will be of utmost importance. If there are any identified health risks or the breakout of an epidemic or pandemic, both Parties will evaluate the situation and will mutually agree on the best way forward. Such

a force majeure event may lead to the temporary suspension of any exchange programmes. After both Parties have evaluated any relevant risks, a decision must be made to send any visiting students or staff back to their home countries.

INDEMNITÉ ET LIMITATION DE LA RESPONSABILITÉ
INDEMNITY AND LIMITATION OF LIABILITY

Chaque partie défendra, indemnisera et dégagera l'autre partie de toutes pertes, réclamations, poursuites et dépenses de quelque nature et description que ce soit, y compris, sans limiter la généralité de ce qui précède, les pertes, réclamations, poursuites et dépenses résultant de ou liées à des dommages matériels, des blessures ou des décès subis par une ou plusieurs personnes, qui peuvent résulter du présent accord ou y être liés.
Each Party shall defend, indemnify and hold harmless the other Party from all losses, claims, suits and expenses of any kind and description, including, without limiting the generality of the foregoing, losses, claims, suits and expenses arising out of or in connection with property damage, injuries or death sustained by any person or persons whatsoever which may result from or arise in connection from this Agreement.

En aucun cas, l'une ou l'autre des parties ne peut être tenue responsable de tout dommage indirect ou consécutif découlant de l'exécution ou de la non-exécution du présent accord ou s'y rapportant.
Under no circumstances shall either Party be liable for any indirect or consequential damages arising out of or relating to its performance or failure to perform under this Agreement.

Aucune des parties n'excluent ou ne limite la responsabilité de l'autre partie en cas de décès, de dommages corporels causés par sa négligence avérée ou celle de ses employés, de fraude ou de vol commis par elle ou ses employés et de violation de l'une des dispositions du présent accord.
Neither Party excludes or limits liability to the other Party for death, personal injury caused by its proven negligence or that of its employees, for fraud or theft by it or its employees and for a breach of any of the provisions in this Agreement.

Rien dans cette clause (Indemnisation et limitation de responsabilité) ne sera considéré comme réduisant ou affectant de quelque manière que ce soit une obligation générale d'atténuer les pertes subies par une partie.
Nothing in this clause (Indemnity and Limitation of Liability) will be taken as in any way reducing or affecting a general duty to mitigate loss suffered by a Party.

TITRE IV : DIVERS / SECTION IV : MISCELLANEOUS

Article 1 : Résiliation
Article 1: Termination

1.1 Conditions de la résiliation
1.1 Conditions for termination

La convention peut être résiliée de plein droit par l'une des Parties en cas d'inexécution par l'une d'entre elles, d'une ou plusieurs des obligations contenues dans ses diverses clauses. Cette résiliation ne devient effective qu'au début de l'année universitaire suivante et uniquement si la Partie plaignante envoie une lettre recommandée avec accusé de réception exposant les motifs de la plainte, au moins six (6) mois avant le début de chaque année

universitaire, à moins que dans ce délai la Partie défaillante n'ait satisfait à ses obligations ou n'ait apporté la preuve d'un empêchement consécutif à un cas de force majeure.

L'exercice de cette faculté de résiliation ne dispense pas la Partie défaillante de remplir les obligations contractées jusqu'à la date de prise d'effet de la résiliation et ce, sous réserve des dommages éventuellement subis par la Partie plaignante du fait de la résiliation anticipée de la convention.

La convention est également résiliée de plein droit dans les cas suivants :
- en cas de soutenance anticipée de la thèse ;
- en cas d'avis défavorable des Directeurs de thèse, au vu des qualités insuffisantes des résultats scientifiques obtenus. Le cas échéant, les Parties pourront décider d'un commun accord de la suspension du salaire du doctorant, au vu des qualités insuffisantes des résultats scientifiques obtenus ;
- en cas d'interruption définitive ou de suspension de la thèse ;
- en cas de refus d'inscription
- en cas de démission du doctorant ;
- le cas échéant en cas de résiliation du contrat de travail du doctorant.

The Convention may be terminated by right by either Party in the event of non-respect of one or several obligations set out herein. The termination will only be effective from the beginning of the next academic year and only if the complaining Party filing a complaint notifies the other Party of the reasons for termination by recorded delivery letter at least six (6) months prior to the beginning of the following academic year further to the defaulting party not having met its obligations or having given proof that such default is due to circumstances beyond its control.

Early termination does not release the defaulting Party from its contracted obligations until the date of effect of termination, and this subject to any prejudice suffered by the applicant Institution arising from early termination of the Convention.

The Convention will also be terminated by right under the following circumstances:
- ***early defence of the Thesis***;
- ***in the event of an unfavourable opinion of PhD supervisors, given the insufficient quality of scientific results. If appropriate, the Parties may by mutual agreement of the suspension of the salary of the doctoral student, given the insufficient quality of scientific results;***
- ***definitive interruption or suspension of the Thesis;***
- ***resignation of the Doctoral Student;***
- ***in case of registration's refusal***
- ***termination of the Doctoral Student's contract of employment, where applicable.***

1.2 Effets de la résiliation
1.2 Effects of termination

Dans tous les cas d'expiration ou de résiliation anticipée de la convention, chaque Partie s'engage à restituer aux autres Parties, sur demande de ces dernières, tous les documents et divers matériels qu'elles lui auraient transmis, sans pouvoir en garder de reproduction.
In all cases of expiry or early termination of the Convention, each Party undertakes to return to the other Parties, upon request, any documents and materials which may have been communicated, without making or keeping any copies.

Article 2 : Intégralité de la Convention
Article 2: Entire Convention

La convention et ses annexes traduisent l'intégralité des engagements pris par les parties dans le cadre défini en préambule.
Elle annule et remplace la totalité des accords et documents, écrits et verbaux, établis et échangés au cours de la période de négociation.
Toutefois, son existence n'affectera pas les droits et obligations résultant de conventions conclues antérieurement entre les Parties et dont l'objet est distinct de celui du la convention ou bien complémentaire.
The present Convention and its Annexes represent the entire agreement made between the Parties within the framework given in the Preamble.
It supersedes any agreements and documents, written and verbal, drawn up and exchanged during the negotiation period.
However, its existence does not affect the rights and duties resulting from prior conventions signed between the Parties where the object is distinct from that of the present Convention.

Article 3 : Invalidité d'une clause
Article 3: Invalidity of a Clause

Si une ou plusieurs stipulations de la convention étaient tenues pour non valides ou déclarées telles en application d'un traité, d'une loi ou d'un règlement, ou encore à la suite d'une décision passée en force de chose jugée d'une juridiction compétente, les autres stipulations garderont toute leur portée et leur force obligatoire.
Les Parties pourront alors rédiger un avenant ayant pour objet le remplacement des stipulations invalides par des stipulations valides, en respectant dans la mesure du possible, l'accord de volonté existant entre les Parties au moment de la conclusion de la convention ainsi que l'objet et l'esprit de ce dernier.
If one or several conditions of the present Convention is found to be invalid or declared as such in application of a treaty, law or regulation, or further to a definitive judgement handed down by a competent jurisdiction, all the other terms and conditions will remain applicable and fully opposable.
The Parties will consequently draw up a rider to replace the invalid section with a valid section, respecting where possible the initial wishes, spirit and object expressed by the Parties upon the signature of the present Convention.

Article 4 : Droit applicable – Litiges
Article 4: Applicable Law - Litigation

La convention est soumise aux lois et règlements du pays du défendeur.

En cas de différend relatif à la validité, à l'interprétation, à l'exécution ou à la résiliation de la convention, les Parties s'obligent, préalablement à tout autre recours, à mettre en œuvre leurs meilleurs efforts afin de trouver une solution amiable.

En cas de désaccord persistant, tous les conflits entre les Parties concernant la présente convention ou n'importe laquelle de ses clauses, que les Parties ne pourraient pas régler à l'amiable, seront portés devant les Tribunaux compétents du pays du défendeur.

The Convention is subject to the applicable laws in the defending country.

In the event of dispute with regards to the validity, interpretation, execution or termination of the Convention, the Parties undertake, prior to any legal action, to make every effort to find an amiable solution.

pp

In the event of persistent disagreement, any dispute between the Parties relative to the present Convention or any of its clauses, which cannot be settled on an amiable basis, will be referred to arbitration in accordance with the rules and laws of the defending country.

Article 5 : Notifications

Toutes les notifications, communications, mises en demeure prévues par la convention seront réputées avoir été valablement délivrées si elles sont adressées aux adresses suivantes :

- Pour l'UM : Direction des Relations Internationales - 163 Rue Auguste Broussonnet, 34090 Montpellier, France

- Pour l'Université de Johannesburg : **Faculty of Science -** Auckland Park Kingsway Campus - Cnr Kingsway and University Road - Auckland Park 2092 / adresse postale : PO Box 524 - Auckland Park – 2006, South Africa

Any notifications, communications and orders given or served for the purposes of the present Convention will be deemed to have been validly issued if sent to the following addresses:

- ***For UM : Direction des Relations Internationales - 163 Rue Auguste Broussonnet, 34090 Montpellier, France***

- ***For the University of Johannesburg:***

  Physical Address:
  Faculty of Science
  Auckland Park Kingsway Campus
  Cnr Kingsway and University Road
  Auckland Park
  2092
  South Africa

  Post address
  PO Box 524
  Auckland Park
  2006
  South Africa

Contact Person:

Prof Jérémie Lehmann

Auckland Park Kingsway Campus, C1 Lab 408
Telephone: +27 (0)11 559 4717/+27(0)767307277
E-mail: jeremiel@uj.ac.za

Les conditions particulières, modifications et prolongations de la présente convention font l'objet d'avenants. Toute modification est soumise à la validation des deux établissements.
Les avenants établis sont signés par l'intéressé(e), les directeurs de thèse et les Présidents des universités.

pp

Whenever necessary, special details, modifications and extensions shall be regulated by specific amendments. Any modification has to be approved by the both institutions. The specific amendments must be established and signed by the PhD student, the co-supervisors of the dissertation and the Presidents of the two universities.

Fait en cinq exemplaires originaux, le ....08/09/22.....
Done in five originals on.....08/09/22....

Laurine Travers La doctorante / ***The PhD student***	
Université de Montpellier	University of Johannesburg
Alain Chauvet Le Directeur de thèse	Jeremie Lehmann The Thesis Supervisor
Philippe Augé Le Président	pp (Acting Vice-Chancellor & Registrar Professor Tshilidzi Marwala The Vice Chancellor

Annexe 1 : Descriptif détaillé de la thèse

Projet Doctoral
Géosciences Montpellier

Titre : Caractérisation et distribution de l'hydrothermalisme dans la ceinture de roches vertes de Barberton (Afrique du Sud) – Approche multi-échelle, implications sur les minéralisations aurifères et sur la géodynamique archéenne.
Mots clés : Géologie structurale et de terrain, Analyse texturale, Veines de quartz, Altération et minéralogie, magmatisme archéen, Analyse multi-échelle (télédétection – microscopie).

Présentation détaillée du projet doctoral
La ceinture de roches vertes de Barberton se localise au Sud-Est de l'Afrique du Sud, à l'Est du craton de Kaapvaal, et contient des gisements d'or de classe mondiale telles que les mines de Fairview, New Consort et de Sheba (e.g., Anhaeusser, 1976 ; Gloyn-Jones et Kisters, 2018)***(Figure)***. Le cadre magmatique, pétrologique et géochronologique est relativement bien connu (Anhaeusser et al., 1981 ; De Ronde and De Wit, 1994 ; Moyen et al., 2006) ainsi que la succession stratigraphique des unités mafiques et volcano-sédimentaires (e.g., Lowe and Byerly, 1999 ; Heubeck et al., 2013). Trois évènements majeurs, datés à 3.4 Ga (phase D1), 3.2 Ga (phase D2) et 3.1 Ga (phase D3), ont permis la construction de la ceinture (Dziggel et Kisters, 2018). Ces évènements sont surtout caractérisés par la mise en place d'importants volumes de magmas dont certains font partie des suites archéennes de type TTG. Située au cœur de ces massifs magmatiques, la ceinture de roche verte est affectée par des déformations plicatives et de nombreux chevauchements. Comme dans tous les domaines archéens, les taux de déformation et le métamorphisme restent faibles. Malgré tout, des conditions proches du faciès amphibolite ont été reconnues dans les roches magmatiques du secteur et attribué à la possible existence de zones de subduction (Moyen et al., 2006). Cependant, cette hypothèse reste encore discutée tout comme les conditions de formation et de déformation de la ceinture archéenne de Barberton.
De nombreuses manifestations hydrothermales sont représentées dans toutes les unités de la ceinture de roche verte (Figure). La majorité correspond à des indices aurifères et a été définie comme "minéralisations de type shear zone" (Metallogenic map, Council for Geoscience, 2000). Toutefois, aucune synthèse n'existe actuellement sur le mode de formation, le contrôle structural et les relations entre ces indices et les mines de plus grande importance. Ainsi, s'il semble acquis jusqu'alors que l'évènement aurifère soit postérieur aux trois évènements tectono-métamorphiques majeurs (D1, D2 et D3 ; Gloyn-Lones et Kisters, 2018), de nombreuses questions restent d'actualité comme :

- i) existe-t-il un lien entre l'évènement aurifère et l'un des évènements majeurs qui caractérisent le secteur et notamment avec un des évènements magmatiques fortement développés dans le secteur étudié ?
- ii) Quelle est la nature du contexte tectonique qui accompagne ces minéralisations, à savoir extension, compression, décrochement, transpression, autres... ? et est-ce que ce contexte est spécifique aux conditions de déformation archéenne ?
- iii) Quelles sont la distribution et l'ampleur de cet évènement à l'échelle de la ceinture de Barberton ?

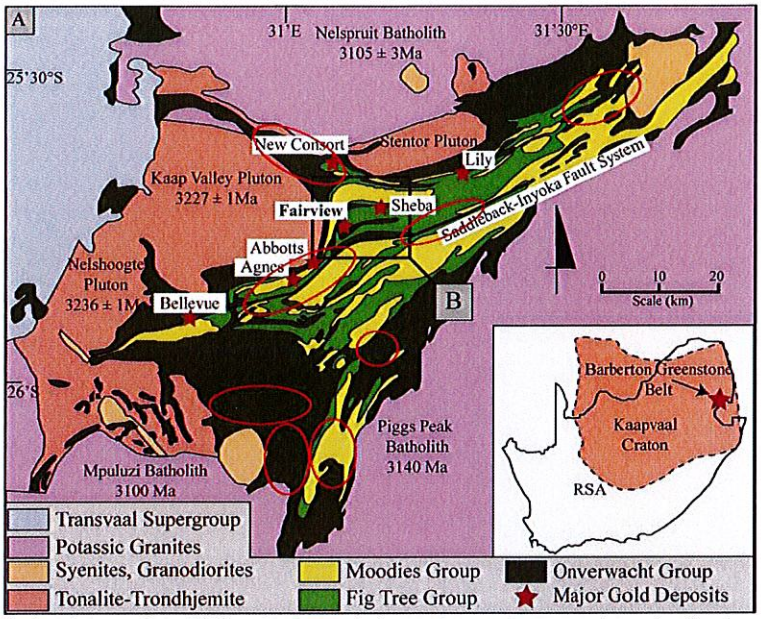

Figure : Carte géologique simplifiée de la ceinture de roches vertes de Barberton montrant la localisation des principales manifestations hydrothermales aurifères (étoiles et cercles rouges, modifié d'après Gloyn et Kisters, 2018)

Les objectifs de ce projet doctoral sont d'apporter des éléments de réponse à ces questions fondamentales et notamment de mieux comprendre les processus d'enrichissement en métaux des ceintures de roches vertes. L'originalité de ce travail sera de proposer une approche multi-échelle des caractérisations hydrothermales depuis la télédétection, l'analyse de terrain, l'échantillon, la lame mince et jusqu'à l'analyse en microscopie électronique à balayage. Dans l'ordre chronologique, les méthodes mises en œuvre seront :

- Etude de terrain combinant à la fois l'analyse structurale, microstructurale, pétrologique, et cartographique à la fois sur les objets cibles (veines de quartz), leur encaissant et les massifs granito-gneissique associés ;
- Echantillonnage précis afin de réaliser une analyse pétro-structurale complémentaire et de bien définir les relations entre minéraux, structures et altération ;
- En complément et à partir de l'étude des altérations (étape précédente), analyse en télédétection à partir des images ASTER afin de caractériser les auréoles d'altération. Pour cette étude, les images seront sélectionnées et traitées en fonction des réflectances nécessaires à la caractérisation des minéraux des altérations identifiés sur le terrain et en lames minces.
- Complément d'analyse des systèmes minéralisés par analyse à la microsonde électronique, MEB, microthermométrie des inclusions fluides et EBSD des objets hydrothermaux. Ces analyses seront déterminantes dans la caractérisation du système hydrothermal (nature des fluides, conditions de mise en place, conditions de cristallisation, etc...) ;
- Etablissement d'un modèle complet de formation du système hydrothermal de la ceinture de Barberton avec prise en compte des contraintes "imagerie satellite", structurales, microtectoniques, minéralogiques et fluides. Ce modèle sera confronté aux grandes idées sur les conditions de déformation et de transfert de fluide à l'Archéen.

En fonction des résultats, deux axes complémentaires pourront également être abordés :

- Analyse prédictive statistique en complément de l'imagerie satellitaire (coll. Univ. Orléans et BRGM) ;

- Modélisation numérique du transfert de fluide dans une croûte continentale chaude (Modélisation COMSOL, coll. Diane Arcay, GM-LIA ou Yannick Branquet, ISTO).

L'étude sera concentrée sur l'exemple de Barberton même si, en fonction de l'avancement du travail, des comparaisons pourront être réalisées avec l'exemple remarquable de l'Abitibi (Canada) pour lequel des contacts sont déjà établis ou bien avec des ceintures de roches vertes du Zimbabwe. Une éventuelle confrontation/comparaison avec les données des principales mines d'or de Barberton en exploitation est également envisagée dans la mesure du possible.

Références citées

Anhaeusser, C.R., 1976a. The nature and distribution of Archaean gold mineralization in Southern Africa. Miner. Sci. Eng. 8, 46–84.

Anhaeusser, C.R., Robb, L.J., Viljoen, M.J., 1981. Provisional Geological Map of the Barberton Greenstone Belt and Surrounding Terrane, Eastern Transvaal and Swaziland Scale 1: 125,000. Geol. Soc. South Africa.

De Ronde, C.E.J., Spooner, E.T.C., De Wit, M.J., Bray, C.J., 1992. Shear zone-related, Au quartz vein deposits in the Barberton Greenstone Belt, South Africa: field and petrographic characteristics, fluid properties and light stable isotope geochemistry. Econ. Geol. 87, 366–402.

Dziggel, A., Kisters, A.F.M., 2018. Tectono-metamorphic controls on Archaean gold mineralization in the Barberton Greenstone Belt, South Africa. In: Van Kranendonk, M., Bennet, V., Hoffmann, J.E. (Eds.), Earth's Oldest Rocks. Dev. Precambrian Geol.

Gloyn-Jones, J., Kisters A., 2018. Regional folding, low-angle thrusting and permeability networks: structural controls of gold mineralization in the Hope reef at Fairview Mine, Barberton Greenstone Belt, South Africa. Ore Geology Reviews, 102, 585-603. https://doi.org/10.1016/j.oregeorev.2018.09.024.

Heubeck, C., Engelhardt, J., Byerly, G.R., Zeh, A., Sell, B., Luber, T., Lowe, D.R., 2013. Timing of deposition and deformation of the Moodies Group (Barberton Greenstone Belt, South Africa): very-high-resolution of Archaean surface processes. Precambrian Res. 231, 236–262. https://doi.org/10.1016/j.precamres.2013.03.021.

Lowe, D.R., Byerly, G.R., 1999. Stratigraphy of the west-central part of the Barberton Greenstone Belt, South Africa. Geol. Soc. Am. Spec. Pap. 329, 1–36.

Moyen, J.F., Stevens, G., Kisters, A.F.M., 2006. Record of mid-Archaean subduction from metamorphism in the Barberton terrain, South Africa. Nature 442, 559–562. https:// doi.org/10.1038/nature04972.

Annex 1: "Detailed description of the thesis".

Title: Characterization and distribution of the hydrothermal event within the Barberton Greenstone Belt (South Africa) – Multi-scale approach and implications on gold mineralization formation and Archean geodynamics.
Keys words: Structural and field geology, Textural analysis, Quartz veins, Alteration and mineralogy, Archean magmatism, Multi-scale analysis (remote sensing – microscopy).

The Barberton greenstone belt (South Africa), located East of the Kaapvaal craton, contains world-class gold deposits such as Fairview, New consort and Shaba mines (e.g., Anhaeusser, 1976 ; Gloyn-Jones et Kisters, 2018)(Figure). The magmatic and geochronological context are well-known (Anhaeusser et al., 1981 ; De Ronde and De Wit, 1994 ; Moyen et al., 2006) such as the lithological succession of volcano-sedimentary units that composes the greenstone belt (e.g., Lowe and Byerly, 1999 ; Heubeck et al., 2013). Three main events, D1, D2 and D3 are supposed to construct the study area between 3.4 and 3.1 Ga (Dziggel et Kisters, 2018). These events were mainly related to intensive magma emplacement sometimes showing a TTG signature. Located in core of the magmatic massifs, the Barberton greenstone belt is affected by low intensity thrust and fold tectonics, as frequently observed within other greenstone belts of the word. Amphibolite facies conditions have been previously described and attributed to subduction-type geodynamics (Moyen et al., 2006). However, this point is still in debate such as the conditions of deformation and formation of this type of belt.
Numerous hydrothermal features are present within the volcano-sedimentary units of the Barberton Greenstone Belt (***Figure***). Most of them are related to gold content and defined as shear-zone related indexes (Metallogenic map, Council for Geoscience, 2000). However, a synthetic model of formation and some information on the structural context of formation don't exist today such as the nature of the relationships between these small indexes and the exploited huge mines. Although it is accepted that the mineralised event certainly post-dates the three main tectono-magmatic events (D1, D2 and D3; Gloyn-Lones et Kisters, 2018), a lot of questions subsist:

- Is there a link between the mineralized event and one of the three main events that characterized the greenstone belt evolution?
- What is the nature of the structural context coeval with the formation of the mineralisation (i.e., extension, compression, transtension, transpression, strike-slip tectonics, others...)?
- What the distribution and the significance of this event at the scale of the Barberton Greenstone Belt?

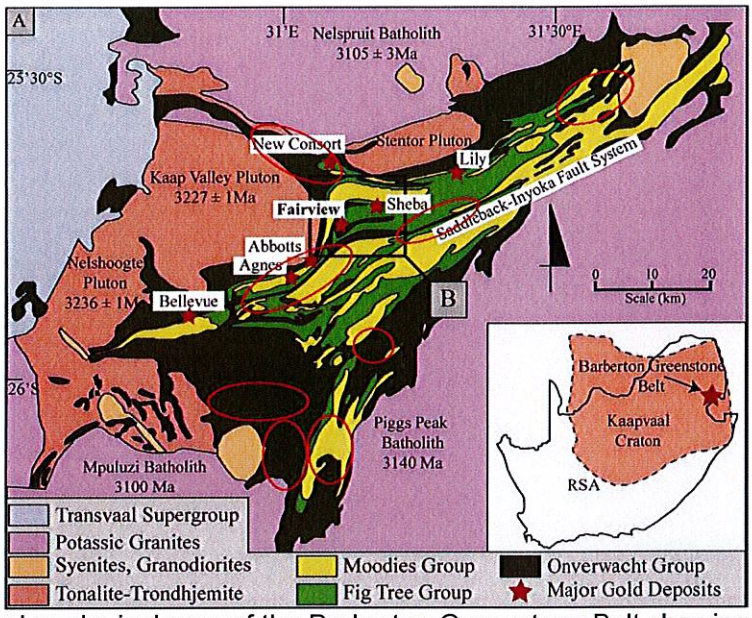

Figure: Simplified geological map of the Barberton Greenstone Belt showing the localisation of the main hydrothermal features (red stars and circles, modified from Gloyn and Kisters, 2018).

The objectives of this research project are to provide some answers to the scientific challenges regarding the systematic process of enrichment within Archean domains of the word. This work will be realised by a multi-scale procedure including remote sensing, field and structural geology, sample and thin section study. Chronologically, the following tasks will be realised:

- Field works combining both structural geology, microtectonics and petrological studies developed on quartz veins and surrounding rocks;
- Sampling and microscopic petro-structural analysis in order to precisely define the relationships between minerals, microstructures and alterations;
- Remote sensing analysis using ASTER images in order to define the width of the alteration halo;
- Fluid and geochemical constraints based of electronic microprobe, MEB and microthermometry analyses;
- Presentation of a complete model of evolution of the studied area that take into account for structural, satellite imagery, mineralogical and fluid constraints. This model will be integrated within the debate regarding the conditions of deformation and fluid transfer of the Archean lithosphere.

In function of the results, two additional tasks can be addressed in this project: i) mineral prospecting approaches using CBA method (Cell Based Associations) (Coll. Univ. Orléans and BRGM; ii) Numerical modelling of fluid transfer within a hot continental crust (COMSOL software, coll. D. Arcay, LIA).

The study will be concentrated on the Barberton Greenstone Belt although a comparison with other Greenstone Belt such as the Abitibi or Swaziland ones could be envisaged. Moreover, a confrontation of our results with the data provided by the three mines still active is also considered.

References

Anhaeusser, C.R., 1976a. The nature and distribution of Archaean gold mineralization in Southern Africa. Miner. Sci. Eng. 8, 46–84.

Anhaeusser, C.R., Robb, L.J., Viljoen, M.J., 1981. Provisional Geological Map of the Barberton Greenstone Belt and Surrounding Terrane, Eastern Transvaal and Swaziland Scale 1: 125,000. Geol. Soc. South Africa.

De Ronde, C.E.J., Spooner, E.T.C., De Wit, M.J., Bray, C.J., 1992. Shear zone-related, Au quartz vein deposits in the Barberton Greenstone Belt, South Africa: field and petrographic characteristics, fluid properties and light stable isotope geochemistry. Econ. Geol. 87, 366–402.

Dziggel, A., Kisters, A.F.M., 2018. Tectono-metamorphic controls on Archaean gold mineralization in the Barberton Greenstone Belt, South Africa. In: Van Kranendonk, M., Bennet, V., Hoffmann, J.E. (Eds.), Earth's Oldest Rocks. Dev. Precambrian Geol.

Gloyn-Jones, J., Kisters A., 2018. Regional folding, low-angle thrusting and permeability networks: structural controls of gold mineralization in the Hope reef at Fairview Mine, Barberton Greenstone Belt, South Africa. Ore Geology Reviews, 102, 585-603. https://doi.org/10.1016/j.oregeorev.2018.09.024.

Heubeck, C., Engelhardt, J., Byerly, G.R., Zeh, A., Sell, B., Luber, T., Lowe, D.R., 2013. Timing of deposition and deformation of the Moodies Group (Barberton Greenstone Belt, South Africa): very-high-resolution of Archaean surface processes. Precambrian Res. 231, 236–262. https://doi.org/10.1016/j.precamres.2013.03.021.

Lowe, D.R., Byerly, G.R., 1999. Stratigraphy of the west-central part of the Barberton Greenstone Belt, South Africa. Geol. Soc. Am. Spec. Pap. 329, 1–36.

Moyen, J.F., Stevens, G., Kisters, A.F.M., 2006. Record of mid-Archaean subduction from metamorphism in the Barberton terrain, South Africa. Nature 442, 559–562. https:// doi.org/10.1038/nature04972.

UNIVERSITY OF JOHANNESBURG

OFFICE OF THE GENERAL COUNSEL ("OGC")
Vetting certificate

Type of document	**Contract**
Contracting Party	**The Universite de Montpellier**
Further desription	**International Joint Doctoral Convention**
Faculty, department or division	**Science**
Contract owner	**Prof Jeremie Lehmann**
Prescribed signatory	**Vice-Chancellor**
Contract vetted by	**Ms P Hlangweni**
Designation	**Legal Advisor**
Date of issue	**31 March 2022**
Signature	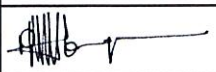

The OGC confirms the following in respect of the document received for vetting:

- It is hereby certified that the above document has been submitted for vetting by a Legal Advisor in terms of the Contract Development Policy and the associated Standard Operating Procedures ("the Policy").
- It is noted that the contract is already in operation and the contract is sought to be concluded retrospectively. The vetting of such a contract falls beyond the mandate of the OGC as provided for by the Policy (§ 13 of the Policy). Such contracts may carry serious reputational, financial, legal and governance risks for the University. In these instances, the contract must be referred to the relevant Executive Dean or Executive Director in terms of the delegation of authority, he or she must be alerted to risks associated with the contract and must be provided with the reasons for the contract having been concluded without first submitting the contract for vetting to the OGC. Having regard to the considerations known to the Legal Advisor, including the contract value, it is the opinion of the Legal Advisor:
  - that the conclusion of the contract should nevertheless not create material risks for the University
- Please note:
  - Legal vetting does not mean that all risks are eliminated or that strict performance under the contract can be guaranteed, nor can the OGC guarantee the outcome or feasibility of the contract.
  - This certificate is not an approval of the contract; the final approval for the conclusion of the contract remains the prerogative of the person authorised to conclude the contract in terms of the Council-approved Delegation of Authority.
  - All risks associated with this document remains with the relevant ELG member and the faculty/division.

- The contract must be signed in terms of the Council-approved Delegation of Authority.

- The following remain the responsibility of the contract owner:
  - That the relevant approvals for concluding this contract had been obtained (which includes authorisation from *inter alia*, the relevant faculty, college, MEC, Council, Senate, MECA, MECCC, Tender Committee, etc.).
  - That the relevant insurance issues arising from the propspective contract had been resolved with the Senior Manager: Risk and Insurance
  - That the relevant financial implications had been authorised.
  - That the relevant financial details, operational provisions, commencement date, terms and all other information in the proposed contract are true and correct.

Appendix 1: Reasons for the Opinion of the Legal Advisor regarding deviations from the Policy

No	Details of deviations from the Policy	Comments
1	**General**	
1.1	The contract is being concluded after performance has already commenced.	
1.1	There is no clause pertaining to Data protection, and the Protection of Personal Information Act ("POPIA") or the proposed clause deviates materially from the University's template.	GDPR will be applicable